

# **Patterned functionalisation of conducting polymer films**

Thesis submitted for the degree of  
Doctor of Philosophy  
at the University of Leicester

By

**Mohammed Qasim Mohammed**

Department of Chemistry  
University of Leicester

2018



UNIVERSITY OF  
**LEICESTER**

## **Abstract**

### **Patterned functionalisation of conducting polymer films**

**Mohammed Qasim Mohammed**

**University of Leicester 2018**

Heavy metals have serious detrimental effects on human health and the environment, even at low concentrations. Therefore, the need to monitor these ions has become an urgent global issue. Although there are many analytical techniques used for the determination of metal ions, electrochemical sensors have a number of advantages, notably construction of small and portable devices with high performance. The application of functionalised polymers as sensing elements offers a means to control selectivity and sensitivity in the detection of metal ions in a solution. In addition, patterned surfaces creates the possibility to form two-dimensional, spatially heterogeneous film surfaces with diverse chemical functionalities. This thesis describes fabrication of patterned electrodes using photolithographic technique for detection of metal ions. Synthetic methods to introduce receptor functionalities into polymer surfaces were developed. This study successfully generated films of two derivatives of pyrrole, aniline and thiophene monomers, which contain carboxylic and amino free groups, through potentiodynamic electropolymerisation. Then, the protection of amino and carboxylic acid groups was performed by using fluorenylmethyloxycarbonyl chloride and pentafluorophenol groups, respectively. Polymerization and electrochemical behaviours of all films were studied and monitored using cyclic voltammetry and EQCM techniques. In the next step, patterned polymer films were made by using a photolithographic technique to control functionalisation of polymer surfaces. Then, patterned ester polymer films were reacted with the  $N\alpha,N\alpha$ -bis(carboxymethyl)-L-lysine and amide polymer films with 2-hydroxyquinoline-4- carboxylic acid. The prepared patterned films (with receptors) were used as electrochemical sensors to detect copper, nickel and cobalt ions at different concentrations in aqueous solution. The voltammetric responses as a function of scan rate were used to determine metal ion uptake and electroactivity. These films gave interesting results for detection of these heavy metals down to 1 ppm. The detection of metal ions was studied as a function of concentration to fit the data to the Langmuir, Frumkin, Temkin and Freundlich isotherms. The relative features of these isotherms were discussed to most appropriately select the isotherm model.

## **Publications**

### **A- Conferences**

#### **(1) Talk**

1- Mohammed Q. Mohammed, A. Robert Hillman and K. Scott Ryder, Patterned polymer electrode surfaces as electrochemical sensors, 26th April 2017, *Midlands Electrochemistry Group Meeting (MEG) 2017*, Department Of Chemistry, University Park, Nottingham, NG7 2RD, UK.

2- Mohammed Q. Mohammed, A. Robert. Hillman and K. Scott Ryder, Patterned polymer electrode surfaces as electrochemical sensors, 4th July 2017, Leicester University Postgraduate Research Day, Department Of Chemistry, University of Leicester, Leicester, UK.

#### **(2) Poster**

1- Mohammed Q. Mohammed, A. Robert. Hillman and K. Scott Ryder, Patterned electrode surfaces for sensing applications, the twelfth Festival of Postgraduate Research 2016, Thursday 7th of July 2016, university of Leicester, Leicester, LE1 7RH, UK.

2- Mohammed Q. Mohammed, A. Robert. Hillman and K. Scott Ryder, Patterned functionalization of conducting polymer films, 22nd June 2015, *Midlands Electrochemistry Group Meeting (MEG) 2015*, University of Warwick, Coventry, UK.

3- Mohammed Q. Mohammed, A. Robert. Hillman and K. Scott Ryder, Patterned electrode surfaces for sensing applications, Leicester University for the 21st meeting of the ELECTROCHEM conference series, 17th-19th August 2016, Stamford Court, Manor Rd, Leicester LE2 2LH, UK.

## **Statement**

The work explained in this thesis for the degree of Ph.D. entitled “Patterned functionalisation of conducting polymer films” was carried out by the author in the Department of Chemistry at the University of Leicester between January 2014 and December 2017.

In this thesis, the work recorded was original except where acknowledged or referenced. None of the work has been submitted for another degree at this or any other university.

Signed ..... Date.....

## **Acknowledgments**

I would like to express my deep gratitude and appreciation to my first supervisor, Prof. Prof. A. Robert Hillman, for giving me the opportunity to pursue my doctoral studies and his encouragement to me throughout my PhD period. I also need to acknowledge the help and suggestions provided by Prof. Karl Ryder my second supervisor for the great help and advices.

Great thanks to Dr. Hudson from the Department of chemistry for his invaluable efforts and assistance for fabrication of patterning polymer films. I am thankful to all my colleagues in the Materials Centre Group for their help and support throughout my studies, particularly. A special thank you to Dr. Andrew Ballantyne, Dr. Rachel Sapstead, Dr. Christopher Zaleski, and Dr Alex Goddard who taught me many of techniques used in this thesis.

I would also like to thank my close friends Dr. Hani Ismail, Hassan Al-Esary, Ahmed Al-Bassam, Dr. Jalil Kareem, Azhar Al-Murshedi, Sahar Alabdullah, and Asuman Unal for their individual contributions and academically to my experiences.

I would also like to acknowledge support of the Higher Committee for Education Development (HCED) and the Iraqi Government for a scholarship and funding this research.

I am very grateful to all the members of my family for their support to complete my research. My immeasurable appreciation for my family, who made me what I am today. Unlimited thanks for all your prayers, sacrifices and love is unmatched and priceless for you.

## **Dedication**

*I would like to dedicate this thesis to:*

*Person, who will rescue of humanity from injustice and delusion.*

*My parents, who have spared no effort for my happiness and my upbringing.*

*My lovely wife, for her support, encouragement and patience.*

*My children; lights and flowers of my life.*

*My brothers and sisters, for their continued support and encouragement.*

**Mohammed  
Leicester, 2017**

## Contents

<b>Chapter one</b>	<b>Introduction</b>	
<b>1.1 Introduction</b>		<b>2</b>
<b>1.2 Conducting Polymers</b>		<b>2</b>
<b>1.3 Electrochemical Properties</b>		<b>5</b>
1.3.1 Conductivity of conducting polymers		5
1.3.2 Synthesis of conducting polymers		6
<b>1.4 Polypyrrole</b>		<b>7</b>
<b>1.5 Polyaniline</b>		<b>8</b>
<b>1.6 Polythiophene</b>		<b>11</b>
<b>1.7 Functionalised conducting polymers</b>		<b>12</b>
<b>1.8 Applications of Conducting Polymers</b>		<b>13</b>
1.8.1 Sensors: principles and applications		13
1.8.1.1 Chemical sensor		14
1.8.2 Patterning of conducting polymers		18
1.8.2.1 Photolithography		19
<b>1.9 Objectives</b>		<b>20</b>
<b>1.10 References</b>		<b>22</b>
<b>Chapter Two</b>	<b>General Methodology</b>	
<b>2.1 Concepts of Electrochemistry</b>		<b>29</b>
2.1.1 Mass Transport		29
2.1.1.1 Diffusion		30
2.1.1.2 Migration		30
2.1.1.3 Convection		31
<b>2.2 Electrochemical Techniques</b>		<b>31</b>
2.2.1 Cyclic voltammetry		31
2.2.2 Chronoamperometry		36
<b>2.3 Quartz crystal Microbalance (QCM)</b>		<b>37</b>
2.3.1 The Piezoelectric Effect		38
2.3.2 The Mass – Frequency Relationship		39
2.3.3 Electrochemical Quartz Crystal Microbalance		40
<b>2.4 Microscopy and Imaging Techniques</b>		<b>41</b>
2.4.1 Scanning Electron Microscopy (SEM)		41
2.4.2 Atomic Force Microscopy (AFM)		43
<b>2.5 Fourier Transform Infrared Spectroscopy</b>		<b>44</b>
<b>2.6 References</b>		<b>45</b>
<b>Chapter three</b>	<b>Experimental</b>	
<b>3.1 Introduction</b>		<b>49</b>
<b>3.2 Reagents and materials</b>		<b>49</b>
<b>3.3 Instrumentations</b>		<b>50</b>

3.3.1 Electrochemical methods .....	50
3.3.1.1 Cyclic Voltammetry .....	50
3.3.1.2 Chronoamperometry .....	52
3.3.1.3 Electrochemical Quartz crystal microbalance (EQCM) .....	52
3.3.2 Non-Electrochemical Measurements .....	53
3.3.2.1 Scanning Electron Microscopy (SEM) .....	53
3.3.2.2 Zeta-200 Optical Profiler .....	53
3.3.2.3 Atomic Force Microscopy (AFM) .....	53
3.3.2.5 Infrared Spectroscopy (FTIR) .....	54
<b>3.4 Preparation of patterned polymer electrodes .....</b>	<b>54</b>
<b>3.5 Preparation of metal ion solutions .....</b>	<b>54</b>
<b>3.6 Procedures .....</b>	<b>55</b>
3.6.1 Monomer Synthesis .....	55
3.6.2 Electropolymerisation of polymer films .....	60
3.6.3 FTIR measurement of compounds .....	61
<b>3.7 References .....</b>	<b>67</b>

## **Chapter Four                      Preparation and patterning of derivatives of polypyrrole**

<b>4.1 Overview .....</b>	<b>69</b>
<b>4.2 Aims and Objectives .....</b>	<b>69</b>
<b>4.3 Results and discussion .....</b>	<b>71</b>
4.3.1 Electropolymerisation of <i>N</i> -(2-carboxyethyl) pyrrole .....	71
4.3.2 Characterization of poly( <i>N</i> -(2-carboxyethyl)pyrrole) .....	74
4.3.3 Electropolymerisation of <i>N</i> -3-aminopropylpyrrole .....	76
4.3.4 Characterization of poly( <i>N</i> -3-aminopropylpyrrole) .....	78
4.3.5 Electropolymerisation of pentafluorophenyl-3-(pyrrol-1-yl) propanoate .....	81
4.3.6 Characterisation of poly(pentafluorophenyl-3-(pyrrol-1-yl) propanoate .....	83
4.3.7 Electropolymerisation of copolymer Py-co-Pyfmoc .....	86
4.3.8 Characterization of copolymer py-co-fmoc .....	88
<b>4.4 Post-Polymerisation Chemical Modifications .....</b>	<b>91</b>
4.4.1 QCM Gravimetric and FTIR Spectroscopic Monitoring of Ester Hydrolysis ..	93
4.4.2 Monitoring of vertical penetration of receptor into ester polymer film .....	95
4.4.3 QCM Gravimetric and FTIR Spectroscopic Monitoring of Amide Hydrolysis...	97
4.4.4 Monitoring of vertical penetration of receptor into amide polymer film .....	99
<b>4.5 Patterning of polymer films .....</b>	<b>101</b>
<b>4.6 Surface imaging characterization of polymer films .....</b>	<b>105</b>
<b>4.7 Conclusion .....</b>	<b>107</b>
<b>4.8 References .....</b>	<b>110</b>

## **Chapter Five                      Preparation and patterning of derivatives of polyaniline**

<b>5.1 Overview .....</b>	<b>113</b>
<b>5.2 Aims and Objectives .....</b>	<b>113</b>
<b>5.3 Result and discussion .....</b>	<b>114</b>

5.3.1 Electropolymerisation of 3-(2-carboxyethyl)aniline .....	114
5.3.2 Characterisation of poly3-(2-carboxyethyl)aniline .....	116
5.3.3 Electropolymerisation of copolymer 3-(Aminomethyl)aniline .....	119
5.3.4 Characterization of copolymer (Ani-co-AniNH <sub>2</sub> ) .....	121
5.3.5 Electropolymerisation of Pentafluorophenyl 3-(3-aminophenyl) propanoate	124
5.3.6 Characterization of poly pentafluorophenyl 3-(3-aminophenyl) propanoate .	125
5.3.7 Electropolymerisation of <i>N</i> -Fmoc-meta-aminobenzylamine .....	128
5.3.8 Characterization of <i>N</i> -Fmoc-meta-aminobenzylamine .....	130
<b>5.4 Post-polymerisation Chemical Modifications .....</b>	<b>133</b>
5.4.1 QCM Gravimetric and FTIR Spectroscopic Monitoring of Ester Hydrolysis....	134
5.4.2 Monitoring of vertical penetration of receptor into ester polymer film .....	136
5.4.3 QCM Gravimetric and FTIR Spectroscopic Monitoring of Amide Hydrolysis..	139
5.4.4 Monitoring of vertical penetration of receptor into amide polymer film .....	141
<b>5.5 Patterning of polymer films .....</b>	<b>143</b>
<b>5.6 Surface imaging characterisation of polymer films .....</b>	<b>147</b>
<b>5.7 Conclusion .....</b>	<b>149</b>
<b>5.8 References .....</b>	<b>152</b>

## **Chapter Six                      Preparation and patterning of derivatives of polythiophene**

<b>6.1 Overview .....</b>	<b>155</b>
<b>6.2 Aims and Objectives .....</b>	<b>155</b>
<b>6.3 Results and discussion .....</b>	<b>156</b>
6.3.1 Electropolymerisation of 3-thiophene acetic acid .....	156
6.3.2 Characterisation of poly(3-thiophene acetic acid) .....	158
6.3.3 Poly(3-thiopheneethylamine) film .....	160
6.3.4 Electropolymerisation of Pentafluorophenyl (thiophen-3-yl) ethanoate .....	161
6.3.5 Characterisation of poly (Pentafluorophenyl(thiophen-3-yl) ethanoate) film ..	163
6.3.6 Electropolymerisation of 9H-fluoren-9-yl(2-(3-thienyl)ethyl) carbamate ... .	166
6.3.7 Characterisation of poly(9H-fluoren-9-yl(2-(3-thienyl)ethyl) carbamate) film	167
<b>6.4 Post-polymerisation Chemical Modifications .....</b>	<b>171</b>
6.4.1 QCM Gravimetric and FTIR Spectroscopic Monitoring of Ester Hydrolysis	171
6.4.2 Monitoring of vertical penetration of receptor into ester polymer film .....	174
6.4.3 QCM Gravimetric and FTIR Spectroscopic Monitoring of Amide Hydrolysis	176
6.4.4 Monitoring of vertical penetration of receptor into amide polymer film .....	179
<b>6.5 Patterning of polymer films .....</b>	<b>181</b>
<b>6.6 Surface imaging characterisation of polymer films .....</b>	<b>184</b>
<b>6.7 Conclusions .....</b>	<b>185</b>
<b>6.8 References .....</b>	<b>188</b>

## **Chapter seven                      Chemical sensor applications**

<b>7.1 Overview .....</b>	<b>191</b>
<b>7.2 Aims and objectives .....</b>	<b>191</b>
<b>7.3 Results and discussion .....</b>	<b>192</b>

7.3.1 Voltammetric response of Poly(Py-NTA) electrode to metal ions .....	192
7.3.1.1 Stability and influence of the sweep rate on metal complexes .....	193
7.3.1.2 Concentration dependence of the characteristic peak charge .....	195
7.3.1.3 Estimate of the molar ratio between metal ions and polymer electrode.....	196
7.3.1.4 Fitting the data to different isotherms .....	198
7.3.2 Voltammetric response of Poly(Py-HQC) to metal ions .....	202
7.3.2.1 Stability and influence of the sweep rate.....	203
7.3.2.2 Concentration dependence of the characteristic peak charge .....	205
7.3.2.3 Estimate of the molar ratio between metal ions and polymer electrode .....	205
7.3.2.4 Fitting the data to the different isotherms .....	206
7.3.3 Voltammetric response of Poly(Ani-NTA) to metal ions .....	209
7.3.3.1 Stability and influence of the sweep rate on metal complexes .....	210
7.3.3.2 Concentration dependence of the characteristic peak charge .....	212
7.3.3.3 Estimate of the molar ratio between metal ions and polymer electrode .....	212
7.3.3.4 Fitting the data to the different isotherms .....	212
7.3.4 Voltammetric response of Poly(Ani-HQC) to metal ions.....	216
7.3.4.1 Stability and influence of the sweep rate on metal complexes .....	216
7.3.4.2 Concentration dependence of the characteristic peak charge .....	218
7.3.4.3 Estimate of the molar ratio between metal ions and polymer electrode .....	219
7.3.4.4 Fitting the data to the different isotherms .....	220
7.3.5 Voltammetric response of poly(Thio-NTA) to of metal ions .....	222
7.3.5.1 Stability and influence of the sweep rate on metal complexes .....	223
7.3.5.2 Concentration dependence of the characteristic peak charge .....	224
7.3.5.3 Estimate of the molar ratio between metal ions and polymer electrode .....	227
7.3.5.4 Fitting the data to the different isotherms .....	227
7.3.6 Voltammetric response of Poly(Thio-HQC) to metal ions .....	229
7.3.6.1 Stability and influence of the sweep rate on metal complexes .....	231
7.3.6.2 Concentration dependence of the characteristic peak charge .....	232
7.3.6.3 Estimate of the molar ratio between metal ions and polymer electrode .....	233
7.3.6.4 Fitting the data to the different isotherms .....	233
<b>7.4 Conclusions .....</b>	<b>237</b>
<b>7.5 References .....</b>	<b>238</b>
<b>Chapter eight</b>	<b>Conclusions and future work</b>
<b>8.1 Conclusions .....</b>	<b>240</b>
8.1.1 Functionalised polypyrrole films .....	240
8.1.2 Functionalised polyaniline films .....	243
8.1.3 Functionalised polythiophene films .....	244
8.1.4 application patterned electrode as chemical sensor .....	245
<b>8.2 Future work .....</b>	<b>246</b>
<b>8.3 References .....</b>	<b>248</b>

## List of abbreviations

Abbreviations	Full name and unit
CV	Cyclic Voltammogram
QCM	Quartz Crystal Microbalance
EQCM	Electrochemical Quartz Crystal Microbalance
FTIR	Fourier Transform Infrared Spectroscopy
SEM	Atomic Absorption Spectroscopy
AFM	Atomic force microscopy
$n$	Number of electrons
$\Gamma$	Surface coverage of the polymer (mol cm <sup>-2</sup> )
$E$	Electrode potential (V)
$E_{pa}$	Anodic peak potential (V)
$E_{pc}$	Cathodic peak potential (V)
$f$	Frequency (Hz)
$F$	Faraday constant (96 486 C mol <sup>-1</sup> )
$i$	Current (A)
$i_p$	Peak current
$m$	Mass of the film (g)
$Q$	Charge (C)
$t$	Time (s)
$\nu$	Scan rate
Ani	Aniline
Py	Pyrrole
Thio	Thiophene
CE	Counter electrode
RE	Reference electrode
WE	Working electrode
Py-NH <sub>2</sub>	<i>N</i> -3-aminopropylpyrrole
Py-COOH	<i>N</i> -(2-carboxyethyl) pyrrole
Py-pfp	pentafluorophenyl-3-(pyrrol-1-yl)propanoate
Py-fmoc	<i>N</i> -Fmoc-aminopyrrole
Ani-NH <sub>2</sub>	3-(Aminomethyl) aniline
Ani-COOH	3-(2-carboxyethyl) aniline
Ani-pfp	Pentafluorophenyl 3-(3-aminophenyl) propanoate
Ani-fmoc	<i>N</i> -Fmoc-meta-aminobenzylamine
Thio-NH <sub>2</sub>	3-Thiopheneethylamine
Thio -COOH	3-thiophene acetic acid
Thio -pfp	Pentafluorophenyl (thiophen-3-yl)ethanoate
Thio -fmoc	9H-fluoren-9-yl(2-(3-thienyl)ethyl)carbamate
NTA	N $\alpha$ , N $\alpha$ -Bis- (carboxymethyl)-L-lysine hydrate
HQC	2- hydroxyquinoline-4-carboxylic acid

## Chapter one

## Introduction

<b>1.1 Introduction.....</b>	<b>2</b>
<b>1.2 Conducting Polymers .....</b>	<b>2</b>
<b>1.3 Electrochemical Properties .....</b>	<b>5</b>
1.3.1 Conductivity of conducting polymers .....	5
1.3.2 Synthesis of conducting polymers .....	6
<b>1.4 Polypyrrole .....</b>	<b>7</b>
<b>1.5 Polyaniline .....</b>	<b>8</b>
<b>1.6 Polythiophene .....</b>	<b>11</b>
<b>1.7 Functionalised conducting polymers.....</b>	<b>12</b>
<b>1.8 Applications of Conducting Polymers.....</b>	<b>13</b>
1.8.1 Sensors: principles and applications .....	13
1.8.1.1 Chemical sensor.....	14
1.8.2 Patterning of conducting polymers .....	18
1.8.2.1 Photolithography .....	19
<b>1.9 Objectives .....</b>	<b>20</b>
<b>1.10 References.....</b>	<b>22</b>

## 1.1 Introduction

Polymers have become an important part of our daily lives due to the multitude of applications in which they can be used, from phones to artificial hearts. Some decades ago, researchers discovered their conducting properties, which launched whole research programs with the aim of improving the conductivity and the stability of these polymers, and finding new applications for them in various areas of life. They have become a highly successful alternative to many materials used in, for example, chemical sensors,<sup>1</sup> corrosion inhibitors,<sup>2</sup> electronics, batteries,<sup>3</sup> actuators, and in the field of medical engineering.<sup>4</sup> The new possibilities offered by conducting polymers have enabled them to revolutionise significant areas of these fields. Recently, there has been growing interest in polymer patterning because of the extensive functionalities of such polymers. The pattern strategy is a technique used to fabricate the pattern of a surface film or pattern functional polymers on the micrometre to nanometre scale.<sup>5</sup> A variety of strategies can be used to pattern conjugated polymer films such as photolithography, direct writing techniques, printing techniques, and particle beam lithography.<sup>6</sup> Recent studies have demonstrated the ability of the pattern technique to design and develop polymers, and this has paved the way for many new applications.<sup>1</sup>

## 1.2 Conducting Polymers

The discovery of conducting polymers in the mid-1970s opened up new horizons in the fields of chemistry and physics.<sup>7</sup> Electrochemistry has enabled these materials to play a substantial role in many applications and in various fields ranging from industrial technologies to health care.<sup>8</sup> Conducting polymers have been widely studied for different purposes since their discovery.<sup>9</sup> They possess electronic properties similar to those of metals due to the conjugated systems that allow electrons to flow throughout polymer chains, which is made possible through doping; sometimes, such polymers are called “synthetic metals.”<sup>10, 11</sup> At the same time, these polymers show traditional organic polymer properties, for example their ease of synthesis, flexibility, processing from solution, and low cost. Generally, conducting polymers (CPs) are a class of polymers with outstanding electrical performance, a property which has been widely taken advantage of in a variety of devices and technologies.<sup>12, 13</sup> Today there are many types of polymers which combine metals properties with traditional polymer characteristics.<sup>14</sup> Electroactive polymers such as polyacetylene, polypyrrole (PPy), polythiophene (PT), polyaniline (PANI), and

poly(3, 4-ethylenedioxythiophene) (PEDOT) (see **Figure 1.1**), amongst others, have been examined over the last thirty years, and have shown promise in many applications in various fields.

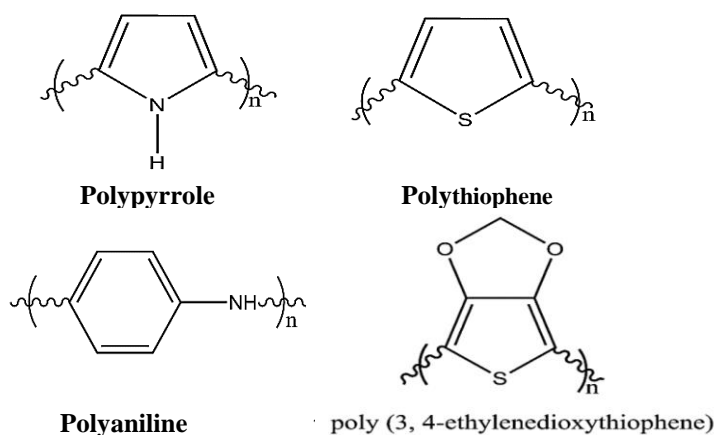


**Figure 1.1:** Structures of several of the most highly conducting polymers: polypyrrole, polythiophene, polyaniline and poly(3, 4-ethylenedioxythiophene).

Conducting polymers can be prepared and manipulated with regard to their characteristics so as to obtain a wide range of desirable features and, indeed, after synthesis a number of distinctive changes to the electrical, chemical and mechanical characteristics of the polymers can be further introduced. The conductivity of traditional materials (metals) depends on electrons and their distribution.<sup>15</sup> With polymers, conductivity is achieved through simple chemical oxidation reactions or, occasionally, through reduction, through a number of chemical species (anionic or cationic) which are called “dopants”.<sup>16</sup> Such studies began with polyacetylene, which has a high conductivity when doped with iodine. The conductivity is increased by a factor of almost ten million compared to undoped polyacetylene, though the doped product shows instability in damp oxygen.<sup>17</sup> Therefore, research efforts have focused on a number of polymers that show greater stabilities and are easier to prepare. In recent years, scientists have concentrated on aromatic and other conjugated, closed-ring molecules such as polyanilines, polypyrroles and polythiophenes because of their stability over a range of different physical conditions, and because the electronic properties of these polymers can be easily modified.<sup>18</sup>

Conducting polymers are organic molecules with conjugated bond systems that consist of alternating double and single bonds. Thus, the  $\pi$ -electrons can easily move from one bond to another along the conjugated system, and it is this ease of movement – this delocalization – that gives these polymers their conductivity. However, whilst these

delocalised electrons allow the movement of charge along polymer backbones and adjacent chains, it is not sufficient in itself to show any appreciable conductivity. In order to improve conductivity, these polymers require doping, and the doping process may change the physical properties of the polymer.<sup>19, 20</sup> When a conducting polymer is oxidised, an electron is removed from the polymer chain, and counterions in the reaction medium are incorporated into the polymer chains in order to maintain the electroneutrality of the polymer system; this process occurs during the polymerisation itself. There are three types of charge carriers that are thus formed, which are called *solitons* (this becomes apparent in polyacetylene because it has a degenerate ground state within the conjugated system  $(CH)_x$ ), *polarons* (radical cations) and *bipolarons* (radical dications). **Figure 1.2** shows the structure of polarons and bipolarons in heterocyclic polymers.<sup>21</sup> Electrons moving between adjacent molecules and chains can enhance the electrical conductivity in these polymers by many orders of magnitude. As a result of this process, the band gaps of such polymers are decreased.<sup>14</sup> A positive polaron will be formed by the oxidation of the conjugated main chain. The emergence of polarons leads to the production of new energy levels in the conjugated polymers that have a spin of 1/2. Bipolarons are charge carriers that have double charges through the coupling of two polarons from the main chain of the conjugated polymer.<sup>22</sup> The electronic levels of polypyrrole proposed by Bredas and co-workers<sup>23</sup> are shown in **Figure 1.3**. The difference in energy between the valence band and conduction band is very wide, and is consequently considered too large for easy transference of electrons; therefore, neutral pyrrole is considered to be an insulator. During electropolymerisation, the polypyrrole chain will react with counterions from the reaction medium to preserve the electroneutrality of the system.

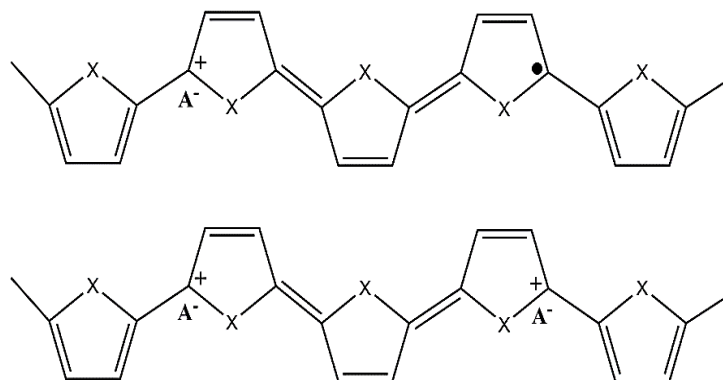


**Figure 1.2:** Structure of polarons and bipolarons formed in conducting polymers.  
 $X = NH$  or  $S$ ,  $A = \text{anion, e.g., } Cl^-, ClO_4^-$ .

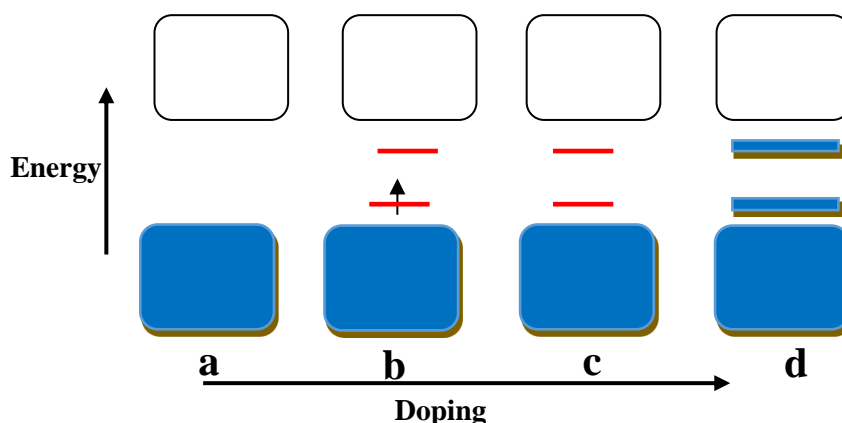


**Figure 1.3:** Electronic levels of polypyrrole with increasing doping. (A) Undoped, (B) polaron form, (C) bipolaron orbital form and (D) bipolaron band form.

### 1.3 Electrochemical Properties

The doping process and the electrochemical properties are the most significant properties of conducting polymers because many of their applications rely on them. The oxidation process of conducting polymers is commonly accompanied by doping (intercalation) with counteranions from the electrolyte; this oxidation process is called *oxidation doping* (or p-doping). In contrast, the reduction of conducting polymers is commonly accompanied by the doping (intercalation) of counteranions from the electrolyte, and the reduction of conducting polymers is called *reduction doping* (or n-doping). Furthermore, an associated electron transfer process on the electrode/electrolyte interface will occur, and there will be both diffusion and expansion of the conducting polymer films because of counterion insertion.<sup>22</sup>

#### 1.3.1 Conductivity of conducting polymers

The electrical attributes of electroactive polymers are important because they determine the transport of information from part of the polymer to another.<sup>24</sup> The conductivity of doped conducting polymers ranges from  $10^{-3}$  to  $10^3$  S cm<sup>-1</sup>, in contrast to the range of conductivities observed for un-doped polymers, which tends to be from  $10^{-9}$  to  $10^{-6}$  S cm<sup>-1</sup>. The mechanism of charge transport in conducting polymers differs from that of conducting materials in that the charge carriers in a conjugated polymer can move easily along the backbone of the polymer.<sup>25</sup> Concentration and transport of charge carriers have an influence on the conductivity of the polymer. This movement depends on two factors: charge transfer along the polymer backbone, referred to as *intrachain*; and charge hopping or tunnelling between chains, referred to as *interchain*. The charge carriers

(polarons and bipolarons) begin moving along the polymer chains when an electrical field is applied. The conduction occurs via both the migration of charge carriers along the conjugated polymer chain and the hopping of charge carriers between conjugated chains, with electrical conductivity ultimately relying on both carrier concentration and mobility.<sup>19, 26</sup>

Polyaniline has a conductivity mechanism that appears to be quite singular among conducting polymers when it undergoes p-type doping similar to pyrrole. This process leads to the production of a radical cation of nitrogen, rather than the cation (carbonium ion) seen for other doped polymers.<sup>1</sup> The conductivity of polyaniline relies on both the oxidation of the polymer and the degree of its protonation. The highly conducting doped state is called *emeraldine*, which consists of amine (-NH-) and imine (=N-) bonds in equal proportion. The imine sites may suffer from protonation,<sup>2</sup> however, resulting in the dication (bipolaron) form of the emeraldine salt. Further rearrangement may occur to form a polaron lattice, which is considered to be a semiquinone radical cation salt. The polaron and bipolaron phases of this process are shown in **Figure 1.4**. According to various studies, it is the charge carriers (polarons) that are responsible for the conductivity of polyaniline.<sup>27, 28</sup>

Like polypyrroles, polythiophene's conductivity is affected by the counterion used during the electropolymerisation process.<sup>29</sup> The concentration of monomer used during polymerisation play a key role in the polymerisation process and the conductivity of the resultant polymers. In addition, the existence of a substituent on the thiophene ring can have a significant effect on conductivity.<sup>30</sup>

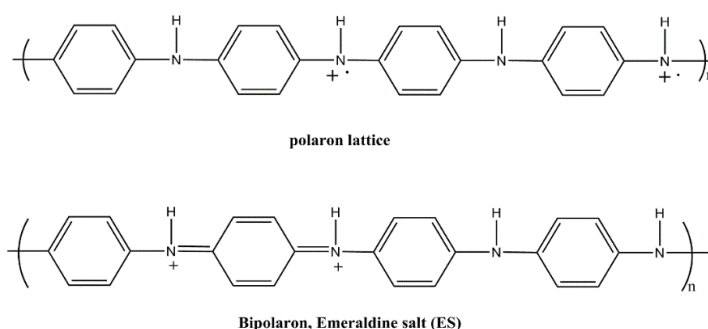


**Figure 1.4:** Structure of polaron and bipolaron modes in conducting polyaniline.<sup>28</sup>

### 1.3.2 Synthesis of conducting polymers

Conducting polymers can be prepared by the oxidation of monomer or its derivatives. This oxidation is often carried out by electropolymerisation or chemical polymerisation;

although there are other methods that allow for the formation of conducting polymers, such as photochemical and enzyme polymerisation, these are less commonly used. In essence, these have generally focused on two main methods: chemical oxidation and electrochemical polymerisation. Electrochemical polymerisation is considered a cheap and simple method for the production for many types of polymers such as heterocyclics (e.g., pyrroles,<sup>31, 32</sup> thiophenes<sup>33, 34</sup>) and aromatics (e.g., aniline,<sup>35, 36</sup> diphenylamine<sup>37</sup>).

At the present time, the majority of scientists prefer the electropolymerisation method because it is an easy, versatile and clean route to obtaining a desired film.<sup>38</sup> Moreover, in recent years, a phenomenal number of studies have focused on the examination of the kinetics and mechanisms of the electrochemical polymerisation in conducting polymer films such as polypyrrole<sup>39</sup> and polyaniline.<sup>36, 40</sup> These studies have mainly focused on two aspects: the mechanism of the chemical reaction, and the growth kinetics of the conducting surface. Generally, these investigations demonstrate that the initial step in the polymerisation reaction is the formation of cation radicals. This step can be followed one of several steps depending on the surrounding conditions, for example the electrolyte, potential, temperature, current density and type of electrode surface.

The electrochemical techniques used in the preparation of conducting polymers include the constant potential (potentiostatic),<sup>41</sup> constant current (galvanostatic),<sup>42</sup> cyclic voltammetry (CV)<sup>42, 43</sup> and pulse galvanostatic methods.<sup>15</sup>

In some aspects, the nucleation of the polymer is similar to the deposition of metals.<sup>15</sup> These stages have been investigated by electrochemical methods such as cyclic voltammetry and the potential step technique. As has been reported in these studies, there is an initial nucleation, followed by coalescence, and a subsequent uniform film growth.<sup>44</sup> <sup>45</sup> As stated above, the nuclei that form will grow readily, and this behaviour leads to characteristic responses in electrochemical experiments.

## 1.4 Polypyrrole

Polypyrrole is a conjugated polymer that contains a system of alternating  $\pi$  and single C-C bonds, which allows for the movement of  $\pi$ -electrons along the polymer chain. The first production of polypyrrole was in 1916 via an oxidation reaction that used hydrogen peroxide, the ultimate product of which was a black powder that was called 'pyrrole black'.<sup>46</sup> In 1979, the electrosynthesis of polypyrrole became a useful method for the

production of highly conductive materials. There are many methods that can be used to modify conducting polymers to increase their suitability for specific functions: (i) use derivatives with functional groups; (ii) use a different counterion during electropolymerisation; (iii) inclusion of molecules with special functions; and (iv) formation of nanoparticles with noble metals.<sup>47</sup>

Over the last four decades, several mechanisms have been proposed in the literature to explain polypyrrole synthesis. Diaz suggested a mechanism, which is generally considered the most popular;<sup>48</sup> however, there are other rival mechanisms that have been put forward, such as those of Kim<sup>49</sup> and Pletcher.<sup>50</sup> The differences between these mechanisms lie in the initiation step of the polymerisation.<sup>51</sup> Briefly, in Diaz's mechanism, the activation of the pyrrole monomer occurs via a multi-step electron transfer from pyrrole to form a radical cation close to the electrode; **Figure 1.5** shows the proposed mechanism.<sup>48</sup>

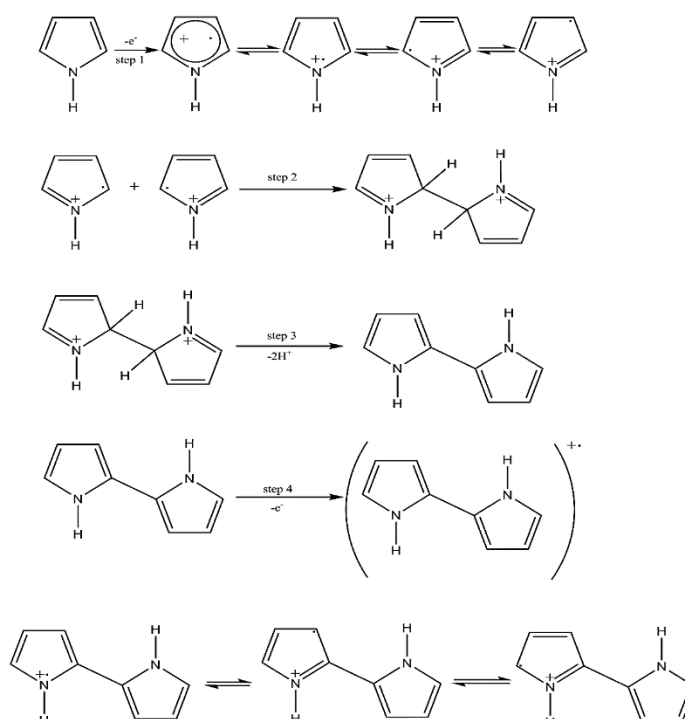


**Figure 1.5:** Steps in the polymerisation mechanism of Pyrrole.<sup>52</sup>

### 1.5 Polyaniline

The second-most studied conductive polymer after polypyrrole is polyaniline.<sup>52</sup> It exists in various forms based on its oxidation level. Polyaniline has a long history among electroactive polymers that can be traced back almost two centuries.<sup>53, 54</sup> It can be prepared using chemical or electrochemical methods. Over the last 30 years, polyaniline

has become one of the most widely studied polymers, and has attracted the attention of the many of research groups in the field of electrochemistry for its promising physical properties such as high conductivity, environmental stability, easy synthesis (both chemically and electrochemically) and reasonable conductivity.<sup>55</sup> These properties suggest a high degree of potential for polyaniline across a wide range of industries such as batteries,<sup>56</sup> optical devices,<sup>57</sup> sensors,<sup>58</sup> catalysts,<sup>59</sup> supercapacitors,<sup>60</sup> anticorrosion coatings,<sup>61</sup> and solar cells.<sup>62</sup> However, polyaniline has limited use in biological system applications because of its non-biodegradability and pH requirements, and has been noted to cause various physiological side effects in such use.<sup>63</sup> Polyaniline can exist in three main structural forms, as shown in **Figure 1.6**; these structural forms can be categorized as either bases or salts,<sup>64</sup> as:

*Leucoemeraldine Base (LB)*: this type has no conducting state because of its unconjugated chain backbone.

*Emeraldine salt (IS)*: this type is the intermediate form and is a partially oxidised state. This type is also characterised by its good conductivity and green colour. The discovery of electrical conductivity properties in the associated emeraldine salt (IS) state has led to an explosion of interest in this promising polymer.

*Pernigraniline Base (PB)*: this type is the fully oxidised form with a characteristic purple or violet colour, and is considered to be an insulating state.<sup>65</sup>

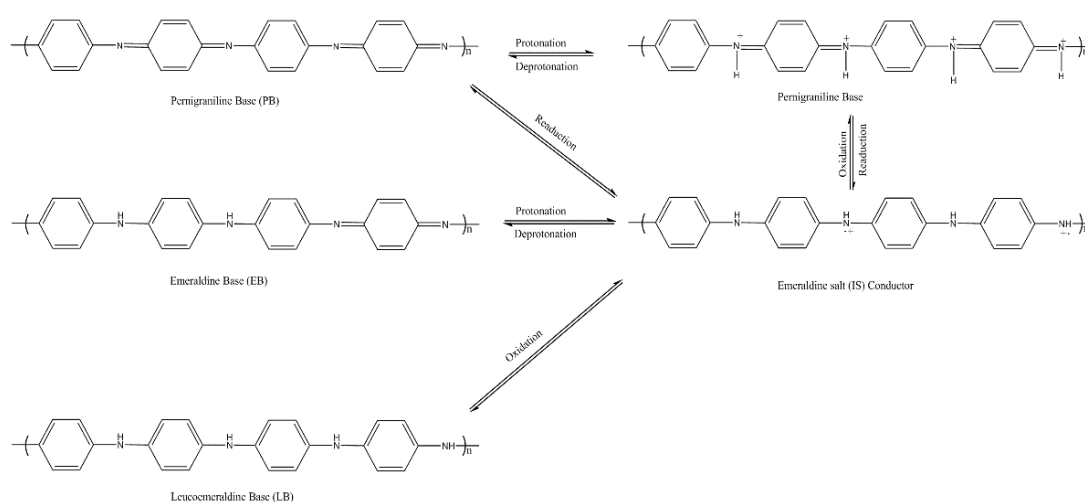
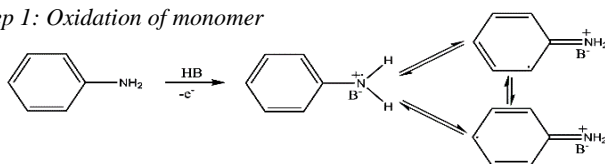


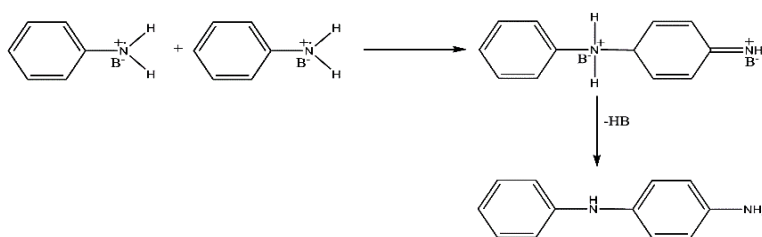
**Figure 1.6:** The various structural forms of polyaniline.<sup>70,71</sup>

Polyaniline can be synthesised using electrochemical polymerisation in a strong acid medium. Popular acidic media used for the preparation of polyaniline are aqueous solutions of 1 M  $\text{H}_2\text{SO}_4$ ,  $\text{HCl}$  or  $\text{HClO}_4$ . The range of conductivities of polyaniline is generally  $10^{-1}$  to  $10^1 \text{ S cm}^{-1}$ .<sup>66</sup> The proposed mechanism for the electrochemical polymerisation of aniline is shown in **Figure 1.7**.<sup>24</sup> In the first step, the aniline monomer undergoes the removal of an electron to form free radical aniline (the anilinium cation). In the second step, two radicals couple together on the N site of one ortho and *para* site of other molecule, which results in the elimination of two protons and the production of a dimer. The next reaction occurs between the anilinium radical cation and the oligomer (radical cation), and it is this step that leads to the start of chain propagation. The reason for the presence of the acid in the reaction solution is to form a counteranion which will act to balance the charge of the chain polymer, producing polyaniline/HA (step 4). Usually, several factors can affect the electropolymerisation of polyaniline such as components of the solution, deposition method, the nature of the anion, electrode type, temperature, pH and the viscosity of the solvent.<sup>67</sup>

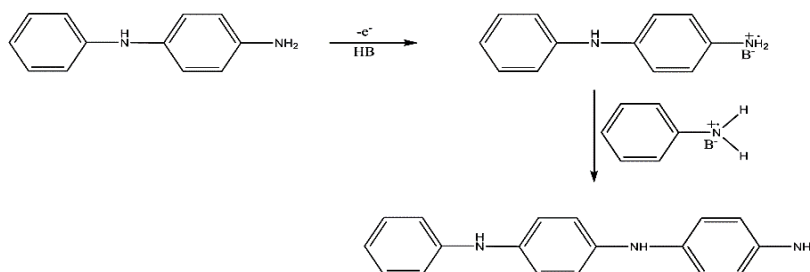
Step 1: Oxidation of monomer



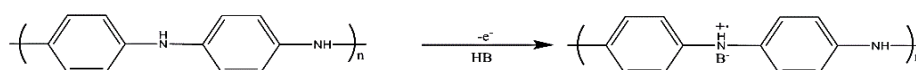
Step 2: Radicals coupling



Step 3: Chain propagation



Step 4: Oxidation and doping of polymer

**Figure 1.7:** Steps in the electropolymerization of aniline.<sup>24</sup>

## 1.6 Polythiophene

Polythiophene (PT) is one of the most widely investigated conducting polymers due to its promising physical properties. It has good environmental stability for doping states that has led to many different applications in electronics.<sup>68</sup> Generally, polythiophenes are similar in many of their properties to polypyrroles. The oxidised form of polythiophene is a conducting electroactive polymer whose large conductivity arises from  $\alpha$ - $\alpha$  linkages. In a similar manner to polyaniline and polypyrrole, polythiophene can be synthesised via chemical and electrochemical methods. The conductivity unsubstituted polythiophene exhibits is in the region of  $10^{-7}$  S  $\text{cm}^{-1}$ , whilst the conductivity of doped polythiophene can reach as high as  $10^2$  S  $\text{cm}^{-1}$ .<sup>69</sup> Polythiophene exhibits significant, and indeed outstanding, properties such as low cost, excellent thermal stability, high mechanical strength and favourable optical properties across a wide range of applications.<sup>68, 70</sup> Polythiophene and its derivatives have potential applications in several areas including sensors,<sup>71</sup> photovoltaics,<sup>72</sup> and biomedicine.<sup>73</sup> Polythiophene can be prepared either chemically or electrochemically through a simple oxidation process. Cyclic voltammetry is the most popular electrochemical route used for the preparation of the polymer. In fact, the electrochemical polymerisation of thiophene requires a high potential to produce polythiophene film in the solution. Electropolymerisation of thiophene follow mechanism shown in **Figure 1.8**.<sup>74</sup>

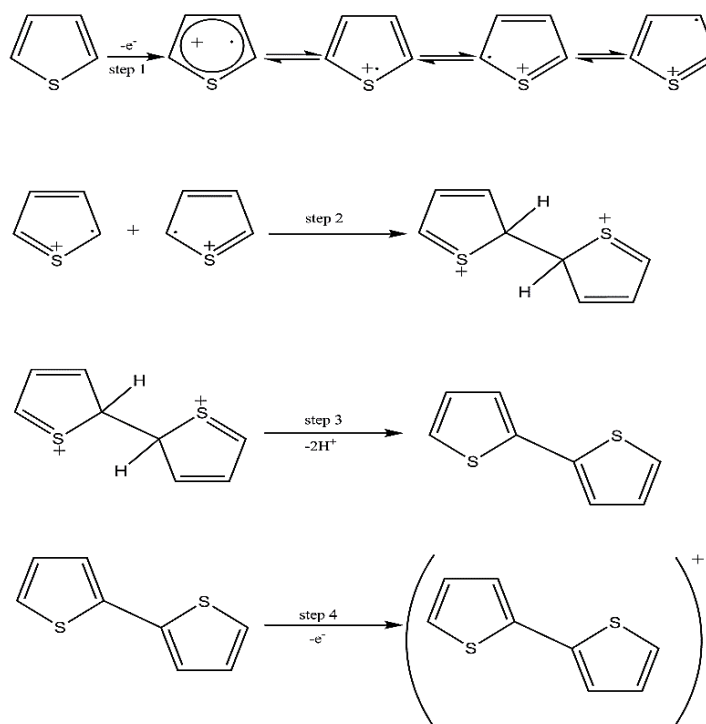


**Figure 1.8:** The steps in the general mechanism of polymerisation of thiophene.<sup>82</sup>

The electropolymerisation mechanism involves the formation of oligomers that then lead to polymer formation. Oligomers are formed by cation radical intermediates at the  $\alpha$ -position of the thiophene monomer. Then, two radical dimers couple to form the bithiophene cation radical, with the subsequent elimination of two protons. The thiophene monomer requires an oxidation potential higher than that of bithiophene because of the conjugated  $\pi$ -bonds in the bithiophene dimer. There are several methods that can be used to polymerise thiophene such as the potentiodynamic, potentiostatic, galvanostatic, or potential pulse methods.<sup>75</sup> Among these methods, potentiodynamic electropolymerisation is the most commonly applied because it can be closely controlled to allow easy production of a film with the desired thickness.

### 1.7 Functionalised conducting polymers

The number of prospective applications for conducting polymers is increased because of their conjugated systems, electronic properties, doping/dedoping properties and optical properties. In spite of these properties and their many applications in many areas, the functionalisation of conducting polymers will improve their various physical properties and open the door to novel applications such as microelectronics, high selectivity sensors, drug delivery and catalysis. There are many functional groups that allow for various functions such as sensors, electrochromism, catalysts and chemiluminescence.<sup>76</sup> Intelligent polymer surfaces have the ability to alter their properties and structure under the influence of certain stimuli. Generally, this work is aimed at controlling molecular design, and has the ability to change the chemical structure of polymer surface films via applied external controls.<sup>77</sup> To achieve such objectives, many studies have concentrated on functional polymer surfaces, which often have end-functional groups. Present studies are examining the reorganisation of functional groups at polymer surfaces and the use of functional surface copolymers to make smart surfaces, and control over reactivity and functionality at polymer surfaces through photoisomerization.<sup>78, 79</sup>

The improvement of surface polymer films and the use of derivatives or copolymerisation are certainly options when seeking to obtain new conducting polymers that have novel properties giving them the potential for use in a wide range of applications. In addition, the patterning of surfaces indicates allows for the possibility of forming two-dimensional, spatially heterogeneous film surfaces with diverse chemical functionalities. This smart technology can be used for the modification and patterning of polymer surfaces towards

special chemical functions.<sup>80</sup> **Figure 1.9** shows a few mechanisms that allow for the modification and immobilisation of polymer backbones.

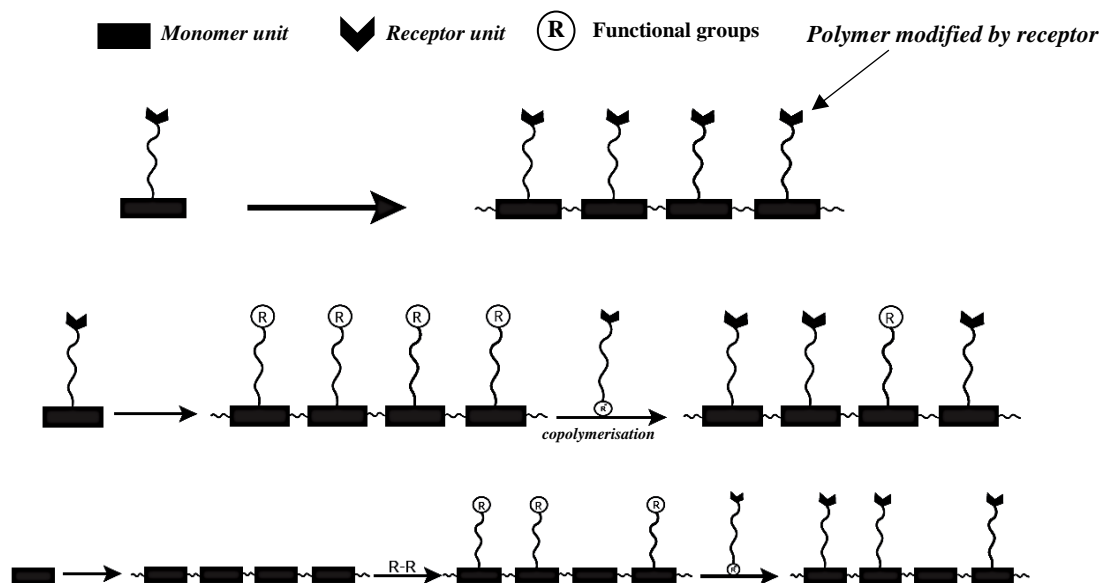


*Figure 1.9: Methods of chemical immobilization of receptor units.*

## 1.8 Applications of Conducting Polymers

Conducting polymers have been described as being key – due to a combination of desirable properties – to a variety of applications such as batteries, supercapacitors, sensors (biosensors and chemical sensors) and corrosion inhibitors. The aromatic structure and conjugated system that extends along the backbone provides the electrical properties and stability of conducting polymers.

### 1.8.1 Sensors: principles and applications

Sensors are detection devices with the ability to convert the chemical or physical changes of an analyte into a measurable signal, which is itself related to the concentration of the analyte.<sup>81</sup> A typical sensor requires many characteristics such as fast response time, high sensitivity and selectivity, long lifetime, excellent reproducibility, good signal-to-noise ratio, low cost, simplicity of operation, easy calibration, reversibility and small dimensions.<sup>82</sup> Sensors can be divided into three categories: (a) physical sensors, e.g., for measuring temperature, distance, mass and pressure; (b) chemical sensors, which detect chemical materials by chemical or physical responses; and (c) biosensors, which measure molecular species using a biosensing element.<sup>83</sup> There are a number of serious problems

one can face with sensing applications, such as non-specific interactions. In general, sensors consist of a transducer, which transforms the response into a signal that can be detected using [modern] instrumentation, and a selective chemical layer, which isolates the response of the analyte.<sup>84</sup> **Figure 1.10** shows the main parts of the sensor.

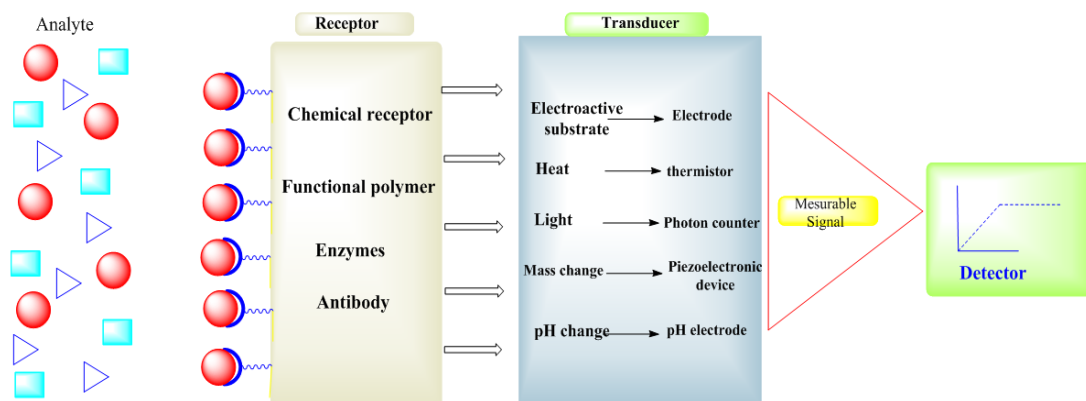


**Figure 1.10:** The main parts of a sensor.

### 1.8.1.1 Chemical sensor

Chemical sensors have received considerable scientific interest in recent years in many and diverse areas such as the chemical industry, food industry, biotechnology, medicine, and environmental control. They are designed to be compatible with the detection and response of any given targeted environment in the liquid, solid or gaseous phases.<sup>2</sup> The enhancement of sensor devices lead to their simplification, and facilitated their use as analytical tools.<sup>85</sup> Many studies and research have been aimed at improving the selectivity of sensors towards specific types of analysis, using chemical sensors which have a high sensitivity to the determination of minimal concentrations and which can be used in complex samples.<sup>86</sup> Continuous improvements in the microfabrication of analytical devices have enabled the production of functional, microscale compositions and tools, with all the consequent advantages of miniaturization.<sup>87</sup> The improvement of chemical sensors represents one of the most promising aims in the field of sensors due to the vast number of applications they have in environmental areas such as fuel analysis and toxic waste identification,<sup>88</sup> the food industry,<sup>89</sup> analysis of water<sup>90</sup> and detection of heavy metal ions.<sup>91</sup> These sensors are capable of giving qualitative and quantitative information about the chemical or physical state of associated analytes. There are various attributes necessary for a useful chemical sensor such as stability, repeatability, sensitivity, selectivity, low limits of detection and low response times. Chemical sensors can be categorized into several types according to the property to be determined, for example

mass, thermal, electrochemical, gas, ionic and optical. Compared to other types of sensors, electrochemical sensors are particularly attractive because of their remarkable detection abilities, experimental simplicity and low production costs.<sup>92</sup> There are three principal types of electrochemical sensors: *conductometric*, *amperometric* and *potentiometric*. Amperometric sensors exploit the oxidation or reduction of electroactive materials to measure a resultant current;<sup>93</sup> potentiometric sensors are similar in that they measure an electrode potential. Conductometric sensors, however, can measure conductivity.<sup>83</sup>

Chemical sensors usually contain three basic elements: a chemical receptor (molecular recognition system), and physicochemical transducers and other additional elements for signal amplification and conditioning.<sup>94</sup> In general, chemical sensors contain a recognition element that is sensitive to the changes produced by different chemical compounds (analyte), and a transduction element, which produces a signal proportional to the concentration of the analyte. They are further categorized as optical, electrochemical, thermometric, and gravimetric according to the operating principle of the transducer. Modification of surfaces, either physically or chemically, allows for novel manipulation of the features of materials.<sup>95</sup> Various operations could be performed through the use of innumerable solid surface techniques, for example high selectivity and sensitivity sensors,<sup>96</sup> or biologically compatible nanoparticles.<sup>97</sup> Modification of surfaces via chemical means could be practically achieved using a wide number of diverse chemical species. The specific groups introduced onto the inert surface should be compatible with the reactive sites on the compound in order to make covalent attachments; popular functional groups in conjugation chemistry include thiols, aldehydes, carboxylic acids, hydroxyls, and primary amines.<sup>98</sup>

The oxidation level of electroactive polymers can be easily affected by their oxidation/reduction mechanisms, causing differences in conductivity, mass and colour. Furthermore, the sensitivity and selectivity of conducting polymers can be modified by attaching particular functional groups to the polymer films, or by using suitable counterions during the polymerisation process. Therefore, considerable effort has been devoted to the production of sensors based on conducting polymers.<sup>76</sup> Sensor technologies that involve the use of modified polymer electrodes to improve sensitivity and selectivity have become the objects of considerable interest in recent years. Electroactive polymers present countless opportunities to allow the interaction of

receptors with analyte groups. Sensors have an extensive range of applications such as in industrial production, food processing, environmental monitoring, and health care.<sup>99</sup>

Selectivity is considered one of the most significant problems that faces chemists in analytical chemistry, in particular when samples contain low concentrations of analyte with [potentially] interfering substances. There are two general methods described in the literature that can be used to create polymer derivatives: *post-polymerisation grafting* and *copolymerisation*.<sup>100</sup> The change of electrochemical behaviour of organic ligands (receptors) in solutions coincides with any change of metal ion “analytes” concentration and this merit can be exploited in sensor technology.<sup>101</sup>

The selectivity can be improved by several methods. One such method is the use of ion-selective membranes, which allow only specific molecules or ions to interact with the conducting polymer.<sup>102</sup> The second method to improve selectivity uses chemically modified polymers by the attachment of functional groups such as amine and carboxylic groups, or enzymes and antibiotics.<sup>103, 104</sup> These functional groups enhance the sensing properties of the surface when exposed to various molecules in different concentrations.<sup>99</sup> The production of modified electrode surfaces with electroactive films ordinarily involves adding several functional properties including reactive sites, a recognition centre to pick up the target species, and an effective means of transporting electrons within the polymer film.<sup>105</sup> The receptors in sensors play a pivotal role in their utility, especially those that are highly selective towards a specific analyte. In conjugated polymers, selectivity can be produced by covalent or physical bonding of receptors; in this regard, conjugated polymers in conjunction with responsive and redox active molecules have been investigated extensively.<sup>106</sup>

Chemical sensors that can detect metal ions are amongst the most studied systems. The studies obtained over several years appear to show that is possible to create very sensitive and selective metal ion sensors using electroactive polymer films.<sup>75</sup> These studies are dependent upon the improvement of molecular recognition and binding chemistry.<sup>100, 107</sup> These conducting polymers often contain alkyl chains, cyclophane,<sup>108</sup> crown ethers,<sup>109-111</sup> aza-crown ethers or calixarenes that complex with specific metal ions such as Na<sup>+</sup>, Li<sup>+</sup> or K<sup>+</sup>, or can use bipyridyl derivatives to form complexes with other ions such as Cu<sup>2+</sup>, Mn<sup>2+</sup>, Pd<sup>2+</sup>, Ba<sup>2+</sup>, and others.<sup>75, 105, 112</sup>

Modified polypyrrole electrodes have been applied as sensors for the detection of cations,<sup>113</sup> anions<sup>114</sup> and heavy metals.<sup>115</sup> More recently, various polyaniline derivative-based sensors have been used for detection of a range of metal ions such as  $\text{Fe}^{3+}$ ,  $\text{Cu}^{2+}$ ,  $\text{Cd}^{2+}$ ,  $\text{Pb}^{2+}$ ,  $\text{Hg}^{2+}$ <sup>116-118</sup> and  $\text{Ag}^+$ .<sup>119</sup> In addition, researchers have introduced salen and acetophenone moieties as selective ligands on thiophene and pyrrole.<sup>120</sup> An increase in the ionic selectivity of conducting polymers can be achieved by doping conducting polymers with metal-complexing anions.

The insertion of metal ion-sensitive groups into conducting polymer can be performed to modified films such as EDTA-polypyrrole, which can be used to determine the presence of  $\text{Cu}^{2+}$ ,  $\text{Pb}^{2+}$  and  $\text{Cd}^{2+}$  ions.<sup>121</sup> Rahman and co-workers reported that an EDTA-bonded terthiophene polymer film can be applied to the detection of  $\text{Pb}^{2+}$ ,  $\text{Cu}^{2+}$ , and  $\text{Hg}^{2+}$  ions.<sup>122</sup> Dai et al.<sup>123</sup> attempted to use phytic acid-functionalised polypyrrole to determine the presence of  $\text{Hg}^{2+}$ ,  $\text{Cd}^{2+}$  and  $\text{Pb}^{2+}$  ions using electrochemical techniques.

Moreover, other ligand groups have been used to detect metal ions, such as the *N*-nitrilotriacetic acid (NTA) group that can bind with polymer film and can then be used to detect metal ions like  $\text{Ni}^{2+}$ ,  $\text{Co}^{2+}$ ,  $\text{Cu}^{2+}$  and  $\text{Zn}^{2+}$ .<sup>124</sup> Wallace et al. used modified poly(3-methylthiophene) film to determine the presence of silver, mercury and chromium ions.<sup>125</sup> In addition, a conducting polymer (poly(3-thiophene acetic acid)) functionalized with tripeptide (Gly–Gly–His) was used for the selective detection of copper ions.<sup>126</sup>

Many studies have used crown ethers as the functional groups in conducting polymer films to employ them as chemical sensors for ions. Garnier et al. used a polypyrrole film electrode with pendant crown units to detect  $\text{Li}^+$ ,  $\text{Na}^+$ , and  $\text{K}^+$ .<sup>127</sup> In another study, crown ethers were attached to polythiophene films and applied for the recognition on  $\text{Li}^+$ ,  $\text{Na}^+$ , and  $\text{K}^+$ .<sup>128</sup>

Copolymerisation is also a straightforward way in which one can modify conducting polymer films. For instance, Somerset and co-workers reported that the presence of mercury ions can be determined using a polyaniline-methylene blue copolymer.<sup>129</sup> Another study noted that copolymer aniline with 2,2'-dithiodianiline (DTDA) gave the same results.<sup>130</sup> Furthermore, researchers were able to manufacture a new copolymer poly(diphenylamine-co-2-aminobenzonitrile) which has the ability to detect  $\text{Cd}^{2+}$  and  $\text{Pb}^{2+}$  ions.<sup>131</sup>

### 1.8.2 Patterning of conducting polymers

Patterning of surfaces can be defined as altering the topography or physiochemical properties of film surfaces in a particular spatial area. The neighbouring sites to this area of the surface, which have other properties, will lead to different interactions between the surface molecules and external atoms. The manipulation of patterned surfaces encourages researchers to use them in different applications such as sensors and molecular diagnostics.<sup>132</sup>

Some applications, for example sensor devices, depend on the ability to discriminate between the molecules that react or interact with their surfaces. This feature requires the use of a smart surface that contains diverse functionalities.<sup>132</sup> The integration of different functional groups (molecules) onto the surface can create a surface that is responsive to various stimuli within particular spatial areas. Fabrication of polymer surface film requires the deposition or etching of different molecules with specific functional groups. In general, the chemical mask used for the transferral of the desired pattern to the surface operates by protecting certain areas from deposits or etchants. Investigations into this topic have mainly concentrated on adding multi-functionality onto surfaces using sequential steps.<sup>133, 134</sup>

The ability to define a spatial location for molecules on a surface provides researchers with a useful tool by which to study the interaction between molecules, cells, and synthetic materials in a highly controlled spatial area. Surface patterning using masks is one of the most developed forms of patterning. A mask is generally defined as a template through which radiation can pass, or a spatial template that determines regions of a substrate that will be exposed to external influences. Creating patterns on surfaces using light-masking techniques is currently the most popular form of patterning with masks. The ability to pattern functional polymers at various length scales (e.g., nanometre, micrometre, etc.) is useful in various research fields including cell biology, tissue engineering and medicinal science. The capabilities of patterned polymers have emerged as a result of the abundance of functionalities of polymers, and a broad range of applications such as medicinal science, development of electronics, cell biology and tissue engineering have subsequently benefitted from them. Over the last twenty years, several techniques have been developed to allow selective positioning of organic molecules such as photolithography,<sup>135</sup> direct writing techniques,<sup>136</sup> printing

techniques,<sup>135</sup> and particle beam lithography.<sup>135, 137</sup> Lithography can be achieved through irradiation using a range of different wavelengths, such as UV and visible light, X-Rays and electron or ion beam bombardment. These devices are able to produce patterns with resolutions ranging from the micrometre to the 100 nm level.<sup>138, 139</sup> In these lithographic techniques, the patterning on surfaces can be controlled at a resolution that is inherent to the beam being applied to the surface.<sup>137</sup>

### 1.8.2.1 Photolithography

Over the last 30 years, photolithography has been one of the key methods used for the patterning of polymers. In photolithographic methods, a polymer-coated surface is selectively exposed to photoirradiation, with the subsequent removal of selected areas of the film through dissolution in appropriate solvents to produce patterning. The resolution of the patterns that can be achieved through photolithography varies from the micrometre to sub-100 nanometre scale.<sup>140</sup>

UV irradiation can lead to different alterations of the surface, for example layer ablation, bond breaking and release of attached molecules, polymerisation reactions or chemical bond formation,<sup>141,142</sup> and can be used to create both 2- and 3-dimensional surface patterns.<sup>143</sup> Photolithography processes have also been used to produce topographical surfaces that can be used to control cell growth.<sup>144</sup> In fact, this process allows for selective control over the production of the topographical features of the surface and directing the attachment of molecules.<sup>137</sup> Photolithography is the process of transferring the geometric patterns of a mask to a thin layer of radiation-sensitive material (called the *resist*, or *photoresist*), where irradiation is achieved via optically clear parts of the mask, leading to changes in the solubility of the parts of the photoresist layer so illuminated. Thereafter, a suitable etching process can be used to remove selective portions of the layer, which leads to the creation of a difference in solubility between irradiated and non-irradiated areas of the polymer. The next steps are those of development, film etching, and photoresist stripping, respectively.<sup>140</sup> **Figure 1.11** shows the steps in the photolithography technique.<sup>145</sup> The mask in the photolithography process can be any material with optically transparent and non-transparent regions. Masks may be solid, such as those fabricated from metals or printed on glass, or they can be printed on elastic substrates, such as transparencies. The principal requirement of

photolithographic patterning is that light should pass through specific spatial regions of the mask so as to result in the formation of a complimentary pattern on the substrate.<sup>132</sup>

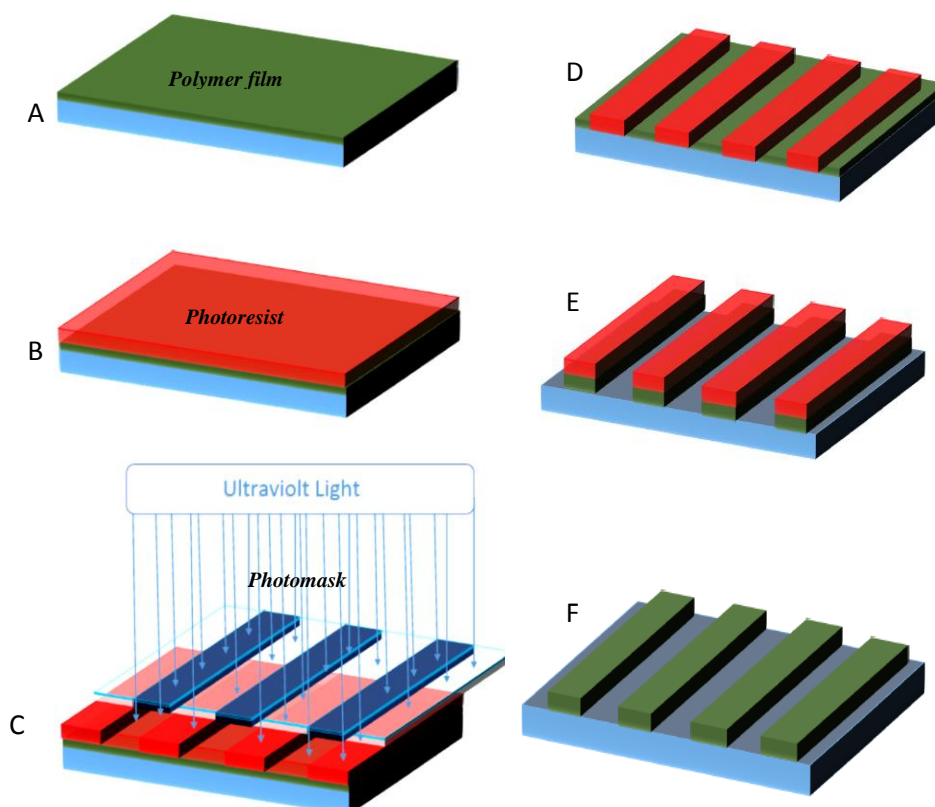


**Figure 1.11:** Process steps in photolithography: A) deposition, B) photoresist, C) UV exposure, D) development, E) film etching and F) photoresist stripping.

### 1.9 Objectives

This project aims to improve understanding of the electrochemical behaviour of functionalised conducting polymer films through the determination of the efficiency of polymer films under different conditions. Moreover, photolithographic methods will be applied to control the spatial distribution of functional groups over polymer films and their use in sensing of metal ions, whereby patterned surfaces with active receptors can be used in many areas such as sensing applications with improved selectivity and sensitivity because of associated increases in effective surface area which leads to enhanced sensitivities and detection limits. The reaction of the receptor molecules with the film surface at a microscale leads to increased performance of analytical devices. In other words, the intention of this project is the production of patterned polymer surfaces with different receptor sites that are capable of sensing different metal ions with improved sensitivity and selectivity through the use of suitable recognition moieties.

The goal of this work can be generally considered as that of gaining a patterning design with the capability to control the spatial distribution of a polymer over a film surface whilst maintaining a well-defined chemical functionality. To accomplish these aims, sophisticated techniques were used to modify surfaces and functional groups present throughout the polymer film surfaces which would hopefully lead to the promotion of a discriminative chemical response. Patterned modified polymer electrodes attached to ligands will be used to determine metal ion concentrations such as copper, cobalt, and nickel in aqueous solution. This work will give the opportunity to produce a measurement device with a number of advantages through control, functionalization and miniaturization of surface, notably the construction of small, portable high-performance devices. The project aims to exploit the photolithographic technique to facilitate the creation of lateral patterns on polymer film surfaces such as polypyrrole, polyaniline and polythiophene derivatives using various chelating elements containing recognition units such as free carboxyl or amino groups, and which possess the ability to sense different analytes. Through the use of such control technology, it can be controlled on the spatial distribution of functional groups and thus have the prospect of being able to create multicomponent analysis systems with the flexibility to allow miniaturisation of analytical devices.

To accomplish these aims, new synthetic methods were used to effect the bulk insertion of receptor molecules over polymer films surfaces in order to determine the distribution of receptors immobilised within the polymer surfaces. Use of electrochemical “iVt” methods led to control of the electrodeposition and electrochemical performance of the resultant polymer films, which offers an excellent opportunity to modify these films to produce the desired film surfaces. QCM was applied to verify the immobilisation process through changes to the polymer film during hydrolysis, and the appropriate functionalisation reaction to obtain a clear picture as to the interaction paths and substitution processes occurring within the polymer surfaces. These techniques are extremely helpful tools in the study and investigation of very low ion concentrations; they are also easy to use and cheap. FTIR spectroscopy was used to identify characteristic bands related to the amide and ester bonds over the polymer surface. The evidence that the immobilisation of surface films had succeed depended on the presence and/or absence of specific bands, such as amide or ester bands within the associated FTIR spectra.

## 1.10 References

1. Z. Nie and E. Kumacheva, *Nature Materials*, 2008, **7**, 277-290.
2. D. Kowalski, M. Ueda and T. Ohtsuka, *Corrosion Science*, 2007, **49**, 3442-3452.
3. M. Sterby, R. Emanuelsson, X. Huang, A. Gogoll, M. Strømme and M. Sjödin, *Electrochimica Acta*, 2017, **235**, 356-364.
4. Z.-B. Huang, G.-F. Yin, X.-M. Liao and J.-W. Gu, *Frontiers of Materials Science*, 2014, **8**, 39-45.
5. J. Jang, *Emissive Materials Nanomaterials*, Springer, Berlin, 2006, pp. 189-260.
6. E. Smela, *Journal of Micromechanics and Microengineering*, 1999, **9**, 1.
7. G. Inzelt, *Conducting Polymers: A New Era in Electrochemistry*, Springer, 2012, p.1.
8. G. Inzelt, *Journal of Solid State Electrochemistry*, 2011, **15**, 1711-1718.
9. P. S. Sharma, A. Pietrzyk-Le, F. D'Souza and W. Kutner, *Analytical and Bioanalytical Chemistry*, 2012, **402**, 3177-3204.
10. C. Chiang, C. Fincher, Y. Park, A. Heeger, H. Shirakawa, E. Louis, S. Gau and A. MacDiarmid, *Physical Review Letters*, 1977, **39**, 1098-1101.
11. T.-H. Le, Y. Kim and H. Yoon, *Polymers*, 2017, **9**, 150.
12. K. Dutta and P. P. Kundu, *Polymer Reviews*, 2014, **54**, 401-435.
13. K. Dutta and P. P. Kundu, *Journal of Colloid and Interface Science*, 2013, **397**, 192-198.
14. D. D. Ateh, H. A. Navsaria and P. Vadgama, *Journal of the Royal Society, Interface / the Royal Society*, 2006, **3**, 741-752.
15. B. Scrosati, *Applications of Electroactive Polymers*, Springer, Netherlands, 1993.
16. P. Chandrasekhar, *Conducting Polymers, Fundamentals and Applications: A Practical Approach*, Springer, USA, 1999.
17. S. Varis, Ph.D. Thesis, Middle East Technical University, 2006.
18. N. K. Guimard, N. Gomez and C. E. Schmidt, *Progress in Polymer Science*, 2007, **32**, 876-921.
19. T. A. Skotheim and J. Reynolds, *Conjugated Polymers: Theory, Synthesis, Properties, and Characterization*, Taylor and Francis, 2006, p.83.
20. M. Wagner, Ph.D Thesis, Åbo Akademi University, 2013.
21. N. V. B. Hemant K. Chitte, Mr. Ajit V. Gore and Ganesh N. Shind *Materials Sciences and Applications*, 2011, **2**, 1491-1498.
22. Y. Li, *Organic Optoelectronic Materials*, Springer, 2015, p.28.
23. J. L. Bredas and G. B. Street, *Accounts of Chemical Research*, 1985, **18**, 309-315.
24. G. G. Wallace, P. R. Teasdale, G. M. Spinks and L. Kane-Maguire, *Conductive Electroactive Polymers: Intelligent Polymer Systems*, CRC Press, 2008, p.12.
25. H. Naarmann and N. Theophilou, *Synthetic Metals*, 1987, **22**, 1-8.
26. Y.-s. Qiao, T. Dou and M. Hu, *Chinese Journal of Polymer Science*, 2010, **28**, 923-930.

27. T. Nakajima and T. Kawagoe, *Synthetic Metals*, 1989, **28**, 629-638.
28. M. C. Bernard and A. Hugot-Le Goff, *Electrochimica Acta*, 2006, **52**, 595-603.
29. G. Tourillon and F. Garnier, *The Journal of Physical Chemistry*, 1983, **87**, 2289-2292.
30. M. a. Sato, T. Shimizu and A. Yamauchi, *Die Makromolekulare Chemie*, 1990, **191**, 313-319.
31. S. Aeiyaeh, B. Zaid and P. Lacaze, *Electrochimica Acta*, 1999, **44**, 2889-2898.
32. M. Grzeszczuk, J. Kalenik and A. Kępas-Suwara, *Journal of Electroanalytical Chemistry and Interfacial Electrochemistry*, 2009, **626**, 47-58.
33. M. Innocenti, F. Loglio, L. Pigani, R. Seeber, F. Terzi and R. Udusti, *Electrochimica Acta*, 2005, **50**, 1497-1503.
34. L. Pigani, R. Seeber, F. Terzi and C. Zanardi, *Journal of Electroanalytical Chemistry and Interfacial Electrochemistry*, 2004, **562**, 231-239.
35. S. Ivanov and V. Tsakova, *Electrochimica Acta*, 2004, **49**, 913-921.
36. A. E. Fischer, T. M. McEvoy and J. W. Long, *Electrochimica Acta*, 2009, **54**, 2962-2970.
37. K. Fehér and G. Inzelt, *Electrochimica Acta*, 2002, **47**, 3551-3559.
38. H. Karamil and A. R. Nezhad, *International Journal of Electrochem. Sci. J*, 2013, **8**, 8905-8921.
39. V. Brandl and R. Holze, *Berichte Der Bunsengesellschaft Für Physikalische Chemie*, 1998, **102**, 1032-1038.
40. A. Diaz and J. Logan, *Journal of Electroanalytical Chemistry and Interfacial Electrochemistry*, 1980, **111**, 111-114.
41. M. B. González and S. B. Saidman, *Electrochemistry Communications*, 2011, **13**, 513-516.
42. J. Petitjean, J. Tanguy, J. C. Lacroix, K. I. Chane-Ching, S. Aeiyaeh, M. Delamar and P. C. Lacaze, *Journal of Electroanalytical Chemistry and Interfacial Electrochemistry*, 2005, **581**, 111-121.
43. S. Geetha and D. C. Trivedi, *Materials Chemistry and Physics*, 2004, **88**, 388-397.
44. A. R. Hillman and E. F. Mallen, *Journal of Electroanalytical Chemistry and Interfacial Electrochemistry*, 1987, **220**, 351-367.
45. A. Hamnett, S. J. Higgins, P. Fisk and W. Albery, *Journal of Electroanalytical Chemistry and Interfacial Electrochemistry*, 1989, **270**, 479-488.
46. H. Nalwa, *Handbook of Advanced Electronic and Photonic Materials and Devices*, Academic Press, 2000, p.16.
47. J. R. a. T. M. K.Mullen, *Conjugated Polymers: A Practical Guide to Synthesis*, The Royal Society of Chemistry, 2013, p.224.
48. M. a. A. Singh, *Polypyrrole Composites: Electrochemical Synthesis, Characterizations and Applications*, In: Ewa Schab-Balcerzak. ed. *Electropolymerization*, InTech, India, 2011.
49. K.-J. Kim, H.-S. Song, J.-D. Kim and J.-K. Chon, *Bulletin of The Korean Chemical Society*, 1988, **9**, 248-251.

50. S. Asavapiriyant, G. Chandler, G. Gunawardena and D. Pletcher, *Journal of Electroanalytical Chemistry and Interfacial Electrochemistry*, 1984, **177**, 229-244.
51. S. Sadki, P. Schottland, N. Brodie and G. Sabouraud, *Chemical Society Reviews*, 2000, **29**, 283-293.
52. R. Balint, N. J. Cassidy and S. H. Cartmell, *Acta Biomaterialia*, 2014, **10**, 2341-2353.
53. A. R. Hillman and M. A. Mohamoud, *Electrochimica Acta*, 2006, **51**, 6018-6024.
54. L. Bauermann and P. Bartlett, *Electrochimica Acta*, 2005, **50**, 1537-1546.
55. A. A. Syed and M. K. Dinesan, *Talanta*, 1991, **38**, 815-837.
56. A. MacDiarmid, L. Yang, W. Huang and B. Humphrey, *Synthetic Metals*, 1987, **18**, 393-398.
57. H. Wang, A. MacDiarmid, Y. Wang, D. Gebier and A. J. Epstein, *Synthetic Metals*, 1996, **78**, 33-37.
58. D. Dutta, T. K. Sarma, D. Chowdhury and A. Chattopadhyay, *Journal of Colloid and Interface Science*, 2005, **283**, 153-159.
59. A. Drelinkiewicz, A. Waksmundzka-Góra, J. Sobczak and J. Stejskal, *Applied Catalysis A: General*, 2007, **333**, 219-228.
60. B. Conway, V. Birss and J. Wojtowicz, *Journal of Power Sources*, 1997, **66**, 1-14.
61. A. Kalendová, D. Veselý and J. Stejskal, *Progress in Organic Coatings*, 2008, **62**, 105-116.
62. M. Chang, C. Wu, Y. Chen, B. Hsieh, W.-Y. Huang, K. Ho, T. Hsieh and Y. Han, *Organic Electronics*, 2008, **9**, 1136-1139.
63. L. Huang, X. Zhuang, J. Hu, L. Lang, P. Zhang, Y. Wang, X. Chen, Y. Wei and X. Jing, *Biomacromolecules*, 2008, **9**, 850-858.
64. C. Dhand, N. Dwivedi, S. Mishra, P. Solanki, V. Mayandi, R. Beuerman, S. Ramarishna, R. Lakshminarayanan and B. Malhotra, *Nanobiosensors in Disease Diagnosis*, 2015, **4**, 25-46.
65. J. Stejskal, P. Kratochvil and A. D. Jenkins, *Polymer*, 1996, **37**, 367-369.
66. M. Skompska and A. R. Hillman, *Journal of the Chemical Society, Faraday Transactions*, 1996, **92**, 4101-4108.
67. G. Zotti, S. Cattarin and N. Comisso, *Journal of Electroanalytical Chemistry and Interfacial Electrochemistry*, 1988, **239**, 387-396.
68. M. Jaymand, M. Hatamzadeh and Y. Omid, *Progress in Polymer Science*, 2015, **47**, 26-69.
69. D. L. Wise, *Electrical and Optical Polymer Systems: Fundamentals: Methods, and Applications*, Taylor and Francis, 1998, p.798.
70. M. Hatamzadeh, M. Jaymand and B. Massoumi, *Polymer International*, 2014, **63**, 402-412.
71. X. Li, Y. Wang, X. Yang, J. Chen, H. Fu and T. Cheng, *TrAC Trends in Analytical Chemistry*, 2012, **39**, 163-179.

72. C. Shi, Y. Yao, Y. Yang and Q. Pei, *Journal of the American Chemical Society*, 2006, **128**, 8980-8986.
73. D. Mawad, E. Stewart, D. L. Officer, T. Romeo, P. Wagner, K. Wagner and G. G. Wallace, *Advanced Functional Materials*, 2012, **22**, 2692-2699.
74. K. Clayton, Ph.D Thesis, University of Huddersfield, 2011.
75. T. Huynh, P. Sharma, M. Sosnowska, F. D'Souza and W. Kutner, *Progress in Polymer Science*, 2015, **47**, 1-25.
76. B. Scrosati, *Applications of electroactive polymers*, Springer, 1993.
77. J. T. Koberstein, *Journal of Polymer Science Part B: Polymer Physics*, 2004, **42**, 2942-2956.
78. J. R. Lancaster, J. Jehani, G. T. Carroll, Y. Chen, N. J. Turro and J. T. Koberstein, *Chemistry of Materials*, 2008, **20**, 6583-6585.
79. G. T. Carroll, N. J. Turro and J. T. Koberstein, *Journal of Colloid and Interface Science*, 2010, **351**, 556-560.
80. P. Theato and H. Klok, *Functional Polymers by Post-Polymerization Modification: Concepts, Guidelines and Applications*, John Wiley, 2013, p.5.
81. L. Dai, *Intelligent Macromolecules for Smart Devices: From Materials Synthesis to Device Applications* Springer, UK, 2004, p.406.
82. L. Dai, P. Soundarrajan and T. Kim, *Pure and Applied Chemistry*, 2002, **74**, 1753-1772.
83. B. R. Eggins, *Chemical Sensor and Biosensor*, John Wiley and Sons, UK, 2004.
84. N. R. Stradiotto, H. Yamanaka and M. V. B. Zanoni, *Journal of the Brazilian Chemical Society*, 2003, **14**, 159-173.
85. M. R. Plata, A. M. Contento and A. Ríos, *Sensors*, 2010, **10**, 2511-2576.
86. J. Gallardo, S. Alegret and M. del Valle, *Sensors and Actuators B: Chemical*, 2004, **101**, 72-80.
87. N. V. Lavrik, M. J. Sepaniak and P. G. Datskos, *Review of Scientific Instruments*, 2004, **75**, 2229-2253.
88. A. Öpik, A. Menaker, J. Reut and V. Syritski, *Proceedings of the Estonian Academy of Sciences*, 2009, **58**, 3-11.
89. B. Deore, Z. Chen and T. Nagaoka, *Analytical Sciences*, 1999, **15**, 827-828.
90. A. R. Hillman, M. J. Swann and S. Bruckenstein, *The Journal of Physical Chemistry*, 1991, **95**, 3271-3277.
91. M. J. Henderson, A. R. Hillman and E. Vieil, *Journal of Electroanalytical Chemistry and Interfacial Electrochemistry*, 1998, **454**, 1-8.
92. G. Price and P. Drake, *Sensors and Actuators B: Chemical*, 2006, **114**, 466-472.
93. T. Lindfors, J. Bobacka, A. Lewenstam and A. Ivaska, *Electrochimica Acta*, 1998, **43**, 3503-3509.
94. D. Thévenot, K. Toth, R. A. Durst and G. S. Wilson, *Biosensors and Bioelectronics*, 2001, **16**, 121-131.
95. W. Senaratne, L. Andruzzi and C. K. Ober, *Biomacromolecules*, 2005, **6**, 2427-2448.
96. H. Hunt, C. Soteropulos and A. M. Armani, *Sensors*, 2010, **10**, 9317-9336.

97. A. E. Nel, L. Mädler, D. Velegol, T. Xia, E. M. Hoek, P. Somasundaran, F. Klaessig, V. Castranova and M. Thompson, *Nature materials*, 2009, **8**, 543-557.
98. J. M. Goddard and J. Hotchkiss, *Progress in Polymer Science*, 2007, **32**, 698-725.
99. W. Knoll and R. C. Advincula, *Functional Polymer Films*, John Wiley and Sons, 2012.
100. U. Lange, N. V. Roznyatovskaya and V. M. Mirsky, *Analytica Chimica Acta*, 2008, **614**, 1-26.
101. D. Compagnone, J. Bannister and G. Federici, *Sensors and Actuators B: Chemical*, 1992, **7**, 549-552.
102. D. G. Pijanowska and W. Torbicz, *Biocybernetics and Biomedical Engineering*, 2008, **28**, 11.
103. X. Liu, S. Cheng, H. Liu, S. Hu, D. Zhang and H. Ning, *Sensors*, 2012, **12**, 9635-9665.
104. A.A. Ciucu, *Journal of Biosensors and Bioelectronics*, 2014, **5**, 2.
105. A. Glidle, A. R. Hillman, K. S. Ryder, E. L. Smith, J. M. Cooper, R. Dalglish, R. Cubitt and T. Geue, *Electrochimica Acta*, 2009, **55**, 439-450.
106. J. Bobacka, A. Ivaska and A. Lewenstam, *Electroanalysis*, 2003, **15**, 366-374.
107. S. Cosnier, *Biosensors and Bioelectronics*, 1999, **14**, 443-456.
108. M. J. Marsella, P. J. Carroll and T. M. Swager, *Journal of the American Chemical Society*, 1995, **117**, 9832-9841.
109. P. Bäuerle and S. Scheib, *Advanced Materials*, 1993, **5**, 848-853.
110. F. Algi and A. Cihaner, *Tetrahedron Letters*, 2008, **49**, 3530-3533.
111. M. Lin, M. Cho, W.-S. Choe, Y. Son and Y. Lee, *Electrochimica Acta*, 2009, **54**, 7012-7017.
112. D. Demeter, P. Blanchard, I. Grosu and J. Roncali, *Journal of Inclusion Phenomena and Macrocyclic Chemistry*, 2008, **61**, 227-239.
113. M. Giannetto, G. Mori, A. Notti, S. Pappalardo and M. F. Parisi, *Chemistry—A European Journal*, 2001, **7**, 3354-3362.
114. M. Nicolas, B. Fabre and J. Simonet, *Journal of Electroanalytical Chemistry and Interfacial Electrochemistry*, 2001, **509**, 73-79.
115. L. M. Goldenberg, M. R. Bryce and M. C. Petty, *Journal of Materials Chemistry*, 1999, **9**, 1957-1974.
116. M. K. Ram, P. Bertinello and C. Nicolini, *Electroanalysis*, 2001, **13**, 574-581.
117. Z. Wang, E. Liu and X. Zhao, *Thin Solid Films*, 2011, **519**, 5285-5289.
118. P. Kumar, A. Joseph, P. C. Ramamurthy and S. Subramanian, *Microchimica Acta*, 2012, **177**, 317-323.
119. Q. Liu, F. Wang, Y. Qiao, S. Zhang and B. Ye, *Electrochimica Acta*, 2010, **55**, 1795-1800.
120. K. Ogura and H. Shiigi, *Electrochemical and Solid-state Letters*, 1999, **2**, 478-480.
121. M. Heitzmann, C. Bucher, J.-C. Moutet, E. Pereira, B. L. Rivas, G. Royal and E. Saint-Aman, *Electrochimica Acta*, 2007, **52**, 3082-3087.

122. M. A. Rahman, M.-S. Won and Y.-B. Shim, *Analytical Chemistry*, 2003, **75**, 1123-1129.
123. H. Dai, N. Wang, D. Wang, H. Ma and M. Lin, *Chemical Engineering Journal*, 2016, **299**, 150-155.
124. J. A. Lori, A. Morrin, A. J. Killard and M. R. Smyth, *Electroanalysis*, 2006, **18**, 77-81.
125. M. J. Peter R., and Gordon G. Wallace, *Electroanalysis*, 1989, **1**, 541-547.
126. M. Lin, M. S. Cho, W. S. Choe and Y. Lee, *Biosensors and Bioelectronics*, 2009, **25**, 28-33.
127. H. K. Youssoufi, M. Hmyene, F. Garnier and D. Delabouglise, *Journal of the Chemical Society, Chemical Communications*, 1993, 1550-1552.
128. T. M. Swager and M. J. Marsella, *Advanced Materials*, 1994, **6**, 595-597.
129. V. Somerset, J. Leaner, R. Mason, E. Iwuoha and A. Morrin, *International Journal of Environmental Analytical Chemistry*, 2010, **90**, 671-685.
130. V. Somerset, J. Leaner, R. Mason, E. Iwuoha and A. Morrin, *Electrochimica Acta*, 2010, **55**, 4240-4246.
131. M. F. Philips, A. I. Gopalan and K. Lee, *Journal of Hazardous Materials*, 2012, **237**, 46-54.
132. K. K. Gleason, *CVD Polymers: Fabrication of Organic Surfaces and Devices*, John Wiley and Sons, 2015, p.323.
133. B. D. Ratner, A. Hoffman, F. Schoen and J. E. Lemons, *Biomaterials Science: an Introduction to Materials in Medicine*, Academic press, 2004, p.276.
134. W. Albery and A. Hillman, *Annual Reports Section "C"(Physical Chemistry)*, 1981, **78**, 377-437.
135. B. Gates, Q. Xu, M. Stewart, D. Ryan, C. Willson and G. M. Whitesides, *Chemical Reviews*, 2005, **105**, 1171-1196.
136. M. Yang, P. E. Sheehan, W. P. King and L. J. Whitman, *Journal of the American Chemical Society*, 2006, **128**, 6774-6775.
137. J.-K. Chen and C.-J. Chang, *Materials*, 2014, **7**, 805-875.
138. S. Persson, P. Dyreklev and O. Inganäs, *Advanced Materials*, 1996, **8**, 405-408.
139. N. Gomez, J. Y. Lee, J. D. Nickels and C. E. Schmidt, *Advanced Functional Materials*, 2007, **17**, 1645-1653.
140. T. Govindarajan and R. Shandas, *Polymers*, 2014, **6**, 2309-2331.
141. T. Cui and J. Wang, *Journal of microelectromechanical systems*, 2005, **14**, 895-902.
142. A. Hook, N. Voelcker and H. Thissen, *Acta Biomaterialia*, 2009, **5**, 2350-2370.
143. H. Otsuka, A. Hirano, Y. Nagasaki, T. Okano, Y. Horiike and K. Kataoka, *ChemBioChem*, 2004, **5**, 850-855.
144. G. Papavasiliou, P. Songprawat, V. Pérez-Luna, E. Hammes, M. Morris, Y.-C. Chiu and E. Brey, *Tissue Engineering Part C: Methods*, 2008, **14**, 129-140.
145. S. Prakash and J. Yeom, *Nanofluidics and Microfluidics: Systems and Applications*, Elsevier Science, USA, 2014, p.88.

## Chapter Two

## General Methodology

<b>2.1</b>	<b>Concepts of Electrochemistry .....</b>	<b>29</b>
2.1.1	Mass Transport .....	29
2.1.1.1	Diffusion.....	30
2.1.1.2	Migration .....	30
2.1.1.3	Convection.....	31
<b>2.2</b>	<b>Electrochemical Techniques .....</b>	<b>31</b>
2.2.1	Cyclic voltammetry .....	31
2.2.2	Chronoamperometry .....	36
<b>2.3</b>	<b>Quartz crystal Microbalance (QCM).....</b>	<b>37</b>
2.3.1	The Piezoelectric Effect .....	38
2.3.2	The Mass – Frequency Relationship .....	39
2.3.3	Electrochemical Quartz Crystal Microbalance .....	40
<b>2.4</b>	<b>Microscopy and Imaging Techniques .....</b>	<b>41</b>
2.4.1	Scanning Electron Microscopy (SEM) .....	41
2.4.2	Atomic Force Microscopy (AFM) .....	43
<b>2.5</b>	<b>Fourier Transform Infrared Spectroscopy .....</b>	<b>44</b>
<b>2.6</b>	<b>References.....</b>	<b>45</b>

## 2.1 Concepts of Electrochemistry

Electrochemistry is concerned with the study of reactions, including electron transfer, that occur between electrodes and reactants within an electrolyte. Oxidation and reduction reactions are the basis of these reactions.<sup>1</sup> Briefly, oxidation involves the loss of electrons from a chemical species, while a reduction involves a gain of electrons. A redox reaction involves the transfer of electrons from an oxidised species to a reduced species.<sup>2</sup>

Electrochemical cells can be divided into two types: electrolytic cells and galvanic cells. In general, a chemical reaction occurs in an electrolytic cell when an external current is applied; a galvanic cell generates this same current via chemical reactions. Reactions within the electrolytic cell are affected by a number of factors such as the surface and nature of the electrode and the potential. The voltage applied to the cell is key to the reaction. The electron transfer (reaction in electrolytic cells) requires a constant supply of new reactant materials and the continuous removal of products.<sup>3</sup> This process involves electron transfer and mass transport. When a certain potential is applied to an electrochemical system, the kinetics of the system will determine the resultant current. These systems, particularly those related to modified polymer electrodes, have been investigated extensively over the past few decades. Cyclic voltammetry<sup>4, 5</sup> and chronoamperometry<sup>6, 7</sup> are the most commonly applied techniques for the electroanalysis of electrochemical systems.

### 2.1.1 Mass Transport

The exchange of mobile species occurs via three steps: firstly, the transport of molecules from the bulk electrolyte solution to the electrode substrate; secondly, the exchange of electrons at the electrode surface and the formation of the reaction product; and, thirdly, the removal of products from the vicinity of the electrode, as shown in **Figure 2.1**. The mass transport of a species is a movement that is entirely necessary to maintaining an electrochemical reaction. Mass transport and electron transfer kinetics are particularly important to the study of electrochemical systems. In general, the transport of ions and/or solvent to/from the surface of the electrode occurs via three disparate processes: diffusion, convection and migration.<sup>8, 9</sup>

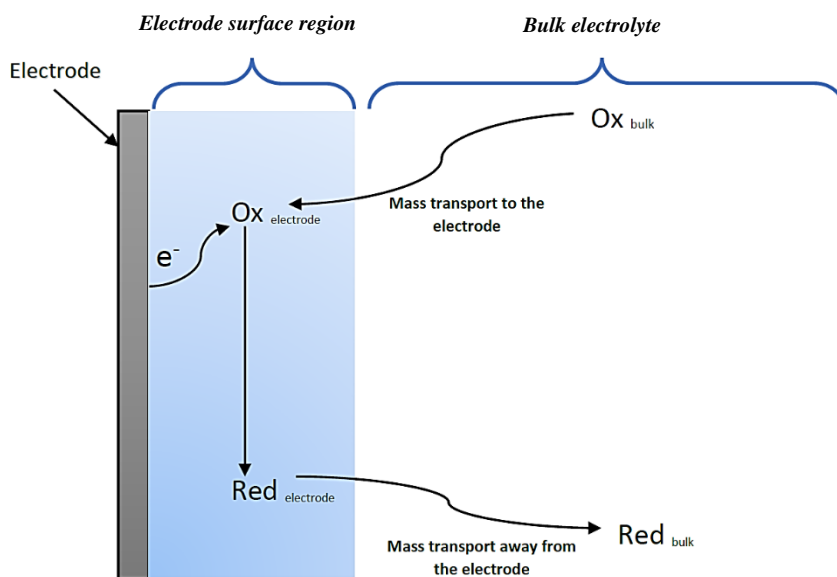


**Figure 2.1:** Electron transfer and mass transport in electrochemical reactions.

### 2.1.1.1 Diffusion

This is the spontaneous motion of ions and/or molecules due to the influence of a concentration gradient in order to reach the equilibrium distribution of the species in the system.<sup>14</sup> In the course of this process, the species will be moved from a region of high concentration to a region of low concentration so as to reach the equilibrium (regular) distribution of the species within the system. In addition, Fick's laws can be used to quantify the rate of transport. Moreover, the diffusion process plays a significant role in electrochemical experiments due to the main reaction occurring at the electrode surface. This process will, of course, lead to an imbalance in concentration between the different regions of the solution.<sup>10, 11</sup>

### 2.1.1.2 Migration

The movement in this process depends on the charges carried by particles as they move towards the electrode.<sup>14</sup> This process takes place in the region immediately around the electrode/electrolyte interface. This process can take place via ion movement under the influence of an electric field. The ion movement in this process depends on the charge and size of the ions, and the viscosity of the solution. Mostly, the effects of migration can be minimized by using a concentrated inert background electrolyte.<sup>11</sup>

### 2.1.1.3 Convection

This process involves the transfer of species from one part of the liquid to another via the motion of the liquid itself, which can occur through stirring, flowing, pumping and vibration.<sup>14,10</sup> This process is also known as hydrodynamic mass transport. Sometimes there is natural convection in an unagitated electrolyte because of small changes in concentration and temperature close to the electrode surface generated by electron transfer reactions in the electrode substrate. Generally speaking, however, natural convection is probably the result of vibrations and noise in the surrounding environment. However, the convection effect is often negligible during short-term experiments within fixed cells. Therefore, diffusion will dominate the rate of mass transport of species.<sup>11</sup>

## 2.2 Electrochemical Techniques

Electrochemical techniques are a particularly popular method by which to investigate and study conducting polymers that have been synthesised via electrochemical methods. These techniques can be used to characterise the growth and nucleation mechanisms of polymer films during electropolymerisation.<sup>3, 11, 12</sup> There are a number of techniques that are commonly used to prepare and monitor conductive polymers, such as the galvanostatic and potentiostatic methods.

### 2.2.1 Cyclic voltammetry

Cyclic voltammetry is one of the most important of techniques used to monitor and study redox processes within electrochemical systems. Moreover, it is considered the most suitable method by which to explain the behaviours of electrochemical processes.<sup>13</sup> The relationship between the potential and current is pivotal to this technique, providing extensive information relating to the electrochemical reactions of electrode films.<sup>14, 15</sup> The redox reaction in the electrochemical system at the surface of the electrode can be represented by the following reaction.



Here, O and R represent the oxidised and reduced forms of a given species, respectively.<sup>16, 17</sup> This technique can provide fundamental information about the redox potentials of polymers.<sup>15, 18</sup> Ordinarily, the technique records the current ( $I$ ) as a function of the potential ( $E$ ) of the working electrode in a figure referred to as a “voltammogram”.

Three-electrode cells are employed in an electrochemical system; the concept of the experiment requires sweeping over a range of potentials whilst the electrode is immersed in an electrolyte solution. A standard electrochemical cell requires a three-electrode system consisting of a working electrode (WE), a counter electrode (CE) and a reference electrode (RE) in an electrolyte solution, as shown in **Figure 2.2**.

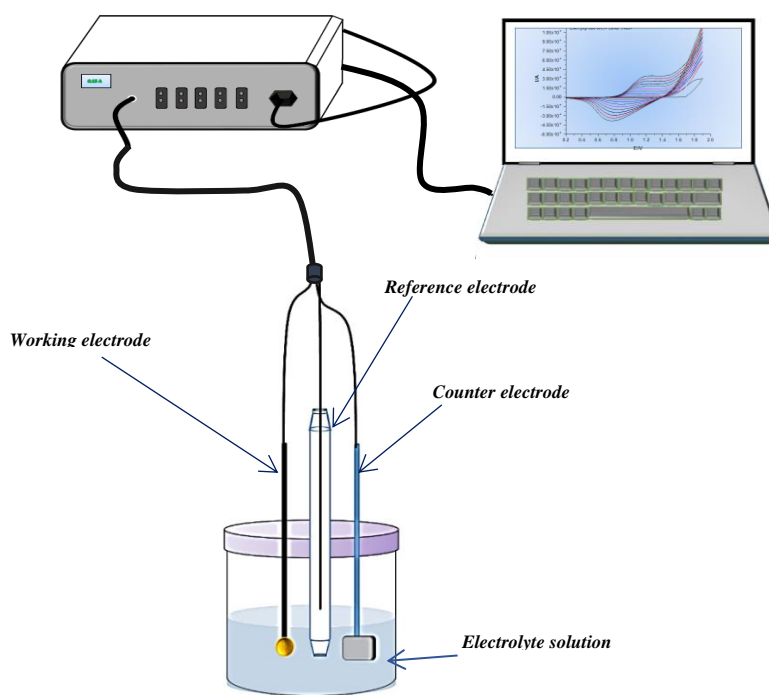


**Figure 2.2** : Schematic diagram of an electrochemical cell.

Cyclic voltammetry is beneficial to various kinds of study, including the deposition of conducting polymers and metals and providing information about kinetics and thermodynamics of charge transfer processes.<sup>19</sup> Moreover, voltammetric methods are used to monitor the activity of analytes in a system.<sup>8, 20</sup>

The 1930s witnessed the first report, and a theoretical description, of the cyclic voltammetry technique by Randles.<sup>21</sup> Cyclic voltammetry involves scanning the potential of a working electrode two or more times between limited points ( $E1$  and  $E2$ ) at a known scan rate ( $v / V s^{-1}$ ). The potential applied to the electrochemical system (working and reference electrodes) can be controlled using the potentiodynamic technique. This process can provide useful information about the features and characteristics of the electrochemical process in the solution or at the surface of the electrode.<sup>19, 22</sup> The integration of this resulting current with time gives the total charge, which is directly

related to the amount of electroactive species present. In the electrochemical cell, electrons will flow between the counter- and working electrodes.<sup>23</sup>

This technique involves repeated regular sweeps of a linear potential between two specific potential values at a scan rate,  $\nu$ , that has been previously chosen. The current resulting from this process is recorded as a function of the potential of the working electrode. Sketch A in **Figure 2.3** illustrates that the potential moves linearly with time in the forward direction at the beginning of the experiment until it reaches a certain value that has been previously identified as being sufficient to oxidise the electroactive species, at which point the scan is reversed and returned to its starting value. Obtaining the required results can be achieved via one cycle only or via repetitive cycles over a fixed number of scans depending on the nature of the experiment.<sup>14, 24</sup> **Figure 2.3** (b) shows a cyclic voltammogram for a reversible electrochemical reaction usually solution species. In this figure, the initial potential value ( $E_i$ ) is set so that only non-faradaic currents flow. Thereafter, as the potential is swept towards  $E^o$ , oxidation reactions will be begin at the surface of the electrode (faradaic current).<sup>25</sup> The current ( $I$ ) at this point begins to rise gradually (positive scanning), and the electroactive molecules (R) that exist at the surface of working electrode convert to their oxidised form (O) and reduced form (RED) until the concentration reaches zero. When all R close to the electrode have been oxidised, the current will reach a higher value called the current peak ( $i_{pc}$ ). Subsequent to this point, the rate of electrochemical consumption of the reduced species will be become faster than the mass transfer of the reduced species from the bulk solution to the surface of electrode, and the diffusion process will be dominated by the voltammetric response. Thereafter, the potential will be scanned in the opposite direction (negative scanning). As a result of this latter step, the current will decrease until it reaches a point where all the oxidized species, O, close to the electrode will be reduced; at this point, the negative current peaks,  $i_{pa}$ , at a potential  $E_{pa}$ , after which the current starts to rise until it reaches its initial value. At this point, the scan is complete. Furthermore, there are diverse and important factors that play important roles in the rate of electrode reaction and the resultant current, including the electron transfer rate at the electrode, mass transfer between the bulk solution and electrode surface, and the nature of the chemical reactions (homogeneous or heterogeneous) during the electron transfer.<sup>26</sup>

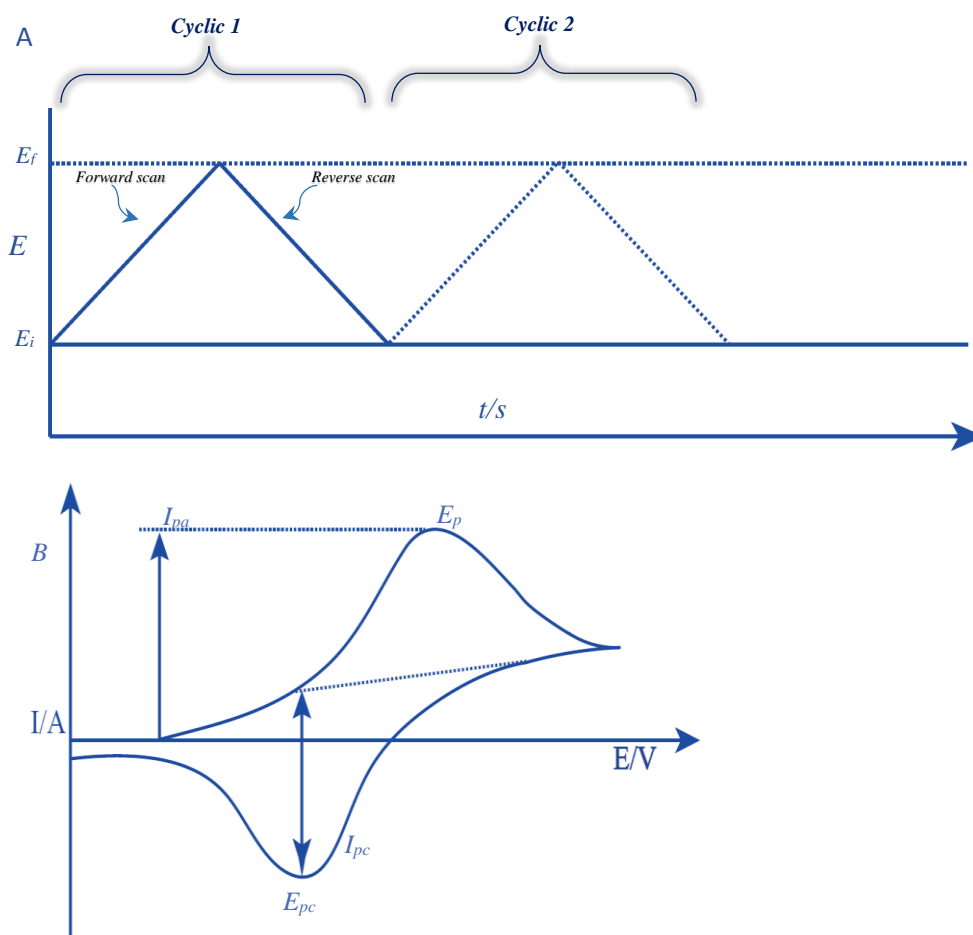


**Figure 2.3:** Cyclic voltammetry schemes. a) Cyclic voltammetry waveform with time; and b) cyclic voltammogram for a reversible process for solution reactant /product.

The form of the cyclic voltammogram is dependent on the reversible electrochemical reaction. Some of the characteristics of a reversible reaction are:<sup>11</sup>

- 1) The value of the potential separation between the anodic and cathodic peak potentials can be measured using **equation 2.1**:<sup>27</sup>

$$\Delta E = E_{pa} - E_{pc} = 59/n \text{ (mV)} \quad \text{Equation 2.1}$$

in practice, there can be small increases in  $n$  with increasing scan rate because of the internal resistance of the electrolyte solution ( $R_s$ ).<sup>28</sup>

- 2) The scan rate plays a vital role in the determination of the peak potential.

- 3) The ratio of the peak anodic current,  $i_{p,a}$ , and the peak cathodic current,  $i_{p,c}$ , is equal to 1, as shown in **equation 2.2**.<sup>8, 11, 29</sup>

$$(i_{pa}/i_{pc} = 1)$$

Equation 2.2

4) The peak current ( $i_p$ ) is proportional to the square root of the scan rate ( $v^{1/2}$ ).

In a reversible electrochemical reaction, the diffusion mechanism dominates, where the rate of electron transfer is faster than the rate of mass transport at any given potential. In addition, the Nernst equation can be used to determine the concentration of electroactive species at the surface of the electrode, as shown in **equation 2.3**:<sup>11</sup>

$$\Delta E = E^\circ + RT/nF \ln C_{OX}/C_{RED}$$

**Equation 2.3**

Where  $E^\circ$  is the reduction potential,  $C_{RED}$  and  $C_{OX}$  are the concentrations of reduced and oxidised species at the electrode surface,  $F$  is the Faraday constant, and  $n$  is the number of electrons transferred during the redox event. In fact, when the mass transport process is faster than the electron transfer process, the cyclic voltammogram curve will change to that of an irreversible electrochemical system. The total charge consumed at the surface of the electrode during the electrochemical reaction can be calculated as the area under the cyclic voltammogram.<sup>8, 30</sup> In reversible electrochemical reactions, the rate of electron transfer is similar in both directions (forward and reverse) and the separation of peaks is close to  $59/n$  mV, where  $n$  is the number of electrons involved in the reaction. One of the characteristics for a reversible process is that the peak potentials will not undergo any shift when the scan rate is altered.

The molar coverage of polymer film per unit area can be determined via **equation 2.4**

$$\Gamma = Q/nFA$$

**Equation 2.4**

Here,  $F$  is the Faraday constant ( $C \text{ mol}^{-1}$ ),  $\Gamma$  is the molar coverage ( $\text{mol cm}^{-2}$ ),  $A$  is the working electrode area which is covered by the film ( $\text{cm}^2$ ), and  $n$  is the number of electrons which are lost from monomer during polymerization. The value of the molar coverage is used to calculate the thickness of the film from **equations 2.5** and **2.6** when molar mass and density are known. Here,  $\rho$  and  $c$  are the density and concentration of the monomer units, respectively, and  $Mr$  is the molecular mass.  $h_f$  is the thickness of the film.<sup>31, 32</sup>

$$C = \frac{\rho}{Mr} \quad \text{Equation 2.5}$$

$$h_f = \frac{\Gamma}{c} \quad \text{Equation 2.6}$$

### 2.2.2 Chronoamperometry

The second technique which can be used in analytical electrochemistry is chronoamperometry. Chronoamperometry is considered an appropriate technique to examine the kinetics of a system, as noted by Gerischer and Vielstich in 1955.<sup>33</sup> It is also used to determine diffusion coefficients, phase transitions and relaxation. This technique is based on applying a fixed potential to the working electrode in order to deposit a polymer film on its surface.<sup>34</sup> Moreover, chronoamperometry can provide information regarding growth processes and nucleation within a system.<sup>35</sup> The current-time curve provides information such as charge and amount of deposition. Here, when a potential is applied to the working electrode in an unstirred solution, it can be noted that the potential will jump immediately from a value,  $E_1$ , where an electrochemical reaction does not occur, to another potential value,  $E_2$ , which represents the point where the electrochemical reaction occurs at the electrode, as shown in **Figure 2.4**. From this kind of experiment, one can measure the reaction rate.<sup>8</sup> Another advantage of this technique is that one can determine the diffusion coefficient of an electrochemical system.<sup>19</sup> Any electroactive species in contact with the surface of the electrode will be immediately oxidized. Therefore, the concentration of electroactive species at the electrode surface will be zero, and the species will then diffuse towards the electrode. With time, the concentration of the electroactive species will be depleted near the electrode.<sup>36</sup> Applying a potential to the system leads to the consumption of all electroactive species at the film/substrate interface. At the beginning of the experiment the current is very high, but after few moments it will decrease rapidly, approaching zero as the electroactive species at electrode surface is fully depleted. The decay of the current in chronoamperometry is proportional to  $t^{-1/2}$ , as can be seen in the Cottrell equation.<sup>36</sup>

$$i = nFAC_{\infty} (D/\pi t)^{1/2} \quad \text{Equation 2.8}$$

Here,  $D$  is the diffusion coefficient and  $C_{\infty}$  is the concentration. The gradient of a plot of  $i$  vs.  $t^{-1/2}$  allows for the determination of the diffusion coefficient,  $D$ .

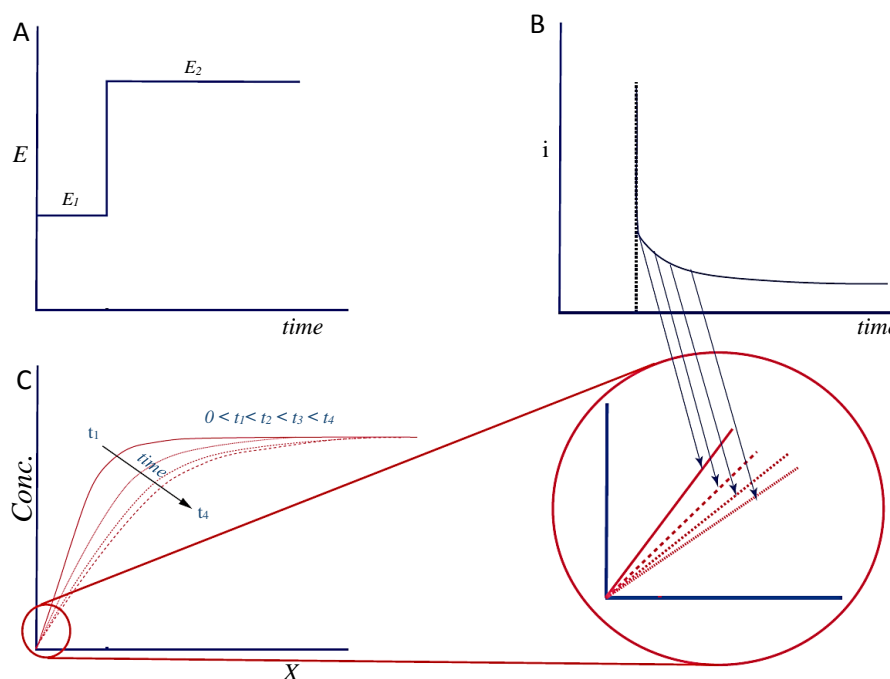


**Figure 2.4:** (A) Chronoamperometry diagram. (B) Chronoamperometric curve. (C) Concentration profile for times in chronoamperometry experiment.

### 2.3 Quartz crystal Microbalance (QCM)

The quartz crystal microbalance (QCM) is a powerful electroanalytical tool in the measurement of mass/frequency changes due to formation of films on an electrode, the viscoelastic properties of deposited films, and the investigation of certain other physical properties of substances.<sup>37, 38</sup> It is an extremely sensitive device, capable of detecting mass changes down to the nanogram level. The QCM technique has become an active contributor, along with other electrochemical techniques, and today is highly considered within the electrochemistry community. This technique can be considered as a gravimetric analytical tool (quantitatively) or can act as the working electrode in an electrochemical system.<sup>39</sup> This small, powerful tool consists of a very thin quartz crystal wafer cut to a particular shape. The quartz crystal wafer used in the QCM technique has two noble metal surfaces (Au or Pt.) coating opposite sides of a crystal wafer, as shown in **Figure 2.5**. These electrode surfaces have two uses: (1) as the working electrode in an electrochemical cell,<sup>40</sup> (2) to allow for an alternating current through the crystal. This technique has a wide variety of applications.<sup>41</sup> The basis of this technique relies on the changes which occur in piezoelectric resonators that are sensitive to changes in frequency and mass.

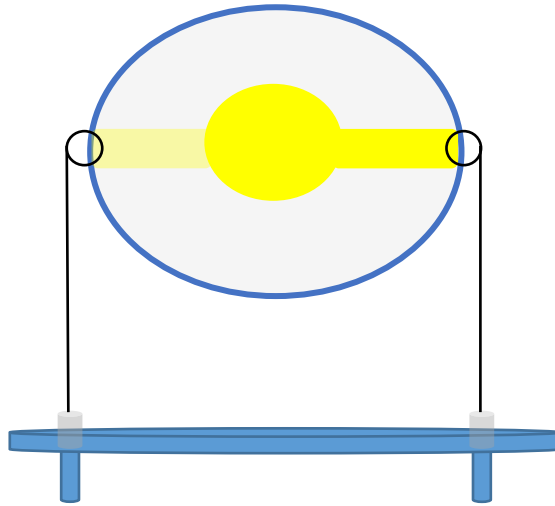


**Figure 2.5:** Scheme representing a typical piezoelectric crystal coated with gold.

### 2.3.1 The Piezoelectric Effect

The discovery of the relationship between the piezoelectric effect and crystal structure date back to the end of the nineteenth century with Jacques and Pierre Curie. They indicated that a mechanical tension applied to the surface of a crystal generates an electrical potential over the crystal; this electrical potential is proportional to the applied tension, which is known as the *direct piezoelectric effect*.<sup>42</sup> The application of the stress that, when applied to crystal surface, will produce a charge similar to that obtained when the displacement of atoms creates a dipole shift. Conversely, the application of an adequate electrical potential over a small crystal produces a symmetric displacement (*converse piezoelectric effect*),<sup>43</sup> as shown in **Figure 2.6**.



**Figure 2.6:** Schematic representation of the converse piezoelectric effect.

Generally, many types of crystal display piezoelectric behaviour, such as quartz, rochelle salts, tourmaline, lead zirconate and barium/lead titanate. Among these types, quartz is the most commonly used material to date because of its high stability, high sensitivity, low cost, elastic deformation properties, and the fact that it is chemically inert. Quartz is

a perfect candidate to utilize in stable oscillator devices where it shows piezoelectric vibrations in diverse directions. **Figure 2.7** shows a typical natural form of quartz.<sup>44</sup>

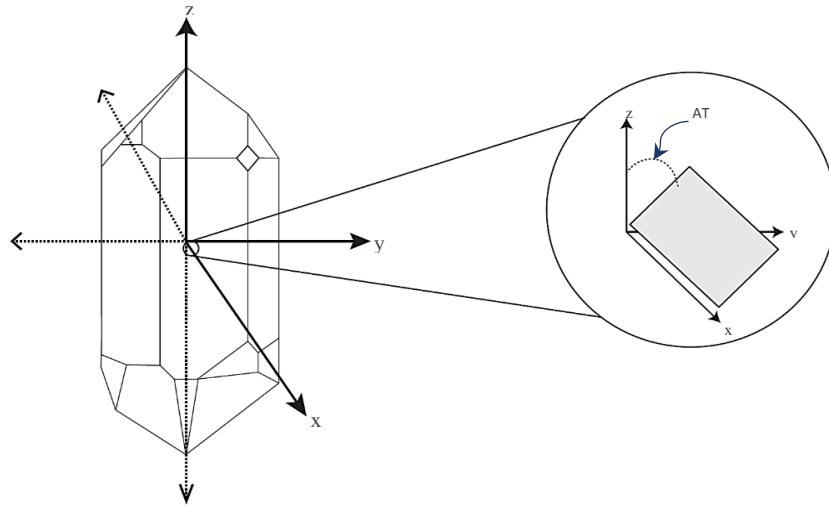


**Figure 2.7:** Schematic diagram showing the assignment of the axes to a quartz block (left) and cutting angle of AT-cut quartz crystal plate.

### 2.3.2 The Mass – Frequency Relationship

In the 1940s, Lord Rayleigh examined the relationship between frequency and mass, pointing out the inverse relationship between the vibration of the body mass and the resonant frequency of the crystal.<sup>28</sup> In 1959, Sauerbrey reported the first mathematical means of considering the sensitivity of a quartz crystal oscillator to mass,<sup>45</sup> also explaining the relationship between the change in mass and the shift in fundamental frequency of the quartz crystal.<sup>29</sup> Scientists have exploited equation 2.9 in order to determine changes in mass for various systems. For example, the surface of a crystal which has been coated using a sensitive film can allow for the recognition of trace ions in the system under study.<sup>46</sup> Sauerbrey reported that the change in the resonant frequency of the quartz crystal,  $\Delta f$ , can be used to calculate the extra mass that has been deposited onto its surface,  $\Delta m$ :<sup>47,39</sup>

$$\Delta f = - \frac{2f_0^2}{A\sqrt{\rho_q\mu_q}} \Delta m \quad \text{Equation 2.9}$$

Here,  $\Delta f$  is the observed resonant frequency change,  $f_0$  is the fundamental resonant frequency,  $A$  is the active electrode area ( $\text{cm}^2$ ),  $\rho_q$  is the density of quartz ( $2.648 \text{ g cm}^{-3}$ ),

$\mu_q$  is the shear modulus of quartz ( $2.947 \times 10^{10} \text{ Nm}^{-2}$ ), and  $\Delta m$  is the change in surface mass.

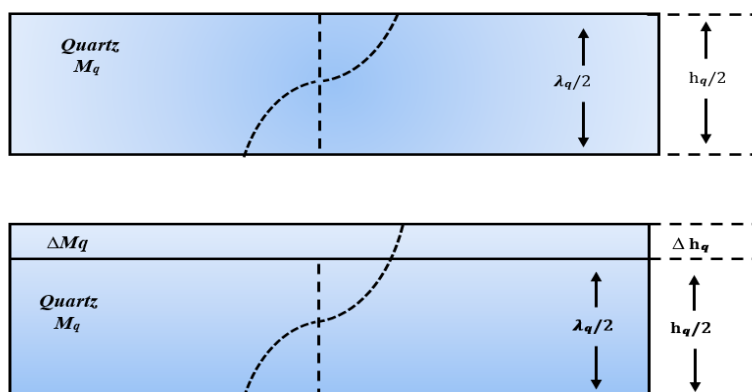


**Figure 2.8:** Schematic representation of a thickness – shear mode resonator. a) The thickness of quartz plate,  $h_q$ , is related to acoustic wavelength,  $\lambda_q$ ; b) an increase in quartz thickness,  $h_q$ , results in an increase in the wavelength,  $\lambda_q$ .

However, there are some limitations to the Sauerbrey equation related to the film thickness and viscoelastic effects of the polymer film such that equation 2.9 can only be applied for rigid and thin polymer films, and analysis of the Sauerbrey equation reveals that the change in the frequency of the quartz crystal during examination must be not be greater than 20% for the equation to hold.<sup>48</sup> Another restriction in applying the Sauerbrey equation is that the polymer film must be thin and uniform over the active areas on the quartz crystal.<sup>49</sup>

### 2.3.3 Electrochemical Quartz Crystal Microbalance

Most electrochemical processes, like electrodeposition, are accompanied by a change in mass at the surface electrode/solution interface. Therefore, the combination of electrochemical measurements and mass sensitive devices will obviously be beneficial. EQCM is a powerful and sensitive technique that can be used to control changes in mass of surface films during electrochemical experiments via the incorporation of the quartz crystal technique into an electrochemical device. The first attempt at such a combination was published in 1981, and was used to detect silver deposition via the QCM technique.<sup>36</sup> Four years later, Bruckenstein and Shay<sup>37</sup> published the first report of an empirical experiment that incorporated electrochemical methods with QCM. Over the subsequent 30 years, QCM has become a vital tool in the examination of the solid/liquid interface as a result of its speed of data acquisition ( $< 0.1 \text{ s}$ ) with high sensitivity down to the nanogram level.<sup>50</sup> This feature has led to QCM becoming an invaluable tool in the

examination of liquid properties and solid-liquid interfaces.<sup>51</sup> Given the above, this technique is now used in many areas such as polymer film characterisation,<sup>52</sup> recognition of metal ions,<sup>53</sup> metal reduction,<sup>54</sup> the study of metal deposition, adsorption of biomolecules on self-assembled monolayers,<sup>55</sup> and monolayer adsorption on diverse metals.<sup>56</sup> Furthermore, EQCM has been exploited in the removal of heavy ions from aqueous solutions using the exchange properties between modified polymer electrodes and the electrolyte solution.<sup>57</sup> The precipitation of electroactive polymer films and ion/solvent exchange through the redox processes of prepared films has been extensively reported in the literature.<sup>58-61</sup> In this technique, one side of the crystal will be directly linked to the electrolyte solution for use as the working electrode, while the second side is exposed to air.<sup>62</sup>

## 2.4 Microscopy and Imaging Techniques

The characterization of polymer surfaces is important in the understanding of a number of polymerisation processes. The analysis of morphology and topography of the surfaces of polymer film electrodes is useful in the study of nucleation and growth mechanisms of polymers on electrode substrates during synthesis.<sup>63</sup> There are many imaging techniques that can be used in this field, but the most commonly used are Scanning Electron Microscopy (SEM) and Atomic Force Microscopy (AFM).<sup>64</sup>

### 2.4.1 Scanning Electron Microscopy (SEM)

SEM can be used to generate high-resolution images of the polymer surface electrode within a high vacuum environment. A beam of electrons, with energies up to 50 keV, is focused on the surface. These electrons will penetrate the sample surface (to a few micrometres depth) and will interact with the associated atoms. This process will generate secondary electrons that are ejected from the surface and are subsequently detected to produce a 2D image of the surface. SEM is one of the most popular techniques used to investigate and examine the surface structures of various materials. This interaction with the surface of the sample and can produce different results such as back-scattered electrons, transmitted electrons and X-rays.<sup>65, 66</sup>

This technique provides high resolution pictures of the electrode at resolutions approaching 10 nm.<sup>67</sup> During this process, the beam of electrons used to scan the surface will be focused by special lenses to form a spot with a diameter of only a few nanometres.

The sample is then bombarded with electrons to a few micrometres depth, producing secondary electrons. The next step is the detection of these secondary electrons, which have originated near the surface, to obtain 2D images.<sup>68</sup> SEM depends on the use of electrons instead of light to allow for surface imaging of polymer film electrodes.<sup>69, 70</sup> It can be used to study a large sample whilst at same time still obtaining high resolution images. The gun produces an electronic beam that is accelerated to energies of 30 keV using an anode. A set of condenser lenses will focus these electrons to a spot with a diameter ranging between 0.4 - 100 nm. Two electromagnetic coils are located directly under the lens. One of these can be used to deflect the beam in the  $x$ -direction, whilst the other deflects the beam in the  $y$ -direction. After this, the electrons will cover all areas on the sample surface, and the secondary electrons will be ejected from the sample surface. The secondary electron current is then recorded, using a detector to create an image. A schematic diagram of the SEM instrumentation is shown in **Figure 2.9**. Generally, there are a number of requirements to working with SEM, such as the sample should be conductive and the operation needs to be conducted in a vacuum environment.<sup>71</sup>

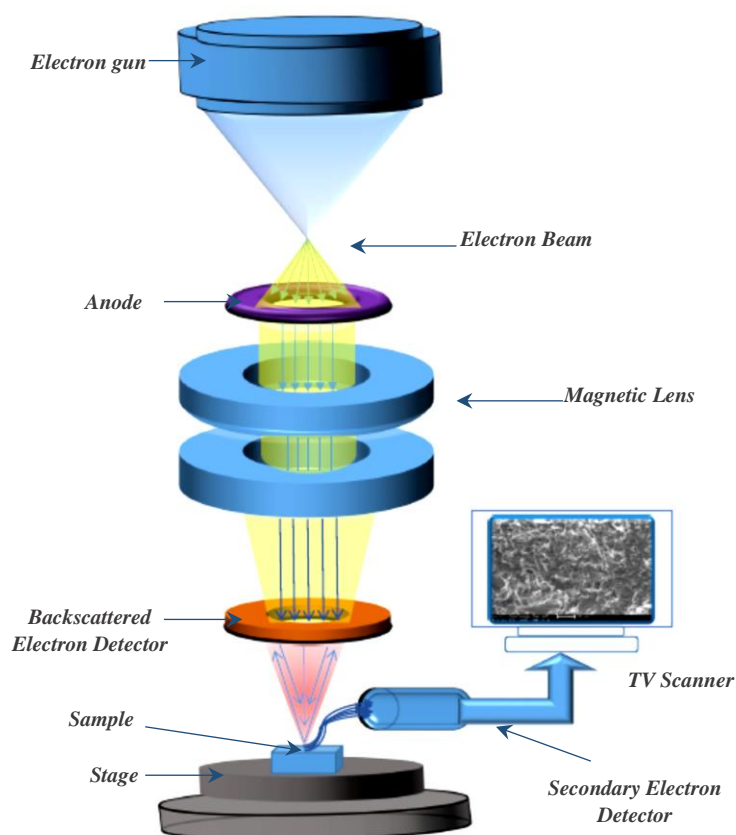


**Figure 2.9:** Schematic representation of the two main parts of a scanning electron microscope, the electron column and electronic console.

### 2.4.2 Atomic Force Microscopy (AFM)

AFM is a method used to obtain a topographical image of a sample surface, and is generally utilized in the morphological characterisation of conducting polymer films.<sup>72-</sup>  
<sup>76</sup> This technique is used to measure surface topography, giving high-resolution images down to the nanometre scale. The changes in the thickness of the surface being examined cause a cantilever to deflect up or down.<sup>77</sup> A probe with a sharp tip is connected to a cantilever located on a scanner that is scanned over the surface along an arbitrary  $x$ -plane to record heights at each point on the sample surface; the probe will then examine the adjacent line. This process will be repeated to cover the entirety of the desired surface area. The monitoring of the cantilever's movement is achieved through a laser beam which detects motion which is reflected from a mirror. A schematic diagram of AFM can be seen in **Figure 2.10**. The implementation of the AFM process can be accomplished through three different approaches: contact mode, tapping mode and non-contact mode. In contact mode, which is destructive, the tip is scanned over the sample surface. Non-contact mode requires a tiny distance between the sample surface and probe that ranges in size between 500 and 1500 nm. In tapping mode, the interatomic forces between the surface and the sharp tip leads to deflection of the cantilever according to changes in the surface topography of the sample. The measurement of the deflection of the cantilever in AFM can be achieved by determining the amount by which the laser deviates from the cantilever. One of the advantages of AFM is that it does not require the sample to be conductive, as in SEM. Another advantage is that the surface does not need a complex preparation process.<sup>78-82</sup>

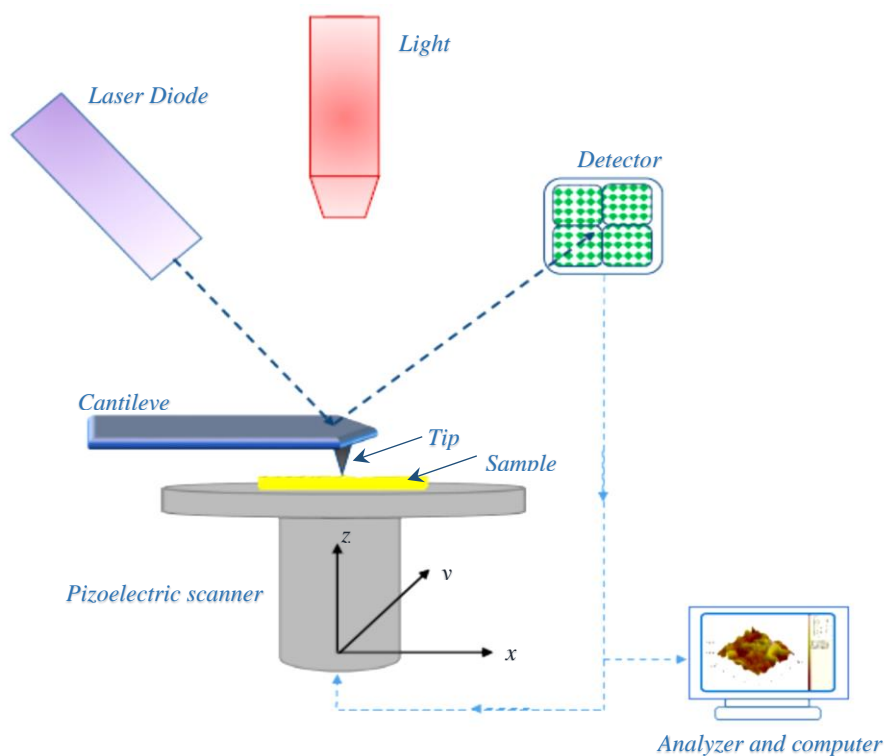


*Figure 2.10: Schematic representation of AFM*

## 2.5 Fourier Transform Infrared Spectroscopy

Infrared spectroscopy is a powerful tool used in the identification of organic and inorganic compounds depending on the vibrational movements and orientation of molecular bonds. These vibrations offer information about the composition and nature of a range of compounds, including polymer films.<sup>83, 84</sup> The FTIR spectrum depends on the absorption and transmission of infrared radiation by the molecules in the sample. This technique is considered a valuable tool in structural elucidation and provides useful data about the polymeric chains and functional groups in polymer films.<sup>85</sup> Absorption of infrared radiation from molecules leads to a change in the vibrational mode of these molecules. Different molecular vibrations lead to the unique frequencies and, therefore, wavenumbers values that can be observed in the IR spectrum. Therefore, the observed infrared bands can be used to distinguish the functional groups existing within the target compound. There are diverse styles of vibrational bonds which can be generated by IR frequencies, such as stretching, wagging and bending, and indeed other more complex motions in larger species. For our purposes, the FTIR technique can provide specific information about the structure of polymer backbones and detect any changes in functional groups on the polymer film surfaces.<sup>86, 87</sup>

## 2.6 References

1. M. Nuñez, *New Topics in Electrochemistry Research*, Nova Science, 2006, p.Vii.
2. R. M. Sapstead, Ph.D thesis University of Leicester, 2014.
3. M. A. Mohamoud, Ph.D Thesis, University of Leicester, 2007.
4. L. Gao, X. Mao, W. Xiao, F. Gan and D. Wang, *Electrochimica Acta*, 2014, **136**, 97-104.
5. X. Feng, N. Gan, H. Zhang, Q. Yan, T. Li, Y. Cao and Q. Jiang, *Electrochimica Acta*, 2015, **170**, 292-299.
6. M. Ates, *Materials Science and Engineering: C*, 2013, **33**, 1853-1859.
7. U. Vanamo and J. Bobacka, *Electrochimica Acta*, 2014, **122**, 316-321.
8. A. J. Bard and L. R. Faulkner, *Electrochemical Methods: Fundamentals and Applications*, Wiley, 2000, p.28.
9. D.T. Sawyer, J.L. Roberts, and A. Sobkowiak, *Electrochemistry for Chemists*, Willey, New York, 1995, p.36.
10. C. Tobias, M. Eisenberg and C. Wilke, *Journal of the Electrochemical Society*, 1952, **99**, 359C-365C.
11. D. Pletcher, R. Greff, R. Peat, L. M. Peter and J. Robinson, *Instrumental Methods in Electrochemistry*, Elsevier, 2001, p. 26.
12. J. Wang, *Analytical Electrochemistry*, Wiley, 2004, pp.29
13. M. Barbooti, *Environmental Applications of Instrumental Chemical Analysis*, CRC Press, 2015, p.166.
14. W. Wu, D. Pan, Y. Li, G. Zhao, L. Jing and S. Chen, *Electrochimica Acta*, 2015, **152**, 126-134.
15. R. S. Nicholson, *Analytical Chemistry*, 1965, **37**, 1351-1355.
16. A. J. Bard and L. R. Faulkner, *Electrochemical Methods, 2nd ed.*; Wiley: New York, 2001.
17. S. Abaci, B. Nessark, R. Boukherroub and K. Lmimouni, *Thin solid films*, 2011, **519**, 3596-3602.
18. Q. Cheng and A. Brajter-Toth, *Analytical Chemistry*, 1992, **64**, 1998-2000.
19. L. Moretto and K. Kalcher, *Environmental Analysis by Electrochemical Sensors and Biosensors: Fundamentals*, Springer, New York, 2014, p.267.
20. R. E. White, *Modern Aspects of Electrochemistry 45*, Springer, New York, 2009.
21. C. Braungardt, E. P. Achterberg and M. Nimmo, *Analytica Chimica Acta*, 1998, **377**, 205-215.
22. D. Pletcher, *A First Course in Electrode Processes*, Royal Society of Chemistry, 2009.
23. J. Sondag-Huethorst and L. Fokkink, *Langmuir*, 1995, **11**, 2237-2241.
24. M. Ertas, R. M. Walczak, R. K. Das, A. G. Rinzler and J. R. Reynolds, *Chemistry of Materials*, 2012, **24**, 433-443.
25. G. Hughes, PhD thesis, University of the West of England, 2015.
26. F. A. Settle, *Handbook of Instrumental Techniques for Analytical Chemistry*, Prentice Hall PTR, 1997.
27. A. J. Bard and I. Rubenstein, *Electroanalytical Chemistry: A Series of Advances*, Taylor and Francis, 1996.
28. P. K. Rai and B. Tripathi, *Toxicological and Environ Chemistry*, 2008, **90**, 247-257.
29. R. Cornelis, J. Caruso, H. Crews and K. Heumann, *Handbook of Elemental Speciation: Techniques and Methodology*, Wiley, 2004, p. 436.
30. F. Scholz, *Electroanalytical Methods*, Springer, 2010, pp.136.
31. R. M. Sapstead, N. Corden and A. R. Hillman, *Electrochimica Acta*, 2015, **162**, 119-128.

32. R. M. Brown and A. R. Hillman, *Physical Chemistry Chemical Physics*, 2012, **14**, 8653-8661.
33. H. Gerischer and W. Vielstich, *Z. Physical Chemistry*, 1955, **3**, 16-33.
34. P. Chandrasekhar, *Conducting Polymers, Fundamentals and Applications: A Practical Approach*, Springer, USA, 1999.
35. A. R. Hillman and E. F. Mallen, *Journal of Electroanalytical Chemistry and Interfacial Electrochemistry*, 1987, **220**, 351-367.
36. C. G. Zoski, *Handbook of Electrochemistry*, Elsevier, 2007, p.836.
37. Z. Jusys, S. Bruckenstein and A. R. Hillman, *Physical Chemistry Chemical Physics*, 2011, **13**, 5373-5382.
38. M. M. Barsan, E. Pinto and C. Brett, *Physical Chemistry Chemical Physics*, 2011, **13**, 5462-5471.
39. A. R. Hillman, D. C. Loveday, A. Glidle, J. G. Vos, A. P. Clarke, D. Kelly and S. Bruckenstein, *Electrochemical Quartz Crystal Microbalance Studies of Redox Polymer Films*, 1994.
40. M. R. Deakin and D. A. Buttry, *Analytical Chemistry*, 1989, **61**, 1147A-1154A.
41. M. Pontié, C. Gobin, T. Pauporté, F. Bedioui and J. Devynck, *Analytica Chimica Acta*, 2000, **411**, 175-185.
42. J. Curie and P. Curie, *Comptes Rendus*, 1880, **91**, 294-295.
43. J. Curie and P. Curie, *Comptes-Rendus de l'Académie des Sciences*, 1881, **93**, 1137-1140.
44. C. Lu and A. Czanderna, *Applications of Piezoelectric Quartz Crystal Microbalances*, Elsevier, 2012.
45. G. Sauerbrey, *Zeitschrift für Physik*, 1959, **155**, 206-222.
46. J. Hlavay and G. G. Guilbault, *Analytical Chemistry*, 1977, **49**, 1890-1898.
47. V. Mecea, *Sensors and Actuators A: Physical*, 2006, **128**, 270-277.
48. C. S. Lu and O. Lewis, *Journal of Applied Physics*, 1972, **43**, 4385-4390.
49. M. D. Ward and E. J. Delawski, *Analytical Chemistry*, 1991, **63**, 886-890.
50. K. K. Kanazawa and J. G. Gordon, *Analytica Chimica Acta*, 1985, **175**, 99-105.
51. A. R. Hillman, *Encyclopedia of Electrochemistry*, 2003.
52. M. Skompska and A. Hillman, *Journal of Electroanalytical Chemistry and Interfacial Electrochemistry*, 1997, **433**, 127-134.
53. S.-Z. Yao, P. Chen and W.-Z. Wei, *Food chemistry*, 1999, **67**, 311-316.
54. T. Nomura, M. Kumagai and A. Sato, *Analytica Chimica Acta*, 1997, **343**, 209-213.
55. A. Olivier, F. Meyer, J.-M. Raquez, P. Damman and P. Dubois, *Progress in Polymer Science*, 2012, **37**, 157-181.
56. J. Rickert, T. Weiss, W. Kraas, G. Jung and W. Göpel, *Biosensors and Bioelectronics*, 1996, **11**, 591-598.
57. M. Hepel, Z. Xingmin, R. Stephenson and S. Perkins, *Microchemical Journal*, 1997, **56**, 79-92.
58. G. Inzelt, M. Pineri, J. Schultze and M. Vorotyntsev, *Electrochimica Acta*, 2000, **45**, 2403-2421.
59. M. Jafeen, M. Careem and S. Skaarup, *Ionics*, 2014, **20**, 535-544.
60. W. Plieth, A. Bund, U. Rammelt, S. Neudeck and L. Duc, *Electrochimica Acta*, 2006, **51**, 2366-2372.
61. C. Barbero, E. Calvo, R. Etchenique, G. Morales and M. Otero, *Electrochimica Acta*, 2000, **45**, 3895-3906.
62. S. Bruckenstein and M. Shay, *Electrochimica Acta*, 1985, **30**, 1295-1300.
63. C. Musumeci, J. A. Hutchison and P. Samorì, *Nanoscale*, 2013, **5**, 7756-7761.
64. K. Grundke, M. Stamm and H. Adler, *Characterization of Polymer Surfaces and Thin Films*, Springer, 2006.
65. F. Guler and A. Sarac, *Express Polymer Letters*, 2011, **5**.

66. A. Madani, B. Nessark, R. Boukherroub and M. Chehimi, *Journal of Electroanalytical Chemistry and Interfacial Electrochemistry*, 2011, **650**, 176-181.
67. S. R. Byrn, G. Zografí and X. Chen, *Solid-State Properties of Pharmaceutical Materials*, Wiley, 2017.
68. D. Dhawale, R. Salunkhe, V. Jamadade, D. Dubal, S. Pawar and C. Lokhande, *Current Applied Physics*, 2010, **10**, 904-909.
69. I. S. Chronakis, S. Grapenson and A. Jakob, *Polymer*, 2006, **47**, 1597-1603.
70. G. Tourillon and F. Garnier, *Journal of Polymer Science: Polymer Physics Edition*, 1984, **22**, 33-39.
71. S. Armes, M. Aldissi, M. Hawley, J. Beery and S. Gottesfeld, *Langmuir*, 1991, **7**, 1447-1452.
72. S. Cetiner, F. Kalaoglu, H. Karakas and A. Sarac, *Polymer composites*, 2011, **32**, 546-557.
73. J. S. Mondschein, A. Kowalski, J. D. Kehlbeck, M. E. Hagerman and R. Cortez, *Materials Letters*, 2014, **131**, 262-265.
74. T. Silk, Q. Hong, J. Tamm and R. G. Compton, *Synthetic metals*, 1998, **93**, 59-64.
75. A. B. Sanghvi, K. P.-H. Miller, A. M. Belcher and C. E. Schmidt, *Nature Materials*, 2005, **4**, 496-502.
76. S. N. Magonov and D. H. Reneker, *Annual Review of Materials Science*, 1997, **27**, 175-222.
77. V. Ferreira, A. Tenreiro and L. Abrantes, *Sensors and Actuators B: Chemical*, 2006, **119**, 632-641.
78. A. Eftekhari, *Nanostructured Conductive Polymers*, Wiley, 2011, p.65.
79. H. Yang, *Atomic Force Microscopy (AFM): Principles, Modes of Operation and Limitations*, Nova Science, 2014.
80. G. Haugstad, *Atomic Force Microscopy: Understanding Basic Modes and Advanced Applications*, John Wiley and Sons, 2012, pp.3-5.
81. G. Friedbacher and H. Bueber, *Surface and Thin Film Analysis: A Compendium of Principles, Instrumentation, and Applications*, Wiley, 2011, p.443.
82. V. Mittal, *Characterization Techniques for Polymer Nanocomposites*, Wiley, 2012, pp.185.
83. P. A. Christensen, A. Hamnett, A. R. Hillman, M. J. Swann and S. J. Higgins, *Journal of the Chemical Society, Faraday Transactions*, 1992, **88**, 595-604.
84. K. S. Ryder, D. G. Morris and J. M. Cooper, *Langmuir*, 1996, **12**, 5681-5688.
85. R. M. Silverstein, F. X. Webster, D. J. Kiemle and D. L. Bryce, *Spectrometric Identification of Organic Compounds*, Wiley, 2014, pp.71.
86. S. Patil, K. Harpale, S. Koiry, K. Patil, D. Aswal and M. More, *Journal of Applied Polymer Science*, 2015, **132**, 41401.
87. R. Deka, M. M. Bora, M. Upadhyaya and D. K. Kakati, *Journal of Applied Polymer Science*, 2015, **132**, 41600.

**Chapter three****Experimental**

<b>3.1 Introduction.....</b>	<b>49</b>
<b>3.2 Reagents and materials .....</b>	<b>49</b>
<b>3.3 Instrumentation .....</b>	<b>50</b>
3.3.1 Electrochemical methods .....	50
3.3.1.1 Cyclic Voltammetry .....	50
3.3.1.2 Chronoamperometry .....	52
3.3.1.3 Electrochemical Quartz crystal microbalance (EQCM).....	52
3.3.2 Non-Electrochemical Measurements .....	53
3.3.2.1 Scanning Electron Microscopy (SEM).....	53
3.3.2.2 Zeta-200 Optical Profiler.....	53
3.3.2.3 Atomic Force Microscopy (AFM).....	53
3.3.2.5 Infrared Spectroscopy (FTIR) .....	54
<b>3.4 Preparation of patterned polymer electrodes .....</b>	<b>54</b>
<b>3.5 Preparation of metal ion solutions .....</b>	<b>54</b>
<b>3.6 Procedures .....</b>	<b>55</b>
3.6.1 Monomer Synthesis .....	55
3.6.2 Electropolymerisation of polymer films.....	60
3.6.3 FTIR characterisation of compounds .....	61
<b>3.7 References.....</b>	<b>67</b>

### 3.1 Introduction

This chapter offers a brief description of the experimental work undertaken, including the general analytical, material and sample preparation techniques used to gain the results presented in chapters four to seven. More specific details, such as that regarding the electropolymerisation of conducting polymer films and characterization of functionalised polymer electrodes and the patterning technique, will be discussed in the following results chapters. Several functionalised polymer electrodes were prepared using pyrrole, aniline and thiophene derivatives. These polymer films were synthesized by electrochemical polymerisation of a suitable monomer at either gold or platinum electrodes.

### 3.2 Reagents and materials

Table 3.1 gives a list of chemicals used in this thesis. Their commercial sources and purities can also be found in this table. All materials in **Table 3.1** were used as received without further purification. All aqueous solutions were prepared using deionised water.

compound	Supplied company	Purity%
1-(2-cyanoethyl)pyrrole	Sigma Aldrich	99
sodium hydroxide	BDH	97.5
sulphuric acid	Fisher Scientific	95
diethyl ether	Fisher Scientific	99
MgSO <sub>4</sub>	Fisher Scientific	99
LiClO <sub>4</sub>	Sigma Aldrich	99
TPAB	Sigma Aldrich	98
acetonitrile	Fisher Scientific	99
LiAlH <sub>4</sub>	Fisher Scientific	95
HBF <sub>4</sub>	Sigma Aldrich	48
HClO <sub>4</sub>	BDH	60
dicyclohexylcarbodiimide dcc	Fisher Scientific	99
pentafluorophenol	Fisher Scientific	99
Hexane	Fisher Scientific	99
Fmoc-Cl	Sigma Aldrich	97

dioxane	Sigma Aldrich	99
Na <sub>2</sub> CO <sub>3</sub>	BDH	99.5
ethyl acetate	Fisher Scientific	99
piperidine	Sigma Aldrich	98
3-(2-carboxyethyl) aniline	Alfa Aesar	97
3-(aminomethyl)aniline	Fisher Scientific	98
aniline	Sigma Aldrich	99
di-tert-butyl dicarbonate) Boc <sub>2</sub> O	Fisher Scientific	99
acetic acid	Fluka	99
dichloromethane	Fisher Scientific	99
trifluoroacetic acid	Fluka	98
3-thiopheneacetic acid	Alfa Aesar	98
tetrabutylammonium hexafluoroborate	Sigma Aldrich	98
3-thiophene acetonitrile	Alfa Aesar	98

*Table 3.1: List of chemicals which used in this thesis*

### 3.3 Instrumentation

Various experimental techniques have been used in this project, including cyclic voltammetry, chronoamperometry and EQCM, which were used to study and control the electropolymerisation of conducting polymers/copolymers and ion exchange of polymer films in aqueous media. Furthermore, SEM, AFM, 3D microscopy and FTIR were also used for the characterisation of the polymer films. All laboratory experiments were carried out in a standard cell that included three electrodes. The gold (or platinum) electrode was used as the working electrode, the platinum sheet was used as the counter electrode and Ag/AgCl was used as the reference electrode (RE).

#### 3.3.1 Electrochemical methods

##### 3.3.1.1 Cyclic Voltammetry

Under experimental conditions, the potential is applied to the working electrode with the counter electrode completing the electrical circuit. The charge transfer process to the

surface of the electrode is a heterogeneous one.<sup>1</sup> The study and analysis of prepared polymer films was undertaken via various techniques. The first was that of cyclic voltammetry, where an Auto Lab PGSTAT20 potentiostat controlled by GPES software (Ecochemie, Holland) was used with a three-electrode cell (gold or platinum as the working electrode, Ag/AgCl as the reference electrode, and a platinum flag as the counter electrode). Cyclic voltammetry used various potential windows vs. Ag/AgCl depending on the type of monomer, and using different supporting electrolyte solutions at various scan rates of 5, 10, 20, 50, and 100 mV s<sup>-1</sup>. All experiments were performed under surrounding conditions at room temperature 20°C (± 2).

There are two kinds of working electrode, Au and Pt, that were used for all experiments. The Au working electrode was built in-house at the University of Leicester, with a 0.7 mm<sup>2</sup> surface area that was covered by glass and araldite; the Pt electrode, also built in-house, was made using the same method and had a 1 mm<sup>2</sup> surface area. The second type of working electrode was located on the AT-cut quartz crystal surfaces as described in chapter two, which were employed for the EQCM measurements. The AT-cut quartz crystal included two gold (Au) faces or one gold and one platinum (Pt) face, which are used as working electrodes. (International Crystal Manufacturing Co., Oklahoma City, USA, active area 0.23 cm<sup>2</sup>.)

A platinum flag electrode was used as a counter electrode in all electrochemical experiments. The surface area of the flag electrode was larger than that of the working electrode in all experiments (nearly 2 cm<sup>2</sup>) to avoid the resultant current from any reaction at the counter electrode. To obtain a uniform film on the working electrode during the experiments requires that the counter electrode is positioned parallel to the working electrode. Obtaining a uniform film over the crystal surface during QCM experiments is a fundamental condition for the correct application of the Sauerbrey equation and the detection of mass changes due to the polymer films.<sup>2, 3</sup>

The silver chloride electrode (Ag/AgCl) ( $E = +0.197$  V, saturated, vs. SHE) was used for all experiments in this thesis. This electrode is stable, inexpensive, and easy to use.<sup>4</sup> It contains an Ag wire (99%) covered with an AgCl layer and is held in a saturated (~3.5 M) KCl solution in a glass tube with a porous piece at the bottom. In fact, the internal reaction of the Ag/AgCl electrode takes place between the Ag(s) and AgCl salt.<sup>5</sup>

### 3.3.1.2 Chronoamperometry

Chronoamperometry was performed using an Autolab PGSTAT 20 Potentiostat (Ecochemie, Holland). The three electrodes used in this method similar to those used in cyclic voltammetry experiments. After the experiment had been completed, the polymer film thus prepared was washed with distilled water and acetone. All polymer film depositions were achieved at room temperature,  $25 \pm 2^\circ\text{C}$ , using different times and monomer concentrations.

### 3.3.1.3 Electrochemical Quartz crystal microbalance (EQCM)

This technique was used to record the change in mass/frequency of a QCM wafer in order to determine the mass and the thickness of the polymer film deposit under investigation. Polished 10 MHz AT-cut quartz crystals were used as supplied by International Crystal Manufacturing (ICM) Co. They are comprised of a thin layer of quartz (0.16 mm) placed between two gold or platinum/gold for another crystal film electrodes, which have a thickness of up to 250 nm, as shown in **Figure 3.1**. Electrochemical and quantitative information were recorded simultaneously using a Hewlett Packard 8751A 5 Hz – 500 MHz network analyser conducted with an Autolab III potentiostat, which was used for the electrodeposition and monitoring of all polymer films. The quartz crystal was used as a working electrode, one side of which was exposed to the electrochemical electrolyte; a special Teflon cell was made for EQCM analysis, as shown in **Figure 3.2**. This cell is designed to prevent any leakage of the solution. All experiments were carried out at room temperature. The polished Au and Pt quartz crystals were used in all EQCM measurements to avoid the negative effects of roughness of surface one encounters with the use of unpolished crystals.<sup>6,7</sup>

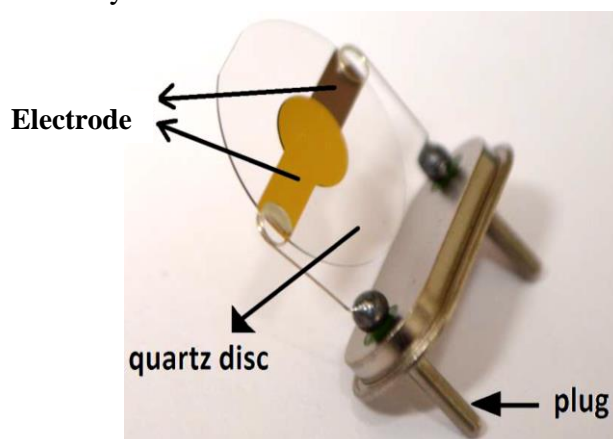


**Figure 3.1:** Au crystal (10 MHz AT-cut polished) which was used as the working electrode in EQCM experiments.

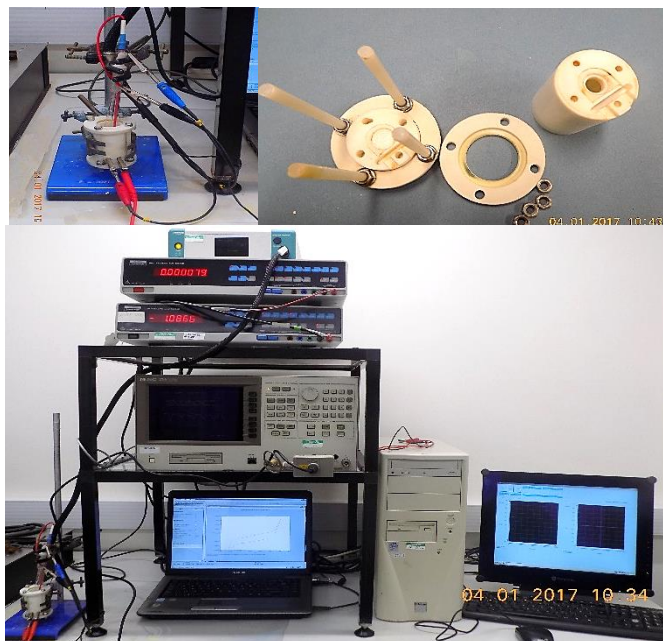


*Figure 3.2: The QCM cell connected to the electrochemical system and the network analyser.*

### 3.3.2 Non-Electrochemical Measurements

#### 3.3.2.1 Scanning Electron Microscopy (SEM)

The surface morphology analysis in this thesis was accomplished using an FEI SIRION SEM. This process was carried out under vacuum ( $10^{-5}$  Pa) conditions using an accelerator voltage that ranged in magnitude between 5 keV and 15 keV without the need for a gold coating on the polymer surfaces.

#### 3.3.2.2 Zeta-200 Optical Profiler

A Zeta-200 optical microscope profiler was used in this thesis to analyse and assess the surfaces of the polymer films and to obtain 3D microscope images. This device is an integrated microscope depending on a system that presents 3D imaging. This tool has the ability to provide images of surfaces which have a very high roughness.

#### 3.3.2.3 Atomic Force Microscopy (AFM)

The AFM used in this thesis was a Digital Instruments Nanoscope IV, Dimension 3100 Scanning Probe Microscope (Veeco Instruments Inc., Santa Barbara, CA), controlled via the Nanoscope version 6.12r1 software (Veeco Instruments Inc., Santa Barbara, CA). The tips used were supplied by Veeco (model: RTESP, part: MPP-11100-10). The calibration

of the instrument was verified by scanning over a silicon reference wafer. The image/scan size was  $1 - 100 \mu\text{m}^2$  and a scan rate of  $0.6 \text{ Hz}/120 \mu\text{m s}^{-1}$  was used.

### 3.3.2.5 Infrared Spectroscopy (FTIR)

FTIR spectra were recorded using a Perkin Elmer Spotlight 400 FTIR imaging system over the region between  $650 - 4000 \text{ cm}^{-1}$ . Additionally, the reflectance mode (at  $20 \pm 2^\circ\text{C}$ ) was used to obtain the spectra that were selected to analyse the films.

## 3.4 Preparation of patterned polymer electrodes

In order to produce the patterned polymer electrodes that were used in later chapters in this thesis, a negative image of a large number of copies of the microfluidic design was drawn in Adobe Illustrator software (Adobe Systems) and converted to the Gerber file format. The image was reproduced at 128,000 dpi on a supported acetate mask layer (JD Photo-Tools). The polymer electrode films were coated with SU-8 2002 (MicroChem Corp.) by spinning at 1500 rpm for 50 seconds and baking at  $90^\circ\text{C}$  for 1 minutes, giving a resist thickness of  $3\mu\text{m}$ . These film-coated electrodes were exposed to a UV light source through a photomask for 10 seconds. They were then baked at  $90^\circ\text{C}$  for 5 min, and the photoresist was developed using AZ developer solvent (MicroChem Corp.) for 90 seconds, and the patterned polymer films thus produced were finally cleaned with acetone.

## 3.5 Preparation of metal ion solutions

Standard solutions (1000 ppm) of each metal ion were prepared by dissolving 3.660 g of copper nitrate (99.9%, Aldrich), 4.955 g of nickel nitrate hexahydrate (99.9%, Aldrich) and 4.938 g of cobalt nitrate hexahydrate (99.9%, Aldrich) in ultra-pure deionised water and diluted to 1 litre. These solutions were used to prepare a series of different concentrations from 1 to 100 ppm for each of the metal ions. All experiments were conducted for individual single metal ion solutions of Cu(II), Ni(II) and Co(II) at the natural pH of the stock solutions (5.4, 5.8 and 5.9 respectively).

## 3.6 Procedures

### 3.6.1 Monomer Synthesis

#### 3.5.1.1 Synthesis of 3-(pyrrol-1-yl)propylamine PyNH<sub>2</sub>

LiAlH<sub>4</sub> (7.58 g, 0.2 mol) was placed in a 250 ml round-bottomed flask containing dry diethyl ether (100 ml) and connected to a condenser. The round-bottom flask was then cooled using an ice bath before the reaction. *N*-cyanoethylpyrrole (5 g, 0.041 mol) was dissolved in dry diethyl ether (50 ml) and was placed in the dropping funnel fitted and connected with the round-bottomed flask and then added slowly to a cold solution containing LiAlH<sub>4</sub> over 30 minutes. The reaction was then left to stir for 20 hours at room temperature. Excess LiAlH<sub>4</sub> was then neutralised using cold water and a 15% NaOH solution. The solution was filtered and dried using MgSO<sub>4</sub>, and then filtered. The solvent was then removed by rotary evaporation yielding 3-(pyrrol-1-yl)propylamine (PyNH<sub>2</sub>) (yellow oil, 78% yield).<sup>8-10</sup>

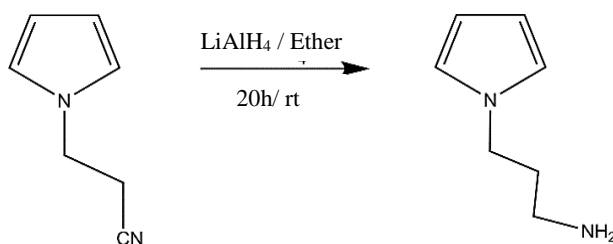


**Figure 3.3:** General reaction schemes for conversion of *N*-cyanoethylpyrrole (PyCN) to 3-(pyrrol-1-yl)propylamine (PyNH<sub>2</sub>)

#### 3.6.1.2 Synthesis of (9H-fluoren-9-yl) methyl-3-(1H-pyrrol-1-yl)propylcarbamate (PyFmoc)

The 3-(pyrrol-1-yl)propylamine (PyNH<sub>2</sub>) (2.5 g, 0.020 mol) was mixed with a solution of Na<sub>2</sub>CO<sub>3</sub> (3 g, 0.028 mol) in a water/dioxane (60 ml, 1:1) mixture in a round-bottomed flask, and then stirred in an ice bath. A Fmoc-Cl (5.2 g, 0.020 mol) in water/dioxane (60 ml, 1:1) mixture was prepared and added to the first solution, and the resultant solution was then stirred at room temperature for 5 hours. After reaction was stopped by the addition of water (50 ml). Py-Fmoc was extracted with ethyl acetate and the solution was dried using MgSO<sub>4</sub>. The solvent was then removed by rotary evaporation, yielding Py-Fmoc (72% yield, white solid). FTIR was used to identify the product Py-Fmoc and showed that all the reactant PyNH<sub>2</sub> had been converted to the product.<sup>11, 12</sup>

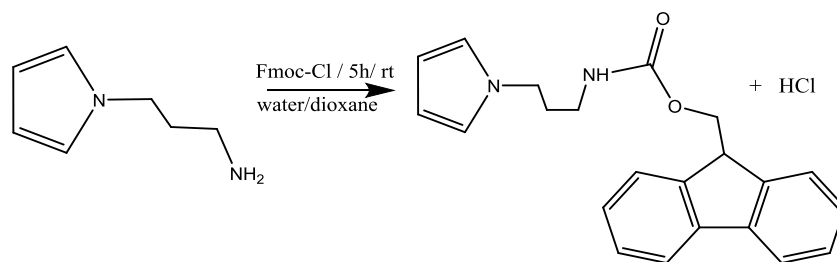


**Figure 3.4:** Schematic of the synthesis of (9H-fluoren-9-yl) methyl-3-(1H-pyrrol-1-yl)propylcarbamate (Py-Fmoc) from N-aminopropylpyrrole (PyNH<sub>2</sub>).

### 3.6.1.3 Synthesis of 1H-Pyrrole-1-propionic acid (Py-COOH)

A 250 ml round-bottomed flask was fitted with a condenser. An aqueous solution of NaOH (8 g, 0.2 mol) was reacted with a 3-(pyrrol-1-yl)propionitrile (5 g, 0.041 mol). The mixture was refluxed until no ammonia evolution was observed. This was tested with indicator paper at the top of the condenser. Then, cold water (25 ml) was added to the mixture and the round-bottomed flask was cooled. Sulphuric acid (50%, 15 ml) was added to mixture to separate the layers. The product was extracted four times with diethyl ether and dried with anhydrous MgSO<sub>4</sub>. The ether was removed by rotary evaporation to yield a waxy solid (77%).<sup>10, 13-15</sup>

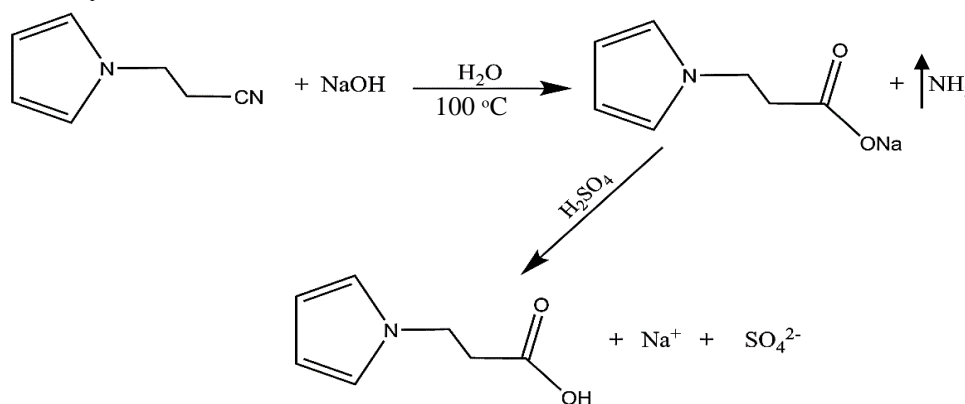


**Figure 3.5:** General reaction scheme for conversion of N-cyanoethylpyrrole (Py- CN) to 3-(pyrrol-1-yl) propanic acid (Py- COOH)

### 3.6.1.4 Coupling of Pentafluorophenol with Py- COOH

A solution of pentafluorophenol (6 g, 0.032 mol) and dicyclohexylcarbodiimide (DCC) (6.7 g, 0.032 mol) and acetonitrile solution (75 ml) was added to a stirred solution of pyrrolpropanoic acid (4.5 g, 0.032 mol) in acetonitrile (25 ml). The mixture was then stirred at room temperature for 20 hours. The white precipitate side reaction (dicyclohexylurea) was filtered off and the acetonitrile was removed under vacuum to yield a golden-coloured oil. This was taken up in hexane and placed in a freezer for about

5 hours. The needles which precipitated out were filtered off and dried under vacuum (83%).<sup>16-19</sup>

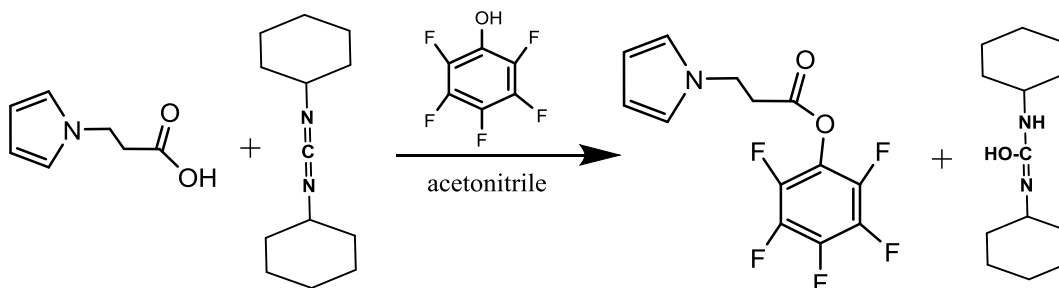


**Figure 3.6:** Schematic of the synthesis of pentafluorophenyl 3-(pyrrol-1-yl)propanoate from 3-(pyrrol-1-yl)propanoic acid (PyCOOH)

### 3.6.1.5 Coupling of Pentafluorophenol with AniCOOH

A coupling reaction between pentafluorophenol and 3-aniline propionic acid was performed under same conditions which were used with 3-(pyrrol-1-yl) propanoic acid (PyCOOH).<sup>19</sup>

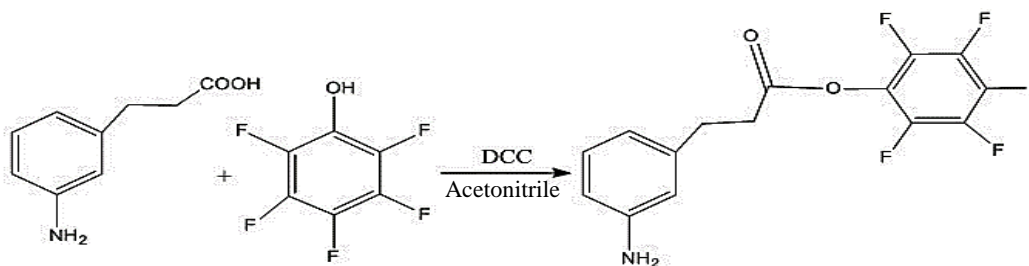


**Figure 3.7:** Schematic of the synthesis of Pentafluorophenyl 3-(3-aminophenyl)propanoate from 3-(3-Aminophenyl) propionic acid

### 3.6.1.6 Monomer formation Aniline-Fmoc

(Aniline-Fmoc) was synthesised in three steps: the first step was the protection of the aromatic amine using (di-tert-butyl dicarbonate) **Boc<sub>2</sub>O**; the aliphatic amine was then protected by using **Fmoc-Cl**; the final step was the deprotection of the aromatic amine group using trifluoroacetic acid to produce the monomer Ani Fmoc, which can be polymerized.

#### Step 1:- protection of aromatic amine

The solution of aminoaniline (2.45 g, 0.02 mol) in 10% acetic acid (20 ml) was added to a solution of **Boc<sub>2</sub>O** (4.3 g, 0.021 mol) in dioxane (20 ml) and the solution was then stirred at room temperature for 24 hours. Water (100 ml) was then added to the mixture and

extracted with diethyl ether (3 x 50 ml). 2 M NaOH was then added to the aqueous phase to gain a solution at pH 14 and extracted with Et<sub>2</sub>O (3 x 75 ml). The organic phase was extracted with H<sub>2</sub>O (2 x 50 ml) and then dried with MgSO<sub>4</sub> and filtered under pressure to give product #1, a pale yellow solid.<sup>20</sup>

**Step 2:- protection of aliphatic amine**

The protected amino aniline 1 (2.0 g, 0.010 mol) was mixed with a solution of Na<sub>2</sub>CO<sub>3</sub> (1.9 g, 0.018 mol) in a water/dioxane (60 ml, 1:1) mixture in a 250 ml round-bottomed flask, and then stirred in an ice bath. A Fmoc (2.6 g, 0.010 mol) in water/dioxane (60 ml, 1:1) mixture was prepared and added to the first solution, which was then stirred at room temperature for 5 hours. 50 ml of water was added to halt the reaction. Ani-Fmoc was extracted using ethyl acetate and the solution was dried using MgSO<sub>4</sub>. The solvent was then removed by rotary evaporation, yielding Ani-Fmoc (68% yield, white colour) product #2.

**Step 2:- deprotection of aromatic amine**

The deprotection of product #2 was achieved using a solution of trifluoroacetic acid in dichloromethane (DCM). The mixture was stirred at room temperature for 5 hours to produce the Ani Fmoc compound (white coloured powder), product #3. The scheme in Figure 3.8 illustrates the reaction steps.

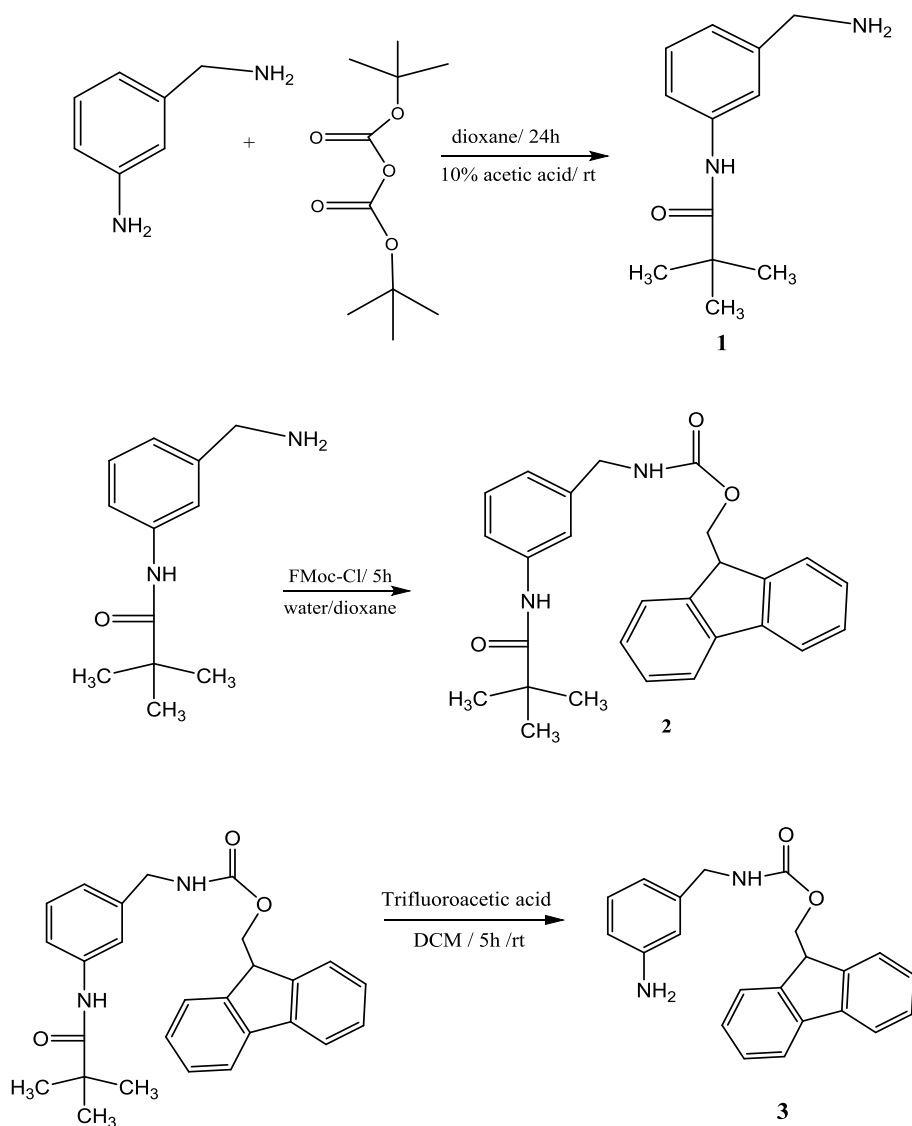


**Figure 3.8:** Schematic of the synthesis of Ani-Fmoc from 3-aminomethylaniline (Ani-NH<sub>2</sub>)

### 3.6.1.7 Reduction of 3-Thiopheneacetonitrile (ThioCN) to Thiophen-3-yl-ethylamine (ThioNH<sub>2</sub>).

Reaction was used same procedure which mentioned above in the section 3.5.1.1 to synthesis thiophen-3-yl-ethylamine (ThioNH<sub>2</sub>) (yellow oil, 62% yield).

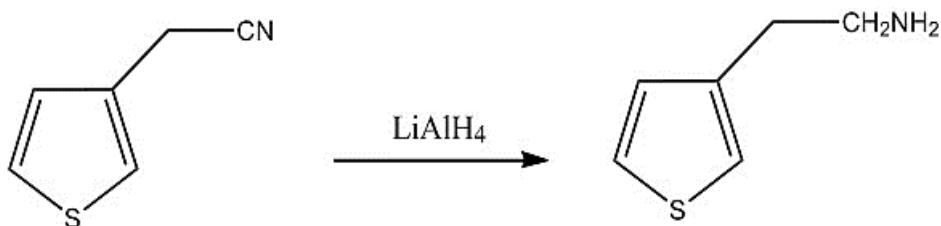


**Figure 3.9:** General reaction schemes for conversion of cyanothiophene (Thio-CN) to aminoethylthiophene (Thio-NH<sub>2</sub>)

## 3.6.1.8 Coupling of Pentafluorophenol with 3- thiophene acetic acid

A coupling reaction between pentafluorophenol and 3- thiophene acetic acid was performed under same conditions which were used with 3-(pyrrol-1-yl) propanic acid (PyCOOH) in section 3.6.1.4.<sup>19</sup>

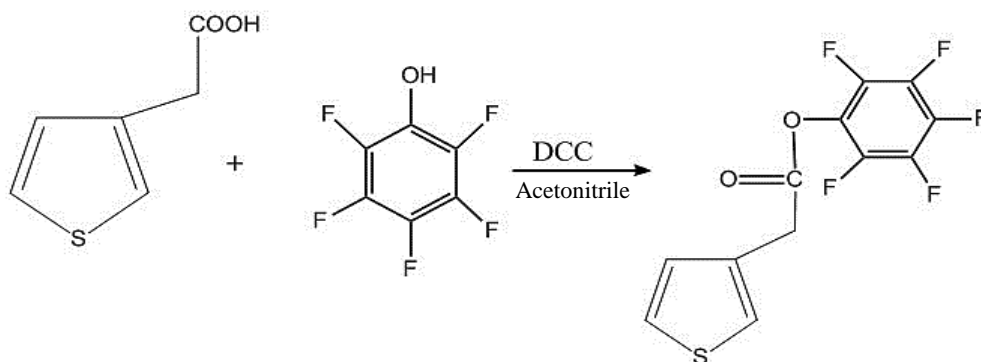


**Figure 3.10:** schematic of the synthesis of pentafluorophenyl 2-(thiophene-3-yl) acetate from 3-TAA.

## 3.6.1.9 Formation of thiophene- Fmoc monomer

Thio- Fmoc compound was synthesized using the same procedure that used to prepare Py-Fmoc. (76% yield, white colour).

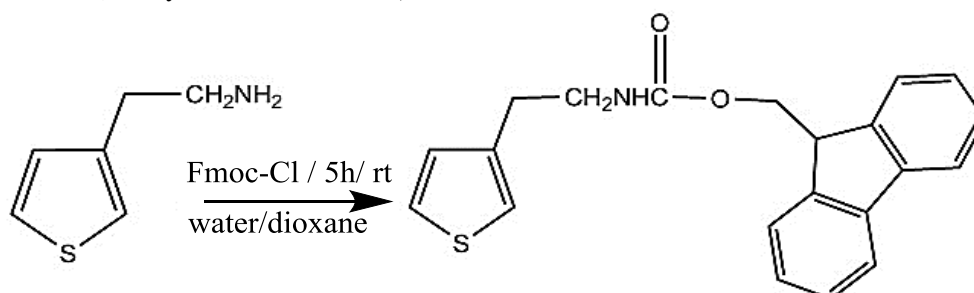


**Figure 3.11:** Schematic of the synthesis of (9H-fluoren-9-yl) methyl-N[2-(thiophen-3-yl)ethyl] carbamate (Thio- Fmoc) from aminothiophene (thio-NH<sub>2</sub>).

## 3.6.2 Electropolymerisation of polymer films

The electropolymerisation of the polymer films, which will be discussed in later chapters, was achieved using the potentiodynamical method. Generally, polymer films were deposited onto a gold or platinum electrode. The polymerisation solution contained a suitable concentration of the monomer (depending on type) in media with 0.5 M tetrabutylammonium perchlorate (TBAP) for experiments involving the electropolymerisation derivatives of pyrrole and thiophene, or acidic media for the polymerisation derivatives of aniline, unless additional conditions are otherwise noted in

the following chapters. Various potential ranges (vs. Ag/AgCl) were applied, depending on the type of monomer, over 10 scans, with each set of scans being conducted at two scan rates, namely 10 and 20  $\text{mV s}^{-1}$ . All details of polymerisation conditions are shown in **Table 2.1**.

Monomer name	Potential window / V	Supporting electrolyte	Conc. / mM	Scan rates $\text{mV s}^{-1}$
3-(pyrrol-1-yl) propionic acid	0.0V - 1.2V	TBAP	10	5 - 100
3-(pyrrole1-l)-propylamine	-0.1V - 1.2 V	TBAP/HBF <sub>4</sub>	10	5 - 100
pentafluorophenyl-3-(pyrrolyl)propanoate	0.0V - 1.3V	TBAP	10	5 - 100
Py-co- Fmoc	-0.6V - 1.1V	TBAP	10	5 - 100
3-(2-carboxyethyl) aniline	0.0 - 1.2	H <sub>2</sub> SO <sub>4</sub>	20	10 and 20
3-(aminomethyl) aniline	0.0 - 1.2	H <sub>2</sub> SO <sub>4</sub>	20	10 and 20
Ani-pfp	0.0 - 1.35	HClO <sub>4</sub> /TBAP	20	10 and 20
Ani- Fmoc	-0.2 - 1.35	HClO <sub>4</sub> /TBAP	20	10 and 20
3-thiophene acetic acid	0.0 – 2.0	TBAP	0.5	10 and 20
Thio-pfp	0.2 - 1.9	TBAP	0.5	10 and 20
Thio- Fmoc	0.3 – 2.0	TBAP	0.5	10 and 20

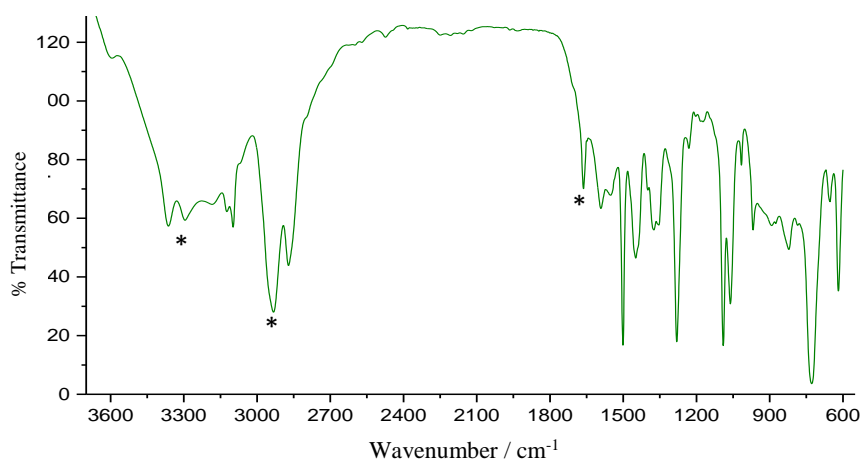
*Table 2.1: Poymerisation condition of all polymers were prepare in this thesis.*

### 3.6.3 FTIR characterisation of compounds

- **Pyrrole monomers**

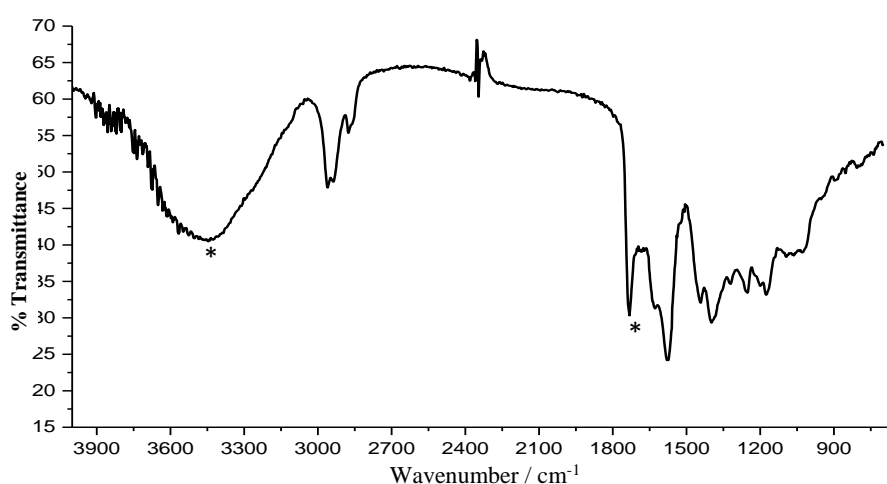
FTIR was used to identify the new compounds prepared in this thesis. Figure 3.12 shows the FTIR spectrum of 3-(pyrrol-1-yl) propylamine. In this figure, two bands at 3360-3290  $\text{cm}^{-1}$  can be seen that are attributable to a free  $\text{NH}_2$  group. The spectrum also shows characteristic absorption bands at 3105, 2968, 1623, 1620 and 1505  $\text{cm}^{-1}$ , which can be assigned to C–H, C=C and N-H vibrations, respectively.<sup>21, 22</sup> In addition, the  $\nu(\text{C-N})$  band

at  $2100\text{ cm}^{-1}$  does not appear in this spectrum due to being converted to a carboxylic group by the oxidation reaction.<sup>23, 24</sup>



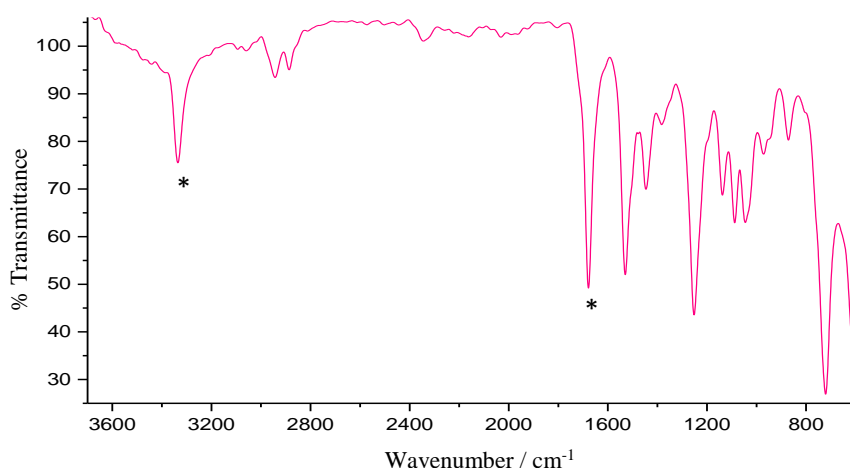
**Figure 3.12:** FTIR spectrum of 3-(pyrrol-1-yl)propylamine. \*denotes the presence of amine and CH aliphatic peaks.

Figure 3.13 shows the FTIR spectrum of 1H-Pyrrole-1-propionic acid (PyCOOH). A broad band is observed around  $3200\text{--}3600\text{ cm}^{-1}$ , characteristic of a carboxylic group.



**Figure 3.13:** FTIR spectrum of 1H-pyrrole-1-propionic acid (PyCOOH). \*denotes the presence of carboxylic and carbonyl peaks.

The Py-FMOC spectrum shows an amide group around  $3325\text{ cm}^{-1}$ , as shown in Figure 3.14. The disappearance of two peaks in this spectrum indicates that the amino groups had reacted with FMOC to form amide bonds. The band at  $1650\text{ cm}^{-1}$  is characteristic of the new amide group (C-N).



**Figure 3.14:** FTIR spectrum of (9H-fluoren-9-yl) methyl-3-(1H-pyrrol-1-yl)propylcarbamate (Py-Fmoc). \*denotes the presence of amide and carbonyl peaks.

The IR spectrum of the Py-pfp shows characteristic bands at 1780, 1525 and 1000  $\text{cm}^{-1}$ , which can be assigned to C–O ester, C=C aromatic and C–F vibrations respectively, as shown in Figure 3.15.

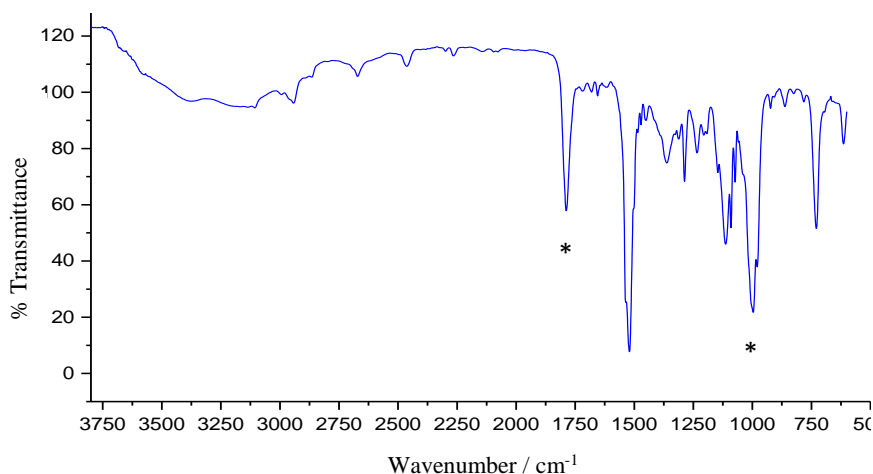


**Figure 3.15:** FTIR spectrum of pentafluorophenyl 3-(pyrrol-1-yl)propanoate. \*denotes the presence of ester carbonyl and C-F peaks.

- **Aniline monomers**

In Figure 3.16, the IR spectrum of Ani-pfp, which was formed by the coupling of pentafluorophenol with carboxylic pyrrole, included a peak at 3050  $\text{cm}^{-1}$  attributable to the C–H aromatic stretching vibration, peaks at 1740  $\text{cm}^{-1}$  attributable to the C–O stretching vibrations of the ester bonds, and a peak at 1500  $\text{cm}^{-1}$  attributable to a C–C bending vibration.

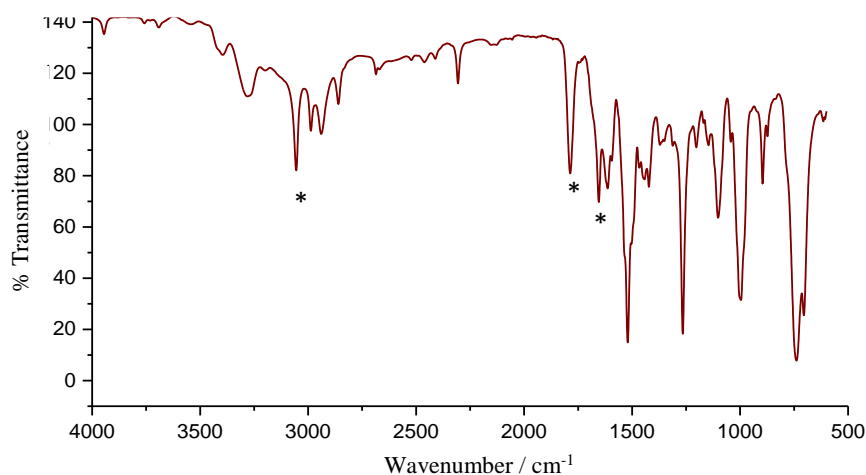


**Figure 3.16:** FTIR spectrum of pentafluorophenyl 3-(3-aminophenyl)propanoate. \*denotes the presence of C-H aliphatic and ester carbonyl peaks.

The structures of the prepared compounds were assigned using FTIR. IR spectrum of compound Ani-Boc showed two absorption bands in the 3420-3360  $\text{cm}^{-1}$  region and a further band in the 3090-2950  $\text{cm}^{-1}$  region related to the  $-\text{NH}_2$  and  $-\text{CH}$  groups, respectively. Appearance of a band around 1670  $\text{cm}^{-1}$  was due to the formation of carbonyl groups related to amide bonds, as shown in the Figure 3.17 A. However, it may be noted from the FTIR spectrum (B) of Ani-Boc/ Fmoc, that two peaks in this spectrum in the 3420-3360  $\text{cm}^{-1}$  region, related to  $\text{NH}_2$  groups, disappeared, supporting of the expected reaction to form an amide group. On the other hand, deprotection of the boc group led to a change in FTIR spectrum (C), it can be seen that spectrum contains two bands at 3450-3345  $\text{cm}^{-1}$  due to deprotection of the  $\text{NH}_2$  group. The mass spectrum showed a peak corresponding to molecular ions of Ani- Fmoc at ESMS (+) 367  $[\text{M}+\text{Na}]^+$ .

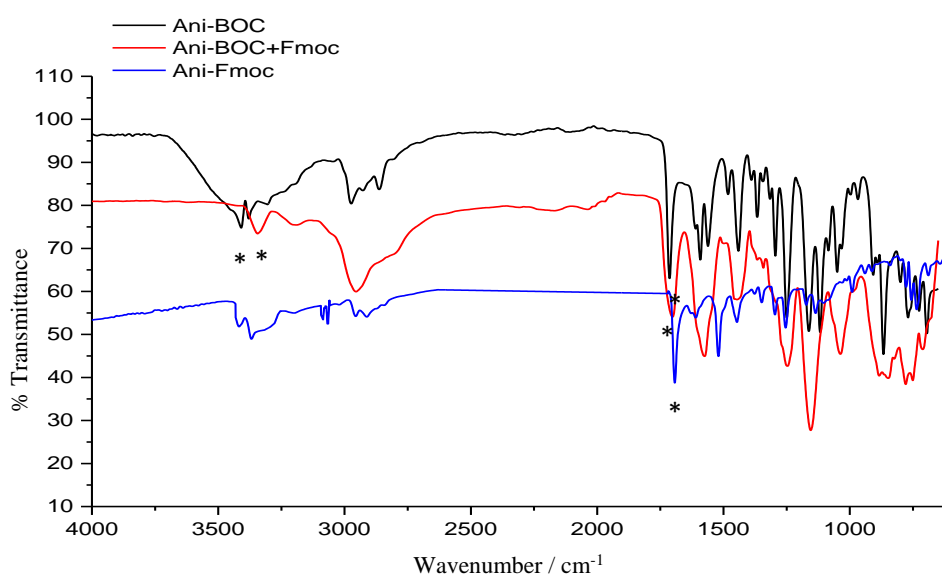


**Figure 3.17:** A) FTIR spectrum of protected aniline-Boc, B) FTIR spectrum of protected aniline-Boc and Fmoc and C) FTIR spectrum of aniline-Fmoc. \*denotes the presence of amide and carbonyl peaks.

- Thiophene monomers

The IR spectrum of thiophen-3-yl-ethylamine (ThioNH<sub>2</sub>) is shown in Figure 3.18. Two bands can be observed in this spectrum at 3400 -3360 cm<sup>-1</sup> attributed to NH<sub>2</sub> stretching vibrations. A band around 3100 cm<sup>-1</sup> was due to a C-H aromatic vibration and the band at 1620 cm<sup>-1</sup> due to an N-H bending mode.

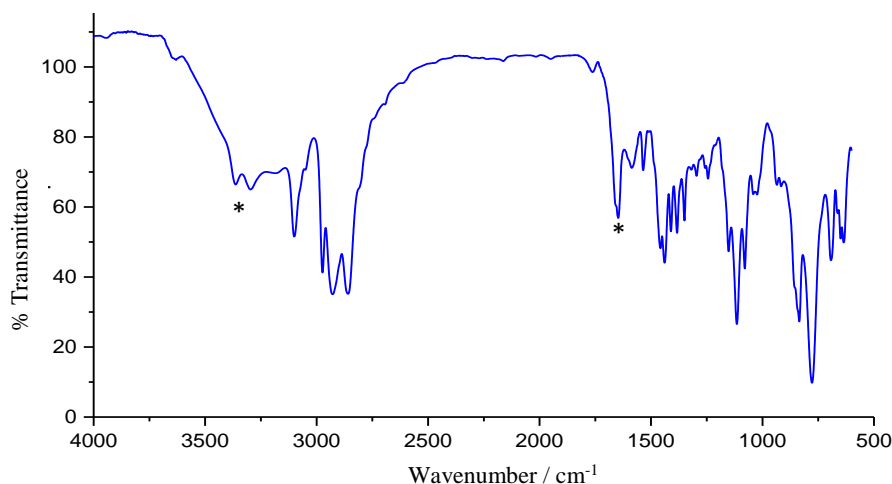


**Figure 3.18:** FTIR spectrum of Thiophen-3-yl-ethylamine (Thio-NH<sub>2</sub>). \*denotes the presence of amine and carbonyl peaks.

The FTIR spectrum of thio-pfp showed the existence of bands characteristic to C-H, C=O and C-F vibrations at around 3100, 1765, and 1000 cm<sup>-1</sup>, respectively, as shown in Figure 3.19.

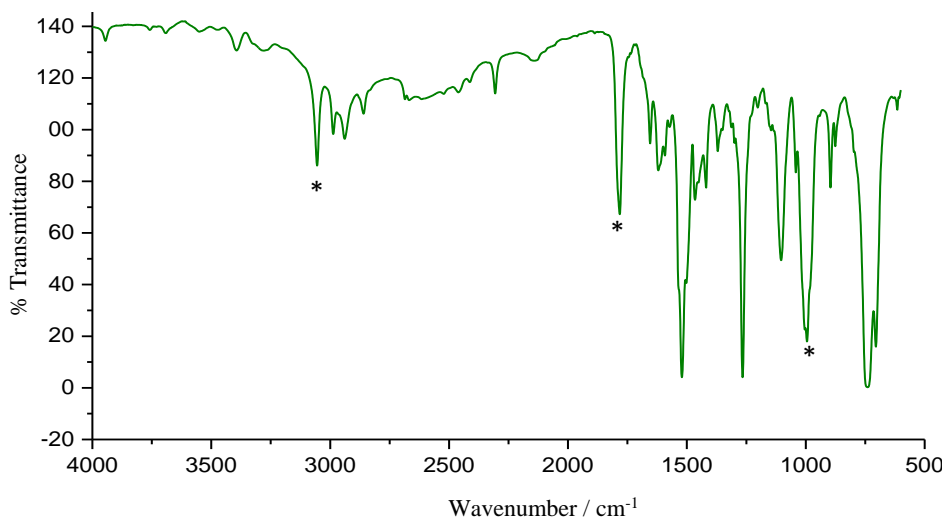


**Figure 3.19:** FTIR spectrum of pentafluorophenyl 2-(thiophene-3-yl) acetate. \*denotes the presence of aromatic, ester carbonyl and C-F peaks.

In the Figure 3.20, the IR spectrum of Thio- Fmoc that was formed by the reaction between aminothiophene with Fmoc-Cl showed a peak at 3280 cm<sup>-1</sup> attributable to the N-H amide stretching vibration, a peak at 1660 cm<sup>-1</sup> attributable to the C-O stretching

vibrations of amide bonds, and a peak at  $1510\text{ cm}^{-1}$  attributable to a C-C bending vibration.

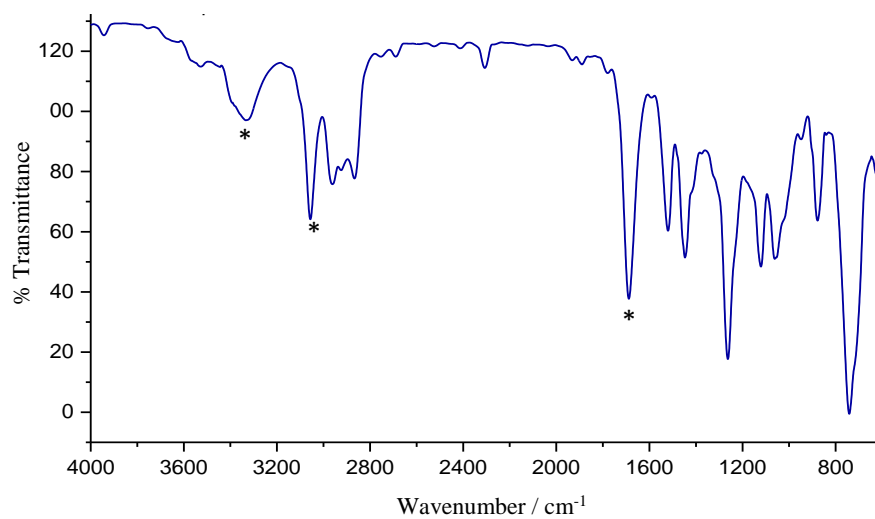


**Figure 3.20:** FTIR spectrum of (9H-Fluoren-9-yl) methyl-N[2-(thiophen-3-yl)ethyl] carbamate (Thio - Fmoc). \*denotes the presence of amide and carbonyl peaks.

### 3.7 References

1. P. Zanello, *Inorganic electrochemistry: Theory, Practice and Applications*, Royal Society of Chemistry, 2003. p.49
2. B. A. Martin and H. E. Hager, *Journal of Applied Physics*, 1989, **65**, 2627-2629.
3. G. Sauerbrey, *Zeitschrift für Physik*, 1959, **155**, 206-222.
4. G. A. East and M. Del Valle, *Journal of Chemical Education*, 2000, **77**, 97.
5. R. Bates and J. Macaskill, *Pure and Applied Chemistry*, 1978, **50**, 1701-1706.
6. R. Schumacher, G. Borges and K. Kanazawa, *Surface Science*, 1985, **163**, L621-L626.
7. D. Buttry and M. Ward, *Chemical Reviews*, 1992, **92**, 1355-1379.
8. K. Kaneto, *Current Applied Physics*, 2005, **5**, 178-183.
9. Rajesh, W. Takashima and K. Kaneto, *Sensors and Actuators B: Chemical*, 2004, **102**, 271-277.
10. J. Hegewald, L. Jakisch and J. Pionteck, *Synthetic Metals*, 2009, **159**, 103-112.
11. S. Kimmins, P. Wyman and N. Cameron, *Polymer*, 2014, **55**, 416-425.
12. M. Gawande and P. Branco, *Green Chemistry*, 2011, **13**, 3355-3359.
13. S. Wolowacz, B. Yon Hin and C. Lowe, *Analytical Chemistry*, 1992, **64**, 1541-1545.
14. W. Khan, M. Kapoor and N. Kumar, *Acta Biomaterialia*, 2007, **3**, 541-549.
15. A. Nan, I. Craciunescu, R. Turcu, D. Reichert and J. Liebscher, *Journal of Optoelectronics and Advanced Materials*, 2008, **10**, 2265-2270.
16. P. Watts, C. Wiles, S. J. Haswell, E. Pombo-Villar and P. Styring, in *Microreaction Technology*, Springer, 2001, pp. 508-517.
17. A. R. Katritzky, K. Suzuki and S. K. Singh, *Arkivoc*, 2004, **1**, 12-35.
18. C. J. Pickett and K. S. Ryder, *Journal of the Chemical Society, Dalton Transactions*, 1994, 2181-2189.
19. S. Kang, J. Kim, J. An, E. Lee, J. Cha, G. Lim, Y. Park and D. Chung, *Polymer Journal*, 2004, **36**, 937-942.
20. V. Perron, S. Abbott, N. Moreau, D. Lee, C. Penney and B. Zacharie, *Synthesis*, 2009, **2009**, 283-289.
21. D. L. Pavia, G. M. Lampman, G. S. Kriz and J. Vyvyan, *Introduction to Spectroscopy*, Cengage Learning, 2014, pp.74.
22. P. S. Kalsi, *Spectroscopy of Organic Compounds*, New Age International (P) Limited, 2007, pp.66.
23. R. M. Silverstein, F. X. Webster, D. Kiemle and D. L. Bryce, *Spectrometric Identification of Organic Compounds*, 8<sup>th</sup> Edition, Wiley, 2014, pp.71.
24. B. H. Stuart, *Infrared Spectroscopy: Fundamentals and Applications*, Wiley, 2004, pp.79.

<b>4.1 Overview.....</b>	<b>69</b>
<b>4.2 Aims and Objectives.....</b>	<b>69</b>
<b>4.3 Results and discussion.....</b>	<b>71</b>
4.3.1 Electropolymerisation of <i>N</i> -(2-carboxyethyl) pyrrole.....	71
4.3.2 Characterization of poly( <i>N</i> -(2-carboxyethyl)pyrrole).....	74
4.3.3 Electropolymerisation of <i>N</i> -3-aminopropylpyrrole.....	76
4.3.4 Characterization of poly( <i>N</i> -3-aminopropylpyrrole).....	78
4.3.5 Electropolymerisation of pentafluorophenyl-3-(pyrrol-1-yl) propanoate.....	81
4.3.6 Characterisation of poly(pentafluorophenyl-3-(pyrrol-1-yl) propanoate.....	83
4.3.7 Electropolymerisation of copolymer Py-co-PyFmoc.....	86
4.3.8 Characterization of copolymer py-co-Fmoc.....	88
<b>4.4 Post-Polymerisation Chemical Modifications.....</b>	<b>90</b>
4.4.1 QCM Gravimetric and FTIR Spectroscopic Monitoring of Ester Hydrolysis.....	92
4.4.2 Monitoring of vertical penetration of receptor into ester polymer film.....	94
4.4.3 QCM Gravimetric and FTIR Spectroscopic Monitoring of Amide Hydrolysis....	97
4.8.4 Monitoring of vertical penetration of receptor into amide polymer film.....	99
<b>4.5 Patterning of polymer films.....</b>	<b>101</b>
<b>4.6 Surface imaging characterization of polymer films.....</b>	<b>105</b>
<b>4.7 Conclusion.....</b>	<b>108</b>
<b>4.8 References.....</b>	<b>110</b>

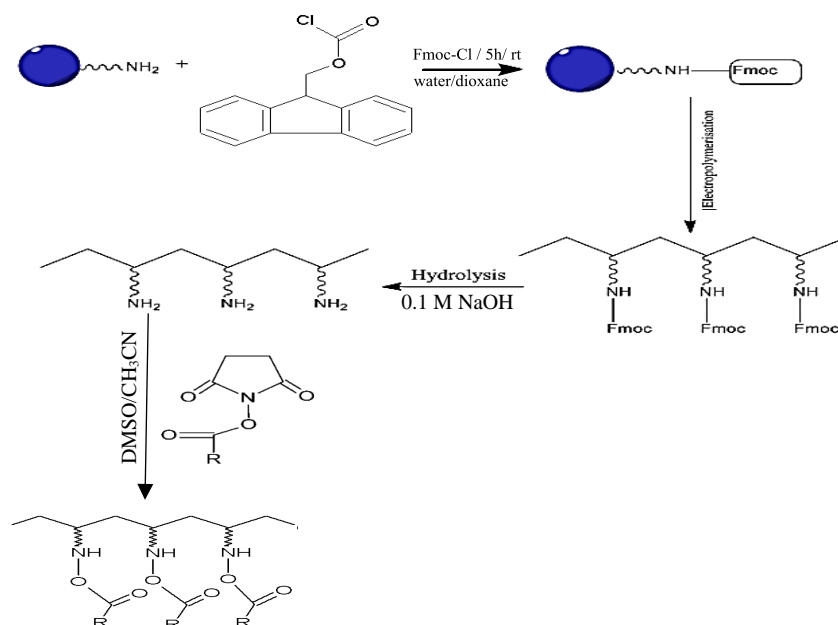
## 4.1 Overview

Conducting polymers have a wide range of applications, such as sensors, electrochemical transistors and solar cells, due to their optical, mechanical and electronic properties.<sup>1, 2</sup> During the last three decades, studies of conducting polymers have increased dramatically, and polypyrrole continues to be one of the most studied conductive polymers.<sup>3, 4</sup> This is attributed to the attractive properties of polypyrrole such as its high conductivity, stability, and ease of preparation, as mentioned in chapter one.<sup>5, 6</sup> Although there are several methods that allow for the preparation of polypyrrole, electrochemical polymerisation is the most favoured technique because of the ability to control the thickness of film, and the fact that it is also a less expensive and straightforward method.<sup>7, 8</sup> The presence of functional groups in monomers and/or polymers can significantly contribute to improving the performance and effectiveness of these molecules in many application areas, thus increasing the potential number of applications available to these molecules. Furthermore, these functional units provide the ability to manipulate and modify chemical and physical properties of conducting polymers to suit the purpose of any particular application.<sup>9</sup> Immobilisation strategies can be accomplished in many ways, such as through physical adsorption or covalent bonding.<sup>10, 11</sup> This process can lead to improving the functionalities of polymer surfaces and provide opportunities for the fabrication and manipulation of surfaces. Continuing studies of surface chemistry have led to the design of surfaces that have more efficient and highly selective properties, and perhaps unsurprisingly these surfaces have taken their place in the manufacture of sensing devices.<sup>12</sup>

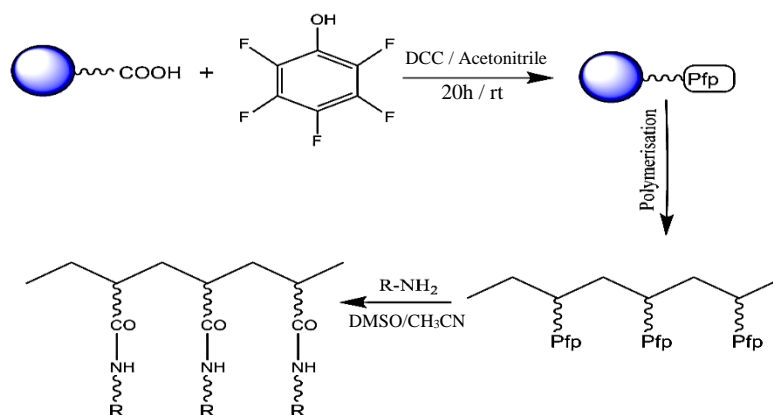
## 4.2 Aims and Objectives

The goal of this chapter are: (i) fabrication of a patterned functionalised electrode from polypyrrole derivatives, here Py-pfp and Py-Fmoc; (ii) determination of mass exchange of polymer films using the QCM technique; and (iii) preparation of spatially heterogeneous (patterned) film surfaces with diverse chemical functionalities to be used later as electrodes in sensing applications. In this chapter, the aim is the functionalisation of film surfaces, through the use of immobilisation strategies, in order to introduce ligands so as to give an enhanced recognition capacity. Various scenarios were used, depending on the electrochemical and synthetic routes available, to manufacture polymer films. This

scenario involves electropolymerisation of the monomer Py-NH<sub>2</sub> (3-(pyrrol-1-yl)propylamine) that contains a large leaving group, namely Fmoc, (9-fluorenylmethoxycarbonyl), and a monomer, py-COOH *N*-(2-carboxyethyl)pyrrol, which contains another large leaving group, pfp (pentafluorophenol). These large groups offer two advantages, namely that they do not appear to inhibit the electropolymerisation and that it is easy to produce polymer film surfaces without causing the collapse of the film itself. After the deposition step, the amide and ester bonds are hydrolysed out to create voids suitable for subsequent insertion of ligand units. **Schemes 4.1** and **4.2** summarise the synthetic reactions and functionalisation of film surfaces.



**Scheme 4.1:** Summary of synthetic reaction and functionalisation of amide polymer film



**Scheme 4.2:** Summary of synthetic reaction and functionalisation of ester polymer film

### 4.3 Results and discussion

Generally, polymer films were deposited using the potentiodynamic method onto a gold electrode. The polymerisation solution contained a 10 mM concentration of the monomers, pyrrole derivatives including 3-(pyrrol-1-yl)propionic acid (Py-COOH), 3-(pyrrole1-1)-propylamine(PyNH<sub>2</sub>), pentafluorophenyl-3-(pyrrolyl)propanoate (Py-pfp), and Py-co-Fmoc, with 0.1 M tetrabutylammonium perchlorate (TBAP) as a supporting electrolyte in dry acetonitrile (CH<sub>3</sub>CN), unless otherwise mentioned. The potential ranges (vs. Ag/AgCl) applied were dependent on the type of monomer and were repeated over 10 scans, with each set of scans being conducted at different scan rates (5, 10, 20, 50 and 100 mV s<sup>-1</sup>).

Monomer name	Potential window (vs. Ag/AgCl)/ V	Supporting electrolyte	Scan rates mV.s <sup>-1</sup>
<i>3-(pyrrol-1-yl) propionic acid</i>	0.0V - 1.2V	TBAP	5 - 100
<i>3-(pyrrole1-1)-propylamine</i>	-0.1 V - 1.2 V	TBAP / HBF <sub>4</sub> <sup>13, 14</sup>	5 - 100
<i>pentafluorophenyl-3-(pyrrolyl)propanoate</i>	0.0V - 1.3V	TBAP	5 - 100
<i>Py-co-Fmoc</i>	-0.6V - 1.1V	TBAP	5 - 100

**Table 4.1:** Potential window and supporting electrolyte for of the four types of monomer (each at 10 mM) used in this chapter.

#### 4.3.1 Electropolymerisation of *N*-(2-carboxyethyl) pyrrole

Py-COOH polymer films were deposited potentiodynamically from TBAP/CH<sub>3</sub>CN solution onto an Au electrode. **Figure 4.1** describes the voltammetric responses of 10 mM *N*-(2-carboxyethyl)pyrrole as the potential was cycled from 0.0 to 1.2 V vs. Ag/AgCl (saturated KCl), for 10 cycles at various scan rates (5 mV s<sup>-1</sup> - 100 mV s<sup>-1</sup>). In the first scan (inset curve in the panel A) the system shows the start of a nucleation loop at  $E_{pa} = 0.95$  V, and the anodic current probably related to the oxidation of the monomer<sup>15, 16</sup> The oxidation potential of *N*-substituted pyrroles is greater than that of the pyrrole monomer, which is due to the electronic effects of the carboxylic groups and the steric hindrance effect on the pyrrole molecule.<sup>17</sup> In the second scan, a new anodic wave appears at  $E_{pa} = 0.80$  V, with cathodic waves at  $E_{pc} = 0.70$  V due to the redox of the polymer film. The

panel B shows cyclic voltammogram (scan 10) of electrodeposition the same monomer with different scan rates at same polymerisation conditions.

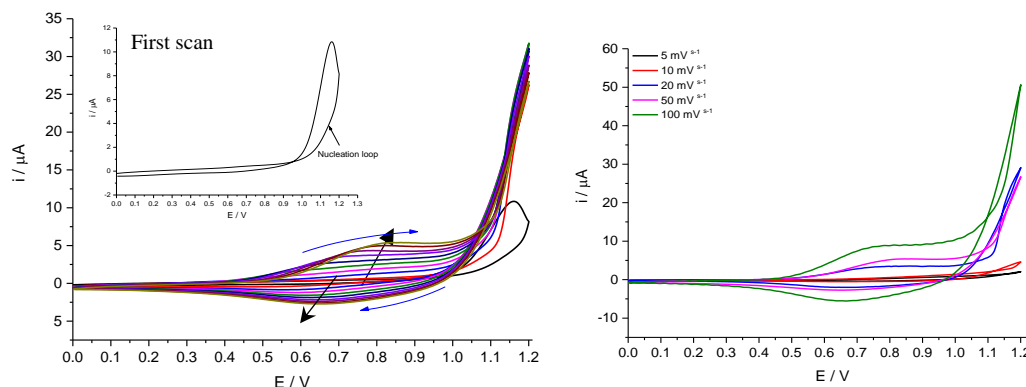


**Figure 4.1:** (A) Cyclic voltammograms of electropolymerisation 10 mM N-(2-carboxyethyl)pyrrole in 0.1 M TBAP/CH<sub>3</sub>CN scan rate  $\nu = 10 \text{ mV s}^{-1}$ . 10 scans (inset curve shows the first scan) (B) Cyclic voltammogram (scan 10) for deposition of Py-COOH at different scan rates,  $\nu$ , 5- 100  $\text{mV s}^{-1}$ . Au electrode area of  $0.0044 \text{ cm}^2$ .

The nature of substituent groups plays a key role in electropolymerisation because of the lead to change the electronic density and steric effects of monomers, where results indicate that there is a shift in potential between poly(Py-COOH) and pyrrole.<sup>18, 19</sup> the oxidation potential of carboxylic pyrrole was higher than that found under the same conditions for the pyrrole (see **Figure 4.1**). This difference is due to the presence of an electron withdrawing group (carboxylic group) which has an electronic effect on the pyrrole cyclic system.<sup>20</sup> As previously mentioned in chapter two, the total deposition cathodic charge,  $Q$ , was used to calculate the surface coverage of the electroactive polymer ( $\Gamma/\text{mol cm}^{-2}$ ) using equation 2.4 ( $\Gamma = Q/nFA$ ). Here,  $n$  is the number of electrons lost from the monomer units (0.33).<sup>6, 21-23</sup> **Table 4.2** shows the cathodic peak charge and surface coverage for all Py-COOH films prepared.

Supporting electrolyte	Number of scans	Scan rate ( $\text{mV s}^{-1}$ )	Reduction peak charge $Q$	Coverage $\Gamma/\text{mol cm}^{-2}$
TBAP	10	5	$5.30 \times 10^{-5}$	$3.78 \times 10^{-7}$
		10	$3.65 \times 10^{-5}$	$2.60 \times 10^{-7}$
		20	$3.40 \times 10^{-5}$	$2.43 \times 10^{-7}$
		50	$3.09 \times 10^{-4}$	$2.02 \times 10^{-7}$
		100	$2.73 \times 10^{-4}$	$1.94 \times 10^{-7}$

**Table 4.2:** Data for figure 4.1 and analyses at different scan rates between 5 – 100  $\text{mV s}^{-1}$ . (Electrode area=  $0.0044 \text{ cm}^2$ ).

Electropolymerisation of a 10 mM solution of *Py-COOH* in TPAP/  $\text{CH}_3\text{CN}$  solution was performed by means of chronoamperometry over different lengths of time (50, 100 and 200 seconds). The  $i$ - $t$  transients are shown in **Figure 4.2** using a potential of 1.2 V. System transitioned from no reaction at 0.0 V to 1.2 V. It can be seen from this figure that the chronoamperogram shows a high initial current peak in the first few seconds after the potential was applied; this was attributed to the charge of the electrical double layer that formed at the polymer-solution interface.<sup>24, 25</sup> The curve then underwent a sharp drop in current, which was due to the oxidation of monomers into radical cations and their diffusion towards the electrodes.<sup>26</sup> The next stage of the polymerisation process shows a clear current increase corresponding to radical cation coupling, which is attributed to the nucleation and growth of polypyrrole on the electrode.<sup>27</sup> After this, a gradual increase in current was observed because of the deposition of the polymer.<sup>26</sup> Panel B shows that the electropolymerisation charge increased with  $t^{1/2}$  as result of diffusion control. The thickness of the *Py-COOH* film (h/ $\mu\text{m}$ ) was estimated from the electrical charge,  $Q$ , using equations 2.5 and 2.6 ( $n = 2.33$ ). **Table 4.2** shows the charge and thickness of the *py-COOH* film at different times.

Monomer conc. / mM	Time / s	Charge $Q$ / C	Thickness / $\mu\text{m}$
10	50	0.0104	0.238
10	100	0.0155	0.337
10	200	0.0278	0.622

**Table 4.3:** Electrical charge due to electropolymerisation of *N*-(2-carboxyethyl)pyrrole films using 50, 100 and 200 second deposition times. Au electrode area was  $0.23\text{cm}^2$ , molecular weight of *Py-COOH* is  $139\text{ g mol}^{-1}$  and its density is ca.  $1.25\text{ g cm}^{-3}$ .

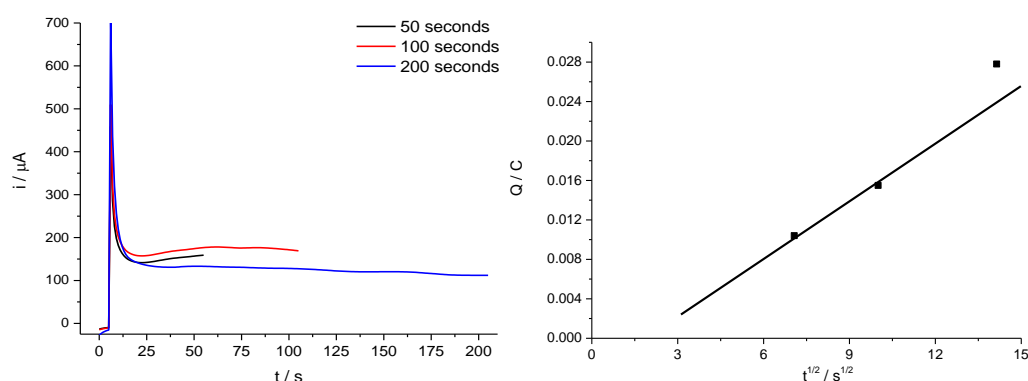


**Figure 4.2:** Current-time transients for potentiostatic electrodeposition of 10 mM *N*-(2-carboxyethyl)pyrrole in 0.1 M TBAP/ $\text{CH}_3\text{CN}$  solution at 1.2 V vs. Ag/AgCl over 50, 100 and 200 seconds. B) Plot of charge vs. square root of time (data from panel A).

4.3.2 Characterization of poly(*N*-(2-carboxyethyl)pyrrole)

Prepared films were rinsed with dry acetonitrile and then placed in a monomer-free electrolyte (0.1 M TBAP/CH<sub>3</sub>CN) to study any chemical changes during redox cycling at different scan rates. Figure 4.3 shows the voltammetric responses of the polymer prepared at 10 mV s<sup>-1</sup> over a potential ranging from 0.2 to 1.1 V vs. an Ag/AgCl. Figure 4.3 A shows cyclic voltammogram of polymer film prepared in TBAP/ CH<sub>3</sub>CN solution at 10 mV s<sup>-1</sup>. This cyclic voltammogram has broad redox peaks at 0.8 V and 0.58 V, respectively. **Figure 4.3 B** shows that both anodic and cathodic peak potentials are proportional to the scan rate for the same film; moreover, both redox peak currents are linearly dependent on scan rates, as shown in **Figure 4.3 C**.

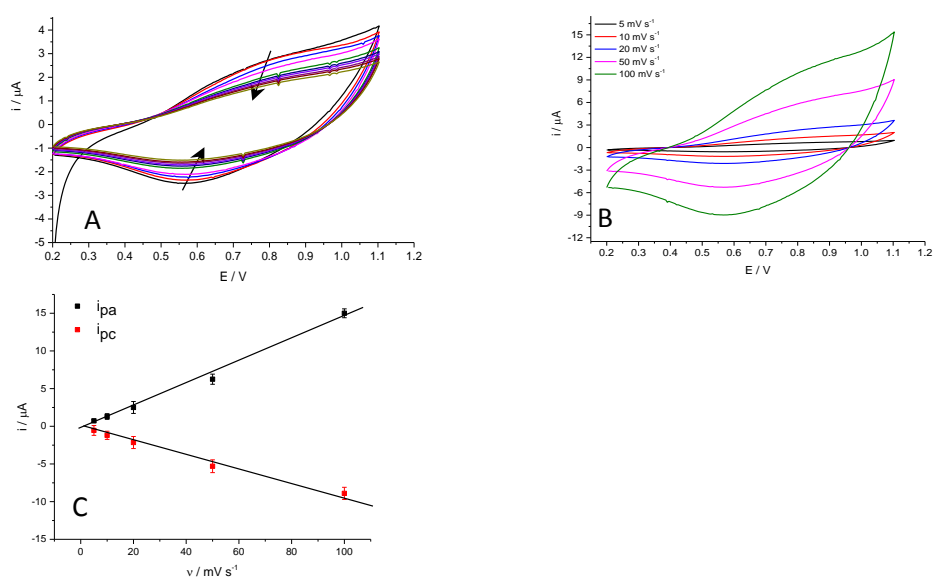


**Figure 4.3:** Voltammetric responses of poly(py-COOH) film prepared at a 10 mV s<sup>-1</sup> scan rate (figure 4.1), and acquired in a 0.1 M TBAP/CH<sub>3</sub>CN solution at 0.2 - 1.1 V vs. Ag/AgCl. B) Voltammetric responses of the same film at different scan rates, 5- 100 mV s<sup>-1</sup>; (C) variation of cathodic peak current (from curves in panel (B)) with scan rate.

Supporting electrolyte	Electrolytes	Scan rate / mV s <sup>-1</sup>	<i>Q</i> red, 1st cycle	<i>Q</i> red, 10th cycle	<i>Q</i> red,10th / <i>Q</i> red, 1st
TBAP	TBAP	5	1.23x 10 <sup>-4</sup>	1.12x10 <sup>-4</sup>	0.91
		10	1.25x10 <sup>-4</sup>	1.09x10 <sup>-4</sup>	0.87
		20	1.09x10 <sup>-4</sup>	1.00x10 <sup>-4</sup>	0.91
		50	1.05x10 <sup>-4</sup>	9.68x10 <sup>-5</sup>	0.92
		100	9.75x10 <sup>-5</sup>	9.12x10 <sup>-5</sup>	0.94

**Table 4.4:** Reduction charge values of Py-COOH panels (a) in Figures 4.4 and 4.5 exposed to TBAP/acetonitrile electrolyte (monomer free).

Electrodeposition of functionalised monomer film was performed successfully using 10 mM monomer in TBAP/CH<sub>3</sub>CN solution on a gold-coated crystal, over a voltage window

of 0.0 V to 1.2 V vs. Ag/AgCl at a scan rate of 10 mV s<sup>-1</sup> for four cycles, as shown in **Figure 4.4**. From Figure 4.4 panel B, it may be noted that there was no significant mass increase in the potential window until 1.05 V in the first scan. It can be concluded that the attached mass increased cycle-to-cycle due to the reduction of the oscillating frequency of the electrode.<sup>28-30</sup> **Figure 4.4** panel D shows that the variation in the mass of film versus of the charge passed during the electropolymerisation of Py-COOH, suggesting that the charge consumed in the electropolymerisation process leads to a change in mass of the quartz crystal. The mass shift,  $\Delta m$ , versus the charge passed,  $Q$ , during the oxidation of the monomer as shown in **Figure 4.4** panel C.<sup>31, 32</sup> Surface coverage of polymer film ( $\Gamma$ /mol cm<sup>-2</sup>) was estimated to be  $4.4 \times 10^{-7}$  mol cm<sup>-2</sup> based on the cathodic charge from the cyclic voltammogram shown in **Figure 4.4** panel A.

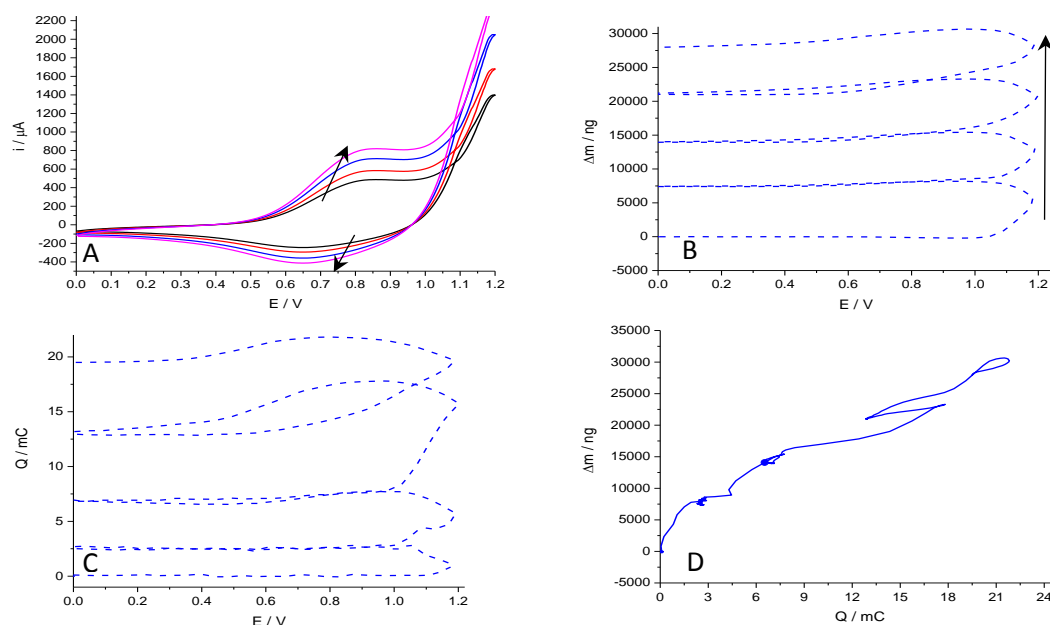


**Figure 4.4:** Representative electrochemical responses for electropolymerisation of 10 mM of Py-COOH (scan rate  $\nu = 10 \text{ mV s}^{-1}$ ) from 0.1 M TBAP/CH<sub>3</sub>CN. (a)  $i$ - $E$ ; (b)  $\Delta m$ - $E$ ; (c)  $Q$ - $E$ ; (d)  $\Delta m$ - $Q$ . Electrode: gold on a QCM crystal with area of 0.23 cm<sup>2</sup>.

Moreover, the slope ( $\Delta m/\Delta q$ ) from Figure 4.6 panel D can be used to estimate the apparent molar mass of electroactive units (include monomer and associated anions and solvent molecules) involved in the electropolymerisation process by using following equation.<sup>33-37</sup>

$$\frac{\Delta m}{\Delta Q} = \frac{M_{app}}{zF} \quad 4.1$$

where  $M_{app}$  is molar mass (g mol<sup>-1</sup>),  $F$  is the Faraday constant (96485 C mol<sup>-1</sup>),  $z$  is the electronic charge of the monomer,  $\Delta m$  is the associated mass change per unit area (g cm<sup>-2</sup>) and  $\Delta q$  is the charge passed per unit area (C cm<sup>-2</sup>) In this case “mol” is used for

monomer redox unit. There are three materials existing in the polymerisation solution: Py-COOH ( $139 \text{ g mol}^{-1}$ ),  $\text{CH}_3\text{CN}$  ( $41.05 \text{ g mol}^{-1}$ ) and  $\text{ClO}_4^-$  ( $99.45 \text{ g mol}^{-1}$ ). According to equation 4.1, the slope ( $\Delta m/\Delta q$ ) is  $1.05 \times 10^{-3} \text{ g / C}$  and thus the  $M_{app}$  is  $236 \text{ g mol}^{-1}$ . Comparing the molar mass of these materials with calculated values for monomer unit refers to that all species have a role during polymerisation processes. Since the molar mass of *Py-COOH* is  $137 \text{ g mol}^{-1}$ , the difference of  $99 \text{ g mol}^{-1}$  was considered as the anions and electrolyte solvent incorporated into the film. This equals ca. 0.33 anion and 0.66 solvent molecules (per monomer unite).

The polymer film was placed in monomer-free electrolyte 0.1 M TBAP/ $\text{CH}_3\text{CN}$  and scanned using a potential window from 0.00 to 1.15 V vs. Ag/AgCl at a scan rate of  $10 \text{ mV s}^{-1}$  for 10 cycles.<sup>38-40</sup> **Figure 4.5** panel A shows a cyclic voltammogram of poly(py-COOH) film in the background electrolyte. From this figure, it can be seen that the first scan has higher redox peaks compared to later cycles where the current peaks are clearly decreased in the second scan until reaching steady state in subsequent scan cycles. In **Figure 4.5** panel B, the mass change over the potential window from 0.00 to 1.15 V is due to the insertion and expulsion of perchlorate ions,  $\text{ClO}_4^-$ , and solvent molecules into and out of the polymer film during the redox process. Surface coverage of polymer film ( $\Gamma/\text{mol cm}^{-2}$ ) was estimated to be  $4.8 \times 10^{-7} \text{ mol cm}^{-2}$  based on the cathodic charge shown in **Figure 4.5** panel A. it can be noted that surface coverage values of polymer film was consistent during deposition and redox process study.

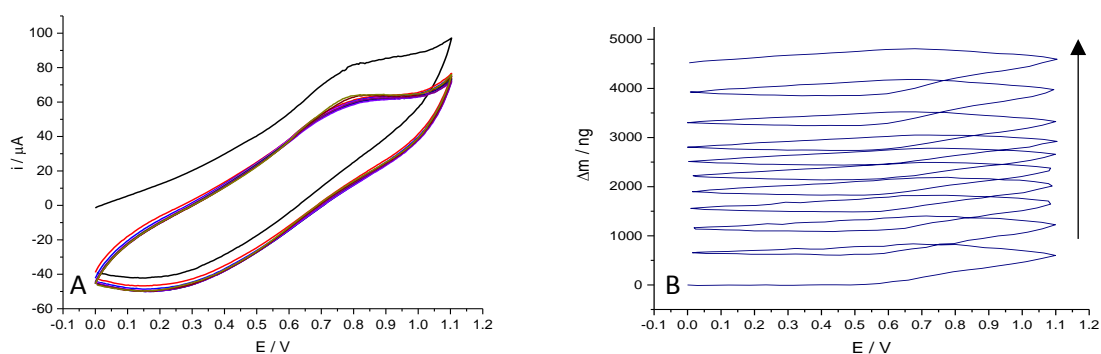


**Figure 4.5:** Representative electrochemical responses for poly-py-COOH from figure 4.6 (scan rate,  $\nu = 10 \text{ mV s}^{-1}$ ) in 0.1 M TBAP/acetonitrile solution (monomer-free). (a)  $i-E$ ; (b)  $\Delta m-E$ . Electrode: gold on a QCM crystal with area of  $0.23 \text{ cm}^2$ .

### 4.3.3 Electropolymerisation of *N*-3-aminopropylpyrrole

Poly(py- $\text{NH}_2$ ) films were grown potentiodynamically on an Au electrode (area =  $0.0044 \text{ cm}^2$ ) from solution containing 10 mM *N*-3-aminopropylpyrrole and 0.1 M TBAP in  $\text{HBF}_4$  50 mM/ $\text{CH}_3\text{CN}$  over 10 cycles and a potential window of -0.1 to 1.1 V at different scan

rates of  $5\text{-}100\text{ mV s}^{-1}$ .<sup>14, 23</sup> **Figure 4.6** panel A shows typical growth curve responses during the electrodeposition of film at  $10\text{ mV s}^{-1}$ . It can be seen that the oxidation of the monomer appears as the peak in the first scan at  $E = 0.9\text{ V}$ . A nucleation loop can be observed in this curve (see inset curve in **Figure 4.6** A). Moreover, new current peaks were observed in voltammograms between ca.  $0.5$  and  $0.7\text{ V}$  and these peak currents rose progressively with sequential potential scans due to the growth of the polymer film. **Figure 4.6** panel B shows the electrochemical response of Py-NH<sub>2</sub> during the electrodeposition at different scan rates of  $5\text{-}100\text{ mV s}^{-1}$ . The surface coverage of (py-NH<sub>2</sub>) film sites was calculated<sup>21, 22</sup> **Table 4.5** shows the cathodic peak charge and surface coverage for all py-NH<sub>2</sub> films prepared.

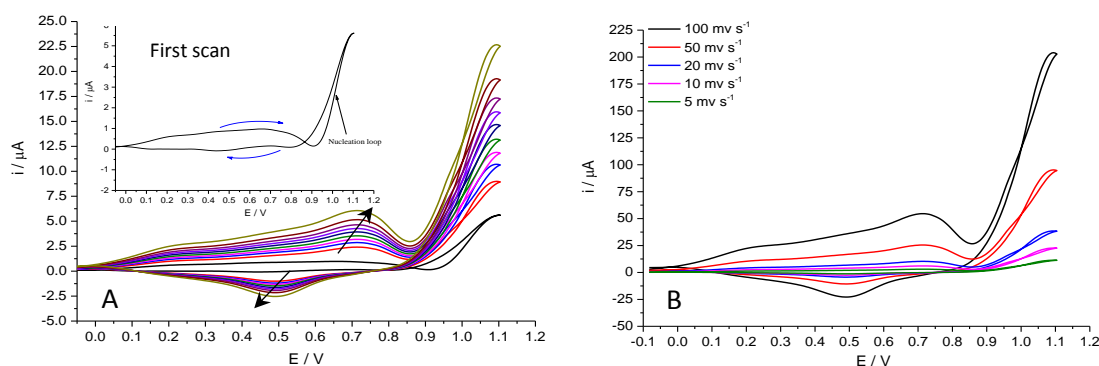


**Figure 4.6:** (A) Cyclic voltammograms during electropolymerisation  $10\text{ mM Py-NH}_2$  in  $0.1\text{M TBAP/CH}_3\text{CN}$  with  $50\text{ mM HBF}_4$  scan rate  $\nu = 10\text{ mV s}^{-1}$  (inset curve shows the first scan cycle) and (B) cyclic voltammogram during electropolymerisation of  $\text{py-NH}_2$  at different scan rates,  $\nu$ ,  $5\text{-}100\text{ mV s}^{-1}$ . Au electrode area of  $0.0044\text{ cm}^2$ .

The amino groups affect the electropolymerisation process because of changes in the electronic density, where the findings above indicate that the oxidation potential of aminopyrrole was higher than that found under the same conditions for the pyrrole monomer (see **Figure 4.6**). This difference is due to the presence of amino groups in the structure of the monomer, which have an electronic effect on the pyrrole cyclic system.<sup>23</sup>

Supporting electrolyte	Number of scans	Scan rate ( $\text{mV s}^{-1}$ )	Reduction peak charge, $Q / \text{C}$	Coverage $\Gamma / \text{mol cm}^{-2}$
TBAP	10	5	$7.4 \times 10^{-5}$	$5.2 \times 10^{-7}$
TBAP	10	10	$7.0 \times 10^{-5}$	$5.0 \times 10^{-7}$
TBAP	10	20	$6.5 \times 10^{-5}$	$4.6 \times 10^{-7}$
TBAP	10	50	$6.2 \times 10^{-5}$	$4.4 \times 10^{-7}$
TBAP	10	100	$6.0 \times 10^{-5}$	$4.2 \times 10^{-7}$

**Table 4.5:** Data for figure 4.6 analyses at different scan rates between  $5\text{ - }100\text{ mV s}^{-1}$ . (Electrode area =  $0.0044\text{ cm}^2$ ) and  $n=0.33$ .

Poly(py-NH<sub>2</sub>) was deposited potentiostatically from a 10 mM solution of the monomer and 0.1 M TBAP in 50 mM HBF<sub>4</sub>/CH<sub>3</sub>CN. Deposition times ranged from 50 to 200 seconds at a potential of 1.1 V. **Figure 4.7** refers that the current increases sharply with applied potential, after which there is an initial rise in the current that decays gradually to give a plateau shape. Generally, this “plateau” in the current can be interpreted as an increase in the number of electroactive sites on the electrode surface.<sup>27, 41</sup> After this, a region where the current remains relatively constant for a long time may be noted. Panel B illustrates that the charge increases with  $t^{1/2}$  because of being a diffusion controlled process. The thickness,  $h_f^*$  (μm), as shown in **Table 4.6** for the py-NH<sub>2</sub> film, was estimated using equations 2.5 and 2.6 in the section 2.2.1.

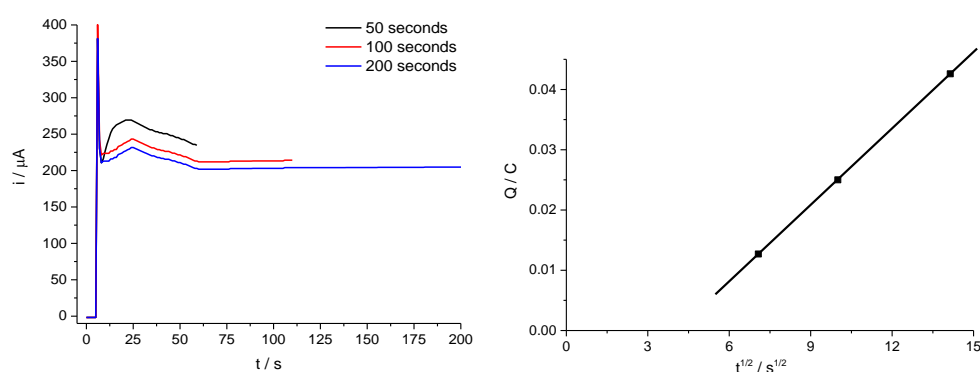


**Figure 4.7:** Current-time transients for potentiostatic electrodeposition of 10 mM *N*-3-aminopropylpyrrole in 0.1 M TBAP/CH<sub>3</sub>CN and 50 mM HBF<sub>4</sub> at 1.1 V vs. an Ag/AgCl over 50, 100 and 200 seconds. B) Plot of charge vs. square root of time (data from panel A).

Monomer conc.(mM)	Time / s	Charge $Q / \text{C}$	Thickness / μm
10	50	0.0127	0.25
10	100	0.0250	0.60
10	200	0.0426	0.84

**Table 4.6:** Electrical charge during electropolymerisation of 20 mM Py-NH<sub>2</sub> for times of 50, 100, and 200 seconds. Au electrode area was 0.23 cm<sup>2</sup>, molecular weight of Ani-NH<sub>2</sub> is 122.16 g mol<sup>-1</sup> and its density is ca. 1.09 g cm<sup>-3</sup>.

#### 4.3.4 Characterization of poly(*N*-3-aminopropylpyrrole)

Polymer films were rinsed with dry acetonitrile and then placed in a monomer-free solution containing 0.1 M TBAP/HBF<sub>4</sub> in acetonitrile. **Figure 4.8** panel A shows the electrochemical response of the polymer film which was prepared at 10 mV s<sup>-1</sup> (**Figure 4.6** panel A). As mentioned previously, the purpose of this examination is to note any electrochemical changes in redox cycling at different scan rates. **Figure 4.8** B shows that

both anodic and cathodic peak potentials are proportional to the scan rate for the same film; moreover, both redox peak currents are linearly dependent on scan rates, as shown in **Figure 4.8 C**.

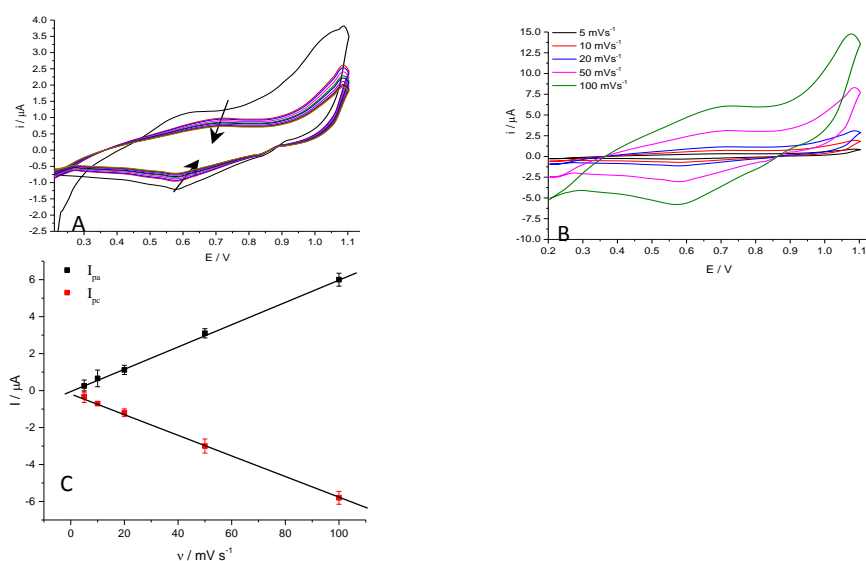


**Figure 4.8:** Voltammetric response of poly-N-3-aminopropylpyrrole film prepared at  $10 \text{ mV s}^{-1}$  (Figure 4.6 panel A), and acquired in  $0.1 \text{ M TBAP/HBF}_4$  in  $\text{CH}_3\text{CN}$  solution at  $-0.1$  to  $1.1 \text{ V}$ . B) Voltammetric responses of the same film at different scan rates,  $5$ – $100 \text{ mV s}^{-1}$ ; (C) variation of cathodic peak current (from curves in panel (B)) with scan rate.

Supporting electrolyte	Electrolytes	Scan rate / $\text{mV s}^{-1}$	$Q_{\text{red, 1st cycle}}$	$Q_{\text{red, 10th cycle}}$	$Q_{\text{red, 10th}} / Q_{\text{red, 1st}}$
TBAP/HBF <sub>4</sub>	TBAP	5	$3.25 \times 10^{-5}$	$2.88 \times 10^{-5}$	0.90
		10	$3.03 \times 10^{-5}$	$2.67 \times 10^{-5}$	0.88
		20	$2.77 \times 10^{-5}$	$2.58 \times 10^{-5}$	0.93
		50	$2.61 \times 10^{-5}$	$2.36 \times 10^{-5}$	0.90
		100	$1.93 \times 10^{-5}$	$2.12 \times 10^{-5}$	0.91

**Table 4.7:** Charge reduction values of Py-NH<sub>2</sub> panels (a) in Figure 4.6 exposed to TBAP/CH<sub>3</sub>CN electrolytes (monomer free) and  $n$  value = 0.33.

Electropolymerisation of Py-NH<sub>2</sub> was carried out potentiodynamically under the same conditions given in section 4.3.3 onto a gold-coated crystal at a scan rate of  $10 \text{ mV s}^{-1}$  for four cycles, as shown in **Figure 4.9**. **Figure 4.9** panel A illustrates an increasing number of cyclic scans led to an increase in the amount of current accompanying the electropolymerisation process. In Figure 4.9 panel B shows that the mass growth clearly starts at  $1.05 \text{ V}$ ; moreover, this curve provides a clear picture as to the increase in polymer mass cycle-to-cycle.<sup>28-30</sup> Another important point can be concluded from this figure, in the sense that during the reduction of the polymer film there was no obvious change in polymeric mass.<sup>30,31, 32</sup> As it was mentioned in the section 4.3.2 the gradient can be used to estimate the apparent molar mass ( $M_{\text{app}}$ ) (monomer, anions and solvent molecules) involved in the electropolymerisation process and the  $M_{\text{app}}$  can be calculated using data

present in **Figure 4.9** panel D.<sup>33,34</sup> According to this, the gradient ( $\Delta m/\Delta q$ ) is  $9.33 \times 10^{-3} \text{ g/C}$  and thus the  $M_{\text{app}}$  was equal to  $119 \text{ g mol}^{-1}$ . This  $M_{\text{app}}$  is close to that of *M.wt* of monomer ( $122 \text{ g mol}^{-1}$ ). The surface coverage was calculated according to equation 2.4 as being  $1.99 \times 10^{-7} \text{ mol cm}^{-2}$  based on the calculated charge ( $1.03 \times 10^{-3} \text{ C}$ ) from the cyclic voltammogram in **Figure 4.9** panel A.

The polymer film thus prepared was washed with dry acetone three times and placed in (monomer- free)  $0.1 \text{ M TBAP/CH}_3\text{CN}$ . It was then used in an EQCM experiment with a potential window ranging from  $0.3$  to  $1.2 \text{ V vs. Ag/AgCl}$  at a scan rate of  $10 \text{ mV s}^{-1}$  for 10 cycles to study the influence of perchlorate ion movement on the electrochemical behaviour of the polymer film during the redox process.<sup>38-40</sup> **Figure 4.10** panel A shows that the first scan has higher anodic and cathodic peaks compared to later cycles, where the current peaks clearly decrease in the second scan until reaching a steady state during subsequent scan cycles. **Figure 4.10** panel B shows that the mass clearly increases at  $0.9 \text{ V}$  due to insertion of perchlorate ions and solvent molecules into the film after the oxidation process. Similarly, the mass of the polymer film decreases with the start of the reduction cycle due to the expulsion of perchlorate ions and solvent molecules from the polymer film. Surface coverage of polymer film ( $\Gamma$ /  $\text{mol cm}^{-2}$ ) was estimated to be  $2.1 \times 10^{-7} \text{ mol cm}^{-2}$  based on the cathodic charge shown in **Figure 4.9** panel A. it can be noted that surface coverage values of polymer film was consistent during deposition and redox process study.

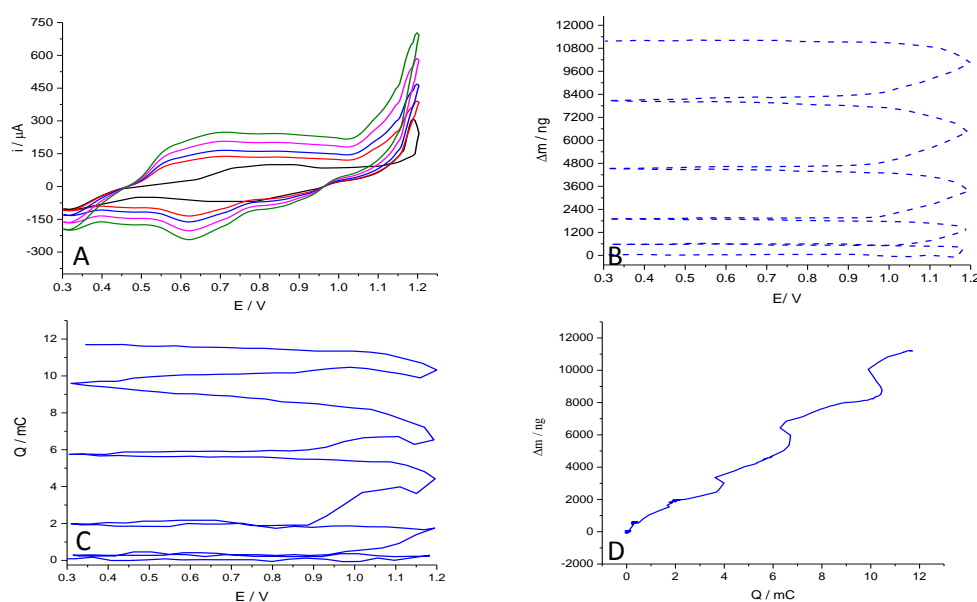


**Figure 4.9:** Representative electrochemical responses for of  $10 \text{ mM py-NH}_2$  (scan rate,  $\nu = 10 \text{ mV s}^{-1}$ ) in  $0.1 \text{ M TBAP/CH}_3\text{CN}$ . (a)  $i-E$ ; (b)  $\Delta m-E$ ; (c)  $Q-E$ ; (d)  $\Delta m-Q$ . Electrode: gold on a QCM crystal with an area of  $0.23 \text{ cm}^2$ .

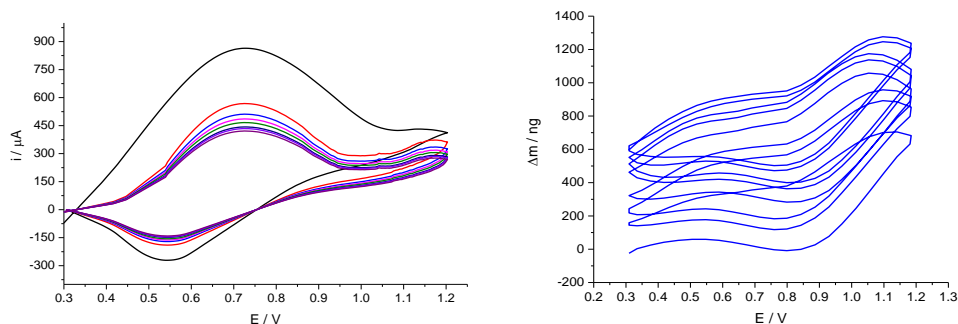


**Figure 4.10:** Representative electrochemical responses for poly-py-NH<sub>2</sub> from Figure 4.9 (scan rate,  $\nu = 10 \text{ mV s}^{-1}$ ) in 0.1 M TBAP/CH<sub>3</sub>CN (monomer free). (a)  $i$ - $E$ ; (b)  $\Delta m$ - $E$ . Electrode: gold on a QCM crystal with an area of  $0.23 \text{ cm}^2$ .

#### 4.3.5 Electropolymerisation of pentafluorophenyl-3-(pyrrol-1-yl) propanoate

Electropolymerisation of Py-pfp film was performed potentiodynamically from a solution of 10 mM Py-pfp with 0.1 M TBAP/CH<sub>3</sub>CN onto an Au electrode at a potential range of 0 V to 1.3 V vs. an AgCl/Ag for 10 cycles at various scan rates (5-100 mV s<sup>-1</sup>). **Figure 4.11** panel A shows, specifically in the first scan, that the formation of the polymer film started at  $E_{pa} = 0.93 \text{ V}$ . After the end of the first scan, the formation of a nucleation loop curve noted, and which often accompanies the electropolymerisation process. In the second scan, the intensity of the current associated with the electro-oxidation process increases with successive deposition scan cycles; this increase in the current peak is indicative of the formation of a polymer film.<sup>42</sup> In the second scan, a new anodic peak appears at  $E_{pa} = 0.85 \text{ V}$ , and a new cathodic peak at  $E_{pc} = 0.77 \text{ V}$ , due to the redox switching of the poly(py-pfp) film that formed during the first scan cycle.<sup>43</sup> **Figure 4.11** panel B shows cyclic voltammogram (scan 10) of electrodeposition the same monomer with different scan rates at same polymerisation conditions.

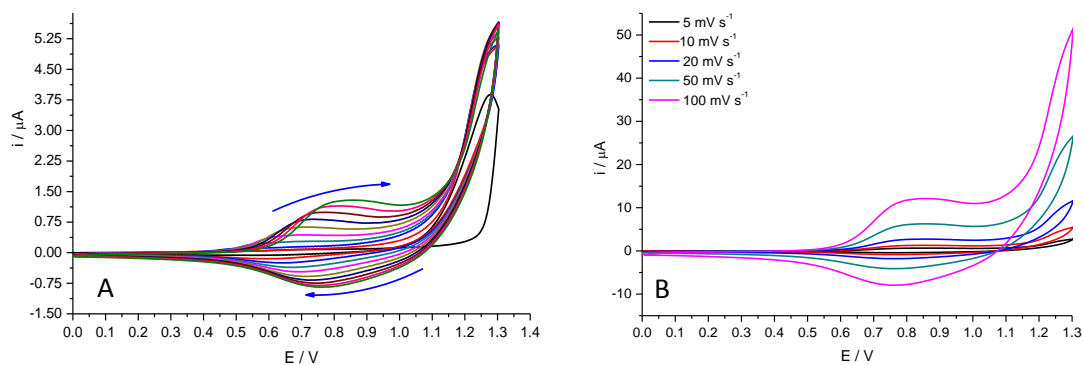


**Figure 4.11:** (A) Cyclic voltammogram resulting during electropolymerization of 10 mM py-pfp in 0.1 M TBAP/CH<sub>3</sub>CN scan rate  $\nu = 10 \text{ mV s}^{-1}$  over 10 scans; (B) cyclic voltammogram of electropolymerisation of py-pfp at different scan rates,  $\nu$ , of 5-100 mV s<sup>-1</sup>. Au electrode area was  $0.0044 \text{ cm}^2$ .

Supporting electrolyte	Number of scans	Scan rate ( $\text{mV s}^{-1}$ )	Reduction peak charge $Q / \text{C}$	Coverage $\Gamma / \text{mol cm}^{-2}$
TBAP	10	5	$7.80 \times 10^{-5}$	$4.13 \times 10^{-7}$
		10	$5.15 \times 10^{-5}$	$3.64 \times 10^{-7}$
		20	$4.32 \times 10^{-5}$	$3.08 \times 10^{-7}$
		50	$4.02 \times 10^{-5}$	$2.85 \times 10^{-7}$
		100	$3.44 \times 10^{-5}$	$2.43 \times 10^{-7}$

**Table 4.8:** Data for figure 4.13 and analyses at different scan rates between 5-100  $\text{mV s}^{-1}$ . (Electrode area =  $0.0044\text{cm}^2$ ) and  $n=0.33$ .

Poly(py-pfp) films were deposited potentiostatically using a potential of 1.3 V in TBAP/ $\text{CH}_3\text{CN}$  solution containing 10 mM py-pfp over various deposition times of 50, 100 and 200 seconds. **Figure 4.12** shows that in the first few seconds the current rises and peaks sharply,<sup>24, 25</sup> followed by a drop because of the oxidation of monomer molecules into radical cations and their diffusion towards the electrode.<sup>26</sup> The current then increases in a gradual manner due to radical cation coupling, and is attributed to the nucleation and growth of poly(py-pfp) on the surface of the electrode. After this stage, the current will reach a steady-state phase.<sup>27</sup> Chronoamperometric measurements show that the electropolymerisation charge increased with  $t^{1/2}$  as result of a diffusion-controlled process as shown in panel B. The thickness,  $h_f^*$  ( $\mu\text{m}$ ), of poly(py-pfp) films was estimated using equations 2.4 and 2.6.<sup>23</sup> As is obvious, the increase in film thickness is proportional to increasing polymerisation time, as shown in **Table 4.9**.

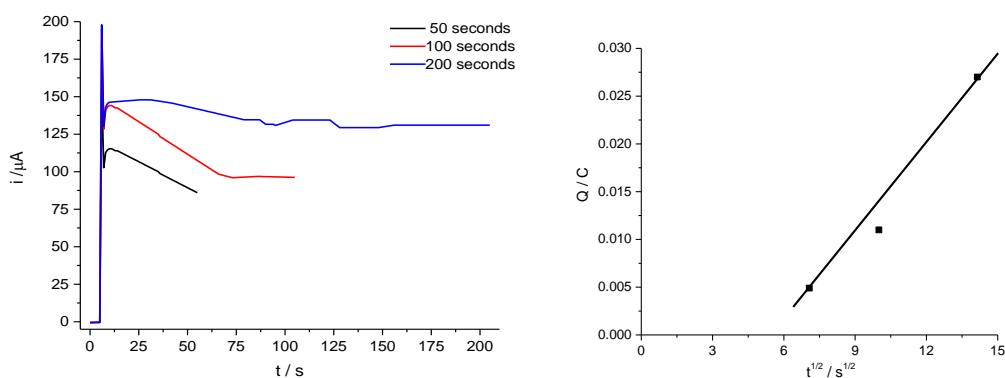


**Figure 4.12:** A) current-time transients for potentiostatic electrodeposition of 10 mM of py-pfp in TBAP/ $\text{CH}_3\text{CN}$  solution at 1.30 V vs. an Ag/AgCl over 50, 100 and 200 seconds. B) Plot of charge vs. square root of time (data from panel A).

Monomer conc. / mM	Time / s	Charge $Q$ / C	Thickness / $\mu\text{m}$
10	50	0.0049	0.23
10	100	0.011	0.53
10	200	0.027	1.30

**Table 4.9:** Electrical charge and thickness of polymer due to electropolymerisation of 20 mM (py-pfp) films at different deposition times of 50, 100 and 200 seconds. Au electrode area was  $0.23\text{ cm}^2$ , molecular weight of Ani-pfp is  $305.06\text{ g mol}^{-1}$  and its density is ca.  $1.2\text{ g cm}^{-3}$ .

#### 4.3.6 Characterisation of poly(pentafluorophenyl-3-(pyrrol-1-yl) propanoate

After deposition, the poly(py-pfp) films were washed with dry acetonitrile and then immersed in monomer-free 0.1 M TBAP/ $\text{CH}_3\text{CN}$  solution. **Figure 4.13** panel A shows the electrochemical response of the polymer electrode thus prepared at  $10\text{ mV s}^{-1}$  scan rates (**Figure 4.11** panel A). Maintaining the electroneutrality of the polymer chains requires an exchange of counterions with the film during the redox process. Polypyrrole film has positive sites over the polymer which, for electroneutrality, requires the entry of anions (in this instance,  $\text{ClO}_4^-$ ) into the polymer chains.<sup>44-46</sup> **Figure 4.13** panel B shows that both anodic and cathodic peak potentials are proportional to the scan rate for the same film; moreover, a linear relationship was observed between the scan rate and peak currents, as shown in **Figure 4.13** panel C.

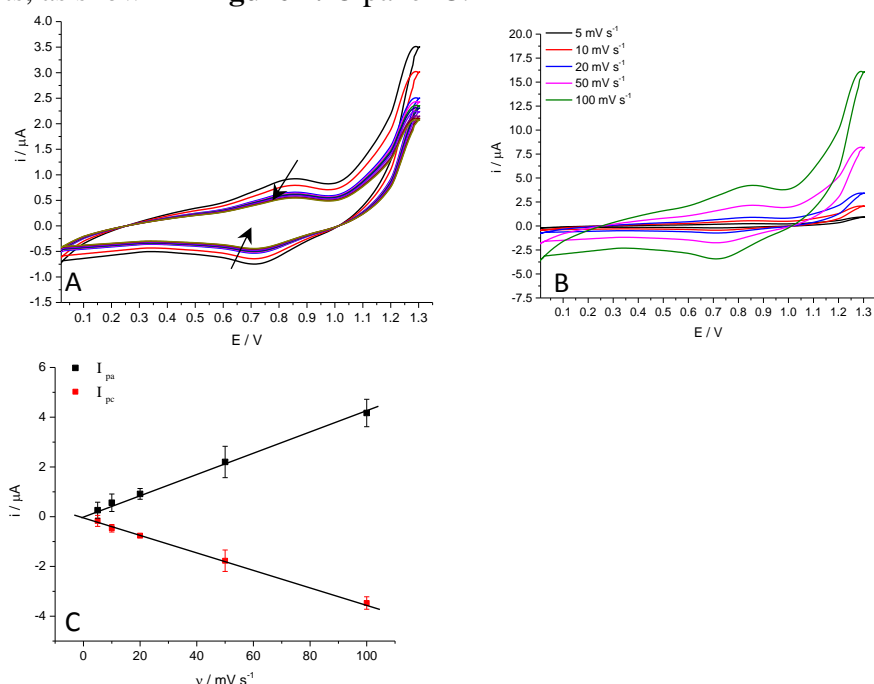


**Figure 4.13:** Voltammetric response of poly(py-pfp) film prepared at  $10\text{ mV s}^{-1}$  with TBAP, and acquired in 0.1 M TBAP/ $\text{CH}_3\text{CN}$  (monomer free) at 0.0 to 1.3 V vs. Ag/AgCl. B) Voltammetric responses of same film at different scan rates, 5-  $100\text{ mV s}^{-1}$ ; (C) variation of cathodic peak current (from curves in panel (B)) with scan rate.

Supporting electrolyte	Electrolytes	Scan rate / $\text{mV s}^{-1}$	$Q_{\text{red, 1st cycle}}$	$Q_{\text{red, 10th cycle}}$	$Q_{\text{red, 10th}} / Q_{\text{red, 1st}}$
TBAP	TBAP	5	$3.91 \times 10^{-5}$	$3.52 \times 10^{-5}$	0.90
		10	$3.38 \times 10^{-5}$	$2.91 \times 10^{-5}$	0.86
		20	$3.04 \times 10^{-5}$	$2.80 \times 10^{-5}$	0.92
		50	$2.68 \times 10^{-4}$	$2.52 \times 10^{-5}$	0.94
		100	$2.52 \times 10^{-3}$	$2.36 \times 10^{-5}$	0.93

**Table 4.10:** Reduction charge values of Py-pfp panels (a) in Figure 4.13 exposed to TBAP/acetonitrile electrolyte (monomer free).

Electrodeposition of 10 mM (Py-pfp) was achieved potentiodynamically in TBAP/ $\text{CH}_3\text{CN}$  solution on an Au layer-coated quartz crystal using a potential window ranging from 0.0 to 1.35 V vs. Ag/AgCl and a scan rate of  $10 \text{ mV s}^{-1}$  over 5 cycles. **Figure 4.14** panel A shows the five cyclic voltammograms recorded during the polymerisation process. Figure 4.14 panel B illustrates that the first cycle scan shows no clear increase in mass over the potential window from 0.0 to 1.15 V. Thereafter, it is obvious that the mass of polymer film deposited onto the electrode began at around 1.15 V; moreover, this curve provides clear evidence as to the increase in polymer mass cycle-to-cycle.<sup>28-30</sup> panel D shows the variation in the mass of the film versus the charge consumed during the electropolymerisation of py-pfp. The gradient of panel D gives the apparent molar mass of electroactive units ( $M_{\text{app}}$ ) involved in the polymerisation as mentioned in section 4.3.2.  $M_{\text{app}}$  was calculated to be  $350 \text{ g mol}^{-1}$  and  $(\Delta m / \Delta q)$  is  $1.71 \times 10^{-3} \text{ g / C}$ . Comparing the molar mass of these materials with calculated values for monomer unit refers to that all species have a role during polymerisation processes. Anions and solvent seem to play role in polymerisation processes. Since  $M_{\text{app}}$  was close to the molar mass of the monomer ( $305 \text{ g mol}^{-1}$ ) and the different could be related to anions and solvent molecules. This equals ca. 0.3 anion and 0.2 solvent molecules (per monomer unite). The surface coverage of poly(py-pfp) was estimated to be  $1.50 \times 10^{-7} \text{ mol cm}^{-2}$ .

The prepared polymer film was placed in monomer-free 0.1 M TBAP/ $\text{CH}_3\text{CN}$ ; this was used for an EQCM experiment with a potential ranging from 0.0 to 1.3 V using a scan rate of  $10 \text{ mV s}^{-1}$  over 10 cycles to study the influence of perchlorate ion movement on the electrochemical behaviour of the polymer film during the redox process.<sup>40, 45</sup> It can be seen from **Figure 4.15** panel A that the first scan has higher anodic and cathodic peaks compared to later cycles, where the current peaks clearly decrease in the second scan until

reaching steady state in subsequent scan cycles. **Figure 4.15** panel B shows the mass clearly increases at 0.9 V due to the insertion of perchlorate ions and solvent molecules into the polymer film, while the mass of the polymer film decreases at the start of the reduction cycle because of the expulsion of perchlorate ions and solvent molecules. Surface coverage of polymer film ( $\Gamma$ / mol cm<sup>-2</sup>) was estimated to be  $1.07 \times 10^{-7}$  mol cm<sup>-2</sup> based on the cathodic charge shown in **Figure 4.15** panel A. Surface coverage values of polymer film was consistent during electrodeposition and redox process study.

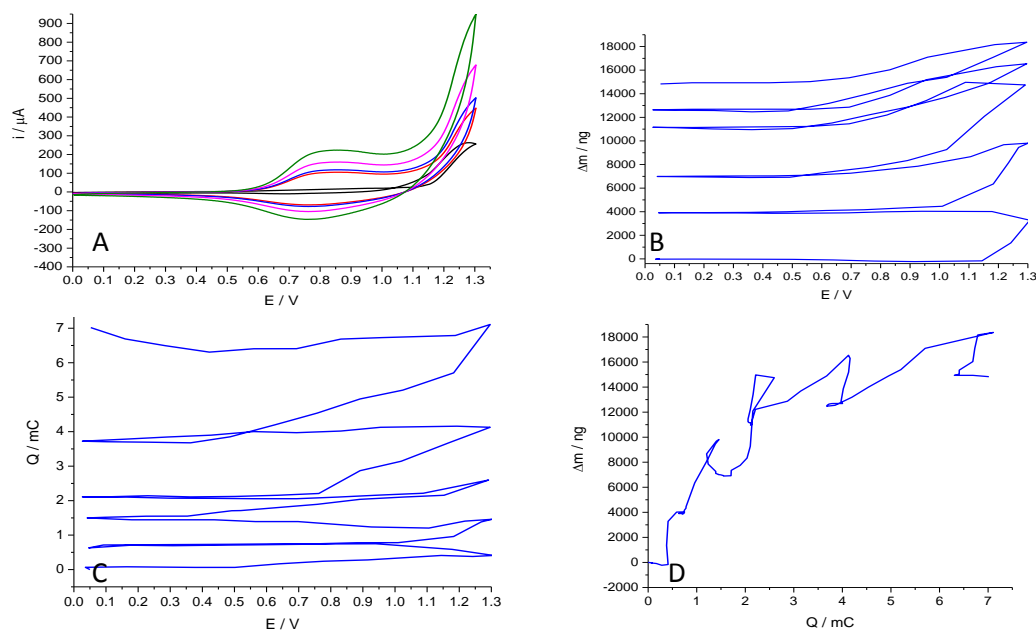


**Figure 4.14:** Representative electrochemical responses for electropolymerisation of 10mM py-pfp (scan rate,  $\nu = 10 \text{ mV s}^{-1}$ ) in 0.1 M TBAP / CH<sub>3</sub>CN. (a)  $i$ - $E$ ; (b)  $\Delta m$ - $E$ ; (c)  $Q$ - $E$ ; (d)  $\Delta m$ - $Q$ . Electrode: gold on a QCM crystal with area of 0.23 cm<sup>2</sup>.

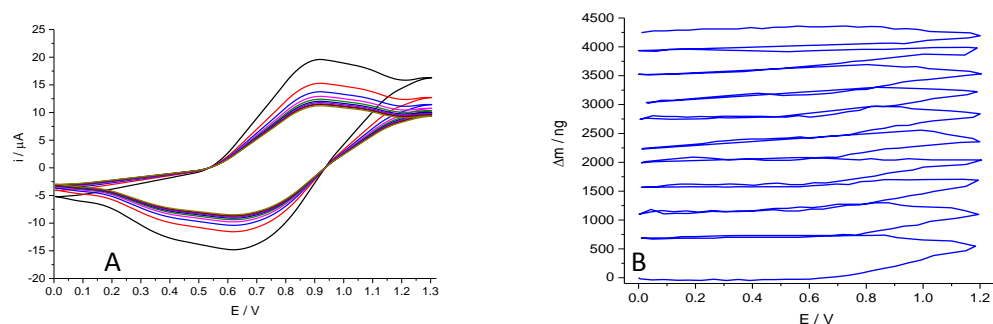


**Figure 4.15:** Representative electrochemical responses for poly(py-pfp) from Figure 4.16 (scan rate,  $\nu = 10 \text{ mV s}^{-1}$ ) in 0.1 M TBAP/CH<sub>3</sub>CN (monomer free). (a)  $i$ - $E$ ; (b)  $\Delta m$ - $E$ . Electrode: gold on a QCM crystal with an area of 0.23 cm<sup>2</sup>.

Analysis of findings show that, The cyclic voltammogram of poly(Py-COOH) has a broad redox peaks at 0.8 V and 0.7 V, whereas the cyclic voltammogram of poly(Py-pfp) film exhibits redox peaks at 0.85 V and 0.77 V. The appearance of the oxidation peak in the poly(Py-pfp) at higher values than for to Py-COOH was attributed to existence of pfp

groups which contain fluoro groups and carbonyl bonds that have electron withdrawing effect that is stronger than that of the carboxylic groups in Py-COOH.<sup>47, 48</sup>

#### 4.3.7 Electropolymerisation of copolymer Py-co-PyFmoc

Figure 4.18 depicts a cyclic voltammogram of the electrodeposition of the copolymer py-Fmoc (10 mM), which was electrodeposited on an Au electrode using a potential range of -0.6 to 1.1 V in a 0.1 M TBAP/CH<sub>3</sub>CN solution at a scan rate of 10 mV s<sup>-1</sup> over 10 scan cycles.<sup>14, 23</sup> Electrodeposition occurred at about 0.9 V vs. Ag/AgCl during the first potential sweep, as shown in **Figure 4.16** panel A. In the second scan, the forward sweep cycle shows new oxidation and reduction peaks at about 0.35 V and 0.25 V, respectively, due to the redox process for the copolymer film. Electrodeposition was conducted at various scan rates of 5-100 mV s<sup>-1</sup> under identical conditions as shown in panel B. As previously mentioned in section 4.1.1, the surface coverage of the copolymer film was estimated.<sup>21, 22</sup> **Table 4.14** shows the cathodic peak charge and surface coverage for all films prepared.

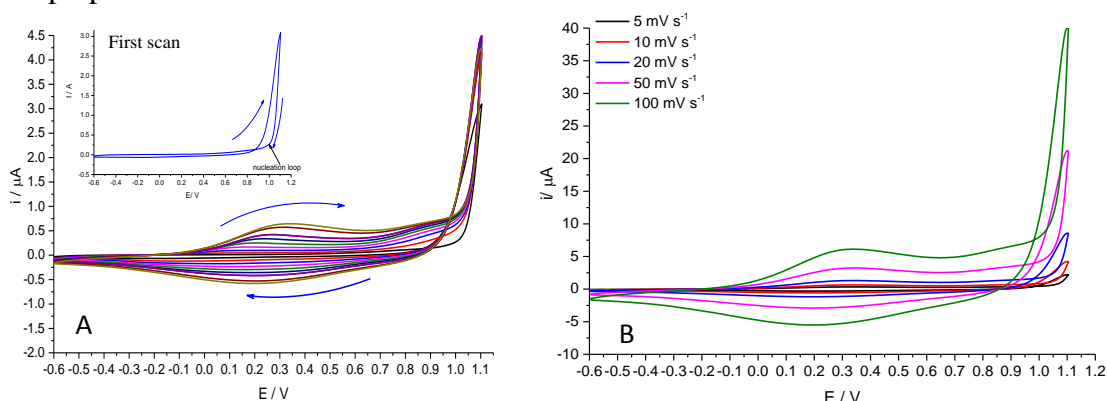


**Figure 4.16:** (A) Cyclic voltammogram resulting from electropolymerisation of 10 mM py-co-pyFmoc in 0.1M TBAP/CH<sub>3</sub>CN scan rate  $v = 10 \text{ mV s}^{-1}$  over 10 scans; (B) cyclic voltammogram of same film at different scan rates,  $v$ , 5-100 mV s<sup>-1</sup> (inset curve shows the first scan cycle).

Supporting electrolyte	Number of scans	Scan rate (m.v.s <sup>-1</sup> )	Reduction peak charge $Q / \text{C}$	Coverage $\Gamma / \text{mol cm}^{-2}$
TBAP	10	5	$6.35 \times 10^{-5}$	$4.53 \times 10^{-7}$
		10	$5.78 \times 10^{-5}$	$4.12 \times 10^{-7}$
		20	$5.65 \times 10^{-5}$	$4.01 \times 10^{-7}$
		50	$5.20 \times 10^{-5}$	$3.71 \times 10^{-7}$
		100	$5.03 \times 10^{-5}$	$3.58 \times 10^{-7}$

**Table 4.11:** Reduction charge and surface coverage for polymerisation of py-co-Fmoc films at different scan rates between 5-100 mV s<sup>-1</sup>. Au electrode area was 0.0044 cm<sup>2</sup> and  $n = 0.33$

Electrodeposition of poly(Py-Fmoc) was achieved potentiostatically using potential 1.1 V for 10 mM py-co-Fmoc in TBAP/CH<sub>3</sub>CN solution over times ranging between 50 to 200 seconds. These ( $i-t$ ) curves in Figure 4.17 show a maximum current peak a few seconds after the potential was applied due to the double layer charge formation at the electrode substrate, followed by a decrease in current value due to the oxidation of monomers.<sup>49</sup> The graduated increase in the current was noted after second the stage (sharp drop) plateau shape, as shown in **Figure 4.17**. The existence of this “plateau” in current value probably corresponds to the gradual growth and formation of the polymeric nuclei, after which the current’s gradual increase may be attributed to an increase in the electroactive area, which occurs due to polymer deposition.<sup>50</sup> Panel B shows that the charge increased with  $t^{1/2}$  as result of a diffusion-controlled process. As expected, and the polymer film thickness increased five-fold on increasing the polymerisation time from 50 to 200 seconds. The thickness,  $h_f^*$  ( $\mu\text{m}$ ), of copolymer film, was calculated, It is clear that the increase in film thickness was proportional to the increase in polymerisation time, as shown in **Table 4.12**.

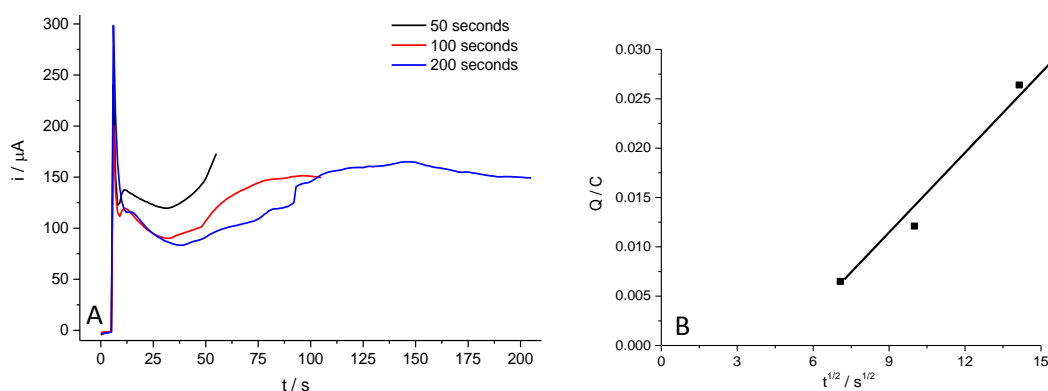


**Figure 4.17:** A) current-time transients for potentiostatic electrodeposition of 20 mM of Ani-Fmoc in HClO<sub>4</sub>/CH<sub>3</sub>CN solution at 1.15 V vs. Ag/AgCl over 50, 100 and 200 seconds. B) Plot charge vs. square root of deposition time.

Monomer conc. / mM	Time / s	Charge, $Q$ / C	Thickness / $\mu\text{m}$
10mM	50	0.0065	0.36
10mM	100	0.0121	0.68
10mM	200	0.0264	1.50

**Table 4.12:** Electrical charge and thickness found from the electropolymerization of py-co-pyFmoc films deposited over 50, 100 and 200 second deposition times on an Au electrode (area 0.23 cm<sup>2</sup>), molecular weight of py-Fmoc is 345 g mol<sup>-1</sup> and its density is ca. 1.2 g cm<sup>-3</sup>.

## 4.3.8 Characterization of copolymer py-co-Fmoc

Copolymer films were studied in a monomer-free 0.1 M TBAP/CH<sub>3</sub>CN solution to determine their electrochemical behaviours of the polymer films after exposing them to the same electrolytes at different scan rates. **Figure 4.18 A** shows the electrochemical response of copolymer py-co-Fmoc at 10 mV s<sup>-1</sup>. **Figure 4.18 B** shows that redox peaks are proportional to the scan rate; moreover, both redox peak currents are linearly dependent on scan rates, as shown in **Figure 4.18 C**.

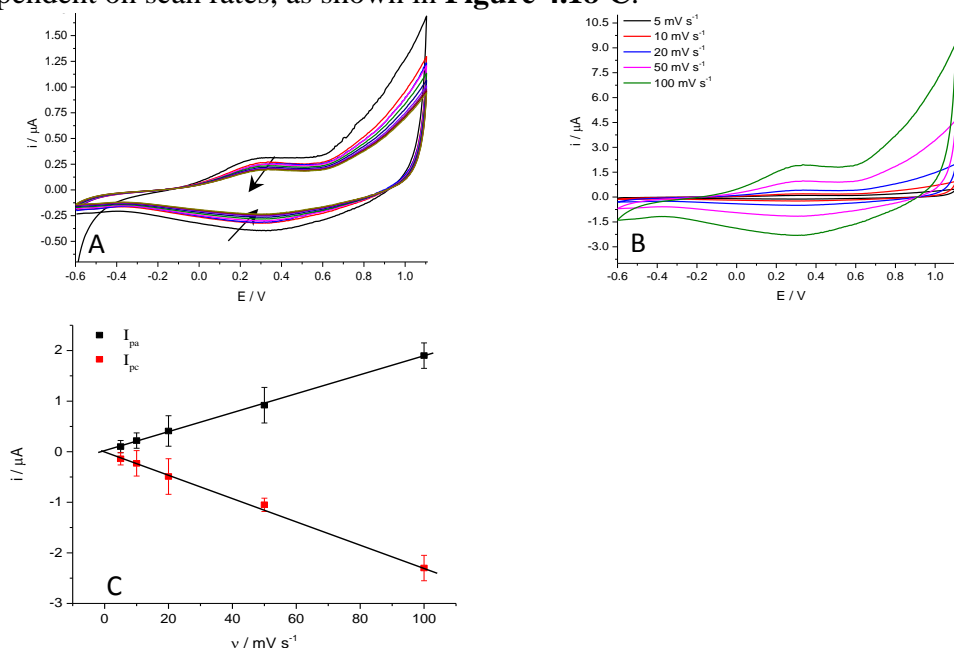


**Figure 4.18:** Voltammetric response of copolymer py-Fmoc film prepared at 10 mV s<sup>-1</sup> (see Figure 4.16) in TBAP/CH<sub>3</sub>CN solution, and acquired in 0.1M TBAP/CH<sub>3</sub>CN with a potential window of -0.6 V to 1.1 V B) Voltammetric responses of the same film at different scan rates, 5- 100 mV s<sup>-1</sup>; (C) variation of cathodic peak current (from curves in panel (B)) with scan rate.

Supporting electrolyte	Electrolyte	Scan rate / mV s <sup>-1</sup>	Q red, 1st cycle	Q red, 10th cycle	Q red,10th / Q red, 1st
TBAP	TBAP	5	3.38 x 10 <sup>-5</sup>	3.05 x 10 <sup>-5</sup>	0.90
		10	3.14 x 10 <sup>-5</sup>	2.70 x 10 <sup>-5</sup>	0.86
		20	2.79 x 10 <sup>-5</sup>	2.57 x 10 <sup>-5</sup>	0.92
		50	2.58 x 10 <sup>-4</sup>	2.43 x 10 <sup>-5</sup>	0.94
		100	2.48 x 10 <sup>-3</sup>	2.31 x 10 <sup>-5</sup>	0.93

**Table 4.12:** Reduction charge values of Py-pfp panels (a) in Figure 4.18 exposed to TBAP/acetonitrile electrolyte (monomer free).

Electrodeposition of copolymer was monitored by EQCM using a 0.1 M TBAP/ CH<sub>3</sub>CN solution over a potential ranging from -0.60 to 1.15 V with scan rate of 10 mV s<sup>-1</sup> for five cycles, as shown in **Figure 4.19**. Panel A shows the current values accompanying the electropolymerisation increase with the number of cyclic scans as a sign of polymer film

growth. The copolymer film growth was reflected in its increasing mass, as shown in panel B. The mass increase clearly starts to take place after 0.9 V. The mass was about 750 ng after 1 cycle and 11,100 ng after 5 cycles. It appears that the mass steadily increases as estimated on a cycle-to-cycle basis.<sup>28-30</sup> The relationship between the film mass and charge consumed is shown in **Figure 4.19** panel D. The  $M_{app}$  of electroactive units (monomer, anions and solvent molecules) involved in the electropolymerisation process can be calculated using data from **Figure 4.19** panel D.<sup>33, 34</sup> According to this, the gradient was found to be  $1.92 \times 10^{-3} \text{ g / C}$  and thus  $M_{app}$  of  $432 \text{ g mol}^{-1}$ . Comparing the molar mass of species involved polymerisation with calculated values for monomer unit refers to that all species play a role during electrodeposition process. Since the molar mass of *Py-Fmoc* is  $343 \text{ g mol}^{-1}$ , the difference of  $89 \text{ g mol}^{-1}$  was considered as the anions and solvent molecules were incorporated into the polymer film. This equals ca. 0.33 anion and 0.56 solvent molecules (per monomer unite). The surface coverage of the polymer film was calculated to be  $1.13 \times 10^{-7} \text{ mol cm}^{-2}$ .

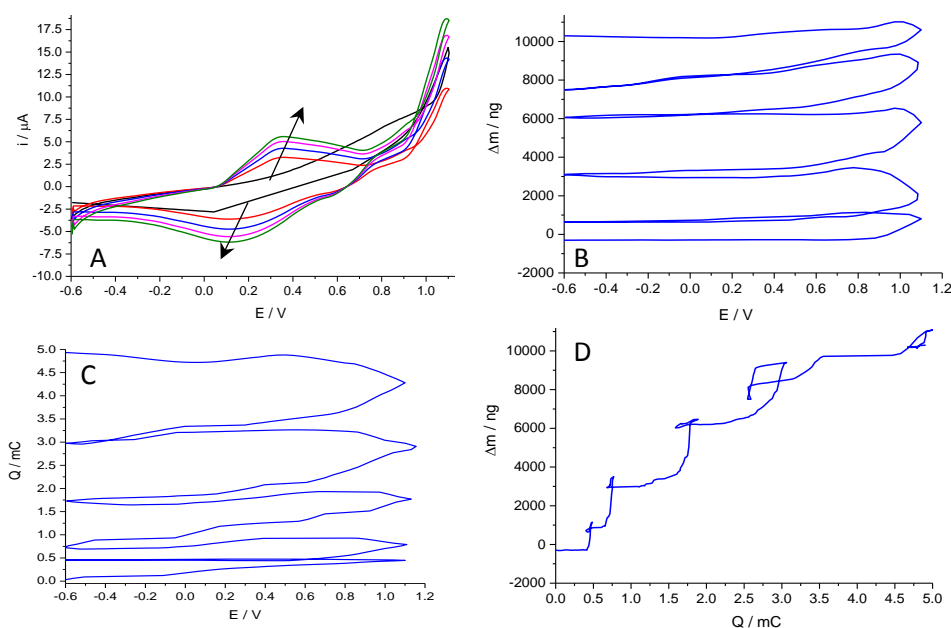


**Figure 4.19:** Representative electrochemical responses for electropolymerization of 10 mM *py-Fmoc* at  $10 \text{ mV s}^{-1}$  from 0.1 M TBAP/ $\text{CH}_3\text{CN}$ . (a)  $i$ - $E$ ; (b)  $\Delta m$ - $E$ ; (c)  $Q$ - $E$ ; (d)  $\Delta m$ - $Q$ . Electrode: gold on a QCM crystal with a surface area of  $0.23 \text{ cm}^2$ .

EQCM was used to monitor the electrochemical behaviour of copolymer film in a 0.1 M TBAP/ $\text{CH}_3\text{CN}$  solution (monomer- free) that by applying a potential from -0.3 to 1.1 V vs. Ag/AgCl at a scan rate of  $10 \text{ mV s}^{-1}$  for 10 cycles.<sup>38-40</sup> **Figure 4.20** panel A shows that the first scan has higher redox peaks compared to later cycles, in which the current peaks clearly decrease in the second scan until reaching steady state in subsequent scan

cycles. **Figure 4.20** panel B shows the mass change over the potential window from -0.3 to 1.0 V. It may be noted that the mass clearly increases at 0.95 V due to the insertion of perchlorate ions and solvent molecules into the polymer film after the oxidation process; similarly, the mass of polymer film decreased with the start of the reduction cycle because of the expulsion of perchlorate ions and solvent molecules. The surface coverage of the polymer film was calculated to be  $8.31 \times 10^{-8} \text{ mol cm}^{-2}$ . The comparison between of surface coverage for polymer film was demonstrated that value was consistent.

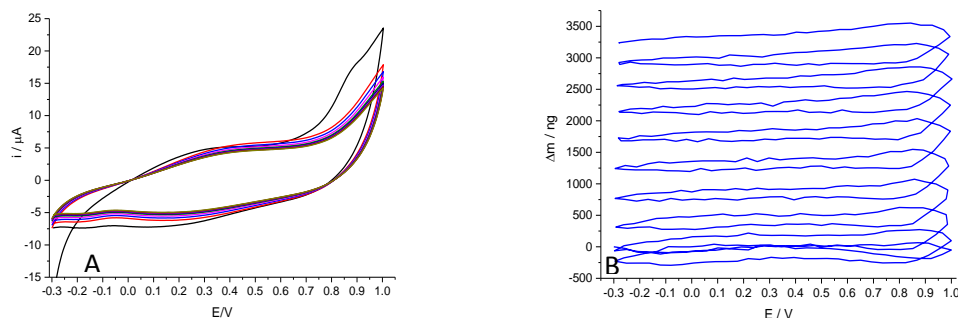


**Figure 4.20:** Representative electrochemical responses for poly-py-co-Fmoc from figure 4.16 (scan rate,  $\nu = 10 \text{ mV s}^{-1}$ ) in 0.1 M TBAP/ $\text{CH}_3\text{CN}$  (monomer free). (a)  $i-E$ ; (b)  $\Delta m-E$ . Electrode: gold on a QCM crystal with surface area of  $0.23 \text{ cm}^2$ .

The comparison between the electrochemical behaviour of poly(Py-NH<sub>2</sub>) and poly(Py-Fmoc) was demonstrated that the both oxidation waves of the poly(Py-Fmoc) (see Figure 4.16) was shifted to lower potentials in comparison to the poly(Py-NH<sub>2</sub>) monomer compound (see Figure 4.6). This shift towards lower potential might be due to the substituent group effect which led to changes in the polymer backbone and alterations in the electrostatic reactions between the oxidised Fmoc groups within the polymer chains themselves. The oxidation peak current is at 0.7 V, and reduction peak current at 0.5 V in the poly(Py-NH<sub>2</sub>). The voltammetric responses of the poly(Py-Fmoc) film illustrate that the oxidation peak at 0.35 V, and a reduction peak at 0.25 V. The difference in the intense of redox peaks for both cyclic voltammogram (Figure 4.6 and Figure 4.16) might be due to the difference in the ingress and egress of counteranions from the polymer film.

#### 4.4 Post-Polymerisation Chemical Modifications

Recently, substitution chemistry has played a key role in the modification and fine-tuning of conducting polymer properties, and in applications where this has contributed in terms of the manipulation and improvement of electroactive polymers.<sup>51</sup> The functional chains in polymers can be considered as being similar to a "molecular wire" that contributes in

terms of facilitating the transport of electrons between the electrode substrate and electrolytes,<sup>52</sup> and through this a number of chemical functionalities, such as identification properties in sensing areas, can be enhanced. In the current section, the hydrolysis reaction of activated esters and amides with suitable solutions will be studied to examine the physical and chemical stability of polymer films after loss of protection groups. **Figure 4.21** illustrates a scheme for the strategy used to incorporate ligands within the polymer film. This scenario involves polymerisation of protected monomers, either PFP (pentafluorophenyl-3-(pyrrol-1-yl) propionate) or FMOC (9-fluorenylmethoxycarbonyl), which can be easily removed and replaced after deposition. The pfp and Fmoc groups were carefully selected to achieve equilibrium between the removed and inserted groups, as well as the fact that these groups are not sufficiently large to inhibit the polymerisation process. Amide formation conjugation was used to covalently bond the receptor groups to the functionalised polymer (pfp or Fmoc) surfaces. A series of measurements were carried out to demonstrate the success of the strategy. EQCM and spectroscopic probe techniques were used to this end. QCM was applied to monitor changes in the polymer film during hydrolysis and the amidation reaction to give a clear indication as to the interaction path and substitution process within the polymer surfaces. Moreover, FTIR was used to provide clear qualitative evidence as to the conjugation between the functionalised polymer surfaces and recognition units.

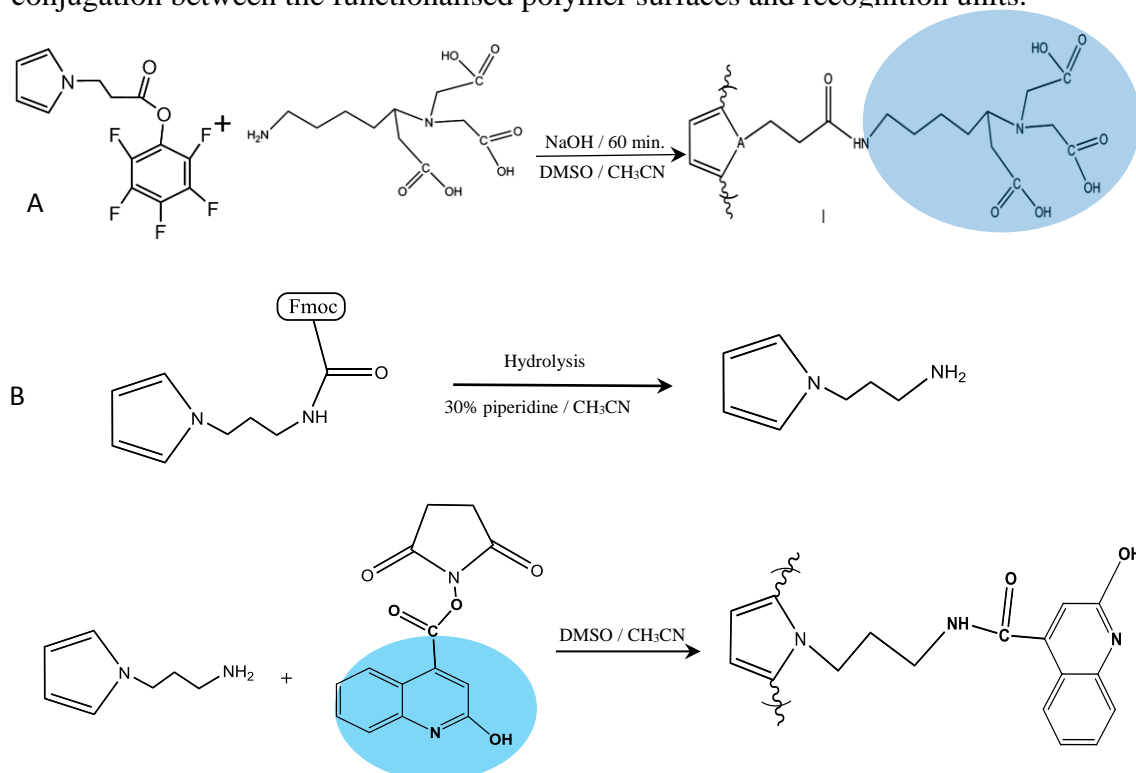


**Figure 4.21:** Scheme represents (A) Poly PFP film reaction with NTA receptor (B) Fmoc group hydrolysis and then reaction with 2-HQC receptor.

#### 4.4.1 QCM Gravimetric and FTIR Spectroscopic Monitoring of Ester Hydrolysis

To investigate the hydrolysis of poly(py-pfp) films in alkaline solution, the experiment considered different reaction times to explore the ratio of the conversion from the ester form to the carboxylic acid polymer. The challenge here was preventing the films from collapsing due to the hydrolysis process and the creation of free volume “voids” in the polymer films. To accomplish the hydrolysis process, films were immersed in 0.1 M NaOH solution for different lengths of time whilst monitoring the reaction using FTIR until the reaction was complete, as shown in **Figure 4.22**. FTIR was applied to show the absence of the carbonyl group due to pfp ester bonds, thus demonstrating the py-pfp had been successfully converted to py-COOH. The carbonyl ester band  $\nu(\text{C}=\text{O})$  at  $1785\text{ cm}^{-1}$  and  $\nu(\text{C}-\text{F})$  band at  $1000\text{ cm}^{-1}$  were not be present in the deprotected film spectrum, as shown in Figure 4.22. Hydrolysis reaction leads to the emergence of certain bands due to the carboxylic film, for instance the broad band at  $3400\text{--}3250\text{ cm}^{-1}$  which is due to the  $\nu(\text{O}-\text{H})$  stretch of the carboxylic acid (indicated by symbol \* in figure) and the band at ( $1735\text{ cm}^{-1}$ ) due to  $\nu(\text{C}=\text{O})$  stretch of the carboxylic acid (indicated by symbol + in figure). All these bands provide further confirmation of the successful removal of pfp from the surface of the polymeric film.

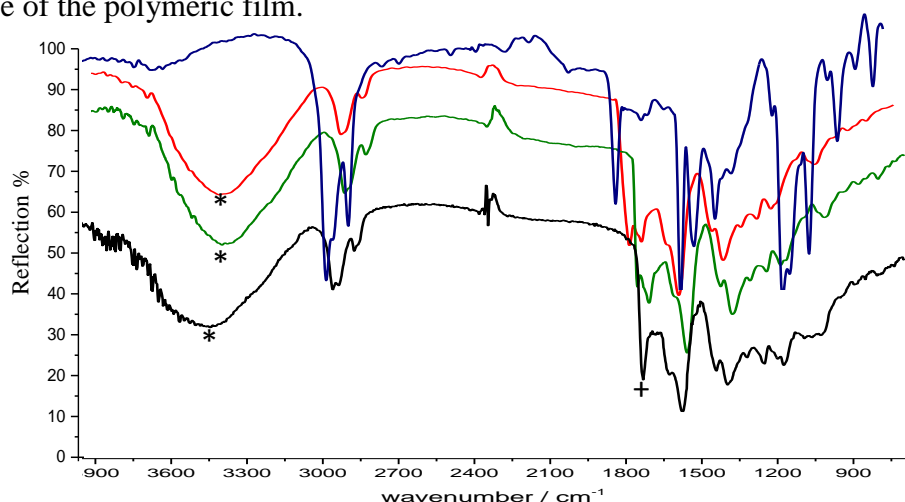


**Figure 4.22:** FTIR spectra showing hydrolysis reaction at different times over the course of the reaction. (a) Ppy-pfp as deposited (navy), (b) film after 5 min. hydrolysis (red), (c) film after 10 min. hydrolysis (green) and (d) film after 20 min. hydrolysis (black).

\*denotes the presence of carboxylic peaks and + denotes the presence of carbonyl peaks.

Moreover, EQCM was applied to study the de-protection of polymer films. EQCM was used to measure the mass changes which can occur in surface polymer films due to the tethering or removal of the desired molecules. To illustrate this point, if the mass of the films after hydrolysis (i.e., having removed the pfp leaving groups) was less than the mass

of the films before hydrolysis, the frequency of the quartz crystal resonator should increase, as can be seen in **Figure 4.23**. During the hydrolysis reaction, solvent molecules' movements can fill the voids left by the leaving groups.

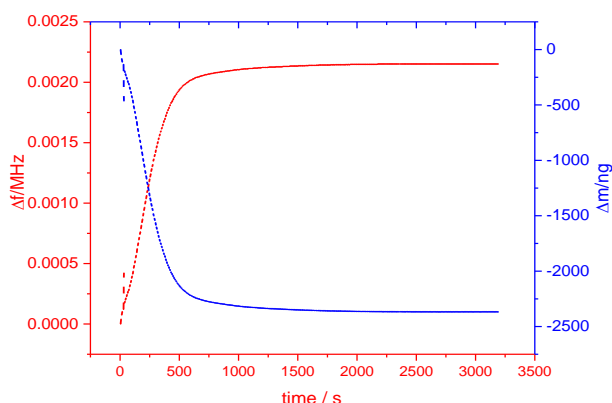


**Figure 4.23:** EQCM recorded during the deprotection of py-pfp film in an alkaline solution of 0.1 M NaOH.

Furthermore, in order to study the electrochemical behaviour of the deprotected polymer films, the cyclic voltammograms was recorded in a monomer-free 0.1 M TBAP/CH<sub>3</sub>CN solution using a 10 mV s<sup>-1</sup> scan rate as shown in **Figure 4.24**. The main aim of this process is to examine the effect of hydrolysis on the electrochemical properties of deprotected films. Result show that redox peaks of deprotected films were similar to the values observed of py-COOH in monomer free solution.

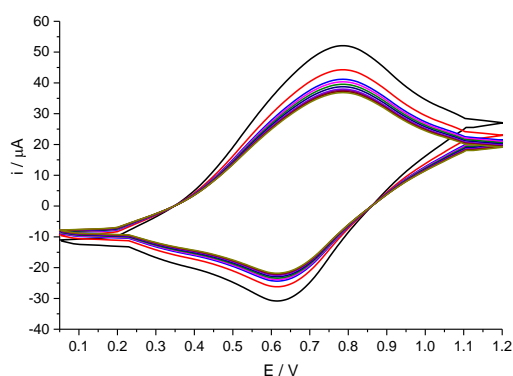


**Figure 4.24:** Cyclic voltammogram of py-pfp film after hydrolysis in a monomer-free 0.1 M TBAP/CH<sub>3</sub>CN solution as a function of repeated scans at 10 mV s<sup>-1</sup>.

From the IR spectrum in **Figure 4.22** it may be noted that the pfp molecules were removed from polymer film during the 12 minutes after the hydrolysis process, which is consistent with the QCM measurement in **Figure 4.23**, which shows that there is no clear change in the mass of the polymer film 12 minutes after hydrolysis. Voltammetric results was used to estimate surface coverage of the polymer using equation 2.4. Results demonstrated that the surface coverage equal to  $1.5 \times 10^{-7}$  mol cm<sup>-2</sup> and this implies mass of polymer ( $m_p$ )

equal to 10.55  $\mu\text{g}$  before hydrolysis (data presented in **Figure 4.14**) and based on QCM data the mass of film was equal to 14  $\mu\text{g}$  (polymer and solvent mass ( $m_p+m_s$ )) implying that solvent represent 34% of polymer film. While after hydrolysis the mass of film was 11.6  $\mu\text{g}$  based on QCM data (presented in **Figure 4.24**) and mass change of hydrolysis was -2.45  $\mu\text{g}$ . Voltammetric results demonstrated that the surface coverage equal to  $1.51 \times 10^{-7} \text{ mol cm}^{-2}$  this implies mass of polymer is 4.4  $\mu\text{g}$  and the difference between mass of polymer before and after hydrolysis was 6  $\mu\text{g}$  (almost 60% of polymer mass). Naturally, surface coverage should be has the same value as indicator of the amount of polymer present on the electrode but the values are comparable (within experimental error). The polymer film contains polymer chains with solvent molecules after polymerisation. After the hydrolysis process the film will lose pfp groups and this leads to voids and a decrease in the mass of the polymer film. In fact, the theoretical calculations show that mass of pfp groups equal to 60% and QCM findings show that the mass change of the polymer film was equal to 18%. This difference in polymer film mass between poly(Py-pfp) and poly(Py-COOH) which contains almost the same  $\Gamma$  values shows the capability for create voids and ingress a large amount of solvent molecules into the polymer film during the hydrolysis process. FTIR gives the evidence to confirm that pfp groups are left in the polymer film during hydrolysis as shown in **Figure 4.22**.

Films	Polymer deposition		polymer hydrolysis		functionalisation	
	$\Gamma \text{ mol cm}^{-2}$	$\Delta M \mu\text{g cm}^{-2}$	$\Gamma \text{ mol cm}^{-2}$	$\Delta M \mu\text{g cm}^{-2}$	$\Gamma \text{ mol cm}^{-2}$	$\Delta M \mu\text{g cm}^{-2}$
Py-pfp	$1.50 \times 10^{-7}$	14.2	$1.51 \times 10^{-7}$	-2.45	$9.87 \times 10^{-8}$	10.6

**Table 4.13:** Mass and surface coverage between polymer films (before and after hydrolysis) functionalisation for poly(Py-pfp) film.

#### 4.4.2 Monitoring of vertical penetration of receptor into ester polymer film

To accomplish the functionalisation process, a chemical bond is formed between the activated ester film, poly(py-pfp) and the receptor,  $N_{\alpha},N_{\alpha}$ -bis-(carboxymethyl)-L-lysine hydrate (NTA-lysine). The film was soaked in a solution of receptor NTA-lysine (0.1 M DMSO/ $\text{CH}_3\text{CN}$  solution (2:8 ml)) for 60 minutes before rinsing with acetonitrile. FTIR was used to monitor the reaction over time to estimate the required time for penetration and demonstrate amide formation throughout the film surface, as discussed below. The ester film, py-pfp, showed characteristic sharp bands in the FTIR spectrum at  $1790 \text{ cm}^{-1}$  due to the  $\nu(\text{C}=\text{O})$  stretch and at  $1010 \text{ cm}^{-1}$  due to the  $\nu(\text{C}-\text{F})$  bend, as shown in **Figure 4.25**. After immersion of the pfp ester film in the NTA-lysine solution, the carbonyl

stretch shifts from  $1790\text{ cm}^{-1}$  to  $1680\text{ cm}^{-1}$  due to formation of amide bonds in the polymer film (indicated by symbol + in figure). Concomitant with this shift in the carbonyl bond is a decrease in the intensity of the peak at approximately  $1010\text{ cm}^{-1}$  due to the removal of the pfp group, further suggesting the loss of the pfp group from the polymer. In addition, the appearance of a broad band at  $3350\text{ cm}^{-1}$  due to the  $\nu(\text{O-H})$  stretch (indicated by symbol \* in figure) and at  $1725\text{ cm}^{-1}$  due to the  $\nu(\text{C=O})$  stretch of the carboxylic groups in the receptor compound.

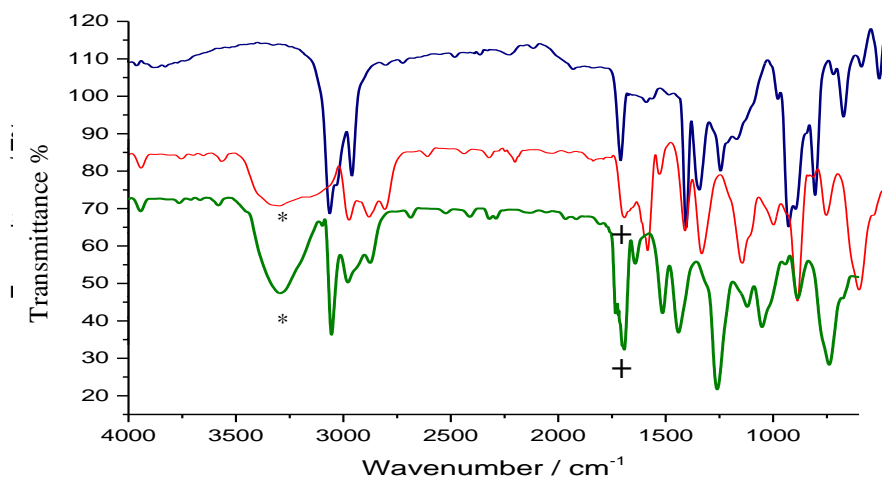


**Figure 4.25:** FTIR spectra showing the amidation reaction at different times after the start of the hydrolysis reaction. (a) Ppy-pfp as deposited (blue), (b) film after 15 min. (red), and (c) film after 60 min. amidation (green). + denotes the presence of amide and \* denotes the presence of carboxylic peaks.

QCM was used to monitor the immobilisation process for the poly(py-pfp) films. Results was demonstrated that the conversion from an ester to an amide bonds led to a progressive decrease in the frequency of the quartz crystal resonator that coincides with an increase in mass as result of the insertion of receptor, as these have a larger molecular weight than the pfp groups being removed. Where the nucleophilic attack on the ester bonds occur and this to creates new amide bonds. The molecular mass of the NTA-lysine group is  $262.2\text{ g mol}^{-1}$  while the molecular mass of the pfp is  $184\text{ g mol}^{-1}$ . **Figure 4.26** shows the changes in mass and frequency during the functionalisation reaction. It should be noted from this figure that the gradual increase in mass is the result of the formation of an amide bond, rather than the pentafluorophenyl leaving group.

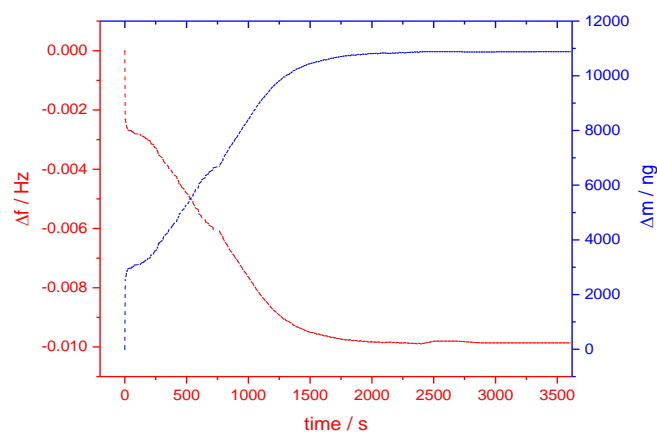


**Figure 4.26:** EQCM recorded during the immobilization process for py-pfp film with the NTA receptor unit over 60 minutes.

The electrochemical properties of py-NTA polymer film were studied and cyclic voltammograms of the film was recorded in monomer-free 0.1 M TBAP/CH<sub>3</sub>CN solution at a scan rate of 10 mV s<sup>-1</sup> as shown in **Figure 4.27**. **Figure 4.27** illustrates redox peaks similar to those observed during the monomer-free study of pfp film after hydrolysis with some shifts towards lower voltage values for both the oxidation and reduction peaks because of the receptor groups being inserted onto the polymer film surface.

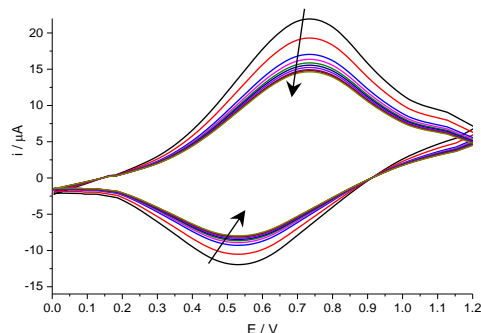


**Figure 4.27:** Cyclic voltammogram of py-NTA film in a monomer-free solution containing 0.1 M TBAP in acetonitrile as a function of repeated scans at 10 mV s<sup>-1</sup>.

Figures 4.25 and 4.26 show the IR spectra and QCM measurements for a functionalisation reaction, where it can be seen from these two figures there is good agreement between these measurements. IR spectra show some of the leaving groups (pfp) remain within the film until 15 minutes after hydrolysis, and the QCM curve demonstrates the existence of pfp molecules in the polymer that have not reacted. The masses of the polymer films were calculated to compare between films before and after functionalisation and the results were demonstrated that the mass of py-NTA increased by 10.6 μg based on QCM data and surface coverage equal to 9.87 x 10<sup>-8</sup> mol cm<sup>-2</sup>. The functionalisation percentage was 77%. This expected increase in the mass of the film is a result of the ingress the receptor

groups (NTA) into polymer film of a larger molecular weight larger than the pfp molecule.

#### 4.4.3 QCM Gravimetric and FTIR Spectroscopic Monitoring of Amide Hydrolysis

The hydrolysis of the copolymer py-Fmoc films with base solution was investigated; as with the previous work with pfp film, this experiment considered different reaction times. This particular hydrolysis experiment involved soaking the copolymer film in 30% piperidine in acetonitrile solution for different lengths of time and monitoring the reaction via FTIR to demonstrate the absence of the carbonyl group due to formation of amide bonds, thus demonstrating the amide film had successfully converted to an amine film. **Figure 4.28** shows that there is no carbonyl band  $\nu(\text{C}=\text{O})$  at  $1675\text{ cm}^{-1}$  in the deprotected film spectrum. Moreover, the hydrolysis reaction should lead to the appearance of a number of IR bands due to the py-NH<sub>2</sub> film; for example, the two bands at  $3400\text{--}3250\text{ cm}^{-1}$  due to the  $\nu(\text{N-H})$  stretching band of the primary amino group (indicated by symbol \* in figure) and the band at  $1625\text{ cm}^{-1}$  due to the  $\nu(\text{N-H})$  bending mode; all these bands provide further confirmation as to the successful removal of the Fmoc group from the polymer surface. The investigation of this hydrolysis reaction provides us with further information about the time required for the receptor units to penetrate the polymer film, therefore leading to an increase of the penetration efficiency of the receptors and an enhancement of the protocols that will be used in the following sections.

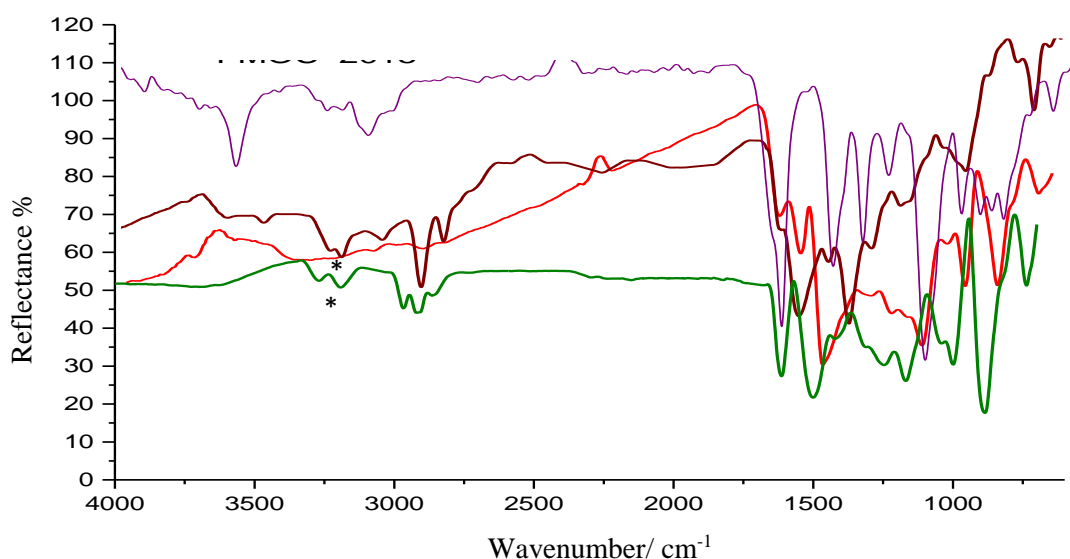


**Figure 4.28:** FTIR spectra showing the effects of hydrolysis at different times during the reaction. (a) Ppy-Fmoc as deposited (purple), (b) film after 5 min. hydrolysis (red), (c) film after 10 min. hydrolysis (brown) and (d) film after 20 min. hydrolysis (green). \*denotes the presence of primary amine peaks.

The QCM can be used to monitor the deprotection process for amide polymers film, as mentioned in the previous section, using the mass changes that can occur as a result of removing the Fmoc molecules. As expected, the mass of the film after hydrolysis (i.e., with the removal of the Fmoc leaving groups) was less than mass of film before hydrolysis, as indicated by the increase in frequency of the quartz crystal resonator that can be seen in **Figure 4.29**.

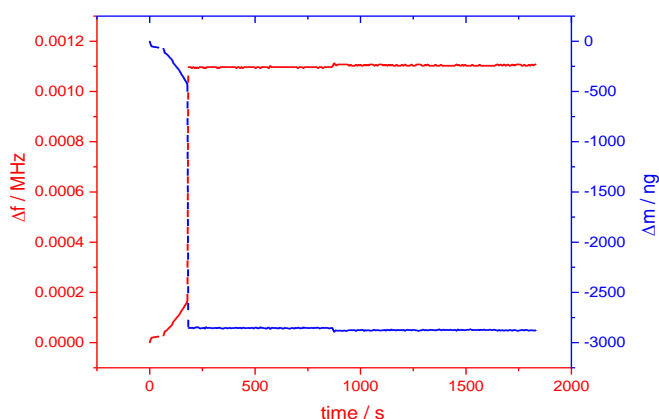


**Figure 4.29:** QCM recorded during the deprotection of py-Fmoc film in 30% piperidine in acetonitrile solution.

The potentiodynamic method was applied to study the electroactivity of deprotected polymer films. This study was recorded in monomer-free 0.1 M TBAP/CH<sub>3</sub>CN at a 10 mV s<sup>-1</sup> scan rate; the cyclic voltammogram is shown in **Figure 4.30**.

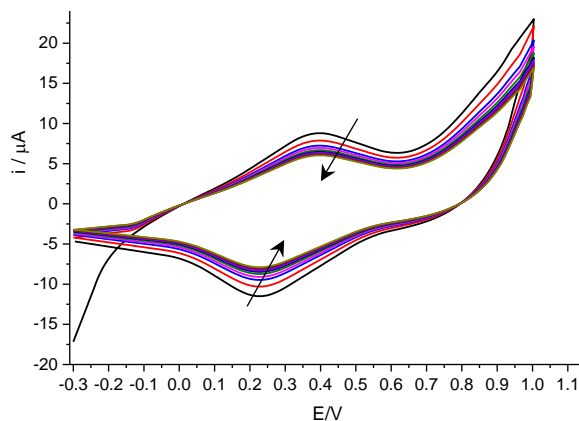


**Figure 4.30:** Cyclic voltammogram of py-Fmoc film after hydrolysis in a monomer-free solution of 0.1 M TBAP/CH<sub>3</sub>CN as a function of repeated scans at 10 mV s<sup>-1</sup>.

The IR spectrum in **Figure 4.28** illustrates that there are Fmoc units remained present in the polymer film after 10 minutes of hydrolysis reaction. However, the QCM results shown in **Figure 4.29** shows that there is no clear change in the mass of the film after 4 minutes of hydrolysis. A possible explanation for this variation is that the polymer film lost the Fmoc molecules in the first few minutes, as shown in the QCM curve, and then

solvent molecules begin to ingress into the polymer film. As mentioned in section 4.4.1 voltammetric and QCM results were used to estimate surface coverage to be  $1.1 \times 10^{-7}$  mol cm<sup>-2</sup> (almost 8.6 µg) and the mass of polymer film before hydrolysis (data presented in **Figure 4.19**) was equal to 10.2 µg based on QCM data. While, after hydrolysis mass of polymer film was equal to 7.35 µg and surface coverage was equal to  $9.65 \times 10^{-8}$  mol cm<sup>-2</sup> and mass change of hydrolysis was -2.85 µg (data presented in Figure 4.30 and 4.31). Fmoc groups were left the film during hydrolysis and this led to create free volumes over polymer film. The theoretical calculations show that mass of Fmoc groups equal to 60% and hydrolysis result show that the mass change was equal to 28%. This difference in film mass between poly(Py-Fmoc) and poly(Py-NH<sub>2</sub>) containing almost same ( $\Gamma$ ) shows the capability for create voids and ingress a large amount of solvent molecules into polymer film. FTIR gives the evidence to confirm that pfp groups was left the polymer film during hydrolysis as shown in Figure 4.28.

Films	Polymer deposition		polymer hydrolysis		functionalisation	
	$\Gamma$ mol cm <sup>-2</sup>	$\Delta M$ µg cm <sup>-2</sup>	$\Gamma$ mol cm <sup>-2</sup>	$\Delta M$ µg cm <sup>-2</sup>	$\Gamma$ mol cm <sup>-2</sup>	$\Delta M$ µg cm <sup>-2</sup>
Py-Fmoc	$1.10 \times 10^{-7}$	10.2	$9.65 \times 10^{-8}$	-2.85	$1.07 \times 10^{-7}$	10.85

**Table 4.14:** Mass and surface coverage between polymer films (before and after hydrolysis) and after functionalisation for poly(Py-Fmoc) film.

#### 4.8.4 Monitoring of vertical penetration of receptor into amide polymer film

The functionalisation of the amino polymer with the receptor requires the polymer film to be exposed to the receptor solution in a suitable solvent. In this reaction, NHS ester strategy was used to activate the carboxylic acid groups on the receptor unit. To accomplish this functionalisation, the film was immersed in a solution of receptor 2HQC (0.1 M in DMSO/CH<sub>3</sub>CN solution (1:9 ml)). The film was allowed to react for 30 minutes before rinsing with acetonitrile. FTIR was used to monitor the reaction as it progressed to determine the time required for the immobilization process to go to completion and to demonstrate amide formation throughout the polymer film surface as shown in **Figure 4.31**. Amide carbonyl stretches were observed at 1680 cm<sup>-1</sup> due to formation of amide bonds (indicated by symbol + in figure), and broad peak was showed at 3320 cm<sup>-1</sup> due to the hydroxyl group on receptor molecule (indicated by symbol \* in figure).

QCM measurements was used to follow the immobilisation process for the deprotected films, to monitor both the degree of immobilisation. The amide formation reaction that occurred on the film surface was accompanied by a change in the molecular weight.

Therefore, it might be expected that the reaction lead to a progressive decrease in frequency, coincident with an increase in mass as a consequence of the insertion of the receptor on the polymer film. In the present study, the molecular weight of 2-hydroxyquinoline-4-carboxylic acid equal  $189.17 \text{ g mol}^{-1}$  was added to polymer film. **Figure 4.32** shows the changes in mass and frequency during the immobilisation reaction.

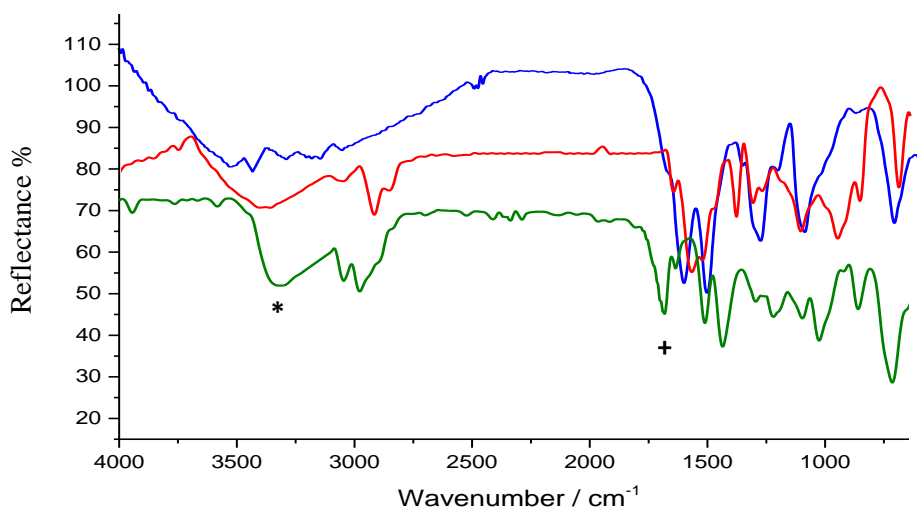


**Figure 4.31:** FTIR spectra showing the immobilisation of the 2-HQC receptor on the polymer film at various times during the course of the reaction. (a) PPyNH<sub>2</sub> (blue), (b) film after 10 min. (red), and (c) film after 25 min. (green). \*denotes the presence of carboxylic peaks and + denotes the presence carbonyl peaks.

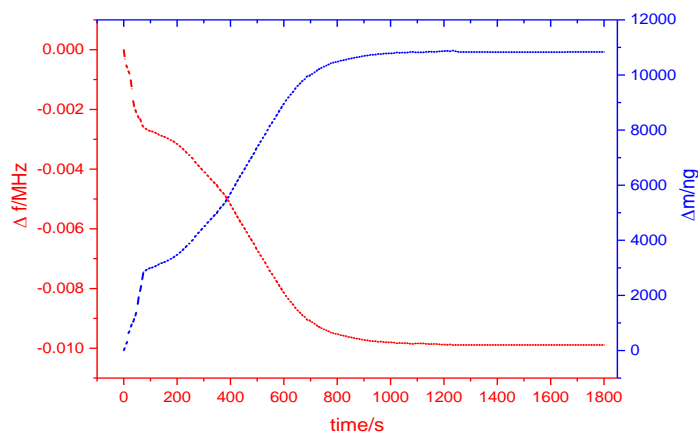


**Figure 4.32:** QCM recorded during the immobilization process of py-Fmoc film with the receptor unit (2-HQC) over a 30 minute duration.

The electroactivity of py-HQC polymer films was performed potentiodynamically using monomer-free 0.1 M TBAP/CH<sub>3</sub>CN at a  $10 \text{ mV s}^{-1}$  scan rate as shown in **Figure 4.33**. This cyclic voltammogram is similar to that recorded for the amino pyrrole film after hydrolysis, though with a number of shifts towards higher potential because of the aforementioned changes in composition.

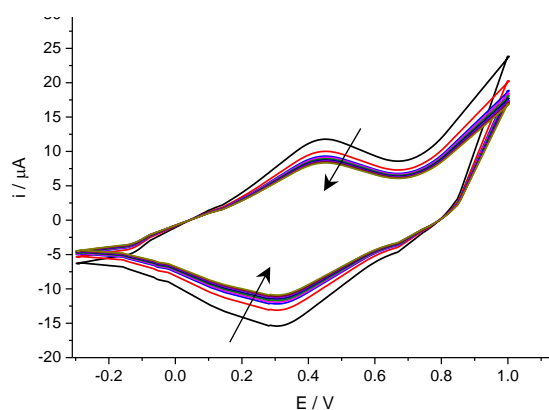


**Figure 4.33:** Cyclic voltammogram of py-HQC film in a monomer-free solution of 0.1 M TBAP in acetonitrile as a function of repeated scans at  $10 \text{ mV s}^{-1}$ .

The IR spectrum and QCM measurement shown in **Figures 4.31** and **4.32**, respectively, demonstrated that the mass of the film was increased as a result of the ingress of HQC into the voids in the polymer film surface. Moreover, there is clear agreement between QCM and IR measurements. IR spectra show that the HQC remained in the polymer film after 10 minutes of the functionalisation process. Calculations showed that the mass of polymer film after the functionalisation (data presented in **Figure 4.33**) was increased by  $10.85 \mu\text{g}$  based on QCM data, with a surface coverage of  $1.07 \times 10^{-7} \text{ mol cm}^{-2}$ , derived from application of Faraday law (see **equation 4.1**). The functionalisation percentage was equal to 87%. This expected increase in the mass of the film as result of the ingress of receptor groups (HQC) into the polymer film.

#### 4.5 Patterning of polymer films

One of the most important goals in the fabrication of chemical sensors is the creation of substrate surfaces that allow a specific reaction with the surrounding environment. Polymer films can provide an easy and effective way to obtain new surfaces for various applications.<sup>53</sup> This project has focused on the design of multifunctional polymeric surfaces, which can combine electrical conductivity and sensing ability. A lithographic approach was used to change the polymer surface properties to make it more appropriate to the needs of potentially desirable applications.

This study used a means of creating a polymer film with functional groups (activated ester pfp and amide Fmoc), which can react with other moieties. Patterning was implemented through two chemical approaches. In the first, a laterally uniform polymer (either py-pfp or py-Fmoc) was deposited, and photolithographic methods were applied directly to these



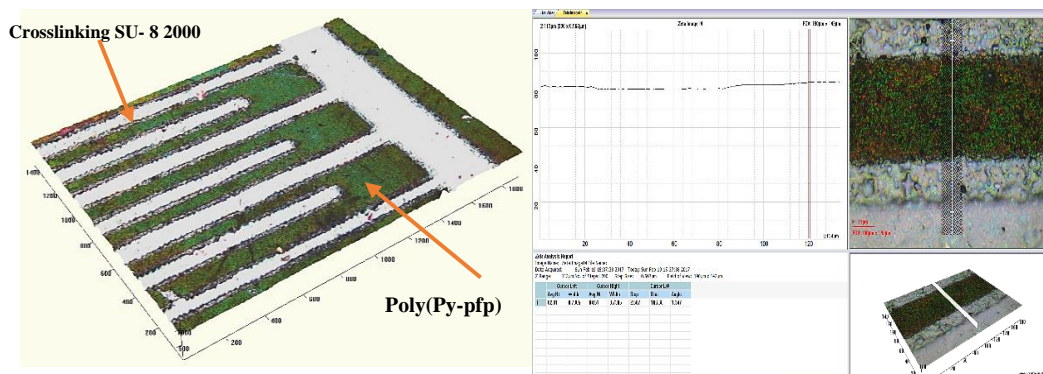


**Figure 4.35:** 3D microscopic image of a cross-section of the poly-pfp electrode after the patterning operation.

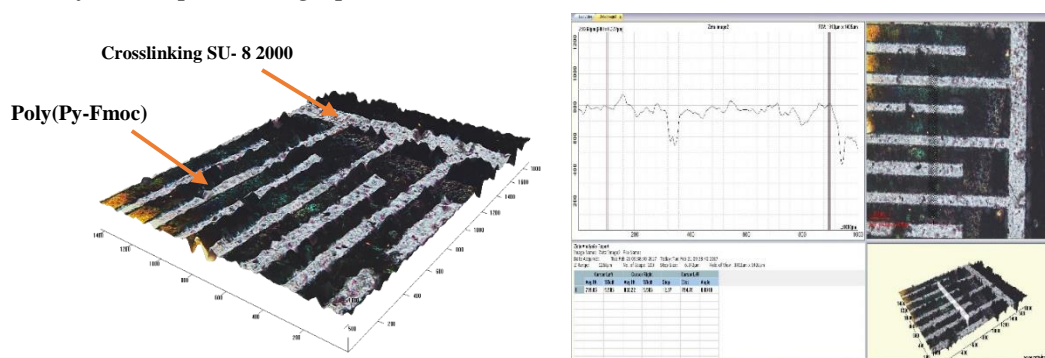


**Figure 4.36:** 3D microscopic image of a cross-section of the poly-Fmoc electrode after the patterning operation.

The electroactivity of patterned films was measured to allow comparison with the films that were deposited after the patterning process. **Figure 4.37** shows the cyclic voltammograms of poly(py-pfp) film before and after irradiation and the functionalised polymer electrode poly(Py-NTA), respectively, in monomer-free solution. The redox peaks in the cyclic voltammogram for patterned py-NTA film were similar to the peaks found for py-NTA before the patterning process, as per **Figure 4.27**. Furthermore, the panels in **Figure 4.38** show the cyclic voltammograms of poly(py-Fmoc) film before and after the patterning process and the functionalised electrode poly(Py-HQC), respectively, in a background electrolyte solution. The redox peaks in the cyclic voltammogram for patterned py-HQC were similar to the peaks found in py-HQC before the patterning process, as per **Figure 4.33**.

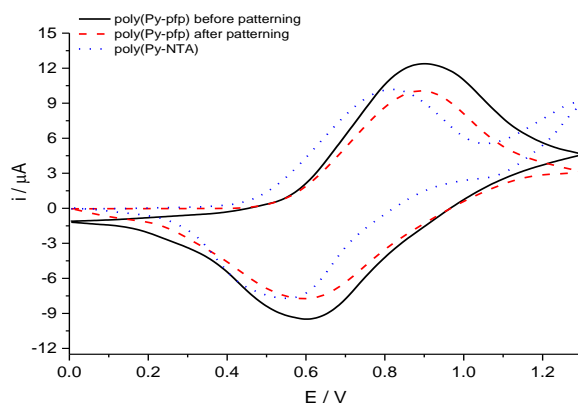


**Figure 4.37:** Voltammetric response of poly(Py-pfp) electrodes, the solid and dashed lines (before and after patterning, respectively) and the chained line, the poly(Py-NTA) electrode, in monomer-free TBAP/acetonitrile solution at a scan rate of  $10 \text{ mV s}^{-1}$ .

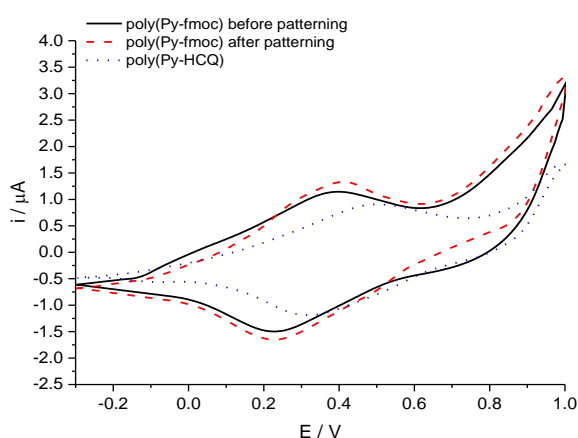


**Figure 4.38:** Voltammetric response of poly(Py-Fmoc) electrodes, the solid and dashed lines (before and after patterning, respectively) and the chained line, the poly(Py-HQC) electrode, in monomer-free TBAP/acetonitrile solution at a scan rate of  $10 \text{ mV s}^{-1}$ .

FTIR was applied to confirm the patterning process had not changed the composition of the polymer film. Also, FTIR was used to demonstrate amide formation on the polymer film surface. **Figure 4.39** shows the FTIR spectrum of pfp film before and after patterning. The ester film, py-pfp, showed characteristic sharp bands in the FTIR spectrum at  $1780 \text{ cm}^{-1}$  due to the  $\nu(\text{C}=\text{O})$  stretch, and at  $1000 \text{ cm}^{-1}$  due to  $\nu(\text{C}-\text{F})$ . After immersion of the pfp ester film in the NTA-lysine solution, the carbonyl stretch shifted from  $1785 \text{ cm}^{-1}$  to  $1660 \text{ cm}^{-1}$  due to the formation of amide bonds in the polymer film (indicated by symbol + in figure). Furthermore, the disappearance of the peak at approximately  $1000 \text{ cm}^{-1}$  was due to the removal of the pfp group. Moreover, the appearance of a broad band at  $3250 \text{ cm}^{-1}$  due to an O-H group and a band at  $1725 \text{ cm}^{-1}$  due to the  $\nu(\text{C}=\text{O})$  stretch of carboxylic groups in the receptor compound were also observed as shown in **Figure 4.40**. The py-NH<sub>2</sub> showed two distinctive band in the FTIR spectrum at  $3310 \text{ cm}^{-1}$  due to the primary  $\nu(\text{NH}_2)$ , and at  $1600 \text{ cm}^{-1}$  due to the  $\nu(\text{N}-\text{H})$

bend. After immersion of the amino film in the HQC solution, the carbonyl stretch was observed at  $1660\text{ cm}^{-1}$  due to the formation of amide bonds. Moreover, the appearance of a broad band at  $3350\text{ cm}^{-1}$  was due to the O-H stretch of the receptor molecule.

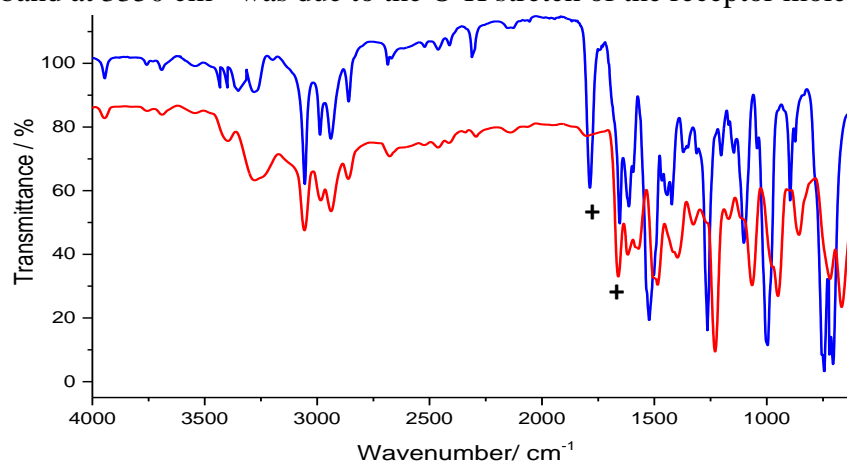


**Figure 4.39:** FTIR spectra of poly(py-pfp) film after patterning (blue) and poly(py-NTA) film (red). + denotes the presence of carbonyl for ester and amide peaks.

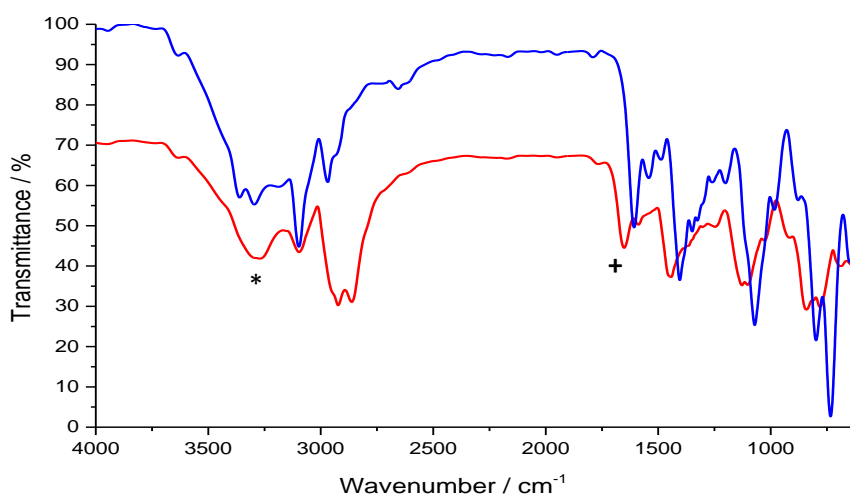


**Figure 4.40:** FTIR spectra of poly(py-NH<sub>2</sub>) film after patterning (blue) and poly(py-HQC) film (red). \* denotes the presence of carboxylic and + denotes amide peaks.

## 4.6 Surface imaging characterization of polymer films

### 4.6.1 Scanning Electron Microscopy (SEM)

The properties of electroactive polymers are highly dependent on their morphology and structure. Scanning electron microscopy (SEM) was used to examine the morphology of the derivatives of pyrrole films. **Figure 4.41** shows the surface morphological structures of the derivatives of pyrrole films. Although the films show different morphologies due to the use of a different monomer composition, there were not any significant differences between these films. This similarity between the film surfaces was due to the fact that we used the same counterions in TBAP (perchlorate ions,  $\text{ClO}_4^-$ ), which have the same effect

on film morphology. Microscopic observation of film surfaces after deposition showed that the electrode surface was completely covered by the polymer. All the films considered demonstrated that there was a uniform distribution of polymer particles over the surface of the electrode, with small spherical particles also apparent from the SEM.

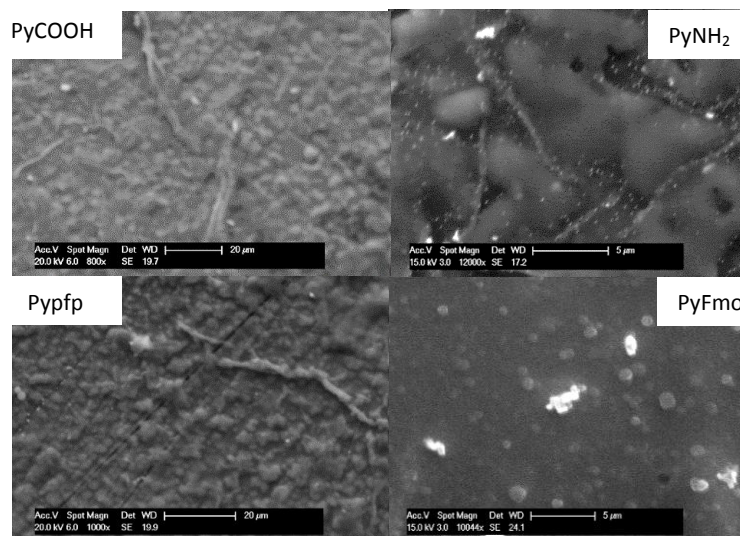


**Figure 4.41:** SEM images of surface films deposited using 10 mM concentrations of (A) py-COOH, (B) py-NH<sub>2</sub>, (C) py-pfp, and (D) copolymer py-co-Fmoc in solutions of 0.1 M TBAP/CH<sub>3</sub>CN at scan rates of 10mVs<sup>-1</sup> over 10 scans.

#### 4.6.2 Atomic Force Microscopy (AFM)

AFM was used to image the film surface and estimate the thickness of the polymer films derived from different monomers (see **Figure 4.42**). In fact, many factors play a role in determining the morphology of the film surface, such as scan rate, monomer concentration, number of potential scans and the applied potential window. In this study, the optical comparison concentrated on a study of nodule size and an examination of the roughness of the film surfaces. The use of different monomers, having different chemical compositions, naturally leads to certain differences in surface topography. From these measurements, we found that these differences were not significant as we used the same scan rate and counterions in all experiments. It was clear that the py-COOH surface gave the smoothest surface in most areas, with a very small range of nodule sizes; the same can be seen for the py-NH<sub>2</sub> surface, which was smoother than the py-COOH surface. Both these film surfaces appeared unwrinkled. On the other hand, the film surface produced from py-pfp was rougher than the above-mentioned films, with some meandering regions apparent across the entire polymer surface. Meanwhile, the py-co-Fmoc copolymer showed a surface topography that was considerably rougher than all the previous polymer surfaces. The differences between the film surfaces here were probably related to

differences in growth and nucleation features, and differences in the amount of electronic charge resulting from the electrodeposition process. A scalpel blade was used to remove polymer films from part of electrode surface to form edge between polymer film and electrode surface, forming a step edge between the film and substrate, (panel E). Analysis of **Figure 4.42** panels A, B, C and D revealed that the surface thickness was in the region of 800, 500, 750 and 500 nm for py-COOH, py-NH<sub>2</sub>, py-pfp and py-Fmoc respectively. While, based on QCM data thickness of films was equal to 900, 530, 730 and 450 nm for py-COOH, py-NH<sub>2</sub>, py-pfp and py-Fmoc respectively. Naturally, films thickness (solvated polymer) was thicker compared with dry polymer. The findings from AFM can be compared with the thickness of polymer film determined from voltammetric and QCM results. The thickness measurements in these methods show some differences. These differences could be due to non-uniform coverage spatially with py-pfp and py-Fmoc films as shown in the **Figure 4.42**, or possibly the existence of some solvent molecules, which would effect on determination of thickness of the polymer film.

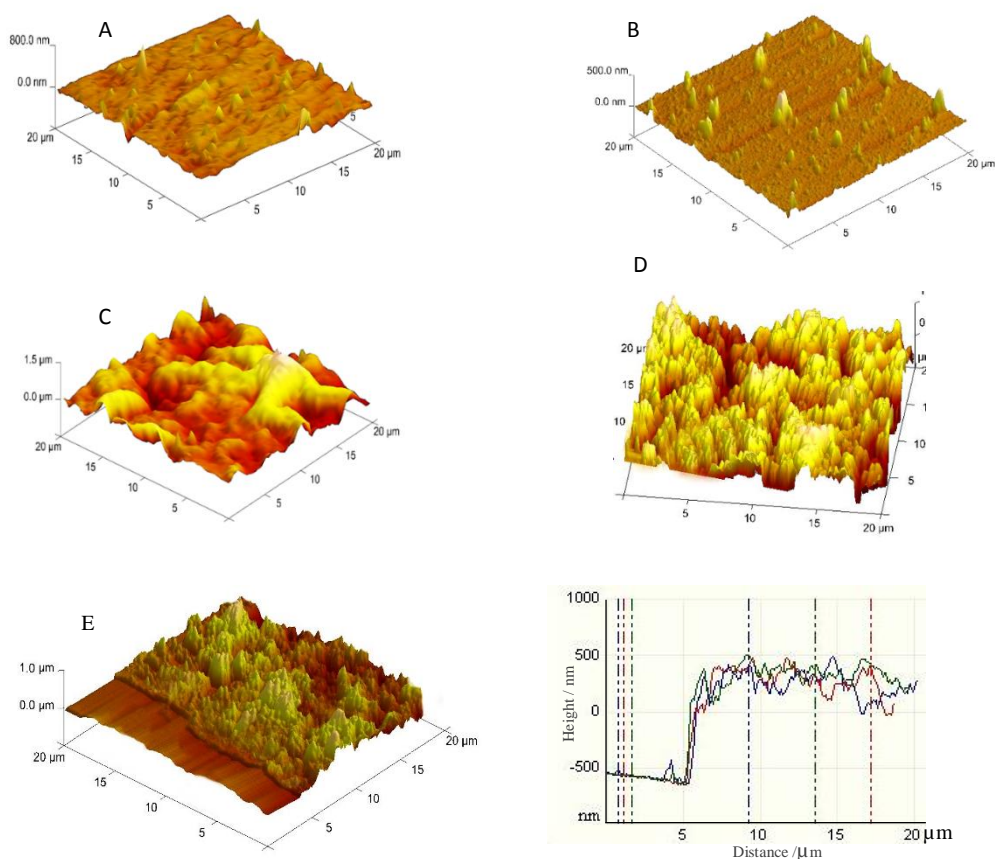


**Figure 4. 42:** AFM images of dry polymers electrodeposited from 10 mM a) py-NH<sub>2</sub>, b) py-COOH, c) py-pfp, d) py-co-Fmoc and e) thickness of polymer film on an Au electrode using a 10 mV s<sup>-1</sup> scan rate over 10 scans.

#### 4.7 Conclusion

The aim of this study was to improve our understanding of the electrochemical behaviour of functionalised polymer films when creating spatially heterogeneous film surfaces with diverse chemical functionalities via photolithography. An investigation into immobilising receptors within patterned films to produce microfabrication-modified films for use as sensors was also undertaken. A set of electrochemical and spectroscopic techniques have been applied to provide a clear picture as to the nature of the electrodeposition, and the subsequent chemical functionalisation processes of patterned polymer films. The deposition of films and overall operational performance was controlled using electrochemical (“*iVt*”) techniques, providing an opportunity for manipulation and electro-coulometric analysis of polymer film. All of these polymer films was prepared and fully functionalised to give mechanically, chemically and redox-stable films. These films were characterized using electrochemical, spectroscopic (FTIR), acoustic (EQCM) techniques.

The results presented in this chapter illustrate the successful fabrication of polymer films using cyclic voltammetry. Another technique used for the deposition of polymer was the potential step technique using different deposition times. The results from chronoamperometric curves show that the electropolymerisation process was that charge increased with  $t^{1/2}$  as result of having a diffusion-controlled process. Following the electrochemical polymerization, polymer films were examined with different scan rates (10 - 100 mV s<sup>-1</sup>) to study stability, the findings of which illustrated that both anodic and cathodic peak currents are linearly dependent on scan rate. EQCM measurements were used to study of polymer films and the slope ( $\Delta m/\Delta q$ ) used to estimate the molar mass of species involved in the charge compensation process. Results show that monomer and solvent seem to play role during polymerisation processes.

Poly(Py-pfp) and poly(Py-Fmoc) films was hydrolysed using NaOH and 30% piperidine solutions, respectively. FTIR measurements confirm that the ester and amide bonds no longer appeared in the prepared films after hydrolysis as a sign of successful deprotection process. QCM was used to monitor the hydrolysis process for both polymer films, the comparison of which demonstrated that the mass of the polymer films after the hydrolysis reaction was lower than before hydrolysis. Moreover, the voltammetric results was used to calculate the mass and surface coverage of the polymer films before and after hydrolysis via Faraday’s law. The difference in mass between the protected and

deprotected polymer films was due to the egress of leaving groups from the films. Findings show that this difference can be explained by ingress of 40% and 30% solvent molecules into Poly(py-pfp) and poly(py-Fmoc) respectively, to fill the voids on the polymer surface for ester and amide film.

The immobilisation process was monitored using an IR spectrometer to confirm the functionalisation reaction between receptors NTA and QCH with poly(Py-COOH) and poly(Py-NH<sub>2</sub>), respectively, had completed. This strategy of reactivity control could be beneficial for the patterning of different species on micro-fabricated polymer films. The electrochemical voltammetric measurements for all patterned polymer surfaces confirmed that electrochemical activity (conductivity) would allow for their use in sensing applications.

This study in this chapter has shown that modification of polymer, by replacing pfp and Fmoc units with NTA and HQC, respectively, had successful. This gives us take a logical scenario to functionalisation control of polymer modified electrodes. Direct measurement and calculations for polymer films providing a greater understanding of the reactivity of functional polymers and redox switching behaviour of these systems.

The AFM data showed that polymer films have rough surfaces and partial collapse were occurred for some polymers due to loss of solvent molecules. These films were less thicker than solvated polymers which calculated from QCM data. AFM data showed that Py-pfp and py-Fmoc were slightly thicker than values which were estimated by QCM and this is perhaps attributed to nonuniform coverage of films across the available deposition area and instrumental bias. **Table 4.14** show the comparison between the thickness of polymer films measured by AFM, cyclic voltammetry and QCM and the differences in thickness of films due to variation of solvent ratio in polymer films.

Films	Voltammetric experiments (dry film)		Molar volume cm <sup>3</sup> mol <sup>-1</sup>	QCM experiments (solvated films)		AFM <i>h<sub>f</sub></i> /cm	Molar volume cm <sup>3</sup> mol <sup>-1</sup>
	<i>I</i> / mol cm <sup>-2</sup>	<i>h<sub>f</sub></i> / cm		$\Delta m/g$	<i>h<sub>f</sub></i> / cm		
Py-COOH	4.4 x 10 <sup>-7</sup>	5.5x10 <sup>-5</sup>	125	2.5x10 <sup>-5</sup>	9.1x10 <sup>-5</sup>	8x10 <sup>-5</sup>	177
Py-NH <sub>2</sub>	2 x 10 <sup>-7</sup>	2.5x10 <sup>-5</sup>	125	1.2x10 <sup>-5</sup>	5.3x10 <sup>-5</sup>	5x10 <sup>-5</sup>	250
Py-pfp	1.55 x 10 <sup>-7</sup>	5x10 <sup>-5</sup>	322	1.6x10 <sup>-5</sup>	7.3x10 <sup>-5</sup>	7.5 x10 <sup>-5</sup>	468
Py-Fmoc	1.13 x 10 <sup>-7</sup>	3.8x10 <sup>-5</sup>	336	1.15x10 <sup>-5</sup>	4.5x10 <sup>-5</sup>	5 x10 <sup>-5</sup>	435

**Table 4.14:** Thickness of polymer films measured by AFM and comparison with those calculated from cyclic voltammetry data based on Faraday law and QCM data (solvated films).

## 4.8 References

1. J. Hegewald, L. Jakisch and J. Pionteck, *Synthetic Metals*, 2009, **159**, 103-112.
2. B. Massoumi, S. E. Afshar, S. Fathalipour, R. Mohammadi and A. A. Entezami, *Designed Monomers and Polymers*, 2013, **16**, 263-273.
3. L.-X. Wang, X.-G. Li and Y.-L. Yang, *Reactive and Functional Polymers*, 2001, **47**, 125-139.
4. H. Eisazadeh, *World Journal of Chemistry*, 2007, **2**, 67-74.
5. J. M. Pringle, J. Efthimiadis, P. C. Howlett, J. Efthimiadis, D. R. MacFarlane, A. B. Chaplin, S. B. Hall, D. L. Officer, G. G. Wallace and M. Forsyth, *Polymer*, 2004, **45**, 1447-1453.
6. S. Sadki, P. Schottland, N. Brodie and G. Sabouraud, *Chemical Society Reviews*, 2000, **29**, 283-293.
7. V. Brandl and R. Holze, *Berichte Der Bunsengesellschaft Für Physikalische Chemie*, 1998, **102**, 1032-1038.
8. G. Inzelt, *Conducting Polymers: a New Era in Electrochemistry*, Springer, 2012.
9. S. Soylemez, F. E. Kanik, S. D. Uzun, S. O. Hacıoglu and L. Toppare, *Journal of Materials Chemistry B*, 2014, **2**, 511-521.
10. Y. Li, W. Zhang, J. Chang, J. Chen, G. Li and Y. Ju, *Macromolecular Chemistry and Physics*, 2008, **209**, 322-329.
11. U. Lange, N. V. Roznyatovskaya and V. M. Mirsky, *Analytica Chimica Acta*, 2008, **614**, 1-26.
12. D. C. Kim and D. J. Kang, *Sensors*, 2008, **8**, 6605-6641.
13. V. Bisht, W. Takashima and K. Kaneto, *Biomaterials*, 2005, **26**, 3683-3690.
14. A. Naji, C. Marzin, G. Tarrago, M. Cretin, C. Innocent, M. Persin and J. Sarrazin, *Journal of Applied Electrochemistry*, 2001, **31**, 547-557.
15. M. Filkusová and R. Oriňáková, *Journal of Biochemical Technology*, 2014, **2**, 13-15.
16. P. A. Mabrouk, *Synthetic Metals*, 2005, **150**, 101-105.
17. D. Stone, *Analyst*, 1997, **122**, 1129-1138.
18. M. D. Levi, C. Lopez, E. Vieil and M. A. Vorotyntsev, *Electrochimica Acta*, 1997, **42**, 757-769.
19. H. Lee, H. Yang and J. Kwak, *Journal of Electroanalytical Chemistry and Interfacial Electrochemistry*, 1999, **468**, 104-109.
20. A. Glidle, C. S. Hadyoon, N. Gadegaard, J. M. Cooper, A. R. Hillman, R. W. Wilson, K. S. Ryder, J. R. P. Webster and R. Cubitt, *The Journal of Physical Chemistry B*, 2005, **109**, 14335-14343.
21. A. Glidle, A. R. Hillman, K. S. Ryder, E. L. Smith, J. M. Cooper, R. Dalgliesh, R. Cubitt and T. Geue, *Electrochimica Acta*, 2009, **55**, 439-450.
22. R. M. Sapstead, N. Corden and A. R. Hillman, *Electrochimica Acta*, 2015, **162**, 119-128.
23. R. M. Sapstead, K. S. Ryder, C. Fullarton, M. Skoda, R. M. Dalgliesh, E. B. Watkins, C. Beebee, R. Barker, A. Glidle and A. R. Hillman, *Faraday Discussions*, 2013, **164**, 391-410.
24. A. A. Arrieta Almarino and R. L. Tarazona Caceres, *Journal of the Chilean Chemical Society*, 2009, **54**, 14-19.
25. R. Okner, A. J. Domb and D. Mandler, *Biomacromolecules*, 2007, **8**, 2928-2935.
26. A. Diaw, D. Gningue-Sall, A. Yassar and J. Aaron, *Synthetic Metals*, 2013, **179**, 74-85.
27. A. R. Hillman and E. F. Mallen, *Journal of Electroanalytical Chemistry and Interfacial Electrochemistry*, 1987, **220**, 351-367.
28. S. Bruckenstein, K. Brzezinska and A. R. Hillman, *Electrochimica Acta*, 2000, **45**, 3801-3811.
29. C. Weidlich, K.-M. Mangold and K. Jüttner, *Electrochimica Acta*, 2005, **50**, 1547-1552.
30. K. Naoi, M. Lien and W. H. Smyrl, *Journal of The Electrochemical Society*, 1991, **138**, 440-445.

31. V. Syritski, A. Öpik and O. Forsen, *Electrochimica Acta*, 2003, **48**, 1409-1417.
32. L. Abrantes, C. Cordas and E. Vieil, *Electrochimica Acta*, 2002, **47**, 1481-1487.
33. A. R. Hillman, K. S. Ryder, C. J. Zaleski, V. Ferreira, C. A. Beasley and E. Vieil, *Electrochimica Acta*, 2014, **135**, 42-51.
34. A. R. Hillman, K. S. Ryder, C. J. Zaleski, C. Fullarton and E. L. Smith, *Zeitschrift für Physikalische Chemie International journal of Research in Physical Chemistry and Chemical Physics*, 2012, **226**, 1049-1068.
35. H. Lee, H. Yang and J. Kwak, *Journal of Electroanalytical Chemistry and Interfacial Electrochemistry*, 1999, **468**, 104-109.
36. R. Kiefer, D. G. Weis, A. Aabloo, G. Urban and J. Heinze, *Synthetic Metals*, 2013, **172**, 37-43.
37. M. A. Skopek, M. A. Mohamoud, K. S. Ryder and A. R. Hillman, *Chemical Communications*, 2009, 935-937.
38. M. Zhou, M. Pagels, B. Geschke and J. Heinze, *The Journal of Physical Chemistry B*, 2002, **106**, 10065-10073.
39. J. Kaufman, K. K. Kanazawa and G. Street, *Physical review letters*, 1984, **53**, 2461.
40. W. Plieth, A. Bund, U. Rammelt, S. Neudeck and L. Duc, *Electrochimica acta*, 2006, **51**, 2366-2372.
41. S. Asavapiriyant, G. K. Chandler, G. A. Gunawardena and D. Pletcher, *Journal of Electroanalytical Chemistry and Interfacial Electrochemistry*, 1984, **177**, 229-244.
42. K. S. Ryder, D. G. Morris and J. M. Cooper, *Journal of the Chemical Society, Chemical Communications*, 1995, 1471-1473.
43. K. S. Ryder, L. F. Schweiger, A. Glidle and J. M. Cooper, *Journal of Materials Chemistry*, 2000, **10**, 1785-1793.
44. R. John and G. G. Wallace, *Journal of Electroanalytical Chemistry and Interfacial Electrochemistry*, 1993, **354**, 145-160.
45. C. Weidlich, K. M. Mangold and K. Jüttner, *Electrochimica Acta*, 2005, **50**, 1547-1552.
46. A. Mirmohseni, M. Milani and V. Hassanzadeh, *Polymer International*, 1999, **48**, 873-878.
47. R. J. Waltman, A. F. Diaz and J. Bargon, *The Journal of Physical Chemistry*, 1984, **88**, 4343-4346.
48. Z. Deng and D. C. Stone, *Analyst*, 1997, **122**, 1129-1138.
49. M. González-Tejera, M. García, E. S. de la Blanca, M. Redondo, M. Raso and I. Carrillo, *Thin Solid Films*, 2007, **515**, 6805-6811.
50. E. De Giglio, M. Guascito, L. Sabbatini and G. Zambonin, *Biomaterials*, 2001, **22**, 2609-2616.
51. A. Dkhissi, D. Beljonne, R. Lazzaroni, F. Louwet, L. Groenendaal and J. Brédas, *International Journal of Quantum Chemistry*, 2003, **91**, 517-523.
52. M. Rodríguez, I. Romero, C. Sens, A. Llobet and A. Deronzier, *Electrochimica Acta*, 2003, **48**, 1047-1054.
53. R. Abargues, P. Rodriguez-Canto, R. Garcia-Calzada and J. Martínez-Pastor, *The Journal of Physical Chemistry C*, 2012, **116**, 17547-17553.
54. V. K. Varadan, K. J. Vinoy and K. A. Jose, *RF MEMS and their applications*, John Wiley and Sons, 2003.
55. J. B. Lee, K.-H. Choi and K. Yoo, *Micromachines*, 2014, **6**, 1-18.

<b>5.1 Overview .....</b>	<b>113</b>
<b>5.2 Aims and Objectives .....</b>	<b>113</b>
<b>5.3 Result and discussion.....</b>	<b>114</b>
5.3.1 Electropolymerisation of 3-(2-carboxyethyl)aniline .....	114
5.3.2 Characterisation of poly3-(2-carboxyethyl)aniline.....	116
5.3.3 Electropolymerisation of copolymer (aniline-co-3-(aminomethyl)aniline).....	119
5.3.4 Characterization of copolymer (aniline-co-3-(aminomethyl)aniline).....	121
5.3.5 Electropolymerisation of pentafluorophenyl 3-(3-aminophenyl) propanoate .....	124
5.3.6 Characterization of poly(pentafluorophenyl 3-(3-aminophenyl) propanoate).....	125
5.3.7 Electropolymerisation of <i>N</i> -Fmoc- <i>m</i> -aminobenzylamine .....	128
5.3.8 Characterization of poly( <i>N</i> -Fmoc- <i>m</i> -aminobenzylamine).....	130
<b>5.4 Post-polymerisation Chemical Modifications .....</b>	<b>133</b>
5.4.1 QCM Gravimetric and FTIR Spectroscopic Monitoring of Ester Hydrolysis.....	134
5.4.2 Monitoring of vertical penetration of receptor into ester polymer film.....	136
5.4.3 QCM Gravimetric and FTIR Spectroscopic Monitoring of Amide Hydrolysis .....	139
5.4.4 Monitoring of vertical penetration of receptor into amide polymer film.....	141
<b>5.5 Patterning of polymer films .....</b>	<b>143</b>
<b>5.6 Surface imaging characterisation of polymer films.....</b>	<b>147</b>
<b>5.7 Conclusion .....</b>	<b>149</b>
<b>5.8 References.....</b>	<b>152</b>

## 5.1 Overview

As explained in previous chapters, the importance of conducting polymers in our lives is considerable, and there is an increase in the number of their applications they can address in many areas.<sup>1</sup> One of the most important electroactive polymers is polyaniline, which has attracted the attention of researchers because of its electrochemical and optical properties.<sup>2,3</sup> There are several functional groups that can be used to alter or improve the electronic structure of the resulting polymers.<sup>4</sup> Instead of using classical, generic ways to functionalise monomer units, a number of new methods have been developed to activate polymer surfaces after deposition by surface grafting via coupling reactions. In this method, electroactive polymers with sensing and complexing abilities can be created. It has been noted that functionalisation, adding desirable groups to the polymer chains, alters the electrochemical properties of these same polymers.<sup>5,6</sup> Surface patterning with diverse functions presents new insights into how molecules (receptors, catalysts, and proteins) can interact with the surfaces of materials.<sup>7</sup> Over the past two decades, scientists have become increasingly interested in developing technologies that allow them to control and manipulate surfaces to acquire intelligent, multi-functional surfaces.<sup>8,9</sup> Patterned surfaces have become important in many research fields such as microelectronics, sensors and catalysis. The ability to control the location of molecules across surfaces offers a powerful tool in the creation of heterogeneous film surfaces with diverse chemical functionalities.<sup>10,11</sup> These new surfaces, with their new characteristics, are highly desirable in many areas such as regenerative medicine<sup>12</sup> and sensors.<sup>13</sup>

## 5.2 Aims and Objectives

The goals here are: (i) fabrication of patterned functionalised electrodes from polyaniline derivatives, here Ani-pfp and Ani-Fmoc, under different conditions; (ii) estimation of mass exchange of polymer films using the QCM device; (iii) the exploration of the morphology and topography of films deposited, and (iv) the preparation of spatially heterogeneous (patterned) film surfaces containing two receptor units. In this chapter, the goal was the functionalisation of polyaniline film surfaces through the use of immobilisation strategies to introduce chelating agents, which would lead to the enhanced recognition ability of analytes. Various scenarios were employed, depending on the electrochemical and synthetic methods available, to create the polymer films. This scenario involves electropolymerisation of the monomer, 3-(aminomethyl)aniline, which

contains a large leaving group, namely 9-fluorenylmethoxycarbonyl (Fmoc), and a monomer, carboxylic aniline 3-(2-carboxyethyl)aniline, which contains another large leaving group, pentafluorophenol (pfp). After the polymerisation step, the amide and ester bonds are hydrolysed out to create voids at the polymer surfaces suitable for the subsequent insertion of the ligand units (see **schemes 4.1** and **4.2**).

### 5.3 Result and discussion

Generally, polyaniline derivative films were deposited onto a gold electrode using the potentiodynamic method. The polymerisation solution contained a suitable concentration of the monomer in an acidic medium with 0.5 M TBAP, detailed procedures for which were given in chapter three. Various potential ranges were applied, depending on the type of monomer, over 10 scans, with each set of scans being conducted at two scan rates, namely 10 and 20  $\text{mV s}^{-1}$ , as shown in **Table 5.1**.

Monomer name	Potential window / V	Supporting electrolyte	Conc. / mM	Scan rates $\text{mV s}^{-1}$
3-(2-carboxyethyl) aniline	0.0 - 1.2	$\text{H}_2\text{SO}_4$	20	10 and 20
3-(aminomethyl) aniline	0.0 - 1.2	$\text{H}_2\text{SO}_4$	20	10 and 20
Py-pfp	0.0 - 1.35	$\text{HClO}_4$ / TBAP	20	10 and 20
Py-fmoc	-0.2 - 1.35	$\text{HClO}_4$ / TBAP	20	10 and 20

**Table 5.1:** Potential window and supporting electrolyte for the electropolymerisation of the four types of monomers used in this chapter.

#### 5.3.1 Electropolymerisation of 3-(2-carboxyethyl) aniline

Poly(Ani-COOH) films were polymerised potentiodynamically using a potential between 0.0 V and 1.20 V from sulphuric acid solution onto an Au electrode. **Figure 5.1** describes the voltammetric responses of 20 mM Ani-COOH for 10 cycles at scan rates of 10 and 20  $\text{mV s}^{-1}$ . Generally, cyclic voltammograms of Ani-COOH show two redox couples and these redox peaks are due to the redox reactions between the aniline forms (leucoemeraldine, emeraldine, and pernigraniline).<sup>14, 15-17</sup> It can be seen from these figures that the intensity of the current of the polymer film increased with sequential deposition scan cycles.<sup>16</sup> More specifically, in the first scan (panel A) there is only one redox peak, and the system shows the start of the polymerisation loop at  $E_{pa} = 0.90$  V,

whilst the anodic current that appears in this scan is attributed to oxidation of the monomer. The  $i$  vs.  $E$  curves show the anodic peak, which was observed at 0.35 V, and which indicated the transformation of the reduced form, i.e., the leucoemeraldine salt to the emeraldine salt form, based on substituted aniline molecules. Further peak current was found at around 0.6 V, which is indicative of the oxidation of pernigraniline.<sup>19-17</sup> The surface coverage and thickness of conducting poly(Ani-COOH) film were determined according to the equations 2.4 and 2.6. According to these equations, the surface coverage of deposition process could be found as  $3.68 \times 10^{-7} \text{ mol cm}^{-2}$  and  $2.07 \times 10^{-7} \text{ mol cm}^{-2}$  for the 10 and 20  $\text{mV s}^{-1}$  scan rates, respectively.<sup>3</sup>

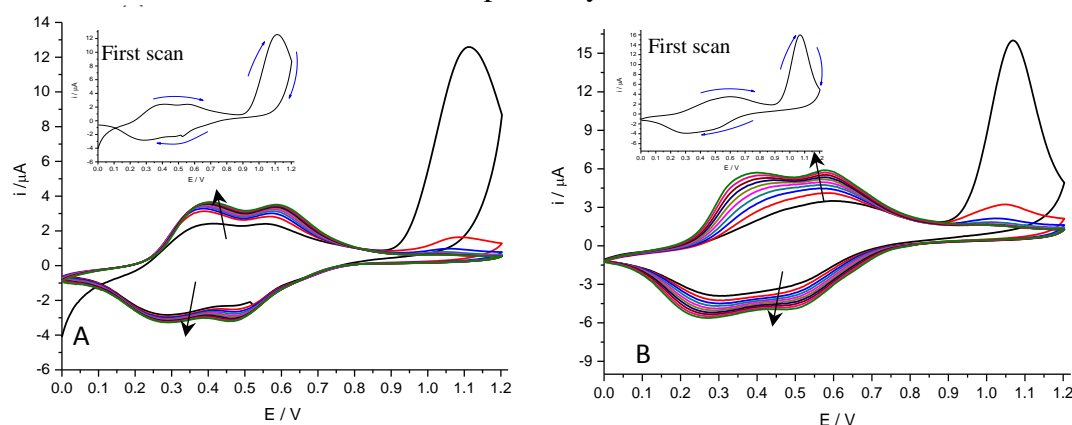


**Figure 5.1:** Cyclic voltammogram of electropolymerisation 20 mM 3-(2-carboxyethyl) aniline on gold electrode in 0.5 M  $\text{H}_2\text{SO}_4$  at (A) 10  $\text{mV s}^{-1}$  and (B) 20  $\text{mV s}^{-1}$  for 10 scans. Electrode area  $0.0044 \text{ cm}^2$ . (Inset curve shows the first scan.)

In general, the two polymer films (see **Figure 5.1**) have similar cyclic voltammograms. In addition, the increase of scan rate led to an increase in peak current. The nature of substituent groups plays a key role in electropolymerisation because of changes in the electronic density and steric effects of monomers, where results indicate that there is a shift in potential between the cyclic voltammogram of poly(Ani-COOH) and unsubstituted aniline, as found in the literature review.<sup>18-20</sup> The cyclic voltammograms illustrated that the oxidation potential of carboxylic aniline was higher than that found under the same conditions for the aniline monomer (see **Figure 5.1**). This difference is due to the presence of an electron withdrawing group in structure of monomer which has an electronic effect on the aniline cyclic system.<sup>21-23</sup>

Poly(Ani-COOH) was deposited potentiostatically from 20 mM monomer and 0.5 M  $\text{H}_2\text{SO}_4$  onto gold electrode over periods ranging from 50 to 200 seconds using a potential of 1.2 V, as shown in **Figure 5.2**. The ( $i$ - $t$ ) transients have many of the characteristics of the electropolymerisation discussed in section 4.4.1. Panel B shows that the

electropolymerisation charge increased with  $t^{1/2}$  as result of diffusion control. As expected, increasing the polymerisation time lead to an increase in polymer film on the electrode surface. The thickness,  $h_f^*$  ( $\mu\text{m}$ ), of the dry polymer film, was calculated using equations 2.4 and 2.6, as reported in **Table 5.2**. The molecular weight of Ani-COOH is  $165.19 \text{ g mol}^{-1}$  and its density is ca.  $1.21 \text{ g cm}^{-3}$ .

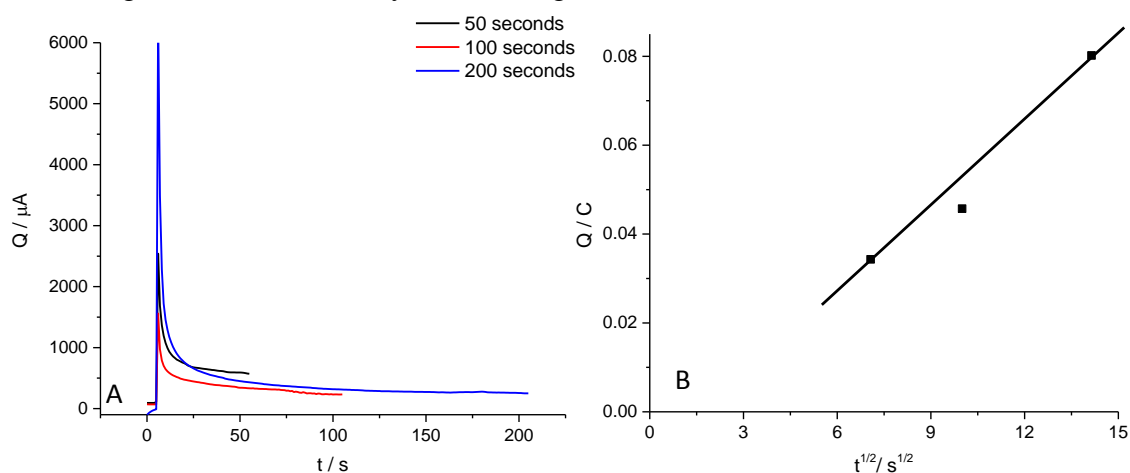


**Figure 5.2:** A) Current-time transients for potentiostatic electrodeposition of 20 mM 3-(2-carboxyethyl) aniline in 0.5 M  $\text{H}_2\text{SO}_4$  solution at 1.2 V vs. an Ag/AgCl over 50, 100 and 200 seconds. B) Plot of charge vs. square root of time (data from panel A).

Monomer conc.(mM)	Time / s	Charge $Q / \text{C}$	Thickness / $\mu\text{m}$
50	50	0.0343	2.05
50	100	0.0457	2.82
50	200	0.0802	4.93

**Table 5.2:** Electrical charge due to electropolymerisation of 20 mM 3-(2-carboxyethyl) aniline films over durations of 50, 100 and 200 seconds. Au electrode area was  $0.23 \text{ cm}^2$  and the molecular weight of the monomer is  $165.19 \text{ g mol}^{-1}$  and its density is ca.  $1.21 \text{ g cm}^{-3}$ .

### 5.3.2 Characterisation of poly3-(2-carboxyethyl)aniline

Following the electropolymerisation process, the prepared films were rinsed with dry acetonitrile and then placed in a monomer-free electrolyte (0.5 M  $\text{H}_2\text{SO}_4$ ). **Figure 5.3** illustrates the voltammetric response of polymer film prepared at  $10 \text{ mV s}^{-1}$  (**Figure 5.1** panel A) over a potential ranging from 0.0 to 1.2 V vs. Ag/AgCl at different scan rates of 5-100  $\text{mV s}^{-1}$ .<sup>3</sup> It can be seen from the figure below that this included two peaks: two anodic peaks at 0.35 V and 0.65 V, and two cathodic peaks at 0.55 V and 0.3 V, which were due to the redox process of the polymer film. Both anodic and cathodic peak currents are linearly dependent on scan rate, as shown in **Figure 5.3** panel C.

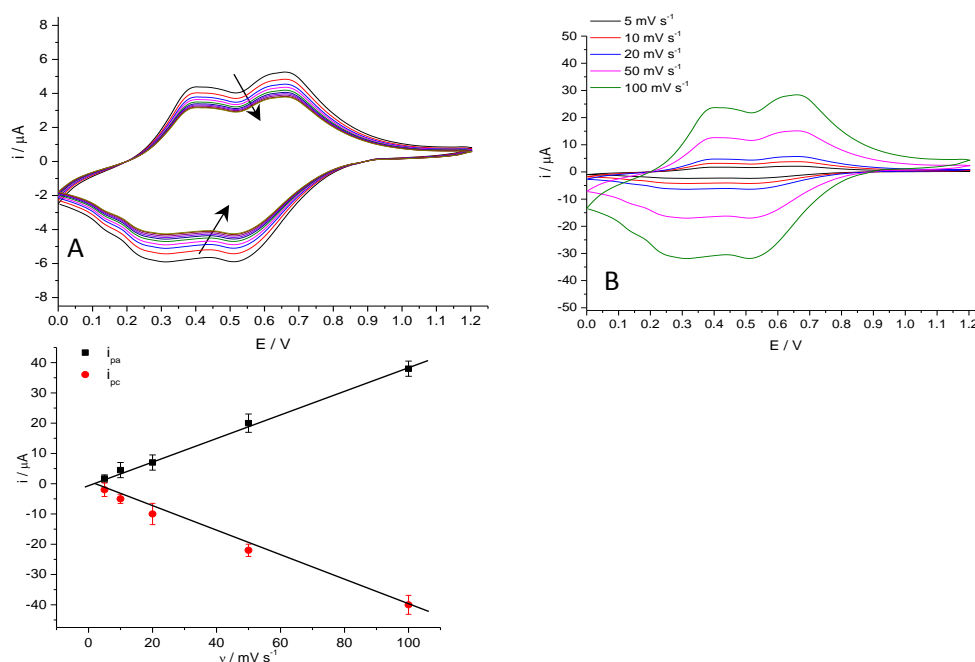


**Figure 5.3:** Voltammetric response of modified electrodes poly(Ani-COOH) prepared at  $10 \text{ mV s}^{-1}$  with  $0.5 \text{ M H}_2\text{SO}_4$  (Figure 5.1 A), and acquired in  $1 \text{ M H}_2\text{SO}_4$  solution (monomer free) at  $0.0 - 1.2 \text{ V}$ . B) Voltammetric responses of the same film at different scan rates,  $5 - 100 \text{ mV s}^{-1}$ ; (C) variation of cathodic peak current (from curves in panel B)) with scan rate.

Polymerisation electrolyte	Electrolyte	Scan rate $\text{mV s}^{-1}$	$Q_{\text{red, 1st cycle}} / \text{C}$	$Q_{\text{red, 10th cycle}} / \text{C}$	$Q_{\text{red, 10th}} / Q_{\text{red, 1st}}$
$\text{H}_2\text{SO}_4$	$\text{H}_2\text{SO}_4$	5	$3.15 \times 10^{-4}$	$2.78 \times 10^{-4}$	0.88
		10	$2.81 \times 10^{-4}$	$2.53 \times 10^{-4}$	0.90
		20	$2.10 \times 10^{-4}$	$1.87 \times 10^{-4}$	0.89
		50	$1.76 \times 10^{-4}$	$1.62 \times 10^{-4}$	0.92
		100	$1.71 \times 10^{-4}$	$1.56 \times 10^{-4}$	0.91

**Table 5.3:** Reduction charge values for Ani-COOH panels (a) in Figure 5.1 exposed to  $\text{H}_2\text{SO}_4$  solution (monomer free). ( $n=1$ )

Electropolymerisation of  $20 \text{ mM Ani-COOH}$  was accomplished via the potentiodynamic method using  $0.5 \text{ M H}_2\text{SO}_4$  solution on a gold-coated quartz crystal using a potential window of  $0.0$  to  $1.2 \text{ V}$  at a scan rate of  $10 \text{ mV s}^{-1}$  for 10 cycles. **Figure 5.4** panels A and B shows the cyclic voltammogram and corresponding mass shift recorded concurrently. Panel A shows the increase in the number of potential cycles that led to an increase in the amount of current accompanying the electropolymerisation. In addition, Figure 5.4 panel B gives a clear indication as to the steady growth of polymer film on the electrode surface. From **Figure 5.4**, it can be seen that mass growth clearly starts at  $1.05 \text{ V}$ .<sup>24, 25</sup> Panel C of **Figure 5.4** shows the amount of charge vs. the applied potential during electropolymerisation. Panel D of **Figure 5.4** illustrates the mass changes vs. the amount of charge. From the gradient determined for panel D, the apparent molar mass of

electroactive units (include monomer and associated anions and solvent molecules) can be estimated using equation 4.1 in chapter four.<sup>36, 37</sup> According to these calculations, the gradient,  $(\Delta m/\Delta q)$ , was  $1.66 \times 10^{-3} \text{ g/C}$  and thus the  $M_{app}$  is  $160 \text{ g mol}^{-1}$ . The molar mass obtained using EQCM was close to the  $M_{app}$  of the monomer at  $165 \text{ g mol}^{-1}$ . Furthermore, cyclic voltammogram data in panel A used to calculate the surface coverage of the polymer film which was  $8.11 \times 10^{-8} \text{ mol cm}^{-2}$ , with a dry polymer film thickness of  $1.15 \times 10^{-5} \text{ cm}$ .

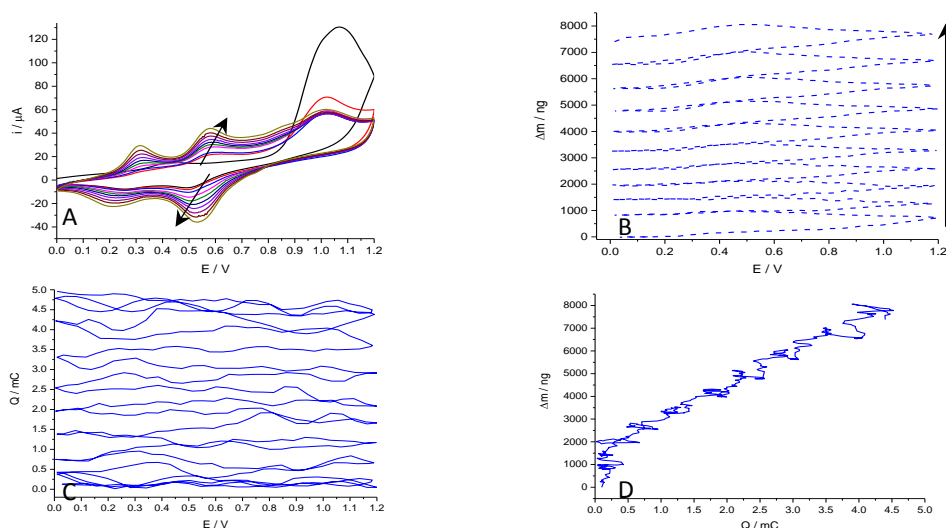


**Figure 5.4:** Representative electrochemical responses for electropolymerisation of 20 mM Ani-COOH (scan rate  $\nu = 10 \text{ mV s}^{-1}$ ) from 0.5 M  $\text{H}_2\text{SO}_4$  solution. (a)  $i$ - $E$ ; (b)  $\Delta m$ - $E$ ; (c)  $Q$ - $E$ ; (d)  $\Delta m$ - $Q$ . Electrode: gold on a QCM crystal with an area of  $0.23 \text{ cm}^2$ . ( $n=1$ )

The prepared polymer film in the previous section was washed in water and acetone three times and then placed in a monomer-free solution of 0.5 M  $\text{H}_2\text{SO}_4$  and scanned using a potential window ranging from 0.0 to 1.2 V vs. Ag/AgCl at a scan rate of  $10 \text{ mV s}^{-1}$  for 10 cycles in order to study the anion doping/dedoping in the polymer film, and its effects on the electrochemical behaviour of the polymer film, using the EQCM technique.<sup>41-43</sup>

**Figure 5.5** panel A shows a cyclic voltammogram of poly(Ani-COOH) film in the monomer-free solution. As expected, the redox peaks of the polymer film corresponded to the electron transfer in the poly(Ani-COOH) film. From this figure, it can be seen that the current peaks are clearly decreased in the second scan until reaching steady state in subsequent scan cycles. **Figure 5.5** panel B shows the increase of mass due to insertion of hydrogen sulphate ions,  $\text{HSO}_4^-$ , and solvent molecules both into an out of the polymer film during the redox process.<sup>26</sup> This was due to the ingress of the solvent electrolyte, leading to the swelling of polymer film and an increase of the polymer mass. The surface coverage of the polymer film was calculated to be  $7.21 \times 10^{-8} \text{ mol cm}^{-2}$ . The comparison

between of surface coverage for polymer film was demonstrated that value was convergent.

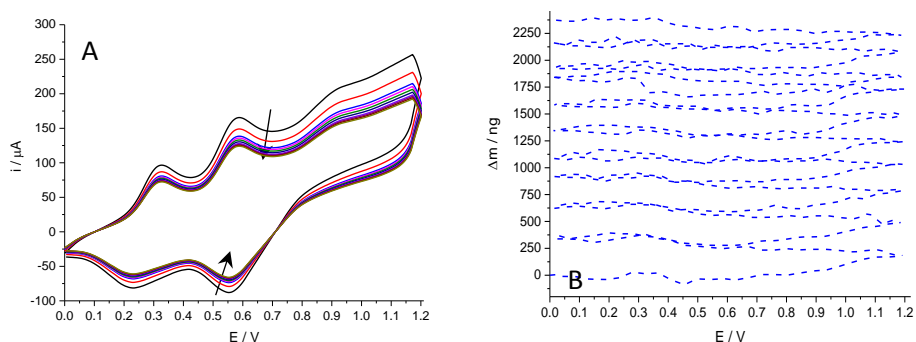


**Figure 5.5:** Representative electrochemical responses for poly(Ani-COOH) from Figure 5.4 (scan rate,  $\nu = 10 \text{ mV s}^{-1}$ ) in  $0.5 \text{ M H}_2\text{SO}_4$  solution (monomer free). (a)  $i-E$ ; (b)  $\Delta m-E$ . Electrode: gold on a QCM crystal with area of  $0.23 \text{ cm}^2$ .

### 5.3.3 Electropolymerisation of copolymer (aniline-co-3-(aminomethyl)aniline)

Copolymerisation was carried out at a total monomer concentration of  $20 \text{ mM}$ , with 3-(aminomethyl)aniline and aniline at a molar ratio of 90:10 in acidic aqueous  $0.5 \text{ M H}_2\text{SO}_4$  using cyclic voltammetry with an applied potential between  $-0.10 \text{ V}$  to  $1.1 \text{ V}$ .<sup>27</sup> **Figure 5.6** illustrates multiple cyclic voltammograms of the comonomer solution as recorded over 10 cycles. The peak currents increased gradually with an increasing number of potential cyclic scans due to the formation of conducting polymer film, which showed a consequent increase in thickness with number of potential cycles.<sup>16, 28, 29</sup> Peak currents were caused by the oxidation of the polymer film, starting from the reduced form (leucoemeraldine salt). The first redox couple at  $0.35 \text{ V}$  and  $0.14 \text{ V}$  can be attributed to the transformation of the leucoemeraldine form into the emeraldine salt form; the third redox couple at  $0.95 \text{ V}$  and  $0.55 \text{ V}$  can be assigned to a further oxidation reaction, namely the transformation of emeraldine into the pernigraniline form. The middle peak was attributed as most probably resulting from the formation of quinone or quinoneimine products during the electropolymerisation process.<sup>30</sup> The surface coverage of deposition process could be found as  $3.42 \times 10^{-6} \text{ mol cm}^{-2}$  and  $1.68 \times 10^{-6} \text{ mol cm}^{-2}$  for the  $10$  and  $20 \text{ mV s}^{-1}$  scan rates, respectively.

Substitution of the aniline monomer by electron donating groups has an effect on the oxidation potentials. In the instance of this copolymer (Ani-co-Ani-NH<sub>2</sub>), the polymer film has an amino functional group, which is expected to have a slight electronic effect on the distribution of charge during the electropolymerisation process. The effect of the amino group on electropolymerisation was attenuated because of the existence of alkyl

groups between the amino group and aromatic ring. In general, the cyclic voltammogram of the copolymer was similar to that of polyaniline.<sup>18-20</sup>

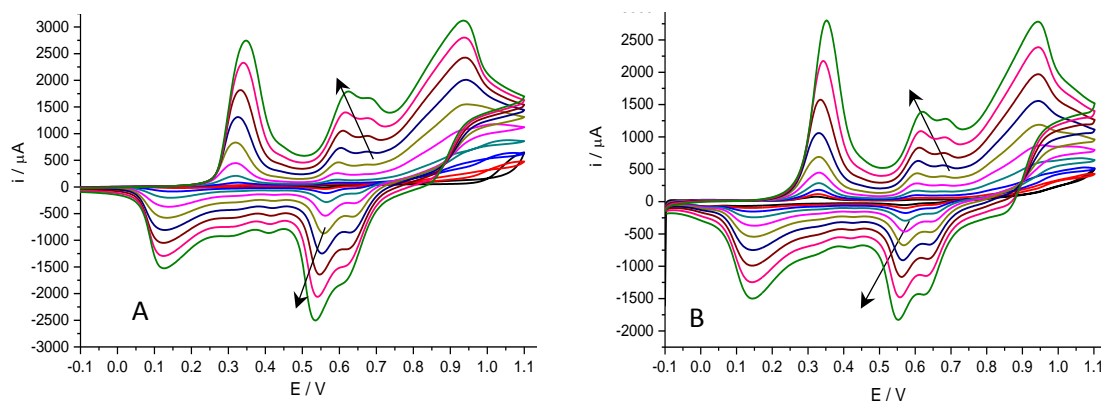


**Figure 5.6:** Cyclic voltammogram during electropolymerisation 20 mM Ani-co-AniNH<sub>2</sub> on gold electrode in 0.5 M H<sub>2</sub>SO<sub>4</sub> at (A) 10 mV s<sup>-1</sup> and (B) 20 mV s<sup>-1</sup> for 10 scans. Electrode area 0.0044 cm<sup>2</sup>.

Electrodeposition of the copolymer was also accomplished using the potentiostatic technique from the same electrolyte solution and using a potential of 1.1 V, with deposition times ranging from 50 to 200 seconds.<sup>31, 32</sup> *I-t* transients for the electropolymerisation are shown in **Figure 5.7**. The general features of these chronoamperogram curves, are similar to those reported for poly(Ani-COOH).<sup>33</sup> From **Figure 5.7**, many of the features associated with the electropolymerisation process discussed in section 4.4.1 can be seen, where the chronoamperometric response of the Ani-co-AniNH<sub>2</sub> copolymer shows the current increases sharply with applied potential and then decays gradually as a result of the electropolymerisation process. Chronoamperometric curves show that the electropolymerisation process was diffusion-controlled as shown in the panel B. As expected, the polymer film thickness increased with increasing polymerisation time. The thickness,  $h_f^*$  (μm), of the dry polymer film was calculated using equations 2.4 and 2.6, as shown in **Table 5.4**.

Monomer conc.(mM)	Time / s	Charge $Q$ / C	Thickness / cm
20	50	$8.81 \times 10^{-3}$	$4.41 \times 10^{-5}$
	100	$1.53 \times 10^{-2}$	$7.74 \times 10^{-5}$
	200	$2.79 \times 10^{-2}$	$1.30 \times 10^{-4}$

**Table 5.4:** Electrical charge of the polymer resulting from the electropolymerisation of 20 mM monomer films for different deposition times of 50, 100 and 200 seconds and an Au electrode area of 0.23 cm<sup>2</sup>. The molecular weight of Ani-NH<sub>2</sub> is 122.16 g mol<sup>-1</sup> and its density is ca. 1.09 g cm<sup>-3</sup>.

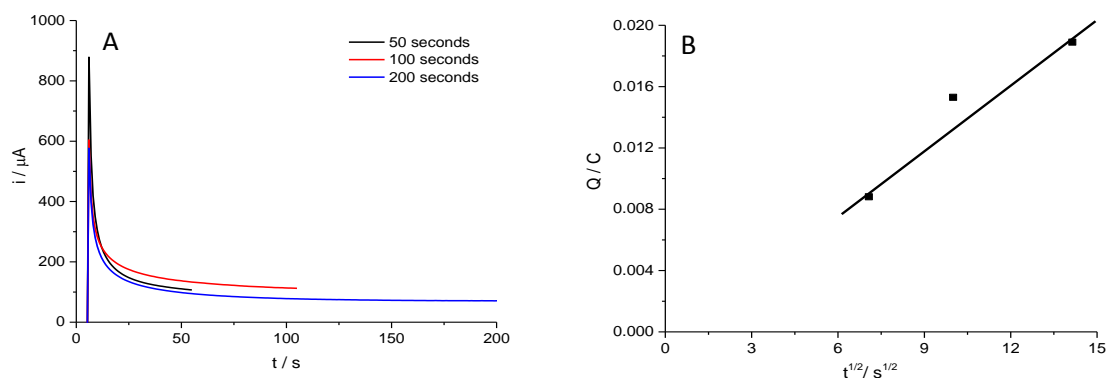


**Figure 5.7:** A) current-time transients for potentiostatic electrodeposition of 20 mM of monomer (3-(aminomethyl)aniline and aniline) in 0.5 M  $\text{H}_2\text{SO}_4$  solution at 1.1 V vs. Ag/AgCl over 50, 100 and 200 seconds. B) plot charge vs. square root of deposition time.

### 5.3.4 Characterization of copolymer (aniline-co-3-(aminomethyl)aniline)

Prepared films were rinsed with water and then placed in a monomer-free electrolyte of 0.5 M  $\text{H}_2\text{SO}_4$  to study the electroactivity during redox cycles. The cyclic voltammetry used an applied potential ranging from -0.2 to 1.1 V vs. Ag/AgCl at different scan rates of between 5 - 100  $\text{mV s}^{-1}$ . Figure 5.8 illustrates the voltammetric response of the resulting polymer film prepared at 10  $\text{mV s}^{-1}$  over 10 scans. It can be seen from Figure 5.8 that there are three reversible peaks, three anodic peaks at 0.45 V, 0.78 V and 0.95 V and three cathodic peaks at 0.83 V, 0.54 V and 0.13 V, which are due to the redox process of the polymer film. **Figure 5.8** panel B shows that both anodic and cathodic peak currents increased linearly with scan number, as shown in **Figure 5.8** panel C.<sup>3, 34, 35</sup>

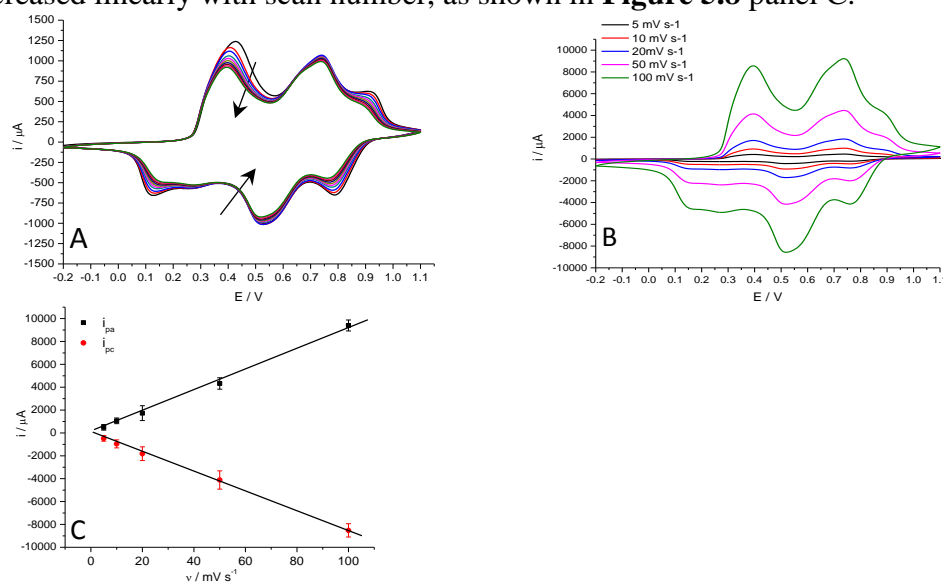


**Figure 5.8:** Voltammetric response of copolymer film prepared at 10  $\text{mV s}^{-1}$  with  $\text{H}_2\text{SO}_4$  (Figure 5.6 panel A), and acquired in 1M  $\text{H}_2\text{SO}_4$  solution (monomer free) at -0.2 to 1.1 V vs. Ag/AgCl. B) Voltammetric responses of the same film at different scan rates, 5- 100  $\text{mV s}^{-1}$ ; C) variation of cathodic peak current (from curves in panel (B)) with scan rate.

Polymerisation electrolyte	Electrolyte	Scan rate $\text{mV s}^{-1}$	$Q$ red, 1st cycle	$Q$ red, 10th cycle	$Q$ red, 10th / $Q$ red, 1st
$\text{H}_2\text{SO}_4$	$\text{H}_2\text{SO}_4$	5	$3.4 \times 10^{-2}$	$3.1 \times 10^{-2}$	0.90
		10	$3.3 \times 10^{-2}$	$3.0 \times 10^{-2}$	0.89
		20	$3.1 \times 10^{-2}$	$2.7 \times 10^{-2}$	0.87
		50	$2.5 \times 10^{-2}$	$2.3 \times 10^{-2}$	0.92
		100	$2.1 \times 10^{-2}$	$1.9 \times 10^{-2}$	0.91

**Table 5.5:** Charge reduction values of Ani-NH<sub>2</sub> panels (a) in Figure 5.6 exposed to H<sub>2</sub>SO<sub>4</sub> solution (monomer free).

Copolymer film was studied using EQCM technique where the polymer film was prepared potentiodynamically using 20 mM in 0.5 M H<sub>2</sub>SO<sub>4</sub> by applying a potential window ranging from -0.2 to 1.1 V vs. Ag/AgCl at a scan rate of 10 mV s<sup>-1</sup> for 10 cycles onto a 10 MHz AT-cut Au polished quartz crystal. **Figure 5.9** shows the cyclic voltammograms and mass curves recorded simultaneously during a sequence of potential cycles in order to deposit the copolymer film. Steady film growth was noted from the increase in mass with the rising number of cycles. **Figure 5.9** panel A shows the increase in the amount of current is proportional to increase in the number of potential cycles. Furthermore, as expected, panel B clearly shows that the mass increased when the potential reached the polymerisation point at ca 0.83 V, as well as the progressive growth of the polymer film on the electrode.<sup>25</sup> Panel C of **Figure 5.9** shows the charge consumed,  $Q$ , versus the applied voltage during electropolymerisation.

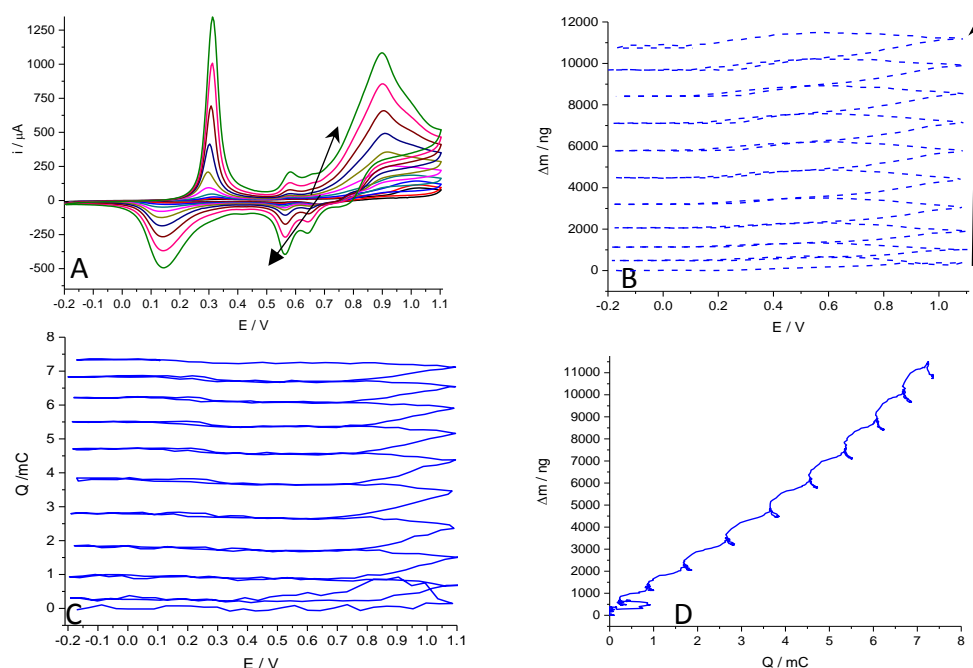


**Figure 5.9:** Representative electrochemical responses for of 20 mM of co-monomer (scan rate  $v = 10 \text{ mV s}^{-1}$ ) from 0.5 M H<sub>2</sub>SO<sub>4</sub> solution. (a)  $i$ - $E$ ; (b)  $\Delta m$ - $E$ ; (c)  $Q$ - $E$ ; (d)  $\Delta m$ - $Q$ . Electrode: gold on a QCM crystal with area of 0.23 cm<sup>2</sup>.

The variation in charge,  $Q$ , and masses are shown in panel D. From the gradient in panel D, the the apparent molar mass ( $M_{app}$ ) (monomer, anions and solvent molecules) involved in the polymerisation process can be calculated.<sup>36, 37</sup> the slope ( $\Delta m/\Delta q$ ) was  $1.50 \times 10^{-3}$  g/C and thus the molar mass is  $146 \text{ g mol}^{-1}$ . The molar mass obtained using EQCM was close to the molar mass of the monomer at  $122 \text{ g mol}^{-1}$ . Furthermore, cyclic voltammogram data was used to calculate the surface coverage of polymer film which was found to be  $6.05 \times 10^{-7} \text{ mol cm}^{-2}$ .

EQCM can be used to monitor doping processes while concurrently recording cyclic voltammograms during redox switching. Copolymer film was placed in a monomer-free solution of  $0.5 \text{ M H}_2\text{SO}_4$ . The cyclic voltammetry used an applied potential ranging from  $0.0$  to  $1.2 \text{ V}$  vs. Ag/AgCl at different scan rates of between  $5 - 100 \text{ mV s}^{-1}$ . To maintain the electroneutrality of the polymer film, counterions will diffuse into the film during oxidation and out of the film during reduction. Protonation of the imine segment in polyaniline leads to the formation of delocalized radical cation sites, into which electroneutrality requires the entry of anions ( $\text{HSO}_4^{1-}$ ) into the polymer chains. Figure 5.10 shows the voltammetric response of the copolymer film prepared at  $10 \text{ mV s}^{-1}$  over 10 scans (**Figure 5.9** panel A). Panel A shows that the current peaks are obviously declining in the second cycle scan until reaching steady state over the next few scan cycles. Moreover, panel B, the mass change during redox switching is due to the influx of  $\text{HSO}_4^-$  ions and water molecules through the polymer film during the redox process. The entrance of solvent molecules into the polymer film lead to swelling and an increase in mass of the polymer film during the redox process. The surface coverage of the polymer film was calculated to be  $6.31 \times 10^{-7} \text{ mol cm}^{-2}$ .

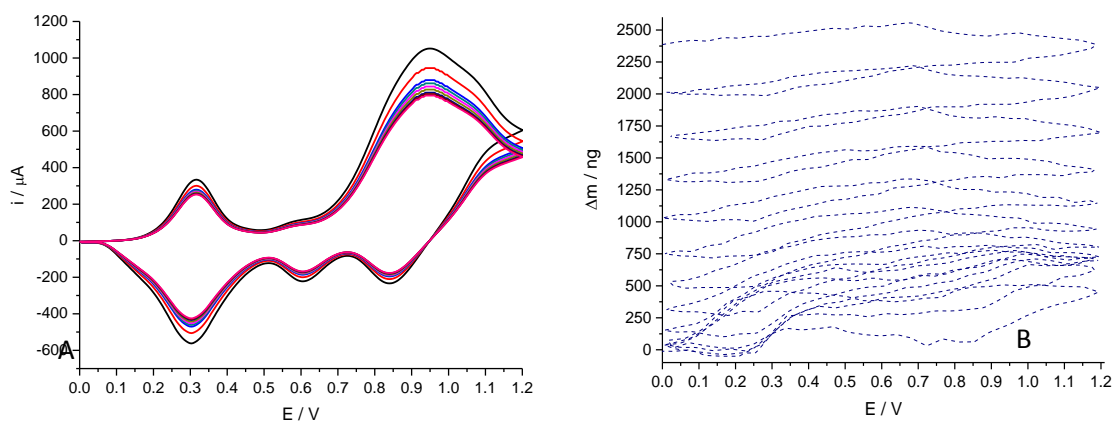


**Figure 5.10:** Representative electrochemical responses for poly(Ani-co-AniNH<sub>2</sub>) from figure 5.10 (scan rate,  $\nu = 10 \text{ mV s}^{-1}$ ) in  $0.5 \text{ M H}_2\text{SO}_4$  solution (monomer free). (a)  $i-E$ ; (b)  $\Delta m-E$ . Electrode: gold on a QCM crystal with an area of  $0.23 \text{ cm}^2$ .

### 5.3.5 Electropolymerisation of pentafluorophenyl 3-(3-aminophenyl) propanoate

The electrochemical polymerisation of (Ani-pfp) on an Au electrode was accomplished by sweeping the potential between 0.0 V and 1.35 V at scan rates of 10 and 20  $\text{mV s}^{-1}$  using 20 mM Ani-pfp in  $\text{HClO}_4/\text{CH}_3\text{CN}$  with 0.05 M TBAP over 10 cycles, as shown in **Figure 5.11** panel A. As shown in **Figure 5.11**, there is an increasing current peak for the redox switching of the polymer film with every potential scan cycle, these increases being indicative of the continuous growth of the polymer film on the gold substrate. These two polymer films exhibit similar cyclic voltammogram curves, and **Figure 5.11** below shows two redox pairs due to polymerisation and the oxidation of the polymer film. The first redox couple at 0.65 V and 0.60 V can be attributed to the redox reaction (the transformation of the leucoemeraldine form into the emeraldine salt form); the second redox couple at 0.78 V and 0.75 V can be assigned to a further oxidation reaction (the transformation of emeraldine into the pernigraniline form). The surface coverage of deposition process was equal to  $5.09 \times 10^{-7} \text{ mol cm}^{-2}$  and  $3.37 \times 10^{-7} \text{ mol cm}^{-2}$  for the 10 and 20  $\text{mV s}^{-1}$  scan rates, respectively.

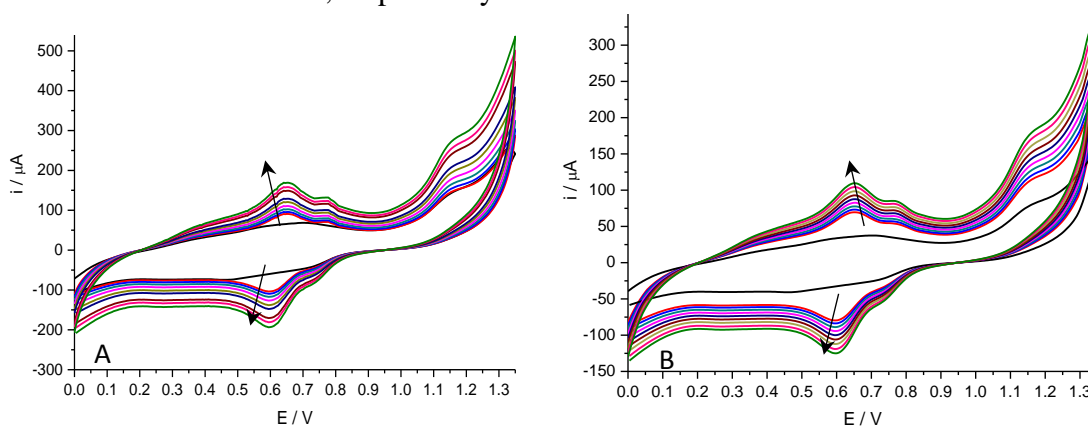


**Figure 5.11:** Cyclic voltammogram during electropolymerisation of 20 mM Ani-pfp on a gold electrode in  $\text{HClO}_4/\text{CH}_3\text{CN}$  at (A) 10  $\text{mV s}^{-1}$  and (B) 20  $\text{mV s}^{-1}$  over 10 scans. Electrode area was  $0.23 \text{ cm}^2$ .

Poly(Ani-pfp) film was formed potentiostatically from 20 mM (Ani-pfp) and  $\text{HClO}_4/\text{CH}_3\text{CN}$  solution over times ranging from 50 to 200 seconds on an Au substrate using a constant potential of 1.35 V. **Figure 5.12** shows the chronoamperometric response recorded during the polymerisation, where the current increases sharply with applied potential and then decays gradually as a result of the electropolymerisation process. The next step was characterised by a slow decrease in current which may have been due to resistive materials being deposited on the electrode. Chronoamperometric measurements show that the electropolymerisation charge increased with  $t^{1/2}$  as result of a diffusion-

controlled process. As expected, the polymer film thickness increased with increasing polymerisation time.<sup>38</sup> The thickness,  $h_f^*$  ( $\mu\text{m}$ ), of the dry polymer film was calculated using equations 2.4 and 2.6, as shown in **Table 5.6**.

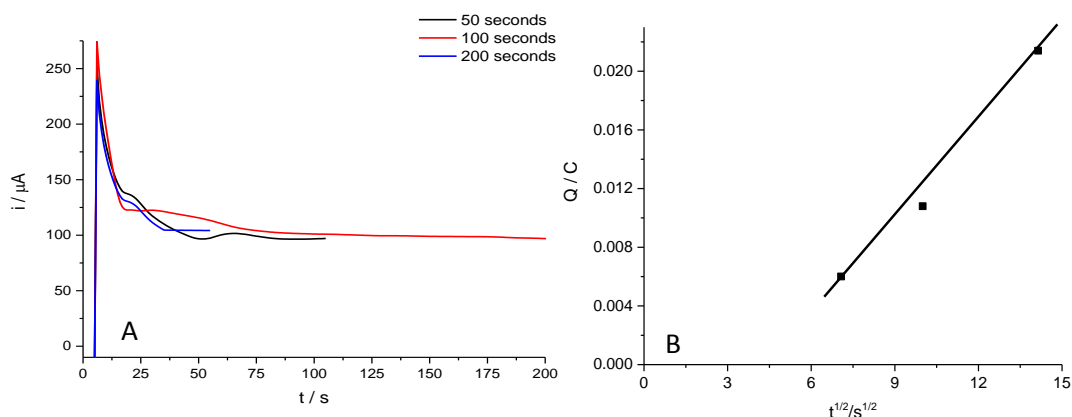


**Figure 5.12:** Current-time transients for potentiostatic electrodeposition of 20 mM Ani-pfp in  $\text{HClO}_4/\text{CH}_3\text{CN}$  solution at 1.35 V vs. Ag/AgCl over 50, 100 and 200 seconds. B) Plot charge vs. square root of deposition time.

Monomer conc.(mM)	Time / s	Charge $Q / \text{C}$	Thickness / cm
20	50	$6.01 \times 10^{-3}$	$7.51 \times 10^{-5}$
	100	$1.08 \times 10^{-2}$	$1.35 \times 10^{-4}$
	200	$2.14 \times 10^{-2}$	$2.66 \times 10^{-4}$

**Table 5.6:** Electrical charge and thickness of polymer due to electropolymerisation of 20 mM ester aniline (Ani-pfp) films at different deposition times of 50, 100 and 200 seconds. Au electrode area was  $0.23 \text{ cm}^2$  and molecular weight of Ani-pfp is  $331.06 \text{ g mol}^{-1}$  and its density is ca.  $1.20 \text{ g cm}^{-3}$ .

### 5.3.6 Characterization of poly(pentafluorophenyl 3-(3-aminophenyl) propanoate)

The poly(Ani-pfp) polymer film was washed with acetonitrile and then transferred to a monomer-free electrolyte containing  $\text{HClO}_4/\text{CH}_3\text{CN}$ . The potentiodynamic method was used to analyse the electroactivity of the polymer film as shown in **Figure 5.13**. The poly(Ani-pfp) prepared in the previous section (see **Figure 5.11**) was scanned in the monomer-free solution over a potential range of 0.0 V to 1.35 V vs. Ag/AgCl at different scan rates between 5 -  $100 \text{ mV s}^{-1}$ . Protonation of polyaniline film leads to the formation of positive sites over the polymer, where the electroneutrality process requires the entry of anions ( $\text{ClO}_4^-$ ) into the polymer chains.<sup>39</sup> It may be noted from **Figure 5.13** that the cyclic voltammogram shows two reversible peaks: two anodic peaks at 0.57 V and 0.73 V, and two cathodic peaks at 0.50 V and 0.70 V, which are due to the redox process of the polymer film. **Figure 5.13** panel B shows that both anodic and cathodic peak

potentials are proportional to the scan rate; moreover, a linear relationship was observed between scan rate and peak currents, as shown in **Figure 5.13** panel C.

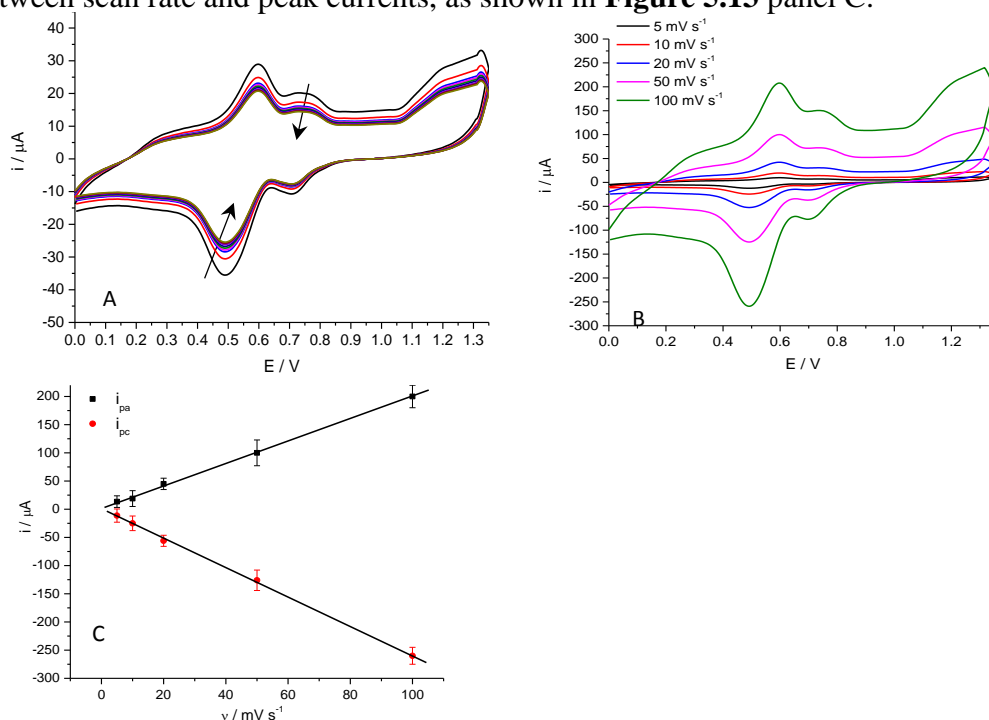


**Figure 5.13:** Voltammetric response of polymer film prepared at  $10 \text{ mV s}^{-1}$  with  $\text{HClO}_4/\text{CH}_3\text{CN}$  solution (Figure 5.11 panel A), and acquired in  $\text{HClO}_4/\text{CH}_3\text{CN}$  solution (monomer free) at 0.0 to 1.35 V vs. Ag/AgCl. B) Voltammetric responses of the same film at different scan rates, 5- 100  $\text{mV s}^{-1}$ ; (C) variation of cathodic peak current (from curves in panel B)) with scan rate.

Polymerisation electrolyte	Electrolyte	Scan rate $\text{mV s}^{-1}$	$Q_{\text{red, 1st cycle}} / \text{C}$	$Q_{\text{red, 10th cycle}} / \text{C}$	$Q_{\text{red, 10th}} / Q_{\text{red, 1st}}$
$\text{HClO}_4 / \text{TBAP}$	$\text{HClO}_4 / \text{TBAP}$	5	$1.07 \times 10^{-3}$	$9.77 \times 10^{-4}$	0.91
		10	$1.06 \times 10^{-3}$	$9.60 \times 10^{-4}$	0.90
		20	$1.03 \times 10^{-3}$	$9.44 \times 10^{-4}$	0.91
		50	$1.02 \times 10^{-3}$	$9.25 \times 10^{-4}$	0.90
		100	$9.70 \times 10^{-4}$	$9.01 \times 10^{-4}$	0.92

**Table 5.7:** Charge reduction values for Ani-pfp panels (a) in Figure 5.13 in  $\text{HClO}_4/\text{CH}_3\text{CN}$  solution (monomer free).

Electrodeposition from 20 mM (Ani-pfp) was achieved using the potentiodynamical method in  $\text{HClO}_4/\text{CH}_3\text{CN}$  solution on an Au layer-coated quartz crystal using a potential window ranging from 0.0 to 1.35 V and a scan rate of  $10 \text{ mV s}^{-1}$  over 10 cycles as shown in **Figure 5.14**. Panels A and B show the cyclic voltammogram and accompanying mass changes recorded concurrently during sequential potential cycles. During the first cycle, it can be seen that an increase in mass could be observed after the oxidation of ester aniline at 0.97 V.<sup>40</sup> Panel C shows the amount of charge vs. applied potential during electropolymerisation. Panel D depicts the mass shifts vs. the amount of charge.<sup>36</sup> the

gradient ( $\Delta m/\Delta q$ ) was  $3.22 \times 10^{-3} \text{ g/C}$  and thus the molar mass is  $308 \text{ g mol}^{-1}$ . This molar mass was close to molar mass of the monomer at  $331 \text{ g mol}^{-1}$ . From these results it can be noted that monomer and solvent have a role during electropolymerisation processes. The molar mass above was lower than expected, and this is probably due to the fact that the polymer film was free of the solvent.<sup>41</sup> The surface coverage of the polymer film was equal to  $1.83 \times 10^{-7} \text{ mol cm}^{-2}$  with a polymer film thickness of  $1.65 \times 10^{-4} \text{ cm}$ .

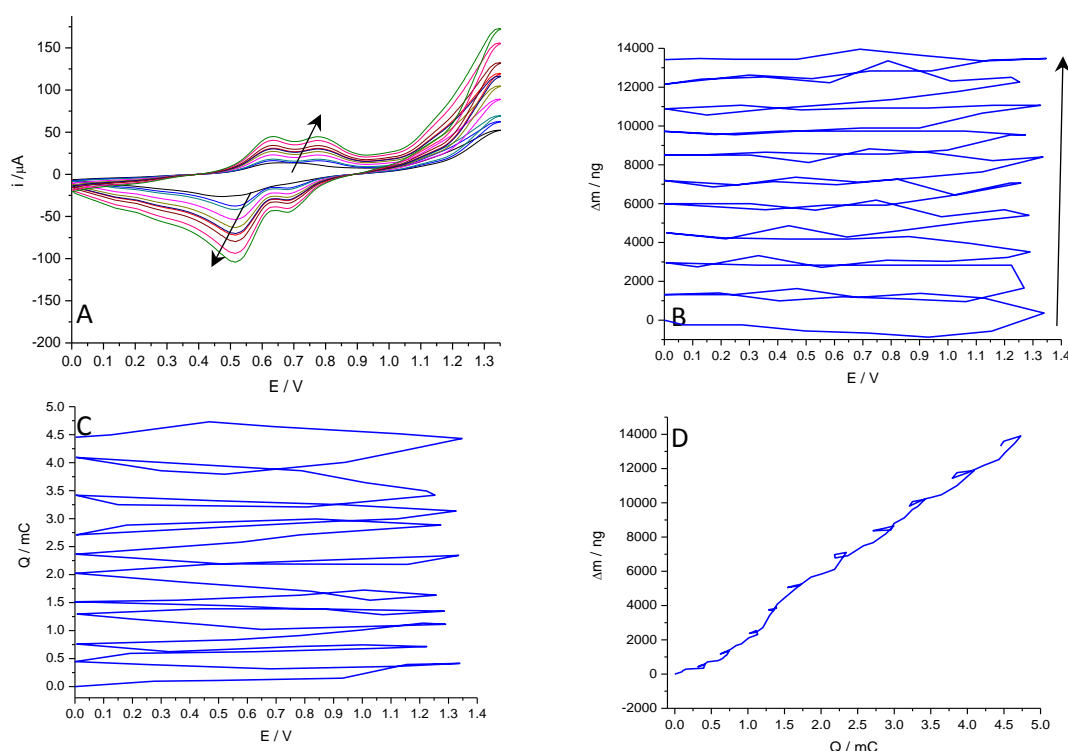


**Figure 5.14:** Representative electrochemical responses for electropolymerisation of 20 mM of Ani-pfp (scan rate  $\nu = 10 \text{ mV s}^{-1}$ ) from  $\text{HClO}_4/\text{CH}_3\text{CN}$  solution. (a)  $i$ - $E$ ; (b)  $\Delta m$ - $E$ ; (c)  $Q$ - $E$ ; (d)  $\Delta m$ - $Q$ . Electrode: gold on a QCM crystal with area of  $0.23 \text{ cm}^2$ .

The poly(Ani-pfp)-coated electrode (which was prepared at a scan rate of  $10 \text{ mV s}^{-1}$ , see **Figure 5.14** panel A) was studied by potential cycling between 0.0 V and 1.3 V vs. Ag/AgCl monomer-free solution  $\text{HClO}_4/\text{CH}_3\text{CN}$  at various scan rates, ranging from 5 to  $100 \text{ mV s}^{-1}$ , over 10 cycles. The film thus produced by the potentiodynamic method showed electroactive characteristics, as can be seen in **Figure 5.15** panel A. From this curve, it may be noted there are two redox peak currents, probably due to the transformation of the leucoemeraldine and emeraldine forms and between the emeraldine and pernigraniline forms, respectively. In **Figure 5.15** panel B, the mass shifts over the potential window from 0.0 to 1.3 V was due to the insertion of perchlorate ions,  $\text{ClO}_4^-$ , and solvent molecules into the polymer film. Although there should be no increase in the polymer mass after each scan cycle, the entry of solvent molecules led to swelling of the

polymer film and a clear increase in mass. The surface coverage of the polymer film was calculated to be  $1.8 \times 10^{-7} \text{ mol cm}^{-2}$  and this value was close to  $\Gamma$  during deposition.

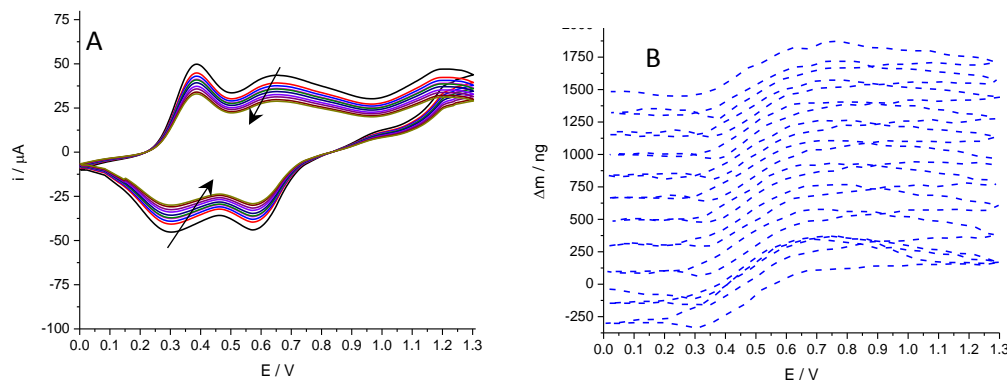


**Figure 5.15:** Representative electrochemical responses for poly(Ani-pfp) from figure 5.14 (scan rate,  $\nu = 10 \text{ mV s}^{-1}$ ) in 0.5  $\text{HClO}_4/\text{CH}_3\text{CN}$  solution (monomer free). (a)  $i$ - $E$ ; (b)  $\Delta m$ - $E$ . Electrode: gold on a QCM crystal with area of  $0.23 \text{ cm}^2$ .

To analyse the findings, the electrochemical properties of the poly(Ani-COOH) and poly(Ani-pfp) films can be compared. The cyclic voltammogram of poly(Ani-COOH) (see **Figure 5.1**) shows two broad oxidation peaks at 0.4V and 0.6 V, and two reduction peaks at 0.25 V and 0.5 V. Whereas, the cyclic voltammogram of poly(Ani-pfp) film (see **Figure 5.11**) exhibits two anodic peaks at 0.65 V and 0.78 V, and two cathodic peaks 0.60 V and 0.75 V. The emergence of an oxidation peak in the poly(Ani-pfp) at a higher potential than Ani-COOH was attributed to the presence of pfp groups, which contain fluoro groups and carbonyl bonds that have a stronger electron withdrawing effect than that of the carboxylic groups in Ani-COOH.<sup>42, 43</sup> This electrochemical behaviour of the conducting polymer (Ani-pfp) can probably be attributed to the existence of potential barriers on the conjugated chains as result of the presence of an electron-withdrawing substituent.

### 5.3.7 Electropolymerisation of *N*-Fmoc-*m*-aminobenzylamine

Poly(Ani-Fmoc) film was polymerized potentiodynamically with an applied voltage between -0.20 V and 1.35 V using an  $\text{HClO}_4/\text{CH}_3\text{CN}$  solution with 0.05 M TBAP onto an Au electrode substrate (area of  $2.3 \text{ cm}^2$ ) at scan rates of 10 and  $20 \text{ mV s}^{-1}$  over 10 cycles as shown in **Figure 5.16** panel A. The peak currents in **Figure 5.16** panel A gradually rise with the number of potential cyclic scans.<sup>44,15</sup> In the first scan (panels A and B), the anodic current at ca.  $E_{pa} = 1.2 \text{ V}$  is due to the oxidation of the Ani-Fmoc monomer. While the subsequent cycles show the appearance of two further redox current

peaks. The first of these redox pairs, at 0.59 V and 0.55 V, is due to the transformation of the leucoemeraldine form into emeraldine salt form; the second pair, which emerged at 0.91 V and 0.79 V, is due to the further oxidation reaction of the transformation of emeraldine into the pernigraniline form. The surface coverages were determined as  $1.81 \times 10^{-6} \text{ mol cm}^{-2}$  and  $7.88 \times 10^{-7} \text{ mol cm}^{-2}$  at 10 and 20  $\text{mV s}^{-1}$  scan rates,

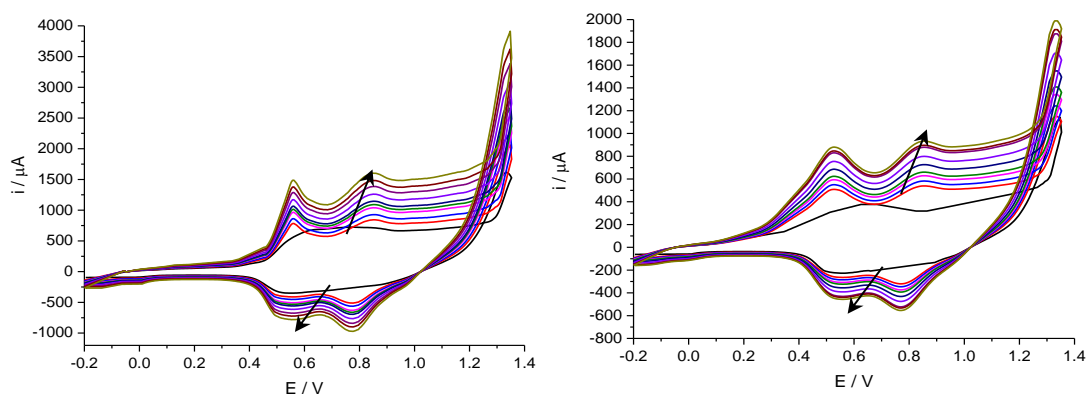


**Figure 5.16:** Cyclic voltammogram during electropolymerisation of 20 mM Ani-pfp on gold electrode in  $\text{HClO}_4/\text{CH}_3\text{CN}$  at (A)  $10 \text{ mV s}^{-1}$  and (B)  $20 \text{ mV s}^{-1}$  over 10 scans. Electrode area of  $0.23 \text{ cm}^2$ .

Electrodeposition of poly(Ani-Fmoc) was achieved using a potential step method from a solution of 20 mM Ani-Fmoc with  $\text{HClO}_4/\text{CH}_3\text{CN}$  and 0.05 M TBAP over various deposition times ranging from 50 to 200 seconds, as shown in **Figure 5.17**. Results from potential step experiments show that the electropolymerisation charge increased with  $t^{1/2}$  as result of diffusion control. The polymer film thickness increased four-fold on increasing the polymerisation time from 50 to 200 seconds. The thickness,  $h_f^*$  ( $\mu\text{m}$ ), of the dry polymer film was estimated as shown in **Table 5.8**.

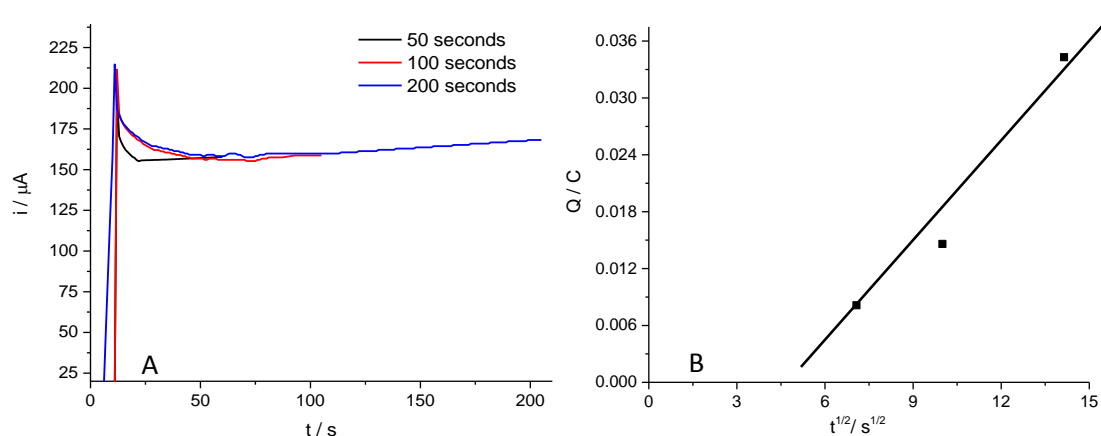


**Figure 5.17:** A) current-time transients for potentiostatic electrodeposition of 20 mM Ani-fmoc in  $\text{HClO}_4/\text{CH}_3\text{CN}$  solution at 1.35 V vs. an Ag/AgCl over 50, 100 and 200 seconds. B) Plot charge vs. square root of deposition time.

Monomer conc.(mM)	Time / s	Charge $Q$ / C	Thickness / cm
20	50	$8.13 \times 10^{-3}$	$1.18 \times 10^{-4}$
	100	$1.46 \times 10^{-2}$	$2.13 \times 10^{-4}$
	200	$3.43 \times 10^{-2}$	$4.95 \times 10^{-4}$

**Table 5.8:** Electrical charge and thickness of polymer resulting from electropolymerisation of 20 mM (Ani-Fmoc) films at different deposition times of 50, 100 and 200 seconds. Au electrode area was  $0.23 \text{ cm}^2$ , and molar mass of Ani-Fmoc is  $344 \text{ g mol}^{-1}$  and its density is ca.  $1.1 \text{ g cm}^{-3}$ .

### 5.3.8 Characterization of poly(N-Fmoc-m-aminobenzylamine)

The resultant films were rinsed three times with dry acetonitrile and then placed in a monomer-free solution containing  $\text{HClO}_4/\text{CH}_3\text{CN}$  to study electroactivity changes and the redox reaction of poly(Ani-Fmoc). Cyclic voltammetry used a voltage ranging from -0.2 to 1.35 V vs. Ag/AgCl over 10 cycles with scan rates ranging from 5 -  $100 \text{ mV s}^{-1}$ . As expected, the redox current peaks are generally assumed to correspond to current peaks during polymer film formation. The doping/dedoping process of the polymer film was accomplished via cyclic voltammetry, as shown in **Figure 5.18**.<sup>14</sup> The figure below shows the voltammetric responses for poly(Ani-Fmoc) prepared at  $10 \text{ mV s}^{-1}$  over 10 cycles (see **Figure 5.16** panel A). **Figure 5.18** shows two reversible peaks could be seen in the associated cyclic voltammograms; the first peak pair appeared at 0.60 V and 0.55 V, and the second at 0.85 V and 0.80 V, which are due to the redox process of the polymer film. **Figure 5.18** panel B shows that the redox current peaks are proportional to scan rate; moreover, a linear relationship was observed between scan rate and peak currents, as shown in **Figure 5.18** panel C.

Polymerisation electrolyte	Electrolyte	Scan rate $\text{mV s}^{-1}$	$Q$ red, 1st cycle/C	$Q$ red, 10th cycle/C	$Q$ red, 10th / $Q$ red, 1st
$\text{HClO}_4$ / TBAP	$\text{HClO}_4$ / TBAP	5	$1.75 \times 10^{-3}$	$1.61 \times 10^{-3}$	0.92
		10	$1.60 \times 10^{-3}$	$1.45 \times 10^{-3}$	0.90
		20	$1.57 \times 10^{-3}$	$1.40 \times 10^{-3}$	0.89
		50	$1.54 \times 10^{-3}$	$1.37 \times 10^{-3}$	0.89
		100	$1.43 \times 10^{-3}$	$1.28 \times 10^{-3}$	0.90

**Table 5.9:** Charge reduction values for Ani-fmoc panels (a) in Figure 5.18 in  $\text{HClO}_4/\text{TBAP}$  solution (monomer free).

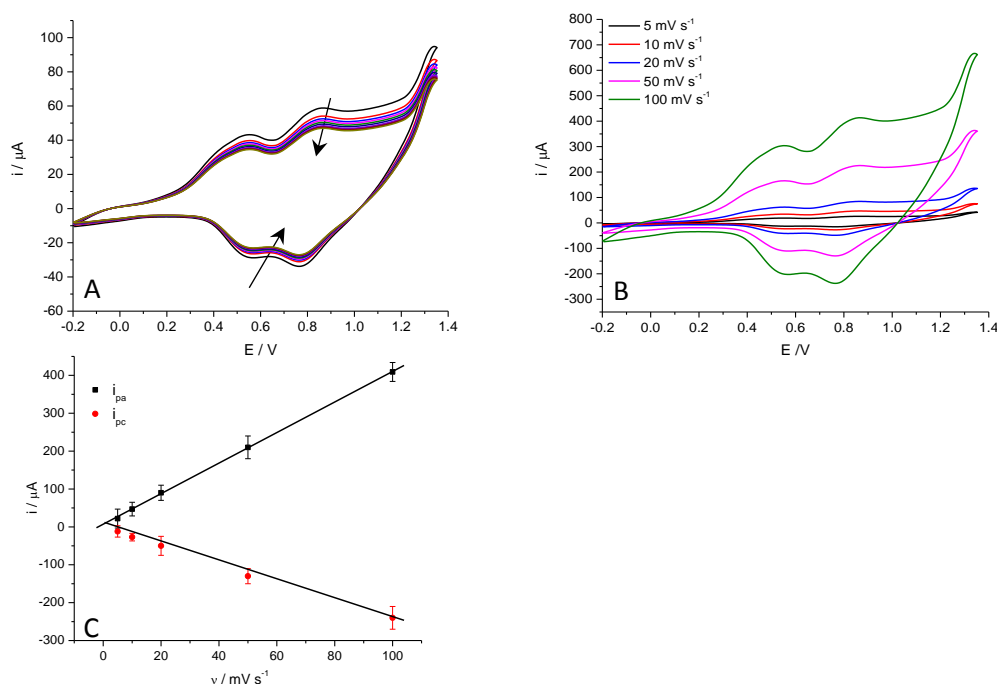


**Figure 5.18:** Voltammetric response of polymer film prepared at  $10 \text{ mV s}^{-1}$  with  $\text{HClO}_4/\text{CH}_3\text{CN}$  solution (Figure 5.16 panel A), and acquired in  $\text{HClO}_4/\text{CH}_3\text{CN}$  solution (monomer free) at 0.0 - 1.35 V vs. Ag/AgCl. B) Voltammetric responses of the same film at different scan rates, 5- 100  $\text{mV s}^{-1}$ ; C) variation of cathodic peak current (from curves in panel (B)) with scan rate.

Electropolymerisation of 20 mM (Ani-Fmoc) was conducted via cyclic voltammetry in a  $\text{HClO}_4/\text{CH}_3\text{CN}$  with 0.05 M TBAP solution onto a gold-coated crystal using a potential window ranging from 0.0 to 1.30 V vs. Ag/AgCl at a scan rate of  $10 \text{ mV s}^{-1}$  over 10 cycles. **Figure 5.19** panels A and B show the cyclic voltammogram and accompanying mass shifts recorded concurrently during sequential potential cycles. **Figure 5.19** panel B clearly shows that the mass of polymer on the crystal increased when the potential reached 1.05 V. Panel C shows the amount of electrical charge vs. the applied potential during the electrodeposition process. The variation of the charge passed,  $Q$ , and mass shift is shown in panel D. Although the curve was nonlinear, as in previous experiments, the value of the gradient and thus molar mass which were calculated from this curve was within an acceptable range. It is possible to assume that the deposition of the polymer in the first cycle was influenced by the electrode surface, and thus decreased the amount of charge consumed in cycles 4 to 10. From this curve, the gradient can be calculated by using the “end-to-end” method, as shown in panel D.<sup>36,37</sup> The gradient ( $\Delta m/\Delta q$ ) was  $3.29 \times 10^{-3} \text{ g/C}$ , and thus the  $M_{app}$  of electroactive units involved in the electrodeposition process was  $320 \text{ g mol}^{-1}$ . This  $M_{app}$  was close to molar mass of the monomer at  $344 \text{ g mol}^{-1}$ . In addition, voltammetric data presented in panel A was used to determine the

surface coverage, which was found to be  $3.02 \times 10^{-7} \text{ mol cm}^{-2}$  with a polymer film thickness of  $7.58 \times 10^{-5} \text{ cm}$ . Moreover, EQCM can be used to monitor the doping/dedoping processes whilst simultaneously recording cyclic voltammograms during redox switching in order to study the electrochemical behaviour and neutralisation processes of the charged polymer film.<sup>45, 46</sup>

To achieve this, the resultant polymer film in the prior section was placed in a monomer-free electrolyte containing  $\text{HClO}_4/\text{CH}_3\text{CN}$  solution and then scanned using a potential window of  $-0.2$  to  $1.35 \text{ V}$  vs.  $\text{Ag}/\text{AgCl}$  at a scan rate of  $10 \text{ mV s}^{-1}$  over 10 cycles. Figure 5.20 panel A illustrates the cyclic voltammogram obtained for poly(Ani-Fmoc) film in the monomer-free solution. Furthermore, **Figure 5.20** panel B shows the mass change during redox switching is due to an influx of perchlorate ions,  $\text{ClO}_4^-$ , and water molecules during the redox process.<sup>47</sup> The increasing of the mass of polymer after each scan cycle can be explained by assuming there is increase in the number of solvent molecules entering the polymer film, therefore causing it to swell. The surface coverage of the polymer film was estimated to be  $3.08 \times 10^{-7} \text{ mol cm}^{-2}$ .

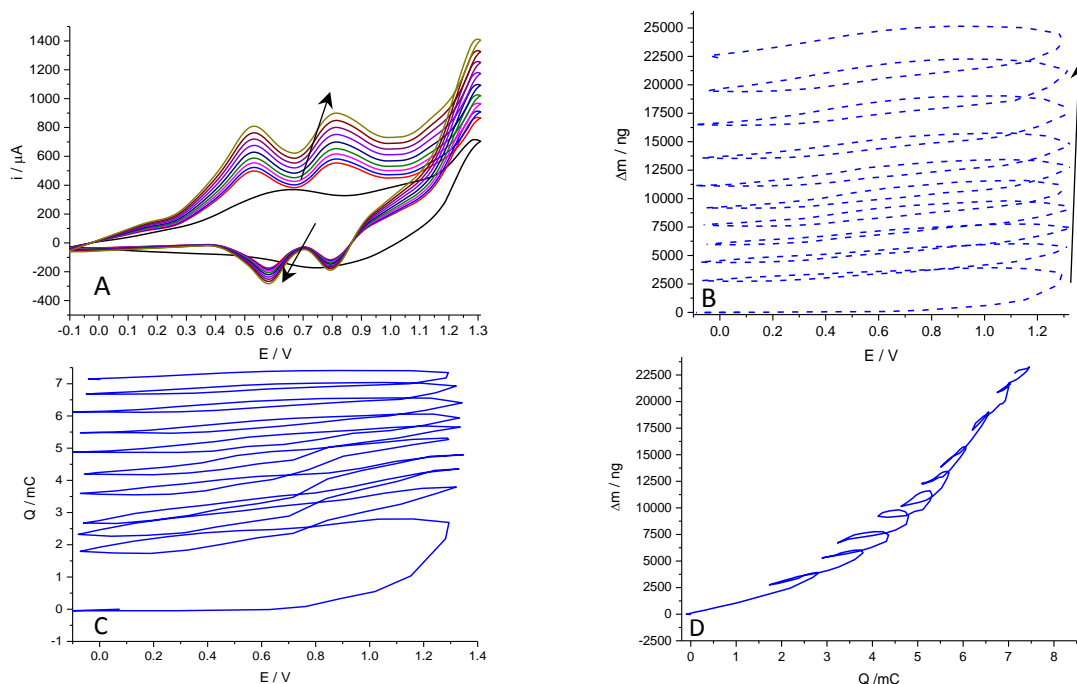


**Figure 5.19:** Representative electrochemical responses for electropolymerization of  $20 \text{ mM Ani-fmoc}$  (scan rate  $v = 10 \text{ mV s}^{-1}$ ) from  $\text{HClO}_4/\text{CH}_3\text{CN}$  solution. (a)  $i$ - $E$ ; (b)  $\Delta m$ - $E$ ; (c)  $Q$ - $E$ ; (d)  $\Delta m$ - $Q$ . Electrode: gold on a QCM crystal with an area of  $0.23 \text{ cm}^2$ .

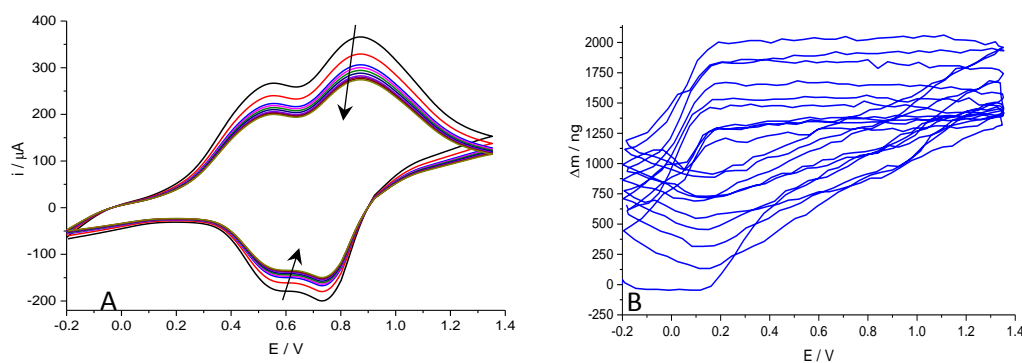


**Figure 5.20:** Representative electrochemical responses for poly(Ani-fmoc) from Figure 5.19 (scan rate,  $v = 10 \text{ mV s}^{-1}$ ) in  $\text{HClO}_4/\text{CH}_3\text{CN}$  solution (monomer free). (a)  $i$ - $E$ ; (b)  $\Delta m$ - $E$ . Electrode: gold on a QCM crystal with area of  $0.23 \text{ cm}^2$ .

A comparison between the electrochemical behaviour of poly(Ani-NH<sub>2</sub>) and poly(Ani-Fmoc) demonstrates that both oxidation waves of the poly(Ani-Fmoc) (**Figure 5.16**) were shifted to higher potentials than were observed for the poly(Ani-NH<sub>2</sub>) monomer (Figure 5.6).<sup>42, 43</sup> This shift to higher potential may have been due to the substituent group effects which led to changes in the polymer backbone and variations in the electrostatic reactions between the oxidised Fmoc groups within the polymer chains. This comparison shows that there are two oxidation peaks at 0.35 V and 0.62 V, and reduction peaks at 0.13 V and 0.53 V, for poly(Ani-NH<sub>2</sub>). Similarly, the voltammetric response of the poly(Ani-Fmoc) film shows that there are two oxidation peaks at 0.55 V and 0.85 V, and two reduction peaks at 0.52 V and 0.77 V. These electrochemical properties of poly(Ani-Fmoc) may be attributed to the existence of steric hindrance due to the substituent groups on the polymer chains as result of the presence of Fmoc units.<sup>48, 49</sup>

#### 5.4 Post-polymerisation Chemical Modifications

As mentioned in chapter four, many post-polymerisation methods are used to modify film surfaces. Immobilisation of functional groups on polymer films has become a key criterion for the enhancement of surface functionalities, especially in sensing applications.<sup>50</sup> In this section, the hydrolysis reactions of protected polymer films and the electrochemical stability of the polymer films were examined. Moreover, the functionalisation of the polymer surface was studied using the FTIR and QCM techniques.<sup>51, 52</sup> The strategy of the hydrolysis and immobilisation of polymer film surface are shown in **Figure 4.22** in chapter four. This section describes the electrodeposition of protected monomers, either pfp or Fmoc that can be easily replaced with suitable groups. In this reaction, amide covalent bonds are formed between receptor groups and the

functionalised polymer (pfp or Fmoc) surfaces. EQCM and spectroscopic probe techniques were used to examine the success of this synthetic strategy as regards the immobilisation of ligands within the polymer films.

#### 5.4.1 QCM Gravimetric and FTIR Spectroscopic Monitoring of Ester Hydrolysis

Poly(Ani-pfp) films were hydrolysed using 0.1 M NaOH solutions over different times to verify their conversion ratio to carboxylic acid groups. Polymer electrodes were placed in solutions of 0.1 M NaOH whilst continuously monitoring the conversion via FTIR until the reaction was complete, as shown in **Figure 5.21**. FTIR was used to identify when the carbonyl group of the ester bond no longer appeared in the resulting film after hydrolysis, Figure 5.21 shows that the carbonyl ester band  $\nu(\text{C}=\text{O})$  at  $1781\text{ cm}^{-1}$  and the  $\nu(\text{C}-\text{F})$  band at  $995\text{ cm}^{-1}$  do not exist in the deprotected film spectrum.<sup>51</sup> Moreover, hydrolysis led to the emergence of new bands that could be attributed to the Ani-COOH film, for example the peak at  $3225\text{ cm}^{-1}$  was due to an amine NH stretch, the broad band at  $3300\text{ cm}^{-1}$  which was due to the  $\nu(\text{O}-\text{H})$  stretch of the carboxylic acid (indicated by symbol \* in figure), while an aliphatic C-H stretch emerged in the range between  $2970$  and  $2910\text{ cm}^{-1}$ ;<sup>53, 54</sup> the band at  $1728\text{ cm}^{-1}$  was attributed to the  $\nu(\text{C}=\text{O})$  stretch of the carboxylic acid (indicated by symbol + in spectrum).<sup>55, 56</sup>

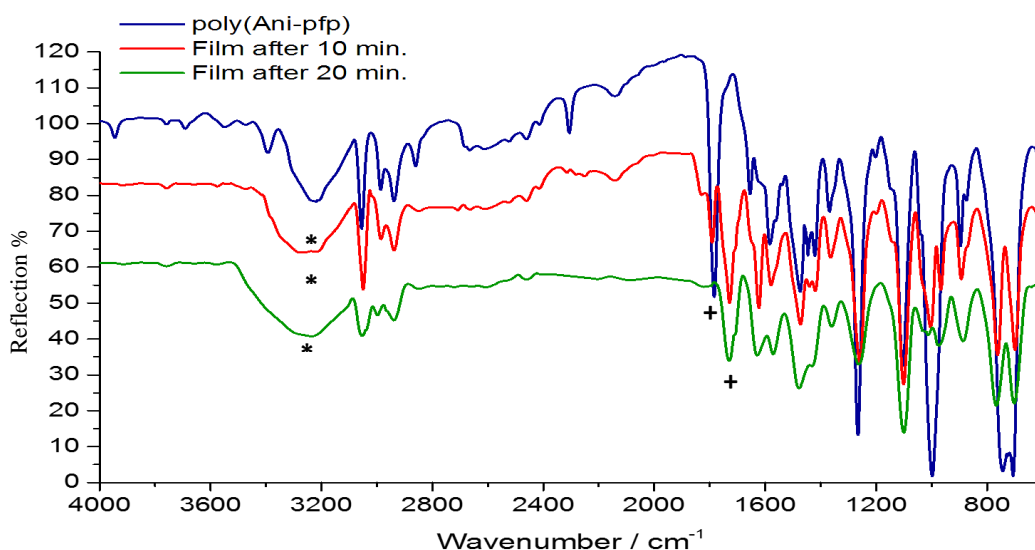


**Figure 5.21:** FTIR spectra showing the hydrolysis reaction at different times over the course of the reaction. (a) Poly(Ani-pfp) as deposited (blue line), (b) film after 10 min. hydrolysis (red line) and (c) film after 20 min. hydrolysis (green line). \*denotes the presence of carboxylic and + denotes the presence of carbonyl peaks.

Moreover, QCM was used to examine the deprotection of poly(Ani-pfp) films.<sup>20</sup> QCM was applied to determine the mass changes accompanying the hydrolysis reaction at the surface of the polymer films as a result of the removal of good leaving groups. **Figure 5.22** shows that the frequency of the quartz crystal resonator increased, and thus mass was decreased, during the hydrolysis reaction.

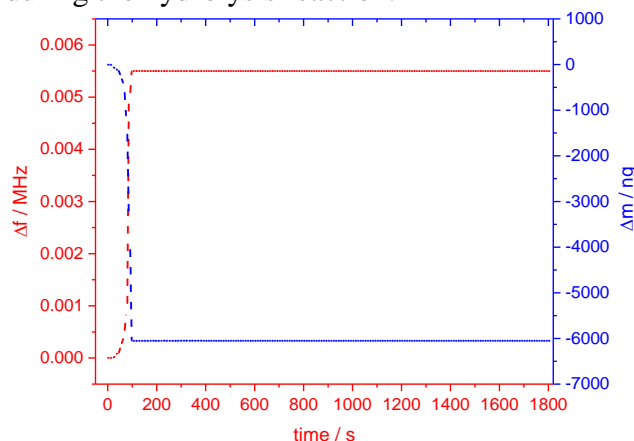


**Figure 5.22:** QCM recorded during the deprotection process of poly(Ani-pfp) film in an alkaline solution of 0.1 M NaOH.

In addition, in order to check that the hydrolysis process had not affected the electroactivity of the polymer films, the electrochemical behaviour of deprotected polymer films via the potentiodynamic method was performed. The cyclic voltammogram was recorded in a monomer-free solution 0.1 M HClO<sub>4</sub>/CH<sub>3</sub>CN at a 10 mV s<sup>-1</sup> scan rate over 10 cycles, as shown in **Figure 5.23**. **Figure 5.23** shows current peaks for the redox process, which were found to be almost identical to those observed during the monomer-free study of Ani-COOH before protection.

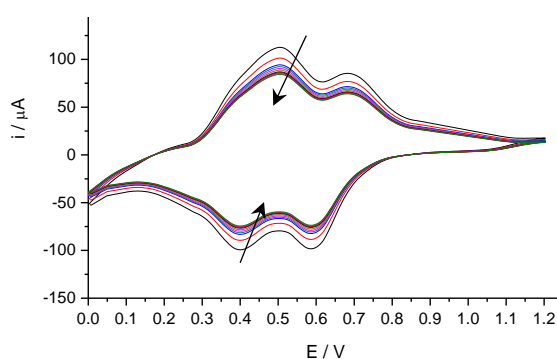


**Figure 5.23:** Cyclic voltammogram of poly(Ani-pfp) film after hydrolysis in a HClO<sub>4</sub>/CH<sub>3</sub>CN with 0.05 M TBAP solution as a function of repeated scans at 10 mV s<sup>-1</sup>.

From the IR spectra in **Figure 5.21**, it may be noted that some of pfp groups remain in the polymer film for up to 10 minutes, while **Figure 5.22** shows that there is no further change in the mass of the polymer film after 3 minutes of hydrolysis. This difference

between techniques can be explained by assuming that the film loses the leaving group (pfp) in the first few minutes of the reaction, and solvent molecules begin to ingress into polymer film to fill the voids caused by the egress of the pfp molecules. It has been confirmed that the hydrolysis reaction was ultimately accomplished via IR measurements, as shown in **Figure 5.21** curve C. As mentioned in section 4.4.1, voltammetric results were used to calculate surface coverage of polymer ( $m_p$ ) using equation 2.4 to be  $1.8 \times 10^{-7} \text{ mol cm}^{-2}$  and this implies mass of polymer equal to  $12 \mu\text{g}$  (data presented in **Figure 5.14**). Based on QCM data the mass of film ( $m_p + m_s$ ) was equal to  $14 \mu\text{g}$ , implying that solvent represent 15% of polymer film. After hydrolysis calculation was showed that surface coverage of polymer equal to  $1.63 \times 10^{-7} \text{ mol cm}^{-2}$  this implies mass of polymer equal to  $7.2 \mu\text{g}$ . Based on QCM data (presented in **Figure 5.22**) the mass of film equal to  $7.9 \mu\text{g}$  and mass change of hydrolysis was  $-6.1 \mu\text{g}$  and.<sup>57, 58</sup> Theoretical calculations show that mass of pfp groups equal to 58% and findings above show that the mass change of polymer film was equal to 43%. This difference in polymer film mass between poly(Ani-pfp) and poly(Ani-COOH) containing almost same  $\Gamma$  values due to ingress a large amount of solvent molecules into polymer film during hydrolysis process.

Films	Polymer deposition		polymer hydrolysis		functionalisation	
	$\Gamma \text{ mol cm}^{-2}$	$\Delta M \mu\text{g cm}^{-2}$	$\Gamma \text{ mol cm}^{-2}$	$\Delta M \mu\text{g cm}^{-2}$	$\Gamma \text{ mol cm}^{-2}$	$\Delta M \mu\text{g cm}^{-2}$
Ani-pfp	$1.80 \times 10^{-7}$	14	$1.63 \times 10^{-7}$	-6.1	$1.5 \times 10^{-7}$	7.3

**Table 5.10:** Mass and surface coverage between polymer films (before and after hydrolysis) functionalisation for poly(Ani-pfp) film.

#### 5.4.2 Monitoring of vertical penetration of receptor into ester polymer film

The immobilisation process was accomplished through the reaction between the poly(Ani-pfp) and (NTA-lysine) molecular using the same procedure which used with Py-pfp in chapter four. **Figure 5.24** illustrates a schematic of the immobilisation reaction between the poly (Ani-pfp) film surface and the receptor (NTA). FTIR was used to monitor the reaction over time to determine the time necessary to ensure the immobilisation process was complete. From the FTIR spectrum, it can be concluded the following: the ester film, poly(Ani-pfp), showed a characteristic sharp band at  $1790 \text{ cm}^{-1}$  that could be attributed to the  $\nu(\text{C}=\text{O})$  stretch of the ester group and a band at  $990 \text{ cm}^{-1}$  due to the  $\nu(\text{C}-\text{F})$  bend before immobilisation, as shown in **Figure 5.25**. After the immobilisation reaction, the carbonyl stretch shifted from  $1790 \text{ cm}^{-1}$  to  $1690 \text{ cm}^{-1}$  as result of the formation of amide bonds (indicated by symbol \* in figure). Concomitant with this shift was the disappearance of the peak at approximately  $995 \text{ cm}^{-1}$  due to the removal of the PFP group. Furthermore, the

emergence of a new broad band at  $3250\text{ cm}^{-1}$  was attributed to the  $\nu(\text{O-H})$  stretch and a band at  $1725\text{ cm}^{-1}$  was attributed to the  $\nu(\text{C=O})$  stretch of the carboxylic groups in the ligand.

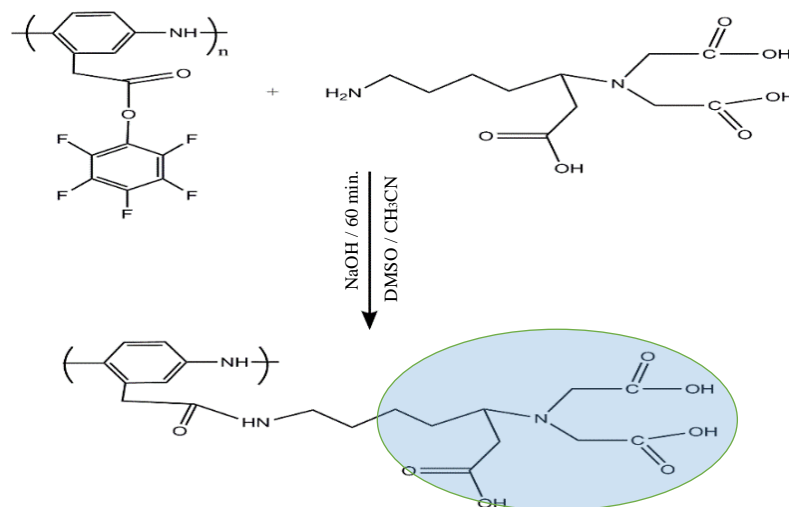


**Figure 5.24:** Reaction scheme illustrating the reaction between the receptor NTA-lysine with the activated ester film, poly(Ani-pfp).

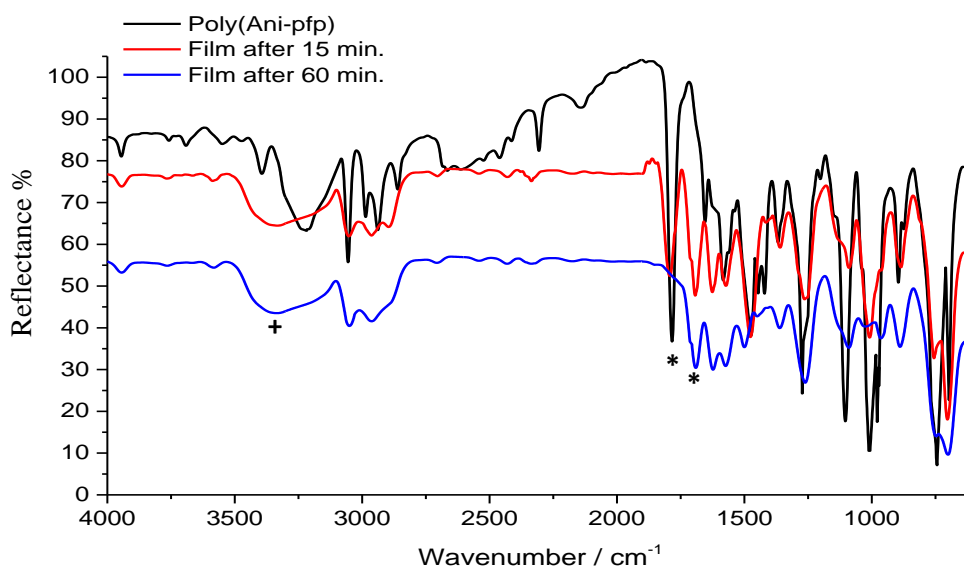


**Figure 5.25:** FTIR spectra showing the amidation at different times. (a) Poly(Ani-pfp) as deposited (black line), (b) film after 15 min. (red line), and (c) film after 60 min. reaction time (blue line). \*denotes the presence of carbonyl of amide and + denotes the presence of carboxylic peaks.

The QCM was used to monitor the immobilisation process for the poly(Ani-pfp) film to verify the degree of penetration over the polymer film surface. As expected, the insertion of receptor units into polymer film led to a gradual decrease in frequency coincident with the increase in mass of the polymer film, as mentioned in chapter four. **Figure 5.26** illustrates the changes in mass and frequency during the immobilisation process.

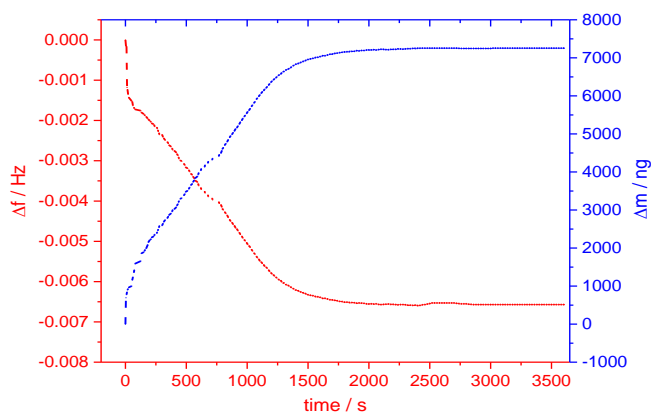


**Figure 5.26:** QCM curve recorded during the immobilization process of poly(Ani-pfp) film with the receptor unit (NTA-lysine) over 60 minutes.

The electrochemical behaviour of poly(Ani-NTA) was examined potentiodynamically in monomer-free 0.1 M HClO<sub>4</sub>/CH<sub>3</sub>CN solution with a 10 mV s<sup>-1</sup> scan rate over 10 cycles, as shown in **Figure 5.26**. The aim of this experiment was to examine the electroactivity of the poly(Ani-NTA) film. **Figure 5.27** shows the redox current peaks differ somewhat to those observed during the monomer-free study of PFP film because of the receptor groups being inserted onto the polymer film surface.

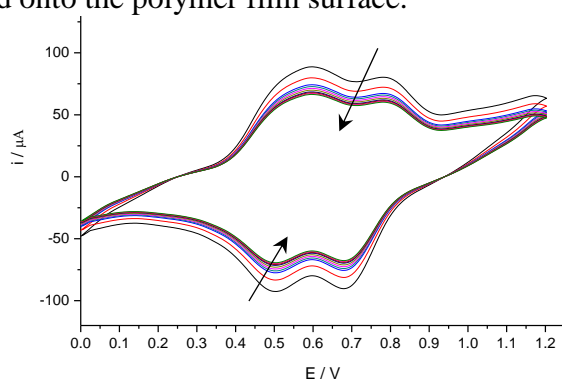


**Figure 5.27:** Cyclic voltammogram of poly(Ani-NTA) film in a monomer-free solution containing 0.1 M HClO<sub>4</sub> in acetonitrile as a function of repeated scans at 10 mV s<sup>-1</sup>.

**Figure 5.25** and **Figure 5.26** show the IR spectra and QCM measurement of the immobilisation reaction; it may be noted from these two figures there is a good agreement between these measurements. The IR spectrum shows some of leaving groups (pfp) remain in film up to 15 minutes after hydrolysis, and the QCM curve illustrates the presence of pfp molecules in the polymer that have not reacted. The immobilisation reaction was confirmed to be complete using IR measurements, as shown in **Figure 5.25** curve C. The determination of the mass of the film, depending on voltammetric responses, was performed to allow the comparison of the mass of film before and after the immobilisation. QCM data was demonstrated that the mass of polymer film after immobilisation (see **Figure 5.26**) was increased by 7.3 μg and surface coverage equal to

$1.5 \times 10^{-7}$  mol  $\text{cm}^{-2}$  and the functionalisation percentage was equal to 77%. This expected increase in the mass of the film is a result of the ingress the receptor groups (NTA) into polymer film of a larger molecular weight larger than the pfp molecule.

### 5.4.3 QCM Gravimetric and FTIR Spectroscopic Monitoring of Amide Hydrolysis

Poly(Ani-Fmoc) films were hydrolysed using 30% piperidine solutions; as with the previous work with the amide pyrrole film. FTIR was utilised to confirm the amide group had been removed from the polymer film surface, thus demonstrating the amide film had been successfully converted to an amine film. **Figure 5.28** shows that the carbonyl amide band  $\nu(\text{C}=\text{O})$  at  $1690 \text{ cm}^{-1}$  had disappeared from the IR spectrum after treatment with the base solution (indicated by symbol + in spectrum). Furthermore, the hydrolysis process resulted in the appearance of a number of bands due to the poly(Ani-NH<sub>2</sub>) film; for example, the two bands in the  $3250\text{-}3150 \text{ cm}^{-1}$  region were due to the  $\nu(\text{N-H})$  stretching band of the primary aliphatic amino group (indicated by symbol \* in spectrum).

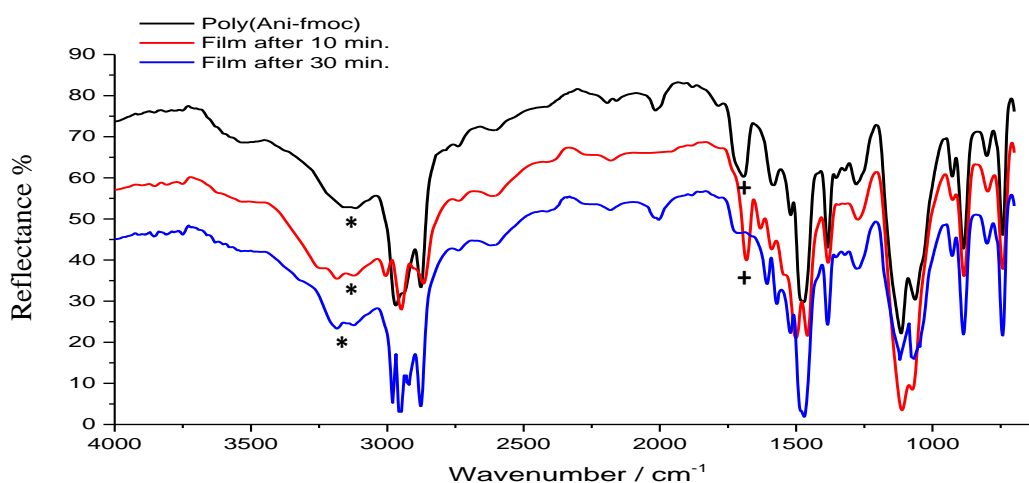


**Figure 5.28:** FTIR spectra showing the effects of hydrolysis at different times during the reaction. (a) Poly(Ani-fmoc) as deposited (black line), (b) film after 10 min. hydrolysis (red line), and (c) film after 30 min. hydrolysis (blue line). \*denotes the presence of primary amine and + for carbonyl peaks.

QCM was used to follow the removal of the Fmoc group from electroactive polymer film using a basic solution (30% piperidine/ $\text{CH}_3\text{CN}$ ). As expected, the weight of the polymer film after hydrolysis was lighter, which can be observed via the increase in frequency of the quartz crystal resonator, as shown in **Figure 5.29**.

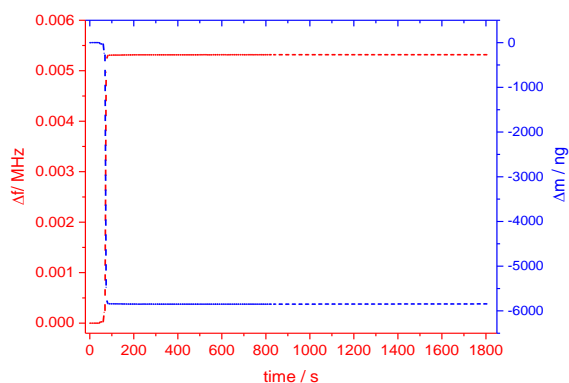


**Figure 5.29:** QCM recorded during the hydrolysis (deprotection) of poly(Ani-Fmoc) film in a 30% piperidine/ $\text{CH}_3\text{CN}$  solution.

The electroactivity of the deprotected polymer film was studied potentiodynamically. The polymer film was placed in a monomer-free  $\text{HClO}_4/\text{CH}_3\text{CN}$  solution and cyclic voltammetry performed at a  $10 \text{ mV s}^{-1}$  scan rate over 10 cycles as shown in **Figure 5.30**. The current redox peaks which emerged during this experiment were significantly different from the redox peaks observed in the monomer-free study of poly(Ani-Fmoc) under same conditions, where these redox peaks were closer to those were recorded for poly(ani- $\text{NH}_2$ ) in monomer-free solution.

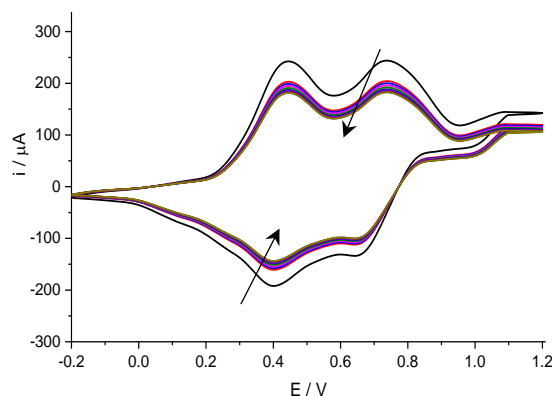


**Figure 5.30:** Cyclic voltammogram of poly(Ani-Fmoc) film after hydrolysis in  $\text{HClO}_4/\text{CH}_3\text{CN}$  with a  $0.05 \text{ M}$  TBAP solution as a function of repeated scans at  $10 \text{ mV s}^{-1}$ .

The IR spectra in **Figure 5.28** show that some Fmoc molecules remained in the polymer film after 10 minutes of the hydrolysis process. However, the QCM measurements shown in **Figure 5.29** indicate that there is no obvious change in the mass of the film after 3 minutes of hydrolysis. The presumed explanation for this is that the polymer film loses Fmoc molecules in the first few minutes, as shown in the QCM curve and then solvent molecules begin their ingress into the polymer film. The hydrolysis reaction was monitored using IR measurements as shown in **Figure 5.28** curve C to confirm that all Fmoc groups had left. The voltammetric results were used to calculate surface coverage to be  $3.02 \times 10^{-7} \text{ mol cm}^{-2}$  ( $20.5 \text{ } \mu\text{g}$ ) and the mass of film ( $m_p+m_s$ ) (data presented in

**Figure 5.19**) was equal to 22  $\mu\text{g}$  based on QCM data. While the mass of polymer film after hydrolysis was 16  $\mu\text{g}$  and surface coverage equal to  $3.1 \times 10^{-7} \text{ mol cm}^{-2}$  and mass change of hydrolysis was -6  $\mu\text{g}$  (data presented in **Figure 5.29** and **5.30**). Fmoc groups were left the film during hydrolysis and this led to create free volumes over polymer film. Theoretically, mass of Fmoc groups equal to 60% of mass of film and hydrolysis result show that the mass change was equal to 27%. This difference in film mass between poly(Ani-Fmoc) and poly(Ani-NH<sub>2</sub>) containing almost same  $\Gamma$  shows the capability for create voids and ingress a large amount of solvent molecules into polymer film.

Films	Polymer deposition		polymer hydrolysis		functionalisation	
	$\Gamma \text{ mol cm}^{-2}$	$\Delta M \mu\text{g cm}^{-2}$	$\Gamma \text{ mol cm}^{-2}$	$\Delta M \mu\text{g cm}^{-2}$	$\Gamma \text{ mol cm}^{-2}$	$\Delta M \mu\text{g cm}^{-2}$
Ani-HQC	$3.02 \times 10^{-7}$	22	$3.1 \times 10^{-7}$	-6	$3.05 \times 10^{-7}$	4.4

**Table 5.11:** Mass and surface coverage between polymer films (before and after hydrolysis) functionalisation for poly(Ani-HQC) film.

#### 5.4.4 Monitoring of vertical penetration of receptor into amide polymer film

Deprotected polymer film, poly(Ani-NH<sub>2</sub>), was immersed in activated NHS ester receptor solution in (0.1 M DMSO/acetonitrile solution, 1:9 ml) for 30 minutes. Activation of the receptor using the NHS strategy facilitated the reaction between the film surface and the 2-HQC (2-hydroxyquinoline-4-carboxylic acid) as shown in the scheme of the immobilisation reaction in **Figure 5.31**. FTIR and QCM techniques were used to monitor the reaction process. The attachment between the polymer film and the receptor led to the production of a new amide film, poly(Ani-HQC). The new film was identified using FTIR, whose spectra showed various features that confirmed amide formation had occurred. **Figure 5.32** shows the FTIR spectra obtained for the polymer film at different times during the reaction. The spectrum showed a new peak at  $1675 \text{ cm}^{-1}$ , which was attributed to the carbonyl stretch of the amide group molecules (indicated by symbol \* in figure); in addition, a broad peak at  $3275 \text{ cm}^{-1}$  was observed because of the hydroxyl groups on the receptor molecules (indicated by symbol + in figure).

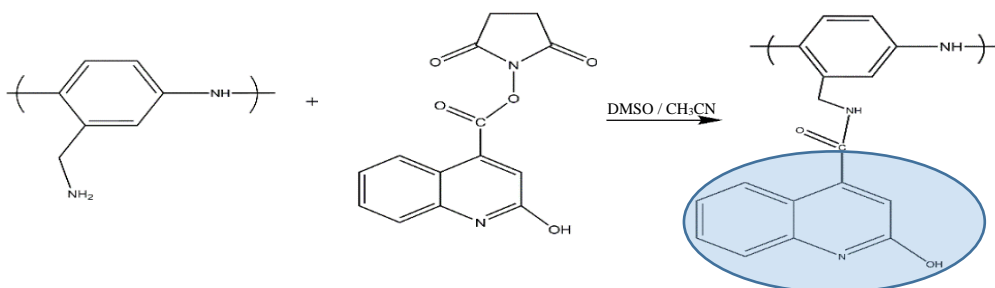


**Figure 5.31:** Reaction scheme illustrating the reaction between the 2-HQC receptor with poly(Ani-NH<sub>2</sub>) film.

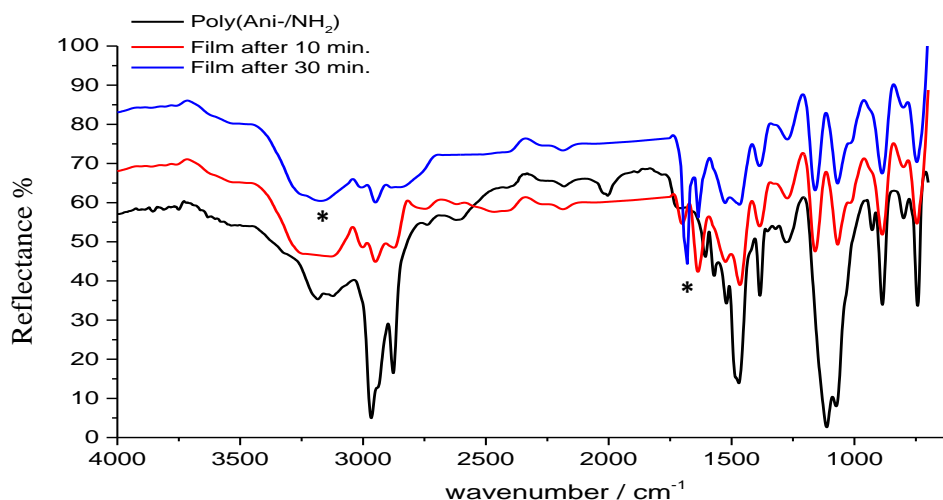


**Figure 5.32:** FTIR spectra showing the immobilisation reaction at various times during the course of the reaction. (a) Poly(Ani-NH<sub>2</sub>) (black line), (b) film after 10 min. (red line), and (c) film after 30 min. reaction time (blue line). + denotes the presence of carboxylic and \* for carbonyl peaks.

Moreover, during the reaction between the poly(Ani-NH<sub>2</sub>) and the receptor solution, QCM was used to follow the immobilisation reaction for electroactivity. The changes in the resulting frequency and mass shifts were useful in monitoring the progress of the reaction and determining the conversion ratio. This reaction led to the generation of new amide bonds across the film surface, which would logically lead to changes in the chemical structure and molecular weight of the monomer units.<sup>20</sup> Thus, it might be expected that the functionalisation reaction would lead to a cumulative increase in weight of the polymer film, detected via a decrease in frequency as a result of the linkage of the receptor molecules to the polymer film, as demonstrated in chapter four. **Figure 5.33** illustrates the changes in mass/frequency over the course of the functionalisation reaction.

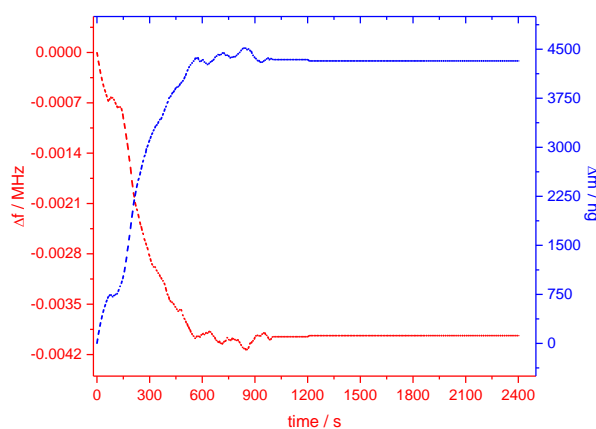


**Figure 5.33:** QCM recorded during the functionalisation reaction of poly(Ani-NH<sub>2</sub>) film with the receptor unit (2-HQC) over a 30 min. duration.

In addition, the electroactivity of the polymer film was examined after the functionalisation to form poly(Ani-HQC) in order to confirm that film had maintained its electrochemical activity. The potentiodynamic method was used to study the doping/dedoping process for poly(Ani-HQC) using a monomer-free 0.1 M HClO<sub>4</sub>/CH<sub>3</sub>CN solution at a 10 mV s<sup>-1</sup> scan rate over 10 cycles, as shown in **Figure 5.34**. The redox current peaks found in this curve differed slightly from those observed during the monomer-free study of the poly(Ani-Fmoc) and poly(Ani-NH<sub>2</sub>) films because of the influence of the receptor molecules after insertion onto the polymer film surface.

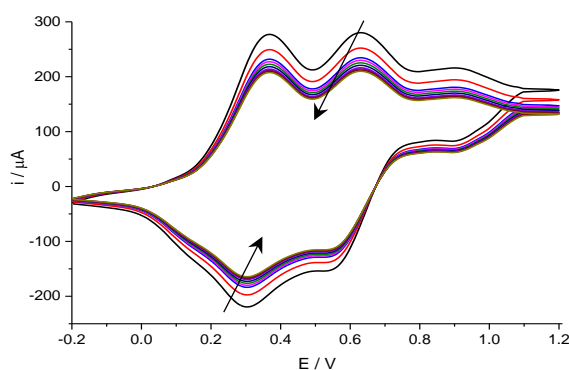


**Figure 5.34:** Cyclic voltammogram of poly(Ani-HQC) film in a monomer-free solution of 0.1 M HClO<sub>4</sub> in acetonitrile as a function of repeated scans at 10 mV s<sup>-1</sup>.

The IR spectra and QCM measurement of the functionalisation reaction are shown in **Figure 5.32** and **Figure 5.33**, respectively. From the QCM curve, it can be seen that mass of the film increased as result of ingress of HQC into polymer film. The functionalisation reaction may be accompanied by several processes such as rearrangement or adsorption, leading to unstable QCM measurements. IR spectra show that HQC remained in the polymer film 10 minutes after the functionalisation process had started. QCM data shows that mass of polymer film after the functionalisation (data presented in **Figure 5.33**) was increased by 4.4 μg based on QCM data, with a surface coverage of 3.05 × 10<sup>-7</sup> mol cm<sup>-2</sup>, derived from application of Faraday law (see equation 4.1). The functionalisation percentage was equal to 53%. This expected increase in the mass of the film as result of the ingress of receptor groups (HQC) into the polymer film.

### 5.5 Patterning of polymer films

The patterning method (photolithography) was implemented through two chemical pathways, as detailed in chapter four.<sup>59</sup> After completing the patterning process, various measurements such as 3D microscopy, FTIR and cyclic voltammetry were undertaken to study the resultant patterned electrodes. **Figures 5.35** and **5.36** show the cross-sections of

the electrodes after the patterning operation for each of the two types of polymer surface, namely the poly(Ani-pfp) and poly(Ani-Fmoc) films. The black part of **Figure 5.33** represents the poly(Ani-pfp) film, whilst the grey part represents the developer (SU-8 2000) which exposed for the UV light.

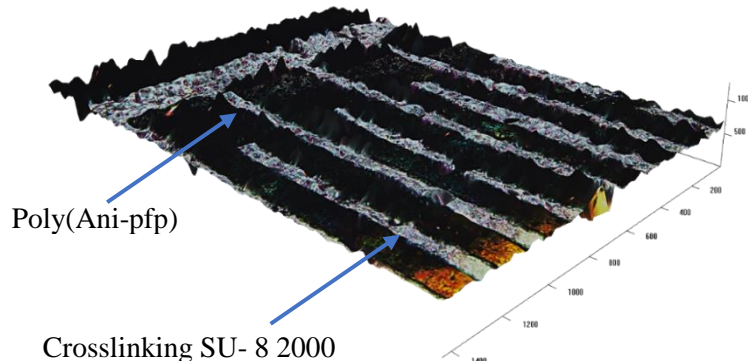


**Figure 5.35:** 3D microscopic image of the cross-section of the poly(Ani-pfp) electrode after the patterning operation.

The black part of this figure represents the poly(Ani-Fmoc) film and the yellow one represents the developer (SU-8 2000) which exposed for UV light.

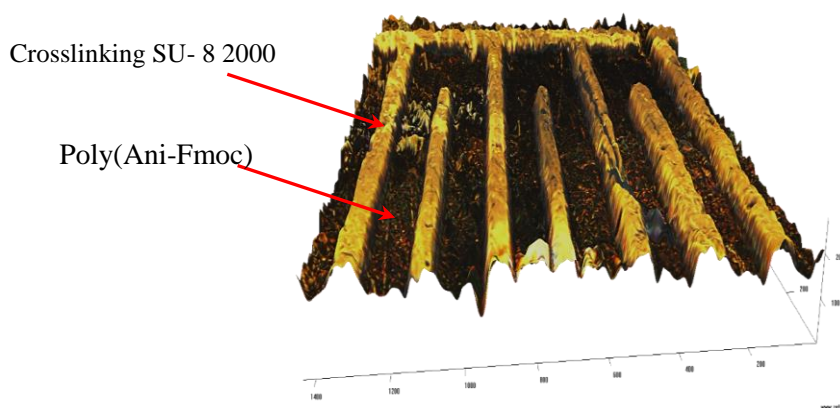


**Figure 5.36:** 3D microscopic image of the cross-section of the poly(Ani-Fmoc) electrode after the patterning operation.

Patterned polymer electrode (with/without polymer film) was investigated using the voltammetric method to verify and measure the electroactivity of the polymer films after exposure to the UV light, and then compared with polymer films which had not been exposed to UV radiation. **Figure 5.37** shows the cyclic voltammograms of poly(Ani-pfp) film before and after UV irradiation and the functionalised polymer electrode poly(Ani-NTA), respectively, in a monomer-free solution containing 0.1 M HClO<sub>4</sub>/CH<sub>3</sub>CN. The current redox peaks in the cyclic voltammogram for non-functionalised polymer films, poly(Ani-pfp), and the functionalised polymer, poly(Ani-NTA). **Figure 5.38** illustrates the cyclic voltammograms of poly(Ani-Fmoc) film before and after the patterning

process, and the patterned poly(Ani-HQC) film, respectively, in background electrolyte solutions containing 0.1 M  $\text{HClO}_4/\text{CH}_3\text{CN}$ . **Figure 5.38** shows the cyclic voltammograms of patterned poly(Ani-HQC) film with redox current peaks that were unlike those found in poly(Ani-Fmoc) because of the changes in chemical structure before and after functionalisation.

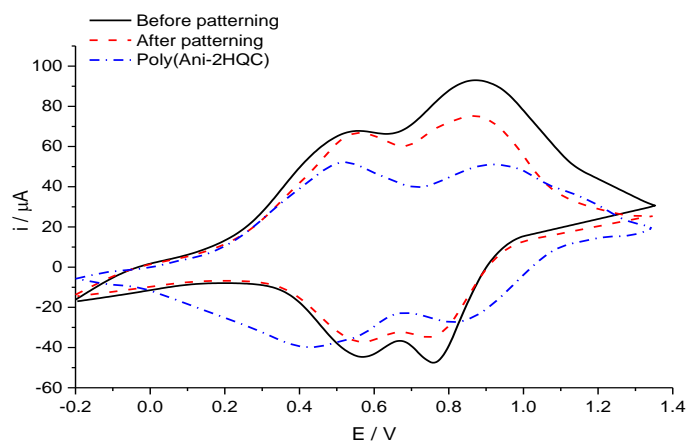


**Figure 5.37:** Voltammetric response of poly(Ani-Fmoc) electrodes, the solid and dashed lines (before and after patterning respectively), and the chained line, the poly(Ani-HQC) electrode, in monomer-free  $\text{HClO}_4/\text{acetonitrile}$  solution at a scan rate of  $10 \text{ mV s}^{-1}$  over a potential window ranging from 0.00 to 1.35 V vs. Ag/AgCl.

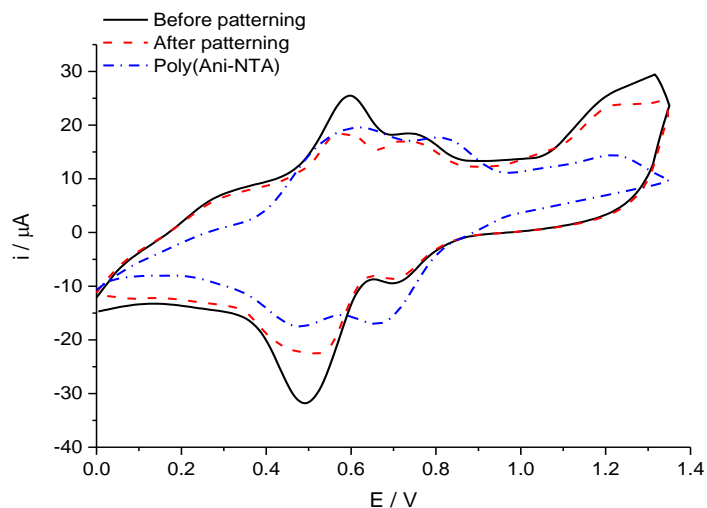


**Figure 5.38:** Voltammetric response of poly(Ani-pfp) electrodes, the solid and dashed lines (before and after patterning, respectively) and the chained line, the poly(Ani-NTA) electrode, in monomer-free  $\text{HClO}_4/\text{acetonitrile}$  solution at a scan rate of  $10 \text{ mV s}^{-1}$  over a potential window ranging from 0.00 to 1.35 V vs. Ag/AgCl.

FTIR was applied technique to emphasise the fact that exposure to UV light during the patterning process had not affected the chemical structure of the polymer film, and that the pfp ester group had remained unchanged and chemically active for later chemical reactions. Furthermore, this tool was used to demonstrate that amide formation on the polymer film surface had been successful. **Figure 5.39** shows the FTIR spectrum of poly(Ani-pfp) film and poly(Ani-NTA) after patterning. This spectrum showed a number of features related to the ester film such as a sharp band at  $1780\text{ cm}^{-1}$  which can be attributed to the carbonyl ester stretch, and the band at  $990\text{ cm}^{-1}$  which was due to  $\nu(\text{C}-\text{F})$ . From this spectrum, it can be deduced that the ester bonds in the polymer film were not affected during UV irradiation. In addition, **Figure 5.39** shows from the FTIR spectrum of poly(Ani-NTA) that there is a conversion from ester to amide bonds as result of the insertion of the receptor onto the polymer film via the immobilisation process. The appearance of the broad band at  $3300\text{ cm}^{-1}$  indicates the existence of hydrogen bonding due to the carboxylic groups in the polymer film(indicated by symbol \* in figure), and the disappearance of the bands at  $1785\text{ cm}^{-1}$  and  $990\text{ cm}^{-1}$  is due to removal of the pfp group during the substitution reaction. Emergence of the band at  $1725\text{ cm}^{-1}$  is due to the  $\nu(\text{C}=\text{O})$  stretch of carboxylic groups in the receptor compound (indicated by symbol + in figure).

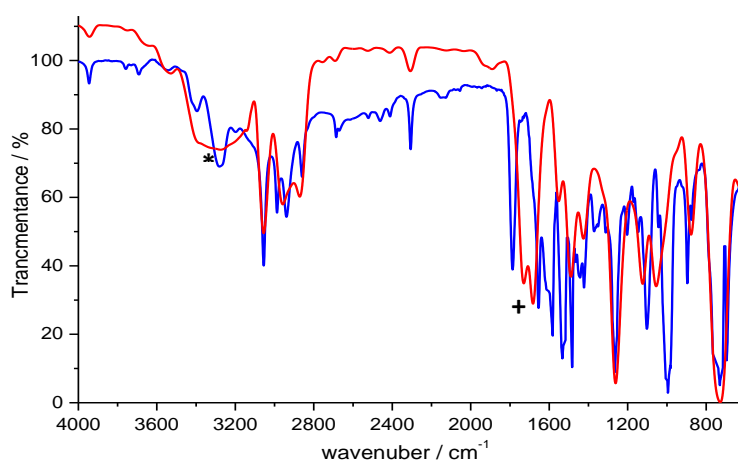


**Figure 5.39:** FTIR spectra of poly(Ani-pfp) film after patterning (blue line) and poly(Ani-NTA) film (red line). \*denotes the presence of carboxylic and + denotes for carbonyl of amide peaks.

The FTIR spectra of poly(Ani-NH<sub>2</sub>) film and poly(Ani-HQC) after patterning are shown in **Figure 5.40**. The amino film showed two distinctive bands in the FTIR spectrum at  $3270\text{ cm}^{-1}$  due to the primary NH<sub>2</sub>, whilst the band at  $1610\text{ cm}^{-1}$  was attributed to the  $\nu(\text{N}-$

H) bending vibration. It can be concluded that the primary amino group was not affected by the patterning process. **Figure 5.40** shows the spectrum of poly(Ani-HQC) after both hydrolysis and the immobilisation reaction with the receptor solution. The emergence of the broad band at  $3300\text{ cm}^{-1}$  was due to an O-H group on the receptor molecules (indicated by symbol \* in figure), whilst the appearance of the band at  $1675\text{ cm}^{-1}$  was attributed to the formation of amide bonds in the polymer film (indicated by symbol + in figure).

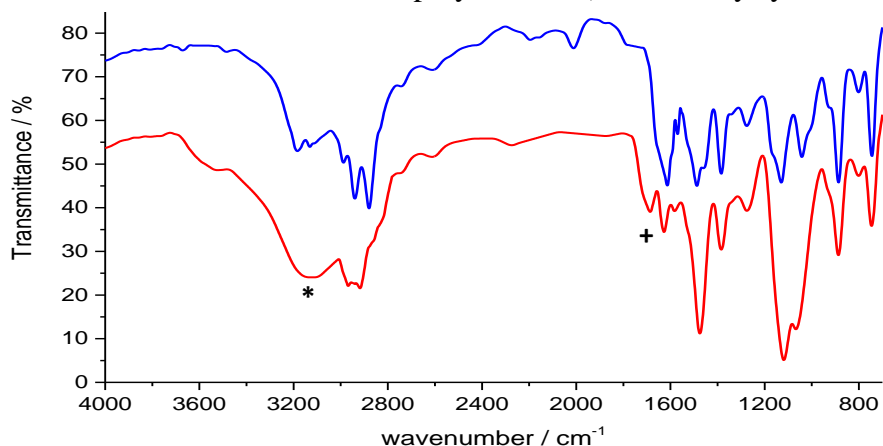


**Figure 5.40:** FTIR spectra of poly(Ani-NH<sub>2</sub>) film after patterning (blue line) and poly(Ani-HQC) film (red line). \* denotes the presence O-H group and + denotes carbonyl of amide peaks.

## 5.6 Surface imaging characterisation of polymer films

### 5.6.1 Scanning Electron Microscopy (SEM)

The morphology of the polymer surfaces plays an important role in the immobilisation of molecules and the activity of the polymer electrode. In this section, scanning electron microscopy (SEM) was applied to study the morphology of the aniline film derivatives. An SEM micrograph of the polymer films (**Figure 5.41** panels A and B) shows a smooth and uniform morphology, whereas a quite tortuous surface was observed for the polymer film due to the nature of the polymer, as shown in panels C and D. These films show different morphologies due to the use of different monomer compositions. The similarity between the film surfaces was due to use the same counterions (perchlorate ions, ClO<sub>4</sub><sup>-</sup>), which have the same effect on film morphology.

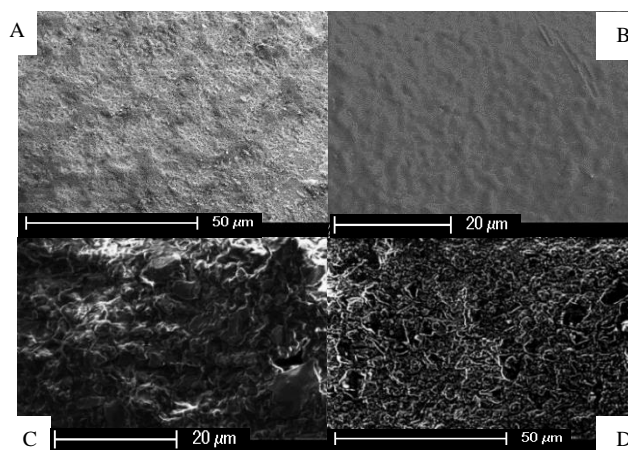


**Figure 4.41:** SEM images of surface films deposited using a solution containing 10 mM concentration of (A) Ani-NH<sub>2</sub>, (B) Ani-COOH, (C) Ani-Fmoc, and (D) Ani-pfp at scan rates of 10 mV s<sup>-1</sup> over 10 scans.

### 5.6.2 Atomic Force Microscopy (AFM)

AFM was applied to image the polymer film surface and estimate the thickness of the films derived from the different aniline monomers. In general, the use of different monomers that possess different chemical structures leads to differences in the associated surface topographies.<sup>60</sup> On the other hand, it may be noted that the film surface produced from poly(An-pfp) was rougher than the above-mentioned films, with a number of tortuous regions found across the entire polymer surface. The poly(Ani-Fmoc) polymer showed a surface topography that was considerably rougher than all the above polymer surfaces. The differences between the film surfaces here was probably related to differences in the associated growth and nucleation features, and to differences in the amount of electronic charge involved in the electrodeposition process. A scalpel blade was used to remove polymer films from part of electrode surface to form edge between polymer film and electrode surface, forming a step edge between the film and substrate, (panel E). Analysis of **Figure 5.42** showed that the surface thickness was equal to 250, 620, 450 and 650 nm for Ani-COOH, Ani -NH<sub>2</sub>, Ani -pfp and Ani- Fmoc respectively. While, based on QCM data thickness of films was equal to 290, 620, 480 and 840 nm for Ani-COOH, Ani -NH<sub>2</sub>, Ani -pfp and Ani- Fmoc respectively. AFM findings were compared with the thickness of films estimated from voltammetric and QCM data. The thickness measurements in these methods show some differences. These differences could be due to rough surface coverage or presence of some solvent molecules, which would effect on determination of thickness. The effect of non-uniform surface on

measurements was clear on especially with Ani-Fmoc films where the calculated thickness using AFM was less than estimated by voltammetric method.

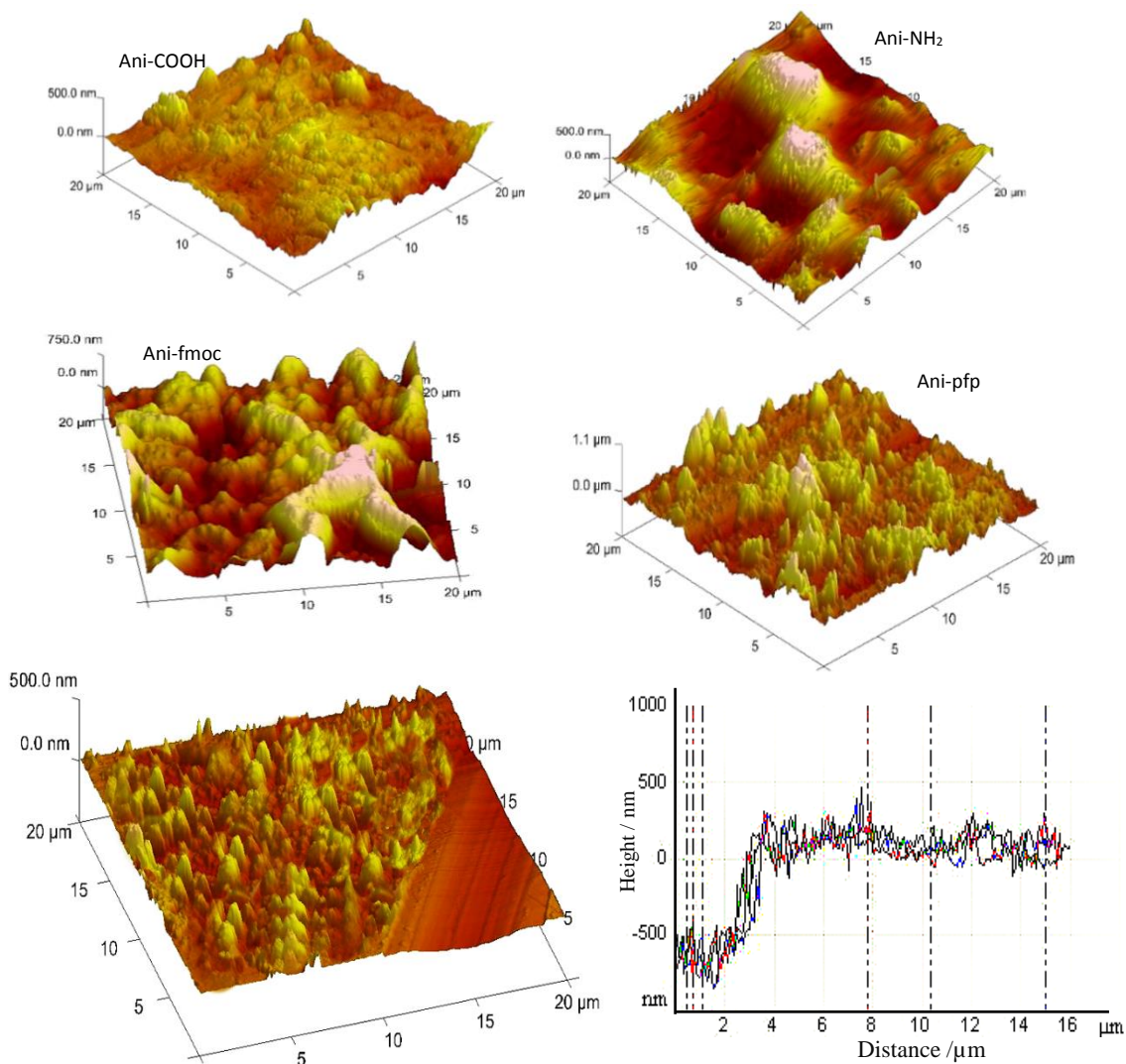


**Figure 5.42:** AFM images of dry polymers electrodeposited from 10 mM a) Ani-NH<sub>2</sub>, b) Ani-COOH, c) Ani-Fmoc, d) Ani-pfp and e) thickness of polymer film on an Au electrode using a 10 mV s<sup>-1</sup> scan rate over 10 scans.

### 5.7 Conclusion

The goal of this project was to understand the electrochemical behaviour of functionalised polyanilines with different functional groups. These polymer films were used as the bases on which to form spatially heterogeneous film surfaces with diverse chemical functionalities using a patterning process, with the intent of later using them as chemical sensors. A series of electrochemical and spectroscopic measurements have been applied to provide further information about the nature of the electrodeposition and

immobilisation processes of patterned polymer films for use in the enhancement of sensing applications.

As it is known that conditions of electropolymerisation can affect the growth and electroactivity of the polymer films. In this chapter it has been shown that composition of monomer and functional groups play a role during electropolymerisation process. The voltammetric findings which recorded at various scan rates (10 - 100 mV s<sup>-1</sup>) showed that polyaniline film has a good stability. The results from chronoamperometric curves show that the electropolymerisation process was that charge increased with  $t^{1/2}$  as result of having a diffusion-controlled process.

QCM and FTIR techniques were applied to verify the immobilisation process through changes to the polymer film during hydrolysis and the appropriate functionalisation reaction to obtain a clear picture regarding the interaction paths and substitution processes within polymer surfaces. Data from EQCM experiments were used to estimate the mass exchange during electropolymerisation process from the slope using on Faraday's law. The gradient ( $\Delta m/\Delta q$ ) was used to calculate the  $M_{app}$  of species involved in electropolymerisation process. Results show that monomer and solvent seem to play role during polymerisation processes. Patterned poly(Ani-pfp) films were reacted with the NTA, and poly(Ani-Fmoc) films and with HQC. This preliminary work focused on the fundamental aspects of fabricating and characterising patterned polymer films to determine if they could maintain their joint polymer-receptor system without it collapsing due to sequential fabrication processes. This strategy of reactivity control could be useful for the patterning of different receptors on micro-fabricated polymer films.

poly(Ani-pfp) and poly(Ani-Fmoc) films were hydrolysed using 0.1 M NaOH and 30% piperidine solutions, respectively. FTIR and QCM measurements were confirmed success of the hydrolysis process. Mass and surface coverage of polymer films before and after hydrolysis were calculated using Faraday's law. Solvation change resultant from entry of solvent molecules to polymer films was calculated. The difference in mass between the protected and deprotected polymer films was due to the egress of leaving groups from the films. In fact, the findings show that this difference can be explained by ingress of 43% and 30% solvent molecules into ester and amide films respectively, to fill the voids on the polymer surface for ester and amide films.

The immobilisation process was monitored using IR spectroscopy to confirm the completion of the functionalisation reaction between the receptors NTA and QCH with the poly(Ani-COOH) and poly(Ani-NH<sub>2</sub>), respectively. Furthermore, the masses of the polymer films were calculated depending on the voltammetric responses of the film before and after the immobilisation process. This expected increase in the mass of the film was a result of the ingress of receptor groups (NTA and HQC) into the polymer films. The electrochemical voltammetric measurements for all patterned polymer surfaces confirmed that electrochemical activity (conductivity) would enable their eventual use in sensing applications. Findings above showed that the hydrolysis, immobilisation and patterning of polymer films have no effect on electroactivity of films and these processes did not led to collapse of polymer films. This chapter has shown that post polymerisation can be used to insert suitable receptors into polymer films. Calculations providing a greater understanding of the reactivity of functional polymers and redox switching behaviour of these systems. It can be deduced from this work that spatial variations of polymer film, reactants and solvent are likely to have considerable influence on properties of films.

The AFM data illustrated that polymer films have rough surfaces and partial collapse were occurred for some polymers due to egress of solvent molecules. These films were less thicker than solvated polymers which were estimated from QCM data. AFM data showed that Ani-Fmoc have thickness more than thus which estimated by QCM and this could be attributed to non-uniform coverage of films over the deposition area and instrumental bias. **Table 5.12** show the comparison between the thickness of polymer films measured by AFM, cyclic voltammetry and QCM and the differences in thickness of films due to variation of solvent ratio in polymer films.

Films	Voltammetric experiments (dry film)		Molar volume cm <sup>3</sup> mol <sup>-1</sup>	QCM experiments (solvated films)		AFM <i>h<sub>f</sub></i> /cm	Molar volume cm <sup>3</sup> mol <sup>-1</sup>
	<i>I</i> / mol cm <sup>-2</sup>	<i>h<sub>f</sub></i> / cm		$\Delta m/g$	<i>h<sub>f</sub></i> / cm		
Ani-COOH	8.8 x 10 <sup>-8</sup>	1.28 x10 <sup>-5</sup>	146	8x10 <sup>-6</sup>	2.9x10 <sup>-5</sup>	2.5x10 <sup>-5</sup>	284
Ani-NH <sub>2</sub>	6 x 10 <sup>-7</sup>	6 x10 <sup>-5</sup>	100	1.2x10 <sup>-5</sup>	6.2x10 <sup>-5</sup>	6.2x10 <sup>-5</sup>	103
Ani-ppp	1.8 x 10 <sup>-7</sup>	4.3 x10 <sup>-5</sup>	238	1.3.5x10 <sup>-5</sup>	4.8x10 <sup>-5</sup>	4.5x10 <sup>-5</sup>	250
Ani-fmoc	3.02 x 10 <sup>-7</sup>	7.55 x10 <sup>-5</sup>	250	2.3x10 <sup>-5</sup>	8.4x10 <sup>-5</sup>	6.5 x10 <sup>-5</sup>	216

**Table 5.12:** Thickness of polymer films measured by AFM and comparison with those calculated from cyclic voltammetry data based on Faraday law and QCM data (solvated films).

## 5.8 References

1. K. M. Molapo, P. M. Ndangili, R. F. Ajayi, G. Mbambisa, S. M. Mailu, N. Njomo, M. Masikini, P. Baker and E. I. Iwuoha, *International Journal of Electrochemical Science*, 2012, **7**, 11859-11875.
2. M. Jaymand, *Progress in Polymer Science*, 2013, **38**, 1287-1306.
3. A. R. Hillman and M. A. Mohamoud, *Electrochimica Acta*, 2006, **51**, 6018-6024.
4. A. Glidle, P. E. Pearson, E. L. Smith, J. M. Cooper, R. Cubitt, R. M. Dalglish, A. R. Hillman and K. S. Ryder, *The Journal of Physical Chemistry B*, 2007, **111**, 4043-4053.
5. S. K. Verma, P. Kar, D. J. Yang and A. Choudhury, *Sensors and Actuators B: Chemical*, 2015, **219**, 199-208.
6. T. Kubo, C. A. Figg, J. L. Swartz, W. L. Brooks and B. S. Sumerlin, *Macromolecules*, 2016, **49**, 2077-2084.
7. R. Ogaki, M. Alexander and P. Kingshott, *Materials Today*, 2010, **13**, 22-35.
8. Z. Nie and E. Kumacheva, *Nature Materials*, 2008, **7**, 277-290.
9. R. K. Pal, A. A. Farghaly, M. M. Collinson, S. C. Kundu and V. K. Yadavalli, *Advanced Materials*, 2016, **28**, 1406-1412.
10. T. Kubo, C. A. Figg, J. L. Swartz, W. L. A. Brooks and B. S. Sumerlin, *Macromolecules*, 2016, **49**, 2077-2084.
11. Y. D. Kim and J. Hone, *Nature*, 2017, **544**, 167-168.
12. S. Khan and G. Newaz, *Journal of Biomedical Materials Research Part A*, 2010, **93**, 1209-1224.
13. J. U. Lind, C. Acikgöz, A. E. Daugaard, T. L. Andresen, S. Hvilsted, M. Textor and N. B. Larsen, *Langmuir*, 2012, **28**, 6502-6511.
14. A. Baba, S. Tian, F. Stefani, C. Xia, Z. Wang, R. C. Advincula, D. Johannsmann and W. Knoll, *Journal of Electroanalytical Chemistry and Interfacial Electrochemistry*, 2004, **562**, 95-103.
15. L. Bauermann and P. Bartlett, *Electrochimica Acta*, 2005, **50**, 1537-1546.
16. J. Yáñez-Heras, G. A. Planes, F. Williams, C. A. Barbero and F. Battaglini, *Electroanalysis*, 2010, **22**, 2801-2808.
17. Y. Wei, F. Fang, W. Yang, H. Guo, X. Niu and L. Sun, *Journal of the Brazilian Chemical Society*, 2015, **26**, 2003-2013.
18. S.-Y. Cui and S.-M. Park, *Synthetic Metals*, 1999, **105**, 91-98.
19. L. Duić and Z. Mandić, *Journal of Electroanalytical Chemistry and Interfacial Electrochemistry*, 1992, **335**, 207-221.
20. S.-J. Choi and S.-M. Park, *Journal of the Electrochemical Society*, 2002, **149**, E26-E34.
21. N. L. Guernion and W. Hayes, *Current Organic Chemistry*, 2004, **8**, 637-651.
22. A. Karyakin, A. Strakhova and A. Yatsimirsky, *Journal of Electroanalytical Chemistry and Interfacial Electrochemistry*, 1994, **371**, 259-265.
23. C. Thiemann and C. M. Brett, *Synthetic Metals*, 2001, **123**, 1-9.
24. K. Naoi, M. Lien and W. H. Smyrl, *Journal of The Electrochemical Society*, 1991, **138**, 440-445.
25. B. Keita, A. Mahmoud and L. Nadjo, *Journal of Electroanalytical Chemistry and Interfacial Electrochemistry*, 1995, **386**, 245-251.
26. A. Singh and M. Mukherjee, *Macromolecules*, 2003, **36**, 8728-8731.
27. S. Chuekachang, R. Janmanee, A. Baba, S. Phanichphant, S. Sriwichai, K. Shinbo, K. Kato, F. Kaneko, N. Fukuda and H. Ushijima, *Surface and Interface Analysis*, 2013, **45**, 1661-1666.
28. A. Abd-Elwahed and R. Holze, *Synthetic Metals*, 2002, **131**, 61-70.
29. Q. Hao, W. Lei, X. Xia, Z. Yan, X. Yang, L. Lu and X. Wang, *Electrochimica Acta*, 2010, **55**, 632-640.
30. A.-u.-H. A. Shah and R. Holze, *Journal of Solid State Electrochemistry*, 2007, **11**, 38-51.

31. E. De Giglio, M. Guascito, L. Sabbatini and G. Zambonin, *Biomaterials*, 2001, **22**, 2609-2616.
32. J. r. Heinze, B. A. Frontana-Uribe and S. Ludwigs, *Chemical Reviews*, 2010, **110**, 4724-4771.
33. H. Randriamahazaka, V. Noël and C. Chevrot, *Journal of Electroanalytical Chemistry and Interfacial Electrochemistry*, 1999, **472**, 103-111.
34. E. Song and J.-W. Choi, *Nanomaterials*, 2013, **3**, 498-523.
35. P. Nunziante and G. Pistoia, *Electrochimica Acta*, 1989, **34**, 223-228.
36. A. R. Hillman, K. S. Ryder, C. J. Zaleski, V. Ferreira, C. A. Beasley and E. Vieil, *Electrochimica Acta*, 2014, **135**, 42-51.
37. A. R. Hillman, K. S. Ryder, C. J. Zaleski, C. Fullarton and E. L. Smith, *Zeitschrift Für Physikalische Chemie*, 2012, **226**, 1049-1068.
38. A. A. Arrieta Almarino and R. L. Tarazona Caceres, *Journal of the Chilean Chemical Society*, 2009, **54**, 14-19.
39. D. C. Kim and D. J. Kang, *Sensors*, 2008, **8**, 6605-6641.
40. A. Glidle, A. R. Hillman, K. S. Ryder, E. L. Smith, J. M. Cooper, R. Dalgliesh, R. Cubitt and T. Geue, *Electrochimica Acta*, 2009, **55**, 439-450.
41. J. Widera, M. Skompska and K. Jackowska, *Electrochimica Acta*, 2001, **46**, 4125-4131.
42. F. Demanze, A. Yassar and F. Garnier, *Synthetic Metals*, 1996, **76**, 269-272.
43. H. Sarker, Y. Gofer, J. Killian, T. Poehler and P. Searson, *Synthetic Metals*, 1998, **97**, 1-6.
44. R. M. Sapstead, K. S. Ryder, C. Fullarton, M. Skoda, R. M. Dalgliesh, E. B. Watkins, C. Beebee, R. Barker, A. Glidle and A. R. Hillman, *Faraday Discussions*, 2013, **164**, 391-410.
45. W. Plieth, A. Bund, U. Rammelt, S. Neudeck and L. Duc, *Electrochimica Acta*, 2006, **51**, 2366-2372.
46. H. Varela and R. M. Torresi, *Journal of the Electrochemical Society*, 2000, **147**, 665-670.
47. E. Smela, W. Lu and B. R. Mattes, *Synthetic Metals*, 2005, **151**, 25-42.
48. S. Weng, Z. Lin, L. Chen and J. Zhou, *Electrochimica Acta*, 2010, **55**, 2727-2733.
49. J. Gu, S. Kan, Q. Shen and J. Kan, *International Journal of Electrochemical Science*, 2014, **9**, 6858-6869.
50. E. Ploetz, B. Visser, W. Slingenbergh, K. Evers, D. Martinez, Y. Pei, B. Feringa, J. T. M. De Hosson, T. Cordes and W. van Dorp, *Journal of Materials Chemistry B*, 2014, **2**, 2606-2615.
51. C. J. Pickett and K. S. Ryder, *Journal of the Chemical Society, Dalton Transactions*, 1994, 2181-2189.
52. C. J. Galvin and J. Genzer, *Progress in Polymer Science*, 2012, **37**, 871-906.
53. L. Li, H. Song, Q. Zhang, J. Yao and X. Chen, *Journal of Power Sources*, 2009, **187**, 268-274.
54. A. Y. Arasi, J. J. L. Jeyakumari, B. Sundaresan, V. Dhanalakshmi and R. Anbarasan, *Spectrochimica Acta Part A: Molecular and Biomolecular Spectroscopy*, 2009, **74**, 1229-1234.
55. F. Xu, G. Zheng, D. Wu, Y. Liang, Z. Li and R. Fu, *Physical Chemistry Chemical Physics*, 2010, **12**, 3270-3275.
56. A. K. Sharma, G. Chaudhary, I. Kaushal, U. Bhardwaj and A. Mishra, *American Journal of Polymer Science*, 2015, **5**, 1-6.
57. J. Heinze, B. A. Frontana and S. Ludwigs, *Chemical Reviews*, 2010, **110**, 4724-4771.
58. A. R. Hillman, K. S. Ryder, H. K. Ismail, A. Unal and A. Voorhaar, *Faraday Discussions*, 2017, **199**, 75-99.
59. Z. Nie and E. Kumacheva, *Nature Materials*, 2008, **7**, 277-290.
60. M. Giz, S. de Albuquerque Maranhao and R. Torresi, *Electrochemistry Communications*, 2000, **2**, 377-381.

**Chapter Six                      Preparation and patterning of derivatives of polythiophene**

**6.1 Overview ..... 155**

**6.2 Aims and Objectives ..... 155**

**6.3 Results and discussion ..... 156**

    6.3.1 Electropolymerisation of 3-thiophene acetic acid ..... 156

    6.3.2 Characterisation of poly(3-thiophene acetic acid) ..... 158

    6.3.3 Poly(3-thiopheneethylamine) film ..... 160

    6.3.4 Electropolymerisation of pentafluorophenyl(thiophen-3-yl)ethanoate ..... 161

    6.3.5 Characterisation of poly(pentafluorophenyl(thiophen-3-yl) ethanoate) film ..... 163

    6.3.6 Electropolymerisation of 9H-fluoren-9-yl(2-(3-thienyl)ethyl) carbamate ..... 166

    6.3.7 Characterisation of poly(9H-fluoren-9-yl(2-(3-thienyl)ethyl) carbamate) film ..... 167

**6.4 Post-polymerisation Chemical Modifications ..... 171**

    6.4.1 QCM Gravimetric and FTIR Spectroscopic Monitoring of Ester Hydrolysis ..... 171

    6.4.2 Monitoring of vertical penetration of receptor into ester polymer film ..... 174

    6.4.3 QCM Gravimetric and FTIR Spectroscopic Monitoring of Amide Hydrolysis ..... 176

    6.4.4 Monitoring of vertical penetration of receptor into amide polymer film ..... 179

**6.5 Patterning of polymer films ..... 181**

**6.6 Surface imaging characterisation of polymer films ..... 183**

**6.7 Conclusions ..... 185**

**6.8 References ..... 188**

## 6.1 Overview

Both functionalised polypyrrole and polyaniline were discussed in previous chapters. In this chapter, polythiophene, which is considered the third main kind of conducting polymer due to both its attractive physical qualities and potential wide range of applications, will be studied.<sup>1-3</sup> Functionalised polythiophene with various substituents that can provide interesting modifications to the physical properties of polythiophene for use as new materials in diverse applications, such as magnetic or optical sensitivity and molecular recognition.<sup>1</sup> Furthermore, these functional units provide the ability to manipulate and modify the chemical and physical properties of conducting polymers to suit the purpose of any particular application.<sup>2</sup> In addition, substituted thiophenes offer a broad area for investigation by researchers in terms of the change in ring composition and the effects of this change on various properties such as polymerisation, conductivity and stability. Among the different possible strategies for functionalisation of conducting polymers, the usual procedure used for the formation of functionalised polythiophene is electropolymerisation.<sup>3</sup> However, there is another method to insert the functional group onto the polymer films, which is the post-polymerisation method.<sup>4,5</sup> Moreover, researchers have become increasingly interested in developing technologies that allow them to control and manipulate such reactions to acquire smart, multi-functional surfaces.<sup>6</sup> Patterning methods allow for new material surfaces containing receptors, catalysts, and proteins, for instance, that can react with different analytes with high sensitivity and selectivity.<sup>7</sup>

## 6.2 Aims and Objectives

The general aims of this chapter are: (i) the fabrication of a patterned functionalised electrode from polythiophene derivatives, here Thio-pfp and Thio-Fmoc; and (ii) the preparation of spatially heterogeneous (patterned) film surfaces containing two receptor units. In this chapter, the aim was the immobilisation of polythiophene film surfaces via the use of functionalisation procedures in order to insert receptor agents; this method will hopefully lead to improved efficiency in the recognition of analytes. Electrochemical and synthetic pathways were applied to create the polymer films. These paths involve the electrodeposition of the monomer derivatives, some of them containing a particular large leaving group such as Fmoc, or pfp. After fabrication of the functionalised polymer electrodes, the amide and ester bonds were substituted to create functionalised polymer

surfaces containing recognition units suitable for subsequent application in sensors (see schemes 4.1 and 4.2 in chapter 4).

### 6.3 Results and discussion

Polythiophene derivative films were deposited using electrochemical techniques, including potentiodynamic and potentiostatic methods, onto a platinum electrode. In general, the electrolyte solution contained a suitable concentration of the monomers with 0.5 M TBAP /CH<sub>3</sub>CN solution, as in the following sections. Diverse potential ranges (vs. Ag/AgCl) were applied, depending on the type of monomer, over 10 scans, with each set of scans being performed at two different scan rates.

Monomer name	Potential window / V	Supporting electrolyte	Concentration. / mM	Scan rates mV s <sup>-1</sup>
3-thiophene acetic acid	0.0 – 2.0	TBAP	0.5	10 and 20
Thio-pfp	0.2 - 1.9	TBAP	0.5	10 and 30
Thio-Fmoc	0.3 – 2.0	TBAP	0.5	30 and 50

**Table 6.1:** Potential window and supporting electrolyte for electropolymerisation of the three types of monomer considered in this chapter.

#### 6.3.1 Electropolymerisation of 3-thiophene acetic acid

The poly(3-thiophene acetic acid) (3-TAA) films were grown potentiodynamically with a potential ranging between 0.0 V and 2.0 V over 10 scans from a 0.5 M solution of 3-TAA in CH<sub>3</sub>CN containing TBAP onto a Pt substrate at different scan rates of 10 and 20 mV s<sup>-1</sup>.<sup>8</sup> **Figure 6.1** shows the cyclic voltammograms of 0.5 M (3-TAA) recorded for each of the two scan rates. The current starts to increase at 1.5 V due to oxidation of the 3-TAA monomer.<sup>9</sup> The doping/dedoping redox processes of poly(3-TAA) resulted in the emergence of current peaks at 1.25 V and 0.60 V in the cyclic voltammogram.<sup>10</sup> The surface coverage and thickness of poly(3-TAA) film were calculated; the surface coverage was 4.62 x 10<sup>-6</sup> mol cm<sup>-2</sup> and 3.25 x 10<sup>-6</sup> mol cm<sup>-2</sup> for the 10 and 20 mV s<sup>-1</sup> scan rates, respectively.

The electronic density and steric effects of substituent groups in the β-position have an influence on electropolymerisation process, where results indicate that there is a difference in redox potential between poly(3-TAA) and thiophene, as mentioned in the literature review.<sup>11</sup> This difference is due to the presence of an electron withdrawing

group (carboxyl groups) in the  $\beta$ -position of thiophene, which has an electronic effect on the thiophene cyclic system.<sup>12, 13</sup>

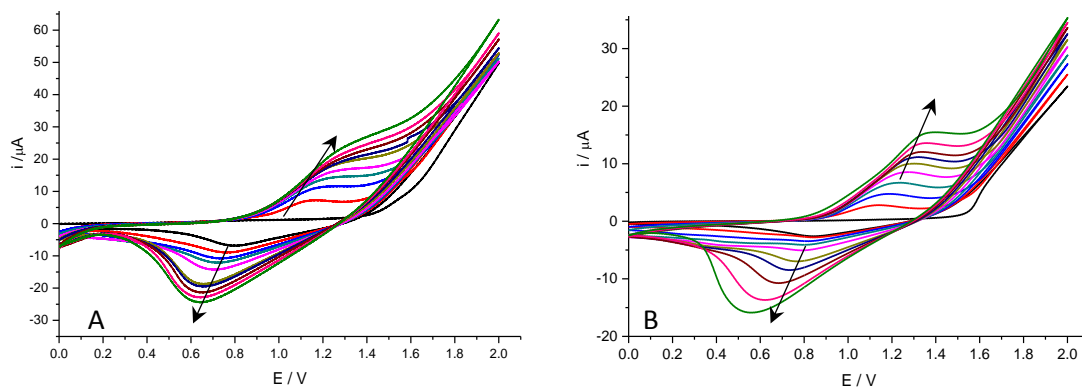


**Figure 6.1:** Cyclic voltammograms resulting from electropolymerisation of 0.5 M 3-TAA on a Pt electrode in 0.1 TBAP/CH<sub>3</sub>CN solution at (A) 10 mV s<sup>-1</sup> and (B) 20 mV s<sup>-1</sup> for 10 scans. Electrode area of 0.00785 cm<sup>2</sup>.

Electrodeposition of poly(3-TAA) films on a Pt electrode at a constant potential of 2.0 V was carried out. These polymers were deposited from a 0.5 M 3-TAA solution over different times ranging from 50 to 200 seconds as shown in **Figure 6.2**.<sup>14</sup> The chronoamperometric response of 3-TAA shows that current increases sharply with applied potential and then decays gradually due to polymer deposition during a nucleation and growth mechanism.<sup>15</sup> Chronoamperometric curves show that the electropolymerisation process was diffusion-controlled as shown in Panel B. As expected, increasing the polymerisation time leads to an increase in the amount of polymer film on electrode surface. The thickness,  $h_f^*$  ( $\mu\text{m}$ ), of the dry polymer film was estimated as reported in **Table 6.2**.

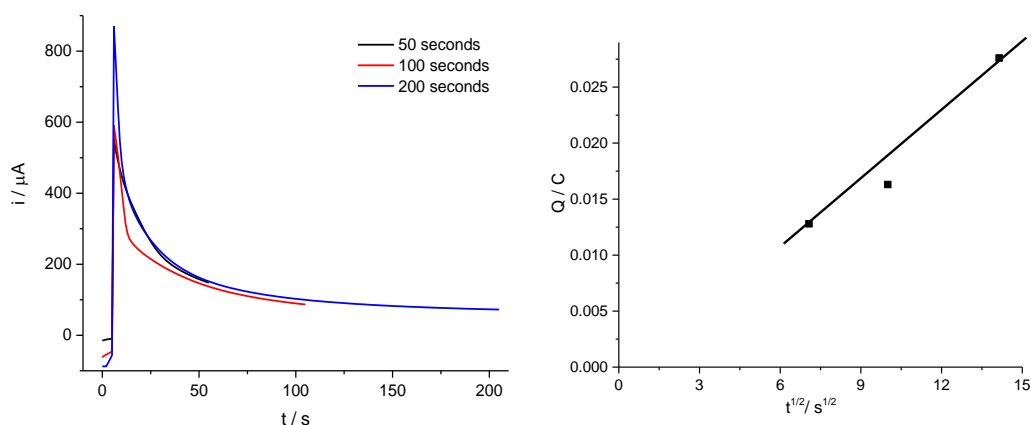


**Figure 6.2:** A) Current-time transients for electrodeposition of 0.5 M 3-TAA in TBAP/CH<sub>3</sub>CN solution at 2 V vs. an Ag/AgCl reference over 50, 100 and 200 seconds onto a Pt electrode (0.23 cm<sup>2</sup>). B) Plot of charge vs. square root of time (data from panel A).

Monomer conc. (M)	Time / s	Charge $Q$ / C	Thickness / $\mu\text{m}$
0.5	50	0.0128	0.27
0.5	100	0.0163	0.35
0.5	200	0.0276	0.59

**Table 6.2:** Electrical charge and thickness of electropolymerisation of 0.5 M 3-TAA at different deposition times of 50, 100 and 200 seconds. Pt electrode area was 0.23 cm<sup>2</sup> and molecular weight of 3-TAA is 142.18 g mol<sup>-1</sup> and its density is ca. 1.336 g cm<sup>-3</sup>.

### 6.3.2 Characterisation of poly(3-thiophene acetic acid)

The electrochemical behaviour of poly(3-TAA) films was studied in monomer-free 0.1 M TBAP/CH<sub>3</sub>CN solution. **Figure 6.3** illustrates the voltammetric response of (poly-3TAA) prepared at 10 mV s<sup>-1</sup> over a potential ranging from 0.0 V to 1.8 V at scan rates of 5 -100 mV s<sup>-1</sup> over 10 cycles. It can be seen from Figure 6.3 that there are redox peaks, an anodic peak at 1.25 V and a cathodic peak at 0.60 V, which were due to the redox process of the polymer film.<sup>16, 17</sup> As shown in **Figure 6.3**, the modified electrode allows for broad redox current peaks for both the anodic and cathodic peaks in the background electrolytes, which was probably due to the counterions diffusing slowly into the polymer film.<sup>18</sup> The density of the peak current was proportional to the scan potential rate; this behaviour of the polymer supports the supposition of good electroactivity and stability as shown in **Figure 6.3** panel C.<sup>19, 20</sup>

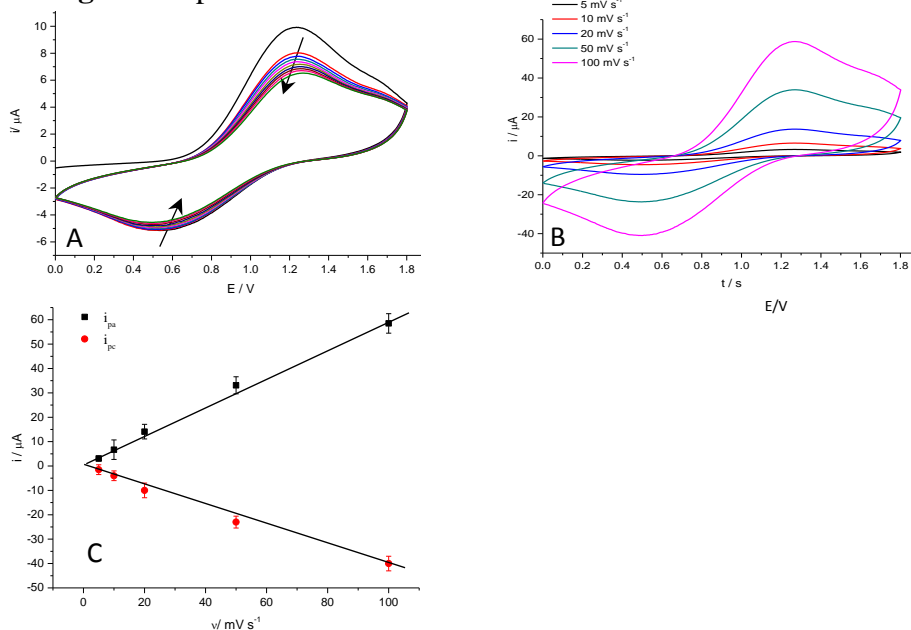


**Figure 6.3:** Voltammetric response of modified poly(3-TAA) electrodes prepared at 10 mV s<sup>-1</sup> with TBAP/CH<sub>3</sub>CN (Figure 6.1 panel A), and acquired in 0.1 M TBAP solution (monomer free) at 0.0 to 1.8 V. B) Voltammetric responses of the same film at different scan rates, 5- 100 mV s<sup>-1</sup>; C) variation of cathodic peak current (from curves in panel B) with scan rate.

Polymerisation electrolyte	Electrolyte	Scan rate mV s <sup>-1</sup>	$Q$ red/C 1st cycle	$Q$ red/C 10th cycle	$Q$ red,10th / $Q$ red,1st
TBAP	TBAP	5	$4.20 \times 10^{-4}$	$3.66 \times 10^{-4}$	0.87
		10	$4.00 \times 10^{-4}$	$3.60 \times 10^{-4}$	0.90
		20	$3.87 \times 10^{-4}$	$3.45 \times 10^{-4}$	0.89
		50	$3.60 \times 10^{-4}$	$3.32 \times 10^{-4}$	0.92
		100	$3.46 \times 10^{-4}$	$3.15 \times 10^{-4}$	0.91

**Table 6.3:** Reduction charge values of poly(3-TAA) film (Figure 6.1 panels A) exposed to TBAP/CH<sub>3</sub>CN solution (monomer free).

In order to obtain additional information about ionic movement and the accompanying electrochemical transformation, EQCM measurements were carried out.<sup>21</sup> The electropolymerisation of 0.5 M 3-TAA was performed potentiodynamically in 0.1 M TBAP/CH<sub>3</sub>CN solution on a Pt-coated quartz crystal using a potential window from 0.0 V to 2.0 V for 10 cycles. **Figure 6.4** panels A and B show the voltammetric response recorded at 30 mV s<sup>-1</sup> with the associated mass changes.<sup>22</sup> **Figure 6.4** panel C shows the amount of consumed charge vs. the applied potential during the electropolymerisation. Moreover, the apparent molar mass  $M_{app}$  of electroactive units was calculated.<sup>23, 24</sup> The gradient was  $6.67 \times 10^{-4}$  g/C and thus the apparent molar mass  $M_{app}$  is 144 g mol<sup>-1</sup>. This  $M_{app}$  was close to molar mass of the monomer at 142 g mol<sup>-1</sup>. Furthermore, cyclic voltammogram data was used to calculate the surface coverage (see equation 2.4), which was found to be  $5.56 \times 10^{-8}$  mol cm<sup>-2</sup>.

Poly(3-TAA) film prepared in the previous section was immersed in a monomer-free solution of 0.1 M TBAP/CH<sub>3</sub>CN and scanned using a potential ranging from 0.0 V to 1.8 V at a scan rate of 30 mV s<sup>-1</sup> for 10 cycles as shown in Figure 6.5 panel A to obtain data about anion doping/dedoping in the polymer film the redox peaks of the poly(3-TAA) film are consistent with the redox current peaks observed during the electropolymerisation process. Furthermore, it can be seen that the current peaks gradually decreased until the seventh scan, but then stabilized until reaching steady state. In **Figure 6.5** panel B, the mass change over the potential window from 0.00 to 1.80 V was due to insertion solvent molecules into the polymer film during the redox process, leading to swelling of the polymer film and increasing polymer mass. Surface coverage of polymer film ( $\Gamma$ / mol cm<sup>-2</sup>) was estimated to be  $6.8 \times 10^{-8}$  mol cm<sup>-2</sup> based on the cathodic charge shown in **Figure 6.5** panel A.

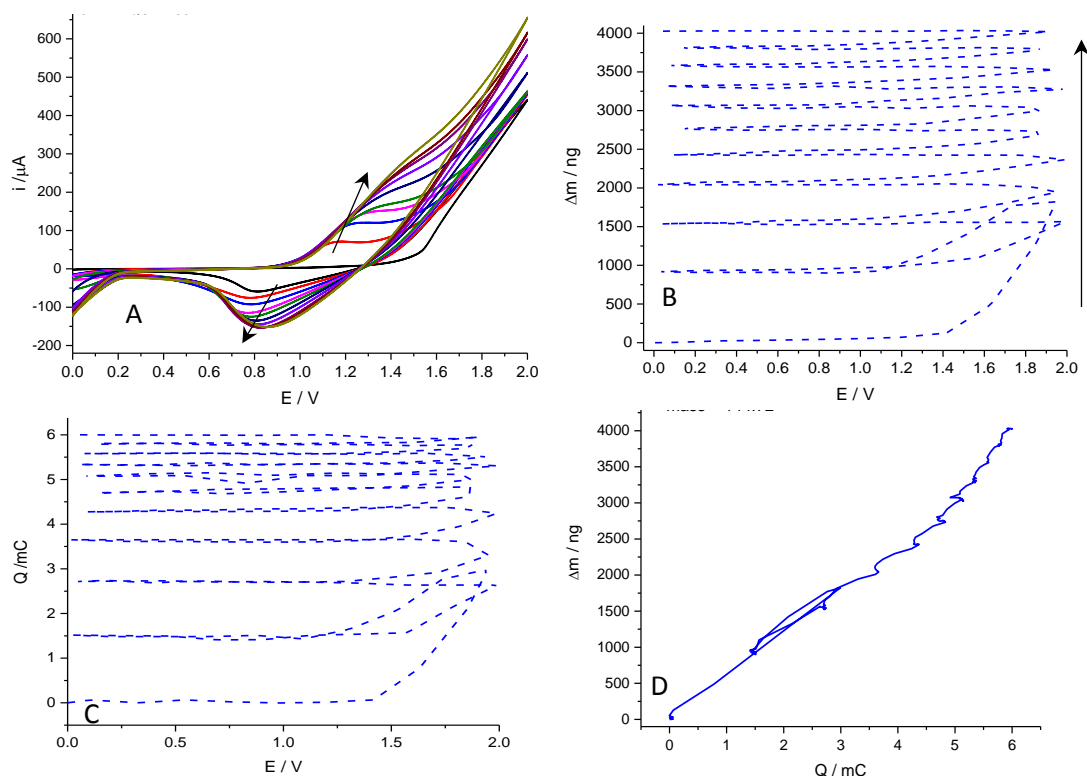


**Figure 6.4:** Representative electrochemical responses for electropolymerisation of 0.5 M 3-TAA (scan rate  $\nu = 30 \text{ mV s}^{-1}$ ) from 0.1M TBAP/ $\text{CH}_3\text{CN}$  solution. (a)  $i-E$ ; (b)  $\Delta m-E$ ; (c)  $Q-E$ ; (d)  $\Delta m-Q$ . Electrode: platinum on a QCM crystal with an area of  $0.23 \text{ cm}^2$ .

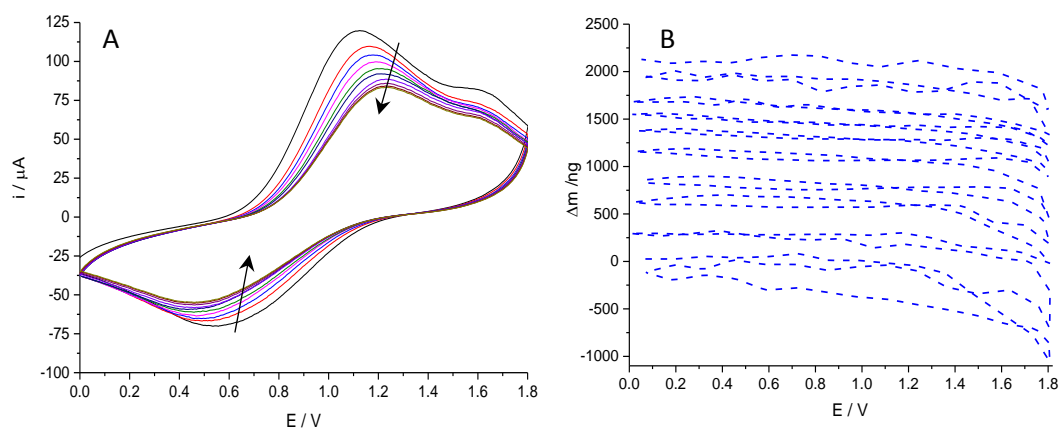


**Figure 6.5:** Representative electrochemical responses for poly(3-TAA) from Figure 6.4 (scan rate,  $\nu = 10 \text{ mV s}^{-1}$ ) in 0.1 M TBAP/ $\text{CH}_3\text{CN}$  solution (monomer free). (a)  $i-E$ ; (b)  $\Delta m-E$ . Electrode: gold on a QCM crystal with area of  $0.23 \text{ cm}^2$ .

### 6.3.3 Poly(3-thiopheneethylamine) film

Attempts to polymerise the 3-thiopheneethylamine monomer was not successful. Figure 6.6 shows the cyclic voltammograms of 0.5 M (Thio- $\text{NH}_2$ ) recorded in the potential range between 0.0 V and 2.0 V vs. Ag/AgCl for 10 cycles at  $10 \text{ mV s}^{-1}$  in TBAP/ $\text{CH}_3\text{CN}$ . From **Figure 6.6**, it may be noted that the peak currents declined with an increasing number of

cycles. Furthermore, the steady dwindling of the anodic current response was observed with the absence of any reduction current peak. A gold electrode substrate was used, but also failed to support the deposition of any polymer. Several attempts were made to increase the monomer concentration, but these experiments were also unsuccessful in producing a polymer film.<sup>25</sup> This failure was probably due to electronic interference from the free NH<sub>2</sub> group in the monomer structure, which inhibited the electropolymerisation process.<sup>26</sup> Moreover, to the best of our knowledge there has been no study in the literature to date that has reported the successful electropolymerisation of 3-thiopheneethylamine.

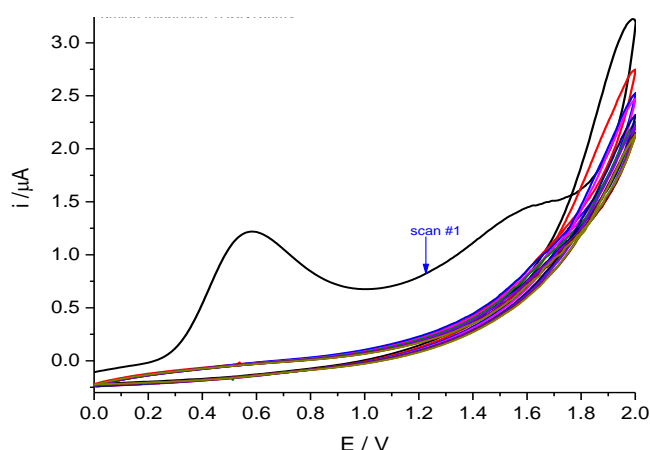


**Figure 6.6:** (A) Cyclic voltammograms resulting from electropolymerisation of 0.5 M Thio-NH<sub>2</sub> on a Pt electrode in TBAP at a scan rate of  $v = 50 \text{ mV s}^{-1}$  over 10 scans.

#### 6.3.4 Electropolymerisation of pentafluorophenyl(thiophen-3-yl)ethanoate

The electropolymerisation of the pentafluorophenyl(thiophen-3-yl) ethanoate (Thio-pfp) was successfully accomplished using cyclic voltammetry as shown in **Figure 6.7**. The electropolymerisation was performed in 0.1 M TBAP/CH<sub>3</sub>CN solution with 0.5 M of Thio-pfp using a Pt electrode and a swept potential of between 0.2 V and 1.9 V at two different scan rates, 10 and 30 mV s<sup>-1</sup>, over 10 cycles. **Figure 6.7** revealed that the anodic current peak appeared at 1.25 V and the cathodic current peak at 0.83 V. The oxidation of the monomer was initiated at  $E = 1.40 \text{ V}$  in the first scan, while the oxidation of the poly(Thio-pfp) was lower, beginning at about 0.80 V. Calculations as to the surface coverage of poly(Thio-pfp) were determined according to the equations 2.4 and 2.6. According to these equations, the surface coverage was equal to  $1.86 \times 10^{-7} \text{ mol cm}^{-2}$  and  $1.34 \times 10^{-7} \text{ mol cm}^{-2}$  for the 10 and 30 mV s<sup>-1</sup>.

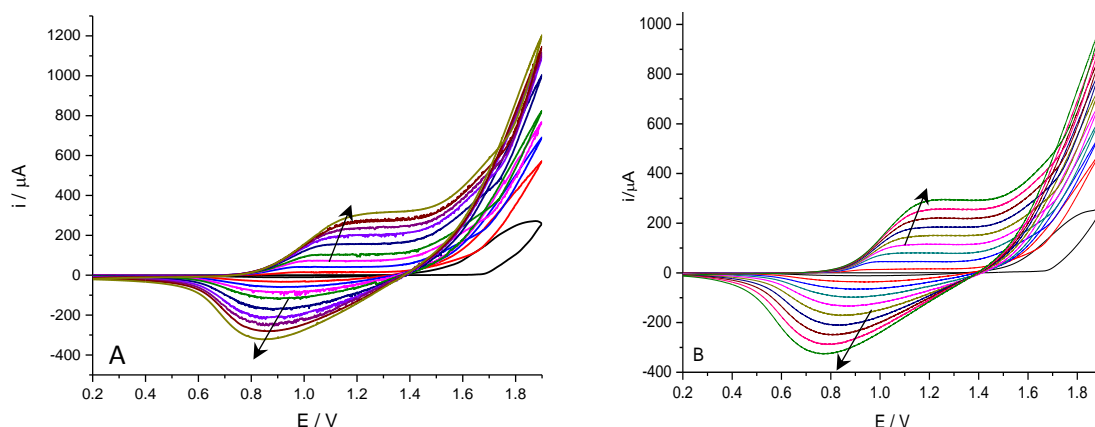


**Figure 6.7:** Cyclic voltammogram resulting from the electropolymerisation of 0.5 M Thio-pfp on a platinum electrode in TBAP/CH<sub>3</sub>CN at (A) 10 mV s<sup>-1</sup> and (B) 30 mV s<sup>-1</sup> over 10 scans. Electrode area was 0.23 cm<sup>2</sup>.

The electropolymerisation of poly(Thio-pfp) can be carried out potentiostatically in 0.5 M TPAB/CH<sub>3</sub>CN solution. In **Figure 6.8**, the chronoamperometric curves recorded on the Pt electrode at 1.9 V are shown with deposition times ranging from 50 to 200 seconds. Characteristics of the chronoamperometric curve were discussed previously in chapter four. Generally, once the voltage was applied to the working electrode, the current first increased, which was then followed by a steady decrease. The panel B shows that the electropolymerisation process was diffusion-controlled. The thickness,  $h_f^*$  (μm), of the dry polymer film was estimated using equations 2.4 and 2.6, as shown in **Table 6.4**.

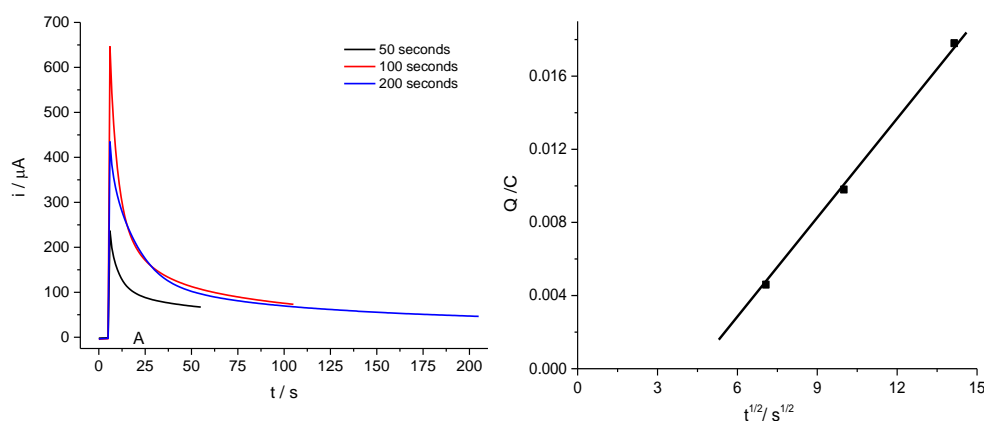


**Figure 6.8:** A) Current-time transients for electrodeposition of 0.5 M Thio-pfp in TBAP/CH<sub>3</sub>CN solution at 2 V vs. an Ag/AgCl reference over 50, 100 and 200 seconds onto a Pt electrode (0.23 cm<sup>2</sup>). B) Plot of charge vs. square root of time (data from figure 6.8)

Monomer conc. (M)	Time / s	Charge $Q$ / C	Thickness / cm
0.5	50	0.0046	$2.12 \times 10^{-5}$
0.5	100	0.0098	$4.56 \times 10^{-5}$
0.5	200	0.0178	$8.27 \times 10^{-5}$

**Table 6.4:** Electrical charge and thickness during electropolymerisation of 0.5 M Thio-pfp films at different times of 50, 100 and 200 seconds. Pt electrode ( $0.23 \text{ cm}^2$ ) and molecular weight of Thio-pfp is  $308.22 \text{ g mol}^{-1}$  and its density is ca.  $1.33 \text{ g cm}^{-3}$ .

### 6.3.5 Characterisation of poly(pentafluorophenyl(thiophen-3-yl) ethanoate) film

Poly(Thio-pfp)-modified platinum electrode prepared in the previous section (**Figure 6.7** panel A) was placed in a monomer-free electrolyte (TBAP/CH<sub>3</sub>CN) to study its electroactivity. The film was scanned over a potential range of 0.2 V to 1.9 V vs. Ag/AgCl at different scan rates between 5 - 100 mV s<sup>-1</sup>. **Figure 6.9** panel A shows a cyclic voltammogram for poly(Thio-pfp) at a 10 mV s<sup>-1</sup> scan rate. **Figure 6.9** clearly shows a stable system during sequential scan cycles and the current redox responses of polymer films. It can be seen from this figure that poly(Thio-pfp) film has both acceptable electroactivity and stability. Furthermore, as illustrated in **Figure 6.9** panel C, the peak currents were linearly proportional to the scan rate, indicating that the poly(Thio-pfp) film was electroactive.

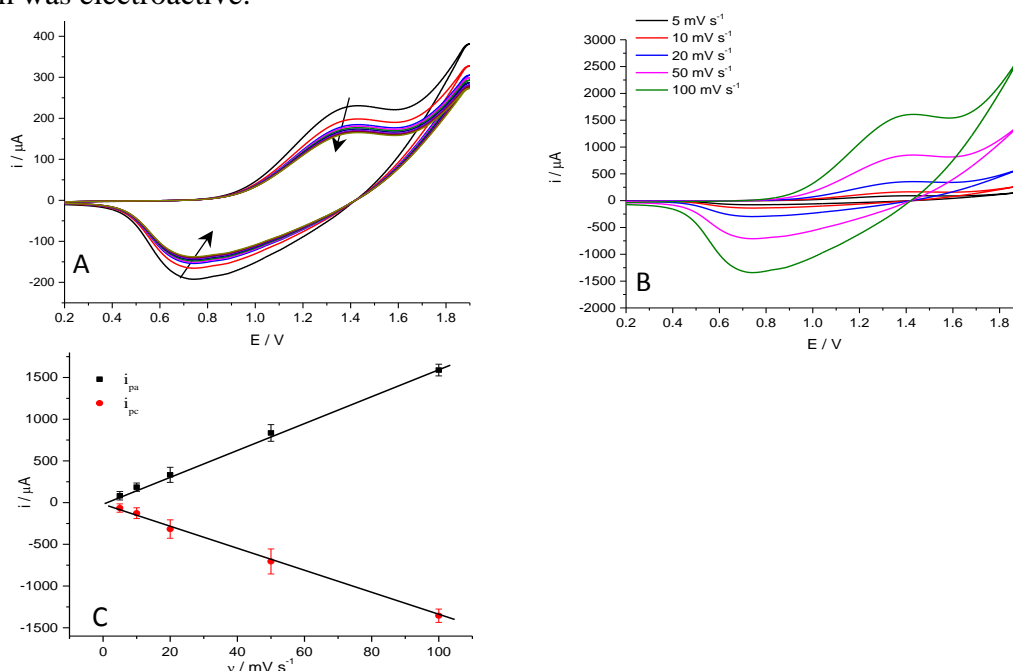


**Figure 6.9:** Voltammetric response of polymer film prepared at  $10 \text{ mV s}^{-1}$  with TBAP/CH<sub>3</sub>CN solution (Figure 6.7 panel A), and acquired in TBAP/CH<sub>3</sub>CN solution (monomer free) at 0.2 to 1.9 V. B) Voltammetric responses of the same film at different scan rates, 5- 100 mV s<sup>-1</sup>; (C) variation of cathodic peak current (from curves in panel B)) with scan rate.

Polymerisation electrolyte	Electrolyte	Scan rate mV s <sup>-1</sup>	$Q_{\text{red}} / C$ 1st cycle	$Q_{\text{red}} / C$ 10th cycle	$Q_{\text{red},10\text{th}} / Q_{\text{red},1\text{st}}$
TBAP	TBAP	5	$9.40 \times 10^{-2}$	$8.50 \times 10^{-2}$	0.89
		10	$9.32 \times 10^{-2}$	$8.47 \times 10^{-2}$	0.91
		20	$8.85 \times 10^{-2}$	$7.96 \times 10^{-2}$	0.90
		50	$8.65 \times 10^{-2}$	$7.86 \times 10^{-2}$	0.91
		100	$8.49 \times 10^{-2}$	$7.81 \times 10^{-2}$	0.92

**Table 6.5:** Reduction charge values of Thio-pfp panels (a) in Figure 6.7 exposed to TBAP / CH<sub>3</sub>CN solution (monomer free).

EQCM experiments used a 0.5 M (Thio-pfp) in 0.1 M TBAP/CH<sub>3</sub>CN solution on a platinum layer-coated crystal with a potential window ranging from 0.3 to 1.9 V and a scan rate of 30 mV s<sup>-1</sup> over 10 cycles. **Figure 6.10** panel A and B shows the voltammetric response and accompanying mass changes recorded concurrently during the electrodeposition process at 30 mV s<sup>-1</sup>. During the first cycle in **Figure 6.10**, it can be seen that the increase in mass starts at 1.25 V. Furthermore, Panel C in Figure 6.10 shows the amount of charge vs. applied potential during the electropolymerisation. Due to the curve D was nonlinear, slope was calculated using "end to end" method to be  $2.1 \times 10^{-3}$  g/C and thus the  $M_{\text{app}}$  was 455 g mol<sup>-1</sup>. The average value was calculated by compact between the lowest value of curve ( $8 \times 10^{-4}$ ) and maximum value ( $3.5 \times 10^{-3}$ ) and thus the  $M_{\text{app}}$  was 465 g mol<sup>-1</sup>. Monomer, anions and solvent seem to play role in charge compensation processes. The surface coverage of the polymer film was found to be  $2.68 \times 10^{-7}$  mol cm<sup>-2</sup>.

The polymer electrode poly(Thio-pfp) film produced in the previous section was placed in a monomer-free electrolyte containing 0.1 M TBAP/CH<sub>3</sub>CN. A potential between 0.0 V to 2.0 V vs. Ag/AgCl was applied with a scan rate of 50 mV s<sup>-1</sup> for 10 cycles to obtain information about the doping/dedoping process of the poly(Thio-pfp) film as shown in **Figure 6.11** panel A. It may be noted that the redox peaks of the polymer film were highly consistent with the redox current peaks in the poly(Thio-pfp) film during the electrodeposition process. Furthermore, the figure demonstrates that the peak currents gradually decreased over the first two scans until stabilizing in subsequent scans. Although there should be no increase in the polymer mass after each scan cycle, the entry of solvent molecules led to the swelling of the polymer film and a clear increase in mass, as shown in **Figure 6.11** panel B. Surface coverage of polymer film was estimated to be  $2.3 \times 10^{-7}$  mol cm<sup>-2</sup> based on the cathodic charge shown in **Figure 6.11** panel A. Surface

coverage values of polymer film was convergent during electrodeposition and redox process study.

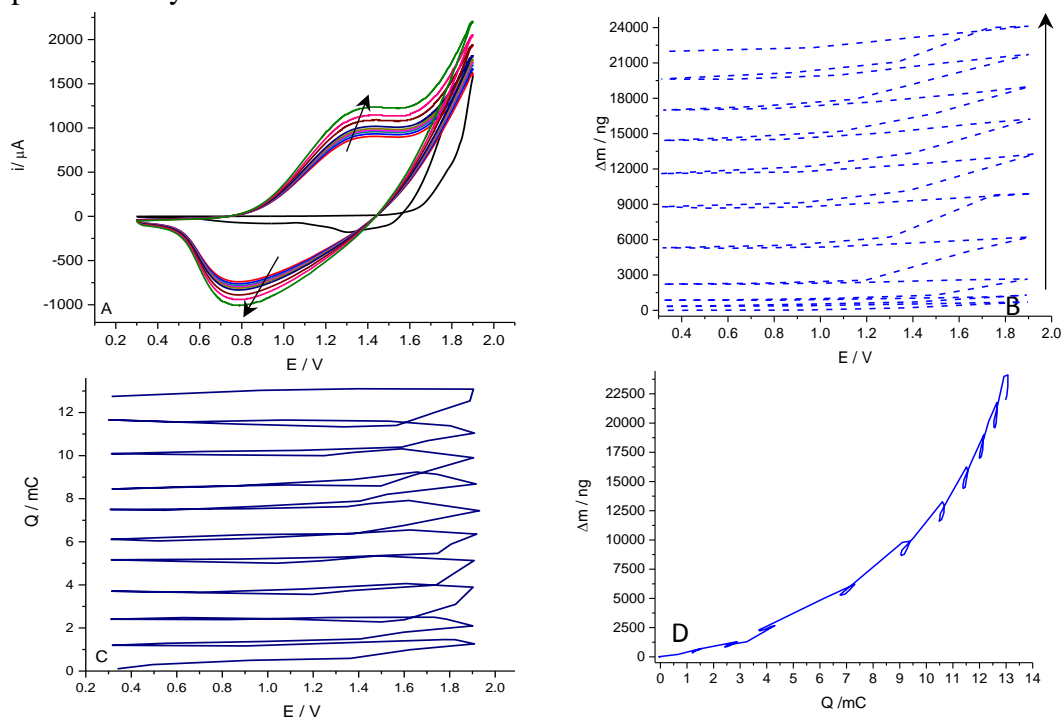


**Figure 6.10:** Representative electrochemical responses for electropolymerisation of 0.5 M Thio-pfp (scan rate  $\nu = 10 \text{ mV s}^{-1}$ ) from TBAP/ $\text{CH}_3\text{CN}$  solution. (a)  $i-E$ ; (b)  $\Delta m-E$ ; (c)  $Q-E$ ; (d)  $\Delta m-Q$ . Electrode: platinum on a QCM crystal with an area of  $0.23 \text{ cm}^2$ .

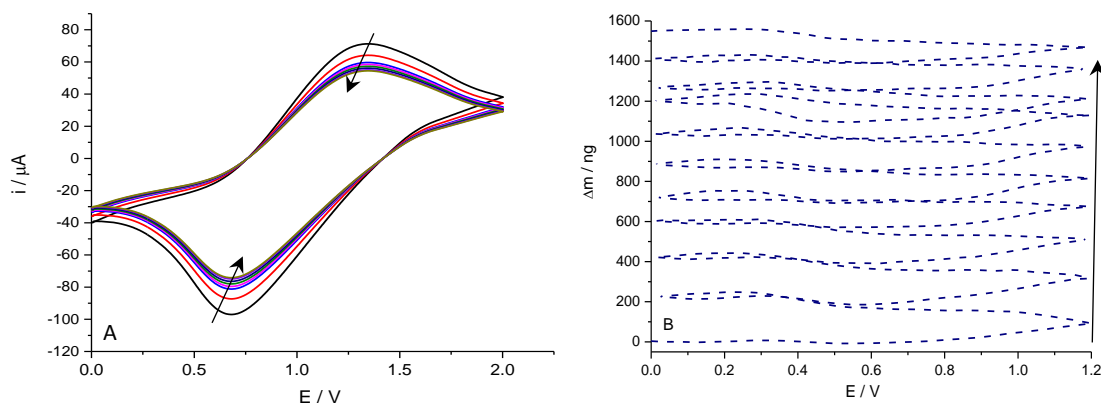


**Figure 6.11:** Representative electrochemical responses for poly(Thio-pfp) from Figure 6.10 (scan rate,  $\nu = 50 \text{ mV s}^{-1}$ ) in 0.1 M TBAP/ $\text{CH}_3\text{CN}$  solution (monomer free). (a)  $i-E$ ; (b)  $\Delta m-E$ . Electrode: platinum on a QCM crystal with an area of  $0.23 \text{ cm}^2$ .

To analyse results, the electrochemical behaviours of poly(3-TAA) and poly(Thio-pfp) films can be compared. The cyclic voltammogram of poly(3-TAA) (see **Figure 6.1**) shows an oxidation peak current at 1.25 V and a reduction peak current at 0.62 V, whereas the cyclic voltammogram of poly(Thio-pfp) film exhibits an oxidation peak current at 1.25 V and a reduction peak current at 0.83 V (see **Figure 6.7**). The differences

in redox locations between the two is due to the presence of pfp groups which contain fluoro groups and carbonyl bonds that have an electron withdrawing effect that leads to a change in the electronic density in the thiophene rings.

### 6.3.6 Electropolymerisation of 9H-fluoren-9-yl(2-(3-thienyl)ethyl) carbamate

Electropolymerisation of amide thiophene (Thio-Fmoc) films were performed in 0.1 M TBAP/CH<sub>3</sub>CN solution using a potential ranging between 0.3 V and 2.0 V vs. Ag/AgCl over 10 scans. **Figure 6.12** panels A and B show the cyclic voltammetric electrodeposition responses of Thio-fmoc recorded during the electropolymerisation process using scan rates of 30 and 50 mV s<sup>-1</sup>, respectively. From **Figure 6.12**, the first positive scan showed the oxidation of the amide derivative started at ca. 1.50 V vs. Ag/AgCl with a notable increase in current due to the generation of Thio-fmoc radicals in the reaction medium. The current peak values increased progressively over consecutive potential scans, where this increase corresponded to the formation of poly(Thio-Fmoc) film. The insertion/repulsion of counterions during the redox of poly(Thio-Fmoc) was noted by the presence of redox current peaks at 1.40 V and 1.30 V in the cyclic voltammogram response of the poly(Thio-Fmoc) film. The surface coverages were found as 3.14 x 10<sup>-7</sup> mol cm<sup>-2</sup> and 2.70 x 10<sup>-7</sup> mol cm<sup>-2</sup> for the 30 and 50 mV s<sup>-1</sup> scan rates, respectively.

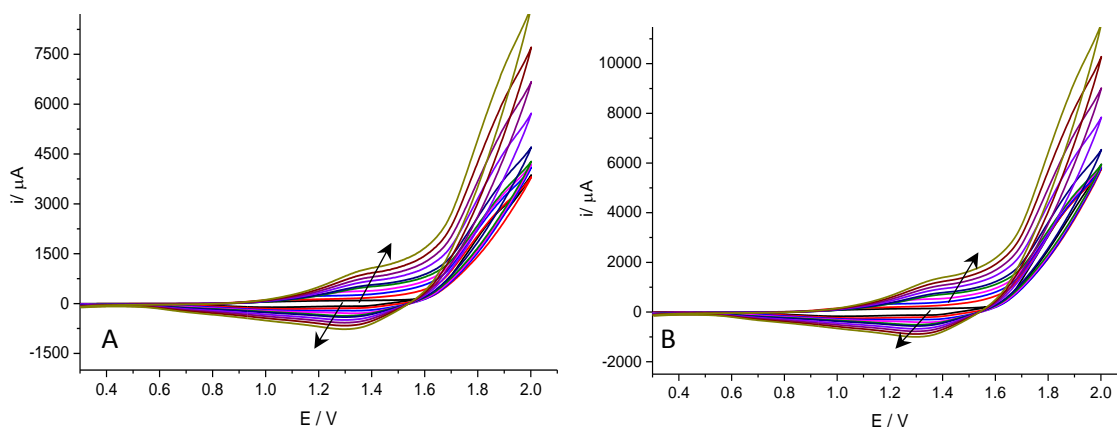


**Figure 6.12:** Cyclic voltammogram during electropolymerisation of 0.5 M amide thiophene on Pt electrode in 0.1 TBAP/CH<sub>3</sub>CN solution at (A) 30 mV s<sup>-1</sup> and (B) 50 mV s<sup>-1</sup> for 10 scans. Electrode area was 0.23 cm<sup>2</sup>.

The electropolymerisation of poly(Thio-Fmoc) film on a Pt electrode with a constant potential of 2.0 V from a 0.5 M Thio-Fmoc with TBAP/ acetonitrile solution over times ranging from 50 to 200 seconds was performed. During potential step polymerisation, the associated *i-t* transient curve is shown in **Figure 6.13**, which indicates the growth of

conducting polymer film. Figure 6.13 shows the chronoamperometric response of amide thiophene, where the current increases sharply with applied potential and then drops gradually due to nucleation and growth processes during the deposition of the polymer film. chronoamperometric measurements show that the electropolymerisation charge increased with  $t^{1/2}$  as result of a diffusion-controlled process as shown in panel B. Thickness of films increased three-fold with increasing the polymerisation time from 50 to 200 seconds. The thickness of the polymer,  $hf^*$  ( $\mu\text{m}$ ) was calculated using equations 2.4 and 2.6, as reported in **Table 6.6**.

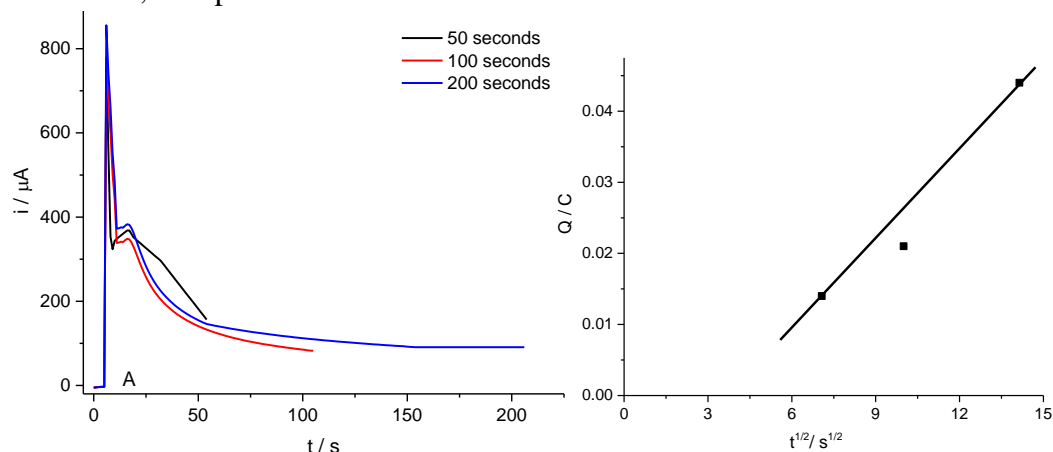


**Figure 6.13:** A) Current-time transients for electrodeposition of 0.5 M Thio-Fmoc in TBAP/ $\text{CH}_3\text{CN}$  solution at 2 V vs. an Ag/AgCl reference over 50, 100 and 200 seconds onto a Pt electrode ( $0.23 \text{ cm}^2$ ). B) Plot of charge vs. square root of time (data from figure 6.13)

Monomer conc. (M)	Time / s	Charge Q / C	Thickness / cm
0.5	50	0.014	$9.80 \times 10^{-5}$
0.5	100	0.021	$1.35 \times 10^{-4}$
0.5	200	0.044	$3.03 \times 10^{-4}$

**Table 6.6:** Electrical charge and thickness of polymer film resulting from electropolymerisation of 0.5 M Thio-Fmoc at different deposition times between 50 - 200 seconds. Pt electrode area was  $0.23 \text{ cm}^2$ ; the molecular weight of Thio-Fmoc is  $349.45 \text{ g mol}^{-1}$  and its density is ca.  $1.03 \text{ g cm}^{-3}$ .

### 6.3.7 Characterisation of poly(9H-fluoren-9-yl(2-(3-thienyl)ethyl) carbamate) film

It is important in this study to obtain information about electrochemical properties, and the redox transformations of poly(Thio-Fmoc) films which accompany the formation of the polymer film. To perform this experiment, poly(Thio-Fmoc) films were washed with acetonitrile and then put in a TBAP/ $\text{CH}_3\text{CN}$  electrolyte. The poly(Thio-Fmoc) film was scanned over a potential range of 0.3 V to 2.0 V at different scan rates between 5 - 100

$\text{mV s}^{-1}$ . **Figure 6.14** panel A shows the cyclic voltammogram of poly(Thio-Fmoc) at a scan rate of  $10 \text{ mV s}^{-1}$  where this curve was a sample for all cyclic voltammograms of polymer films under study. The cyclic voltammogram of the polymers recorded at different potential scan rates provided redox current peaks similar to those seen for the polymer during the electrodeposition process, as per **Figure 6.12**. **Figure 6.14** illustrates the cyclic voltammogram responses including anodic current peaks at  $1.50 \text{ V}$  and a cathodic peak at  $1.25 \text{ V}$ , which are due to the redox process of the polymer film. A linear relationship was observed between scan rate and peak currents, as shown in **Figure 6.14** panel C.

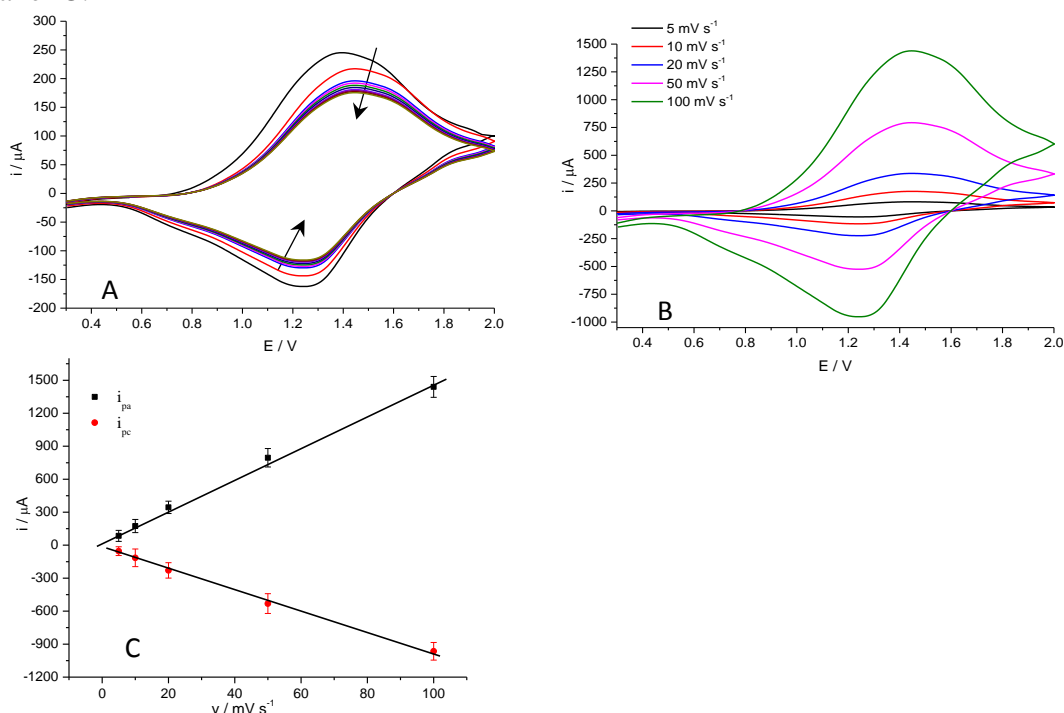


**Figure 6.14:** Voltammetric response of polymer film prepared at  $10 \text{ mV s}^{-1}$  with TBAP/ $\text{CH}_3\text{CN}$  solution (Figure 6.12 panel A), and acquired in TBAP/ $\text{CH}_3\text{CN}$  solution (monomer free) at  $0.3 - 2.0 \text{ V}$  vs. Ag/AgCl. B) Voltammetric responses of the same film at different scan rates,  $5- 100 \text{ mV s}^{-1}$ ; (C) variation of cathodic peak current (from curves in panel (B)) with scan rate.

Polymerisation electrolyte	Electrolyte	Scan rate $\text{mV s}^{-1}$	$Q_{\text{red}}/C$ 1st cycle	$Q_{\text{red}}/C$ 10th cycle	$Q_{\text{red,10th}} / Q_{\text{red,1st}}$
TBAP	TBAP	5	$8.39 \times 10^{-2}$	$7.30 \times 10^{-2}$	0.87
		10	$7.77 \times 10^{-2}$	$6.92 \times 10^{-2}$	0.89
		20	$6.78 \times 10^{-2}$	$6.17 \times 10^{-2}$	0.91
		50	$6.13 \times 10^{-2}$	$5.64 \times 10^{-2}$	0.92
		100	$5.92 \times 10^{-2}$	$5.33 \times 10^{-2}$	0.90

**Table 6.7:** Reduction charge values of poly(Thio-Fmoc) panels (A) in Figure 6.14 exposed to TBAP/ $\text{CH}_3\text{CN}$  solution (monomer free).

The poly(Thio-Fmoc) film was grown on a platinum-coated crystal using a potential ranging from 0.3 to 2.0 V vs. Ag/AgCl with scan rate of  $30 \text{ mV s}^{-1}$  over 10 cycles from 0.5 M Thio-fmoc in 0.1 M TBAP/ $\text{CH}_3\text{CN}$  solution. Figure 6.15 panel A and B shows the voltammetric response during the potentiodynamic growth of polymer film and the accompanying mass changes. From **Figure 6.15** panels A and B it can be seen that both redox current peaks and changes in mass increased as a result of the successive deposition of poly(Thio-Fmoc). Panel C illustrates the amount of electrical charge vs. the applied potential during the electrodeposition process. The variation of the charge passed,  $Q$ , and mass shift is shown in panel D. Although the curve was nonlinear, as in previous experiments, the value of the gradient and thus  $M_{app}$  mass so calculated were within an acceptable range. It can be assumed that the deposition of the polymer in the first cycle was influenced by the electrode surface, and thus decreased the amount of consumed charge in following cycles. As it was mentioned in the section 4.3.2 in chapter four the  $M_{app}$  of all electroactive sites which involved in electropolymerisation can be calculated using data from **Figure 6.15** panel D. According to this, the slope was found to be  $1.68 \times 10^{-3} \text{ g/C}$  and thus  $M_{app}$  of  $364 \text{ g mol}^{-1}$ . The surface coverage of the polymer film was calculated to be  $1.83 \times 10^{-7} \text{ mol cm}^{-2}$ .

The poly(Thio-Fmoc) film electrosynthesised in the previous section was placed in monomer-free 0.1 M TBAP/ $\text{CH}_3\text{CN}$  and a potential applied between 0.0 V to 2.0 V vs. Ag/AgCl at a scan rate of  $10 \text{ mV s}^{-1}$  for 20 cycles as shown in **Figure 6.16** panel A. In addition, this experiment was used to examine the influence of ionic movement on the stability and electrochemical properties of the polymer film. Furthermore, **Figure 6.16** panel B shows the mass change during redox switching is due to both the influx of solvent into the polymer film during the redox process. The increasing mass of the polymer after each scan cycle can be explained by assuming there is an increase in the number of solvent molecules entering the polymer film, therefore causing it to swell. The surface coverage of the polymer film was calculated to be  $1.87 \times 10^{-7} \text{ mol cm}^{-2}$ .

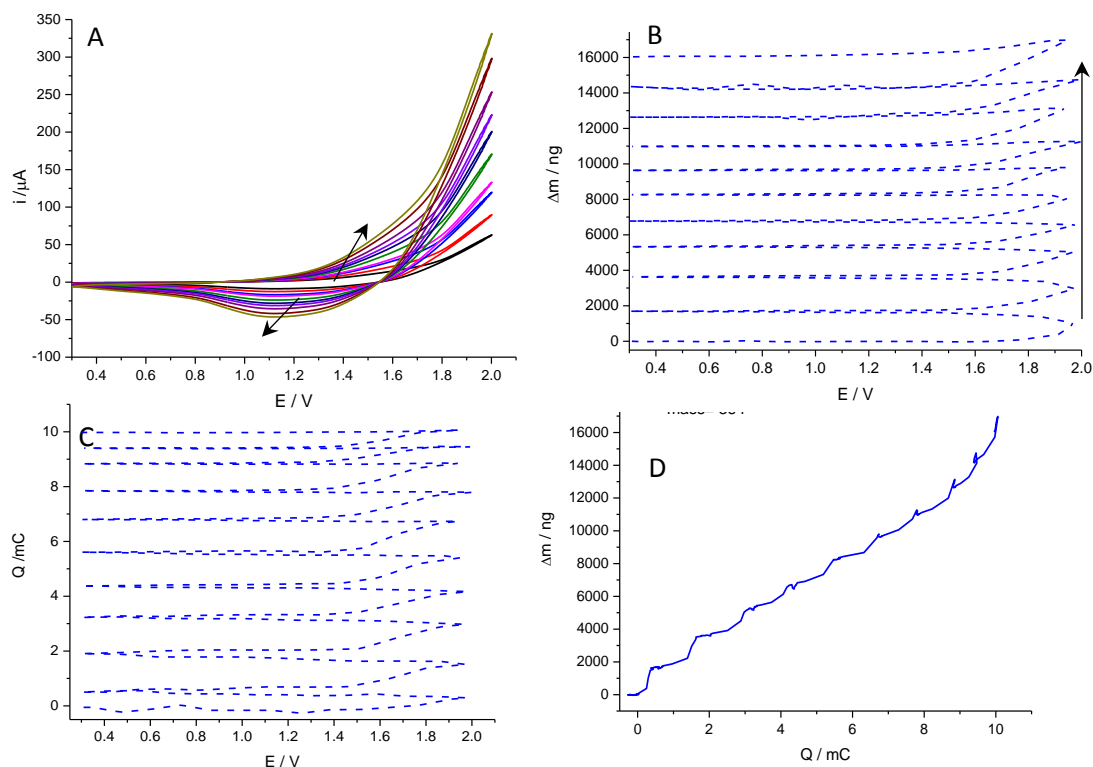


**Figure 6.15:** Representative electrochemical responses for electropolymerisation of 0.5 M Thio-Fmoc (scan rate  $v = 30 \text{ mV s}^{-1}$ ) from TBAP/ $\text{CH}_3\text{CN}$  solution. (a)  $i$ - $E$ ; (b)  $\Delta m$ - $E$ ; (c)  $Q$ - $E$ ; (d)  $\Delta m$ - $Q$ . Electrode: platinum on a QCM crystal with an area of  $0.23 \text{ cm}^2$ .

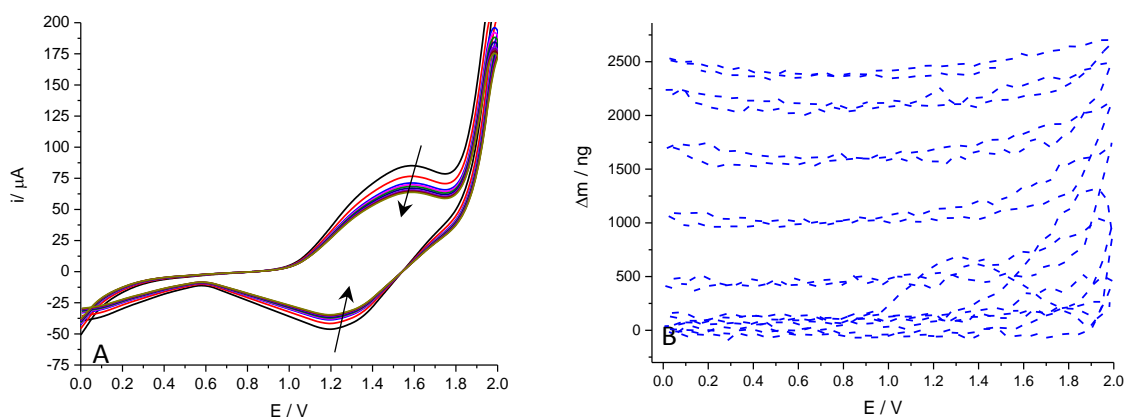


**Figure 6.16:** Representative electrochemical responses for poly(Thio-Fmoc) from Figure 6.15 (scan rate,  $v = 20 \text{ mV s}^{-1}$ ) in 0.1 M TBAP/ $\text{CH}_3\text{CN}$  solution (monomer free). (a)  $i$ - $E$ ; (b)  $\Delta m$ - $E$ . Electrode: platinum on a QCM crystal with an area of  $0.23 \text{ cm}^2$ .

The electronic influence of the amino group on the thiophene molecular leads to inhibition of the electropolymerisation process of the monomer. After protection of the amino group using fmoc, the ability to polymerise the functionalised monomer is significantly improved; the polymer thus obtained as shown in the **Figure 6.12**.

## 6.4 Post-polymerisation Chemical Modifications

As mentioned in previous chapters, tailored positioning of molecules on surfaces is considered a key criterion for the creation of smart devices in various applications.<sup>27</sup> The functionalisation of the structure of polythiophene with specific groups such as recognition units has been extensively investigated, and which leads to the improved functionality of polymer electrode surfaces, such as for selectivity and sensitivity.<sup>4,28,29</sup> In this section of the thesis, protected polymer films (ester and amide) were hydrolysed in appropriate solutions. The electrochemical and physical stabilities of the polymer films after deprotection process were evaluated. FTIR and QCM were used to examine the functionalisation of the polymer surface and the influence of this process on the electroactivity of polymer films. Practically, functionalised polymer films were fabricated by electropolymerisation of a monomer containing functional groups, either pfp or Fmoc, which can subsequently be removed and substituted for other suitable groups. In this strategy, amide bonds are formed between receptor groups and the polythiophene surfaces. QCM and FTIR spectroscopy were used to examine the success of this synthetic strategy with regards to the immobilisation of the receptor molecules within the polymer films.

### 6.4.1 QCM Gravimetric and FTIR Spectroscopic Monitoring of Ester Hydrolysis

Poly(Thio-pfp) films was hydrolysed using alkaline solutions. Practically, polymer electrodes were immersed in 0.1 M NaOH for different lengths of time with continuous monitoring of the conversion using FTIR as shown in **Figure 6.17**. FTIR was used to identify when the carbonyl group of the ester bond no longer appeared in the resulting film as an indication of the successful and complete conversion to poly(3-TAA). A carbonyl ester band  $\nu(\text{C}=\text{O})$  at  $1775\text{ cm}^{-1}$  and the  $\nu(\text{C}-\text{F})$  band at  $1000\text{ cm}^{-1}$  are no longer present in the spectrum of the deprotected film (blue line) in **Figure 6.17**.<sup>30,31</sup> Moreover, hydrolysis led to the appearance of new bands attributed to the poly(3-TAA) film, for instance the broad band at  $3270\text{ cm}^{-1}$  was due to the  $\nu(\text{O}-\text{H})$  stretch of the carboxylic acid (indicated by symbol \* in figure), the band at  $1718\text{ cm}^{-1}$  was attributed to the  $\nu(\text{C}=\text{O})$  stretch of the carboxylic acid (indicated by symbol + in figure).<sup>32-34</sup>

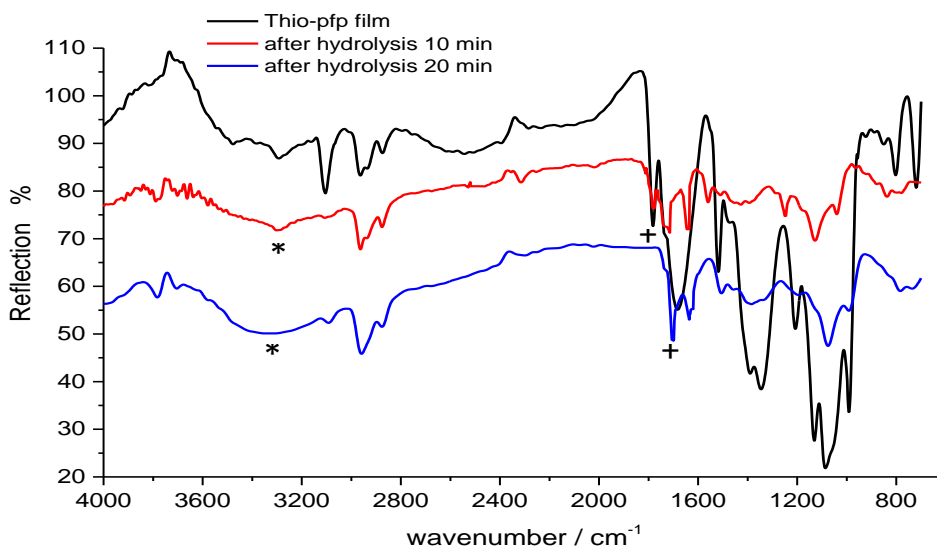


**Figure 6.17:** FTIR spectra showing the hydrolysis reaction at different times over the course of the reaction. (a) Poly(Thio-pfp) as deposited (black line), (b) film after 10 min. hydrolysis (red line) and (c) film after 20 min. hydrolysis (blue line). \* denotes the presence of carboxylic and + denotes the presence carbonyl peaks.

The QCM was used to examine the deprotection reaction of poly(Thio-pfp) films<sup>15,35</sup> in terms of monitoring the mass change accompanying the hydrolysis reaction at the surfaces of the polymer films, as caused by the removal of good leaving groups (here, the pfp groups). **Figure 6.18** shows the increasing frequency of the quartz crystal resonator accompanying a decrease in the mass of the film during the hydrolysis process.

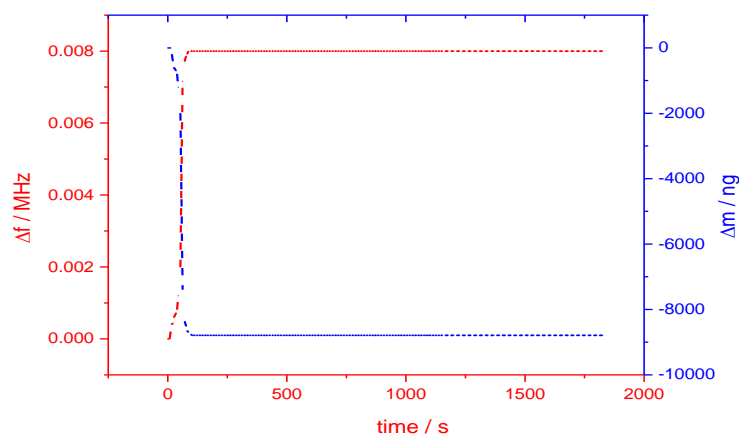


**Figure 6.18:** EQCM recorded during the deprotection process of poly(Thio-pfp) film in an alkaline solution of 0.1 M NaOH.

To confirm that the hydrolysis process had not had any negative influence on the electroactivity of the polymer films, the electrochemical behaviour of deprotected polymer films was recorded in a monomer-free solution of 0.1 M TBAP in acetonitrile at a 10 mV s<sup>-1</sup> scan rate over 10 cycles, as shown in **Figure 6.19**. The voltammetric response

shows that the current peaks were almost identical to those observed during the monomer-free study of 3-TAA before protection.

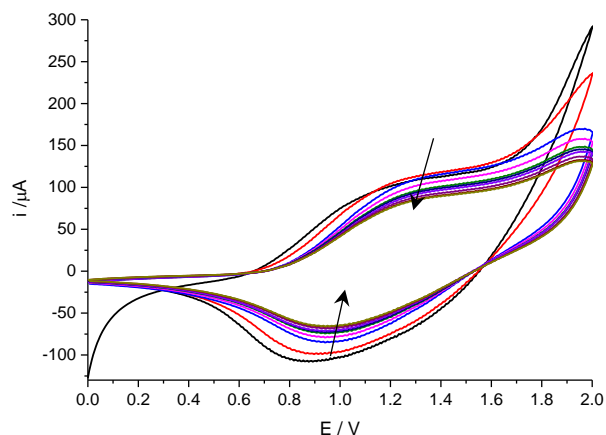


**Figure 6.19:** Cyclic voltammogram of poly(Thio-pfp) film after hydrolysis in a TBAP/CH<sub>3</sub>CN monomer-free solution as a function of repeated scans at 10 mV s<sup>-1</sup>.

From the IR spectra curve B (red line) in **Figure 6.17**, it may be noted that some (pfp) molecules remained in the polymer film, whilst QCM curve shows that there is no change in the mass until third minutes of hydrolysis. The voltammetric results were used to estimate mass of polymer films according to equation (mass =  $M.wt \times \Gamma$ ) and surface coverage of the polymer films was calculated by equation 2.4. Voltammetric results demonstrated that the surface coverage of polymer ( $m_p$ ) before hydrolysis equal  $2.6 \times 10^{-7}$  mol cm<sup>-2</sup> (equal to 19 μg) (data presented in **Figure 6.10**) and based on QCM data the mass of film ( $m_p + m_s$ ) was equal to 22 μg. After hydrolysis the mass of film was 13 μg based on QCM data (presented in **Figure 6.18**) and mass change of hydrolysis was -9 μg and surface coverage of polymer equal to  $2.15 \times 10^{-7}$  mol cm<sup>-2</sup> (equal to 7 μg). Decreasing film mass due to leave pfp groups from polymer. In fact, the theoretical calculations show that mass of pfp groups equal to 57% and findings based QCM data show that the mass change of film was equal to 41%. This difference in polymer film mass between poly(Thio-pfp) and poly(Thio-COOH) which containing almost same  $\Gamma$  values shows the capability for create voids and ingress a large amount of solvent molecules into polymer film during hydrolysis process. FTIR gives the evidence to confirm that pfp groups was left the polymer film during hydrolysis as shown in **Figure 6.17**.

Films	Polymer deposition		polymer hydrolysis		functionalisation	
	$\Gamma$ / mol cm <sup>-2</sup>	$\Delta M$ / μg cm <sup>-2</sup>	$\Gamma$ / mol cm <sup>-2</sup>	$\Delta M$ / μg cm <sup>-2</sup>	$\Gamma$ / mol cm <sup>-2</sup>	$\Delta M$ / μg cm <sup>-2</sup>
Thio-pfp	$2.6 \times 10^{-7}$	22	$2.15 \times 10^{-7}$	-9	$2.16 \times 10^{-7}$	4.9

**Table 6.8:** Mass and surface coverage between polymer films (before and after hydrolysis) functionalisation for poly(Thio-pfp) film.

### 6.4.2 Monitoring of vertical penetration of receptor into ester polymer film

In order to achieve the immobilisation process, the activated ester polymer film, poly(Thio-pfp), and the receptor molecule (NTA-lysine) were allowed to react. The film was placed in a solution of receptor NTA-lysine (0.1 M DMSO/CH<sub>3</sub>CN solution, 2:8 ml) for 60 minutes and then rinsed with dry acetonitrile. **Figure 6.20** shows the proposed schematic for the immobilisation reaction between the poly (Thio-pfp) film surface and the receptor (NTA-lysine). FTIR was used to monitor the reaction over time to determine the time necessary to ensure the functionalisation process was complete throughout the polymer film surface, as shown in **Figure 6.21**. The FTIR spectrum gave the following data: the ester film, poly(Thio-pfp), showed a characteristic sharp band at 1780 cm<sup>-1</sup> due to the  $\nu(\text{C}=\text{O})$  stretch of the ester group and a band at 1000 cm<sup>-1</sup> that was attributed to the  $\nu(\text{C}-\text{F})$  bend before functionalisation, as shown in **Figure 6.21**. After the functionalisation reaction, the carbonyl stretch was observed to have shifted from 1780 cm<sup>-1</sup> to 1650 cm<sup>-1</sup> as result of formation of amide bonds in the polymer film (indicated by symbol + in figure), with the disappearance of the peak at 1000 cm<sup>-1</sup> as a result of the removal of the pfp group. Furthermore, the emergence of a new broad band at 3250 cm<sup>-1</sup> was attributed to the  $\nu(\text{O}-\text{H})$  stretch (indicated by symbol \* in figure).

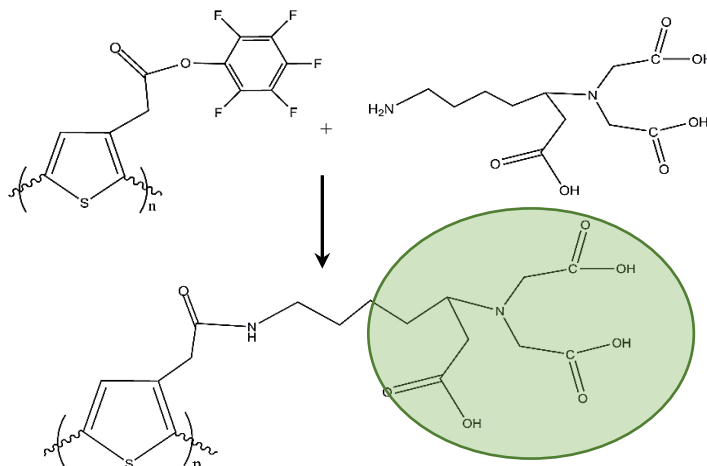


**Figure 6.20:** Reaction scheme illustrating the reaction between the receptor NTA-lysine with the activated ester film, poly(Thio-pfp).

The QCM was used to monitor the functionalisation process for the poly(Thio-pfp) film to confirm the penetration over the polymer film surface. The insertion of new molecules into the polymer chains, and the conversion from ester to amide bonds, led to a gradual decrease in frequency in the crystal indicative of an increase in the mass of the polymer film due to the insertion of receptor units. The molecular mass of the NTA-lysine group

is  $262.2 \text{ g mol}^{-1}$  while the molecular mass of the pfp is  $184 \text{ g mol}^{-1}$ . **Figure 6.22** demonstrates the changes in mass and frequency during the immobilisation process.

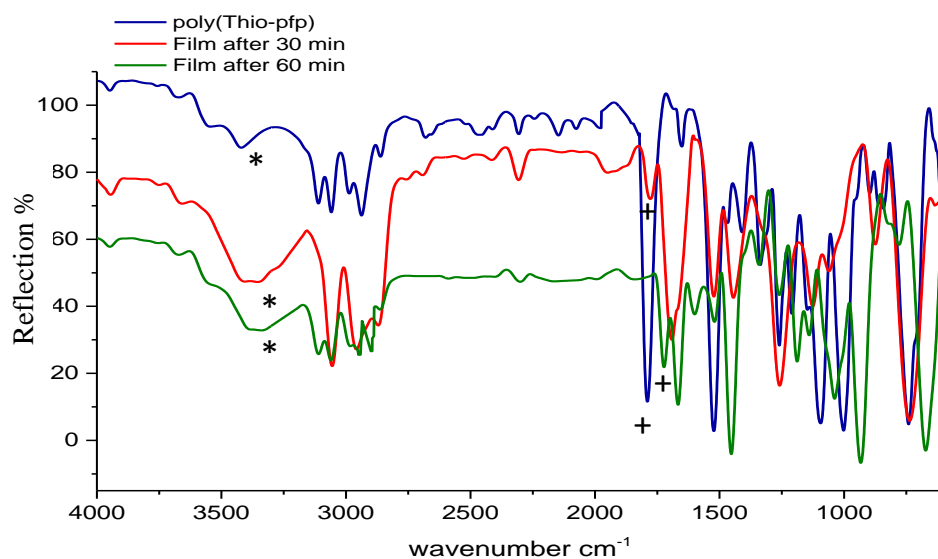


**Figure 6.21:** FTIR spectra showing the amidation reaction at different times. (a) Poly(Thio-pfp) as deposited (blue line), (b) film after 30 min. (red line), and (c) film after 60 min. reaction time (green line). \*denotes the presence of carboxylic and + denotes the presence of carbonyl peaks

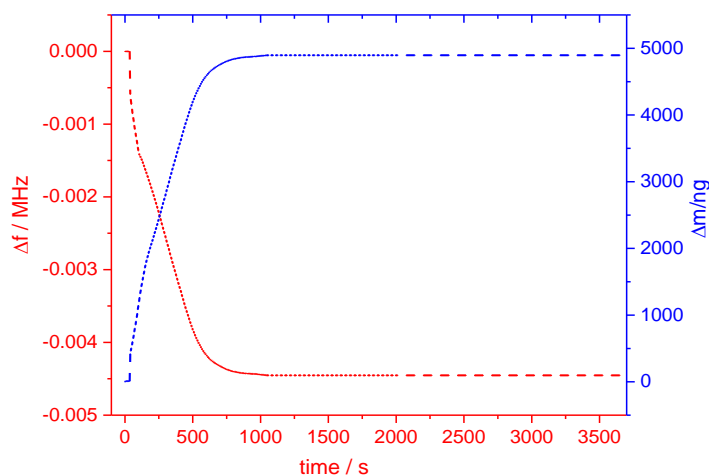


**Figure 6.22:** QCM recorded during the immobilization process of poly(Thio-pfp) film with the receptor unit (NTA-lysine) over 60 mins.

The electrochemical behaviour of polymer films after functionalisation was studied using a monomer-free  $0.1 \text{ MTBAP/CH}_3\text{CN}$  solution at a  $10 \text{ mV s}^{-1}$  scan rate over 10 cycles, as shown in **Figure 6.23**. **Figure 6.23** shows the redox current peaks differ from those observed during the redox study of poly(Thio-pfp) film as result of insertion of the receptor groups on the polymer film surface.

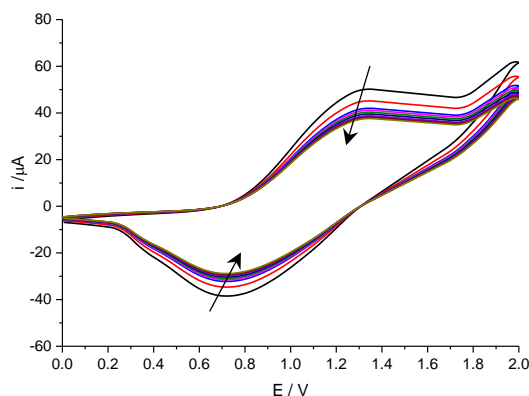


**Figure 6.23:** Cyclic voltammogram of poly(Thio-NTA) film in a monomer-free 0.1 M TBAP/CH<sub>3</sub>CN solution as a function of repeated scans at 10 mV s<sup>-1</sup>.

**Figure 6.21** and **Figure 6.22** show the IR spectra and QCM measurements of the immobilisation reaction. The completion of the immobilisation reaction was confirmed using IR measurements, as shown in Figure 6.22 curve C. Mass of polymer films were calculated to compare between films before and after functionalisation and results were demonstrated that the mass of Thio-NTA was increased by 4.9 μg based on QCM data and surface coverage equal to 2.16 × 10<sup>-7</sup> mol cm<sup>-2</sup>. The functionalisation percentage was equal to 53%. This increase was expected due to the ingress of receptor groups (NTA) into the polymer film, whose molecular weight is greater than that of pfp.

#### 6.4.3 QCM Gravimetric and FTIR Spectroscopic Monitoring of Amide Hydrolysis

poly(Thio-fmoc) films was hydrolysed using a basic solution (30% piperidine) as with the previous work with amide pyrrole and aniline films. FTIR was utilised to identify and confirm that the amide group had been removed from the polymer film surface, thus demonstrating the amide film had successfully converted to an amine film. **Figure 6.24** shows that the carbonyl amide band  $\nu(\text{C}=\text{O})$  at 1690 cm<sup>-1</sup> had disappeared from the IR spectrum. Furthermore, the hydrolysis reaction led to the emergence of a number of bands due to the poly(Thio-NH<sub>2</sub>) film; for instance, the two bands in the 3300-3200 cm<sup>-1</sup> region were due to  $\nu(\text{N-H})$  stretching bands of the primary aliphatic amino group (indicated by symbol \* in figure), whilst the band at 1630 cm<sup>-1</sup> was due to the  $\nu(\text{N-H})$  bending mode (indicated by symbol + in figure).

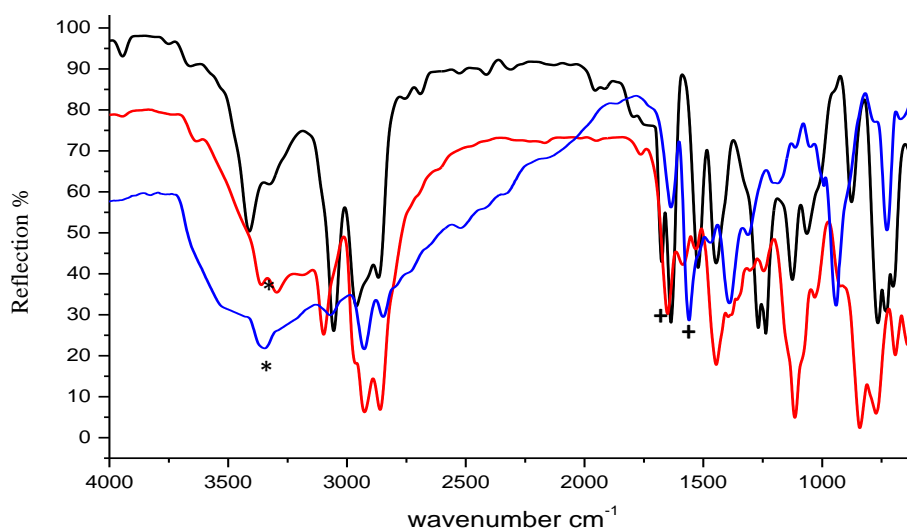


**Figure 6.24:** FTIR spectra showing the effects of hydrolysis at different times during the reaction. (a) Poly(Thio-Fmoc) as deposited (black line), (b) film after 10 min. hydrolysis (blue line), and (c) film after 30 min. hydrolysis (red line). \*denotes the presence of primary amine and + denotes the presence of carbonyl peaks.

QCM was used to follow the removal of the fmoc group from polymer film as shown in **Figure 6.25**. The resulting changes in frequency and weight of the polymer film offer an obvious indication as to the nature of the reactions on the polymer film surface. The electroactivity of the deprotected poly(Thio-NH<sub>2</sub>) film was studied potentiodynamically. The polymer film was placed in a monomer-free TBAP/CH<sub>3</sub>CN solution and cyclic voltammetry performed at a scan rate of 10 mV s<sup>-1</sup>. The resultant cyclic voltammogram was recorded over 10 cycles, as shown in **Figure 6.26**. The current redox peaks which emerged during this experiment were different from those observed in the monomer-free study of poly(Thio-Fmoc).

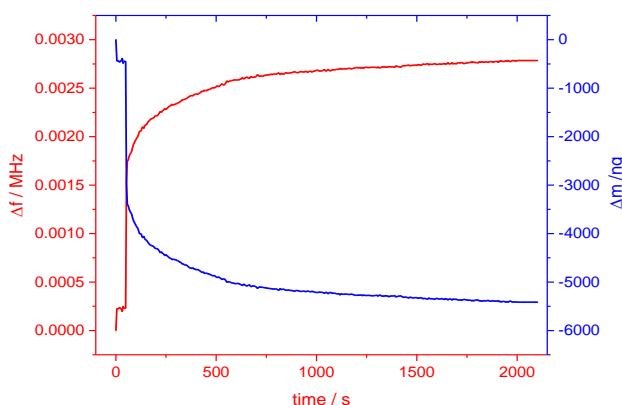


**Figure 6.25:** QCM recorded during the hydrolysis (deprotection) of poly(Thio-Fmoc) film in a 30% piperidine/CH<sub>3</sub>CN solution.

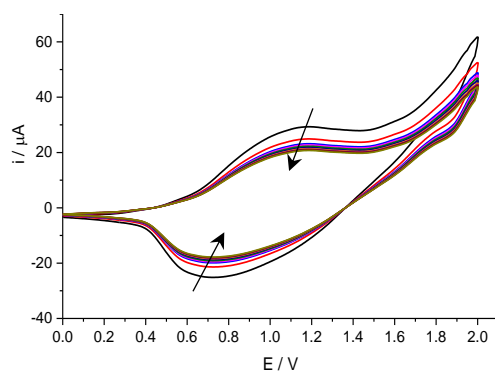


**Figure 6.26:** Cyclic voltammogram of poly(Thio-Fmoc) film after hydrolysis in a TBAP/CH<sub>3</sub>CN monomer-free solution as a function of repeated scans at 10 mV s<sup>-1</sup>.

**Figure 6.24** and **Figure 6.25** show the IR spectra and QCM measurements of the hydrolysis reaction. The IR spectra curve B shows that some amide bands remain within the film, whilst the QCM curve illustrates the presence of pfp molecules in the polymer that have not reacted. The completion of the hydrolysis reaction was confirmed using IR measurements, as shown in **Figure 6.24** curve C. The voltammetric results were used to estimate surface coverage to be  $1.8 \times 10^{-7}$  mol cm<sup>-2</sup> (14.5 μg) and the mass of film (data presented in **Figure 6.15**) was equal to 16 μg based on QCM data. While the mass of polymer film after hydrolysis was 10.5 μg and surface coverage was equal to  $1.9 \times 10^{-7}$  mol cm<sup>-2</sup> and mass change of hydrolysis was -5.5 μg (data presented in **Figure 6.25** and **6.26**). Theoretical calculations show that mass of fmoc groups equal to 62% and hydrolysis result show that the mass change was equal to 35%. This difference in film mass between poly(Thio-Fmoc) and poly(Thio-NH<sub>2</sub>) containing almost same  $\Gamma$  shows the capability for create voids and ingress a large amount of solvent molecules into polymer film. FTIR gives the evidence to confirm that pfp groups was left the polymer film during hydrolysis as shown in **Figure 6.24**.

Films	Polymer deposition		polymer hydrolysis		functionalisation	
	$\Gamma$ / mol cm <sup>-2</sup>	$\Delta M$ / μg cm <sup>-2</sup>	$\Gamma$ / mol cm <sup>-2</sup>	$\Delta M$ / μg cm <sup>-2</sup>	$\Gamma$ / mol cm <sup>-2</sup>	$\Delta M$ / μg cm <sup>-2</sup>
Thio-fmoc	$1.8 \times 10^{-7}$	16	$1.9 \times 10^{-7}$	-5.5	$1.95 \times 10^{-7}$	4.8

**Table 6.9 :** Mass and surface coverage between polymer films (before and after hydrolysis) functionalisation for poly(Thio-Fmoc) film.

#### 6.4.4 Monitoring of vertical penetration of receptor into amide polymer film

The reaction between the poly(Thio-NH<sub>2</sub>) and the receptor 2-HQC is shown in Figure 6.27. The deprotected poly(Thio-NH<sub>2</sub>) film was immersed in activated NHS-ester receptor solution in a suitable solvent (0.1 M DMSO/CH<sub>3</sub>CN solution, 1:9 ml) for 30 minutes. FTIR and QCM were used to monitor the reaction process. The interaction between the polymer film and receptor led to the production of a new amide film, poly(Thio-HQC). This amino film was identified using FTIR, whose spectrum showed various features that confirmed amide formation had occurred. **Figure 6.28** shows the FTIR spectra obtained for the polymer film at different times during the reaction. The spectrum showed a new peak at 1690 cm<sup>-1</sup>(indicated by symbol + in figure), which was due to the carbonyl stretch of the amide group; in addition, a broad peak at 3275 cm<sup>-1</sup> was observed because of the hydroxyl groups on the receptor molecules (indicated by symbol \* in figure).

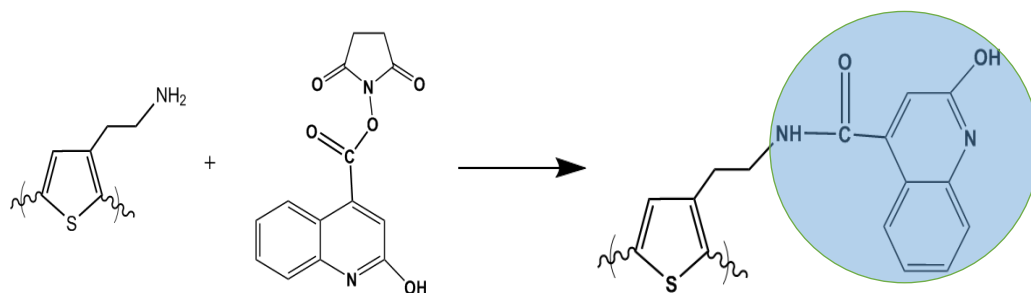


**Figure 6.27:** Reaction scheme illustrating the reaction between the 2-HQC receptor with poly(Thio-NH<sub>2</sub>) film.

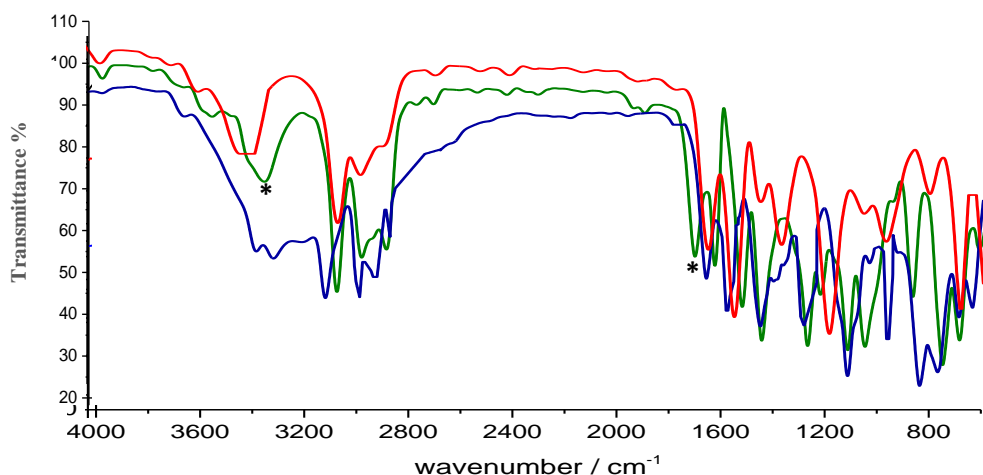


**Figure 6.28:** FTIR spectra showing the immobilisation reaction at various times during the course of the reaction. (a) Poly(Thio-NH<sub>2</sub>) as deposited (blue line), (b) film after 10 min. reaction time (red line), and (c) film after 30 min. reaction time (green line). \*denotes the presence of hydroxyl and +denotes the presence of carbonyl of amide peaks.

QCM was used to follow the functionalisation reaction between the poly(Ani-NH<sub>2</sub>) and 2-HQC. The changes in the resulting frequency and mass shifts gave us an idea as to the nature of the reaction, which had led to the generation of new amide bonds across the film surface, this logically leading to changes in the chemical structure and molecular weight of the monomer units. Thus, it might be expected that the functionalisation reaction would lead to a cumulative increase in weight of the polymer film. **Figure 6.29** illustrates the changes in mass/frequency over the course of the functionalisation reaction.

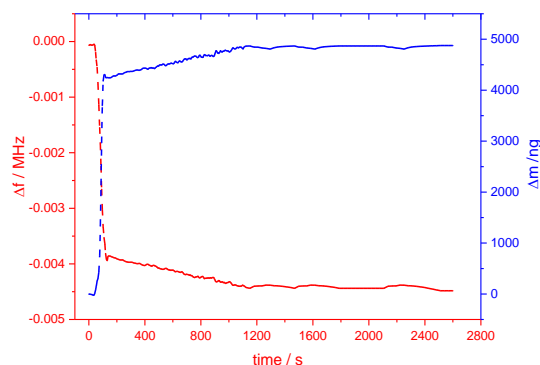


**Figure 6.29:** QCM recorded during the functionalisation reaction of poly(Thio-NH<sub>2</sub>) film with the receptor unit (2-HQC) over a 30 min. duration.

The electroactivity was studied for film after the immobilisation reaction to demonstrate that the film had maintained its electrochemical activity. Study was recorded in a monomer-free 0.1 M TBAP/CH<sub>3</sub>CN solution with a 10 mV s<sup>-1</sup> scan rate over 10 cycles, as shown in **Figure 6.30**. The redox current peaks observed in this voltammogram differed slightly from those observed during the monomer-free studies of poly(Thio-Fmoc) and poly(Thio-NH<sub>2</sub>) films because of the influence of the receptor molecules after insertion on the polymer film surface.

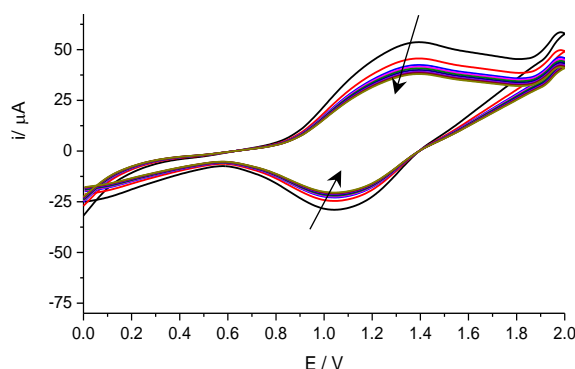


**Figure 6.30:** Cyclic voltammogram of poly(Thio-HQC) film in a monomer-free solution of 0.1 M TBAP/CH<sub>3</sub>CN as a function of repeated scans at 10 mV s<sup>-1</sup>.

From the QCM curve, it can be seen that mass of the film increased as a result of the ingress of HQC into the polymer film surface. IR spectra show that the HQC is still

present in the polymer film after the functionalisation process had been allowed to proceed for 15 minutes. The mass of the film was estimated for polymer film, depending of redox process, before and after functionalisation. Calculations showed that the mass of polymer film after the functionalisation (data presented in **Figure 6.29**) was increased by 4.8  $\mu\text{g}$  based on QCM data, with a surface coverage of  $1.95 \times 10^{-7} \text{ mol cm}^{-2}$ . The functionalisation percentage was equal to 79%. This expected increase in the mass of the film as result of the ingress of receptor groups (HQC) into the polymer film.

### 6.5 Patterning of polymer films

In this section, the patterning method detailed in chapter four was used. After completing the patterning process, various measurements were undertaken, such as 3D microscopy, FTIR and cyclic voltammetry, to examine the patterned electrodes. **Figures 6.31** and **6.32** show cross-sections of the electrodes after the patterning operation. The black part of **Figure 6.32** represents the polymer film, whilst the grey region represents the developer (SU-8 2000) as exposed to UV light.

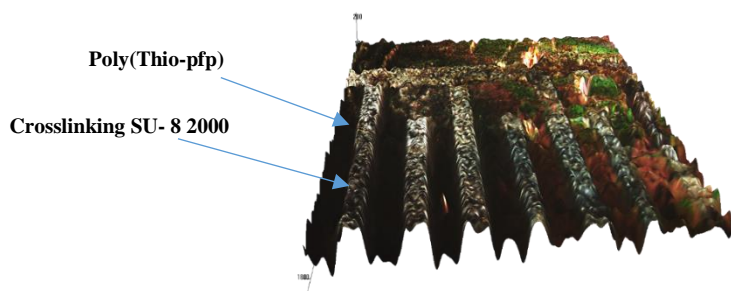


**Figure 6.31:** 3D microscopic image of a cross-section of the poly(Thio-pfp) electrode after the patterning operation.

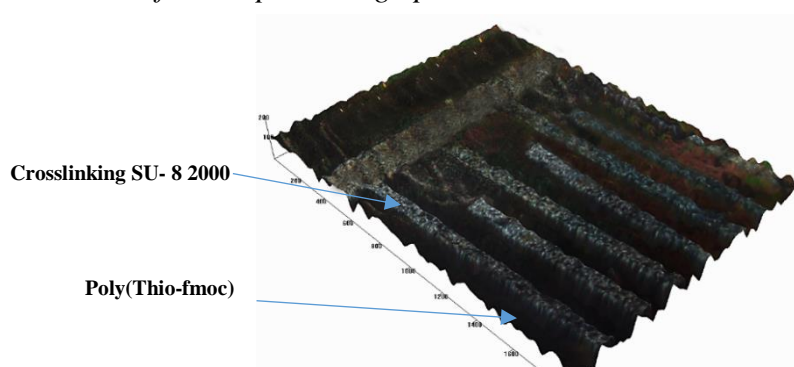


**Figure 6.32:** 3D microscopic image of a cross-section of the poly(Thio-Fmoc) electrode after the patterning operation.

The patterned surface was examined potentiodynamically to measure its electroactivity after patterning, and then compared with polymer films which had not been exposed to UV radiation. **Figure 6.33** shows the cyclic voltammograms of a poly(Thio-pfp) film

before and after UV irradiation and the functionalised polymer electrode poly(Thio-NTA), respectively, in a monomer-free solution containing 0.1 M TBAP/CH<sub>3</sub>CN. The current peaks in the cyclic voltammogram for non-functionalised polymer film, poly(Thio-pfp), and the functionalised polymer, poly(Thio-NTA), differed due to their differing chemical compositions. Figure 6.34 illustrates the cyclic voltammograms of a poly(Thio-Fmoc) film before and after the patterning process, and the patterned poly(Thio-HQC) film, respectively, in background electrolyte solutions containing 0.1 M TBAP in acetonitrile. From **Figure 6.34**, we note the shifts that occurred in the redox current peaks between poly(Thio-fmoc) and poly(Thio-HQC) film as result of the changes in chemical composition before and after functionalisation.

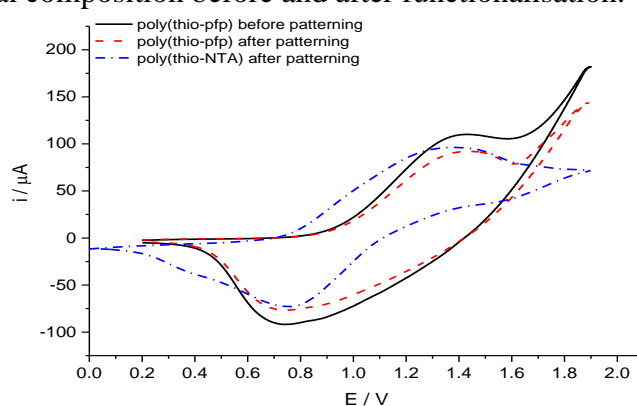


**Figure 6.33:** Voltammetric response of poly(Thio-pfp) electrodes, the solid and dashed lines (before and after patterning, respectively) and the chained line, the poly(Thio-NTA) electrode, in monomer-free TBAP/CH<sub>3</sub>CN solution at a scan rate of 10 mV s<sup>-1</sup>.

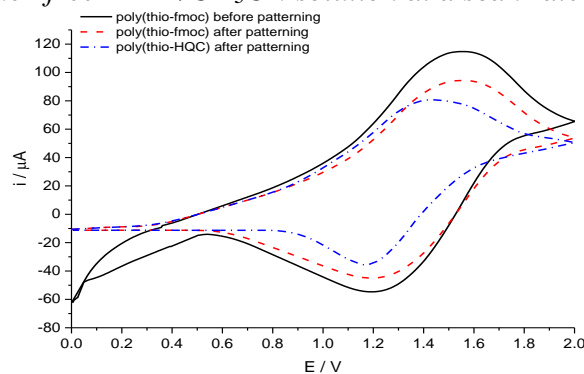


**Figure 6.34:** Voltammetric response of poly(Thio-Fmoc) electrodes, the solid and dashed lines (before and after patterning, respectively) and the chained line, the poly(Thio-HQC) electrode, in monomer-free TBAP/CH<sub>3</sub>CN solution at a scan rate of 10 mV s<sup>-1</sup>.

FTIR measurements were used to confirm that exposure to UV light during the patterning process had not affected the chemical composition of the polymer film. In this regard, **Figure 6.35** illustrates the FTIR spectrum of poly(Thio-pfp) film and poly(Thio-NTA) after patterning. This spectrum showed a number of features related to the ester film, such as a sharp band at 1770 cm<sup>-1</sup> that can be attributed to the carbonyl ester stretch, and the

band at  $995\text{ cm}^{-1}$  which was due to  $\nu(\text{C-F})$ . From this spectrum, it can be deduced that the ester groups were not affected during UV irradiation. In addition, **Figure 5.36** shows that, from the FTIR spectrum for poly(Thio-NTA), the conversion from ester to amide bonds as result of the immobilisation process has been successful. The appearance of the broad band at  $3350\text{ cm}^{-1}$  indicates the existence of hydrogen bonding because of the carboxylic groups in the polymer film (indicated by symbol \* in figure), and the disappearance of the bands at  $1770\text{ cm}^{-1}$  and  $995\text{ cm}^{-1}$  is due to the removal of the pfp group during the substitution reaction. Moreover, the emergence of the bands at  $1720\text{ cm}^{-1}$  and  $1665\text{ cm}^{-1}$  are due to the  $\nu(\text{C=O})$  stretch of carboxylic groups in the receptor compound and amide bonds, respectively (indicated by symbol + in figure). **Figure 6.36** shows the FTIR spectrum of poly(Thio-NH<sub>2</sub>) film and poly(Thio-HQC) after patterning. The amino film showed two distinctive bands at  $3200\text{ cm}^{-1}$  due to the primary NH<sub>2</sub> (indicated by symbol \* in figure). **Figure 6.36** shows the spectrum of poly(Thio-HQC) after hydrolysis and the immobilisation reaction. The emergence of the broad band at  $3350\text{ cm}^{-1}$  was due to an O-H group from the receptor molecules, whilst the appearance of the band at  $1680\text{ cm}^{-1}$  was attributed to the formation of amide bonds in the polymer film(indicated by symbol + in figure).

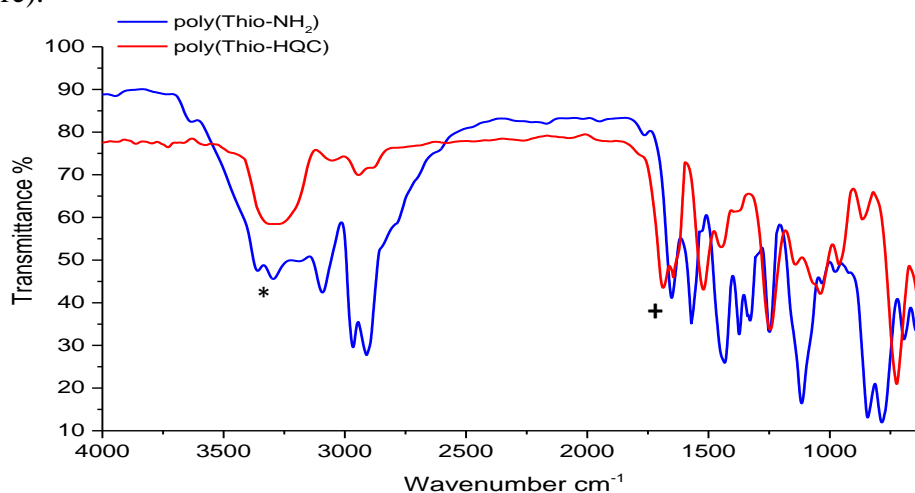


**Figure 6.36:** FTIR spectra of poly(Thio-Fmoc) film after patterning (blue line) and poly(Thio-HCQ) film (red line). \*denotes the presence of amine and + denotes the presence of carbonyl peaks.

## 6.6 Surface imaging characterisation of polymer films

### 6.6.1 Scanning Electron Microscopy (SEM)

In this section, scanning electron microscopy (SEM) was used to examine the morphology of the thiophene film derivatives. Microscopic observation of film surfaces

after deposition showed that the electrode surface was completely covered by the polymer. **Figure 6.37** shows the surface morphological structures of the derivatives of the thiophene films. These films show various morphologies due to the use of different monomer structures. All films demonstrated a regular distribution of polymer particles over the surface of the electrode.

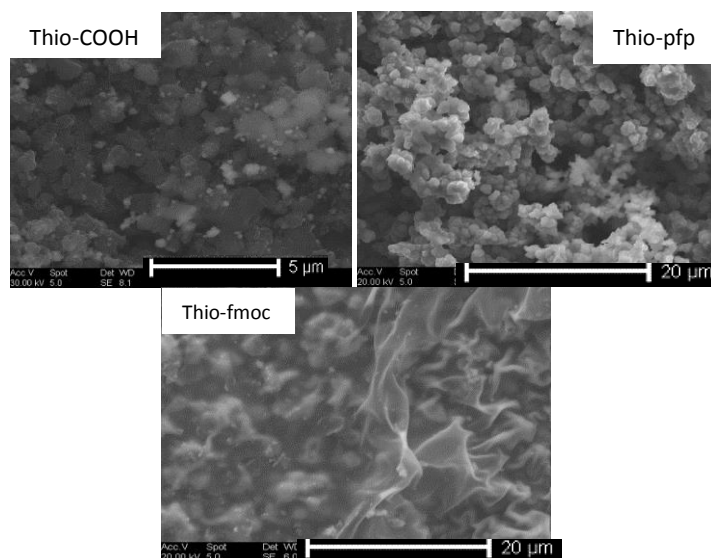


**Figure 6.37:** SEM images of surface films deposited using 0.5 M concentrations of (A) Thio-COOH, (B) Thio-pfp, and (C) Thio-Fmoc at scan rates of  $10 \text{ mV s}^{-1}$  over 10 scans.

### 6.6.2 Atomic Force Microscopy (AFM)

AFM was used to image the polymer film surface and estimate the thickness of the films derived from the different aniline monomers. In general, the use of different monomers that possess different chemical structures leads to certain differences in surface topography.<sup>53</sup> The few differences between the film surfaces here were probably related to differences in growth and nucleation features, and differences in the amount of electronic charge in the electrodeposition process. A scalpel blade was used to remove polymer films from part of electrode surface to form edge between polymer film and electrode surface, forming a step edge between the film and substrate, (panel D). Analysis of **Figure 6.38** showed that the surface thickness was equal to 170, 750 and 500 nm for Thio-COOH, Thio -pfp and Thio- fmoc respectively. AFM findings were compared with the thickness of films estimated from voltammetric and QCM data. Based on QCM data thickness of films was equal to 140, 775 and 630 nm for Thio-COOH, Thio -pfp and Thio- fmoc respectively. Naturally, the thickness from QCM data more thicker than the AFM measurements because partial collapse of films but Thio-COOH and Thio-fmoc

showed slightly less thickness than thickness which estimated by QCM data this contrast could be due to non-uniform deposition of films on electrode area.

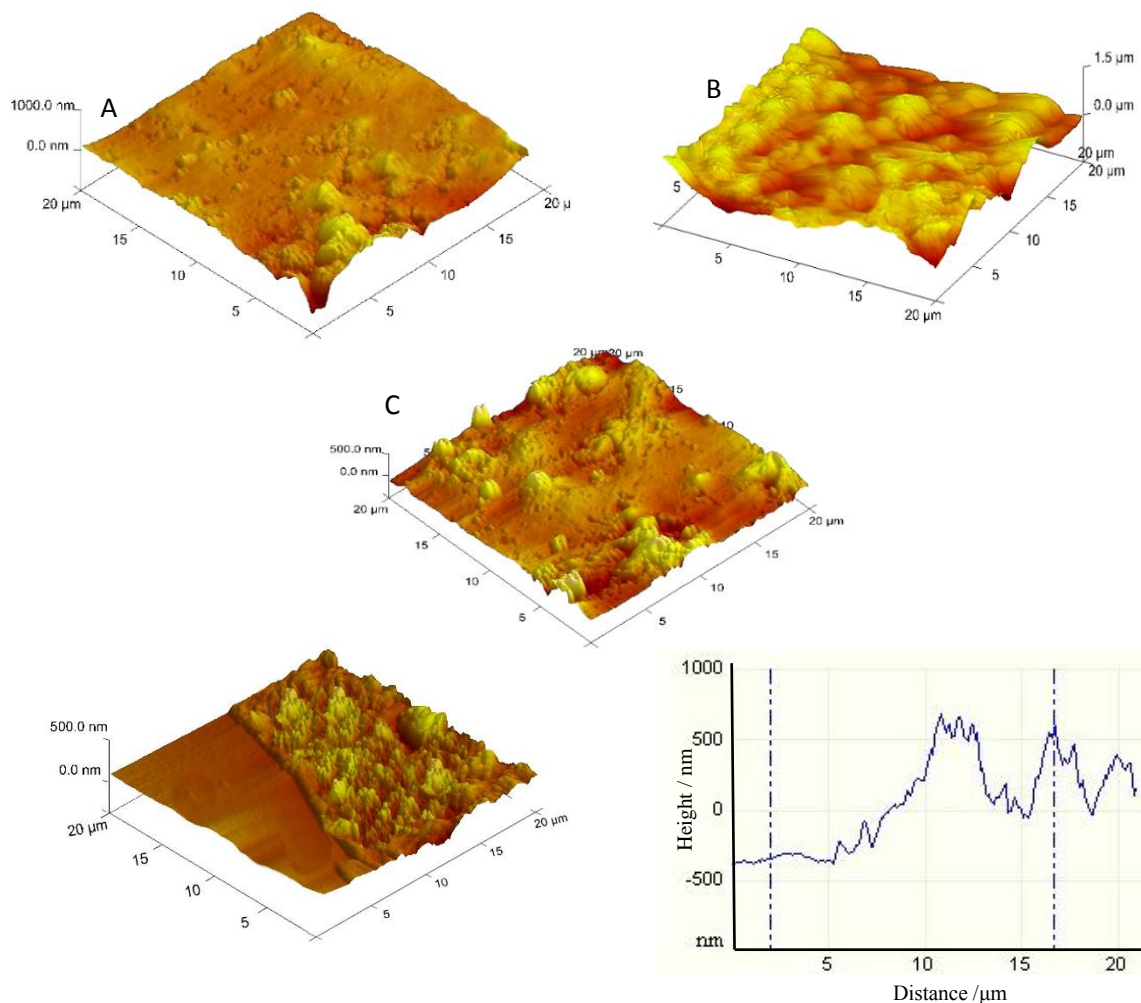


**Figure 6.38:** AFM images of dry polymers electrodeposited from 0.5 M a) Thio-COOH, b) Thio-pfp, c) Thio-Fmoc and d) thickness of polymer film on an Pt electrode using a  $10 \text{ mV s}^{-1}$  scan rate over 10 scans on a Pt electrode using a  $10 \text{ mV s}^{-1}$ .

## 6.7 Conclusions

The goal of this chapter was preparation of functionalised polythiophenes with different functional groups and study of electrochemical behaviour of these polymer films. As it is known that structure of monomers and conditions polymerisation can affect the growth and electrical properties of the polymer films. In this chapter it has been shown that composition of monomer and various functional groups have a key role during electropolymerisation process. The voltammetric findings which recorded at various scan rates ( $10 - 100 \text{ mV s}^{-1}$ ) showed that polythiophene films have a good electro-stability. The results from chronoamperometric curves show that the electropolymerisation process was that charge increased with  $t^{1/2}$  as result of having a diffusion-controlled process.

QCM and FTIR techniques were used to verify the immobilisation process through changes to the polymer film during hydrolysis and the appropriate functionalisation reaction. Data from EQCM experiments were used to estimate the mass exchange during electropolymerisation process from the slope using on Faraday's law. The gradient ( $\Delta m/\Delta q$ ) was used to calculate the  $M_{app}$  of electroactive species involved in electropolymerisation process. Results show that monomer and solvent seem to play role during polymerisation processes. Patterned poly(Ani-pfp) films were reacted with the  $N_{\alpha},N_{\alpha}$ -bis(carboxymethyl)-L-lysine, and poly(Ani-Fmoc) films and with 2-hydroxyquinoline-4-carboxylic acid. This preliminary work focused on the fundamental aspects of fabricating and characterising patterned polymer films to determine if they could maintain their joint polymer-receptor system without it collapsing due to sequential fabrication processes.

poly(Thio-pfp) and poly(Thio-Fmoc) films were hydrolysed using 0.1 M NaOH and 30% piperidine solutions, respectively. FTIR and QCM measurements were confirmed success of the hydrolysis process. Mass and surface coverage of polymer films before and after hydrolysis were calculated using Faraday's law. Solvation change resultant from entry of solvent molecules to polymer films was calculated. The difference in mass between the protected and deprotected polymer films was due to the egress of leaving groups from the films. In fact, the findings show that this difference can be explained by ingress of 16% and 25% solvent molecules into ester and amide films respectively, to fill the voids on the polymer surface for ester and amide films.

The immobilisation process was monitored using IR spectroscopy and QCM. Masses of the polymer films were calculated depending on the voltammetric responses of the film before and after the immobilisation process. This expected increase in the mass of the film was a result of the ingress of receptor groups (NTA and HQC) into the polymer films. The electrochemical voltammetric measurements for all patterned polymer surfaces confirmed that electrochemical activity (conductivity) would enable their eventual use in sensing applications. Findings above showed that the hydrolysis, immobilisation and patterning of polymer films have no effect on electroactivity of films and these processes did not led to collapse of polymer films. Patterning strategy of reactivity control could be useful for preparation of functionalised micro-fabricated polymer films.

The AFM data illustrated that polymer films have different topographic surfaces and partial collapse were occurred for some polymers due to egress of solvent molecules. AFM data showed that Thio-COOH and Thio-fmoc have thickness more than thus which were estimated by QCM and this could be attributed to non-uniform coverage of films over the deposition area or instrumental bias. Table 6.10 show the comparison between the thickness of polymer films measured by AFM, cyclic voltammetry and QCM and the differences in thickness of films due to variation of solvent ratio in polymer films.

Films	Voltammetric experiments (dry film)		Molar volume $\text{cm}^3 \text{mol}^{-1}$	QCM experiments (solvated film)		AFM $h_f/\text{cm}$	Molar volume $\text{cm}^3 \text{mol}^{-1}$
	$\Gamma/\text{mol cm}^{-2}$	$h_f/\text{cm}$		$\Delta m/\text{g}$	$h_f/\text{cm}$		
Thio-COOH	$5.5 \times 10^{-8}$	$7.1 \times 10^{-6}$	125	$4.0 \times 10^{-6}$	$1.45 \times 10^{-5}$	$1.7 \times 10^{-5}$	309
Thio -pfp	$2.6 \times 10^{-7}$	$6.7 \times 10^{-5}$	256	$2.1 \times 10^{-5}$	$7.75 \times 10^{-5}$	$7.5 \times 10^{-5}$	288
Thio -fmoc	$1.8 \times 10^{-7}$	$6.0 \times 10^{-5}$	344	$1.6 \times 10^{-5}$	$6.3 \times 10^{-5}$	$5.0 \times 10^{-5}$	278

**Table 6.10:** Thickness of polymer films measured by AFM and comparison with those calculated from cyclic voltammetry data based on Faraday law and QCM data (solvated films).

## 6.8 References

1. T.-P. Huynh, P. S. Sharma, M. Sosnowska, F. D'Souza and W. Kutner, *Progress in Polymer Science*, 2015, **47**, 1-25.
2. G. Li, G. Koßmehl, H. P. Welzel, W. Plieth and H. Zhu, *Macromolecular Chemistry and Physics*, 1998, **199**, 2737-2746.
3. G. Li, G. Koßmehl, Y. Zhang, S. Bhosale and W. Plieth, *Polymer Bulletin*, 2003, **51**, 217-224.
4. C. J. Pickett and K. S. Ryder, *Journal of the Chemical Society, Dalton Transactions*, 1994, 2181-2189.
5. C. Xue, F.-T. Luo and H. Liu, *Macromolecules*, 2007, **40**, 6863-6870.
6. Z. Nie and E. Kumacheva, *Nature Materials*, 2008, **7**, 277.
7. Y. D. Kim and J. Hone, *Nature*, 2017, **544**, 167-168.
8. H.-J. Kim, S.-H. Choi, K.-P. Lee, A. I. Gopalan, S.-H. Oh and J. Woo, *Ultramicroscopy*, 2008, **108**, 1360-1364.
9. S. Hardy, *Journal of Materials Chemistry*, 1995, **5**, 631-637.
10. C. Lete, B. Gadgil and C. Kvarnström, *Journal of Electroanalytical Chemistry and Interfacial Electrochemistry*, 2015, **742**, 30-36.
11. J. Dai, J. L. Sellers and R. E. Nofle, *Synthetic Metals*, 2003, **139**, 81-88.
12. P. S. Tóth, C. Janáky, Z. Hiezl and C. Visy, *Electrochimica Acta*, 2011, **56**, 3447-3453.
13. J. Roncali, *Chemical Reviews*, 1992, **92**, 711-738.
14. A. R. Hillman and E. F. Mallen, *Journal of Electroanalytical Chemistry and Interfacial Electrochemistry*, 1987, **220**, 351-367.
15. F. B. Li and W. J. Albery, *Langmuir*, 1992, **8**, 1645-1653.
16. Y. He, W.-j. Guo, M.-s. Pei and G.-y. Zhang, *Chinese Journal of Polymer Science*, 2012, **30**, 537-547.
17. P.-C. Nien, P.-Y. Chen and K.-C. Ho, *Sensors*, 2009, **9**, 1794-1806.
18. G. A. Sotzing, J. R. Reynolds and P. J. Steel, *Chemistry of Materials*, 1996, **8**, 882-889.
19. K. Lin, S. Ming, S. Zhen, Y. Zhao, B. Lu and J. Xu, *Polymer Chemistry*, 2015, **6**, 4575-4587.
20. H.-P. Welzel, G. Kossmehl, H.-J. Stein, J. Schneider and W. Plieth, *Electrochimica Acta*, 1995, **40**, 577-584.
21. A. R. Hillman, M. J. Swann and S. Bruckenstein, *Journal of Electroanalytical Chemistry and Interfacial Electrochemistry*, 1990, **291**, 147-162.
22. A. K. Singh and M. Singh, *Biosensors and Bioelectronics*, 2015, **74**, 711-717.
23. C. Visy, C. Janáky and E. Kriván, *Journal of Solid State Electrochemistry*, 2005, **9**, 330-336.
24. M. Skompska, A. Jackson and A. R. Hillman, *Physical Chemistry Chemical Physics*, 2000, **2**, 4748-4757.
25. H. Akbulut, M. Yavuz, E. Guler, D. O. Demirkol, T. Endo, S. Yamada, S. Timur and Y. Yagci, *Polymer Chemistry*, 2014, **5**, 3929-3936.

26. G. Li, G. Koßmehl, W. Kautek, W. Plieth, H. Zhu, H. S. O. Chan and S. Choon Ng, *Macromolecular Chemistry and Physics*, 2000, **201**, 21-30.
27. E. Ploetz, B. Visser, W. Slingenbergh, K. Evers, D. Martinez-Martinez, Y. Pei, B. Feringa, J. T. M. De Hosson, T. Cordes and W. van Dorp, *Journal of Materials Chemistry B*, 2014, **2**, 2606-2615.
28. F. Brétagnot, A. Valsesia, G. Ceccone, P. Colpo, D. Gilliland, L. Ceriotti, M. Hasiwa and F. Rossi, *Plasma Processes and Polymers*, 2006, **3**, 443-455.
29. A. Glidle, A. R. Hillman, K. S. Ryder, E. L. Smith, J. M. Cooper, R. Dalgliesh, R. Cubitt and T. Geue, *Electrochimica Acta*, 2009, **55**, 439-450.
30. M. Nasrollahzadeh, M. Jahanshahi, M. Salehi, M. Behzad and H. Nasrollahzadeh, 2013.
31. B. Senthilkumar, P. Thenamirtham and R. Kalai Selvan, *Applied Surface Science*, 2011, **257**, 9063-9067.
32. D. Pourjafari, A. Vazquez, J. Cavazos and I. Gomez, *Soft Materials*, 2014, **12**, 380-386.
33. R. Liu and Z. Liu, *Chinese Science Bulletin*, 2009, **54**, 2028-2032.
34. Z. Durmus, B. Unal, M. S. Toprak, H. Sozeri and A. Baykal, *Polyhedron*, 2011, **30**, 1349-1359.
35. M. N. Akieh, W. E. Price, J. Bobacka, A. Ivaska and S. F. Ralph, *Synthetic Metals*, 2009, **159**, 2590-2598.

## Chapter seven

## Chemical sensor applications

<b>7.1 Overview .....</b>	<b>191</b>
<b>7.2 Aims and objectives .....</b>	<b>191</b>
<b>7.3 Results and discussion .....</b>	<b>192</b>
7.3.1 Voltammetric response of Poly(Py-NTA) electrode to metal ions .....	192
7.3.1.1 Stability and influence of the sweep rate on metal complexes .....	193
7.3.1.2 Concentration dependence of the characteristic peak charge .....	195
7.3.1.3 Estimate of the molar ratio between metal ions and polymer electrode .....	196
7.3.1.4 Fitting the data to different isotherms .....	198
7.3.2 Voltammetric response of Poly(Py-HQC) to metal ions .....	202
7.3.2.1 Stability and influence of the sweep rate.....	203
7.3.2.2 Concentration dependence of the characteristic peak charge .....	205
7.3.2.3 Estimate of the molar ratio between metal ions and polymer electrode .....	205
7.3.2.4 Fitting the data to the different isotherms .....	206
7.3.3 Voltammetric response of Poly(Ani-NTA) to metal ions .....	209
7.3.3.1 Stability and influence of the sweep rate on metal complexes .....	210
7.3.3.2 Concentration dependence of the characteristic peak charge .....	212
7.3.3.3 Estimate of the molar ratio between metal ions and polymer electrode .....	212
7.3.3.4 Fitting the data to the different isotherms .....	212
7.3.4 Voltammetric response of Poly(Ani-HQC) to metal ions.....	216
7.3.4.1 Stability and influence of the sweep rate on metal complexes .....	216
7.3.4.2 Concentration dependence of the characteristic peak charge .....	218
7.3.4.3 Estimate of the molar ratio between metal ions and polymer electrode .....	219
7.3.4.4 Fitting the data to the different isotherms .....	220
7.3.5 Voltammetric response of poly(Thio-NTA) to of metal ions .....	222
7.3.5.1 Stability and influence of the sweep rate on metal complexes .....	223
7.3.5.2 Concentration dependence of the characteristic peak charge .....	224
7.3.5.3 Estimate of the molar ratio between metal ions and polymer electrode .....	227
7.3.5.4 Fitting the data to the different isotherms .....	227
7.3.6 Voltammetric response of Poly(Thio-HQC) to metal ions .....	229
7.3.6.1 Stability and influence of the sweep rate on metal complexes .....	231
7.3.6.2 Concentration dependence of the characteristic peak charge .....	232
7.3.6.3 Estimate of the molar ratio between metal ions and polymer electrode .....	233
7.3.6.4 Fitting the data to the different isotherms .....	233
<b>7.4 Conclusions.....</b>	<b>237</b>
<b>7.5 References.....</b>	<b>238</b>

## 7.1 Overview

Depending on the nature of the metal, metal ions can either play useful roles or otherwise be harmful to the environment and human health. The main concern with metal ions is that they are non-biodegradable and also contribute to the production of free radicals.<sup>1-3</sup> Hence, sensitive and rapid detection of these ions has become a critical issue in the analytical sciences, and considerable effort has been devoted to the improvement of different chemical sensors.<sup>3, 4</sup> Electrochemical sensors have been developed to detect metal ions using several interfaces such as receptor units, enzymes, and nanomaterials.<sup>1</sup> Electrochemical sensors are distinguished from other detection techniques through their high performance with sensitivity, rapid response, and their economical use.<sup>5</sup> Electroactive polymers are attractive materials for sensing applications because they can convert chemical and physical changes into electrical signals. These polymers can be modified chemically with special functional groups for use in the recognition of various analytes. Over the last two decades, modified polymer electrodes have been used abundantly in analytical applications.<sup>6, 7</sup> Conducting polymers are particularly interesting materials for the manufacture of electrochemical sensors.<sup>8-10</sup> Various chemical interactions can be accomplished on polymer surfaces to introduce special functionalities.<sup>11</sup> Scientists have shown particular interest in applying patterned surfaces, which contain special chemical functionalities that allow for their use in highly specific applications such as sensor devices, nanomedicines, food technology, and catalysis.<sup>12, 13</sup>

## 7.2 Aims and objectives

The aim of the work described in this chapter is the development of electrochemical sensors from patterned polymer electrodes which have been modified with special receptors (NTA and HQC), and to study the possibility of their use as sensing systems for certain metal cations. In this part of the study, modified electrodes formed from three types of polymers (polypyrrole, polyaniline and polythiophene) and two types of receptors, (NTA-lysine) and (2-HQC) were used to detect ions in concentrations in the range of 1 ppm - 5000 ppm. The transport processes and electrochemical behaviour occurring at the patterned electrodes have been analysed.

### 7.3 Results and discussion

This chapter describes the use of patterned functionalised polymer electrodes as chemical sensors to determine the presence of metal ions. Cyclic voltammetry was applied to study the electrochemical properties of these film electrodes in aqueous solution containing metal ions (copper, nickel and cobalt) using different scan rates (10, 20, 50 and 100 mV s<sup>-1</sup>) to examine the stability of electrode films under the conditions studied. Generally, patterned functionalised electrodes' ion recognition ability can be examined using nitrate salts of Cu<sup>2+</sup>, Ni<sup>2+</sup> and Co<sup>2+</sup>.

#### 7.3.1 Voltammetric response of Poly(Py-NTA) electrode to metal ions

This section describes the use of patterned poly(Py-NTA) electrodes to detect copper, nickel and cobalt ions using potentiodynamic measurements as a qualitative tool. This study involves the use of different concentrations of metal ions (1 ppm to 5000 ppm) with the NTA ligand. Coulometric data is used to estimate metal coverage through integration of the voltammetric responses of the complexed metal surfaces. Concentration effects and influence of scan rates on coordination binding have been examined.

NTA ligand (structure presented in **Figure 4.21**) was examined to detect Cu<sup>2+</sup>, Ni<sup>2+</sup> and Co<sup>2+</sup> in solution using electrochemical voltammetric responses. The metal ions binding with the films were determined by integration of the charge required for reduction/oxidation of the bound ions on the modified electrode. The prepared Py-NTA modified electrodes were immersed in 10 ml 100 ppm solutions of Cu(NO<sub>3</sub>)<sub>2</sub>, Ni(NO<sub>3</sub>)<sub>2</sub> and Co(NO<sub>3</sub>)<sub>2</sub> in 0.1 M potassium nitrate solution without stirring. The Py-NTA electrodes, including metal ions, were rinsed with ultra-pure water. Next, cyclic voltammetry measurements were performed directly using a metal-free solution of 0.1 M potassium nitrate with potentials ranging between -0.6 to 0.6, -0.7 to 0.6 and -0.5 to 0.7 V vs. Ag/AgCl for Cu<sup>2+</sup>, Ni<sup>2+</sup> and Co<sup>2+</sup>, respectively, at different scan rates (100, 50, 20 and 10 mV s<sup>-1</sup>). The voltammetric studies of the Py-NTA electrode were carried out using potassium nitrate as a supporting electrolyte for detection of metal ions because the pH of the KNO<sub>3</sub> was appropriate for detection experiments. **Figure 7.1** shows the cyclic voltammograms of the Py-NTA electrode obtained with a metal-free solution using 10 mV s<sup>-1</sup> (black curve). After immersion in 100 ppm metal ion solution for 20 min (curve b). A pair of current peaks at  $E_{p,a} = 0.185$  V,  $E_{p,c} = -0.096$  V for the redox of Cu<sup>2+</sup>/Cu<sup>+</sup> is shown in **Figure 7.1** (panel I).<sup>7, 14-17</sup> In addition, **Figure 7.2** (panel II) represents the

voltammetric response of the Py-NTA electrode after exposure to a  $\text{Ni}^{2+}$  ion solution with oxidation/reduction current peaks at  $E_{p,a} = 0.17 \text{ V}$ , and  $E_{p,c} = -0.056 \text{ V}$  for the redox of  $\text{Ni}^{2+}/\text{Ni}^{\circ}$ .<sup>18</sup> Furthermore, the current peaks for the Py-NTA electrode which had been immersed in a  $\text{Co}^{2+}$  ion solution appeared at  $E_{p,a} = 0.20 \text{ V}$ ,  $E_{p,c} = -0.021 \text{ V}$ , as shown in **Figure 7.3** (panel III).<sup>18</sup> The emergence of these current peaks in the voltammetric curves were considered evidence of the successful binding of each of these three metal ions to the modified electrode surface. Moreover, to confirm that the current peaks occurred due to the formation of metal complexes, the voltammetric measurements were applied to a film electrode (Py-NTA) with blank solution (metal ion free) under the same conditions shown in the figures (black curve). From this, it can be demonstrated that the film electrode will not give any peak currents as result of there being no metal ions in the solution and there is no redox reaction of polymer within this potential window. Thus, the voltammetric response of the electrode to metal ions is attributed to the interaction between py-NTA and metal ions.

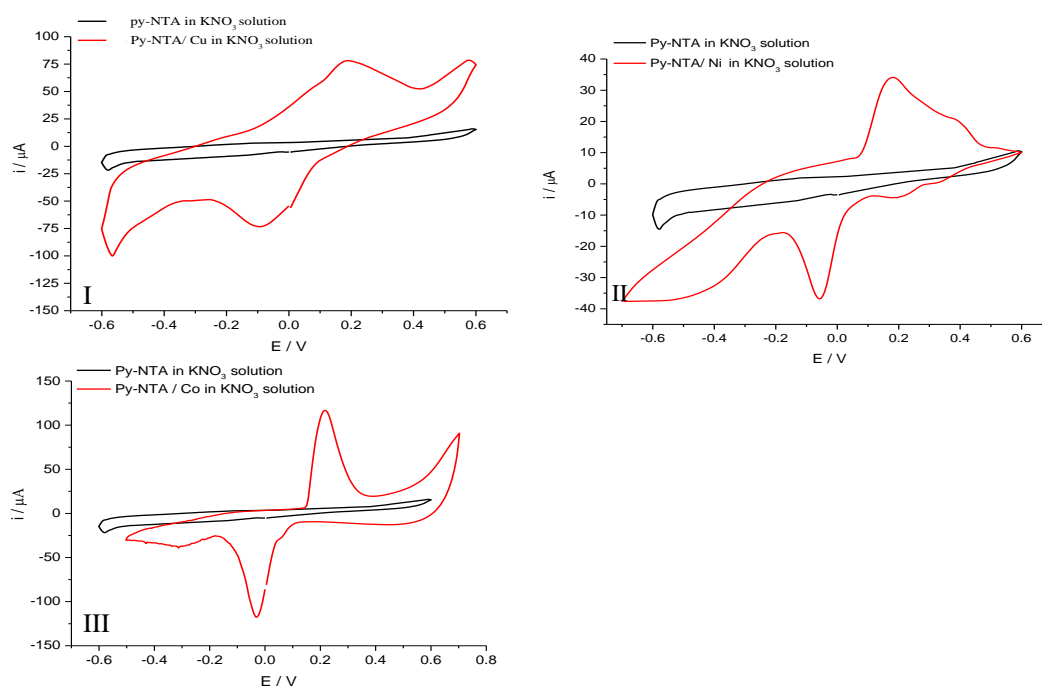


**Figure 7.1:** Cyclic voltammogram of Py-NTA modified electrode (black curve) in metal-free  $\text{KNO}_3$  solution at  $10 \text{ mV s}^{-1}$ , (red curve) Py-NTA electrode in  $\text{KNO}_3$  solution after exposure to 100 ppm of metal ions solution: I)  $\text{Cu}^{2+}$  II)  $\text{Ni}^{2+}$  III)  $\text{Co}^{2+}$  at  $100 \text{ mV s}^{-1}$ .

### 7.3.1.1 Stability and influence of the sweep rate on metal complexes

Cyclic voltammogram experiments were repeated for Py-NTA electrode using a metal ion-free solution over ten cycles, as shown in **Figure 7.2**. It may be noted that the voltammograms of the film electrode decreased over the first and second cycles, but after

the third cycle stable voltammograms were obtained with no subsequent change in peak potentials and only a slight decrease in peak current. It may also be noted that a stable voltammetric response was recorded during the fourth to tenth cycles in the blank electrolyte solution as result of the formation of a stable complex at the film surface. These results indicate that  $\text{Cu}^{2+}$  ions remain strongly bound to the ligand at the electrode surface within the potential range of the experiment.

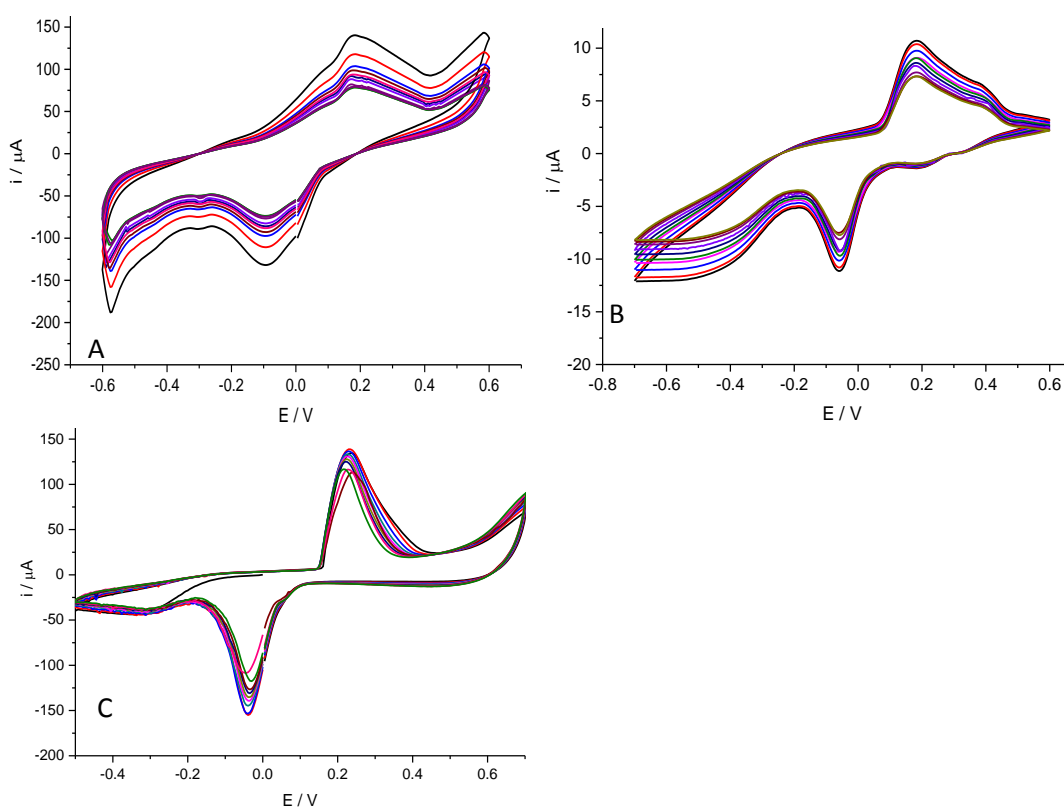


**Figure 7.2:** Cyclic voltammograms of Py-NTA-modified electrode in 0.1 M  $\text{KNO}_3$ , after adsorbing A)  $\text{Cu}^{2+}$  ions, B)  $\text{Ni}^{2+}$  ions, and C)  $\text{Co}^{2+}$  ions (100 ppm). From the first to the tenth cycles, the scan rate used was  $100 \text{ mV s}^{-1}$ .

The stability of the cyclic voltammograms recorded for the three metals at different scan rates, from 10 to  $100 \text{ mV s}^{-1}$ , is shown in **Figures 7.3, 7.4, and 7.5** for copper, nickel and cobalt, respectively. It can be seen from panel B in each of these figures that the peak currents increased linearly with increasing sweep rate for the redox reaction, indicating a surface redox reaction. The comparison between surface coverage of metal ions ( $\Gamma_m$ ) and surface coverage of ligand ( $\Gamma_p$ ) was calculated in the section 7.3.1.3.

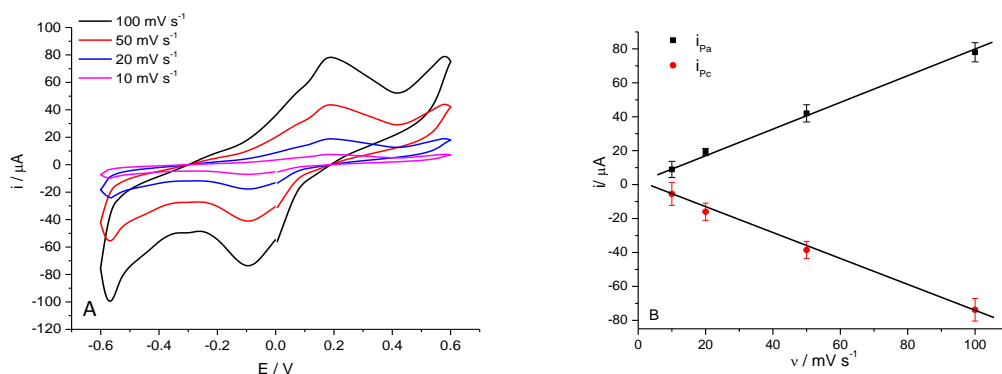


**Figure 7.3:** A) Influence of scan rate (from 10 to 100  $\text{mV s}^{-1}$ ) on the  $\text{Cu}^{2+}/\text{Cu}^0$  peak current in 0.1 M  $\text{KNO}_3$  solution B) Variation of anodic and cathodic peak currents vs. scan rate. Electrode area =  $0.11\text{cm}^2$

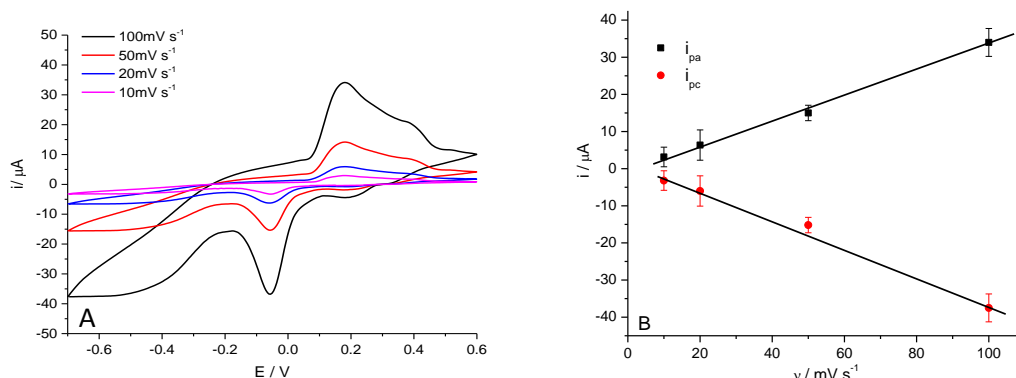


**Figure 7.4:** A) Influence of scan rates (from 10 to 100  $\text{mV s}^{-1}$ ) on the  $\text{Ni}^{2+}/\text{Ni}^0$  peak current in 0.1 M  $\text{KNO}_3$  solution B) Variation of anodic and cathodic peak currents vs. scan rate. Electrode area =  $0.11\text{cm}^2$

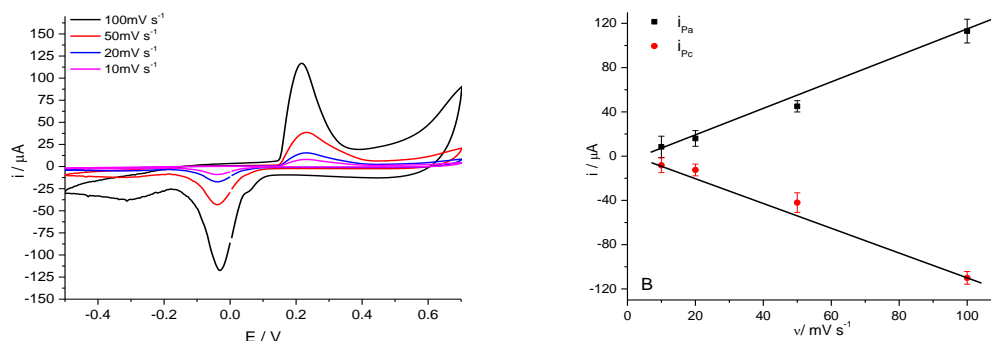


**Figure 7.5:** A) Study influence of scan rates (from 10 to 100  $\text{mV s}^{-1}$ ) on the  $\text{Co}^{2+}/\text{Co}^0$  peak current in 0.1 M  $\text{KNO}_3$  solution B) Variation of anodic and cathodic peak currents vs. scan rate. Electrode area =  $0.11\text{cm}^2$

### 7.3.1.2 Concentration dependence of the characteristic peak charge

Using the same the procedures described above, the relation between the peak redox current and metal ion concentration was studied. **Figures 7.6, 7.7, and 7.8** show the cyclic voltammograms obtained with a Py-NTA-modified electrode with different  $\text{Cu}^{2+}$ ,  $\text{Ni}^{2+}$  and  $\text{Co}^{2+}$  concentrations from 1 to 5000 ppm. It is clear from these figures that the peak

redox currents increased with increasing concentration of metal ions. The total charge density value of copper at 5000 ppm was  $4500 \mu\text{C cm}^{-2}$ , corresponding to a copper of  $19.7 \text{ nmol cm}^{-2}$  and charge density of  $\text{Ni}^{2+}$  ions at saturation coverage surface was  $3000 \mu\text{C cm}^{-2}$ , corresponding to a nickel was  $15.8 \text{ nmol cm}^{-2}$ , as shown in **Figure 7.6** panel B. However, the charge density, as obtained from the voltammetric responses of  $\text{Co}^{2+}$  ions at 5000 ppm, was equal to  $3550 \mu\text{C cm}^{-2}$ , corresponding to a cobalt coverage of  $15.1 \text{ nmol cm}^{-2}$ , as shown in **Figure 7.6** panel C. The lowest metal ion concentration detected was 1 ppm.

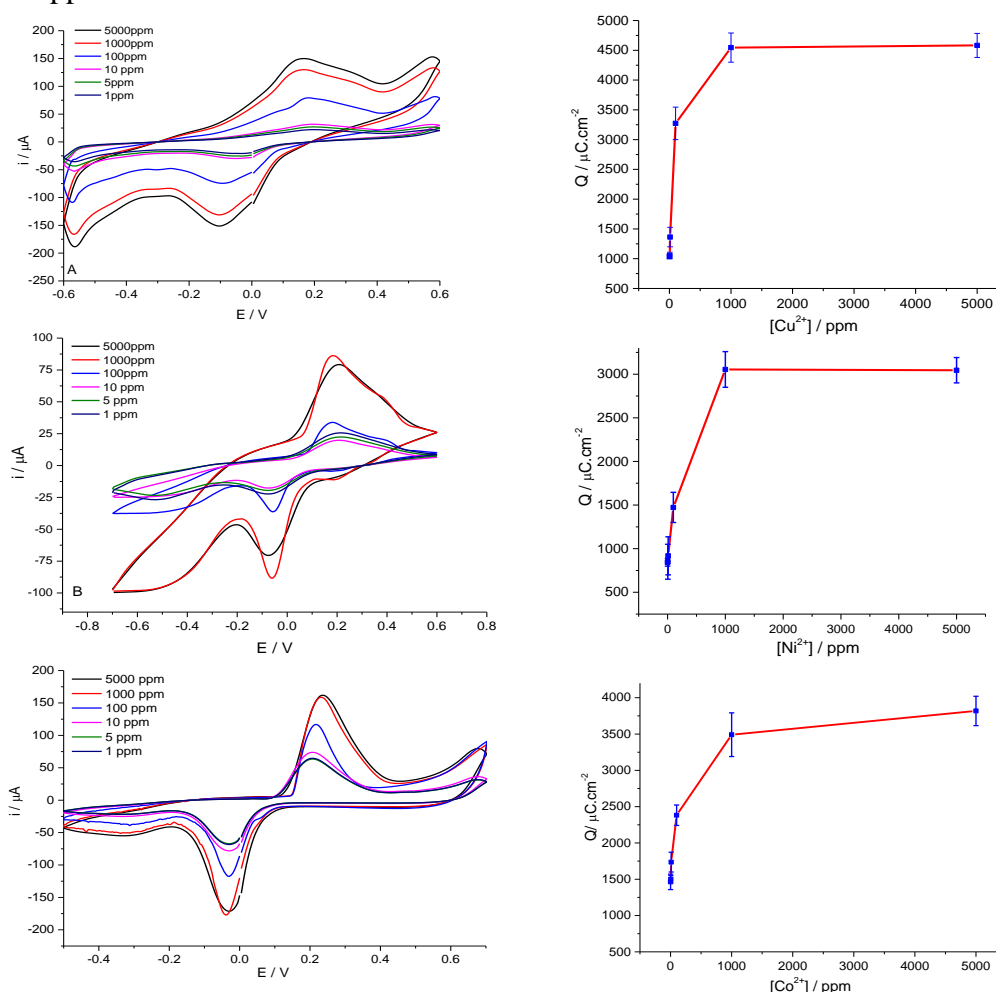


**Figure 7.6:** A) Cyclic voltammograms in blank  $\text{KNO}_3$  solution for a Py-NTA-modified electrode, as exposed to 1 ppm to 5000 ppm A)  $\text{Cu}^{2+}$ , B)  $\text{Ni}^{2+}$  and C)  $\text{Co}^{2+}$  at a scan rate of  $100 \text{ mV s}^{-1}$ . Electrode area =  $0.11 \text{ cm}^2$ .

### 7.3.1.3 Estimate of the molar ratio between metal ions and polymer electrode

The surface coverage of metal ions ( $\Gamma_m$ ) was estimated by the integration of the peaks using Faraday's laws. **Table 7.1** shows the coverage of metal ions and the mole ratio ( $\Gamma_m / \Gamma_{\text{polymer}}$ ) between metal ions and Py-NTA. From the data in the table, it may be noted

that the saturated surface coverage of the three metal ions on the Py-NTA electrode obtained from 1000 and 5000 ppm solution was varied, at 19.7, 15.8, and 15.1 nmol cm<sup>-2</sup> for Cu<sup>2+</sup>, Ni<sup>2+</sup> and Co<sup>2+</sup>, respectively. The surface coverage of the ligand film (after functionalisation) was estimated using equation 2.4 ( $\Gamma = Q/nFA$ ) to be 20.5 nmol cm<sup>-2</sup> using charge integration from cyclic voltammetry which was recorded at 100 mV s<sup>-1</sup> with monomer free solution (TBAP /CH<sub>3</sub>CN).

Metal	Concentration	charge / C	$\Gamma_m$ (nmol.cm <sup>-2</sup> )	Molar ratio $\Gamma_m/\Gamma_{\text{polymer}}$
Cu <sup>2+</sup>	5000 ppm	4.2x 10 <sup>-4</sup>	19.7	0.96
	1000 ppm	4.0 x 10 <sup>-4</sup>	18.8	0.92
	100 ppm	2.5 x 10 <sup>-4</sup>	11.8	0.57
	10 ppm	1.3 x 10 <sup>-4</sup>	6.12	0.29
	5 ppm	1.13 x 10 <sup>-4</sup>	5.3	0.26
	1 ppm	1.04 x 10 <sup>-4</sup>	4.7	0.23
Ni <sup>2+</sup>	5000 ppm	3.35 x 10 <sup>-4</sup>	15.8	0.77
	1000 ppm	3.34 x 10 <sup>-4</sup>	15.7	0.76
	100 ppm	1.62 x 10 <sup>-4</sup>	7.6	0.78
	10 ppm	1.01 x 10 <sup>-4</sup>	4.7	0.23
	5 ppm	9.35 x 10 <sup>-5</sup>	4.4	0.21
	1 ppm	9.28 x 10 <sup>-5</sup>	4.37	0.21
Co <sup>2+</sup>	5000 ppm	3.2 x 10 <sup>-4</sup>	15.10	0.74
	1000 ppm	2.84 x 10 <sup>-4</sup>	13.4	0.65
	100 ppm	1.65 x 10 <sup>-4</sup>	7.80	0.38
	10 ppm	1.41 x 10 <sup>-4</sup>	6.65	0.32
	5 ppm	1.04x 10 <sup>-4</sup>	4.95	0.24
	1 ppm	1.02x 10 <sup>-4</sup>	4.80	0.23

**Table 7.1:** Charge values, surface coverage and the molar ratio for metals/Py-NTA-modified electrode at various concentrations. Scan rate was fixed at 100 mV s<sup>-1</sup>. The surface coverage of the polymer film was estimated to be 20.5 nmol cm<sup>-2</sup>.

Repeated use of the electrode for detection of metal ions requires the reactivation of the modified electrode. This can be achieved using EDTA solution, where the coordinated metal ions were easily removed from the Py-NTA film electrode by immersion of the NTA/metal in 0.1 M EDTA solution for a few minutes and then washing with pure water. A cyclic voltammogram recorded for Py-NTA after regeneration (using EDTA) was almost identical to the cyclic voltammogram of the Py-NTA electrode before reaction with copper ions, as shown in **Figure 7.1** (red curve). This voltammetric response indicates that the incorporated copper ions had been completely removed from the Py-NTA-modified electrode, as shown in **Figure 7.7** (for copper ions in this example). Then,

the regenerated Py-NTA can be used for the determination of metal ions without any appreciable decline in the electroactivity of the modified electrode.

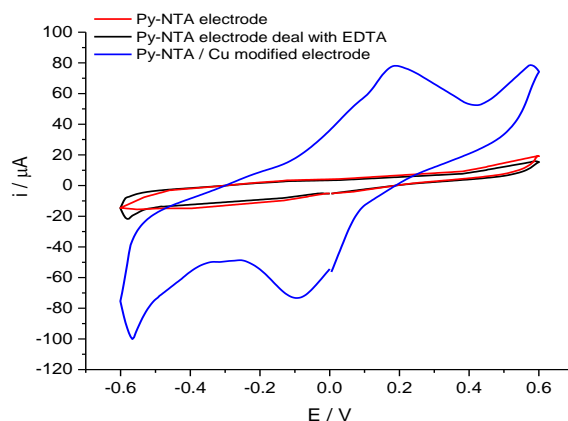


**Figure 7.7:** Cyclic voltammogram of the Py-NTA-modified electrode, red curve: Py-NTA in  $KNO_3$  solution, black curve) after treating with 0.1 M EDTA, and blue curve Py-NTA in  $KNO_3$  solution after exposure to 100 ppm  $Cu^{2+}$ .

#### 7.3.1.4 Fitting the data to different isotherms

In this part of study, the adsorption isotherms of the metal ions were investigated, and four isotherm modes (*Langmuir*, *Temkin*, *Freundlich*, and *Frumkin*) were selected to examine the experimental data.<sup>19, 20</sup> **Table 7.2** shows the mathematical forms for these models. The Langmuir isotherm model was developed to explain the adsorption of species on activated carbon in the gas phase.<sup>21</sup> The second model used was the Freundlich isotherm, which is widely used in heterogeneous systems and organic compounds<sup>21, 22</sup> The third model was the Temkin isotherm, which was applied to study the effects of adsorbate interactions on isotherms.<sup>23</sup> Finally, the Frumkin isotherm was applied, which is often used for the study of non-ionic surfactants.<sup>22</sup> These four models were applied to the experimental findings. The changes in charge over a range of different concentrations (1 - 5000 ppm) were utilized to draw all experimental data, as shown in **Figures 7.8, 7.9,** and **7.10** for  $Cu^{2+}$ ,  $Ni^{2+}$  and  $Co^{2+}$ , respectively. The four models above were applied to select the isotherm model that gave the better adsorption. The results extracted from the figures show that the Frumkin isotherm offered the best fitting for the adsorption of all metal ions with the polymer electrode depending on the R-value, with the results arranged from best to least appropriate isotherm as follows: Frumkin > Freundlich > Temkin > Langmuir.

Isotherm model	Mathematical Equation	Assumptions
Langmuir	$\frac{1}{\theta} = 1 + \frac{1}{KC}$	Monolayer and homogenous surface No interactions between sites
Freundlich	$\ln\theta = \frac{1}{n} \ln C + \ln K$	Rough and heterogeneous surface No interactions between sites
Temkin	$\theta = \frac{1}{x} \ln K + \frac{1}{x} \ln C$	Interactions between sites
Frumkin	$\ln \left[ \frac{\theta}{(1-\theta)C} \right] = \ln K + a\theta$	Interactions between sites

**Table 7.2:** The mathematical models for the different types of isotherm model.  $\theta$  = fractional surface coverage of sites (estimated by dividing every charge for every concentration by the maximum charge for saturation with metal ions).  $K$  = binding constant,  $C$  = concentration metal ions; and  $x, a$  = molecular interaction constant.

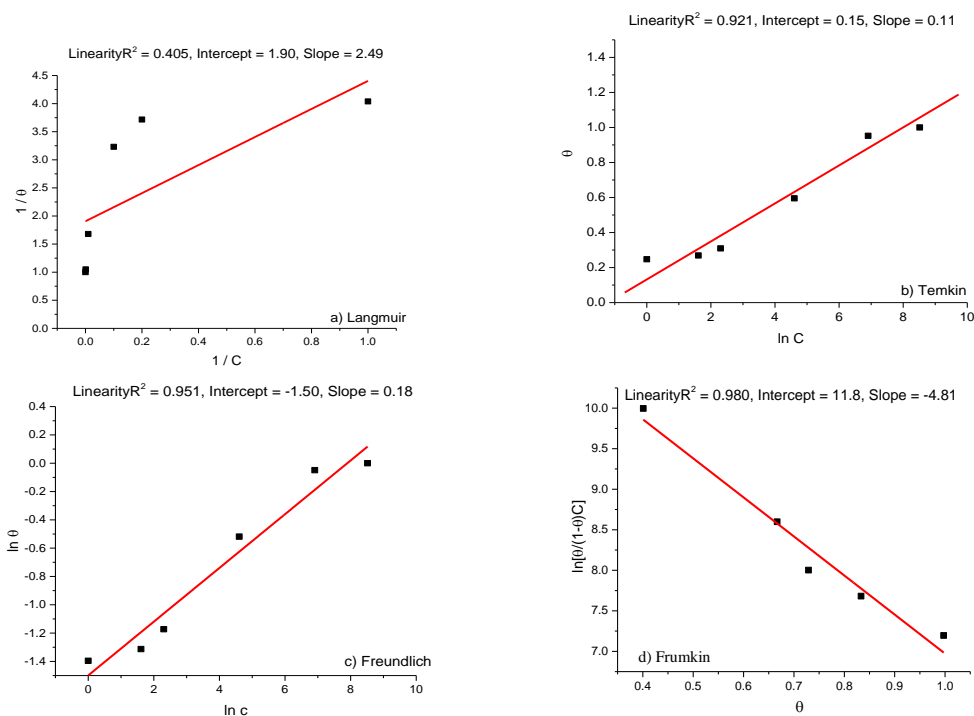


**Figure 7.8:** Plots of four isotherms: a) Langmuir isotherm, b) Temkin isotherm, c) Freundlich isotherm, and d) Frumkin isotherm for binding between copper and the Py-NTA electrode.

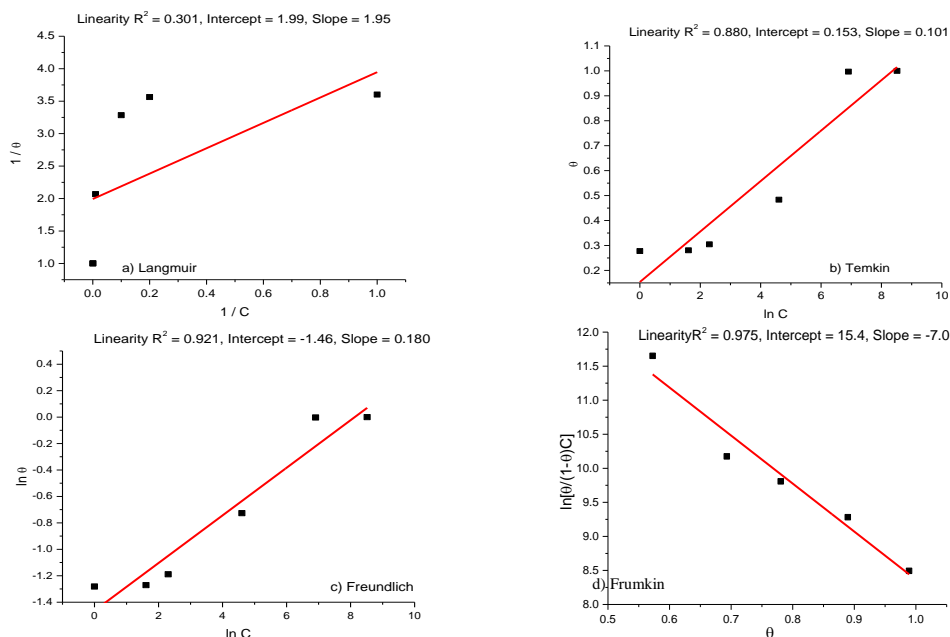


**Figure 7.9:** Plots of four isotherms: a) Langmuir isotherm, b) Temkin isotherm, c) Freundlich isotherm, and d) Frumkin isotherm for binding between Nickel and Py-NTA electrode.

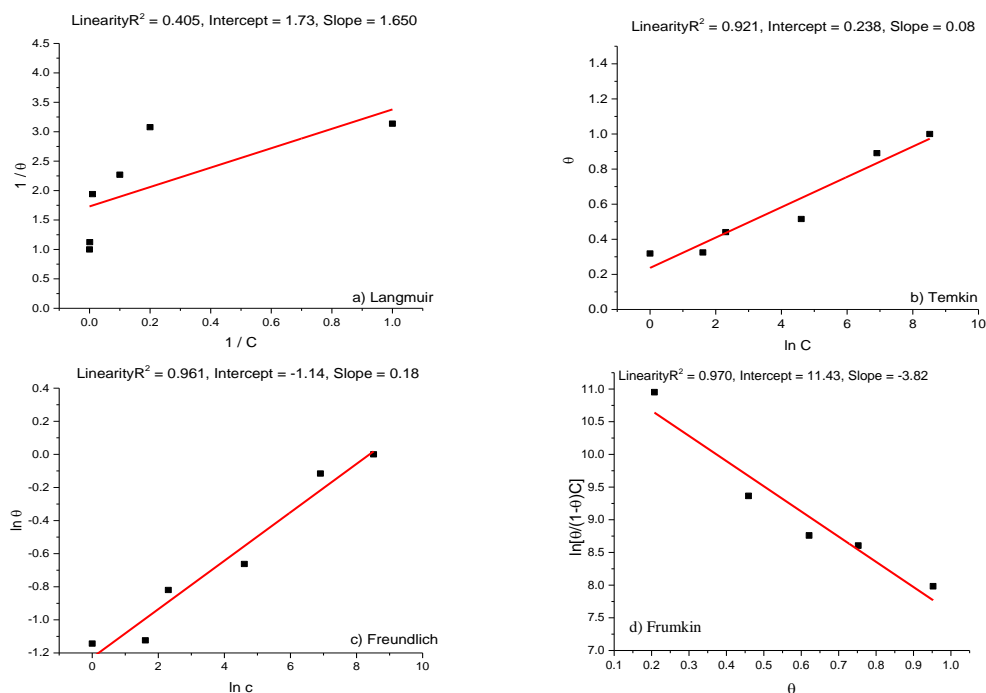


**Figure 7.10:** Plots of four isotherms: a) Langmuir isotherm, b) Temkin isotherm, c) Freundlich isotherm, and d) Frumkin isotherm for binding between cobalt and Py-NTA electrode.

The metal ions have a relative similar properties and have a different redox chemistry that be appeared in the voltammogram. With the polymer system it show the same effect for all ions. The Langmuir isotherm was lowest one due to it assumed that homogeneous surface has an equivalent sites and no interactions will be occurred between these sites

and this not fitting with polymer which has functional groups close together and so it can be used another isotherm model to analysis the results. While, Frumkin has a good fit with experimental data because it assumes these are heterogeneous surfaces with ability to interactions between sites on surface. Since Frumkin isotherm gave best fitting, characteristic parameters  $K$  and  $a$  can be calculated for each metal ions using this equation, where  $K$  represents the adsorption constant and  $a$  a molecular interaction constant, as reported in **Table 7.3**. The binding constant of adsorption,  $K$ , is related to the standard free energy  $\Delta G^\circ$  by the equation:  $\Delta G^\circ = -RT \ln K$ , where  $R$  is the universal gas constant ( $8.314 \text{ J mol}^{-1} \text{ K}^{-1}$ ) and  $T$  is absolute temperature. The thermodynamics of adsorption can provide useful evidences about the nature of adsorption process. Where the negative value of  $\Delta G^\circ$  indicates that the adsorption was spontaneous process and takes place via chemical adsorption because the adsorption free energy is more negative than  $25 \text{ kJ mol}^{-1}$  for all isotherms as mentioned in **Table 7.3**. The variations in observed negative values of  $a$  (interaction parameter) for all isotherms indicates that there is force of repulsion between adsorbed species. These  $a$ -values can be effected by coulombic and steric influences.

Metal ions	$\ln K$	$10^6 K / \text{M}^{-1}$	$\log K$	$a$	$\Delta G^\circ \text{ K J.mol}^{-1}$
Copper	11.8	0.13	5.1	-4.8	-29.5
Nickel	12.2	0.19	5.2	-7.0	-30.5
Cobalt	11.4	0.09	4.9	-3.8	-28.5

**Table 7.3:** Values of calculated  $a$ ,  $\log K$  and  $\Delta G$  parameters for metal binding to the Py-NTA electrode based on the Frumkin isotherm.

The experimental binding constant calculated using Frumkin equation was compared with the binding constant values for metal ions complexes with succinic acid, propane-1,2,3-tricarboxylic acid and NTA (nitrilotriacetic acid) in aqueous solution, as shown in **Table 7.4**.<sup>24</sup> These values of  $\log K$  calculated from the experimental data were bigger than succinic acid and propane-1,2,3-tricarboxylic acid because the NTA ligand has a nitrogen atom can interact with the metal ions. Furthermore, experimental results ( in the **Table 7.3**) show that NTA in solution has bigger binding constant because in modified electrode the ligand was restricted into polymer film surface, while values from literature relate to the free ligands in aqueous media meaning more freedom for complexation to occur.

Metal ions \ Ligand	<i>log K</i>		
	Succinic acid	Propane tricarboxylic acid	NTA
Copper	2.6	2.5	11.5
Nickel	1.6	2.4	11.5
Cobalt	1.7	1.6	10

**Table 7.4:** Values of *log K* for metal binding to the in aqueous solution for different carboxylic ligands

### 7.3.2 Voltammetric response of Poly(Py-HQC) to metal ions

This section describes the use of patterned poly(Py-HQC) electrodes for the qualitative detection of metal ions (copper, nickel and cobalt) in aqueous solution. This study involves the same procedures described in section 7.3.1. From this experimental data, the metal coverage can be estimated through integration of the voltammetric responses of the complex film surfaces. (HQC) was studied as a recognition element for  $\text{Cu}^{2+}$ ,  $\text{Ni}^{2+}$  and  $\text{Co}^{2+}$  in solution using the electrochemical voltammetric technique. The Py-HQC-modified electrodes were placed in 10 ml of 100 ppm metal nitrate solutions,  $\text{Cu}(\text{NO}_3)_2$ ,  $\text{Ni}(\text{NO}_3)_2$  and  $\text{Co}(\text{NO}_3)_2$ , in 0.1 M  $\text{KNO}_3$  without stirring. The Py-NTA/metal electrodes were rinsed with ultra-pure water and then cyclic voltammetry was applied directly using 0.1 M  $\text{KNO}_3$  solution with potentials ranging between -0.75 to 0.70, -0.75 to 0.65 and -0.50 to 0.50 V vs. Ag/AgCl for  $\text{Cu}^{2+}$ ,  $\text{Ni}^{2+}$  and  $\text{Co}^{2+}$ , respectively, at different scan rates (10, 20, 50 and 100  $\text{mV s}^{-1}$ ).

**Figure 7.11** depicts the cyclic voltammograms for the Py-HQC electrode obtained with  $\text{KNO}_3$  solution using 10  $\text{mV s}^{-1}$  (black curve). From this, it can be demonstrated that the film electrode will not give any peak currents as result of there being no metal ions in the solution and there is no redox reaction of polymer within this potential window. After the reaction step with 100 ppm metal ion solutions for 20 min (red curve). The current peaks at ( $E_{p,a} = 0.157$  V,  $E_{p,c} = -0.175$  V) for the redox of  $\text{Cu}^{2+}/\text{Cu}^{\circ}$  are shown in **Figure 7.11** (panel I). In addition, **Figure 7.11** (panel II) displays the voltammetric response of the modified electrode having been immersed in the  $\text{Ni}^{2+}$  ions solution with peak currents at  $E_{p,a} = 0.126$  V and  $E_{p,c} = -0.127$  V for the  $\text{Ni}^{2+}/\text{Ni}^{\circ}$  couple.<sup>18</sup> Furthermore, a pair of current peaks for the Py-HQC electrode due to the reaction with the  $\text{Co}^{2+}$  ion solution were found at  $E_{p,a} = 0.26$  V and  $E_{p,c} = 0.10$  V, as shown in **Figure 7.11** (panel III). The appearance of the above current peaks in the voltammetric response curves were

considered proof of the successful formation of coordination bonds between each of the three metal ions and the modified electrode surface.

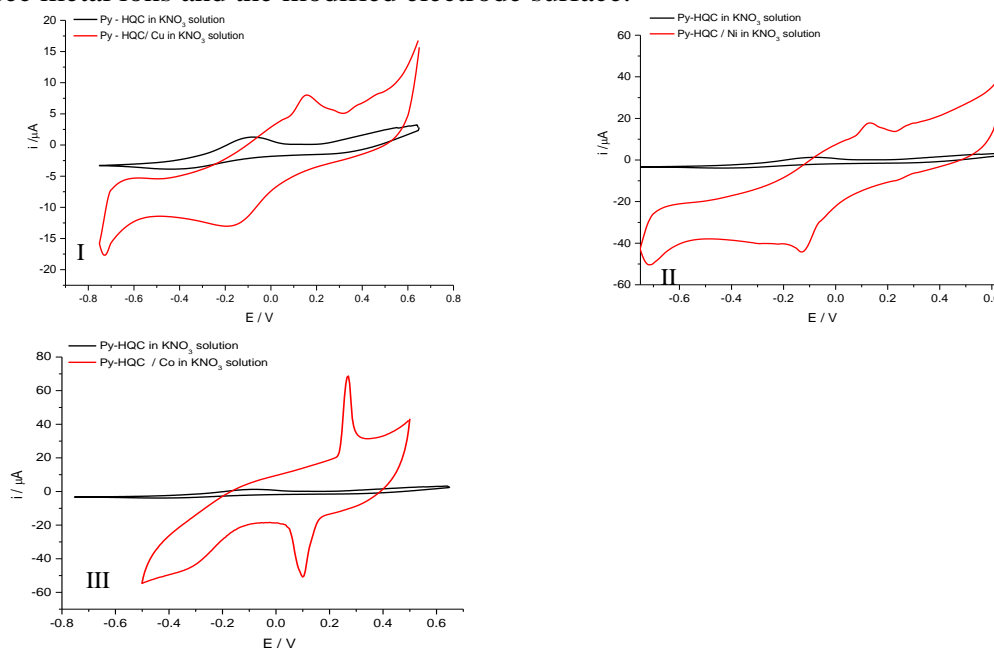


**Figure 7.11:** Cyclic voltammogram of the Py-HQC electrode (black curve) in metal free  $\text{KNO}_3$  solution at  $10 \text{ mV s}^{-1}$ , (red curve) Py-HQC electrode in  $\text{KNO}_3$  solution after exposed it to 100 ppm of metal ions solution: I)  $\text{Cu}^{2+}$  II)  $\text{Ni}^{2+}$  III)  $\text{Co}^{2+}$  at  $100 \text{ mV s}^{-1}$ .

### 7.3.2.1 Stability and influence of the sweep rate

**Figure 7.12** depicts the cyclic voltammograms of a Py-HQC electrode obtained with  $\text{KNO}_3$  solution (curve a) and after exposure to 100 ppm metal ion solution for 20 min (curve b). The current peaks at  $E_{p,a} = 0.157 \text{ V}$  and  $E_{p,c} = -0.175 \text{ V}$  for the  $\text{Cu}^{2+}/\text{Cu}^\circ$  couple are shown in **Figure 7.13** (panel I). In addition, **Figure 7.12** (panel II) displays the voltammetric response of the modified electrode having been immersed in the  $\text{Ni}^{2+}$  ion solution with peak currents at  $E_{p,a} = 0.126 \text{ V}$  and  $E_{p,c} = -0.127 \text{ V}$  for the  $\text{Ni}^{2+}/\text{Ni}^\circ$  couple. Furthermore, the pair of current peaks for the Py-HQC electrode that was reacted with  $\text{Co}^{2+}/\text{Co}^\circ$  ions solution emerged at  $E_{p,a} = 0.26 \text{ V}$  and  $E_{p,c} = 0.10 \text{ V}$ , as shown in **Figure 7.12** (panel III). The appearance of the above current peaks in the voltammetric response curves were considered proof of the successful coordination of the three metal ions with the modified electrode surface.

Stability of the cyclic voltammograms for the three complexes formed was recorded over 10 cycles using various scan rates ranging from  $10$  to  $100 \text{ mV s}^{-1}$ , as shown in **Figures 7.13, 7.14, and 7.15** for copper, nickel and cobalt, respectively. It can be seen from panel

B in each of these figures that their peak currents increased linearly with increasing sweep rate, indicating a surface redox reaction.

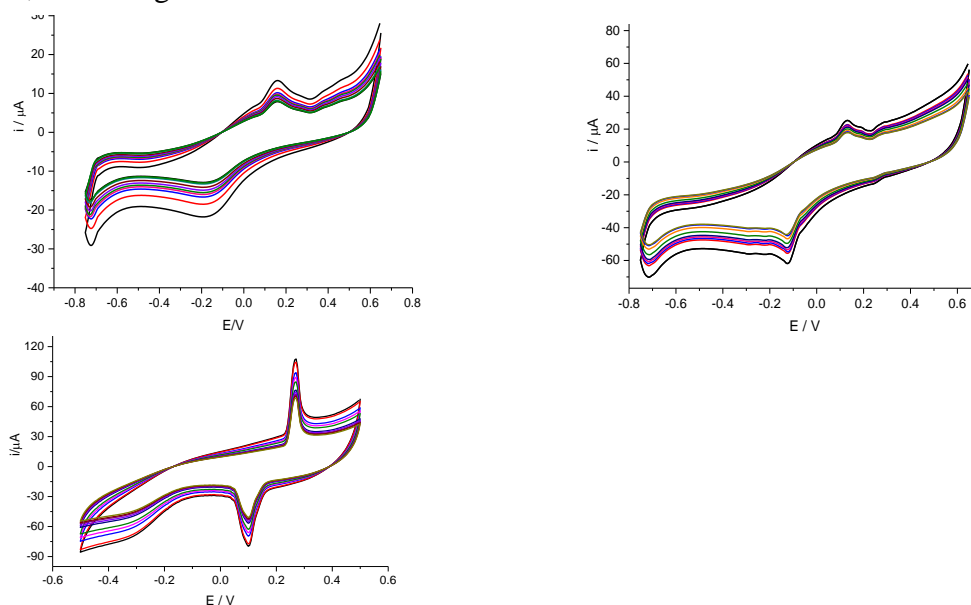


**Figure 7.12:** Cycling voltammograms of Py-HQC modified electrode, after adsorbing A)  $\text{Cu}^{2+}$  ions, B)  $\text{Ni}^{2+}$  ions, and C)  $\text{Co}^{2+}$  ions (100 ppm), in 0.1M  $\text{KNO}_3$ . From first to 10th cycles, scan rate  $100 \text{ mV s}^{-1}$ .

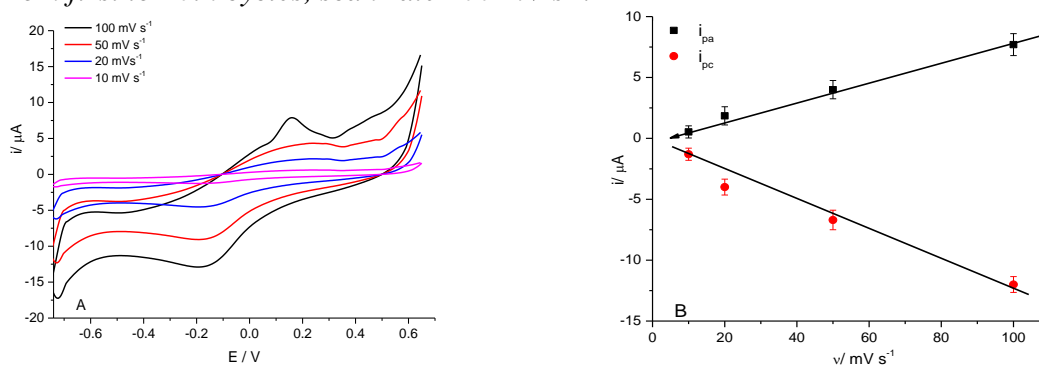


**Figure 7.13:** Influence of scan rates (from 10 to  $100 \text{ mV s}^{-1}$ ) on the  $\text{Cu}^{2+/0}$  peak current in 0.1 M  $\text{KNO}_3$  solution. B) Variation of anodic and cathodic peak currents vs. scan rate. Electrode area  $=0.11 \text{ cm}^2$

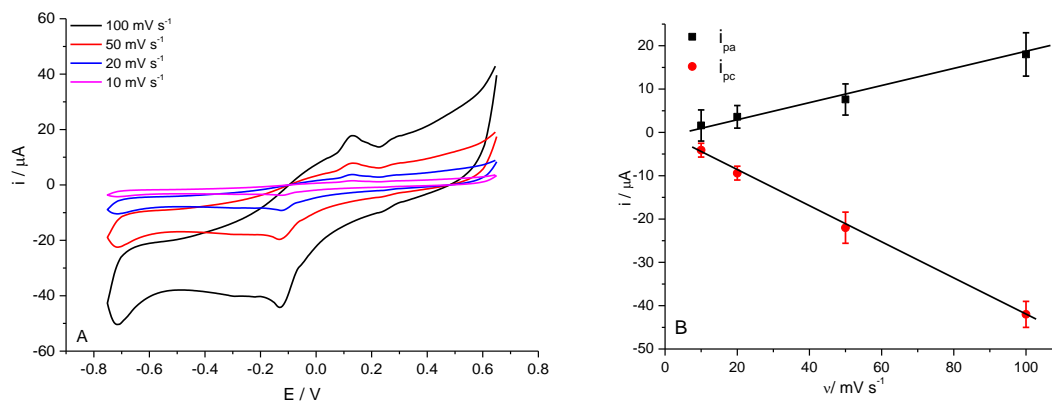


**Figure 7.14:** A) A study of the influence of scan rates (from 10 to  $100 \text{ mV s}^{-1}$ ) on the  $\text{Ni}^{2+/0}$  peak current in 0.1 M  $\text{KNO}_3$  solution. B) Variation of anodic and cathodic peak currents vs. scan rate. Electrode area  $=0.11 \text{ cm}^2$

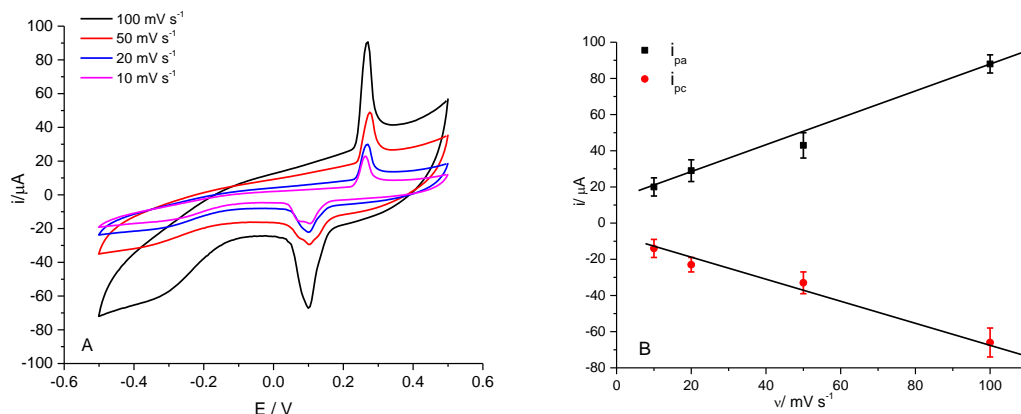


**Figure 7.15:** A) A study of the influence of scan rates (from 10 to 100  $\text{mV s}^{-1}$ ) on the  $\text{Co}^{2+/\circ}$  peak current in 0.1 M  $\text{KNO}_3$  solution. B) Variation of anodic and cathodic peak currents vs. scan rate. Electrode area =  $0.11\text{cm}^2$

### 7.3.2.2 Concentration dependence of the characteristic peak charge

Py-HQC can be studied using the same the procedures for Py-NTA. **Figures 7.16** shows the voltammogram response recorded for film exposed to different  $\text{Cu}^{2+}$ ,  $\text{Ni}^{2+}$  and  $\text{Co}^{2+}$  concentrations. Inset show a calibration curve for the detection of copper by the film electrode. The charge density was  $2100\ \mu\text{C cm}^{-2}$  at 5000 ppm, corresponding to a copper ion coverage of  $11\ \text{nmol cm}^{-2}$  on the electrode, whereas the charge density for nickel ions was  $2375\ \mu\text{C cm}^{-2}$  at 5000 ppm, corresponding to a nickel coverage of  $12.3\ \text{nmol cm}^{-2}$ , as illustrated in **Figure 7.16**. The charge density obtained from the voltammetric responses of cobalt ions was equal to  $1500\ \mu\text{C cm}^{-2}$  at saturation coverage, corresponding to a cobalt coverage  $8.7\ \text{nmol cm}^{-2}$ , as shown in **Figure 7.16**.

### 7.3.2.3 Estimate of the molar ratio between metal ions and polymer electrode

Faraday's law was applied to estimate the surface coverage of metal ions ( $\Gamma_m$ ). **Table 7.5** presents the coverage surface values of metal ions and the molar ratios ( $\Gamma_m / \Gamma_{\text{polymer}}$ ). From these experimental findings it can be noted that the saturation surface coverage of three metal ions on Py-HQC film electrodes obtained from the 1000 and 5000 ppm solutions was varied at 11, 12.3, and  $8.7\ \text{nmol cm}^{-2}$  for  $\text{Cu}^{2+}$ ,  $\text{Ni}^{2+}$  and  $\text{Co}^{2+}$ , respectively. The surface coverage of the ligand film was calculated using equation 2.4 to be  $15.1\ \text{nmol cm}^{-2}$  using charge integration from cyclic voltammetry which was recorded at  $100\ \text{mV s}^{-1}$  with monomer free solution (TBAP / $\text{CH}_3\text{CN}$ ). Regeneration of the modified electrode for the detection of metal ions was performed a number of times as described in the previous section using EDTA solution.

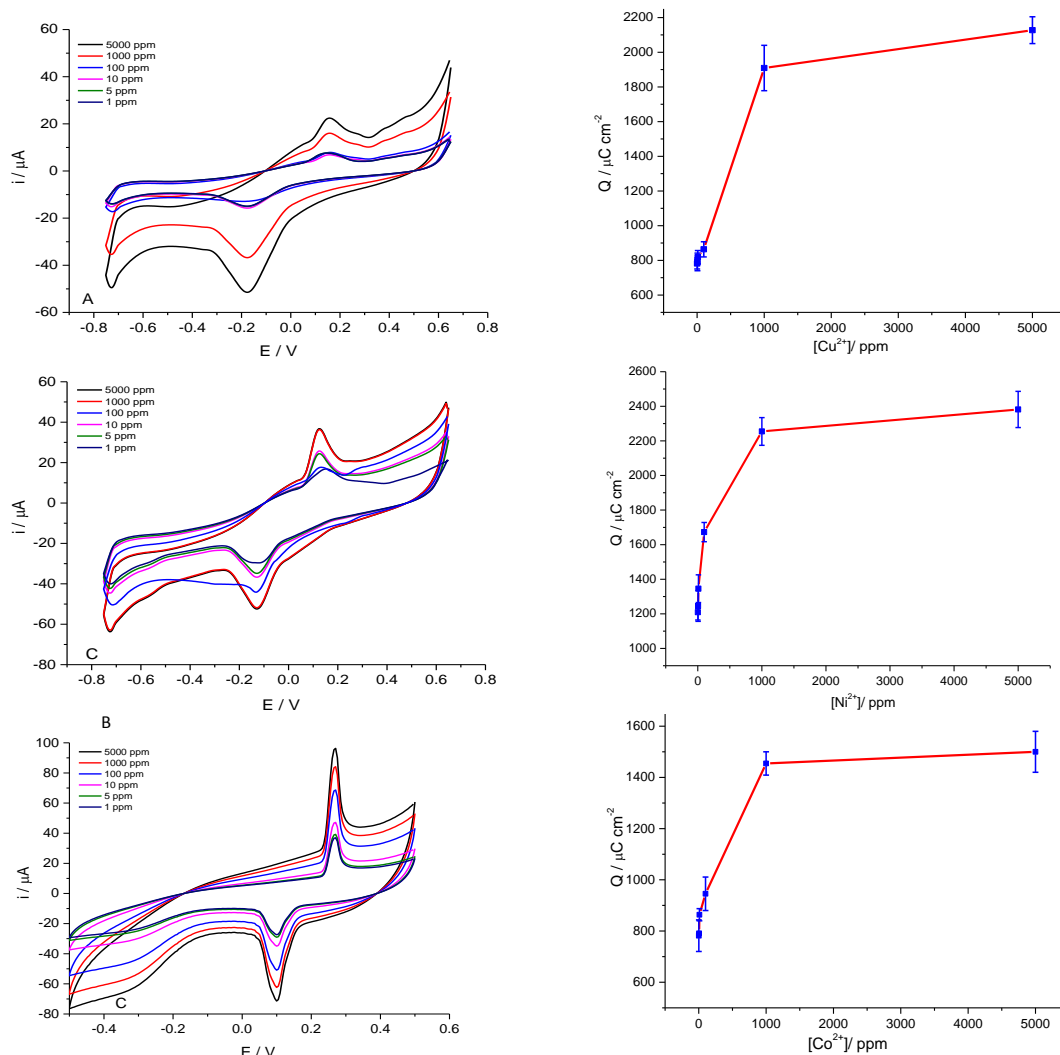


**Figure 7.16:** A) Cyclic voltammograms in blank  $\text{KNO}_3$  solution for the Py-HQC-modified electrode when exposed to 1 ppm to 5000 ppm A)  $\text{Cu}^{2+}$ , B)  $\text{Ni}^{2+}$  and C)  $\text{Co}^{2+}$  at a scan rate of  $100 \text{ mV s}^{-1}$ . (Inset curve charge response as a function of

### 7.3.2.4 Fitting the data to the different isotherms

The adsorption isotherms for the metal ions were examined, and the four isotherm modes discussed above were applied to interpret the experimental data. The data are presented in Figures 7.17, 7.18, and 7.19 for  $\text{Cu}^{2+}$ ,  $\text{Ni}^{2+}$  and  $\text{Co}^{2+}$ , respectively. The results extracted from the figures show that the Freundlich isotherm offered the best fit for the adsorption of nickel and cobalt ions onto the polymer electrode, depending on the R-value, with the results arranged from best to least appropriate as follows: Frumkin > Freundlich > Temkin > Langmuir. Characteristic parameters  $K$ ,  $a$  and  $\Delta G^\circ$  were calculated for each metal ions using Frumkin equation, as reported in Table 7.6 as mentioned in section 7.3.1.4.

Metal	Concentration	Charge / C	$\Gamma_m$ nmol cm <sup>-2</sup>	Molar ratio $\Gamma_m / \Gamma_{\text{polymer}}$
Cu <sup>2+</sup>	5000 ppm	2.34 x 10 <sup>-4</sup>	11	0.73
	1000 ppm	2.10 x 10 <sup>-4</sup>	9.9	0.65
	100 ppm	9.5 x 10 <sup>-5</sup>	4.5	0.30
	10 ppm	9.0 x 10 <sup>-5</sup>	4.25	0.28
	5 ppm	8.7 x 10 <sup>-5</sup>	4.1	0.27
	1 ppm	8.6 x 10 <sup>-5</sup>	4.1	0.27
Ni <sup>2+</sup>	5000 ppm	2.62 x 10 <sup>-4</sup>	12.3	0.81
	1000 ppm	2.48 x 10 <sup>-4</sup>	11.7	0.77
	100 ppm	1.82 x 10 <sup>-4</sup>	8.6	0.57
	10 ppm	1.43 x 10 <sup>-4</sup>	6.7	0.44
	5 ppm	1.37 x 10 <sup>-4</sup>	6.4	0.42
	1 ppm	1.33 x 10 <sup>-4</sup>	6.25	0.41
Co <sup>2+</sup>	5000 ppm	1.85 x 10 <sup>-4</sup>	8.7	0.57
	1000 ppm	1.60 x 10 <sup>-4</sup>	7.5	0.49
	100 ppm	1.02 x 10 <sup>-4</sup>	4.8	0.31
	10 ppm	9.56 x 10 <sup>-5</sup>	4.5	0.29
	5 ppm	8.68 x 10 <sup>-5</sup>	4.1	0.27
	1 ppm	8.63 x 10 <sup>-5</sup>	4.08	0.27

**Table 7.5:** Charge values, surface coverage and the molar ratio for metals/Py-HQC-modified electrode at different concentrations. Scan rate was 100 mV s<sup>-1</sup>. The surface coverage of ligand sites on the polymer film was 15.1 nmol cm<sup>-2</sup>

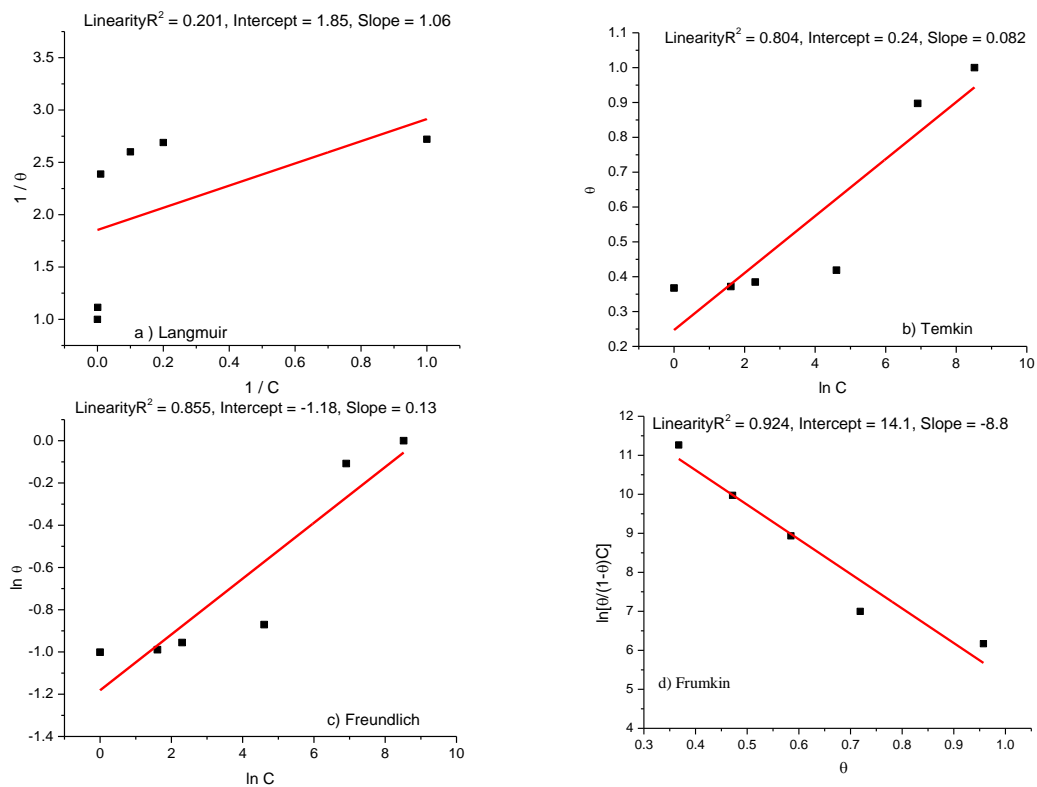


**Figure 7.17:** Plots of four isotherms: a) Langmuir isotherm, b) Temkin isotherm, c) Freundlich isotherm, and d) Frumkin isotherm for the binding between copper and the Py-HQC electrode.

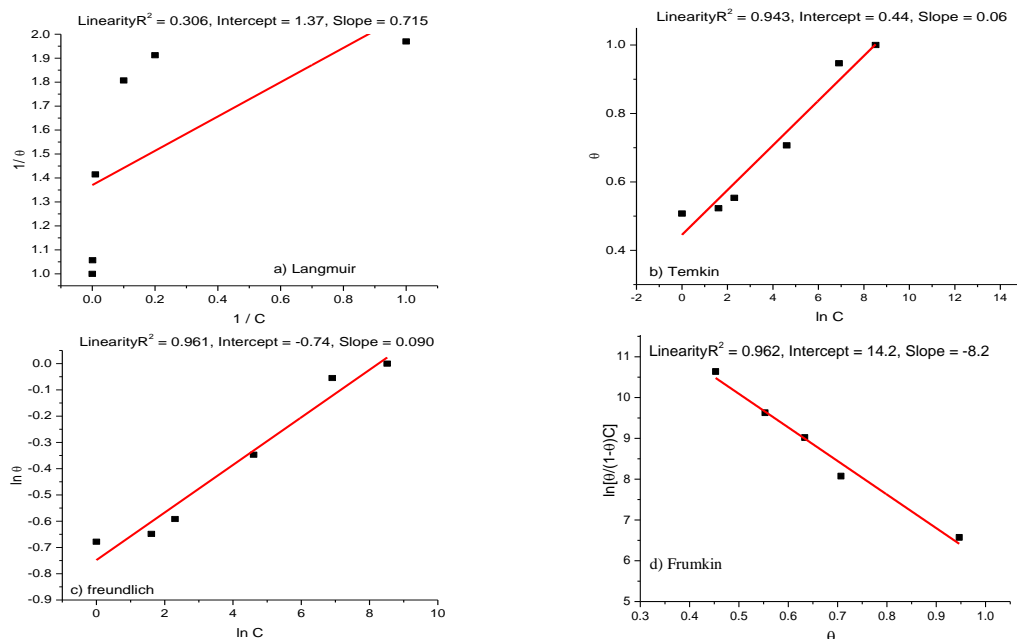


**Figure 7.18:** Plots of four isotherms: a) Langmuir isotherm, b) Temkin isotherm, c) Freundlich isotherm, and d) Frumkin isotherm for the binding between nickel and the Py-HQC electrode.

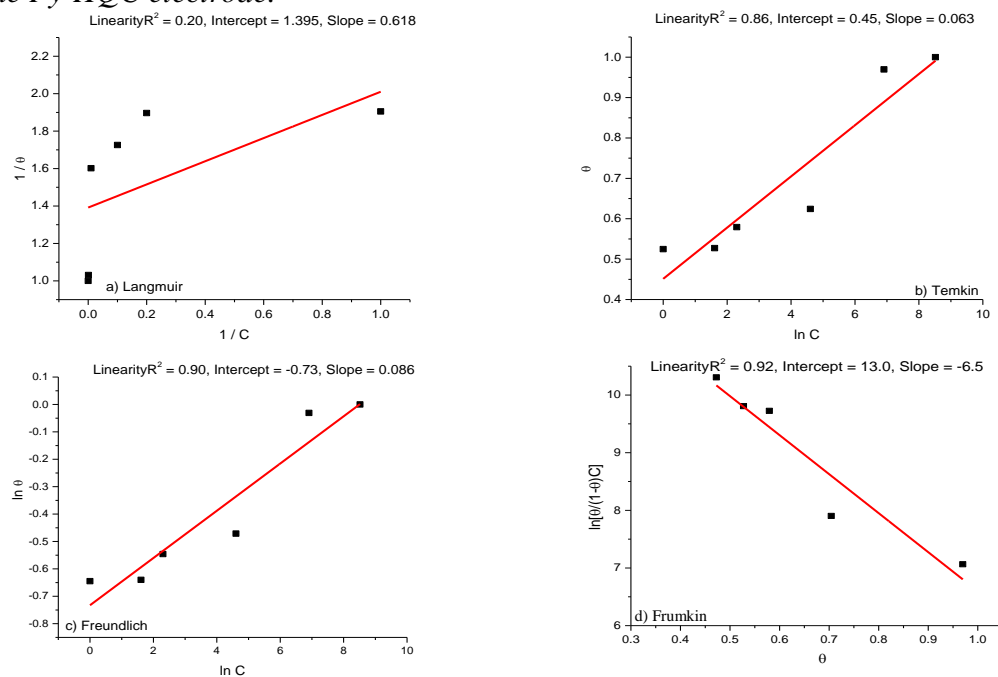


**Figure 7.19:** Plots of four isotherms: a) Langmuir isotherm, b) Temkin isotherm, c) Freundlich isotherm, and d) Frumkin isotherm for the binding between cobalt and the Py-HQC electrode.

Metal ions	$\ln K$	$10^6 K / M^{-1}$	$\log K$	$a$	$\Delta G^\circ$ K J.mol <sup>-1</sup>
Copper	14.1	1.32	6.1	-8.8	-35.3
Nickel	14.2	1.46	6.1	-8.2	-35.5
Cobalt	13	0.44	5.6	-6.5	-32.5

**Table 7.6:** Values of calculated  $a$ ,  $\log K$  and  $\Delta G$  parameters for metal binding to the Py-HQC electrode based on Frumkin isotherm.

The calculated binding constant was compared with the binding constant values for metal ions complexes with 8-hydroxyquinoline and 8-hydroxyquinoline 5-sulphonic acid in aqueous solution, as reported in **Table 7.7**.<sup>25</sup> These  $\log K$  calculated from the results were smaller than those in the aqueous mediums because in polymer - ligand system the ligand was restricted into polymer film surface, while values from literature relate to the free ligands in aqueous media meaning more freedom for complexation to occur.

Metal ions \ Ligand	$\log K$	
	8-hydroxyquinoline	8-hydroxyquinoline 5-sulphonic acid
Copper	12.3	11.5
Nickel	9.9	10
Cobalt	9	9.2

**Table 7.7:** Values of  $\log K$  for metal binding to the in aqueous solution for different ligands

### 7.3.3 Voltammetric response of Poly(Ani-NTA) to metal ions

This section describes the use of modified poly(Ani-NTA) electrodes to detect metal ions (copper, nickel and cobalt) in aqueous solutions using voltammetric measurements. This study involves use the same procedure described in the previous **section 7.3.1**, though this time using Py-NTA as the surface modifier. Patterned Ani-NTA electrodes were examined as recognition units for  $\text{Cu}^{2+}$ ,  $\text{Ni}^{2+}$  and  $\text{Co}^{2+}$  in solution using electrochemical voltammetry. In this procedure, the Ani-NTA-modified electrodes were immersed in 10 ml of 100 ppm of metal nitrate solutions,  $\text{Cu}(\text{NO}_3)_2$ ,  $\text{Ni}(\text{NO}_3)_2$  and  $\text{Co}(\text{NO}_3)_2$ , with a 0.1 M  $\text{KNO}_3$  solution without stirring. Then, cyclic voltammetry was used to measure electrochemical responses with potentials ranging between -0.60 to 0.65, -0.70 to 0.65 and -0.50 to 0.70 V vs. (Ag/AgCl) for  $\text{Cu}^{2+}$ ,  $\text{Ni}^{2+}$  and  $\text{Co}^{2+}$ , respectively, at different scan rates (10, 20, 50 and 100  $\text{mV s}^{-1}$ ).

The results for binding  $\text{Cu}^{2+}$ ,  $\text{Ni}^{2+}$  and  $\text{Co}^{2+}$  to Ani-NTA using voltammetry showed that these metal ions can be detected using an Ani-NTA-modified electrode in aqueous solutions. **Figure 7.20** shows the cyclic voltammograms of the modified electrodes (black curve) before and (red curve) after immersion in 100 ppm metal ion solutions in 0.1 M  $\text{KNO}_3$  for 20 mins. In the metal-free solutions, modified electrodes were inert under the potential windows used as result of there is no metal ions in the solution and there is no redox reaction of polymer within studied potential window, whereas the cyclic voltammetric responses of the modified electrodes were clear in the same potential

window. **Figure 7.20** panel I illustrates cyclic voltammograms for the redox current of  $\text{Cu}^{2+}/\text{Cu}^{\circ}$  at  $E_{p,a} = 0.21$  V and  $E_{p,c} = -0.06$  V. However, the oxidation/reduction peaks of  $\text{Ni}^{2+}/\text{Ni}^{\circ}$  emerged ( $E_{p,a} = 0.18$  V and  $E_{p,c} = -0.09$  V) as shown in **Figure 7.20** (panel II). Furthermore, **Figure 7.20** (panel III) shows the voltammetric response of the modified electrode when exposed for  $\text{Co}^{2+}$  ion solution with current peaks at  $E_{p,a} = 0.21$  V and  $E_{p,c} = -0.03$  V. Successful coordination between the metals and the Ani-NTA surface electrode was apparent.

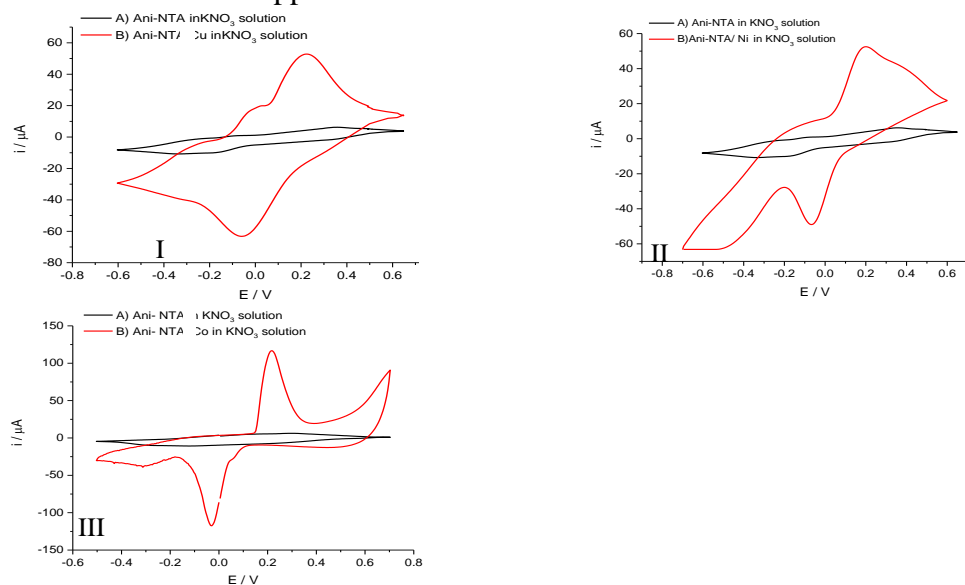


**Figure 7.20:** Cyclic voltammograms of Ani-NTA-modified electrodes :(black curves) in metal-free  $\text{KNO}_3$  solution, (red curve) Ani-NTA electrode in  $\text{KNO}_3$  solution after exposed it to 100 ppm of metal ions solution: I)  $\text{Cu}^{2+}$  II)  $\text{Ni}^{2+}$  III)  $\text{Co}^{2+}$  at  $100 \text{ mV s}^{-1}$ .

### 7.3.3.1 Stability and influence of the sweep rate on metal complexes

Under the same experiment conditions were mentioned in section 7.3.3, repeated cyclic potential scans were performed for metal complexes with Ani-NTA film in  $\text{KNO}_3$  solution over 10 cycles. Voltammetric responses show two current peaks due to oxidation/reduction reaction, as shown in **Figure 7.21**. These findings indicate that the metal complexes formed were strongly coordinated within the potential window of our experiment.

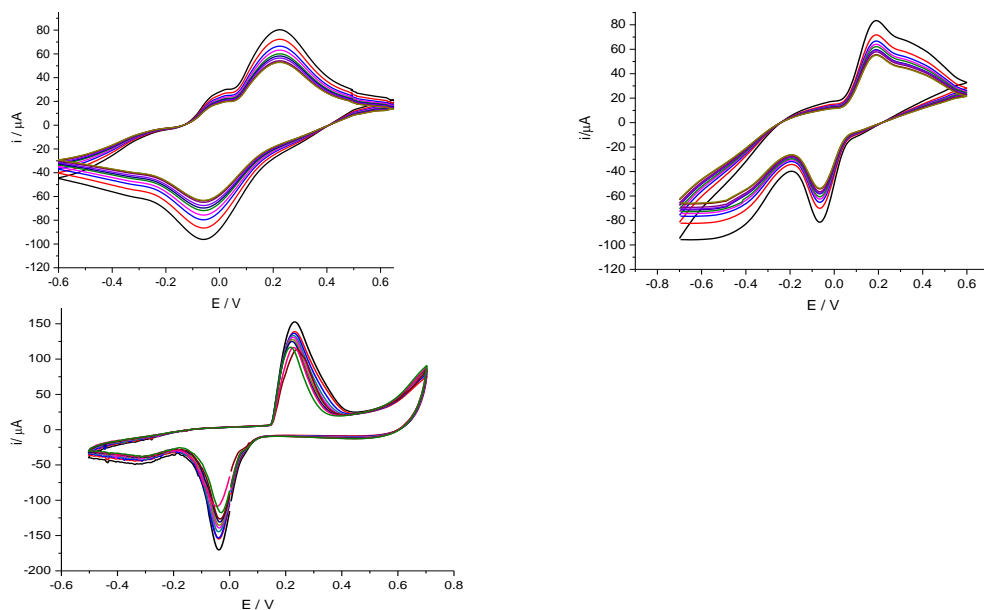


**Figure 7.21:** Cyclic voltammograms of Ani-NTA-modified electrode in 0.1M  $\text{KNO}_3$  solution, after adsorbing A)  $\text{Cu}^{2+}$  ions, B)  $\text{Ni}^{2+}$  ions, and C)  $\text{Co}^{2+}$  ions (100 ppm). From first to the tenth cycle. The scan rate was  $100 \text{ mV s}^{-1}$ .

The effect of scan rate on the voltammetric response of the modified electrodes was examined in the range  $10\text{-}100 \text{ mV s}^{-1}$ , as shown in Figures 7.22, 7.23 and 7.24 for copper, nickel and cobalt, respectively. These findings show that both the oxidation and reduction peaks increased linearly with sweep rate.

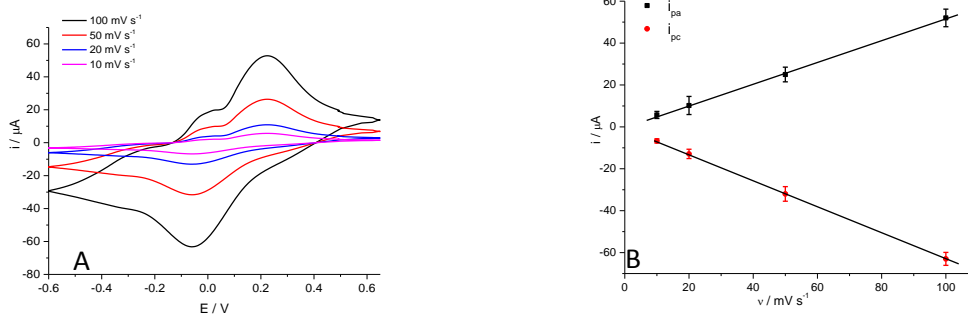


**Figure 7.22:** Influence of scan rate (from 10 to  $100 \text{ mV s}^{-1}$ ) on the  $\text{Cu}^{2+}/^0$  peak current in 0.1 M  $\text{KNO}_3$  solution. B) Variation of anodic and cathodic peak currents vs. scan rate. Electrode area =  $0.11 \text{ cm}^2$

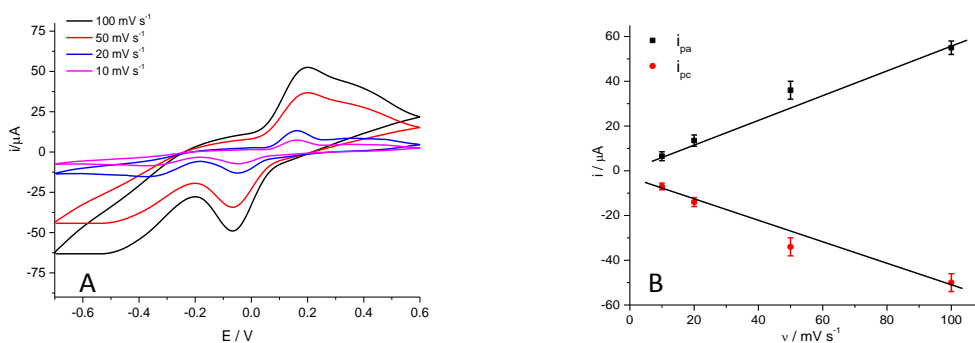


**Figure 7.23:** Influence of scan rate (from 10 to  $100 \text{ mV s}^{-1}$ ) on the  $\text{Ni}^{2+}/^0$  peak current in 0.1 M  $\text{KNO}_3$  solution. B) Variation of anodic and cathodic peak currents vs. scan rate. Electrode area =  $0.11 \text{ cm}^2$

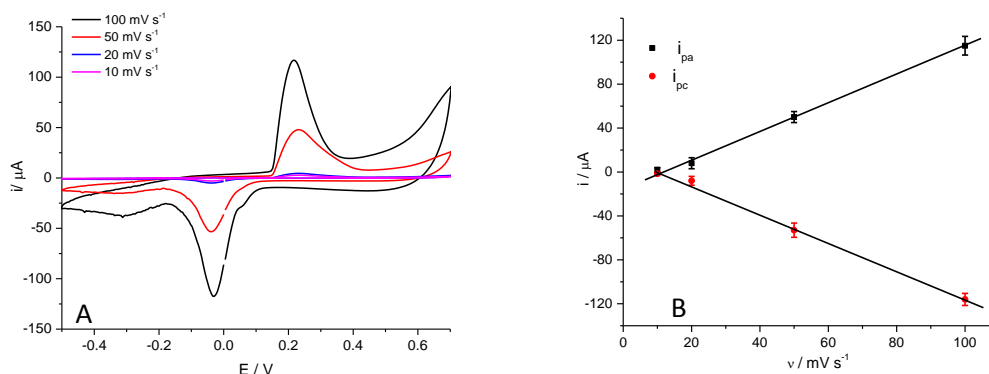


**Figure 7.24:** Influence of scan rate (from 10 to 100  $\text{mV s}^{-1}$ ) on the  $\text{Co}^{2+/0}$  peak current in 0.1 M  $\text{KNO}_3$  solution. B) Variation of anodic and cathodic peak currents vs. scan rate. Electrode area =  $0.11 \text{ cm}^2$

### 7.3.3.2 Concentration dependence of the characteristic peak charge

Using the same the procedures described above in section 7.3.3, the relationship between metal ion concentration and peak current was investigated. The electrochemical responses were recorded in each case via the voltammetric measurements for different  $\text{Cu}^{2+}$ ,  $\text{Ni}^{2+}$  and  $\text{Co}^{2+}$  concentrations ranging from 1 to 5000 ppm with a constant scan rate of  $100 \text{ mV s}^{-1}$  for all samples, as shown in **Figure 7.25**. From these results, total charge density value of  $\text{Cu}^{2+}$ ,  $\text{Ni}^{2+}$  and  $\text{Co}^{2+}$  was 3600, 1620 and  $2700 \mu\text{C cm}^{-2}$  at saturation coverage surfaces, corresponding to metal coverage of 15.2, 8.95, and  $13.5 \text{ nmol cm}^{-2}$  respectively.

### 7.3.3.3 Estimate of the molar ratio between metal ions and polymer electrode

The surface coverage of metal ions ( $\Gamma$ ) was calculated by using Faraday's law and **Table 7.8** reports surface coverages and molar ratios. The saturated surface coverages for copper, nickel and cobalt on Ani-NTA-modified electrodes, as obtained from 1000 and 5000 ppm solutions, were equal to 15.2, 8.95, and  $13.5 \text{ nmol cm}^{-2}$  for  $\text{Cu}^{2+}$ ,  $\text{Ni}^{2+}$  and  $\text{Co}^{2+}$  respectively. The surface coverage of the ligand was estimated using area under the peak method as mentioned in section 7.3.1.3 and was equal to  $16.8 \text{ nmol cm}^{-2}$ .

### 7.3.3.4 Fitting the data to the different isotherms

The adsorption isotherms were examined to study the experimental data as described in the previous section and as shown in Figures 7.26, 7.27, and 7.28 for  $\text{Cu}^{2+}$ ,  $\text{Ni}^{2+}$  and  $\text{Co}^{2+}$ , respectively. The results extracted from these figures illustrate that the Frumkin isotherm represents the best fit for the adsorption of nickel and cobalt ions with the polymer

electrode, depending on the R-value, with the results arranged from best to least appropriate isotherm as follows: Frumkin > Freundlich > Temkin > Langmuir. Characteristic parameters  $K$ ,  $a$  and  $\Delta G^\circ$  were calculated for metal ions using Frumkin equation, as shown in **Table 7.9** as mentioned in **section 7.3.1.4**. Comparison between the experimental  $\log K$  in the **Table 7.9** and  $\log K$  of complexes in aqueous solution (mentioned in **Table 7.4**) was illustrated that the experimental  $\log K$  was bigger than ligands which contain two or three carboxylic acid groups because the NTA ligand has a nitrogen atom can interact with the metal ions. Whereas, experimental results show that NTA in solution has smaller binding constant because the free ligands in aqueous solution have more freedom for complexation to occur.

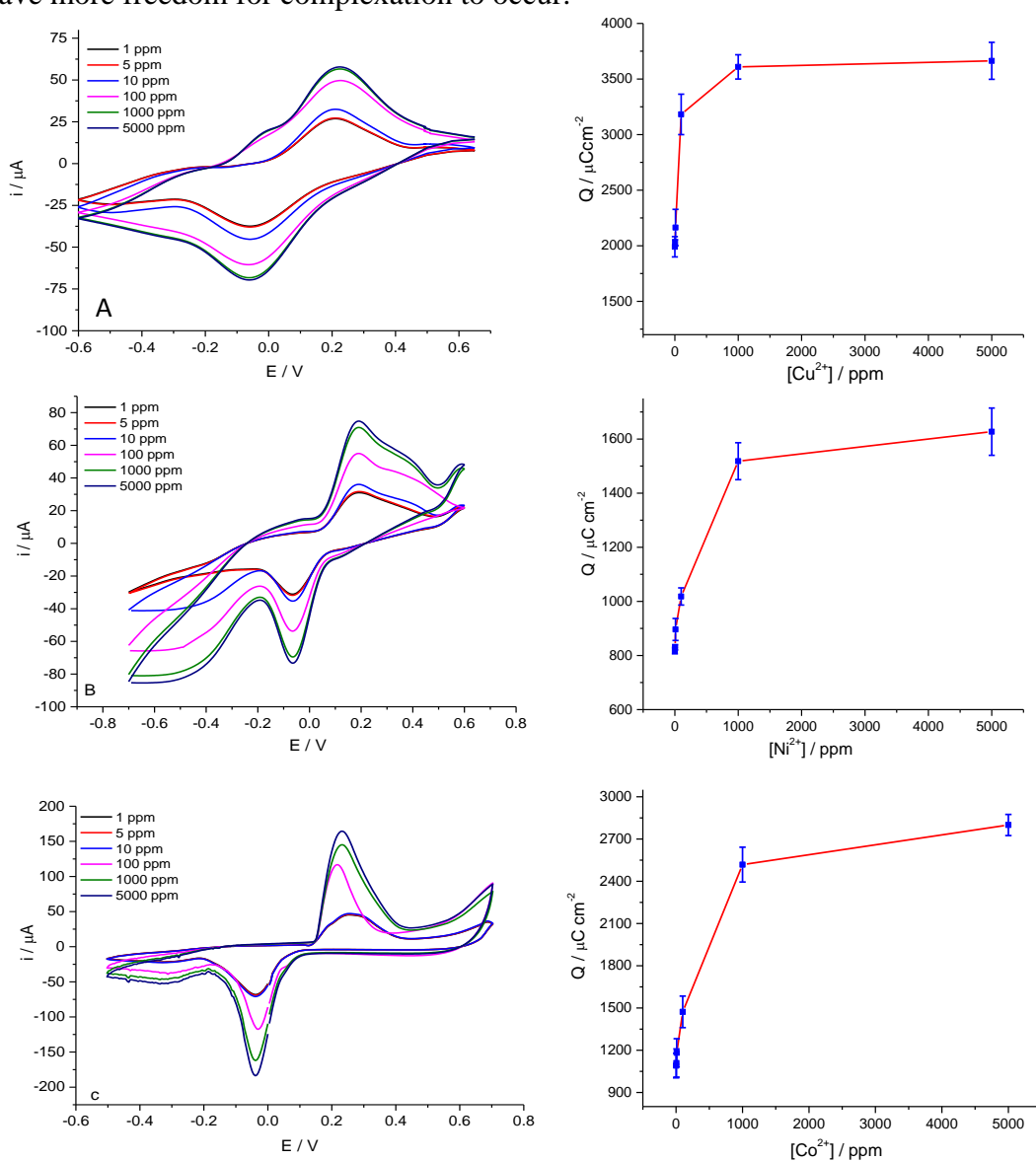


**Figure 7.25:** A) Cyclic voltammograms in blank  $\text{KNO}_3$  solution for the Ani-NTA-modified electrode exposed to 1 ppm to 5000 ppm A)  $\text{Cu}^{2+}$ , B)  $\text{Ni}^{2+}$  and C)  $\text{Co}^{2+}$  at a scan rate of  $100 \text{ mV s}^{-1}$ . (Inset curve charge response as a function of concentration).

Metal	Concentration	charge / C	$\Gamma_m$ (nmol.cm <sup>-2</sup> )	Molar ratio $\Gamma_m / \Gamma_{\text{polymer}}$
Cu <sup>2+</sup>	5000 ppm	3.23 x 10 <sup>-4</sup>	15.2	0.91
	1000 ppm	2.97 x 10 <sup>-4</sup>	14	0.83
	100 ppm	2.1 x 10 <sup>-4</sup>	9.9	0.59
	10 ppm	1.48 x 10 <sup>-4</sup>	6.9	0.41
	5 ppm	9.72 x 10 <sup>-5</sup>	4.6	0.27
	1 ppm	9.56 x 10 <sup>-5</sup>	4.5	0.26
Ni <sup>2+</sup>	5000 ppm	1.89 x 10 <sup>-4</sup>	8.95	0.53
	1000 ppm	1.67 x 10 <sup>-4</sup>	7.8	0.46
	100 ppm	1.12 x 10 <sup>-4</sup>	5.2	0.32
	10 ppm	9.86 x 10 <sup>-5</sup>	4.7	0.28
	5 ppm	9.16 x 10 <sup>-5</sup>	4.4	0.26
	1 ppm	9.03 x 10 <sup>-5</sup>	4.25	0.25
Co <sup>2+</sup>	5000 ppm	2.88 x 10 <sup>-4</sup>	13.5	0.80
	1000 ppm	2.65 x 10 <sup>-4</sup>	12.5	0.74
	100 ppm	1.62 x 10 <sup>-4</sup>	7.6	0.45
	10 ppm	1.3 x 10 <sup>-4</sup>	6.12	0.36
	5 ppm	1.22 x 10 <sup>-4</sup>	5.8	0.34
	1 ppm	1.19 x 10 <sup>-4</sup>	5.6	0.33

**Table 7.8:** Charge values, surface coverages and the molar ratios for metals/Ani-NTA-modified electrode at different concentrations. Scan rate was 100 mV s<sup>-1</sup>. The surface coverage of the polymer film was estimated at 16.8 nmol cm<sup>-2</sup>.

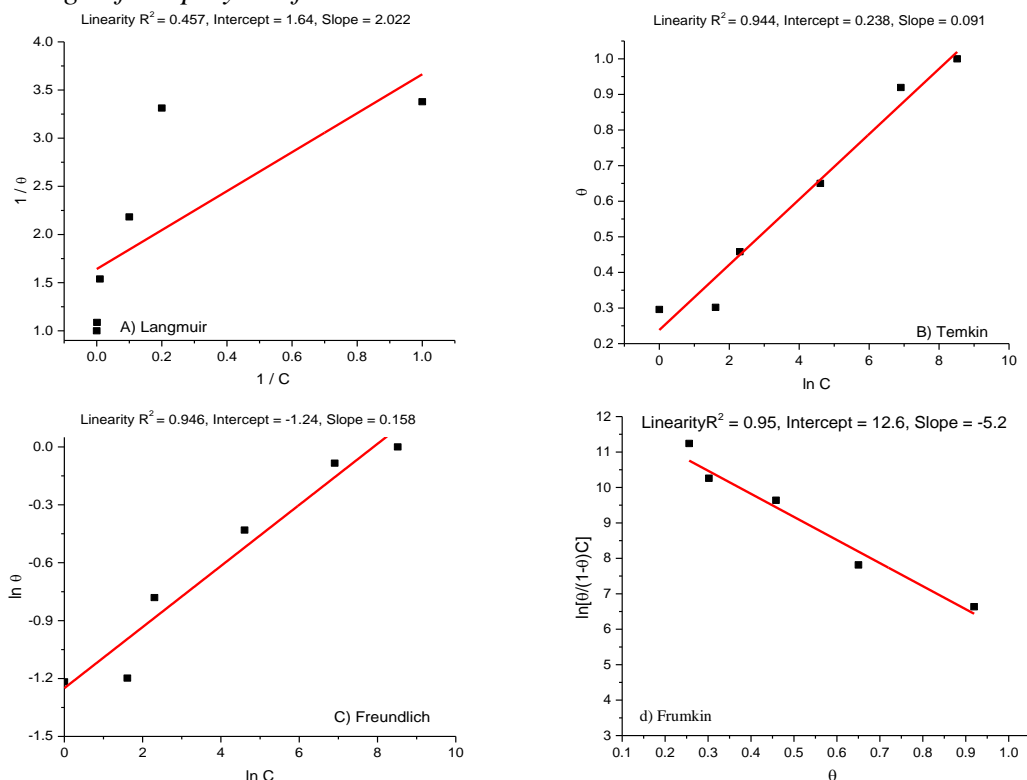


**Figure 7.26:** Plots of four isotherms: a) Langmuir isotherm, b) Temkin isotherm, c) Freundlich isotherm, and d) Frumkin isotherm for the binding between copper and the Ani-NTA electrode.

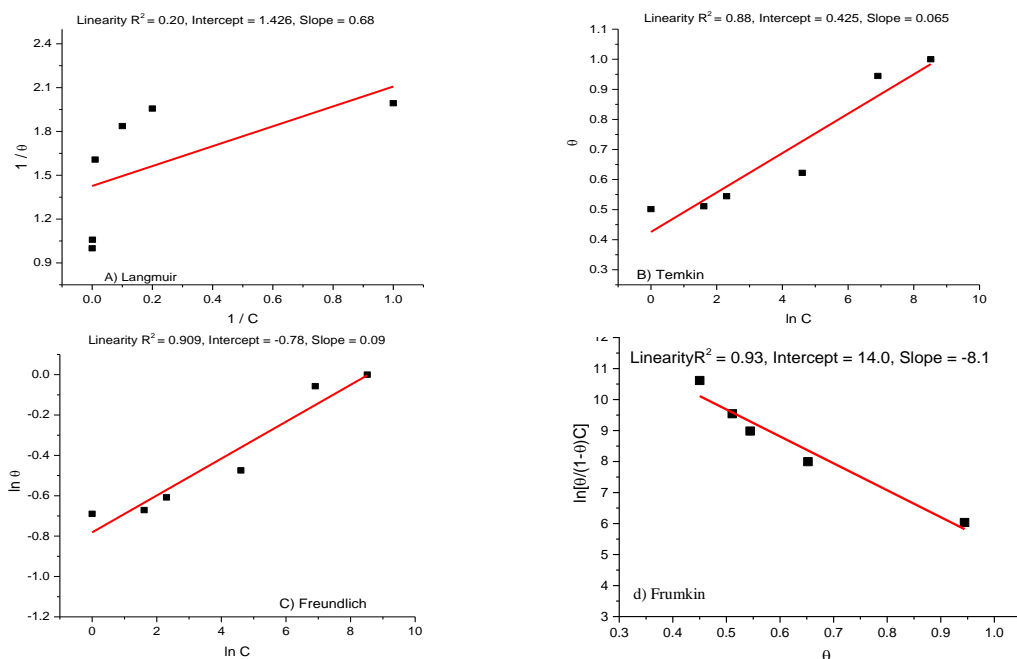


**Figure 7.27:** Plots of four isotherms: a) Langmuir isotherm, b) Temkin isotherm, c) Freundlich isotherm, and d) Frumkin isotherm for the binding between nickel and the Ani-NTA electrode.

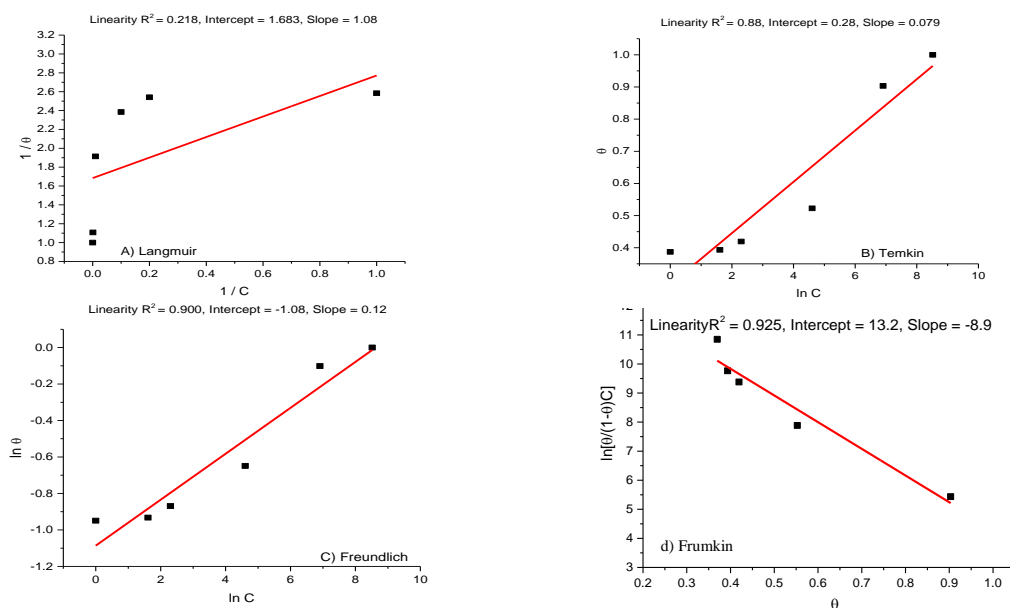


**Figure 7.28:** Plots of four isotherms: a) Langmuir isotherm, b) Temkin isotherm, c) Freundlich isotherm, and d) Frumkin isotherm for the binding between cobalt and the Ani-NTA electrode.

Metal ions	$\ln K$	$10^6 K / M^{-1}$	$\log K$	$a$	$\Delta G^\circ K J.mol^{-1}$
Copper	12.6	0.29	5.4	-5.2	-31.5
Nickel	14.0	1.20	6.0	-8.1	-35
Cobalt	13.2	0.54	5.7	-8.9	-33

**Table 7.9:** Values of calculated  $a$ ,  $\log K$  and  $\Delta G$  parameters for metal binding to the Ani-NTA electrode based on the Frumkin isotherm.

### 7.3.4 Voltammetric response of Poly(Ani-HQC) to metal ions

The electrochemical behaviour between copper, nickel and cobalt ions and the Ani-HQC electrode were investigated using cyclic voltammetry. Fresh Ani-HQC electrodes were placed in prepared solutions of three metal ions as described in section 7.3.3. The free hydroxyl groups and nitrogen atom in the HQC molecules can coordinate with the metal ions to form stable complexes. The experimental procedures used were similar to those described in the previous section for Ani-NTA. Cyclic voltammograms were recorded using a potential ranging between -0.9 to 0.7, -0.5 to 0.5 and -0.7 to 0.6 V vs (Ag/AgCl) for  $\text{Cu}^{2+}$ ,  $\text{Ni}^{2+}$  and  $\text{Co}^{2+}$ , respectively, at different scan rates (10, 20, 50 and 100  $\text{mV s}^{-1}$ ). The electrochemical responses in terms of the coordination of  $\text{Cu}^{2+}$ ,  $\text{Ni}^{2+}$  and  $\text{Co}^{2+}$  to Ani-HQC observed via cyclic voltammetry illustrated that the Ani-HQC-modified electrode can be used as recognition element to detect these metal ions in aqueous solution. The cyclic voltammograms recorded for the modified electrodes (black curve) before and (red curve) after immersion in 100 ppm in 0.1 M  $\text{KNO}_3$  are shown in **Figure 7.29**. It can be seen that black curves for all the cyclic voltammograms recorded for films in blank solutions ( $\text{KNO}_3$ ) over the potential window were not showed redox peaks as result of there is no metal ions in the solution and there is no redox reaction of polymer within studied potential window, while curve B shows the cyclic voltammetric responses for the modified electrodes when exposed to metal ion solutions, with clear peaks due to the formation of complexes in this same potential window. **Figure 7.29** panel I depicts cyclic voltammetric response for the redox current of  $\text{Cu}^{2+}/\text{Cu}^{\circ}$  at  $E_{p,a} = 0.22$  V and  $E_{p,c} = -0.17$  V. However, the oxidation/reduction peaks of  $\text{Ni}^{2+}/\text{Ni}^{\circ}$  emerged at  $E_{p,a} = 0.159$  V and  $E_{p,c} = 0.03$  V, as shown in **Figure 7.29** (panel II). **Figure 7.29** (panel III) shows the voltammetric response of the modified electrode on exposure to the cobalt ion solution, with redox peak currents at  $E_{p,a} = 0.25$  V and  $E_{p,c} = -0.03$  V. The successful coordination of the metals to the Ani-HQC electrode surface was apparent.

#### 7.3.4.1 Stability and influence of the sweep rate on metal complexes

Using the same procedure in Ani-NTA, the voltammetric responses were examined in blank  $\text{KNO}_3$  solution over 10 cycles. Cyclic voltammetry demonstrates that there are two current peaks corresponding to a redox process, as shown in **Figure 7.30**. It can be seen that the current peaks were slightly decreased after the first and second scan cycles until

electro-stability was achieved in subsequent scans. These results indicate that the complex bonds formed were strongly coordinated within the potential window of our experiment.

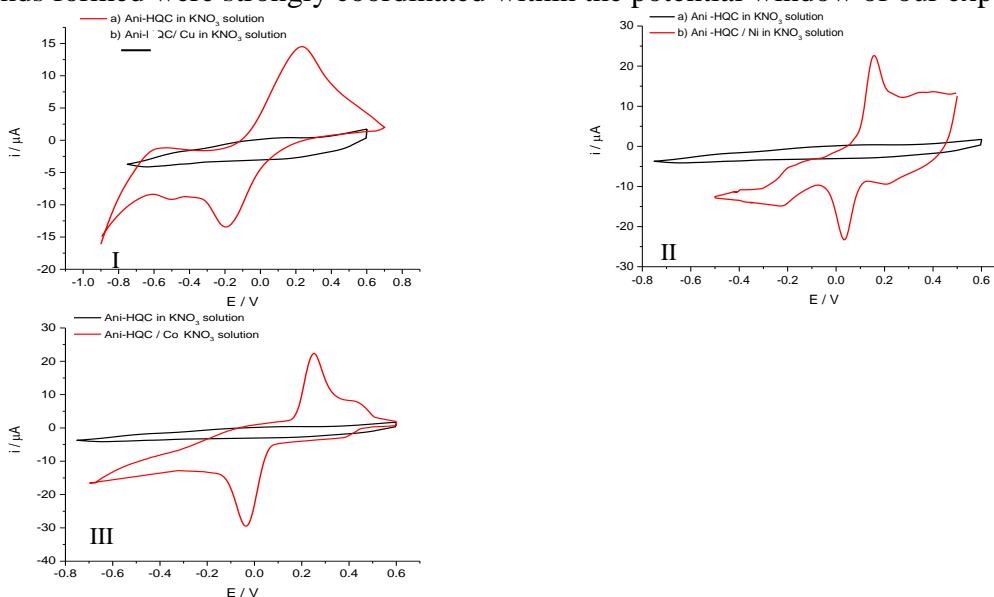


**Figure 7.29:** Cyclic voltammograms of Ani-HQC-modified electrode (black curve) in metal-free solution at  $10 \text{ mV s}^{-1}$ , (red curve) Ani-HQC electrode in  $\text{KNO}_3$  solution after exposure to 100 ppm ions solutions: I)  $\text{Cu}^{2+}$  II)  $\text{Ni}^{2+}$  III)  $\text{Co}^{2+}$ . Scan rate  $100 \text{ mV s}^{-1}$ .

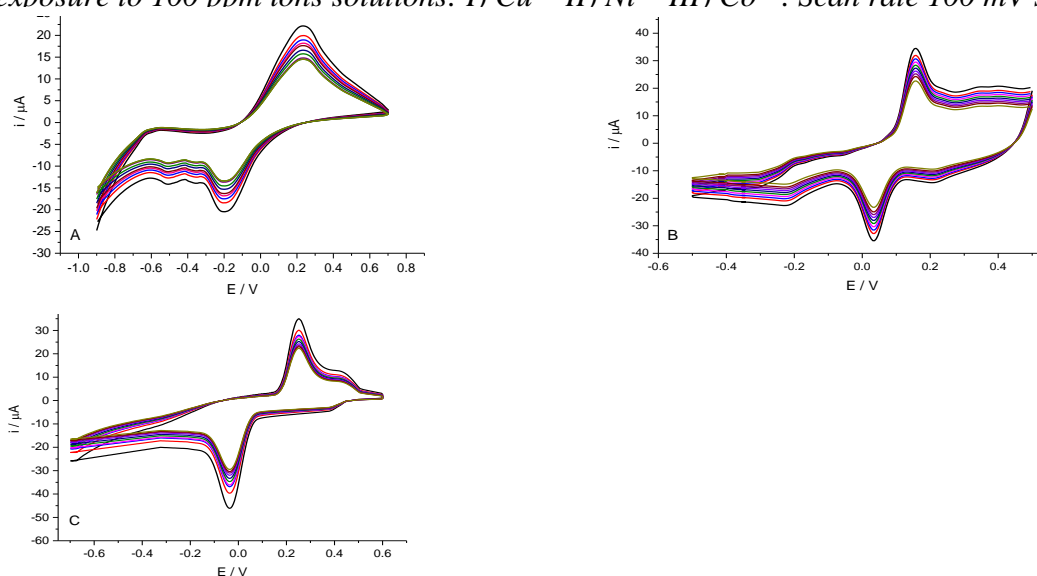


**Figure 7.30:** Cyclic voltammograms of an Ani-HQC-modified electrode in  $0.1 \text{ M KNO}_3$  solution, after adsorbing A)  $\text{Cu}^{2+}$  ions, B)  $\text{Ni}^{2+}$  ions, and C)  $\text{Co}^{2+}$  ions (at 100 ppm concentrations). The scan rate was  $100 \text{ mV s}^{-1}$ .

The stability of the cyclic voltammograms for the three metal complexes was recorded at various scan rates, from  $10$  to  $100 \text{ mV s}^{-1}$ , as shown in **Figures 7.31, 7.32, and 7.33** for copper, nickel and cobalt, respectively. It can be noted from panel B in each of these figures that oxidation and reduction peaks increased linearly with increasing sweep rate, indicating a surface redox reaction.

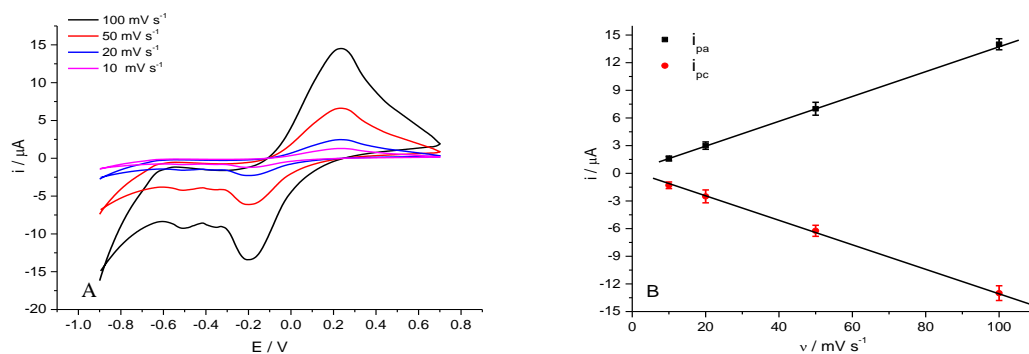


**Figure 7.31:** A) Influence of scan rate (from 10 to  $100 \text{ mV s}^{-1}$ ) on the  $\text{Cu}^{2+}$  peak current in  $0.1 \text{ M KNO}_3$  solution. B) Variation of anodic and cathodic peak currents vs. scan rate. Electrode area  $=0.11 \text{ cm}^2$

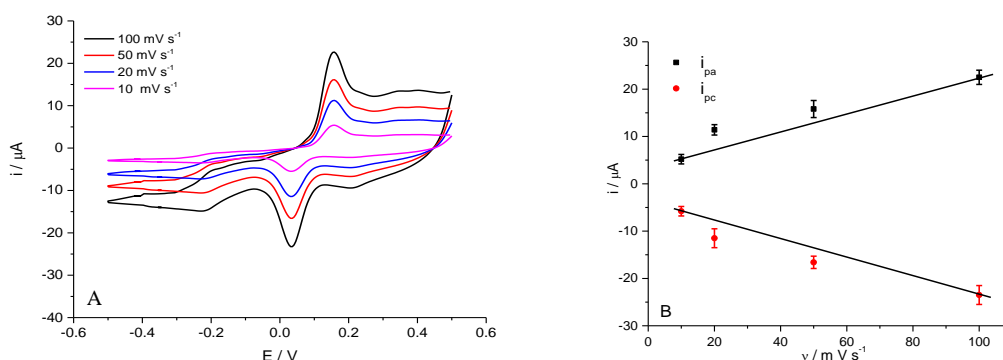


**Figure 7.32:** A) Influence of scan rate (from 10 to  $100 \text{ mV s}^{-1}$ ) on the  $\text{Ni}^{2+}$  peak current in  $0.1 \text{ M KNO}_3$  solution. B) Variation of anodic and cathodic peak currents vs. scan rate. Electrode area  $=0.11 \text{ cm}^2$

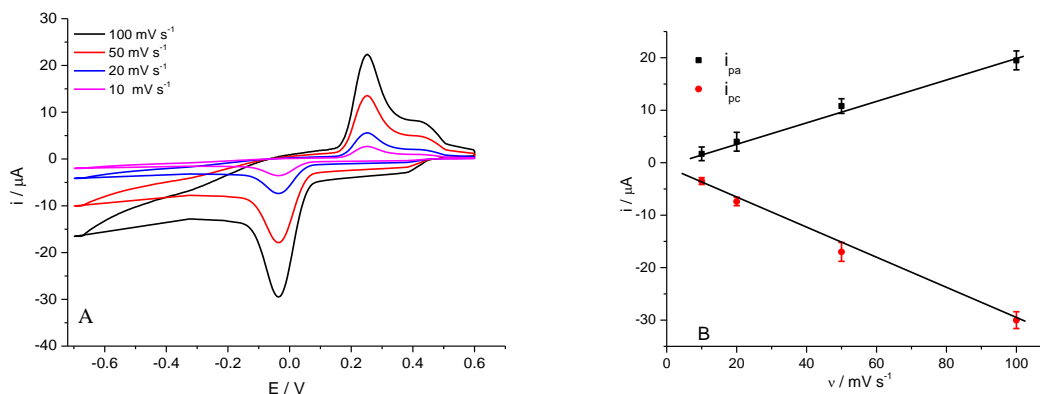


**Figure 7.33:** A) Influence of scan rate (from 10 to  $100 \text{ mV s}^{-1}$ ) on the  $\text{Co}^{2+}$  peak current in  $0.1 \text{ M KNO}_3$  solution. B) Variation of anodic and cathodic peak currents vs. scan rate. Electrode area  $=0.11 \text{ cm}^2$

#### 7.3.4.2 Concentration dependence of the characteristic peak charge

The same experimental conditions as described above were used to study the relation between the redox peak and metal ion concentration. **Figure 7.34** shows the cyclic voltammograms obtained using a Thio-HQC electrode film with different  $\text{Cu}^{2+}$ ,  $\text{Ni}^{2+}$  and  $\text{Co}^{2+}$  concentrations from 1 to 5000 ppm. These figures demonstrate that the current peaks increased with increasing concentration of the metal ions. The inset curves in all three

figures depict the calibration curve for the detection of metal ions via the modified electrode. The density charge value was reached at  $1100 \mu\text{C cm}^{-2}$ , corresponding to a copper coverage of  $5.85 \text{ nmol cm}^{-2}$  on the electrode when the copper concentration was 5000 ppm. The density charge due to  $\text{Ni}^{2+}$  ions was reached at  $1100 \mu\text{C cm}^{-2}$ , corresponding to a nickel coverage  $5.85 \text{ nmol cm}^{-2}$  at 5000 ppm, as shown in Figure 7.34. The density charge, as obtained from the voltammetric responses to the cobalt ions, was equal to  $800 \mu\text{C cm}^{-2}$  at 5000 ppm, corresponding to a cobalt coverage of  $4.4 \text{ nmol cm}^{-2}$ , as shown in **Figure 7.34**. The lowest metal ion concentration that was detected was 1 ppm.

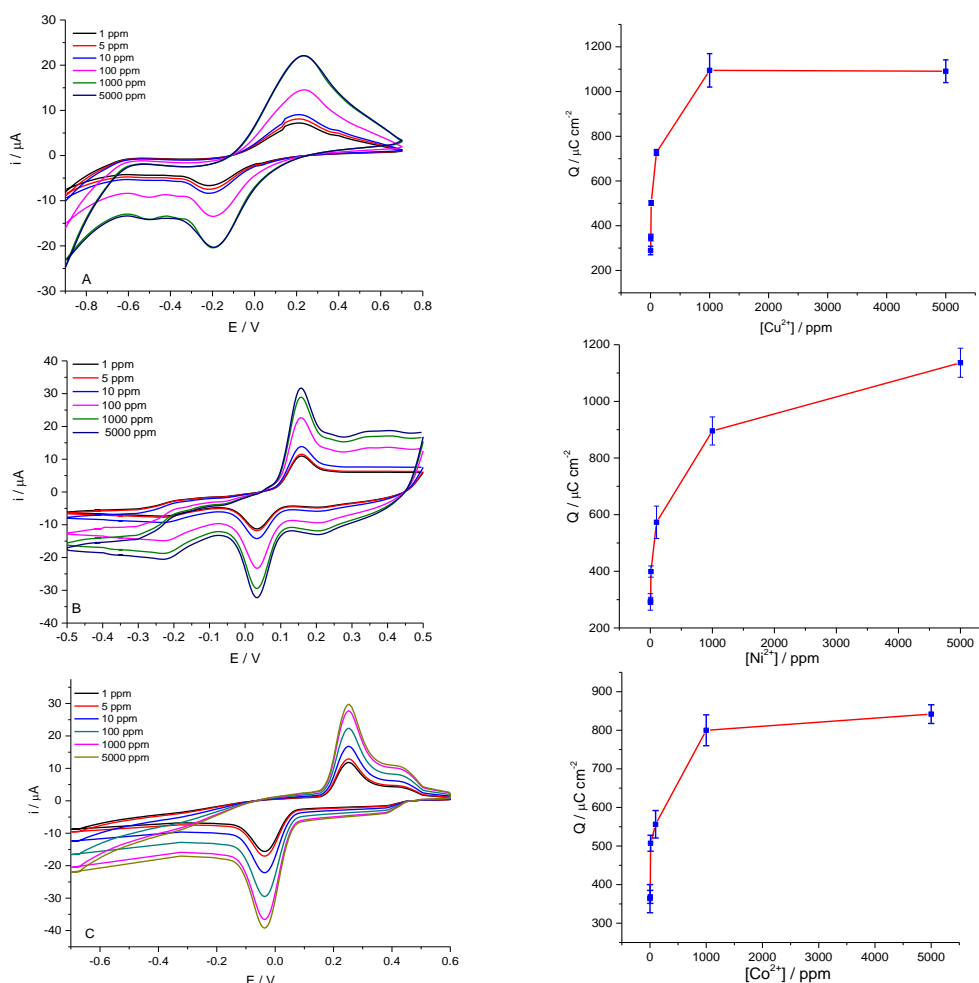


**Figure 7.34:** A) Cyclic voltammograms in blank  $\text{KNO}_3$  solution for an Ani-HQC-modified electrode exposed to 1 ppm to 5000 ppm A)  $\text{Cu}^{2+}$ , B)  $\text{Ni}^{2+}$  and C)  $\text{Co}^{2+}$  at a scan rate of  $100 \text{ mV s}^{-1}$ . (Inset curve charge response as a function of concentration).

### 7.3.4.3 Estimate of the molar ratio between metal ions and polymer electrode

The surface coverage of metal ions ( $\Gamma$ ) was estimated by integration of peaks (see chapter 4). The molar ratios of metal ions to the Ani-HQC electrode are presented in **Table 7.10**. From this table, it can be seen that the saturated surface coverage of the three metal ions

on the Ani-HQC electrode was 5.85, 5.85, and 4.4 nmol cm<sup>-2</sup> for Cu<sup>2+</sup>, Ni<sup>2+</sup> and Co<sup>2+</sup>, respectively. The surface coverage of the ligand was estimated using cyclic voltammetry and equal to 8.5 nmol cm<sup>-2</sup>.

#### 7.3.4.4 Fitting the data to the different isotherms

The adsorption isotherms were examined as described in the previous section with Ani-NTA as shown in **Figures 7.35, 7.36, and 7.37** for Cu<sup>2+</sup>, Ni<sup>2+</sup> and Co<sup>2+</sup>, respectively. These results show that the fitting of isotherm modes shows the same ordering obtained for the poly(Ani-HQC) electrode Frumkin > Freundlich > Temkin > Langmuir. Characteristic parameters  $K$ ,  $a$  and  $\Delta G^\circ$  were calculated for metal ions using Frumkin equation, as reported in **Table 7.11**. The comparison between the experimental  $\log K$  and  $\log K$  of complexes in aqueous solution (values was mentioned in **Table 7.7**) was showed that the experimental  $\log K$  was smaller  $\log K$  than complexes in aqueous solution due to ligands have more freedom to complexation.

Metal	Concentration	charge / C	$\Gamma_m$ (nmol.cm <sup>-2</sup> )	Molar ratio $\Gamma_m / \Gamma_{\text{polymer}}$
Cu <sup>2+</sup>	5000 ppm	1.25 x 10 <sup>-4</sup>	5.85	0.70
	1000 ppm	1.20 x 10 <sup>-4</sup>	5.65	0.66
	100 ppm	8.05 x 10 <sup>-5</sup>	3.7	0.43
	10 ppm	5.53 x 10 <sup>-5</sup>	2.6	0.30
	5 ppm	3.82 x 10 <sup>-5</sup>	1.8	0.21
	1 ppm	3.18 x 10 <sup>-5</sup>	1.3	0.15
Ni <sup>2+</sup>	5000 ppm	1.25 x 10 <sup>-4</sup>	5.85	0.70
	1000 ppm	9.84 x 10 <sup>-5</sup>	4.65	0.55
	100 ppm	6.35 x 10 <sup>-5</sup>	3	0.35
	10 ppm	4.39 x 10 <sup>-5</sup>	2.1	0.24
	5 ppm	3.24 x 10 <sup>-5</sup>	1.55	0.18
	1 ppm	3.21 x 10 <sup>-5</sup>	1.53	0.17
Co <sup>2+</sup>	5000 ppm	9.26 x 10 <sup>-5</sup>	4.4	0.51
	1000 ppm	8.83 x 10 <sup>-5</sup>	4.2	0.49
	100 ppm	6.12 x 10 <sup>-5</sup>	2.9	0.35
	10 ppm	5.58 x 10 <sup>-5</sup>	2.7	0.31
	5 ppm	4.03 x 10 <sup>-5</sup>	1.9	0.22
	1 ppm	3.90 x 10 <sup>-5</sup>	1.83	0.21

**Table 7.10:** Charges, surface coverages and the molar ratios for metal/Ani-HQC-modified electrode at different metal ion concentrations. Scan rate was 100 mV s<sup>-1</sup>. The surface coverage of the polymer film was estimated to be 8.5 nmol cm<sup>-2</sup>.

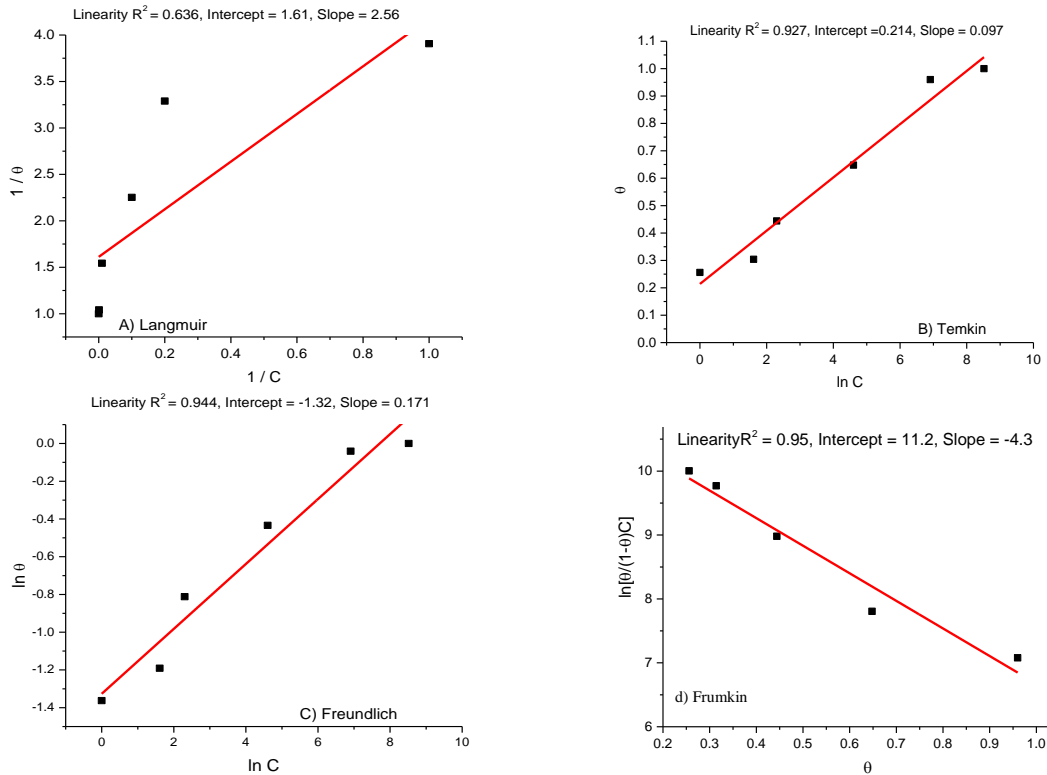


**Figure 7.35:** Plots of four isotherms: a) Langmuir isotherm, b) Temkin isotherm, c) Freundlich isotherm, and d) Frumkin isotherm for the binding between copper and the Ani-HQC electrode.

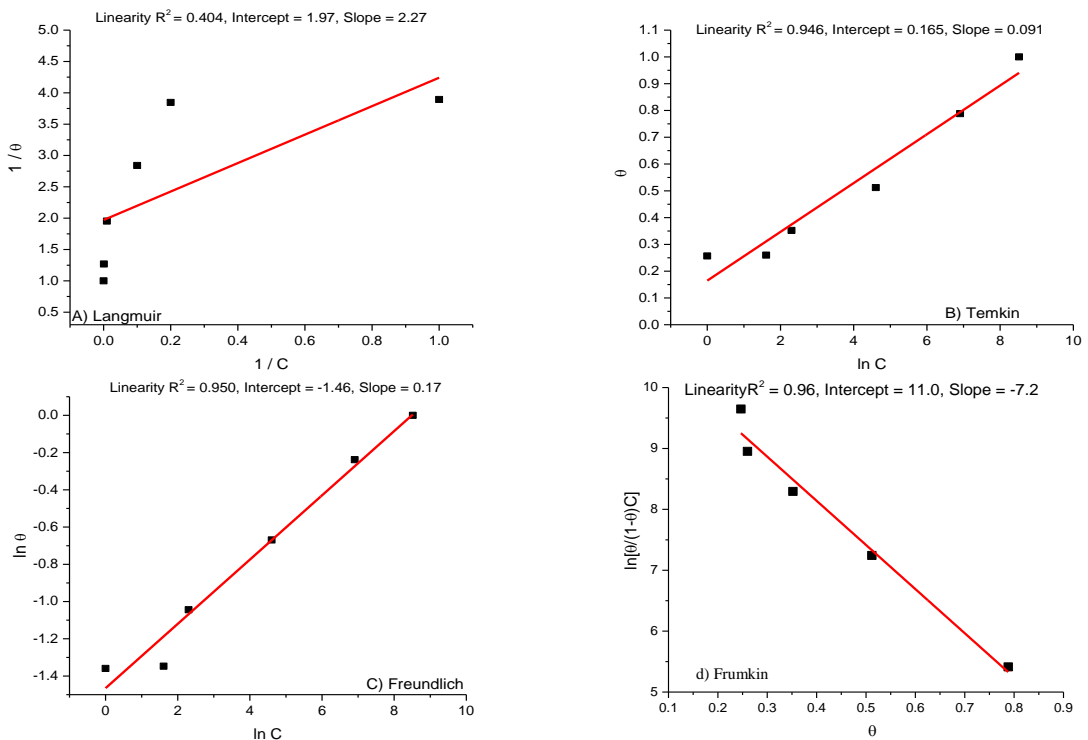


**Figure 7.36:** Plots of four isotherms: a) Langmuir isotherm, b) Temkin isotherm, c) Freundlich isotherm, and d) Frumkin isotherm for the binding between nickel and the Ani-HQC electrode.

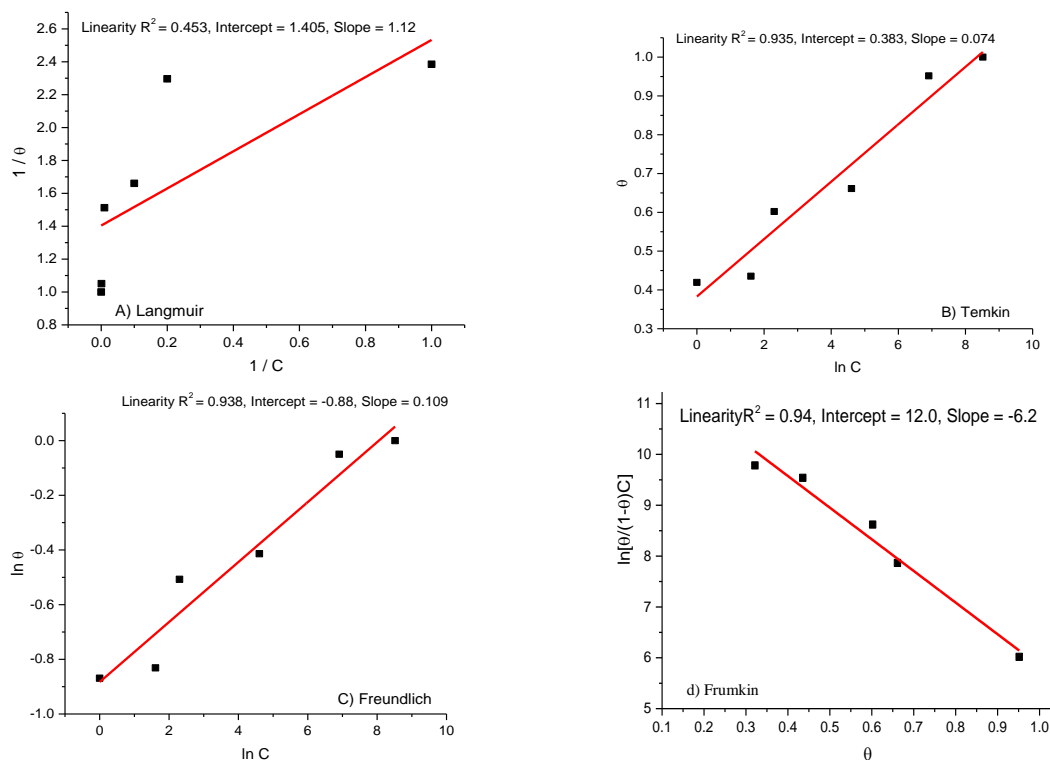


**Figure 7.37:** Plots of four isotherms: a) Langmuir isotherm, b) Temkin isotherm, c) Freundlich isotherm, and d) Frumkin isotherm for the binding between cobalt and the Ani-HQC electrode.

Metal ions	$\ln K$	$10^6 K / M^{-1}$	$\log K$	$a$	$\Delta G^\circ K J.mol^{-1}$
Copper	11.2	0.07	4.8	-4.3	-28
Nickel	11	0.05	4.7	-7.2	-27.5
Cobalt	12	0.16	5.2	-6.2	-30

**Table 7.11:** Values of calculated  $a$ ,  $\log K$  and  $\Delta G$  parameters for metal binding to the Ani-HQC electrode based on the Frumkin isotherm.

### 7.3.5 Voltammetric response of poly(Thio-NTA) to of metal ions

This section describes the electrochemical responses of patterned poly(Thio-NTA) electrodes using the same potentiometric measurements as for poly(Py-NTA) and poly(Ani-NTA). The metal ions solutions used contain 100 ppm of the metal nitrate combined with 0.1 M  $KNO_3$ . Cyclic voltammograms were recorded using a potential ranging between -0.6 to 0.6, -0.7 to 0.6 and -0.5 to 0.6 V vs. (Ag/AgCl) for  $Cu^{2+}$ ,  $Ni^{2+}$  and  $Co^{2+}$ , respectively, at different scan rates (10, 20, 50 and 100  $mV s^{-1}$ ). Cyclic voltammetry was used to investigate the possibility of the coordination of metal ions to the Thio-NTA-modified electrode. **Figure 7.38** shows the cyclic voltammograms of the Thio-NTA electrode obtained with a metal-free solution at 10  $mV s^{-1}$  (black curve) and after an immersion step in 100 ppm metal ions solution for 20 mins. (red curve). The electrochemical behaviour due to the reduction and oxidation of complex film-metal ions

supposes the metal ions are bound to the Thio-NTA film via the carboxylate groups and nitrogen atom. A pair of current peaks at  $E_{p,a} = 0.120$  V and  $E_{p,c} = -0.124$  V for the oxidation/reduction of  $\text{Cu}^{2+}/\text{Cu}^{\circ}$  is shown in **Figure 7.38** (panel I), whereas **Figure 7.38** (panel II) shows the voltammetric response of the Thio-NTA electrode on exposure to a  $\text{Ni}^{2+}$  ion solution, with oxidation/reduction peak currents at  $E_{p,a} = 0.125$  V and  $E_{p,c} = -0.039$  V for the redox of  $\text{Ni}^{2+}/\text{Ni}^{\circ}$ . Furthermore, the voltammetric responses in **Figure 7.38** (panel III) showed the appearance of redox peaks due to the Thio-NTA electrode which were placed in a cobalt ion solution at  $E_{p,a} = 0.217$  V and  $E_{p,c} = 0.09$  V. Voltammetric measurements were conducted for a film electrode (Thio-NTA) with a blank solution (metal-ion free) under the same conditions for which no redox peak current was observed because of there is no metal ions in the solution and there is no redox reaction of polymer within studied potential window, as shown in the figures (black curve). From this, it was demonstrated that the film electrode will not give any peak currents if there are no metal ions in the solution.

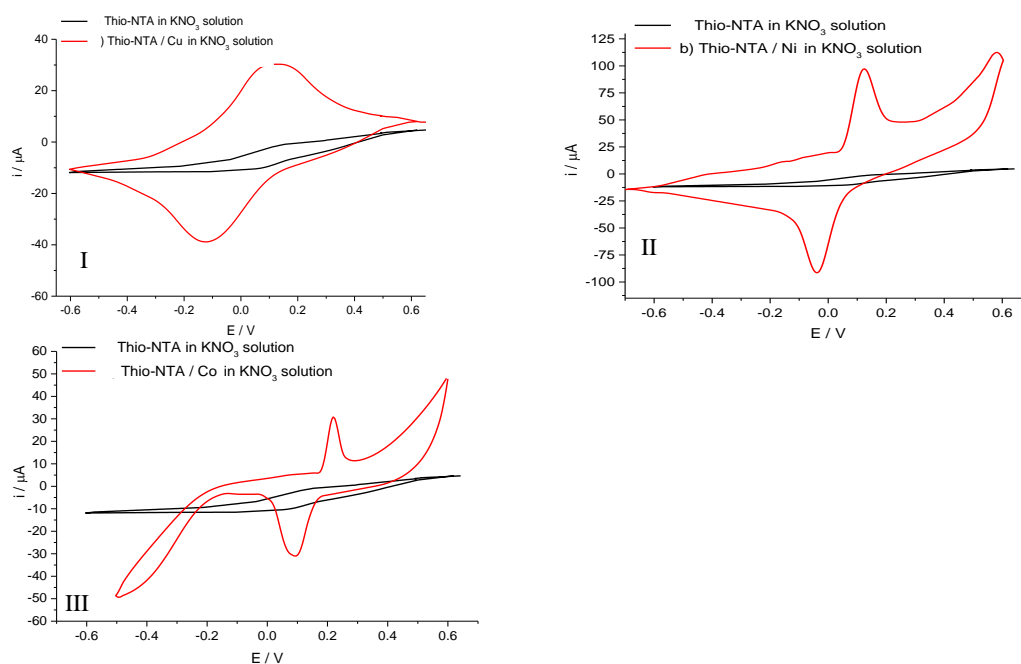


**Figure 7.38** Cyclic voltammogram of a Thio-NTA-modified electrode (black curve) in metal-free  $\text{KNO}_3$  solution at  $10 \text{ mV s}^{-1}$ , (red curve) Thio-NTA electrode in  $\text{KNO}_3$  solution in 100 ppm metal ion solutions: I)  $\text{Cu}^{2+}$  II)  $\text{Ni}^{2+}$  III)  $\text{Co}^{2+}$  at  $100 \text{ mV s}^{-1}$ .

### 7.3.5.1 Stability and influence of the sweep rate on metal complexes

Cyclic voltammetry technique was used to study the effects of frequent cyclic scans on metal complexation with a Thio-NTA electrode in  $\text{KNO}_3$  solution over ten cycles, as shown in **Figure 7.39**. These voltammograms show that the complex-film electrode maintain electrostability over the ten sweep cycles. The cyclic voltammograms recorded

from the fourth to the tenth cycles in blank electrolyte solution were stable, with a slight decrease in redox current peaks as a consequence of the formation a stable complex within the polymer films. These findings data indicate that metal ions are strongly bound to receptor at the electrode surface within the potential range examined in this experiment. The cyclic voltammogram of copper with Thio-NTA electrode showed quite different shape from other metal ions. None of these cyclic voltammograms were ideal and none of them confirms to Langmuir isotherms model and this could be due to interactions with surface, where cations are attracted to electrode surface. This also indication that the anodic and cathodic peak currents are associated with surface-bound copper ions on Thio-NTA modified electrode.

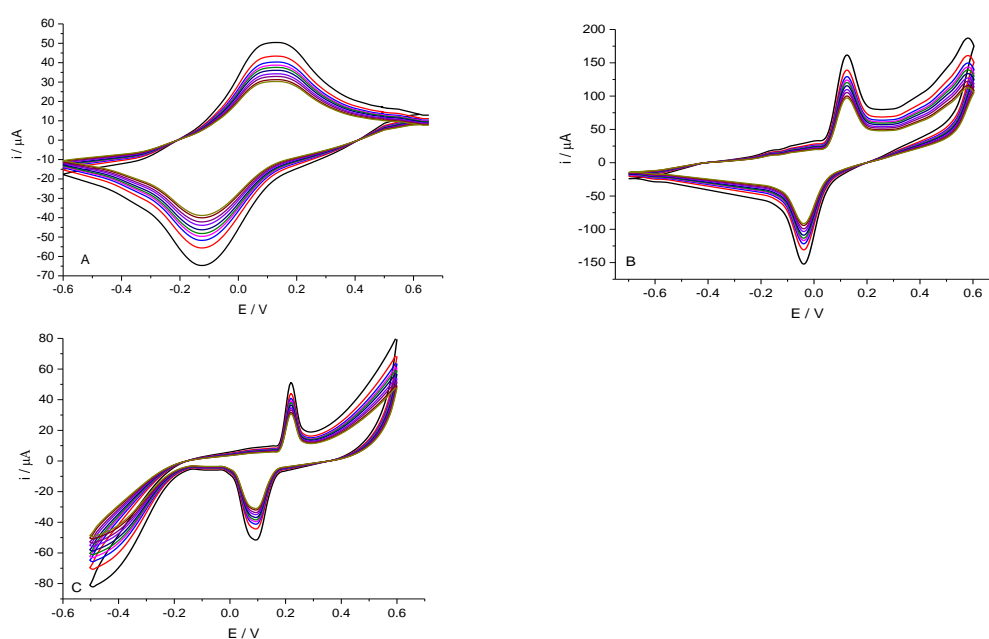


**Figure 7.39:** Cyclic voltammograms of a Thio-NTA-modified electrode in 0.1 M  $KNO_3$  after adsorbing A)  $Cu^{2+}$  ions, B)  $Ni^{2+}$  ions, and C)  $Co^{2+}$  ions (100 ppm). From the first to the tenth cycle, the scan rate was held constant at  $100\text{ mV s}^{-1}$ .

The voltammetric responses for the three metals were recorded at various sweep rates, from 10 to  $100\text{ mV s}^{-1}$ , to examine influence of variation in scan rate on the electrochemical behaviour of complexes, as shown in **Figures 7.40, 7.41, and 7.42** for copper, nickel and cobalt, respectively. Panel B in each of these figures shows that the redox peaks increased with increasing scan rate.

### 7.3.5.2 Concentration dependence of the characteristic peak charge

Using the experimental conditions described in the previous section, the ability of poly(Thio-NTA) electrodes to detect metal ions in solution was investigated using

different concentrations of the latter. **Figure 7.43** show the cyclic voltammograms recorded during the examination of a Thio-NTA-modified electrode with different  $\text{Cu}^{2+}$ ,  $\text{Ni}^{2+}$  and  $\text{Co}^{2+}$  concentrations ranging from 1 to 5000 ppm. The anodic and cathodic peak currents showed a clear increase with increasing metal ion concentration in all cases. The density charge reached to  $2300 \mu\text{C cm}^{-2}$ , corresponding to a copper coverage of  $12.48 \text{ nmol cm}^{-2}$  on the electrode when the copper concentration was 5000 ppm. The calculated peak charge for the  $\text{Ni}^{2+}$  ions was  $2840 \mu\text{C cm}^{-2}$  at 5000 ppm, corresponding to a nickel coverage of  $14.2 \text{ nmol cm}^{-2}$ , as shown in **Figure 7.43**. The charge, as obtained from the voltammetric responses of  $\text{Co}^{2+}$  ions, was equal to  $850 \mu\text{C cm}^{-2}$  at 5000 ppm, corresponding to a cobalt coverage of  $4.3 \text{ nmol cm}^{-2}$ , as shown in **Figure 7.53**. As it mentioned in the section 7.3.5.1 the cyclic voltammograms have a different shapes and these could be attributed to diverse interactions were occurs between metal ions and electrode surfaces.

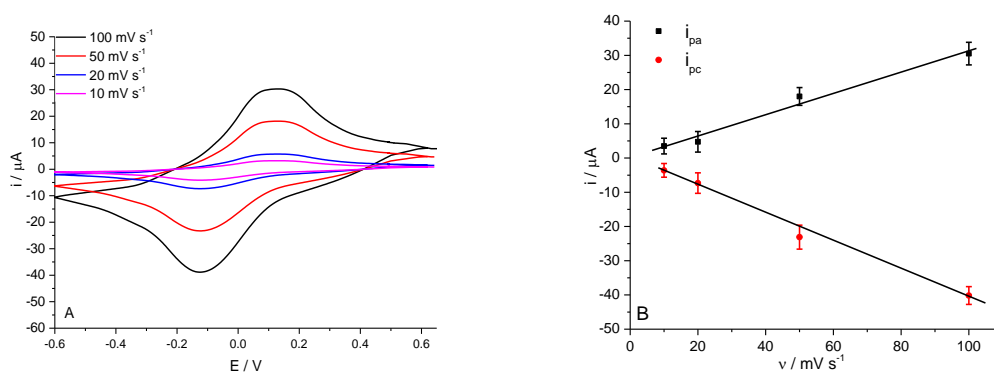


**Figure 7.40:** A) Influence of scan rate (from 10 to  $100 \text{ mV s}^{-1}$ ) on the  $\text{Cu}^{2+}/^0$  peak current in  $0.1 \text{ M KNO}_3$  solution. B) Variation of anodic and cathodic peak currents vs. scan rate. Electrode area =  $0.11 \text{ cm}^2$

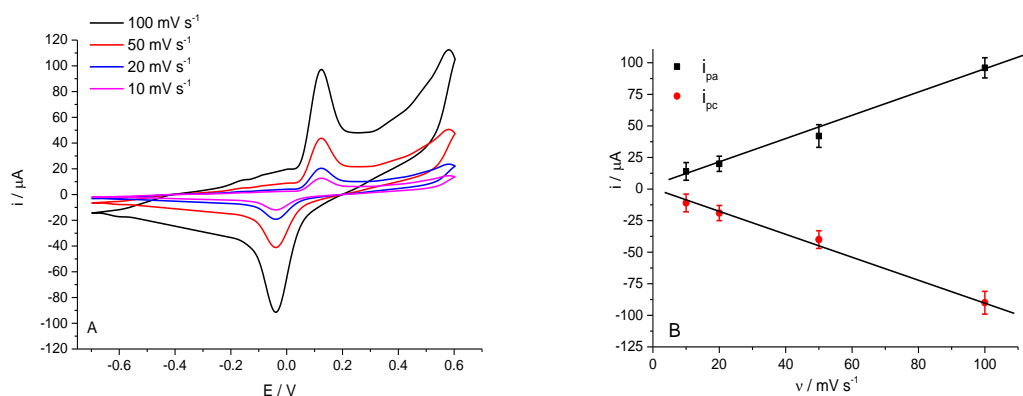


**Figure 7.41:** A) Influence of scan rate (from 10 to  $100 \text{ mV s}^{-1}$ ) on the  $\text{Ni}^{2+}/^0$  peak current in  $0.1 \text{ M KNO}_3$  solution. B) Variation of anodic and cathodic peak currents vs. scan rate. Electrode area =  $0.11 \text{ cm}^2$

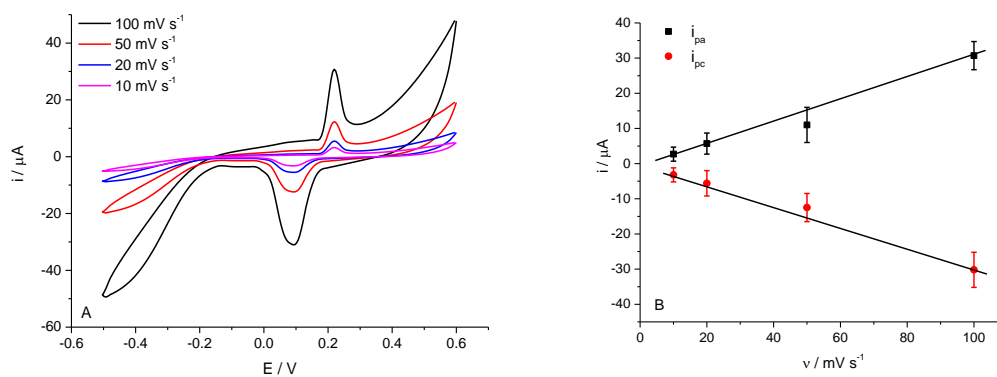


**Figure 7.42:** A) Influence of scan rate (from 10 to  $100 \text{ mV s}^{-1}$ ) on the  $\text{Co}^{2+}/^0$  peak current in  $0.1 \text{ M KNO}_3$  solution. B) Variation of anodic and cathodic peak currents vs. scan rate. Electrode area  $= 0.11 \text{ cm}^2$

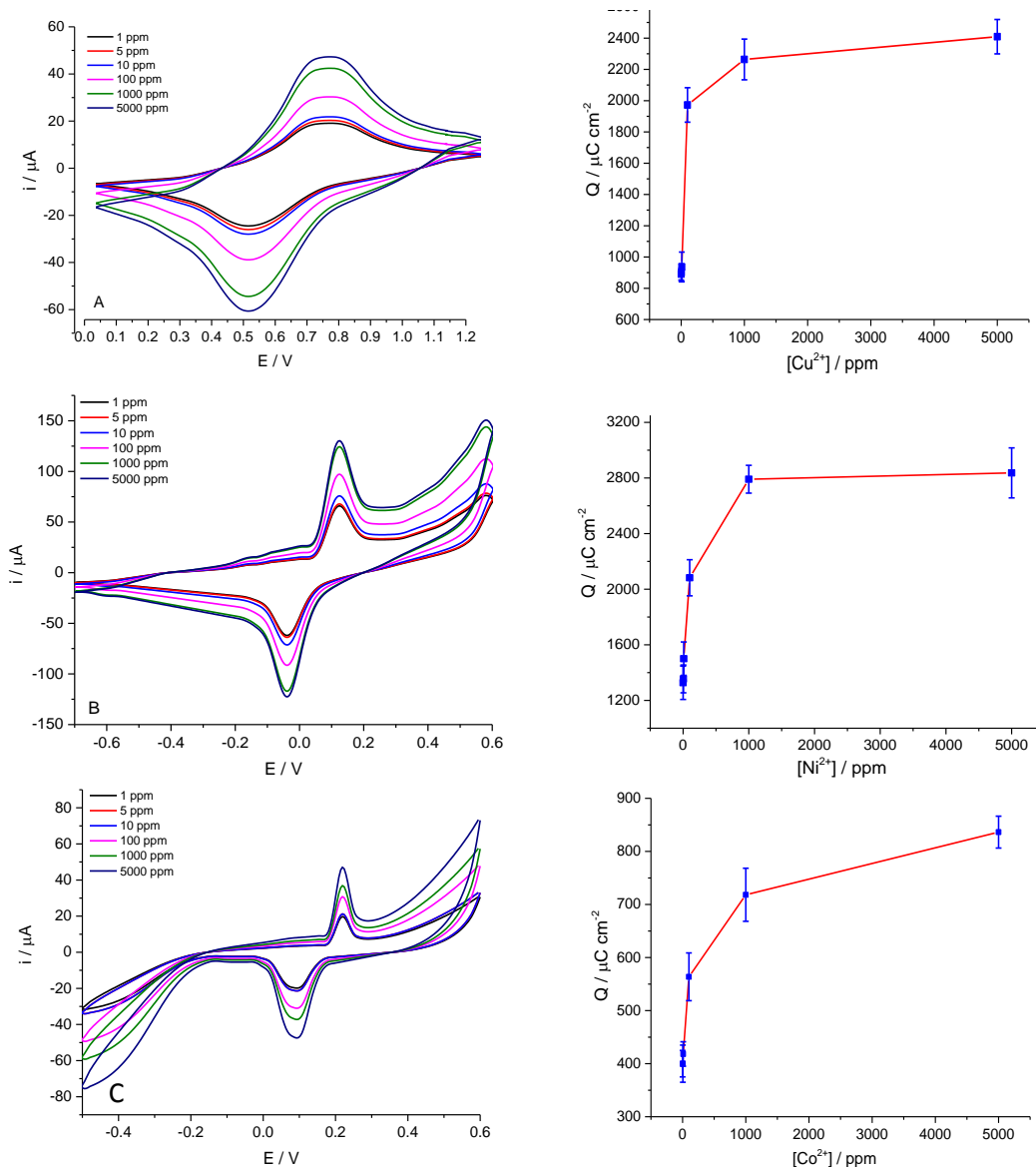


**Figure 7.43:** A) Cyclic voltammograms in blank  $\text{KNO}_3$  using a Thio-NTA modified electrode exposed to between 1 ppm to 5000 ppm A)  $\text{Cu}^{2+}$ , B)  $\text{Ni}^{2+}$  and C)  $\text{Co}^{2+}$  at a scan rate of  $100 \text{ mV s}^{-1}$ . (Inset curve charge response as a function of concentration).

### 7.3.5.3 Estimate of the molar ratio between metal ions and polymer electrode

The surface coverage of complexed metal ions ( $\Gamma_m$ ) was calculated by integration of peaks by using Faraday's laws. **Table 7.12** shows the coverage of metal ions and the molar ratio between metal ions and Thio-NTA. From the data in the table, it can be seen that the saturation surface coverage of the three metal ions on the Thio-NTA electrode obtained from the 1000 and 5000 ppm solutions was varied, at 12.48, 14.2, and 4.3 nmol cm<sup>-2</sup> for Cu<sup>2+</sup>, Ni<sup>2+</sup> and Co<sup>2+</sup>, respectively. The surface coverage of the ligand was estimated using cyclic voltammetry and was equal to 12.6 nmol cm<sup>-2</sup>.

### 7.3.5.4 Fitting the data to the different isotherms

The adsorption isotherms were investigated to study the experimental results, as shown in **Figures 7.44, 7.45, and 7.46** for Cu<sup>2+</sup>, Ni<sup>2+</sup> and Co<sup>2+</sup>, respectively. The findings here show that the Frumkin isotherm gives the best fit for the adsorption of all metal ions onto the modified electrode; the results can be arranged from best to worst isotherm as follows: Frumkin > Temkin > Freundlich > Langmuir. Characteristic parameters were calculated using Frumkin equation, as reported in **Table 7.13**.

Metal	Concentration	charge / C	$\Gamma_m$ (nmol.cm <sup>-2</sup> )	Molar ratio $\Gamma_m / \Gamma_{\text{polymer}}$
Cu <sup>2+</sup>	5000 ppm	2.65 x 10 <sup>-4</sup>	12.48	0.99
	1000 ppm	2.49 x 10 <sup>-4</sup>	11.73	0.93
	100 ppm	2.17 x 10 <sup>-4</sup>	10.3	0.81
	10 ppm	1.03 x 10 <sup>-4</sup>	4.9	0.38
	5 ppm	9.92 x 10 <sup>-5</sup>	4.67	0.37
	1 ppm	9.88 x 10 <sup>-5</sup>	4.65	0.36
Ni <sup>2+</sup>	5000 ppm	3.02 x 10 <sup>-4</sup>	14.2	1.12
	1000 ppm	2.87 x 10 <sup>-4</sup>	13.5	1.07
	100 ppm	2.29 x 10 <sup>-4</sup>	10.7	0.85
	10 ppm	1.65 x 10 <sup>-4</sup>	7.8	0.61
	5 ppm	1.48 x 10 <sup>-4</sup>	7	0.55
	1 ppm	1.46 x 10 <sup>-4</sup>	6.87	0.54
Co <sup>2+</sup>	5000 ppm	9.18 x 10 <sup>-5</sup>	4.3	0.35
	1000 ppm	7.94 x 10 <sup>-5</sup>	3.8	0.30
	100 ppm	6.27 x 10 <sup>-5</sup>	3	0.23
	10 ppm	4.53 x 10 <sup>-5</sup>	2.15	0.17
	5 ppm	4.36 x 10 <sup>-5</sup>	2.05	0.16
	1 ppm	4.35 x 10 <sup>-5</sup>	2.05	0.16

**Table 7.12:** Charges, surface coverages and the molar ratios for metal/Thio-NTA-modified electrode at different metal ion concentrations. Scan rate was fixed at 100 mV s<sup>-1</sup>. The surface coverage of the polymer film was estimated at 12.6 nmol cm<sup>-2</sup>.

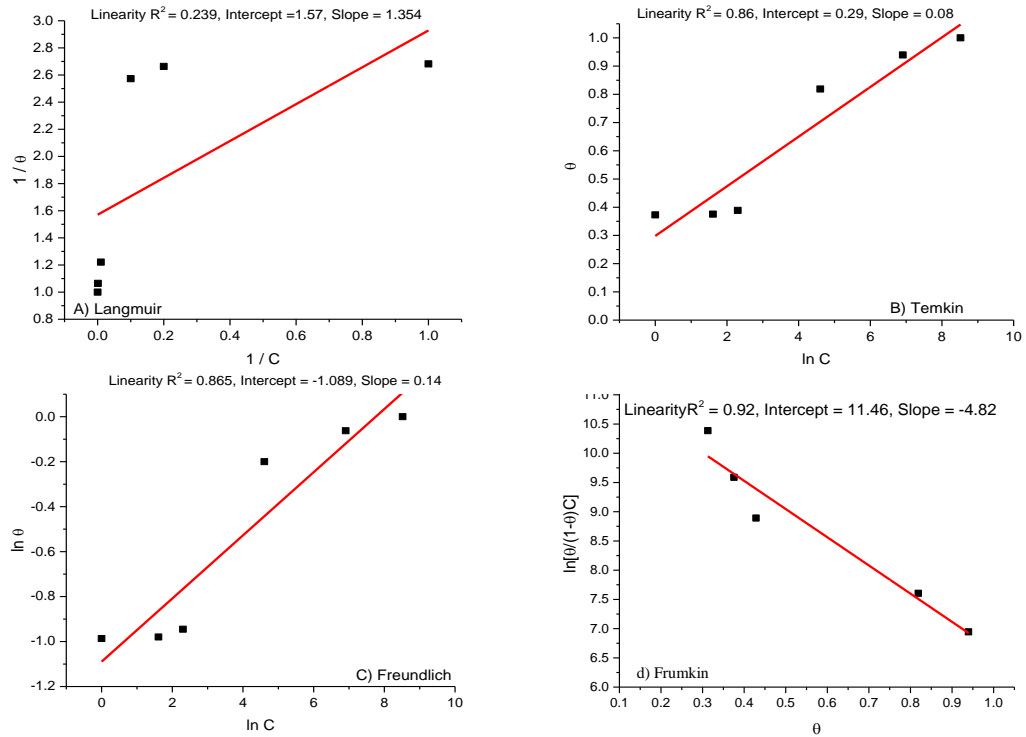


Figure 7.44: Plots of four isotherms: a) Langmuir isotherm, b) Temkin isotherm, c) Freundlich isotherm, and d) Frumkin isotherm for the binding between copper and the Thio-NTA electrode.

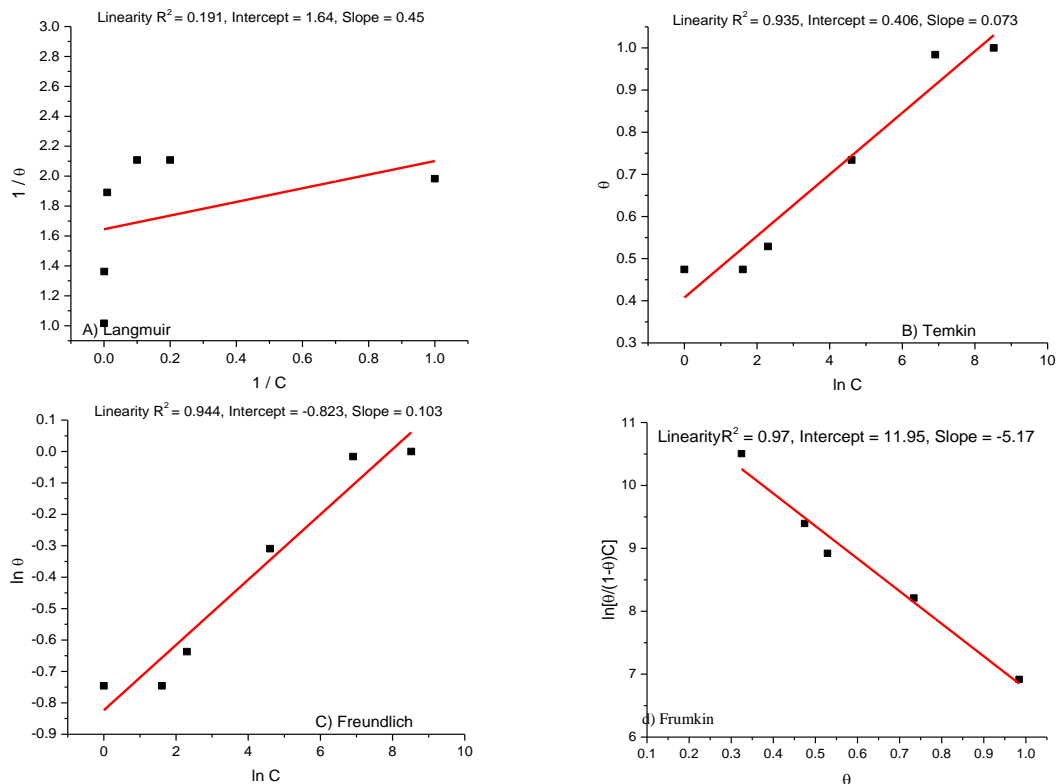
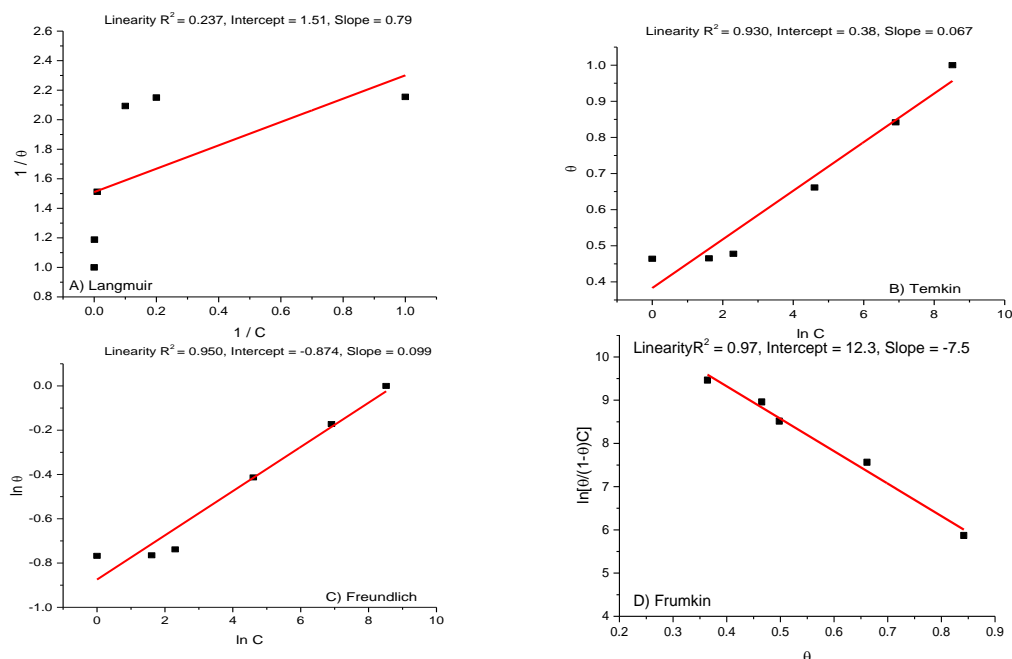


Figure 7.45: Plots of four isotherms: a) Langmuir isotherm, b) Temkin isotherm, c) Freundlich isotherm, and d) Frumkin isotherm for the binding between nickel and the Thio-NTA electrode.



**Figure 7.46:** Plots of four isotherms: a) Langmuir isotherm, b) Temkin isotherm, c) Freundlich isotherm, and d) Frumkin isotherm for the binding between cobalt and the Thio-NTA electrode.

Metal ions	$\ln K$	$10^6 K / M^{-1}$	$\log K$	$a$	$\Delta G^\circ \text{ K J.mol}^{-1}$
Copper	11.6	0.10	5.0	-4.8	-29
Nickel	11.9	0.14	5.1	-5.1	-29.8
Cobalt	12.3	0.21	5.3	-7.5	-30.8

**Table 7.13:** Values of calculated  $a$ ,  $\log K$  and  $\Delta G^\circ$  parameters for metal binding to the Thio-NTA electrode based on the Frumkin isotherm.

### 7.3.6 Voltammetric response of Poly(Thio-HQC) to metal ions

The electrochemical behaviour between metal ions and the Thio-HQC-modified electrode were examined in this section using potentiodynamic measurement. To accomplish these experiments, poly(Thio-HQC) electrodes were immersed in individual metal ion solutions, as described in the previous **section 7.3.5**. The free hydroxyl groups and nitrogen atom in the HQC molecules can bind with these metal ions to form stable complexes. Cyclic voltammograms were obtained using a potential ranging between -0.8 to 0.7, -0.5 to 0.5 and -0.7 to 0.7 V vs. (Ag/AgCl) for  $\text{Cu}^{2+}$ ,  $\text{Ni}^{2+}$  and  $\text{Co}^{2+}$ , respectively, at different scan rates (10, 20, 50 and 100  $\text{mV s}^{-1}$ ). The cyclic voltammetry measurements show that the Thio-HQC has high affinities for copper, nickel and cobalt ions in aqueous solution. The cyclic voltammetry responses showed that the Thio-HQC-modified electrode has the ability to recognise metal ions in aqueous solutions. **Figure 7.47** shows the cyclic voltammogram of an electrode modified with poly(Thio-HQC) obtained in a

metal-free nitrate solution at  $10 \text{ mV s}^{-1}$  (black curve) and after an immersion step in 100 ppm metal ion solution for 20 mins. (red curve). From curve a, it can be seen that all cyclic voltammograms were electrochemically inert within the potential windows applied. Conversely, curve B in each instance demonstrates the electrochemical responses of the polymer-modified electrodes after exposure to metal ion solutions with clear redox peaks due to the formation of metal complexes. **Figure 7.47** panel I shows the cyclic voltammogram of the redox current of  $\text{Cu}^{2+}/\text{Cu}^{\circ}$  at  $E_{p,a} = 0.18 \text{ V}$  and  $E_{p,c} = -0.15 \text{ V}$ , whereas the voltammetric responses to the oxidation/reduction of  $\text{Ni}^{2+}/\text{Ni}^{\circ}$  appeared at  $E_{p,a} = 0.122 \text{ V}$  and  $E_{p,c} = -0.01 \text{ V}$ , as shown in the Figure 7.47 (panel II). However, the **Figure 7.47** (panel III) depicts the voltammetric response of poly(Thio-HQC) having been exposed to a  $\text{Co}^{2+}$  ion solution with redox peak currents at  $E_{p,a} = 0.26 \text{ V}$  and  $E_{p,c} = 0.05 \text{ V}$ . These findings indicate that the redox peaks of metal complexes are undoubtedly due to the formation an ion/metal redox transition, where the voltammetric response of poly(Thio-HQC) without exposure to any metal ion solution formed a “control experiment” which, when performed under identical conditions, demonstrated that the polymer electrode itself does not show redox peaks within same potential windows because of there is no redox reaction of polymer within studied potential window.

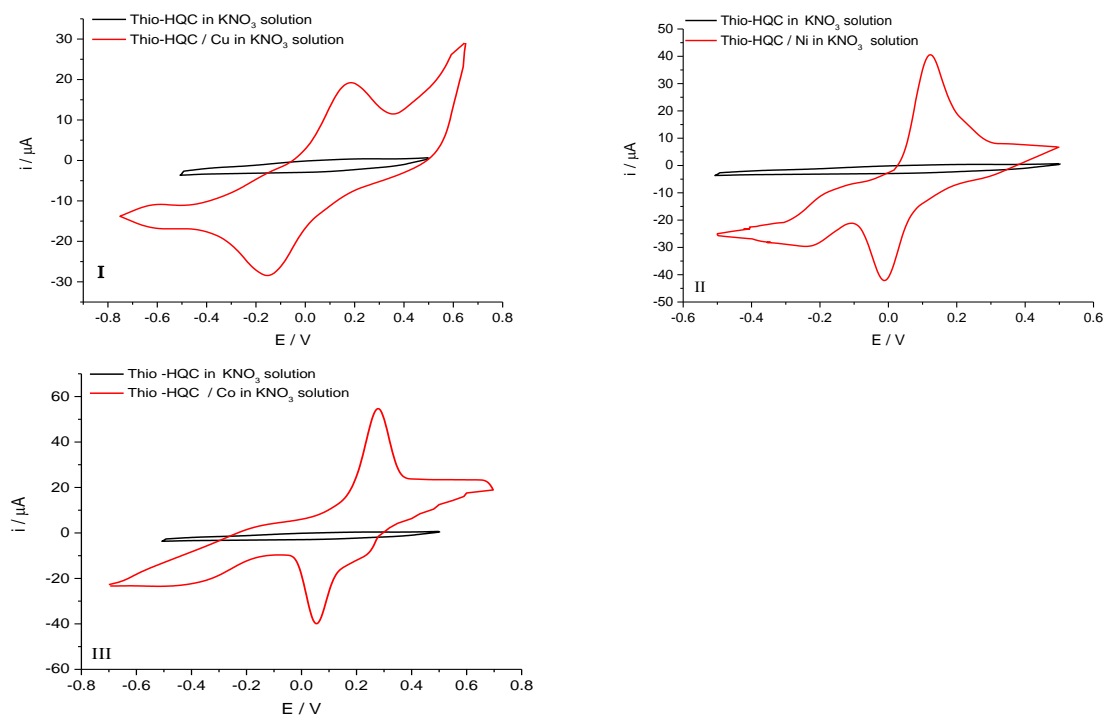


**Figure 7.47:** Cyclic voltammogram of Thio -HQC modified electrode (black curve) in metal-free  $\text{KNO}_3$  solution at  $10 \text{ mV s}^{-1}$ , (red curve) Thio-NTA electrode in  $\text{KNO}_3$  solution after exposure to 100 ppm of metal ions solution: I)  $\text{Cu}^{2+}$  II)  $\text{Ni}^{2+}$  III)  $\text{Co}^{2+}$  at  $100 \text{ mV s}^{-1}$ .

### 7.3.6.1 Stability and influence of the sweep rate on metal complexes

Any voltammetric response of the poly(Thio-HQC) electrode to metal ions should be attributable to the coordination between these metals and the Thio-HQC electrode surface when in solution. The voltammetric behaviour of the metal-poly(Thio-HQC) electrodes over ten cycles are shown in **Figure 7.48**. These cyclic voltammograms show that there are two current peaks corresponding to a redox process. It may be noted that these peaks decreased slightly after the first and second scan cycles, but stabilised in subsequent scans. These voltammetric properties indicate that there is strong complexation between the metal ions and the polymer surface.

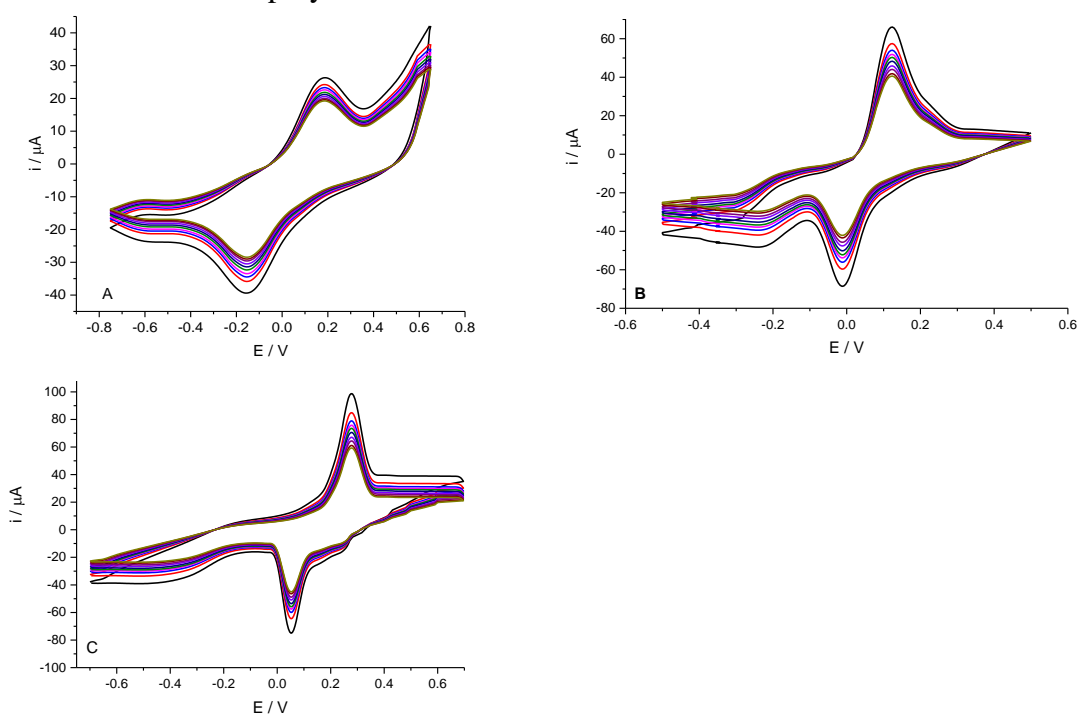


**Figure 7.48:** Cyclic voltammograms of Thio-HQC modified electrode in 0.1 M  $\text{KNO}_3$ , after adsorbing A)  $\text{Cu}^{2+}$  ions, B)  $\text{Ni}^{2+}$  ions, and C)  $\text{Co}^{2+}$  ions (100 ppm). From first to 10th cycles, scan rate was  $100 \text{ mV s}^{-1}$ .

The stability of the cyclic voltammograms for the three metal complexes was examined for various scan rates, ranging from 10 to  $100 \text{ mV s}^{-1}$ , as shown in **Figures 7.49**, **7.50**, and **7.51** for copper, nickel and cobalt, respectively. It may be noted from panel B in each of these figures that the oxidation and reduction peaks increased linearly with increasing sweep rate, indicating a surface redox reaction

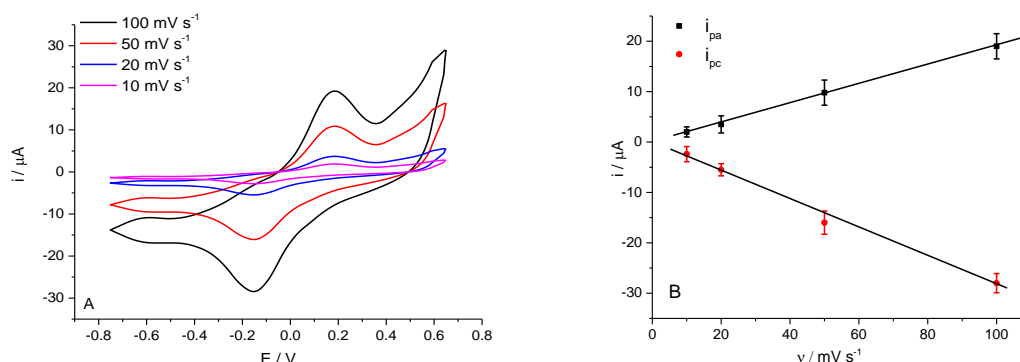


**Figure 7.49:** A) Influence of scan rate (from 10 to 100  $\text{mV s}^{-1}$ ) on the  $\text{Cu}^{2+}$  peak current in 0.1 M  $\text{KNO}_3$  solution. B) Variation of anodic and cathodic peak currents vs. scan rate. Electrode area =  $0.11 \text{ cm}^2$

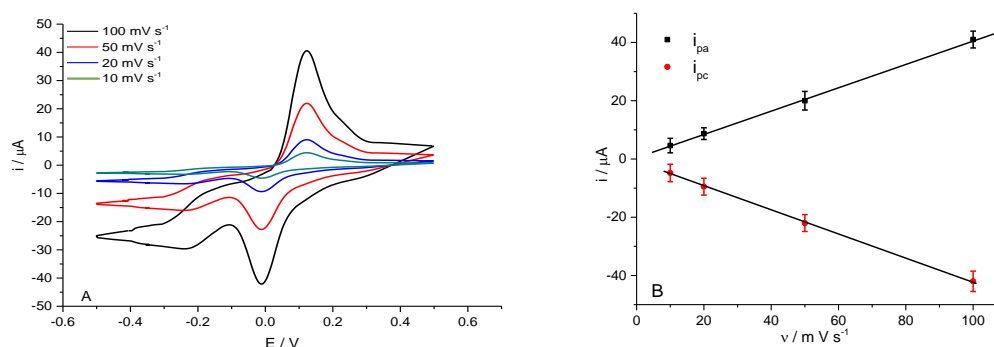


**Figure 7.50:** A) Influence of scan rate (from 10 to 100  $\text{mV s}^{-1}$ ) on the  $\text{Ni}^{2+}$  peak current in 0.1 M  $\text{KNO}_3$  solution. B) Variation of anodic and cathodic peak currents vs. scan rate. Electrode area =  $0.11 \text{ cm}^2$

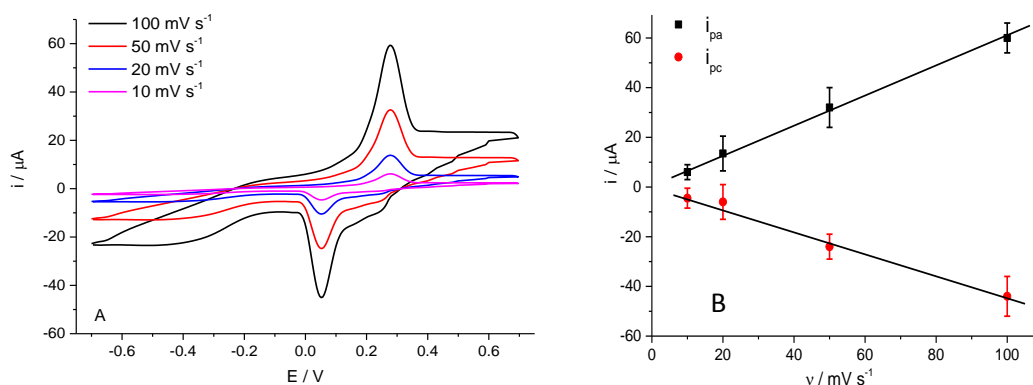


**Figure 7.51:** A) Influence of scan rate (from 10 to 100  $\text{mV s}^{-1}$ ) on the  $\text{Co}^{2+}$  peak current in 0.1 M  $\text{KNO}_3$  solution. B) Variation of anodic and cathodic peak currents vs. scan rate. Electrode area =  $0.11 \text{ cm}^2$

### 7.3.6.2 Concentration dependence of the characteristic peak charge

The ability of the poly(Thio-HQC)-modified electrode to detect metal ions in different concentrations was investigated over a 1 ppm to 5000 ppm range under identical experimental conditions to those described above. **Figure 7.52** shows the cyclic voltammograms obtained using a Thio-HQC electrode film with  $\text{Cu}^{2+}$ ,  $\text{Ni}^{2+}$  and  $\text{Co}^{2+}$  ions,

respectively. These results demonstrate that the redox peaks increased with increasing concentration of metal ions. The inset curves in all three figures depict the calibration curve for the detection of metal ions via the modified electrode. The density charge clearly increased with increasing copper ion concentration. The density charge was  $1230 \mu\text{C cm}^{-2}$ , corresponding to a copper coverage of  $6.41 \text{ nmol cm}^{-2}$  on the electrode at 5000 ppm, whereas the density charge value of  $\text{Ni}^{2+}$  ions was equal to  $1870 \mu\text{C cm}^{-2}$ , corresponding to a nickel coverage of  $10.1 \text{ nmol cm}^{-2}$  at 5000 ppm, as shown in **Figure 7.52**. The density charge obtained from the voltammetric responses of  $\text{Co}^{2+}$  ions was  $1750 \mu\text{C cm}^{-2}$ , corresponding to a cobalt coverage of  $9 \text{ nmol cm}^{-2}$  at 5000 ppm, as shown in **Figure 7.52**.

### 7.3.6.3 Estimate of the molar ratio between metal ions and polymer electrode

The surface coverage of metal ions ( $\Gamma_m$ ) was calculated by integration of peaks by using Faraday's law (see **chapter 4**). The molar ratios between the metal ions and Thio-HQC-modified electrode are reported in **Table 7.14**. From the results shown in this table, it can be seen that the ratio of the saturated coverage of metal ions varies depending on the nature of the metal ions at a fixed scan rate of  $100 \text{ mV s}^{-1}$ .

### 7.3.6.4 Fitting the data to the different isotherms

The adsorption isotherms were investigated to study the experimental results, as shown in Figures 7.53, 7.54, and 7.55 for  $\text{Cu}^{2+}$ ,  $\text{Ni}^{2+}$  and  $\text{Co}^{2+}$ , respectively. The findings illustrate that the Frumkin isotherm represents the best fit to experimental data for the adsorption of the metal ions onto the modified electrode; the isotherms can be arranged from best to least appropriate as follows: Freundlich > Frumkin > Temkin > Langmuir Characteristic parameters  $\log K$ ,  $a$ ,  $\Delta G^\circ$  were calculated using Frumkin equation, as reported in **Table 7.15**.

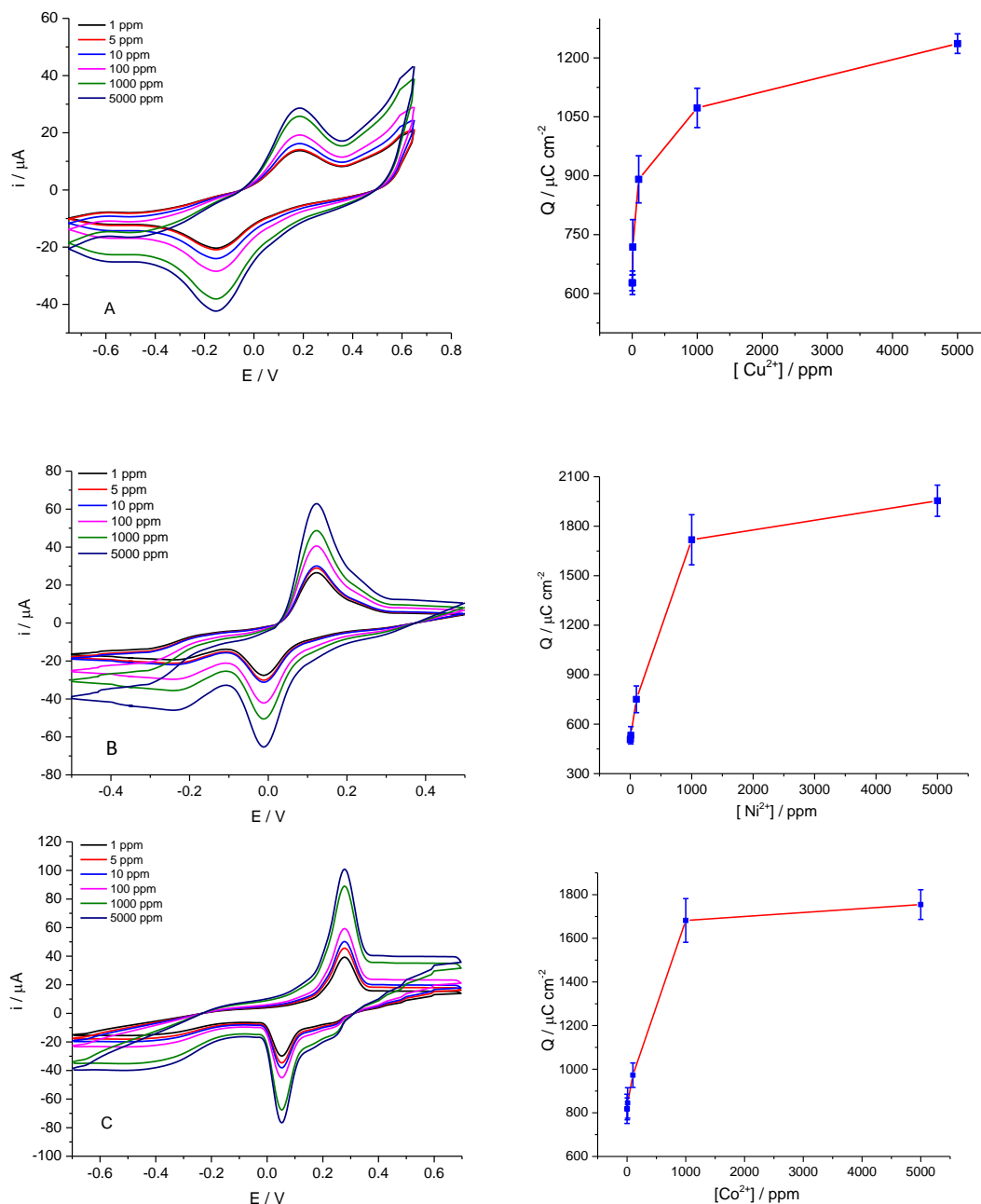


**Figure 7.52:** A) Cyclic voltammograms in blank  $\text{KNO}_3$  solution using a Thio-HQC-modified electrode exposed to between 1 ppm to 5000 ppm A)  $\text{Cu}^{2+}$ , B)  $\text{Ni}^{2+}$  and C)  $\text{Co}^{2+}$  at a scan rate of  $100 \text{ mV s}^{-1}$ . (Inset curve cathodic peak charge response as a function of concentration).

Metal	Concentration	charge / C	$\Gamma_m$ (nmol.cm <sup>-2</sup> )	Molar ratio $\Gamma_m / \Gamma_{\text{polymer}}$
Cu <sup>2+</sup>	5000 ppm	$1.36 \times 10^{-4}$	6.41	0.68
	1000 ppm	$1.18 \times 10^{-4}$	5.6	0.59
	100 ppm	$9.55 \times 10^{-5}$	4.5	0.48
	10 ppm	$7.96 \times 10^{-5}$	3.7	0.39
	5 ppm	$6.97 \times 10^{-5}$	3.2	0.34
	1 ppm	$6.94 \times 10^{-5}$	3.2	0.34
Ni <sup>2+</sup>	5000 ppm	$2.15 \times 10^{-4}$	10.1	1.06
	1000 ppm	$1.89 \times 10^{-4}$	8.9	0.95
	100 ppm	$8.26 \times 10^{-5}$	3.9	0.42
	10 ppm	$5.86 \times 10^{-5}$	2.76	0.29
	5 ppm	$5.60 \times 10^{-5}$	2.63	0.28
	1 ppm	$5.55 \times 10^{-5}$	2.61	0.27
Co <sup>2+</sup>	5000 ppm	$1.93 \times 10^{-4}$	9	0.96
	1000 ppm	$1.85 \times 10^{-4}$	8.7	0.93
	100 ppm	$1.07 \times 10^{-4}$	5	0.53
	10 ppm	$9.38 \times 10^{-5}$	4.4	0.47
	5 ppm	$9.02 \times 10^{-5}$	4.2	0.44
	1 ppm	$9.00 \times 10^{-5}$	4.2	0.44

**Table 7.14:** Charges, surface coverages and molar ratios for metal/Thio-HQC-modified electrode at different metal ion concentrations. Scan rate was fixed at 100 mV s<sup>-1</sup>. The surface coverage of the polymer film was estimated at 9.35 nmol cm<sup>-2</sup>.

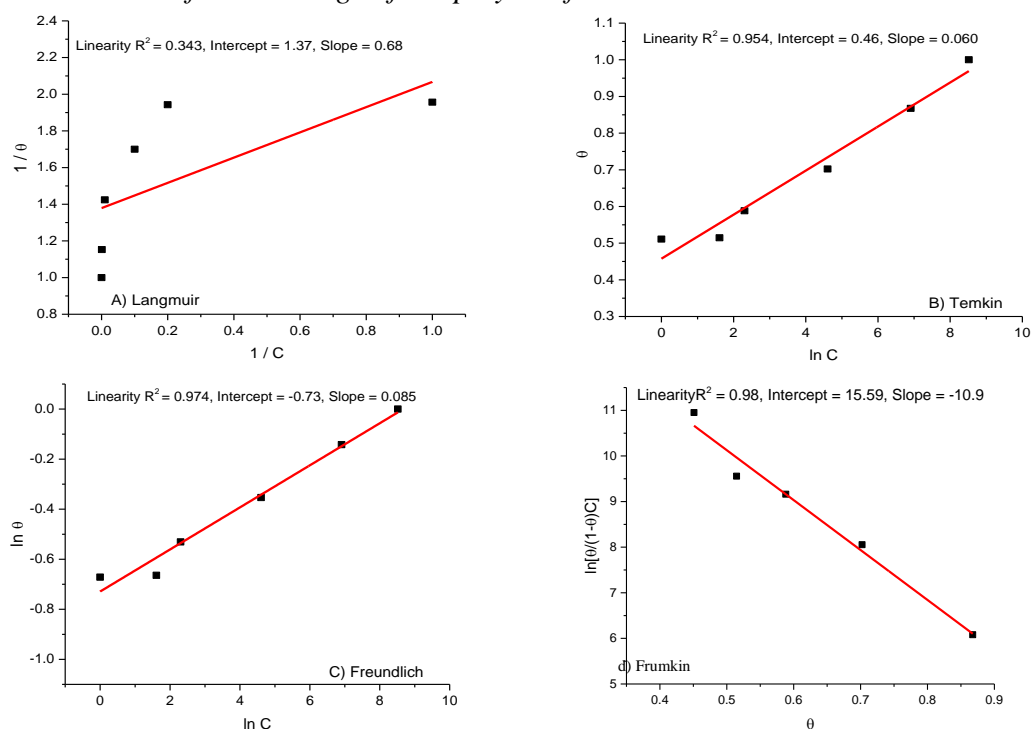


**Figure 7.53:** Plots of four isotherms; a) Langmuir isotherm, b) Temkin isotherm, c) Freundlich isotherm, and d) Frumkin isotherm for binding between copper and Thio-HQC electrode.

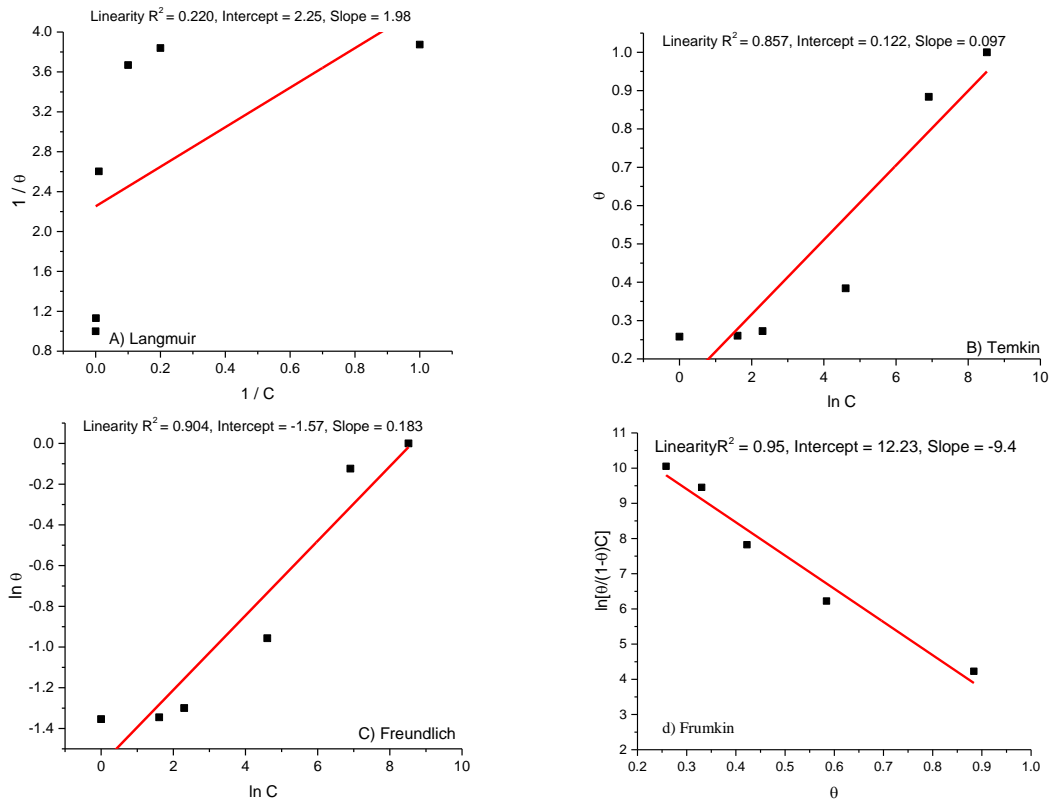


**Figure 7.54:** Plots of four isotherms: a) Langmuir isotherm, b) Temkin isotherm, c) Freundlich isotherm, and d) Frumkin isotherm for the binding between nickel and the Thio-HQC electrode.

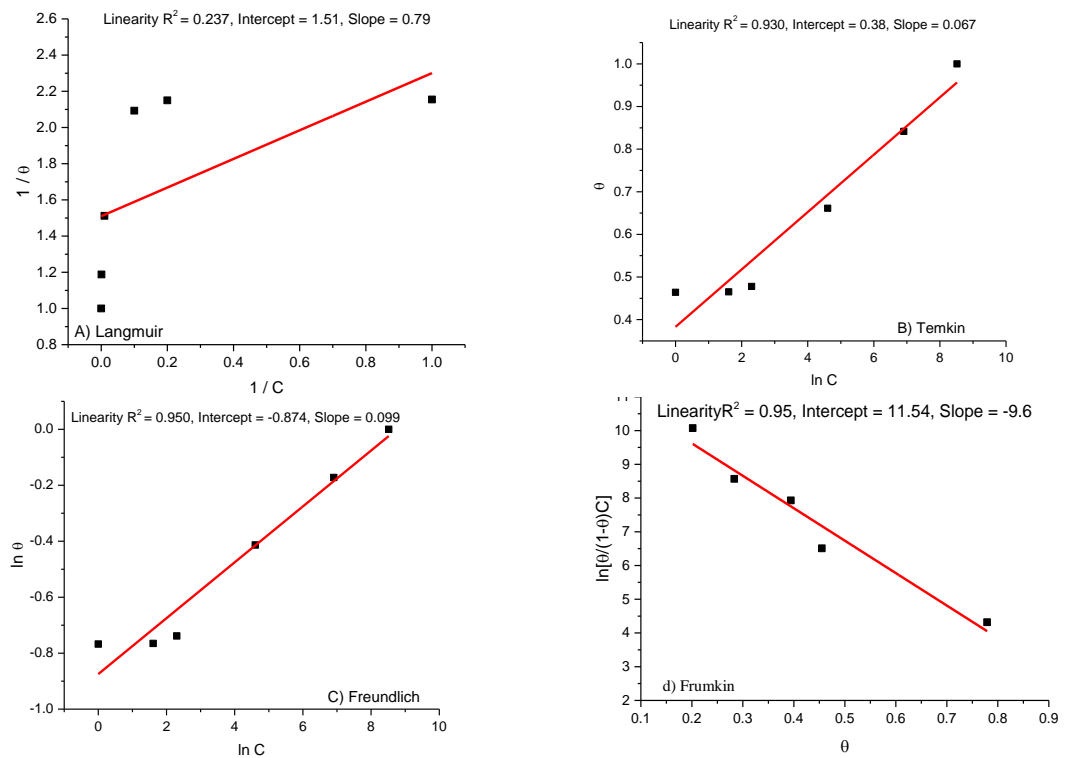


**Figure 7.55:** Plots of four isotherms: a) Langmuir isotherm, b) Temkin isotherm, c) Freundlich isotherm, and d) Frumkin isotherm for the binding between cobalt and the Thio-HQC electrode.

Metal ions	$\ln K$	$10^6 K / M^{-1}$	$\log K$	$a$	$\Delta G^\circ$ K J.mol <sup>-1</sup>
Copper	15.5	5.38	6.7	-10.9	-38.8
Nickel	12.2	0.19	5.3	-9.4	-30.5
Cobalt	11.5	0.09	5	-9.6	-28.8

**Table 7.15:** Values of calculated  $a$ ,  $\log K$  and  $\Delta G$  parameters for metal binding to the Thio-NTA electrode based on the Frumkin isotherm.

#### 7.4 Conclusions

The experiments discussed in this chapter have demonstrated the successful electrochemical responses of various polymer-modified electrodes to copper, nickel and cobalt ions in solution. The findings indicate that complex formation can be applied to detect target metal ions in aqueous solution. Voltammetric responses between the polymer surfaces and the metal ions were examined in terms of several experimental variables, namely scan rate, repetitive cycling, and concentration of metal ions. This study involved the use of different concentrations of metal ions (1 ppm to 5000 ppm) and use electrochemical monitoring to study the recognition efficiency for metal ions. The results illustrated that peak charge for metal complexes depends on the metal ion concentration, and that this method can be applied to detect trace metal ion concentrations at the ppm level. The stability of the cyclic voltammograms was obtained at different scan rates, from 10 to 100 mV s<sup>-1</sup>. The saturated surface coverage of metal ions was calculated for different concentrations of metal ions using the integrated peak charge; the molar ratio of the metal ions to the receptors that was found. Freundlich, Frumkin, Temkin and Langmuir models were applied to select which isotherm best represented progress. Results illustrate that the Frumkin isotherm offered the best fitting for all of metal ions with polymer electrodes. From these findings it can be concluded there are interactions occurred between sites on heterogeneous surface as assumptions of Frumkin and Freundlich models. While, the Langmuir equation was least appropriate model because it assumes there is a monolayer surface without interactions. The thermodynamics of adsorption was provided useful evidences about the nature of adsorption process. Where the negative value of  $\Delta G^\circ$  indicated that the adsorption was spontaneous process and happened via chemical adsorption.

## 7.5 References

1. M. B. Gumpu, S. Sethuraman, U. M. Krishnan and J. B. B. Rayappan, *Sensors and Actuators B: Chemical*, 2015, **213**, 515-533.
2. W.-W. Zhao, J.-J. Xu and H.-Y. Chen, *Analyst*, 2016, **141**, 4262-4271.
3. G. Zhu and C.-y. Zhang, *Analyst*, 2014, **139**, 6326-6342.
4. D. T. McQuade, A. E. Pullen and T. M. Swager, *Chemical Reviews*, 2000, **100**, 2537-2574.
5. A. Ramanavičius, A. Ramanavičienė and A. Malinauskas, *Electrochimica Acta*, 2006, **51**, 6025-6037.
6. H. Yoon, *Nanomaterials*, 2013, **3**, 524-549.
7. M. Lin, M. Cho, W.-S. Choe, Y. Son and Y. Lee, *Electrochimica Acta*, 2009, **54**, 7012-7017.
8. M. A. Rahman, P. Kumar, D.-S. Park and Y.-B. Shim, *Sensors*, 2008, **8**, 118-141.
9. C. Li, H. Bai and G. Shi, *Chemical Society Reviews*, 2009, **38**, 2397-2409.
10. G. March, T. D. Nguyen and B. Piro, *Biosensors*, 2015, **5**, 241-275.
11. C. Nicosia and J. Huskens, *Materials horizons*, 2014, **1**, 32-45.
12. A. Sassolas, L. J. Blum and B. D. Leca-Bouvier, *Biotechnology advances*, 2012, **30**, 489-511.
13. Y. Lei, S. Yang, M. Wu and G. Wilde, *Chemical Society Reviews*, 2011, **40**, 1247-1258.
14. E. Chow, E. L. S. Wong, T. Böcking, Q. T. Nguyen, D. B. Hibbert and J. J. Gooding, *Sensors and Actuators B: Chemical*, 2005, **111**, 540-548.
15. M. Lin, M. Cho, W. Choe, J.-B. Yoo and Y. Lee, *Biosensors and Bioelectronics*, 2010, **26**, 940-945.
16. I. Kerekovic, S. Milardovic, M. Palcic and Z. Grabaric, *Journal of Electroanalytical Chemistry and Interfacial Electrochemistry*, 2014, **724**, 103-110.
17. G. O. Buica, C. Bucher, J. Moutet, G. Royal, E. Saint-Aman and E. M. Ungureanu, *Electroanalysis*, 2009, **21**, 77-86.
18. A. M. Hewas, pH.D Thesis, University of Leicester, 2013.
19. Z. Xu, J.-g. Cai and B.-c. Pan, *Journal of Zhejiang University Science A*, 2013, **14**, 155-176.
20. B. Crittenden and W. J. Thomas, *Adsorption Technology and Design*, Elsevier Science, 1998.
21. N. Ünlü and M. Ersoz, *Journal of Hazardous Materials*, 2006, **136**, 272-280.
22. R. T. Loto, C. A. Loto and T. Fedotova, *Research on Chemical Intermediates*, 2014, **40**, 1501-1516.
23. M. G. Bridelli and P. R. Crippa, *Adsorption*, 2008, **14**, 101-109.
24. A. E. Martell and R. M. Smith, *Critical stability constants: Other organic ligands*, Plenum Press, 1977.
25. A. Albert, *Biochemical journal*, 1953, **54**, 646-654.

<b>8.1 Conclusions</b> .....	<b>240</b>
8.1.1 Functionalised polypyrrole films .....	240
8.1.2 Functionalised polyaniline films .....	243
8.1.3 Functionalised polythiophene films .....	244
8.1.4 Application of patterned electrode as chemical sensor .....	245
<b>8.2 Future work</b> .....	<b>246</b>
<b>8.3 References</b> .....	<b>248</b>

## 8.1 Conclusions

Conducting polymers have a number of prospective applications based on their electronic properties. These properties can be exploited via functionalisation, leading to high selectivity sensors and catalysts, for instance.<sup>1</sup> Current studies are focused on the immobilisation of functional groups on polymer surfaces to create smart surfaces and allow control over reactivity and functionality at polymer surfaces in general.<sup>2, 3</sup> The fabrication of patterned surfaces and smart surfaces that contain diverse functionalities has allowed for the creation of materials that are responsive to various stimuli within particular spatial areas of the film surface.<sup>4</sup> This project aimed to prepare patterned functionalised conducting polymer films and determine the efficiency of these resultant polymer films under different conditions. The main goal of the project described in this thesis is to prepare modified electrode films by systematic modification of functionalised conducting polymers, such that they can be used as analytical devices to detect and quantify metal ions in solution. This involves studying the characteristics of polymer films using electrochemical techniques (including cyclic voltammetry, EQCM and chronoamperometry) with surface characteristic methods (3D optical microscopy, SEM, AFM and vibrational spectroscopy).

### 8.1.1 Functionalised polypyrrole films

Functionalised polypyrrole films were formed electrochemically by using cyclic voltammetry and chronoamperometry. Cyclic voltammograms of Py-COOH (structure shown in **Figure 8.1**) illustrated that the oxidation potential of the functionalised monomer was higher than that found for pyrrole monomer, due to the electronic effect of the carboxylic acid group and its steric hindrance on the pyrrole molecule.<sup>5</sup> For the same reason, cyclic voltammograms of amino pyrrole (Py-NH<sub>2</sub>), ester pyrrole (Py-pfp) and amide pyrrole (Py-Fmoc) showed that oxidation potential of functionalised monomers was higher than for pyrrole.<sup>6-8</sup> Polymer films which were polymerised using potential step method show that the electropolymerisation charge increased with  $t^{1/2}$  as result of diffusion control. Data from EQCM experiments were used to estimate the mass change associated with electropolymerisation and to study electrochemical behaviour of polymer films in monomer-free solutions.

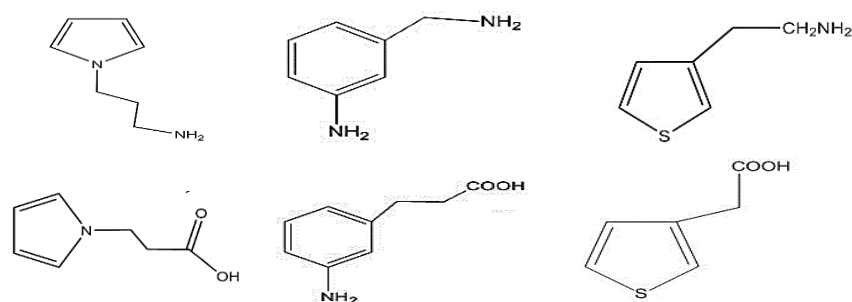


**Figure 8.1:** Chemical structures of monomers used in this thesis.

Furthermore, poly(Py-pfp) and poly(Py-Fmoc) films were hydrolysed using 0.1 M sodium hydroxide and 30% piperidine solutions, respectively. FTIR results confirmed that the ester and amide groups no longer appear in the spectrum of the film after hydrolysis: this is evidence of successful hydrolysis. The QCM technique was applied to monitor the hydrolysis process for both polymer films. Mass and electroactive site coverage of polymer films before and after hydrolysis were interpreted using Faraday's law. The voltammetric data were used to estimate surface coverage of the representative polymer film to be  $1.5 \times 10^{-7} \text{ mol cm}^{-2}$  (14.2  $\mu\text{g}$ ) and  $1.1 \times 10^{-7} \text{ mol cm}^{-2}$  (10.2  $\mu\text{g}$ ) for py-pfp and py-Fmoc, respectively. The mass change was equal to -2.45  $\mu\text{g}$  and -2.85  $\mu\text{g}$  for py-pfp and py-Fmoc, respectively, based on QCM data as shown in the Table 8.1. The hydrolysis process led to loss of pfp and Fmoc groups from polymer chains, creating free volume and decrease of film mass. Findings demonstrated that the solvation changes were 40% and 30% for Poly(py-pfp) and poly(py-Fmoc) respectively. This difference in polymer film mass between poly(Py-pfp) and poly(Py-COOH), with almost the same  $\Gamma$  values, shows the capability to create voids leading to ingress of a large amount of solvent into the polymer film during hydrolysis. **Table 8.1** shows the mass and surface coverage for all polymer films (before and after hydrolysis).

Films	Polymer deposition		polymer hydrolysis	
	$\Gamma / \text{mol cm}^{-2}$	$\Delta M / \mu\text{g cm}^{-2}$	$\Gamma / \text{mol cm}^{-2}$	$\Delta M / \mu\text{g cm}^{-2}$
Py-pfp	$1.50 \times 10^{-7}$	14.2	$1.51 \times 10^{-7}$	-2.45
Py-Fmoc	$1.10 \times 10^{-7}$	10.2	$9.65 \times 10^{-8}$	-2.85
Ani-pfp	$1.80 \times 10^{-7}$	14	$1.63 \times 10^{-7}$	-6.1
Ani- Fmoc	$3.02 \times 10^{-7}$	22	$3.1 \times 10^{-7}$	-6
Thio-pfp	$2.6 \times 10^{-7}$	22	$2.15 \times 10^{-7}$	-9
Thio-Fmoc	$1.8 \times 10^{-7}$	16	$1.9 \times 10^{-7}$	-5.5

**Table 8.1:** Mass, surface coverage and solvation changes between polymer films (during deposition and hydrolysis).

The functionalisation process was monitored using FTIR and QCM measurements to confirm immobilisation reaction between NTA and QCH receptors with poly(Py-COOH) and poly(Py-NH<sub>2</sub>), respectively, as shown in **Figure 8.2**. The mass of representative polymer film after functionalization was increased by 10.6  $\mu\text{g}$  based on QCM data and surface coverage equal to  $9.87 \times 10^{-8} \text{ mol cm}^{-2}$  based on Faraday law. While, the mass of (Py-HQC) increased by 10.85  $\mu\text{g cm}^{-2}$  and surface coverage equal to  $1.07 \times 10^{-7} \text{ mol cm}^{-2}$ . These results showed that the functionalisation percentage was equal to 77% and 87% for py-pfp and py-Fmoc, respectively. This expected increase in mass film is a result of ingress the receptor NTA and HQC groups into polymer film. Voltammetric measurements for all patterned polymer surfaces confirmed that electrochemical activity (conductivity) would enable them to be used in sensing applications.

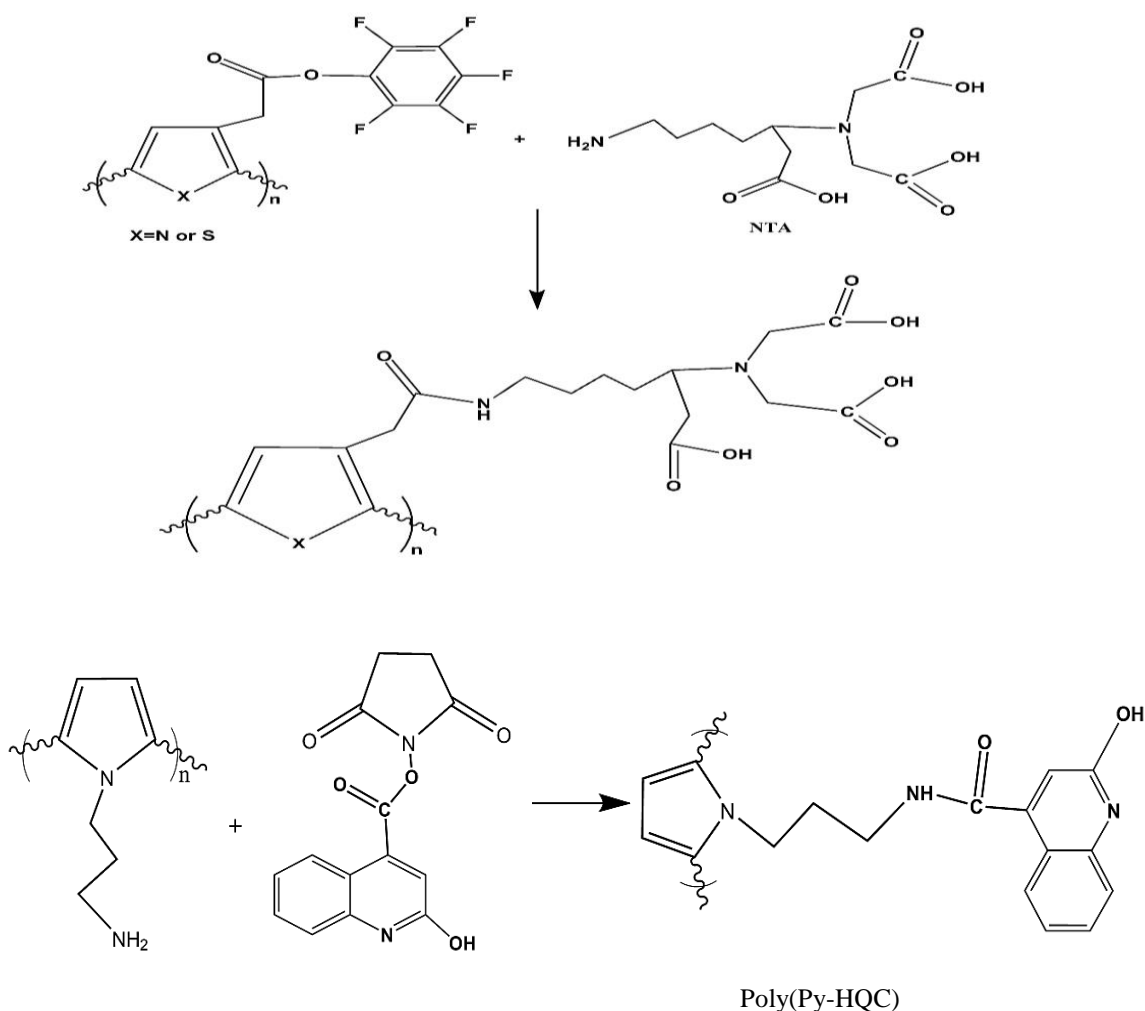


**Figure 8.2:** Reaction scheme illustrating the reaction of receptors (NTA and HQC) with the activated ester within polymer films.

### 8.1.2 Functionalised polyaniline films

Functionalised polyaniline films were synthesised electrochemically using potentiodynamic and potentiostatic methods. Cyclic voltammograms show that there is a difference in oxidation potential between Ani-COOH and un-substituted aniline due to an electronic effect on the aniline cyclic system. This difference is due to the presence of electron withdrawing groups in the structure of the monomer (see **Figure 8.1**). This difference in oxidation potential was also present in the cyclic voltammograms for other monomers (Ani-pfp and Ani-Fmoc) because of the presence of pfp and Fmoc groups.<sup>9-11</sup> Furthermore, chronoamperometric measurements show that the electropolymerisation charge increased with  $t^{1/2}$  as result of a diffusion-controlled process. Data from EQCM experiments were used to estimate the mass change during electropolymerisation process. The  $(\Delta m/\Delta q)$  data can be used to estimate  $M_{app}$  (which is equivalent mass of matter associated with one mole of monomer and any associated anions and solvent) with of species involved in the polymerisation process. The  $M_{app}$  of these species was equal to  $160 \text{ g mol}^{-1}$ ,  $146 \text{ g mol}^{-1}$ ,  $308 \text{ g mol}^{-1}$  and  $320 \text{ g mol}^{-1}$  for Ani-COOH, Ani-NH<sub>2</sub>, Ani-pfp and Ani-Fmoc, respectively. These values were close to molar mass of monomers ( $165 \text{ g mol}^{-1}$ ,  $122 \text{ g mol}^{-1}$ ,  $331 \text{ g mol}^{-1}$  and  $344 \text{ g mol}^{-1}$ ) for Ani-COOH, Ani-NH<sub>2</sub>, Ani-pfp and Ani-Fmoc, respectively. This indicates that the polymer films have very little solvent within chains.

Poly(Ani-pfp) and poly(Ani-Fmoc) films were hydrolysed using 0.1 M NaOH and 30% piperidine solutions, respectively. FTIR and QCM measurements results confirm that the carbonyl groups of the ester and amide functionalisation were hydrolysed completely. The voltammetric data for representative polymer film were used to estimate surface coverage to be  $1.8 \times 10^{-7} \text{ mol cm}^{-2}$  and mass change of hydrolysis was equal to  $-6.1 \text{ } \mu\text{g}$  for poly(Ani-pfp). While the electroactive site coverage of poly(Ani-Fmoc) was equal to  $3.02 \times 10^{-7}$  and mass change of hydrolysis was  $-6 \text{ } \mu\text{g}$  based on QCM data as shown in Table 8.1. Naturally, hydrolysis process led to decrease of polymer mass because of losing pfp and Fmoc groups from polymer film and this lead to creating voids over the film. Solvent molecules ingress into polymer to fill these voids and solvation changes were equal to 15% and 30% for Ani-pfp and Ani-Fmoc, respectively.

The immobilisation process was monitored using IR and QCM measurements to confirm the functionalisation reaction between NTA and QCH receptors and representative poly(Ani-COOH) and poly(Ani-NH<sub>2</sub>) respectively. Furthermore, the mass of the

representative polymer films were calculated depending of QCM technique. Voltammetric result showed that the surface coverage equal to  $1.5 \times 10^{-7} \text{ mol cm}^{-2}$  and  $3.05 \times 10^{-7}$  for poly (Ani-NTA) and poly (Ani-HQC) respectively based on Faraday law. QCM data demonstrated that the mass increased by  $7.3 \mu\text{g}$  and  $4.4 \mu\text{g}$  for poly (Ani-NTA) and poly (Ani-HQC) respectively. The functionalisation percentage estimated to be 77% and 53% for poly (Ani-NTA) and poly (Ani-HQC) respectively.

### 8.1.3 Functionalised polythiophene films

Polythiophene films were prepared successfully by electrochemical techniques. Cyclic voltammograms of (3-TAA) showed that the oxidation potential of monomer was higher than that for thiophene monomer,<sup>12</sup> because of electronic density and steric effects of substituent groups in the  $\beta$  position, as shown in **Figure 8.1**. However, electrodeposition of 3-thiopheneethylamine monomer (Thio-NH<sub>2</sub>) was not successful. For the same reason, cyclic voltammograms Thio-pfp and Thio- Fmoc showed that the oxidation potential of functionalised monomers was higher than potential oxidation of thiophene. All of these films showed shifting in oxidation peaks attributed to existence of pfp and Fmoc groups, which affect the electronic properties of monomers.<sup>13</sup> Chronoamperometric curves show that the electropolymerisation process was diffusion-controlled. EQCM measurements were used to study of polymer films and calculate the gradient ( $\Delta m/\Delta q$ ) using Faraday's law.  $M_{app}$  was equal to  $144 \text{ g mol}^{-1}$ ,  $367 \text{ g mol}^{-1}$  and  $364 \text{ g mol}^{-1}$  for thio-COOH, thio-pfp and thio-Fmoc, respectively. These values were close to molar mass of monomers  $142 \text{ g mol}^{-1}$ ,  $308 \text{ g mol}^{-1}$  and  $349 \text{ g mol}^{-1}$  respectively. These values indicate that in the reduced state (which contains no anions) monomer and associated only a small amount of solvent involved in polymerisation process.

Voltammetric measurements were used to calculate the mass and surface coverage of representative polymer films before and after hydrolysis using Faraday's law as shown in **Table 8.1**. The voltammetric data were used to estimate surface coverage to be  $2.6 \times 10^{-7} \text{ mol cm}^{-2}$  and mass change of hydrolysis was equal to  $-9 \mu\text{g}$  for poly(Thio-pfp ). While the surface coverage of poly(Thio-Fmoc) was equal to  $1.8 \times 10^{-7}$  and mass change of hydrolysis was  $-5.5 \mu\text{g}$  based on QCM data as shown in **Table 8.1**. Solvation changes was equal to 16% and 25% for poly(Thio-pfp) and poly(Thio-Fmoc) films, respectively. These values refer to engress some of solvent molecules into films instead of pfp and Fmoc groups that left the polymer films.

The functionalisation process was monitored using IR and QCM measurements to confirm the functionalisation reaction between NTA and QCH receptors and poly(3-TAA) and poly(Thio-NH<sub>2</sub>), respectively. Surface coverage of representative films above calculated using Faraday's law to be  $2.16 \times 10^{-7}$  mol cm<sup>-2</sup> and  $1.95 \times 10^{-7}$  for poly (Thio-NTA) and poly (Thio-HQC), respectively. QCM data demonstrated that the mass increased by 4.9 µg and 4.8 µg for poly (Thio-NTA) and poly (Thio-HQC) respectively. The functionalisation percentage estimated to be 53% and 79% for poly (Thio -NTA) and poly (Thio-HQC), respectively. The electrochemical voltammetric results showed that all patterned electrodes have electrochemical activity, enabling them to be used as electrochemical sensors.

#### 8.1.4 Application of patterned electrode as chemical sensor

All patterned polymer electrodes were tested as electrochemical sensors for detection of copper, nickel and cobalt ions in aqueous solutions. Voltammetric responses for modified polymer surfaces exposed to metal ions were examined as function of scan rate, repetitive cycling, and metal ion concentration. The patterned poly(Py-NTA) electrodes were examined using potentiodynamic measurements as a qualitative tool. This study involved the use of different concentrations of metal ions (1 ppm to 5000 ppm) and use electrochemical monitoring to study the recognition efficiency for metal ions. The metal binding to the films was determined by integration of anodic and cathodic charges. The stability of the cyclic voltammograms was obtained at different scan rates, from 10 to 100 mV s<sup>-1</sup>. Using the same the procedures with Py-NTA, the relation between the peak redox current and metal ion concentration was studied.

Surface coverage of metal ions ( $\Gamma$ ) was estimated by integration of reduction peaks by using Faraday's laws. These findings show that formed modified patterned electrodes have molar ratio less than or equal to 1. This can be attributed in part to incomplete functionalisation and, most probably, incomplete access to receptor sites in the films interior.

Freundlich, Frumkin, Temkin and Langmuir models were applied to select which isotherm best represented progress quantitatively. The voltammetric responses showed that the Frumkin isotherm offered the best fitting for all of metal ions with polymer electrodes. It can be concluded from these results that there are interactions occurred between sites on the heterogeneous surface, as considered in the Frumkin and Freundlich

models. The Langmuir model was least useful model, because it assumes there is a monolayer surface without interactions. The thermodynamics of adsorption was provided useful evidences about the nature of adsorption process. Where the negative value of  $\Delta G^\circ$  indicated that the adsorption was spontaneous process and happened via chemical adsorption.

Patterned poly(Ani-NTA) and poly(Ani-HQC) electrodes were studied using the same procedures and experimental conditions as for the pyrrole electrodes. Characteristic parameters  $n$  and  $x$  were calculated for each metal ion, depending on Freundlich and Temkin isotherms. Stability, scan rates and relation between concentration of metal ions and surface coverage ( $\Gamma$ ) were studied depending on voltammetric results.

Poly(Thio-NTA) and poly(Thio-HQC) electrodes were investigated using the same the procedures and experimental conditions described above with patterned pyrrole and aniline. Stability, scan rates, and concentration effects were studied depending on voltammetric results. Isotherm models result was shown that Frumkin isotherm offered the best fitting with Poly(Thio-NTA) electrode while Freundlich model offered the best fitting with poly(Thio-HQC). Characteristic parameters  $n$  and  $x$  were calculated for each metal ion, depending on Freundlich and Temkin isotherms.

## 8.2 Future work

This project has showed that patterned modified polymer electrodes with NTA and HQC receptor groups are promising devices to be used as electrochemical sensors for detecting some metal ions in aqueous solutions. Therefore, it is recommended that further research be undertaken in the following areas:

Patterned electrodes can used to detect metal ions with various values of the pH for metal ion solutions with different analytical procedures and to study effect of pH on electrodes at room temperature to obtain optimal conditions for sensor devices performance and to determine sensitivity and selectivity of the chemical sensor with different values of pH. Future study can be aimed to use other metal ions in such Fe(III), Cr(III), Cd(II), Zn(II), Pb(II) and As(III) in aqueous solutions<sup>14</sup> using the same patterned modified polymer electrodes or using other conducting polymers like poly(3,4-ethylenedioxythiophene) and poly(aminophenol) or use a copolymerisation strategy to create polymer films with interesting properties.<sup>15-19</sup> In addition, the same receptor units in this study or use other

chelating groups such as EDTA (Ethylenediaminetetraacetic acid) ( which could be used to make a selective sensor device but could not be regenerated), NOTA (1,4,7-triazacyclononane-1,4,7-trisacetic acid), DOTA (1,4,7,10-tetraazacyclododecane-1,4,7,10-tetraacetic acid), EGTA (ethyleneglycol-bis(2-aminoethylether)-N,N,N'N'-tetraacetic acid),<sup>20</sup> dimethylglyoxime (DGM)<sup>21</sup> and Schiff bases<sup>22</sup> which contain various free terminal functional groups and examine the capability of these electrodes as electrochemical sensors. Nanomaterials such as carbon nanotubes, fullerenes and graphene,<sup>23, 24</sup> which have many outstanding electric properties can be used with polymer films to enhance the performance of sensor devices and detection limit by increasing the electrode surface area, electrical conductivity and connectivity.<sup>20, 25, 26</sup>

Patterning of functionalised surfaces could be accomplished by photolithography or electron beam lithography techniques to develop polymer film surfaces that can promote a specific chemical response during examination. Various photoresists such as negative type like *SU-8 2000* or positive type like SPR- 220 and S1813 could be used. Detection measurements could involve a series of electrochemical techniques such as cyclic voltammetry,<sup>27</sup> square-wave voltammetry (SWV)<sup>16</sup> anodic stripping voltmmetry (ASV)<sup>28</sup> and electrochemical impedance spectroscopy (EIS)<sup>20</sup> and EQCM experiments.<sup>29</sup> Non-electrochemical techniques can be applied to assess aspects of film reactivity and structure. Morphology techniques such as 3D optical microscopy, SEM and AFM can be used to examine the surfaces. Neutron reflectivity could be used to determine the spatial profiles of polymer component and precise solvation levels. FTIR spectroscopy can be used to monitor the chemical structure of polymer films before, during and after functionalisation.

### 8.3 References

1. G. Stienen, *Applications of Electroactive Polymers*, Springer Netherlands 2012.
2. J. R. Lancaster, J. Jehani, G. T. Carroll, Y. Chen, N. J. Turro and J. T. Koberstein, *Chemistry of Materials*, 2008, **20**, 6583-6585.
3. G. T. Carroll, N. J. Turro and J. T. Koberstein, *Journal of Colloid and Interface Science*, 2010, **351**, 556-560.
4. K. K. Gleason, *CVD Polymers: Fabrication of Organic Surfaces and Devices*, Wiley, 2015.
5. A. Glidle, C. S. Hadyoon, N. Gadegaard, J. M. Cooper, A. R. Hillman, R. W. Wilson, K. S. Ryder, J. R. P. Webster and R. Cubitt, *The Journal of Physical Chemistry B*, 2005, **109**, 14335-14343.
6. R. M. Sapstead, K. S. Ryder, C. Fullarton, M. Skoda, R. M. Dalgliesh, E. B. Watkins, C. Beebee, R. Barker, A. Glidle and A. R. Hillman, *Faraday Discussions*, 2013, **164**, 391-410.
7. A. Mirmohseni, M. Milani, and V. Hassanzadeh, *Polymer International*, 1999, **48**, 873-878.
8. R. Waltman, A. Diaz, J. Bargon, *The Journal of Physical Chemistry*, 1984, **88**, 4343
9. S. Cui and S. Park, *Synthetic Metals*, 1999, **105**, 91-98.
10. C. Thiemann and C. M. A. Brett, *Synthetic Metals*, 2001, **123**, 1-9.
11. H. Sarker, Y. Gofer, J. Killian, T. Poehler and P. Searson, *Synthetic Metals*, 1998, **97**, 1-6.
12. P. S. Tóth, C. Janáky, Z. Hiezl and C. Visy, *Electrochimica Acta*, 2011, **56**, 3447-3453.
13. J. Roncali, *Chemical Reviews*, 1992, **92**, 711-738.
14. M. B. Gumpu, S. Sethuraman, U. M. Krishnan and J. Rayappan, *Sensors and Actuators B: Chemical*, 2015, **213**, 515-533.
15. M. A. Deshmukh, M. Gicevicius, A. Ramanaviciene, M. D. Shirsat, R. Viter and A. Ramanavicius, *Sensors and Actuators B: Chemical*, 2017, **248**, 527-535.
16. N. Thinakaran, S. E. Subramani, T. Priya, N. Dhanalakshmi, T. V. Vineesh and V. Kathikeyan, *Electroanalysis*, 2017, **29**, 1903-1910.
17. M. F. Philips, A. I. Gopalan and K.-P. Lee, *Journal of Hazardous Materials*, 2012, **237-238**, 46-54.
18. V. Somerset, J. Leaner, R. Mason, E. Iwuoha and A. Morrin, *International Journal of Environmental Analytical Chemistry*, 2010, **90**, 671-685.
19. N. Wang, H. Dai, D. Wang, H. Ma and M. Lin, *Materials Science and Engineering: C*, 2017, **76**, 139-143.
20. M. A. Deshmukh, R. Celiesiute, A. Ramanaviciene, M. D. Shirsat and A. Ramanavicius, *Electrochimica Acta*, 2018, **259**, 930-938.
21. K. Pokpas, N. Jahed, P. G. Baker and E. I. Iwuoha, *Sensors*, 2017, **17**, 1711.
22. S. Rana, S. K. Mittal, N. Singh, J. Singh and C. E. Banks, *Sensors and Actuators B: Chemical*, 2017, **239**, 17-27.
23. L. Cui, J. Wu and H. Ju, *Biosensors and Bioelectronics*, 2015, **63**, 276-286.
24. L. R. Pokhrel, N. Ettore, Z. L. Jacobs, A. Zarr, M. H. Weir, P. R. Scheuerman, S. R. Kanel and B. Dubey, *Science of The Total Environment*, 2017, **574**, 1379-1388.
25. H. Liu, L. Weng and C. Yang, *Microchimica Acta*, 2017, **184**, 1267-1283.
26. C. Zhu, G. Yang, H. Li, D. Du and Y. Lin, *Analytical Chemistry*, 2015, **87**, 230-249.
27. Y. Lu, X. Liang, C. Niyungeko, J. Zhou, J. Xu and G. Tian, *Talanta*, 2018, **178**, 324-338.
28. R. Manikandan and S. Sriman Narayanan, *Electroanalysis*, 2017, **29**, 609-615.
29. T. Neubert, F. Rösicke, G. Sun, S. Janietz, M. Gluba, K. Hinrichs, N. Nickel and J. Rappich, *Applied Surface Science*, 2017, **421**, 755-760.